C–H-Bond Activation
by
Rare-Earth-Metallocene Compounds

Dissertation

der Mathematisch-Naturwissenschaftlichen Fakultät

der Eberhard Karls Universität Tübingen

zur Erlangung des Grades eines

Doktors der Naturwissenschaften

(Dr. rer. nat.)

vorgelegt von

Dipl.-Chem. Martin Bonath

aus Wolfach

Tübingen

2021

Gedruckt mit Genehmigung der Mathematisch-Naturwissenschaftlichen Fakultät der Eberhard Karsl Universität Tübingen.

Tag der mündlichen Qualifikation:	22.12.2021
Dekan:	Prof. Dr. Thilo Stehle
1. Berichterstatter:	Prof. Dr. Reiner Anwander
2. Berichterstatter:	Prof. Dr. Lars Wesemann
3. Berichterstatter:	Prof. Dr. Rüdiger Beckhaus

C–H-Bond Activation

by

Rare-Earth-Metallocene Compounds

Martin Bonath

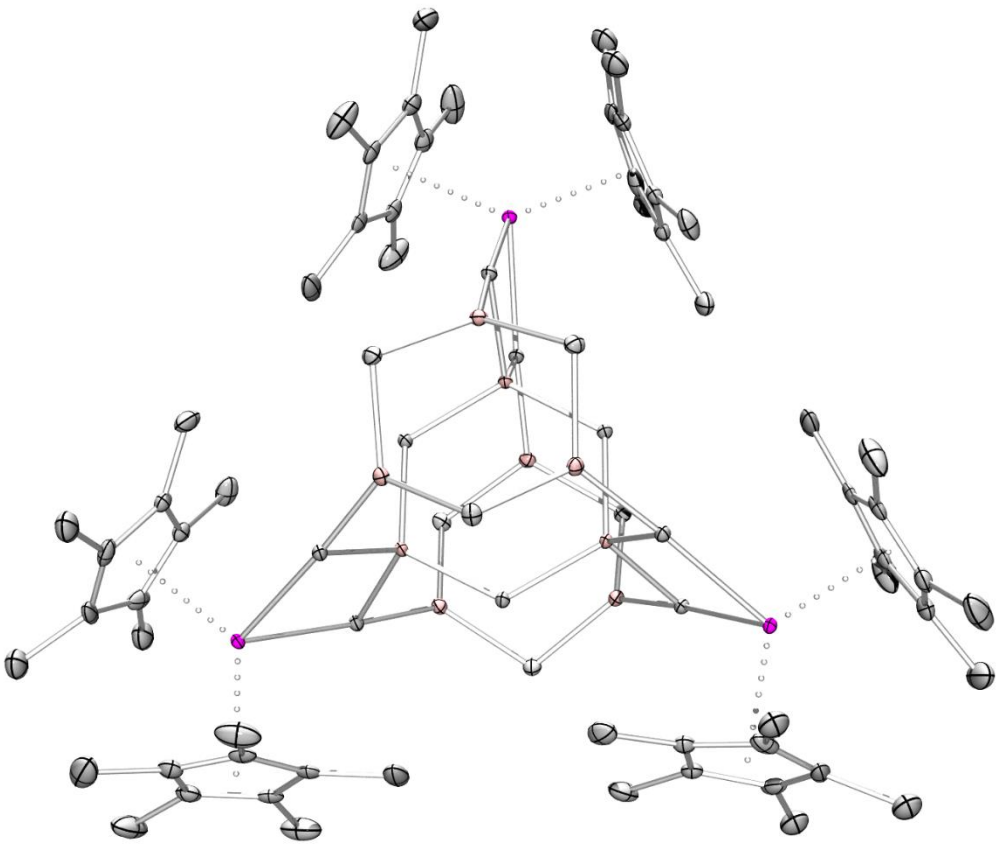

Preface

The following thesis consists of a survey on σ-bond-metathesis reactions of rare-earth-metallocene compounds, a summary of the main results, one manuscript, and four scientific papers. The work has been carried out at the Institut für Anorganische Chemie of the Eberhard Karls Universität Tübingen, Germany, over the period October 2014 to September 2018 under the supervision of Prof. Dr. Reiner Anwander.

Parts of this thesis have been presented at international and national conferences and meetings as oral and poster contributions.

Wem sonst als dir

Meiner lieben Frau Olga gewidmet

Acknowledgements

First, I want to express my deep gratitude to my supervisor Prof. Dr. Reiner Anwander for the confidence he put in me by offering me the great opportunity to join his research group and providing me with the interesting research topic for this thesis. In particular I am thankful for the opportunity to present some of my work at the 253rd ACS conference in San Francisco.

I wish to thank Dr. Peter Sirsch for performing the DFT calculations and the jovial discussions concerning chemistry and non-chemistry topics.

Special thanks also go to Dr. Cäcilia Maichle-Mössmer, for all the efforts she put in crystal picking, mounting and structural model refinement in the course of this thesis.

Special thanks go to Dr. Dorothea Schädle for all the support as glovebox colleague and for proofreading my publications and this thesis.

Moreover, I thank Dr. Klaus Eichele and Kristina Strohmaier for providing help with all aspects related to NMR spectroscopy. My thanks also go to Wolfgang Bock for measuring the elemental analysis, to Tobias Wolf for help and support with any technical issues and especially Elke Niquet for picking and mounting numerous of my crystals and her unresting efforts to provide a tidy and well-equipped lab stock.

I also would like to thank all the coworkers of the Anwander Group during my PhD work, Dr. Nicole Dettenrieder, Dr. Sonja König, Dr. Christoph Hollfelder, Dr. Tatiana Spallek, Dr. Jochen Friedrich, Dr. Daniel Werner, Dr. Lars Jende, Dr. Dominic Diether, Dr. Verena Birkelbach, Dr. Lorenz Bock, Dr. Uwe Bayer, Andrea Sonström, Dr. Leilei Luo, Dr. Ning Yuan, Dr. Yucang Liang, Denis Buschmann, Markus Katzenmayer, Georgios Spiridopoulos, Alexandros Mortis and Simon Trzmiel for all the joyful moments and helpful discussions. In happy memory I keep all members of the ‘Kommandozentrale’, Dr. Renita Thim, Damir Barisic, Dr. David Schneider and Dr. Christoph Stuhl. As well, I want to thank Dr. Benjamin Wolf for all the helpful and entertaining discussions and the great time during our stay in California.

Meine tiefste Dankbarkeit gilt jedoch meiner Familie, meinen Geschwistern Konrad und Franziska und insbesondere meinen Eltern, die mich über all die Jahre während des Studiums immer unterstützt haben und mir durch ihr Vertrauen und ihre Zuversicht auch in schwierigen Zeiten einen festen Rückhalt gegeben haben.

Olga, Moritz und Helena, eure Liebe und Lebensfreude erfüllt mich jeden Tag. So wart ihr mir immer wieder aufs Neue meine Motivation um diese Arbeit abzuschließen.

Contents

Abbreviations

Ar	aryl	EXSY	exchange spectroscopy
av	average	HMBC	heteronuclear multiple bond correlation
*t*Bu	*tert*-butyl	HSQC	heteronuclear single quantum coherence
cat.	catalytically	Ln	rare-earth metal (Sc, Y, La - Lu)
COSY	correlated spectroscopy	M	metal
Cp	cyclopentadienyl	*m*-	*meta*-
Cp*	1,2,3,4,5-pentamethylcyclo-pentdienyl	Me	methyl
CP/MAS	cross polarization/magic angel spinning	NMR	nuclear magnetic resonance spectroscopy
DEPT	distortionless enhancement by polarization transfer	*o*-	*ortho*-
DFT	density functional theory	*p*-	*para*-
Dipp	2,6-diisopropylphenyl	Ph	phenyl
DMAP	4-dimethylaminopyridine	ppm	parts per million
do	donor ligand	py	pyridine
DOSY	diffusion ordered spectroscopy	r.t.	ambient (room) temperature
DRIFT	diffuse reflectance infrared fourier transform spectroscopy	THF	tetrahydrofuran
eqiv	equivalent	$Tp^{tBu,Me}$	hydrotris(3-*tert*-butyl-5-methyl-pyrazolyl)borate
Et	ethyl	VT	variable temperature

Abstract

The synthesis of complexes $[Cp^*_2LnMe]_x$ and the examination on the exceptional reactivity toward various substrates resulted in the development of σ-bond metathesis as the most important mechanism for C–H-bond activation by rare-earth-metal alkyl complexes. Ever since, complexes $[Cp^*_2LnMe]_x$ emerged as archetypical compounds for σ-bond-metathesis chemistry. However, owing to the high reactivity of these compounds, their synthesis is challenging and the reaction pathways hard to control. As such, it is of interest to develop synthesis strategies based on stabilized derivatives of $[Cp^*_2LnMe]_x$ such as $[Cp^*_2LnMe(do)]$ and $[Cp^*_2Ln(MMe_4)]$ (M = Al, Ga) to investigate into σ-bond metathesis reactions.

In a first approach, thermal treatment of $[Cp^*_2YMe(THF)]$ resulted in the activation of THF to afford $[Cp^*_2Y(OC_2H_3)(THF)]$ and the substituted tetrahydrofuranyl compound $[Cp^*_2Y(2\text{-}C_2H_2\text{-}OC_4H_7)]$. The attempted synthesis of elusive $[Cp^*_2LaMe(THF)]$ by donor induced aluminate cleavage of $[Cp^*_2La(AlMe_4)]$ resulted in formation of polymeric $[Cp^*_2La(AlMe_4)(THF)]_n$. This compound was found to be thermally labile cleanly converting into $AlMe_3$-stabilized tetrahydrofuranyl compound $[Cp^*_2La(2\text{-}AlMe_3\text{-}OC_4H_7)]$.

Thermal treatment of $[Cp^*_2Y(MMe_4)]$ (M = Al, Ga) in benzene solutions led to C–H-bond activation of benzene to afford complexes $[Cp^*_2Y(Me_2MPh_2)]$ and $[Cp^*_2Y(MPh_4)]$. The proposed mechanism involves thermally induced dissociation of MMe_3 to liberate highly reactive $[Cp^*_2YMe]$. In a similar vein, the sterically demanding boryl moiety $\{B(NDippCH)_2\}^-$ was implemented to promote dissociative aluminate cleavage. As a result, $[Cp^*_2YMe_3Al\{B(NDippCH)_2\}]$ activates benzene already at ambient temperatures affording $[Cp^*_2YMe_2AlPh\{B(NDippCH)_2\}]$ and $[Cp^*_2YPh_3Al\{B(NDippCH)_2\}]$.

This concept was successfully extended to the corresponding lutetium and lanthanum compounds $[Cp^*_2Ln(MMe_4)]$ (Ln = Lu, La). Accordingly, the sandwich complexes $[Cp^*_2Ln(MMe_4)]$ gave access to lanthanide-based C–H-bond activation chemistry covering the full range of ionic radii in the lanthanide series.

In a final approach, the reactivity of $[Cp^*_2Ln(GaMe_4)]$ (Ln = Lu, Y) toward an excess of $GaMe_3$ at elevated temperatures was explored. Interestingly, complexes $[Cp^*_2Ln(GaMe_4)]$ triggered the formation of molecular homoleptic gallium methylene $[Ga_8(CH_2)_{12}]$ from $GaMe_3$ via a cascade C–H-bond activation involving dodecametallic clusters $[Cp^*_6Ln_3Ga_9(CH_2)_{15}]$ as crucial intermediates.

Zusammenfassung

Die Synthese der Methyl-Komplexe $[Cp^*_2LnMe]_x$ und die daraus resultierende Erforschung ihrer herausragenden Reaktivität gegenüber einer Vielzahl von Substraten gemäß der σ-Bindungsmetathese als dem wichtigsten Reaktionsmechanismus zur C–H-Bindungsaktivierung ist ein Meilenstein in der Organometallchemie der Lanthanoide. Seitdem gelten die Alkyle $[Cp^*_2LnMe]_x$ als archetypische Verbindungen für die Chemie der σ-Bindungsmetathese. Aufgrund der hohen Reaktivität dieser Verbindungen ist die Synthese jedoch anspruchsvoll und involvierte Reaktionsprozesse schwer zu kontrollieren. Daher ist es von Interesse Synthesestrategien ausgehend von stabilisierten Derivaten wie $[Cp^*_2LnMe(do)]$ und $[Cp^*_2Ln(MMe_4)]$ zu entwickeln um Reaktionen basierend auf σ-Bindungsmetathese näher zu untersuchen.

In einem ersten Ansatz resultierte aus der thermischen Behandlung von $[Cp^*_2YMe(THF)]$ eine Aktivierung des THF-Moleküls unter Ausbildung von $[Cp^*_2Y(OC_2H_3)(THF)]$ sowie der substituierten Tetrahydrofuranylverbindung $[Cp^*_2Y(2\text{-}C_2H_2\text{-}OC_4H_7)]$. Bestrebungen, ausgehend von $[Cp^*_2La(AlMe_4)]$, durch donorinduzierte Aluminatspaltung die bislang unbekannte Verbindung $[Cp^*_2LaMe(THF)]$ zu erhalten führten zur Bildung von polymerem $[Cp^*_2La(AlMe_4)(THF)]_n$. Diese Verbindung erwies sich als thermisch labil und reagierte zur $AlMe_3$-stabilisierten Tetrahydrofuranylverbindung $[Cp^*_2La(2\text{-}AlMe_3\text{-}OC_4H_7)]$.

Durch anhaltendes Erwärmen einer Lösung von $[Cp^*_2Y(MMe_4)]$ (M = Al, Ga) in Benzol führte die Aktivierung des Aromaten zur Bildung von $[Cp^*_2Y(Me_2MPh_2)]$ und $[Cp^*_2Y(MPh_4)]$. Der vermutete Reaktionsmechanismus wird durch thermisch-induzierte Dissoziation von MMe_3 eingeleitet was die Freisetzung des hochreaktiven $[Cp^*_2YMe]$ zur Folge hat. Diesem Gedanken folgend wurde die sterisch anspruchsvolle Borylgruppe $\{B(NDippCH)_2\}^-$ eingeführt um eine dissoziative Aluminatspaltung zu begünstigen. Dies hatte zum Ergebnis, dass $[Cp^*_2YMe_3Al\{B(NDippCH)_2\}]$ bereits bei Umgebungstemperatur Benzol aktiviert und dabei die Heteroaluminate $Cp^*_2YMe_2AlPh\{B(NDippCH)_2\}]$ und $[Cp^*_2YPh_3Al\{B(NDippCH)_2\}]$ gebildet werden.

Dieses Konzept wurde erfolgreich auf die entsprechenden Lutetium- und Lanthan-Verbindungen $[Cp^*_2Ln(MMe_4)]$ (Ln = Lu, La) übertragen. Somit ermöglichen die Sandwich-Verbindungen $[Cp^*_2Ln(MMe_4)]$ Zugang zu einer Lanthanoid-basierten C–H-Bindungsaktivierungschemie über die komplette Reihe der Seltenerdmetalle.

In einem weiteren Ansatz wurde die Reaktivität von [Cp*$_2$Ln(GaMe$_4$)] (Ln = Lu, Y) gegenüber einem Überschuss an GaMe$_3$ bei höheren Temperaturen untersucht. Als Ergebnis zeigte sich, dass Komplexe des Typs [Cp*$_2$Ln(GaMe$_4$)] die Bildung von molekularem, homoleptischem Galliummethylen [Ga$_8$(CH$_2$)$_{12}$] ausgehend von GaMe$_3$ über eine Kaskade von C–H-Bindungsaktivierungen bewirken. Dabei sind die dodekametallischen Cluster [Cp*$_6$Ln$_3$Ga$_9$(CH$_2$)$_{15}$] die entscheidenden Zwischenstufen.

Publications

Publications incorporated into this thesis

Paper I C–H-Bond Activation and Isoprene Polymerization by Lutetium Alkylaluminate/gallate Complexes Bearing a Peripheral Boryl and a Bulky Hydrotris(pyrazolyl)borate Ligand
M. Bonath, C. O. Hollfelder, D. Schädle, C. Maichle-Mössmer, P. Sirsch, R. Anwander
Eur. J. Inorg. Chem. **2017**, 4683-4692.

Paper II Gallium Methylene
M. Bonath, C. Maichle-Mössmer, P. Sirsch, R. Anwander
Angew. Chem. **2019**, *131*, 8290-8294.
Angew. Chem. Int. Ed. **2019**, *58*, 8206-8210.

Paper III Rare-Earth-Metallocene Alkylaluminates Trigger Distinct Tetrahydrofuran Activation
M. Bonath, V. M. Birkelbach, C. Stuhl, C. Maichle-Mössmer, R. Anwander
Chem. Commun. **2021***, 57,* 7918-7921.

Paper IV The Alkylaluminate/gallate Trap: Metalation of Benzene by Heterobimetallic Yttrocene Complexes [Cp*$_2$Y(MMe$_3$R)] (M = Al, Ga)
M. Bonath, D. Schädle, C. Maichle-Mössmer, R. Anwander
Inorg. Chem. **2021**, *60*, 14952−14968.

Paper V [Cp*Y{C$_5$Me$_4$(μ-CH$_2$)MPh$_3$}] (M = Al, Ga): Group 13-Assisted Metalation of Permethylyttrocene
M. Bonath, C. Maichle-Mössmer, R. Anwander
Manuscript

Publications with minor contributions

Paper VI Pentamethylcyclopentadienyl-Supported Rare-Earth-Metal Benzyl, Amide, and Imide Complexes
R. Thim, H. M. Dietrich, M. Bonath, C. Maichle-Mössmer, R. Anwander
Organometallics **2018**, *37*, 2769-2777.

Oral and poster presentations

Metalation of C–H bonds by $Cp^*_2Y(\mu\text{-}Me)_2MMe_2$ (M = Al, Ga)
253rd American Chemical Society National Meeting and Exposition, San Francisco, USA, *April 2-6*, **2017**.
Oral Presentation

Metallierung von C–H-Bindungen durch Yttrocenderivate $Cp^*_2Y(\mu\text{-}Me)_2MMe_2$ (M = Al, Ga)
Inorganic Chemistry Colloquium, University of Tübingen, Tübingen, Germany, *June 26*, **2017**.
Oral Presentation

C–H-Bond Activation by Lutetium Alkylaluminate/gallate Complexes Bearing a Peripheral Boryl and a Bulky Hydrotris(pyrazolyl)borato Ligand
M. Bonath, C. Maichle-Mössmer, R. Anwander
XXVIII. Tage der Seltenen Erden, Tübingen, Germany, *October 4-6*, **2017**.
Poster Presentation

Personal Contribution

Paper I: C–H-Bond Activation and Isoprene Polymerization by Lutetium Alkylaluminate/gallate Complexes Bearing a Peripheral Boryl and a Bulky Hydrotris(pyrazolyl)borate Ligand

All reactions and analyses described as well as paper writing, were conducted by the candidate and C. O. Hollfelder. Analyses include 1D NMR (^{1}H, VT ^{1}H, ^{13}C{^{1}H}, ^{11}B{^{1}H}) and 2D NMR spectroscopy (^{1}H-^{1}H COSY, ^{1}H-^{1}H EXSY, ^{1}H-^{13}C HSQC, ^{1}H-^{13}C HMBC) and DRIFT spectroscopy. Therein, C. O. Hollfelder performed the polymerizations including data acquisition and writing of the corresponding chapter. Interpretation of ^{1}H NMR spectroscopic data concerning the activation scenario of [(Tp$^{t\mathrm{Bu,Me}}$)Lu(Me)(AlMe$_3${B(NDippCH)$_2$})] and [(Tp$^{(t\mathrm{Bu\text{-}H})_2/t\mathrm{Bu,Me}}$)Lu(AlMe$_2${B(NDippCH)$_2$})] with cocatalyst [PhNMe$_2$H][B(C$_6$F$_5$)$_4$] was done by the candidate.

Dr. Peter Sirsch performed the DFT calculations, interpretation of the data and writing of the corresponding chapter.

Elemental analyses were performed by Wolfgang Bock. The structural analyses by single crystal X-ray diffraction were performed by Dr Cäcilia Maichle-Mössmer.

Paper II: Gallium Methylene

All reactions and analyses described were conducted by the candidate. Analyses include 1D NMR (^{1}H, VT ^{1}H, ^{13}C{^{1}H}, ^{13}C{^{1}H} DEPT135) and 2D NMR spectroscopy (^{1}H-^{1}H COSY, ^{1}H-^{13}C HSQC) and DRIFT spectroscopy. Paper writing was done by the candidate and Dr. Reiner Anwander.

Dr. Peter Sirsch performed the DFT calculations, interpretation of the data and writing of the corresponding chapter.

Dr. Klaus Eichele supported us in setting up the ^{1}H DOSY NMR experiment. Kristina Strohmaier performed the ^{13}C CP/MAS NMR experiments. Elemental analyses were performed by Wolfgang Bock. The structural analyses by single crystal X-ray diffraction were performed by Dr Cäcilia Maichle-Mössmer.

Paper III: Rare-Earth-Metallocene Alkylaluminates Trigger Distinct Tetrahydrofuran Activation

All reactions and analyses described were conducted by the candidate. Analyses include 1D NMR (^{1}H, ^{13}C{^{1}H}) and 2D NMR spectroscopy (^{1}H-^{1}H COSY, ^{1}H-^{13}C HSQC) and DRIFT spectroscopy. Paper writing was done by the candidate.

Dr. Verena M. Birkelbach provided crystals of $[Cp^*_2La(AlMe_4)(THF)]_n$ suitable for X-ray diffraction analysis. Dr. Christoph Stuhl performed X-ray diffraction determination for $[Cp^*_2La(AlMe_4)(THF)]_n$. Further structural analyses by single crystal X-ray diffraction were performed by Dr Cäcilia Maichle-Mössmer. Elemental analyses were performed by Wolfgang Bock.

Paper IV: The Alkylaluminate/gallate Trap: Metalation of Benzene by Heterobimetallic Yttrocene Complexes $[Cp^*_2Y(MMe_3R)]$ (M = Al, Ga)

All reactions and analyses described were conducted by the candidate. Analyses include 1D NMR (^{1}H, ^{2}H, VT ^{1}H, ^{13}C{^{1}H}, ^{11}B{^{1}H}) and 2D NMR spectroscopy (^{1}H-^{1}H COSY, ^{1}H-^{13}C HSQC, ^{1}H-^{13}C HMBC) and DRIFT spectroscopy. Paper writing was done by the candidate.

Dr. Dorothea Schädle performed ^{1}H-^{89}Y HSQC spectroscopy.

Elemental analyses were performed by Wolfgang Bock. The structural analyses by single crystal X-ray diffraction were performed by Dr Cäcilia Maichle-Mössmer.

Paper V: $[Cp^*Y\{C_5Me_4(\mu\text{-}CH_2)MPh_3\}]$ (M = Al, Ga): Group 13-Assisted Metalation of Permethylyttrocene

All reactions and analyses described were conducted by the candidate. Analyses include 1D NMR (^{1}H, ^{13}C{^{1}H}) and 2D NMR spectroscopy (^{1}H-^{13}C HSQC, ^{1}H-^{13}C HMBC) and DRIFT spectroscopy. Paper writing was done by the candidate.

Elemental analyses were performed by Wolfgang Bock. The structural analyses by single crystal X-ray diffraction were performed by Dr Cäcilia Maichle-Mössmer.

Paper VI: Pentamethylcyclopentadienyl-Supported Rare-Earth-Metal Benzyl, Amide, and Imide Complexes

The synthesis procedure for $[Cp^*Y(CH_2Ph)_2(THF)]$ and starting material of $[Cp^*Y(CH_2Ph)_2(THF)]$ was provided by the candidate.

The synthesis of $[Cp^*LnI_2(THF)]_x$ was planned by Dr. H. Martin Dietrich. All further reactions and analyses described were planned and conducted by Dr. Renita Thim. Elemental analyses were performed by Wolfgang Bock. The structural analyses by single crystal X-ray diffraction were performed by Dr Cäcilia Maichle-Mössmer.

Objective of the Thesis

The activation of C–H bonds by donor or Lewis-acid stabilized derivatives of highly reactive methyl complexes [Cp*$_2$LnMe] is in the focus of this thesis. The synthesis of well-established compounds, e. g. [Cp*$_2$Ln(MMe$_4$)] (Ln = Y, Lu, La; M = Al, Ga) and [Cp*$_2$YMe(THF)], and new complexes [Cp*$_2$LnMe$_3$Al{B(NDippCH)$_2$}] (Ln = Y, Lu) and [Cp*$_2$La(AlMe$_4$)(THF)]$_n$ were optimized and the feasibility for σ-bond metathesis of THF, arenes and GaMe$_3$ was examined.

Chapter A of this thesis gives a brief survey on metallocene-based σ-bond metathesis in rare-earth-metal chemistry. The main emphasis is put on synthesis protocols for rare-earth-metallocene compounds [Cp*$_2$LnR] (R = Me, Et, Ph, CH(SiMe$_3$)$_2$, CH$_2$CMe$_3$, H) capable to perform σ-bond metathesis and an overview on their reactivity toward different substrates is given. Moreover, catalytic applications are described and rapid progress can be anticipated.

Chapter B summarizes the main results of this thesis. The emphasis is put on the following aspects:

- Metalation of THF by rare-earth-metallocene tetramethylaluminates
- Metalation of benzene by rare-earth-metallocene complexes
- Activation of GaMe$_3$ by rare-earth-metallocene complexes to form gallium methylene
- C–H-bond activation of the Tp$^{t\mathrm{Bu,Me}}$ ligand

Chapter E is a compilation of papers and manuscripts.

A

σ-Bond Metathesis in Rare-Earth-Metal Chemistry

1 σ-Bond Metathesis

Activation of nonpolar single bonds, such as C–H, C–C, and H–H are of fundamental interest in organometallic chemistry.[1] As such, the oxidative addition (OA) to a metal center is the most important elementary reaction step at transition metals (Scheme 1, **A**). However, this requires a metal center with an accessible "+2" oxidation state and two vacant coordination sites. In a first step the nonpolar single bond coordinates at the metal center to form a σ complex, followed by bond cleavage. As a result, the oxidation state and coordination number at the metal center increase by +2. The reverse reaction, the reductive elimination (RE) would liberate the initial substrate or allows formation of a new product if other suitable ligands are present at the metal center. This reaction sequence is of great importance in many catalytic cycles and therefore plays a pivotal role in synthetic and sustainable processes.

Since d^0 and d^0f^n metal compounds lack an accessible "+2" oxidation state, oxidative addition is ruled out for these cases. An alternative reaction sequence is posed by σ-bond metathesis where in a concerted [2σ + 2σ] cycloaddition a metal-ligand σ bond and a substrate σ bond form a four-centered transition state (Scheme 1, **B**). In the following, reformation of the starting materials or exchange of the metal-ligand σ bond and the substrate σ bond to form new compounds can occur. Although the final outcome parallels the oxidative addition/reductive elimination sequence, the oxidation state at the metal center does not change along this pathway and only one vacant coordination site is necessary to enable this reaction step.

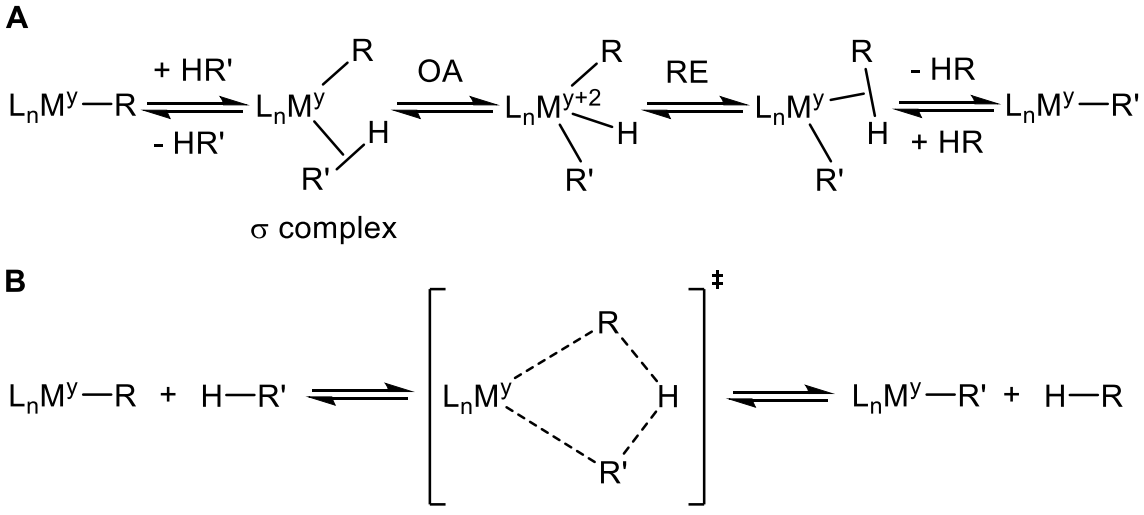

Scheme 1. Comparison of important mechanisms in organometallic chemistry; **A** oxidative addition (OA)/reductive elimination (RE); **B** σ-bond metathesis.

2 σ-Bond Metathesis in Rare-Earth-Metallocene Chemistry

2.1 Methyl complexes $[Cp^*_2LnMe]_x$ ($\mathbf{1^{Ln}}$)

The use of cyclopentadienyl ligands is well established in organolanthanide chemistry, starting 1954 when WILKINSON reported the successful synthesis of homoleptic $[Cp_3Ln]$ ($Cp = C_5H_5$; Ln = Sc, Y, La, Ce, Pr, Nd, Sm, Gd; Scheme 2)[2] as the first organolanthanide compounds.

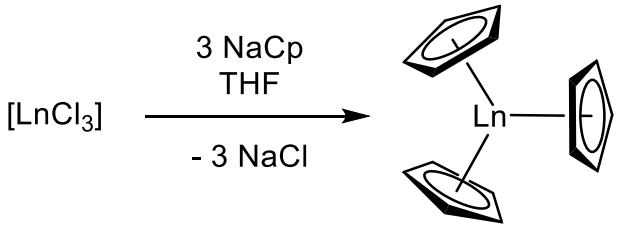

Scheme 2. Synthesis of Cp_3Ln (Ln = Sc, Y, La, Ce, Pr, Nd, Sm, Gd).[2]

Since then, cyclopentadienyl derivatives have emerged as the most ubiquitous ancillary ligands utilized to stabilize rare-earth metal complexes. In particular, the sterically demanding Cp* ligand ($Cp^* = C_5Me_5$) is routinely used due to its enhanced solubilizing ability. Also, the increased steric demand at the rare-earth metal center markedly affect stability and thus reactivity. For example, LAPPERT and co-workers synthesized donor-solvent free $[Cp_2Y(\mu\text{-}Me)]_2$ via donor-induced cleavage of $AlMe_3(py)$ from $[Cp_2Y(\mu\text{-}Me_2AlMe_2)]$.[3] Complex $[Cp_2Y(\mu\text{-}Me)]_2$ lacks terminal ligands and open coordination sites owing to its dimeric constitution in the solid state and solution featuring two bridging methyl groups. Hence, $[Cp_2Y(\mu\text{-}Me)]_2$ does not engage in σ-bond metathesis reactions and is thermally stable in hydrocarbon solutions.[4] In contrast, $[Cp^*_2YMe]_2$ ($\mathbf{1^Y}$) is not accessible by this route since donor assisted cleavage of the $[AlMe_4]$ functionality affords monomeric donor stabilized $[Cp^*_2YMe(do)]$.[5]

However, WATSON achieved $[Cp^*_2LnMe]_2$ ($\mathbf{1^{Ln}}$ Ln = Y, Yb, Lu) by repeated treatment of $[Cp^*_2LnMe(OEt_2)]$ with NEt_3 and subsequent evaporation under vacuum.[6] In the solid state, complexes $\mathbf{1^{Ln}}$ (Ln = Y, Yb, Lu) are dimeric with a bridging and a terminal methyl group, whereas in solution those compounds undergo a quick monomer-dimer equilibrium (Scheme 3).[6b,d]

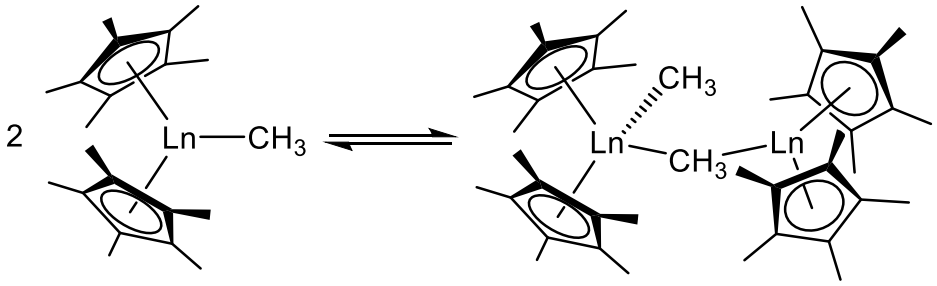

Scheme 3. Monomer-dimer equilibrium found for $\mathbf{1^{Ln}}$ (Ln = Y, Lu) in solutions.[6a,c]

WATSON discovered outstanding reactivities of $\mathbf{1^{Lu}}$ toward various substrates. As such, hydrogenolysis afforded $[Cp^*_2LuH]_2$ ($\mathbf{2^{Lu}}$), while C–H-bond activation of benzene, pyridine and tetramethylsilane resulted in the formation of $[Cp^*_2LuPh]$ ($\mathbf{3^{Lu}}$), $[Cp^*_2Lu(C,N\text{-}\eta^2\text{-}NC_5H_4)]$ ($\mathbf{4^{Lu}}$) and $[Cp^*_2Lu(CH_2SiMe_3)]$ ($\mathbf{5^{Lu}}$), respectively (Scheme 5).[7] The phenyl compound is prone to further arene metalation to form the *p*-phenylene bridged dimer, $[Cp^*_2Lu(\mu\text{-}1,4\text{-}C_6H_4)LuCp^*_2]$ ($\mathbf{6^{Lu}}$). In the course of further investigations on methane exchange reactions by $\mathbf{1^{Y}}$ and $\mathbf{1^{Lu}}$, respectively, WATSON postulated a four-centered transition state as the key step in the mechanism of the exchange reactions (Scheme 4). Detailed kinetic studies also strongly suggested a competing intramolecular C–H-bond activation process to produce a highly reactive intermediate "tuck-in" complex $[Cp^*Ln(\eta^1,\eta^5\text{-}CH_2C_5Me_4)]$ ($\mathbf{7^{Ln}}$).[6d, 8]

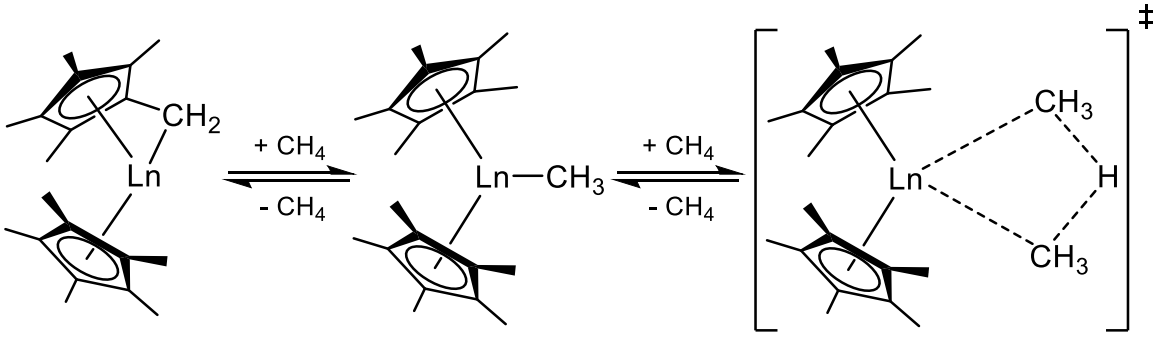

Scheme 4. Methane activation by unsolvated rare-earth metallocene compounds, $[Cp^*_2LnMe]_x$ (x = 1, $\mathbf{1^{Sc}}$; x = 2, $\mathbf{1^{Lu}}$, $\mathbf{1^{Y}}$), via formation of "tuck-in" complexes (left) and four-centered transition states (right).[6a,c, 9]

For comparison, complex $\mathbf{1^{Yb}}$ does not react with any C–H bonds and hydrogenolysis leads to formation of mixed valent $[Cp^*_2Yb(\mu\text{-}H)YbCp^*_2]$ (**8**). This surprising finding may be attributed to the thermodynamic stability and kinetic accessibility of the ytterbium(II) electronic configuration.[10]

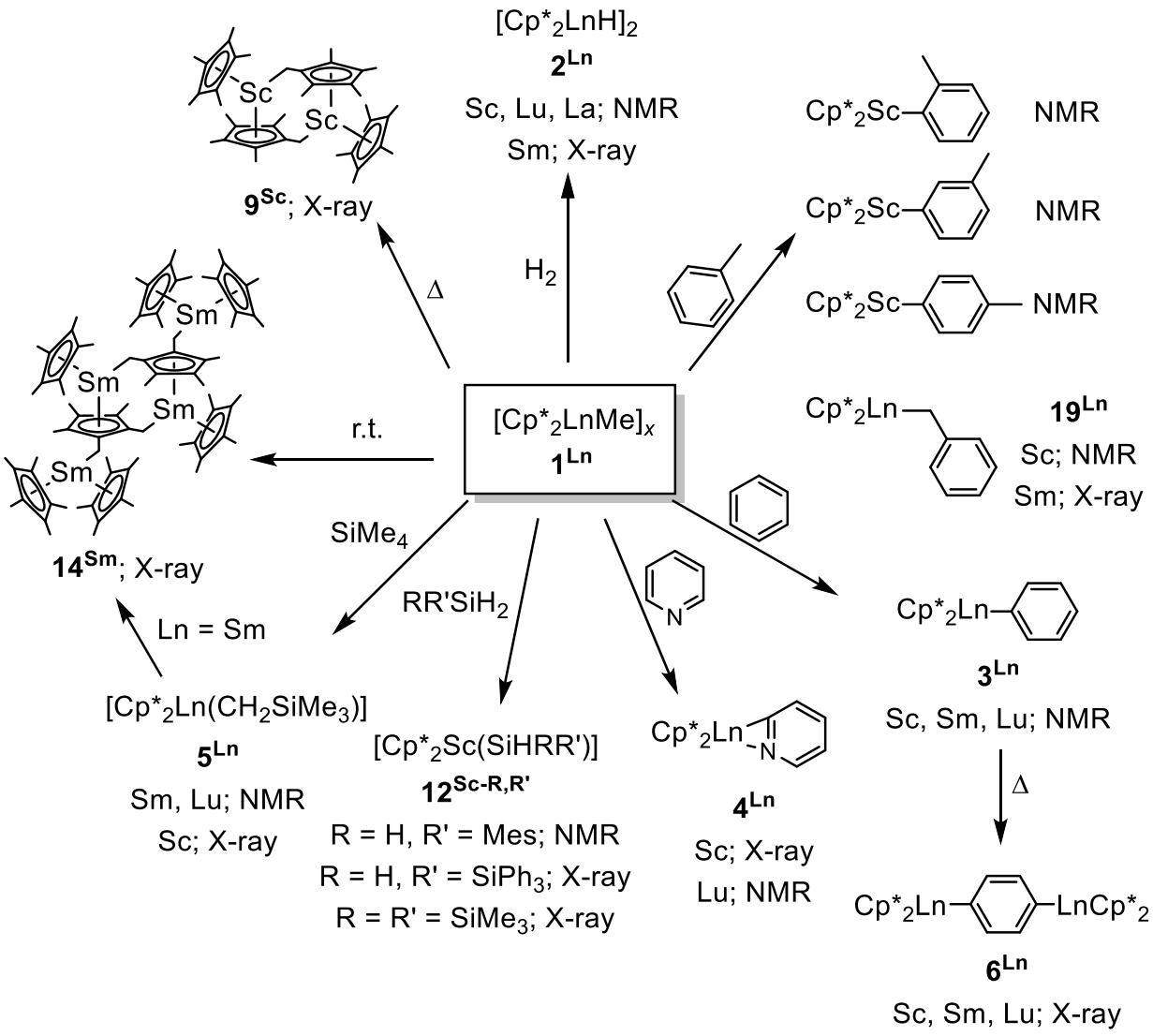

Scheme 5. Reactivity of $[Cp^*_2LnMe]_x$ ($\mathbf{1^{Sc}}$ x = 1, $\mathbf{1^{Lu}}$/$\mathbf{1^{Y}}$ x = 2, $\mathbf{1^{Sm}}$ x = 3, $\mathbf{1^{La}}$ x = unknown; compound is not isolable) and reaction products characterized by single crystal X-ray diffraction (XRD) or NMR spectroscopy.[7, 9, 11]

Shortly after the seminal studies by WATSON, THOMPSON et al. published detailed studies on C–H-bond activation by scandocene derivatives via "σ-bond metathesis", indicating comparable reactivity for $\mathbf{1^{Sc}}$ toward hydrogen, methane, benzene and pyridine, as well as further arenes (e.g. toluene), alkenyls, alkynyls and methyl iodide.[9b] Thermolysis of $\mathbf{1^{Sc}}$ at 80 °C in cyclohexane produced CH_4 and a dimeric "tuck-over" compound $[Cp^*Sc(\mu\text{-}CH_2C_5Me_4)]_2$ (**9**).[9b, 12]

In 2003 SADOW and TILLEY examined the potential application of $\mathbf{1^{Sc}}$ for the catalytic functionalization of methane. As such, they demonstrated that catalytic hydromethylation can be realized in the presence of methane and propene (9-10 equiv.). This system provided

[Cp*$_2$Sc(CH$_2$CHMe$_2$)] (**10**), [Cp*$_2$Sc(CH=CMe$_2$)] (**11**) and 3 equivalents isobutane within three days at ambient temperature (Scheme 6).[13]

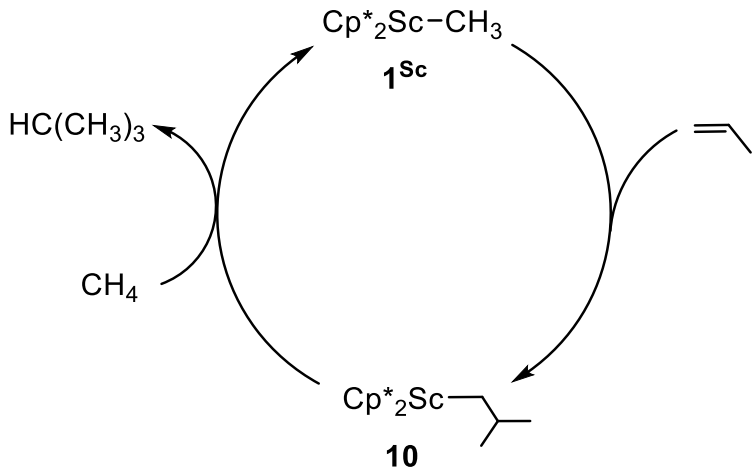

Scheme 6. Proposed catalytic cycle for hydromethylation of propene by **1**^{Sc} (adopted from Ref. [13]).

In another study SADOW and TILLEY reported on the dehydrosilylation of methane by **1**^{Sc} and found a strong correlation of steric constraints of the silane and the product formation.[11f,g] As such, sterically congested primary silane MesSiH$_3$ and **1**^{Sc} rather produced the silyl complex [Cp*$_2$Sc(SiH$_2$Mes)] (**12**$^{Sc\text{-}H,Mes}$) and MesMeSiH$_2$ as a minor side product (15%) in the presence of excessive methane.[11f] In contrast, unhindered primary and secondary silanes, respectively, (RSiH$_3$, R = H, Me, Ph, C$_6$H$_{11}$, *p*-MeC$_6$H$_4$, 3,5-Me$_2$C$_6$H$_3$; Ph$_2$SiH$_2$, PhMeSiH$_2$, Me$_2$SiH$_2$, Et$_2$SiH$_2$) and **1**^{Sc} afford a methyl to silicon transfer to form the hydride **2**^{Sc} (Scheme 7 **A**).[11g] Therefore, small primary and secondary silanes are potential substrates for the catalytic dehydrosilylation with the concomitant activation of methane (Scheme 7, **B**). Hence, a mixture of **1**^{Sc} and Ph$_2$SiH$_2$ afforded 5 equivalents of Ph$_2$MeSiH at 80 °C under 150 atm of methane after 7 days (Scheme 7 **C**).[11f]

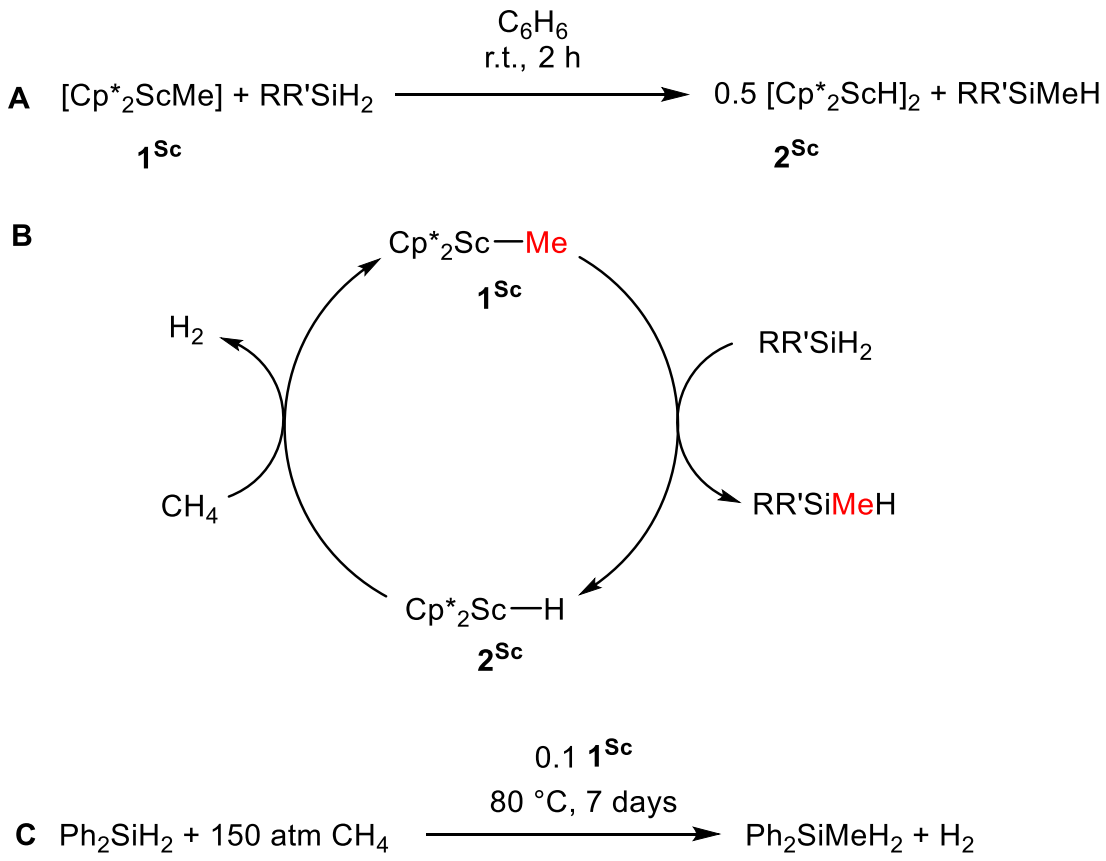

Scheme 7. A Reaction of primary and secondary hydrosilanes with $\mathbf{1}^{Sc}$; **B** Possible catalytic cycle for methane dehydrosilylation via the metalation of methane by $\mathbf{2}^{Sc}$ (adopted from Ref. [11g]); **C** Catalytic dehydrosylilation of methane by $\mathbf{1}^{Sc}$.[11f]

Noteworthy, complex $\mathbf{1}^{Sc}$ is monomeric in solution and in the solid state and methane exchange proceeds rather slow, approximately 50 times slower than observed for $\mathbf{1}^{Lu}$ and 250 times slower than observed for $\mathbf{1}^{Y}$. Clearly, the reactivity increases with increasing size of the ionic radii of the rare-earth metal center and enhanced steric unsaturation, a well-known phenomenon in organolanthanide chemistry.[14] Accordingly, the synthesis of the larger rare-earth-metal congeners is challenging and it was not until 2005 that EVANS successfully achieved the samarocene methyl compound from [Cp*$_2$Sm{(μ-Ph)$_2$BPh$_2$}] ($\mathbf{13}^{Sm}$) and MeLi by following a salt-metathesis protocol. Single-crystal structure determination revealed an asymmetric trinuclear core structure for $\mathbf{1}^{Sm}$ (Scheme 8).[11c]

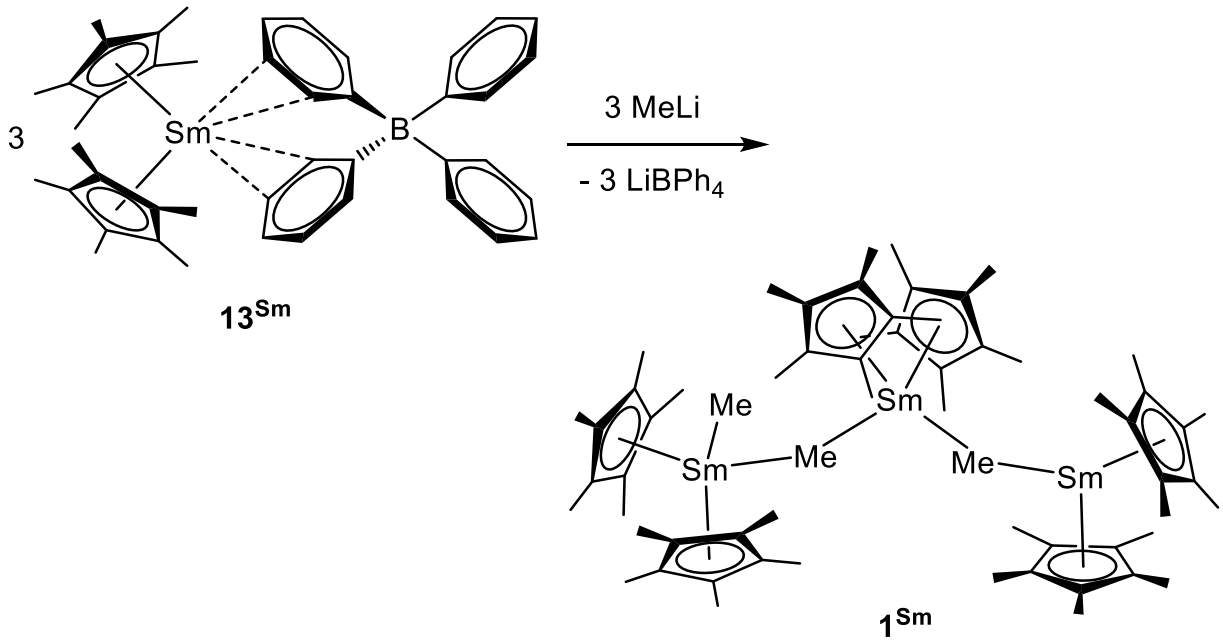

Scheme 8. Synthesis of complex $\mathbf{1}^{\mathbf{Sm}}$.[11c]

Following the same protocol also complex $\mathbf{1}^{\mathbf{La}}$ was prepared.[11c] The instability of this compound did not allow for characterization by single crystal X-ray crystallography. However, EVANS established the system $\mathbf{13}^{\mathbf{Ln}}$/MeLi as readily accessible synthon for highly reactive $\mathbf{1}^{\mathbf{Ln}}$ compounds for the lanthanide series (Ln = Y, Lu, Sm, La).[11c, 15] EVANS and co-workers exhaustively examined the chemistry of $\mathbf{1}^{\mathbf{Sm}}$ and found an overall similar reactivity as established for the smaller rare-earth-metal analogues. However, compound $\mathbf{1}^{\mathbf{Sm}}$ metalates toluene preferentially at the methyl group to form the corresponding benzyl compound $[Cp^*_2Sm(CH_2C_6H_5)]$ ($\mathbf{19}^{\mathbf{Sm}}$) as the main product. Formation of *m*-tolyl samarocene $[Cp^*_2Sm(m\text{-}C_6H_4CH_3)]$ and dimetalated toluene product $[Cp^*_2Sm(CH_2C_6H_4)SmCp^*_2]$ were mentioned only as minor side products. Metalation of $SiMe_4$ by $\mathbf{1}^{\mathbf{Sm}}$ generated compound $[Cp^*_2Sm(CH_2SiMe_3)]$ ($\mathbf{5}^{\mathbf{Sm}}$). This complex was also achieved directly by a salt metathesis protocol. Furthermore, at ambient temperature in C_6D_{12} solutions complexes $\mathbf{1}^{\mathbf{Sm}}$ and $\mathbf{5}^{\mathbf{Sm}}$, respectively, decompose slowly to afford a higher aggregated tretranuclear complex $[Cp^*_3(\mu_3\text{-}\eta^5,\eta^1,\eta^1\text{-}C_5Me_3\{CH_2\}_2)Sm_2]_2$ ($\mathbf{14}^{\mathbf{Sm}}$) comprising two doubly metalated Cp* ligands (Scheme 5).[11c]

2.2 Ethyl complexes [Cp*$_2$LnEt] ($\mathbf{15^{Ln}}$)

The reaction of $\mathbf{1^Y}$ and $\mathbf{1^{Lu}}$, respectively, with ethane or propane to afford the alkyl analogs [Cp*$_2$LnR] (R = ethyl, propyl) was also mentioned by WATSON.[6a] However, these compounds eluded from isolation due to their proneness to undergo β-hydride elimination. In contrast, the less reactive ethyl complex [Cp*$_2$ScEt] ($\mathbf{15^{Sc}}$) was easily obtained from scandium hydride [Cp*$_2$ScH]$_2$ ($\mathbf{2^{Sc}}$) and ethene and is stable at ambient temperature.[9b] Although severe disorder in the single crystal structure could not verify a β-agostic interaction for $\mathbf{15^{Sc}}$ in the original study, the obtained IR data strongly suggested a β-agostic structure in the solid state. This assumption was confirmed later by single crystal X-ray diffraction for the yttrium derivative [Cp*$_2$YEt] ($\mathbf{15^Y}$)[15] and detailed solid-state NMR studies for $\mathbf{15^{Sc}}$.[16] For compound $\mathbf{15^Y}$ MACDONALD et al. revealed a rich chemistry comparable to $\mathbf{1^Y}$. As such, $\mathbf{15^Y}$ activates benzene and toluene and reacts to $\mathbf{1^Y}$ under methane atmosphere via σ-bond metathesis (Scheme 9). At ambient temperature $\mathbf{15^Y}$ forms the hydride [Cp*$_2$YH]$_2$ ($\mathbf{2^Y}$)[17] under ethane elimination which is prone to H_2 elimination to form the mixed hydride "tuck-over" compound [Cp*$_2$Y(μ-H)(μ-CH$_2$C$_5$Me$_4$)YCp*] ($\mathbf{16^Y}$).[15]

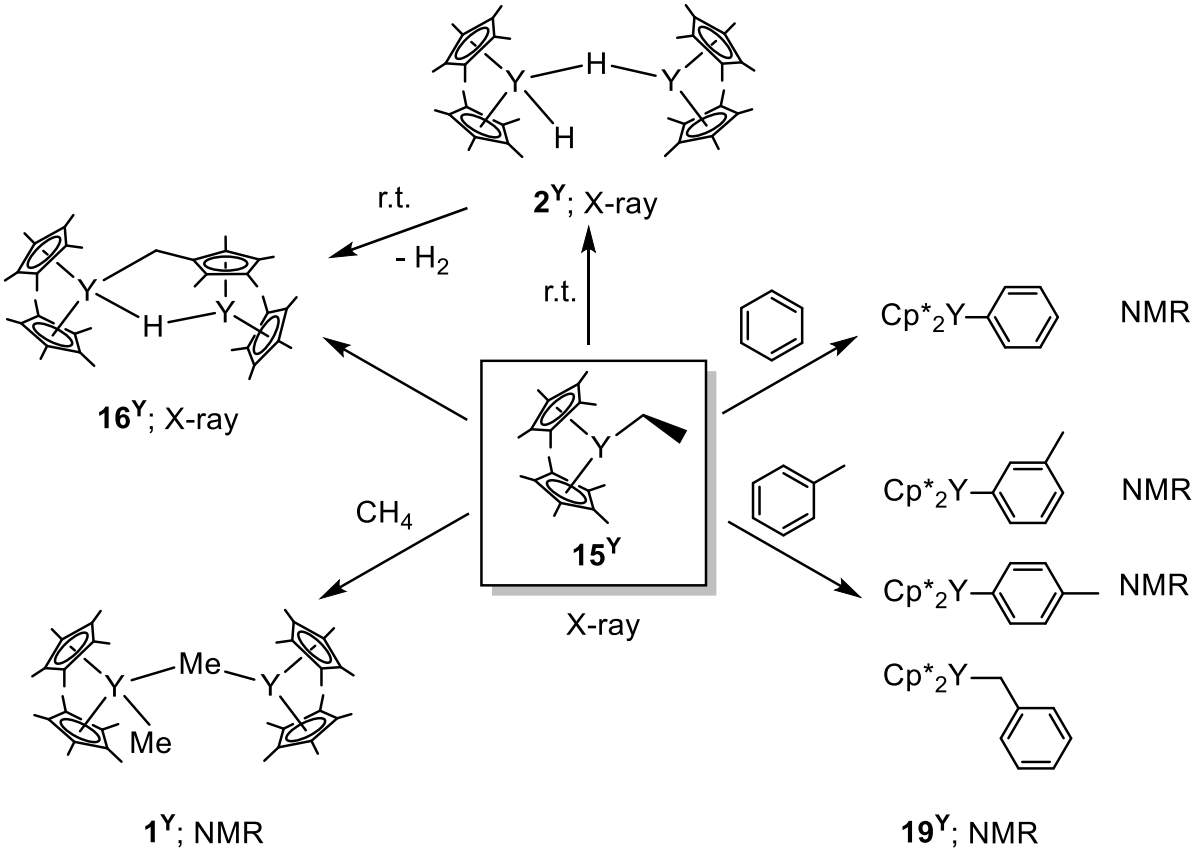

Scheme 9. Reactivity of $\mathbf{15^Y}$ and reaction products characterized by single crystal XRD or NMR spectroscopy.[15]

2.3 Phenyl complexes $[Cp^*_2LnPh]_x$ ($\mathbf{3^{Ln}}$)

The C–H-bond activation of benzene is commonly observed by rare-earth metallocene alkyls to produce $[Cp^*_2LnPh]_x$ ($\mathbf{3^{Ln}}$).[6a, 7-9, 11c,e, 15, 18] Closer investigations of compounds $\mathbf{3^{Ln}}$ addressed the pivotal role of lanthanide phenyl species as intermediates in the rare-earth-metal catalyzed C–Si bond cleavage and rearrangement in redistribution reactions of $PhSiH_3$ to Ph_2SiH_2 and SiH_4.[11e, 19]

Rare-earth-metallocene phenyl compounds $\mathbf{3^{Ln}}$ (Ln = Sc, Y, Lu) are available from the respective hydrides $[Cp^*_2LnH]_2$ ($\mathbf{2^{Ln}}$) in benzene solutions (Scheme 10, **A**). However, the equilibrium strongly prefers the hydride compound. Thus, liberated hydrogen needs to be removed from the reaction vessel to access the phenyl compounds $\mathbf{3^{Ln}}$ in good yields.

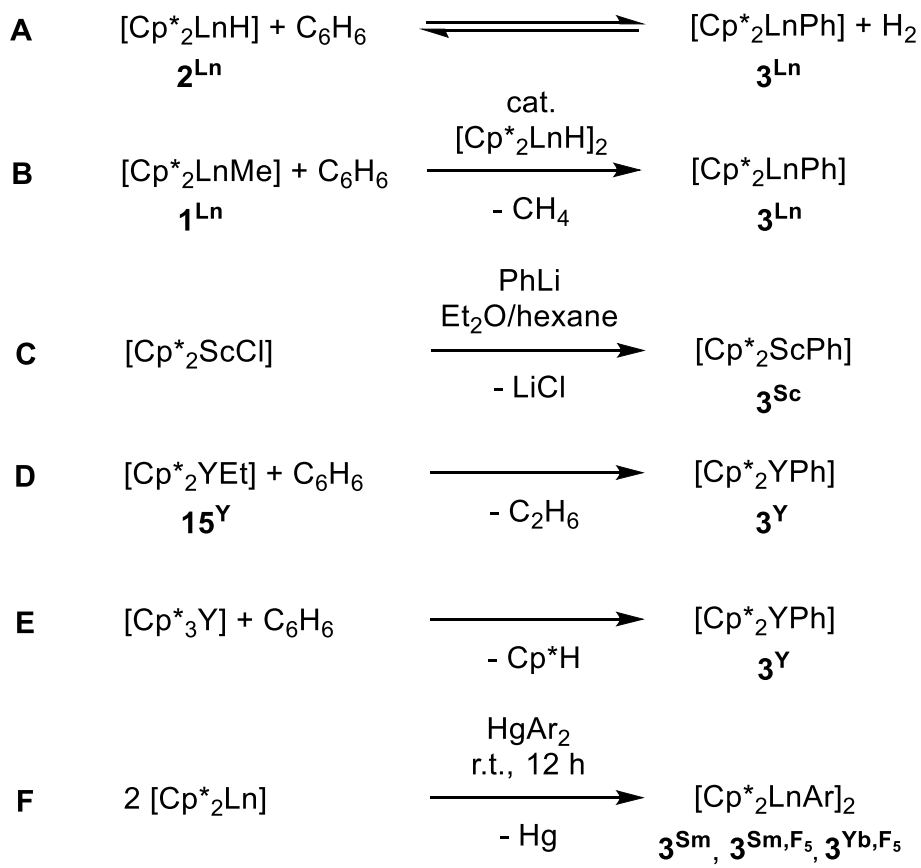

Scheme 10. A, **B** Synthesis of phenyl compounds $\mathbf{3^{Ln}}$ (Ln = Sc, Y, Lu) via σ-bond metathesis starting from $\mathbf{1^{Ln}}$ and $\mathbf{2^{Ln}}$, respectively; **C** Synthesis of $\mathbf{3^{Sc}}$ by salt metathesis; **D**, **E** Metalation of benzene by $[Cp^*_2YEt]$ and $[Cp^*_3Y]$, respectively, to afford $\mathbf{3^{Y}}$; **F** Synthesis of $[Cp^*_2LnAr]_2$ (Ln = Sm, Ar = Ph ($\mathbf{3^{Sm}}$), C_6F_5 ($\mathbf{3^{Sm,F_5}}$); Ln = Yb, Ar = C_6F_5 ($\mathbf{3^{Yb,F_5}}$)) in a redox reaction.[6a, 7-10, 11c,e, 15, 18, 19b, 20]

Treatment of the methyl compounds $\mathbf{1}^{\mathbf{Ln}}$ in benzene solutions is an alternative approach to afford $\mathbf{3}^{\mathbf{Ln}}$ (Scheme 10, **B**). Since metalation of benzene by $\mathbf{1}^{\mathbf{Ln}}$ for the smaller to intermediate-sized rare-earth metals (Ln = Sc, Lu, Y) proceeds rather slow, catalytic amounts of the hydride $\mathbf{2}^{\mathbf{Ln}}$ are necessary to accelerate the methyl/phenyl exchange reaction.[7, 19b] In addition, scandium phenyl $\mathbf{3}^{\mathbf{Sc}}$ is accessible by the salt-metathesis reaction of sandwich complex [Cp*$_2$ScCl] and PhLi (Scheme 10, **C**).[9b] This route is not available for the larger rare-earth metal analogues due to robust adduct formation with phenyl lithium. Reaction of either the ethyl complex [Cp*$_2$YEt] or sterically crowed [Cp*$_3$Y] with benzene affords yttrium phenyl compound $\mathbf{3}^{\mathbf{Y}}$ (Scheme 10, **D**/**E**).[15, 20] A further approach for the synthesis of $\mathbf{3}^{\mathbf{Sm}}$ and $\mathbf{3}^{\mathbf{Ln,F_5}}$ (Ln = Sm, Yb) is the oxidation of Ln(II)-compounds [Cp*$_2$Ln] with HgAr$_2$ (Ar = Ph, C_6F_5) (Scheme 10, **F**; $\mathbf{3}^{\mathbf{Yb}}$ is not achievable by this route).[10, 11e]

The thermal stability of compounds $\mathbf{3}^{\mathbf{Ln}}$ strongly correlates with the ionic radius of the respective rare-earth-metal center. Hence, scandium phenyl $\mathbf{3}^{\mathbf{Sc}}$ is stable at ambient temperatures and thermolysis experiments with various hydrocarbons in benzene solutions only resulted in slow decomposition to a mixture of uncharacterized scandium containing products but no detectable concentrations of permethylscandocene derivatives other than $\mathbf{3}^{\mathbf{Sc}}$.[18a] However, derivative $\mathbf{3}^{\mathbf{Sc}}$ eluded from structural characterization and solid samples needed to be stored at 10 °C to prevent decomposition.[21] In stark contrast, the samarium congener $\mathbf{3}^{\mathbf{Sm}}$ decomposes spontaneously in cyclohexane solutions and in the solid state at –35 °C.[11c,e] Decomposition of $\mathbf{3}^{\mathbf{Sm}}$ results in clean formation of the *p*-phenylene-bridged dimer [Cp*$_2$Sm(μ-1,4-C_6H_4)SmCp*$_2$] ($\mathbf{6}^{\mathbf{Sm}}$) as confirmed by X-ray crystallography.[11e] Similar reactivity was mentioned by WATSON and TILLEY for the lutetium compound to form $\mathbf{6}^{\mathbf{Lu}}$.[7, 19b] However, decomposition of $\mathbf{3}^{\mathbf{Lu}}$ proceeds slowly and the formation of $\mathbf{6}^{\mathbf{Lu}}$ might be promoted by catalytical amounts of the hydride $\mathbf{2}^{\mathbf{Lu}}$.

In good agreement with the methyl compounds $\mathbf{1}^{\mathbf{Ln}}$, the phenyl homologs $\mathbf{3}^{\mathbf{Ln}}$ revealed that increasing radii of the rare-earth metal center are attributed with increased reactivity and a higher propensity to form dimeric species. As such, the scandium phenyl $\mathbf{3}^{\mathbf{Sc}}$ is monomeric in benzene solutions[9b] while samarocene complex $\mathbf{3}^{\mathbf{Sm}}$ exists predominantly as a dimer in benzene solutions in rapid equilibrium with the monomeric species.[11e] According to detailed kinetic studies TILLEY and co-workers postulated competing intra- and intermolecular reaction pathways for the decomposition of $\mathbf{3}^{\mathbf{Sm}}$ in good analogy as described for the $\mathbf{1}^{\mathbf{Lu}}$ system (Scheme 11).

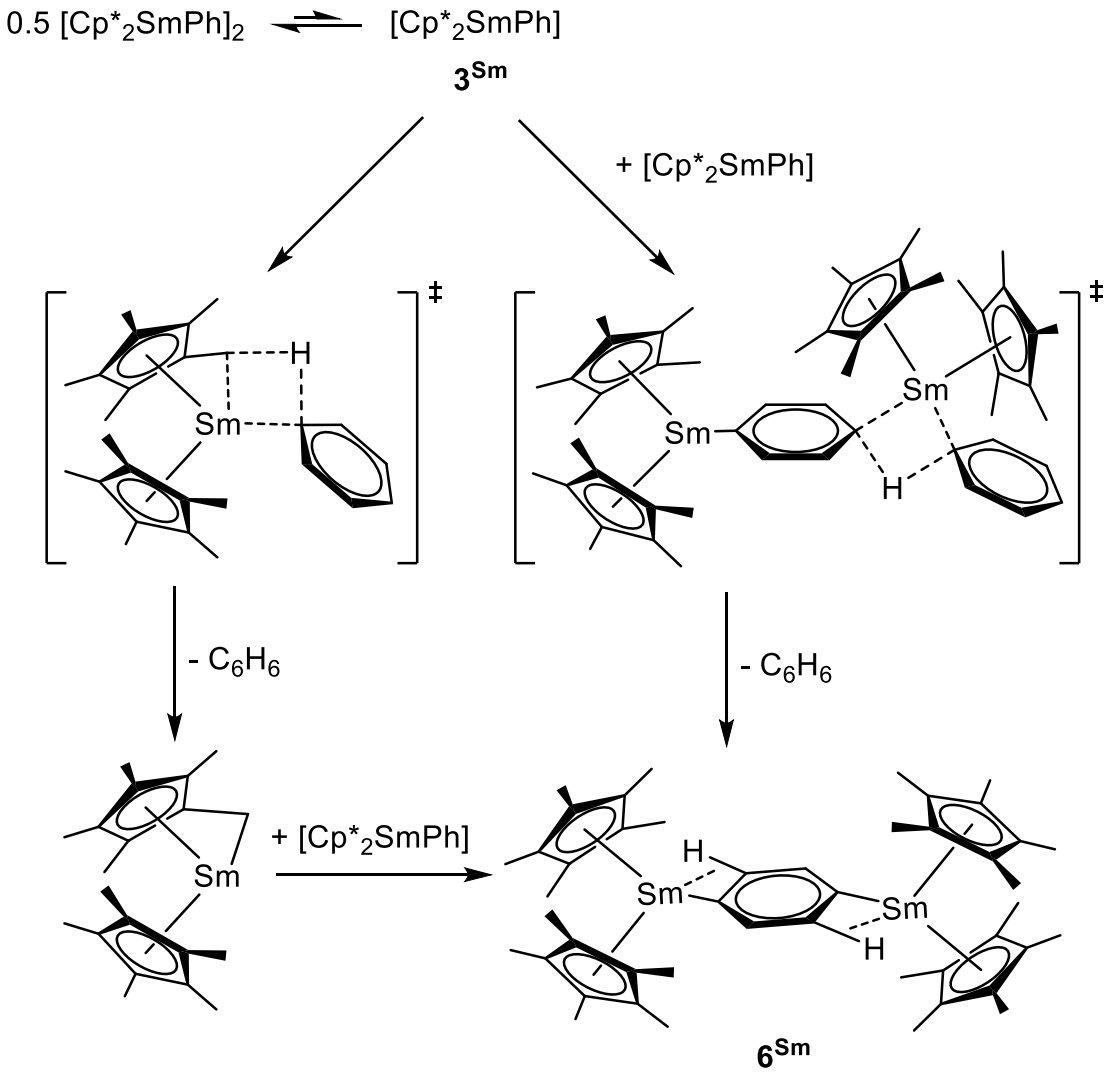

Scheme 11. Proposed decomposition route of $\mathbf{3}^{Sm}$ for the formation of $\mathbf{6}^{Sm}$ (adopted from ref. [11e]).

Since the samarium phenyl $\mathbf{3}^{Sm}$ is thermally labile, TILLEY targeted the more robust perfluorophenyl derivative $[Cp^*_2Sm(C_6F_5)]_2$ ($\mathbf{3}^{Sm,F_5}$) (Scheme 10, **F**) and revealed the dimeric constitution of $\mathbf{3}^{Sm,F_5}$ in solution by ^{19}F NMR spectroscopy and in the solid state by X-ray diffraction analysis.[11e]

2.4 Synthesis and reactivity of complexes [Cp*$_2$Ln{CH(SiMe$_3$)$_2$}] (**17^{Ln}**)

A convenient strategy to overcome decomposition of alkyl compounds [Cp*$_2$LnR] via β-hydrogen elimination utilizes bulky alkyl moieties carrying no hydrogen atoms in β position. As such, MARKS, and SCHUMANN and co-workers synthesized a series of rare-earth-metallocene alkyls [Cp*$_2$Ln{CH(SiMe$_3$)$_2$}] (**17^{Ln}**; Ln = La, Nd, Sm, Lu) by a salt metathesis protocol (Scheme 12, **A**).[22] In a similar approach, TEUBEN et al. obtained **17^{Y}**[23] and **17^{Ce}**[24] by the reaction of either [Cp*$_2$Y{N(SiMe$_3$)$_2$}] or [Cp*$_2$CeCl] and [Li{CH(SiMe$_3$)$_2$}], respectively (Scheme 12, **B**/**C**). In the solid state, complexes **17^{Ln}** (Ln = Y, Nd, Ce) are monomeric.[22-24]

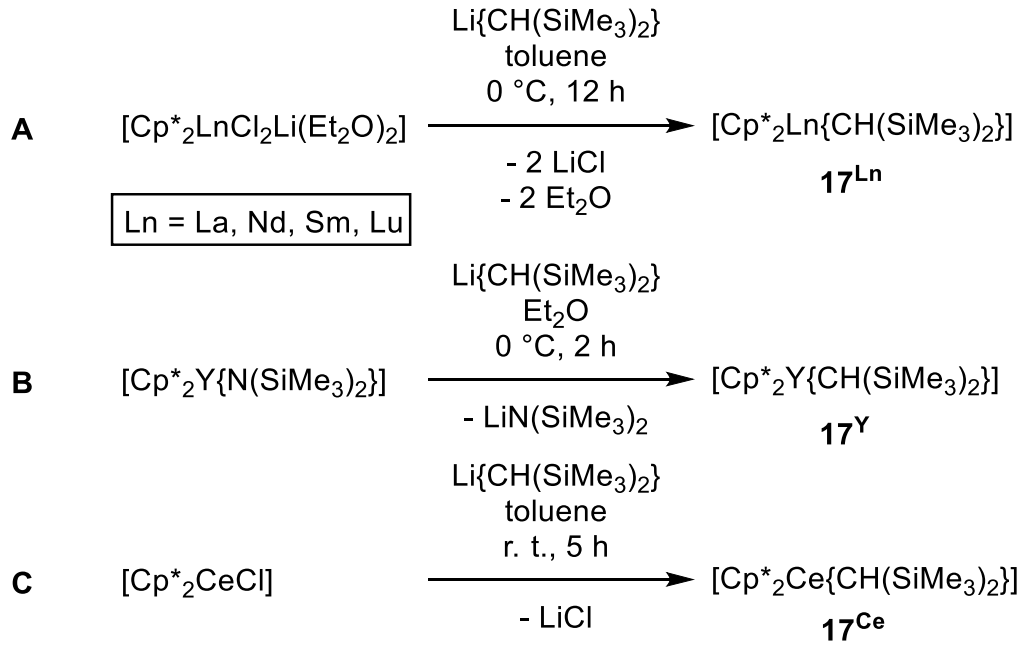

Scheme 12. A Salt-metathesis protocol for the synthesis of **17^{Ln}** (Ln = La, Nd, Sm, Lu);[22] **B** Synthesis of **17^{Y}** by lithium silylamid elimination;[23] **C** Synthesis of **17^{Ce}**.[24]

In contrast to complexes with less congested alkyl groups R, compounds [Cp*$_2$Ln{CH(SiMe$_3$)$_2$}] (**17^{Ln}**) are not coordinated by ethers (e.g. THF and Et$_2$O) and are unreactive toward olefins due to steric constraints and additional α-agostic Ln···H–C interactions. However, *ortho*-metalation was observed in the reaction of the yttrium compound **17^{Y}** and pyridine to form the *o*-pyridyl complex [Cp*$_2$Y(η^2-NC$_5$H$_4$)] (**4^{Y}**).[25] The corresponding hydride complexes **2^{Ln}** (Ln = La, Nd, Sm, Lu, Y, Ce) are formed in quantitative yields under an H$_2$ atmosphere in *n*-pentane solutions at 0 °C.[22, 24-25] Thermolysis of **17^{Y}** in toluene produced a mixture of benzyl-, *o*-, *m*-, and *p*-tolylyttrocenes similar to the reactivity of **1^{Sc}**.[25] For comparison, the reaction of **17^{Y}** and mesitylene at 150 °C selectively produced the yttrocene

complex [Cp*$_2$Y{CH$_2$(C$_6$H$_3$Me$_2$-3,5)}] (**18**).[25] In contrast, thermolysis in toluene of the "larger" rare-earth-metal derivatives **17^{La}** and **17^{Ce}**, respectively, afforded exclusively the benzyl derivatives [Cp*$_2$Ln(CH$_2$Ph)] (**19^{Ln}**; Ln = La, Ce).[26] In cyclohexane solutions **17^{Y}** is inert at temperatures up to 130 °C (decomposition starting at 155 °C). The thermal treatment of **17^{La}** and **17^{Ce}** led to elimination of H$_2$C(SiMe$_3$)$_2$ under these conditions to form the tetranuclear "tuck-over" complexes **14^{La}** and **14^{Ce}** with the same structural motif later found for the samarium analog starting from [Cp*$_2$SmMe]$_3$ (Scheme 13).[11c, 26]

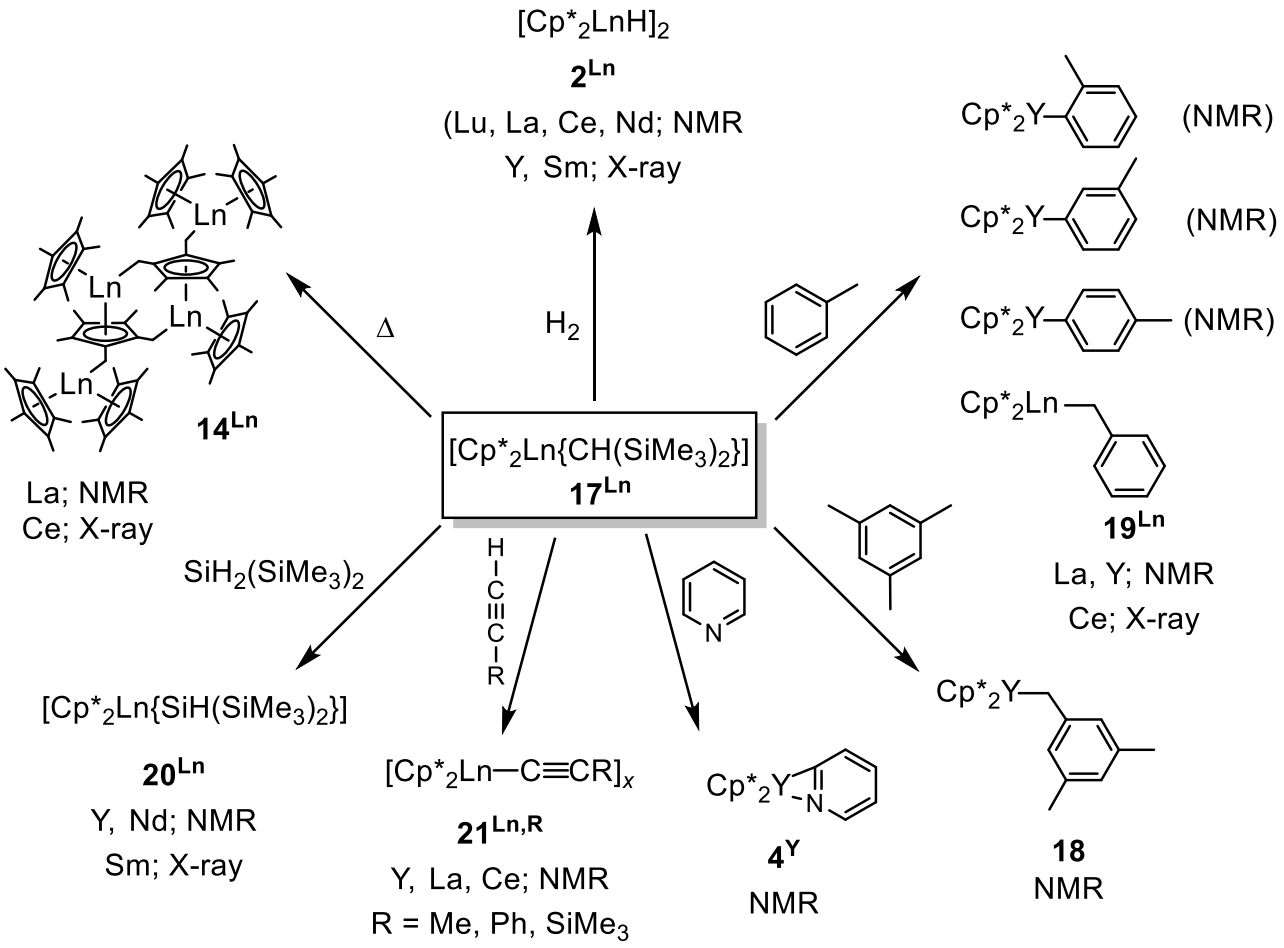

Scheme 13. Reactivity of **17^{Ln}** (Ln = Y, Lu, Nd, Sm, Ce, La) and reaction products characterized by single-crystal X-ray diffraction or NMR spectroscopy.[22, 24-27]

The reactivity of alkyl complexes **17^{Ln}** (Ln = Nd, Sm, Y) toward a series of silanes was assessed by RADU and co-workers. Depending on the steric bulk of the silane dehydrocoupling or the formation of silyl complexes was observed. As such, reaction of primary silane MesSiH$_3$ and **17^{Ln}** produced CH$_2$(SiMe$_3$)$_2$, the corresponding hydride **2^{Ln}** and the dehydrocoupling product

$MesH_2SiSiH_2Mes$ (not depicted in Scheme 13). The reaction of alkyls **17^{Ln}** with 5 equivalents of secondary silane $SiH_2(SiMe_3)_2$ at 85 °C afforded the silyl complexes $[Cp^*_2Ln\{SiH(SiMe_3)_2\}]$ (**20^{Ln}**; Ln = Nd, Sm, Y; Scheme 13), which are monomeric in hydrocarbon solutions but form dimers in the solid state.[27b-d]

TEUBEN and co-workers also employed compounds **17^{Ln}** (Ln = Y, La, Ce) for the catalytic oligomerization of terminal alkynes. In the presence of alkynes, complexes **17^{Y}**, **17^{La}** and **17^{Ce}** gave acetylides $[Cp^*_2Ln(C{\equiv}CR)]_n$ (**21^{Ln,R}**) (R = Me, Ph, $SiMe_3$).[25, 27a] The oligomerization of alkynes by complexes **21^{Ln,R}** is efficiently catalyzed via the coordination and insertion of further alkynes into the Ln–C bond to afford transient rare-earth-metal alkenyl complex $[Cp^*_2Ln(CHCRC{\equiv}CR)]$. The σ-bond metathesis reaction step with an incoming alkyne molecule regenerates the catalyst and liberates free enynes (Scheme 14).

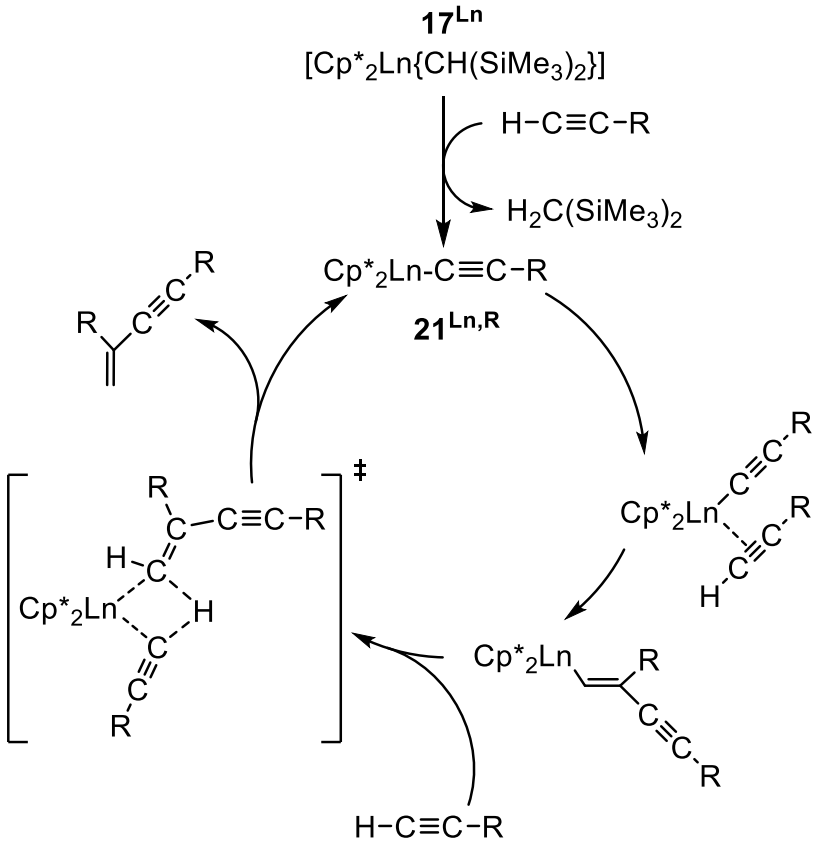

Scheme 14. Catalytic cycle for alkyne dimerization by **17^{Ln}** (Ln = Y, Ce, La; R = Me, Ph, $SiMe_3$; adopted from ref. [25]).

2.5 Neopentyl complexes [Cp*$_2$Ln(CH$_2$CMe$_3$)] (**22^{Ln}**)

Neopentyl derivatives [Cp*$_2$Ln(CH$_2$CMe$_3$)] (**22^{Ln}**) are exceedingly rare despite the absence of any β-hydrogen atoms. Attempts to prepare **22^{Sm}** via a salt-metathesis protocol by EVANS and co-workers failed, since the initially produced **22^{Sm}** rapidly decomposes via β-methyl elimination.[28] In a multistep reaction, the trimethylenemethane dianion in complex [Cp*$_2$Sm(μ-η^3:η^3-C(CH$_2$)$_3$)SmCp*$_2$] (**23**) is formed (Scheme 15). SADOW et al. successfully synthesized and structurally characterized the scandocene analog **22^{Sc}** from the reaction of [Cp*$_2$ScCl] and [Li(CH$_2$CMe$_3$)] in *n*-pentane solutions at –78 °C (Scheme 16).[13] Compound **22^{Sc}** is sensitive to ambient light but is stable in the dark at temperatures below –30 °C. In the presence of methane **22^{Sc}** forms **1^{Sc}** and neopentane at rate constants even faster than for the reported activation of methane by **1^{Sc}** itself while the reaction of **22^{Sc}** with cyclopropane to produce cyclopropyl complex [Cp*$_2$Sc(*c*Pr)] (**24**) and neopentane proceeds rather slow.

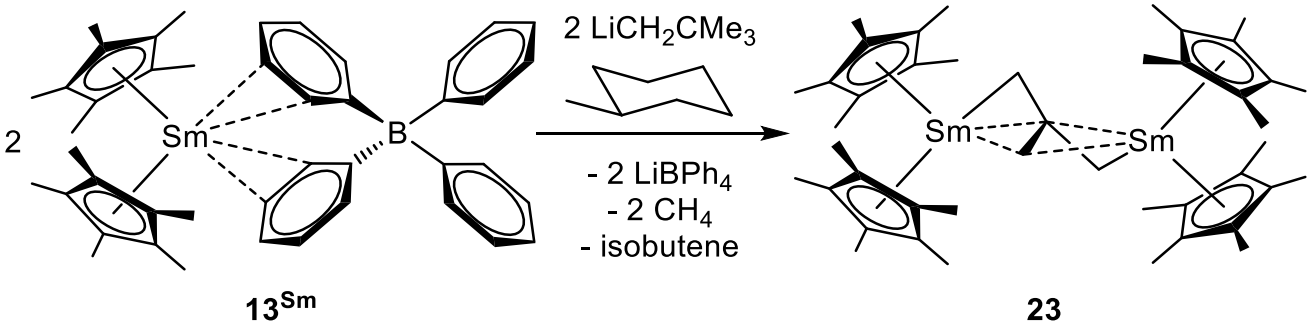

Scheme 15. Synthesis of **23** (adopted from Ref. [28]).

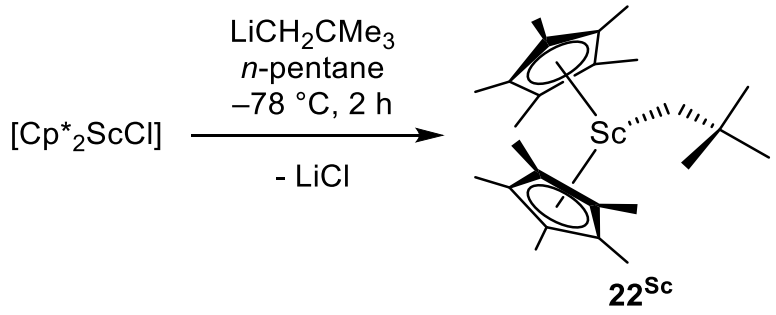

Scheme 16. Salt-metathesis protocol for the synthesis of **22^{Sc}**.[13]

2.6 Hydride complexes $[Cp^*_2LnH]_2$ (2^{Ln})

The metallocene-hydrides $[Cp^*_2LnH]_2$ ($\mathbf{2^{Ln}}$) are readily formed by hydrogenolysis of unsolvated alkyl complexes $[Cp^*_2LnR]_x$ since hydrogenolysis of the Ln–C bond is thermodynamically favored.

Hence, investigations on the formation and reactivity of the hydrides $\mathbf{2^{Ln}}$ were already part of the early studies on σ-bond metathesis by WATSON and BERCAW. Thus, hydride complexes $\mathbf{2^{Lu}}$ and $\mathbf{2^{Sc}}$ were accessed by hydrogenolysis of the corresponding methyl complexes $\mathbf{1^{Ln}}$ (Scheme 17, **A**).[7, 9] According to low-temperature ^{1}H NMR spectroscopy (–95 °C), $\mathbf{2^{Lu}}$ forms an asymmetric dimer in solution analogous to $\mathbf{1^{Lu}}$ (Chart 1, **B**). However, at 25 °C hydride $\mathbf{2^{Lu}}$ is in equilibria with the monomer $[Cp^*_2LuH]$.[6d, 29] In a different study, EVANS achieved $\mathbf{2^{Sm}}$ by hydrogenolysis of the samarocene enediyl $[Cp^*_2Sm(PhC{=}CPh)SmCp^*_2]$ (**25**).[11d] Despite its thermal lability in solutions and the solid state, complex $\mathbf{2^{Sm}}$ was characterized by X-ray diffraction analysis and found to be dimeric in the solid state.

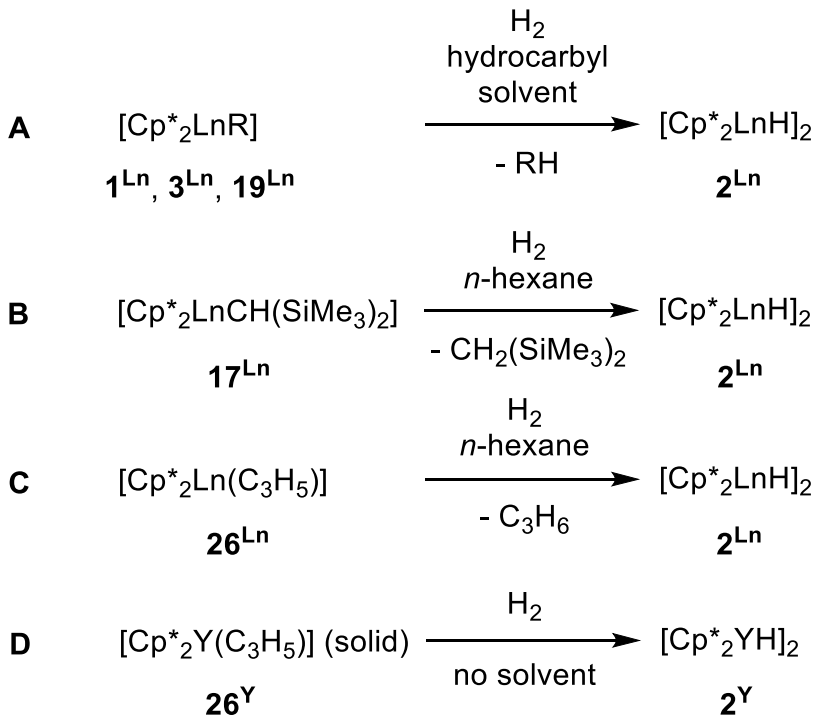

Scheme 17. Synthesis of hydride compounds $\mathbf{2^{Ln}}$; **A** Ln = Lu, Sc; R = Me, Ph, Tol or Ln = Sm; R = C_2Ph_2; **B** Ln = La, Ce, Nd, Sm, Lu, Y; **C** Ln = Gd, Tb, Dy, Y; **D** Ln = Y.[7, 9, 11d, 18b, 22, 24-25, 30]

A different approach for the synthesis of $\mathbf{2^{Ln}}$ was developed by TEUBEN and MARKS utilizing the thermally robust rare-earth metallocenes $\mathbf{17^{Ln}}$ (Ln = La, Ce, Nd, Sm, Lu, Y)[18b, 22, 24-25] to access hydrides across the lanthanide series (Scheme 17, **B**). In benzene solutions spectroscopic

data strongly suggest a dimeric constitution for complexes $\mathbf{2^{Ln}}$ of the larger lanthanides Nd and Ce, while the lutetium compound $\mathbf{2^{Lu}}$ appeared significantly dissociated,[22, 24] which is in good agreement with previous findings by WATSON.[6a]

A further route toward the synthesis of rare-earth-metallocene hydrides was investigated by EVANS and coworkers utilizing metallocene allyls [Cp*$_2$Ln(C_3H_5)] ($\mathbf{26^{Ln}}$) to isolate the hydrides $\mathbf{2^{Ln}}$ for Gd, Tb, Dy and Y (Scheme 17, **C**).[30a, b] This synthesis protocol allows the synthesis of such hydride compounds even in the solid state (Scheme 17, **D**).[30c]
According to X-ray diffraction analysis the crystal structures of $\mathbf{2^{Gd}}$ and $\mathbf{2^{Tb}}$ have the same space group *C*2/*c* as revealed for $\mathbf{2^{Sm}}$. However, the hydride positions could be located only for $\mathbf{2^{Tb}}$. Thus, the symmetric dimer [Cp*$_2$Tb(μ-H)$_2$TbCp*$_2$] with two bridging hydrido ligands was found (Chart 1, **A**). On the other hand, for the smaller rare-earth metal dysprosium the XRD analysis revealed an asymmetrical dimer [Cp*$_2$Dy(μ-H)DyHCp*$_2$] (Chart 1, **B**).[30b] The same structural motif was elucidated for the yttrium derivative $\mathbf{2^{Y}}$ in a different study.[30c]

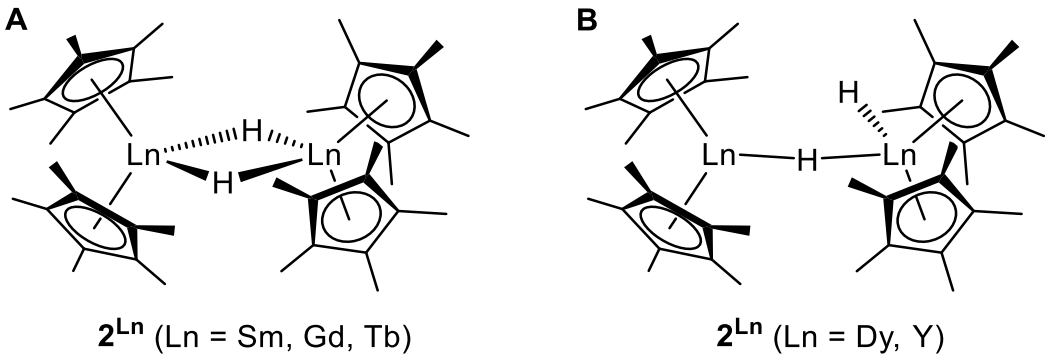

Chart 1. Structural motifs of hydride complexes $\mathbf{2^{Ln}}$; **A** Ln = Sm, Gd, Tb; **B** Ln = Dy, Y.[11d, 17, 30b]

The hydride compounds $\mathbf{2^{Ln}}$ (Ln = La, Sm, Nd, Lu, Y, Sc) show a rapid H/D exchange at ambient temperatures in C_6D_6 solutions (Scheme 18).[9a, 22, 25] The exchange rates increase with decreasing rare-earth-metal size.[22]

Furthermore, compounds $\mathbf{2^{Ln}}$ (Ln = Lu, Sc)[7, 9] are in rapid equilibrium with the phenyls $\mathbf{3^{Ln}}$ in benzene solutions wherein hydrogen is liberated (Scheme 10, **A**; Scheme 18). Noteworthy, the formation of $\mathbf{3^{Lu}}$ in minor amounts was observed whereas benzene solutions of $\mathbf{2^{Sc}}$ predominantly contain $\mathbf{3^{Sc}}$.

The coordination of pyridine to $\mathbf{2^{Ln}}$ (Ln = Lu, Sc, Y) leads to metalation at the 2-position of pyridine and concomitant evolution of hydrogen (Scheme 18).[7, 9, 31]

Compounds $\mathbf{2^{Ln}}$ are thermally labile and thermolysis starting at ambient temperature liberates hydrogen to form tuck-over hydrides $\mathbf{16^{Ln}}$ (Ln = Y, Lu, Er, Sm, La; Scheme 18).[18c, 30c, 32]

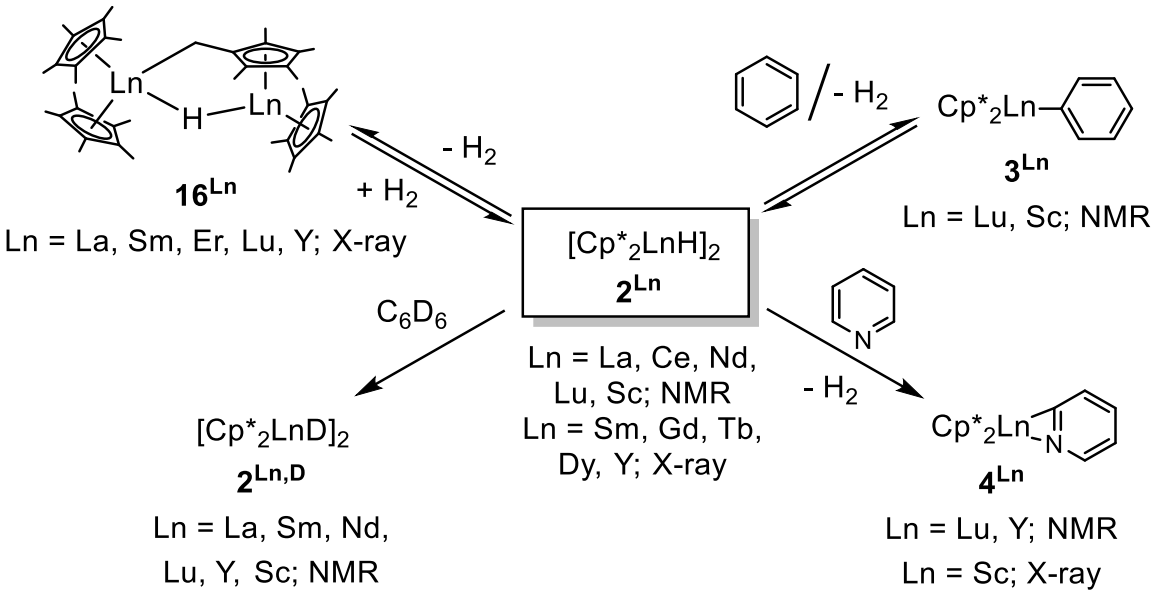

Scheme 18. Reactivity of $\mathbf{2^{Ln}}$ and reaction products characterized by single crystal XRD or NMR spectroscopy.[7, 9, 18c, 22, 25, 30c, 31-32]

B

Summary of the Main Results

1 Metalation of THF by Rare-Earth-Metallocene Tetramethylaluminates

(Half-)sandwich rare-earth-metal complexes are routinely used to perform polymerization, heterofunctionalization, and hydrometalation reactions by initial alkyl or vinylic C–H-bond activation.[9b, 13, 22, 33] However, metalation of cyclic ethers commonly results either in ring opening or intractable degradation reactions since the high negative charge at the oxygen atom causes severe destabilization of the ring system.[34] Accordingly, it appears to be very difficult to balance the high basicity crucial for C–H-bond activation and to stabilize the highly charged α-carbon atom. Hence, structurally characterized 2-tetrahydrofuranyl compounds are exceedingly rare and not described for rare-earth-metal complexes. We thus investigated further into the reactivity of heterobimetallic rare-earth metallocene tetramethylaluminate compounds toward THF (**Paper III**).

As reported in literature, treating [Cp*$_2$Y(AlMe$_4$)] with THF affords [Cp*$_2$YMe(THF)] by donor-induced aluminate cleavage.[5] However, further thermal treatment of [Cp*$_2$YMe(THF)] in THF solutions led to complete consumption of the starting material and extrusion of methane. The ^{1}H NMR spectrum of the crude products accounted for the presence of vinyl oxide compound [Cp*$_2$Y(OC$_2$H$_3$)(THF)] (**A**) and chiral ethylene-2-tetrahydrofuranyl compound [Cp*$_2$Y(2-C$_2$H$_4$-OC$_4$H$_7$)] (**B**) in the ^{1}H NMR spectrum (Scheme S1) in an approximate ratio of 3:2. Fractional crystallization from *n*-pentane solutions allowed for the separation of **A** and **B** and their isolation in high purities. The obtained solid-state structures depicted in Figure S1 revealed that yttrocene compounds **A** and **B** are monomeric in the solid state.

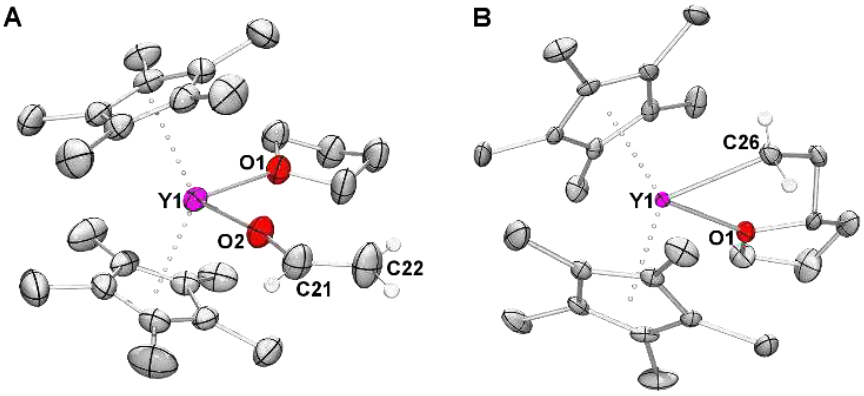

Figure S1. A: Solid-state structure of [Cp*$_2$Y(OC$_2$H$_3$)(THF)] (**A**); **B:** Solid-state structure of [Cp*$_2$Y(2-C$_2$H$_4$-OC$_4$H$_7$)] (**B**).

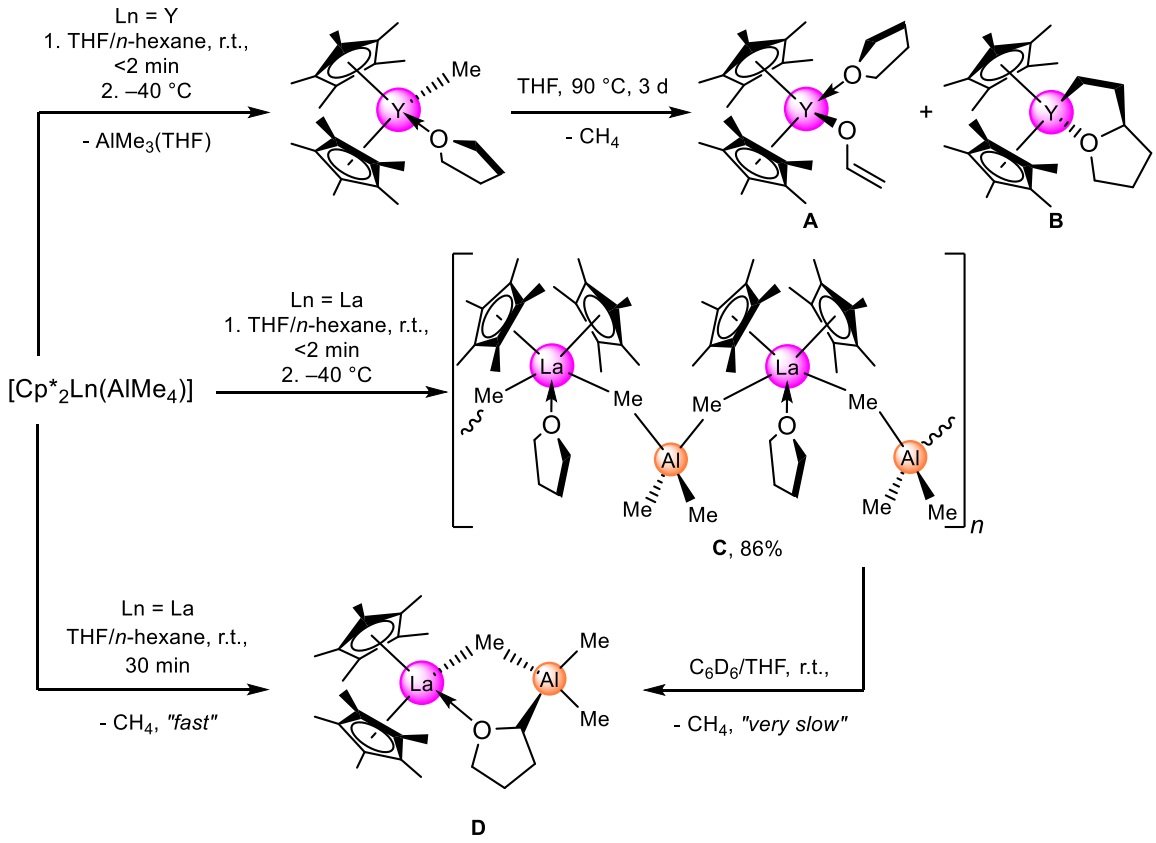

Scheme S1. Metalation of THF by [Cp*$_2$Ln(AlMe$_4$)] (Ln = Y, La).

A mechanistic scenario for the formation of **A** and **B** involves THF degradation and ethylene insertion (Scheme S2). The reaction proceeds presumably via σ-bond metathesis of [Cp*$_2$YMe(THF)] (step **i**) under elimination of methane to form transient tetrahydrofuranyl compound [Cp*$_2$Y(η^2-OC$_4$H$_7$)]. Subsequent cleavage of THF under release of ethylene[34a] and addition of a second THF molecule would afford compound **A** (stepp **ii**). The liberated ethylene adds to [Cp*$_2$Y(η^2-OC$_4$H$_7$)] and inserts at the α position to produce compound **B** (step **iii**).

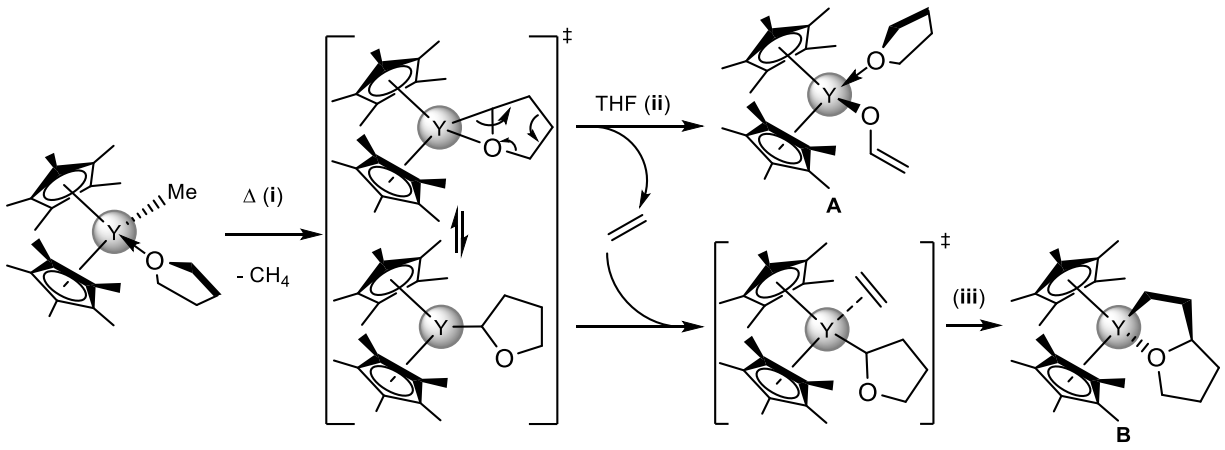

Scheme S2. Possible reaction sequence for THF C–H-bond activation and rearrangements to afford **A** and **B**.

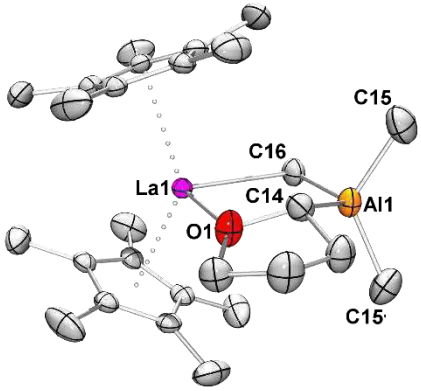

Figure S2. Solid-state structure of $[Cp^*_2La(2\text{-}AlMe_3\text{-}OC_4H_7)]$ (**D**).

In stark contrast, treatment of $[Cp^*_2La(AlMe_4)]$ with THF (<2 min) and subsequent crystallization from THF/*n*-hexane mixtures at –40 °C did not result in cleavage of the $[AlMe_4]$ unit to form elusive $[Cp^*_2LaMe(THF)]$, but afforded polymeric $[Cp^*_2La\{(\mu\text{-}Me)_2AlMe_2\}(THF)]_n$ (**C**) in high yields (Scheme S1). At ambient temperature compound **C** is, however, labile benzene/THF mixtures and slowly converts to compound $[Cp^*_2La(2\text{-}AlMe_3\text{-}OC_4H_7)]$ (**D**) under elimination of methane. Much to our delight, stirring a solution of $[Cp^*_2La(AlMe_4)]$ in THF/*n*-hexane for 30 minutes at ambient temperature resulted in quantitative formation of **D**. In contrast to **B**, degradation of THF and formation of ethylene did not occur under these conditions. Single crystal X-ray analysis revealed a monomeric constitution of **D** and unequivocally evidenced the formation of $AlMe_3$ stabilized 2-tetrahydrofuranyl lanthanocene (Figure S2), representing the first structurally characterized rare-earth metal complex featuring a 2-tetrahydrofuranyl moiety.

2 Methyl/Iodide Exchange by Rare-Earth-Metallocene Tetramethylaluminates

Iodide complexes of the rare-earth metals can be advantageous precursors for salt-metathesis reactions over the lighter halide analogues in order to prevent ate complexation. Fortunately, the high affinity of the lanthanides toward halides allows for straightforward alkyl/halide exchange. As such, DIETRICH et al. utilized Me_3SiI on half-sandwich compounds $[Cp^*Ln(AlMe_4)_2]$ (Ln = Y, La, Lu) under elimination of volatile $SiMe_4$ and $AlMe_3$ concomitant with the formation of $[Cp^*LnI_2]_x$ (Ln = Y, $x = 4$; La, $x = 9$).[35] Spurred by this study the concept was adopted for readily accessible lanthanide metallocenes $[Cp^*_2Ln(AlMe_4)]$ (Ln = Y, La) to facilitate access to rare-earth metallocene iodide complexes $[Cp^*_2LnI]_x$.

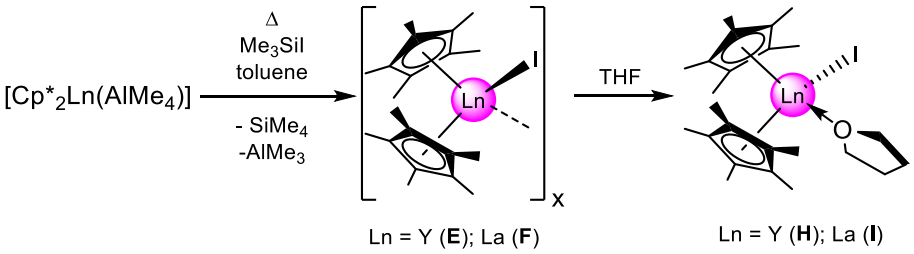

Scheme S3. Methyl/iodide exchange by $[Cp^*_2Ln(AlMe_4)]$ (Ln = Y, La) and Me_3SiI.

Treating $[Cp^*_2Ln(AlMe_4)]$ (Ln = Y, La) with one equivalent Me_3SiI at 90-100 °C afforded the corresponding solvent-free rare-earth metallocene iodide complexes $[Cp^*_2YI]_x$ (**E**) and $[Cp^*_2LaI]_x$ (**F**) in quantitative yields as amorphous powders (Scheme S3). Compounds **E** and **F** are insoluble in hydrocarbons and aromatic solvents, impeding recrystallization to afford single crystals suitable for X-ray analysis while condensing excess Me_3SiI at ambient temperature to a saturated benzene solution of $[Cp^*_2(LaAlMe_4)]$ resulted in the formation of $[Cp^*_4La_4(\mu_4\text{-}I)(\mu_3\text{-}I)_2(\mu\text{-}I)_6LaCp^*_2]$ (**G**) (Figure S3).

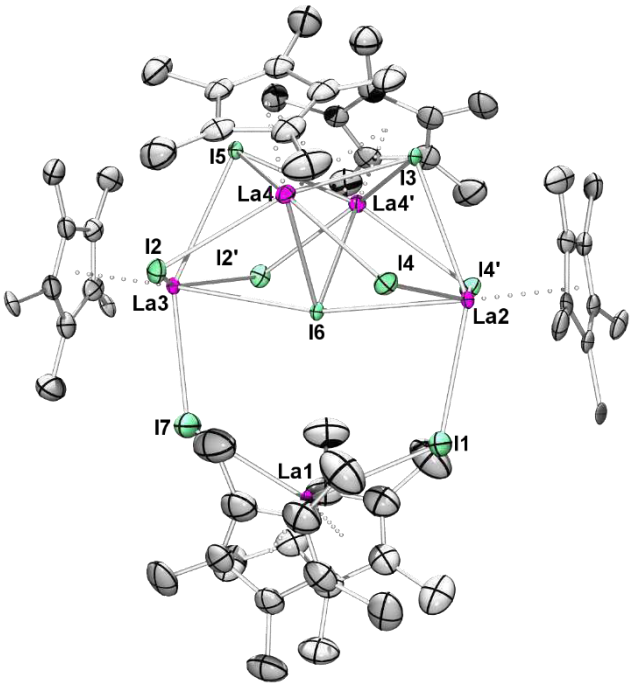

Figure S3. Connectivity of $[Cp^*_4La_4(\mu_4\text{-}I)(\mu_3\text{-}I)_2(\mu\text{-}I)_6LaCp^*_2]$ (**G**).

However, **E** and **F** readily dissolve in THF to form monomeric [Cp*$_2$YI(THF)] (**H**) and [Cp*$_2$LaI(THF)] (**I**), respectively. The ^{1}H NMR spectra in THF-d_8 show one singlet for the Cp* ligands. The high purity of compounds **E** and **F**, respectively, is emphasized by the absence of signals diagnostic for $AlMe_3$(THF). In the solid state, compounds **H** and **I** are isostructural with comparable Ln–I distances (Y–I = 3.009(1) Å; La–I = 3.161(2) Å, Figure S4), considering the differences in the ionic radii.

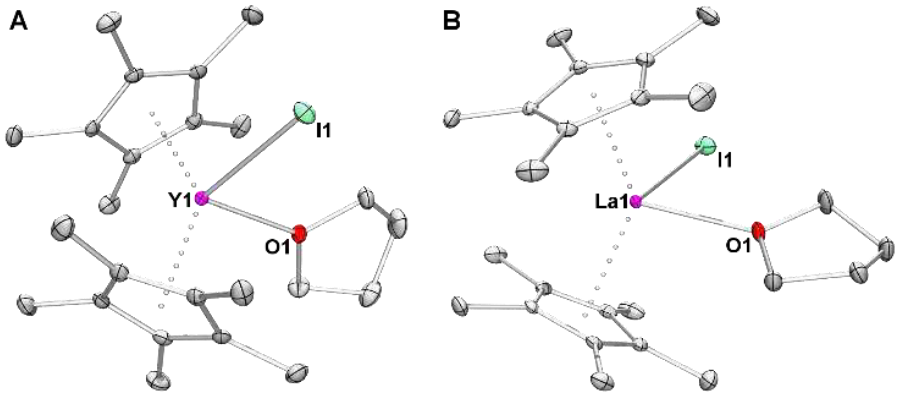

Figure S4. A: Solid-state structure of [Cp*$_2$YI(THF)] (**H**); **B**: solid-state structure of [Cp*$_2$LaI(THF)] (**I**).

3 C–H-Bond Activation by Rare-Earth-Metallocene Complexes

Rare-earth-metallocene methyl complexes $[Cp^*_2LnMe]_x$ (x = 1, Ln = Sc; x = 2, Ln = Y, Lu; x = 3, Ln = Sm) display extraordinary reactivity in hydrogenolysis and C–H-bond activation reactions toward various substrates, for instance, benzene, toluene, pyridine and tetramethylsilane.[6a, 7, 9, 11c,d, 12, 17] Initial studies in this field by WATSON and BERCAW in the 1980s identified σ-bond metathesis as the most important mechanism for C–H bond activation by lanthanide(III) complexes.

The associated rare-earth-metallocene tetramethylaluminates and -gallates, $[Cp^*_2Ln(MMe_4)]$ (M = Al, Ga), can be described as the formal addition products of MMe_3 and $[Cp^*_2LnMe]$. The saturated coordination sphere at the rare-earth-metal center is beneficial in terms of relatively high thermal robustness at ambient temperature and increased solubility in aromatic solvents. However, $[Cp^*_2Ln(MMe_4)]$ and $[Cp^*_2LnMe]_x$ show comparable reactivities, for example, as pre-catalysts in ethylene polymerization. Moreover, considering the concept of the reversible donor-induced tetramethylaluminate cleavage reaction,[4] we were intrigued if further analogies could be derived with respect C–H bond activation of benzene (**Paper IV**).

3.1 Yttrocene Derivatives

In an initial attempt, treatment of $[Cp^*_2Y(AlMe_4)]$ in benzene solutions at 100 °C for 42 hours (Scheme S4) resulted in liberation of methane and formation of $[Cp^*_2Y(Me_2AlPh_2)]$ (**J**) in high yield, while no reaction was observed at 90 °C. In analogy to the starting material $[Cp^*_2Y(AlMe_4)]$, the ^{1}H NMR spectrum of compound **J** features two sets of signals, accounting for a monomer-dimer equilibrium at ambient temperatures in C_6D_6 solutions.

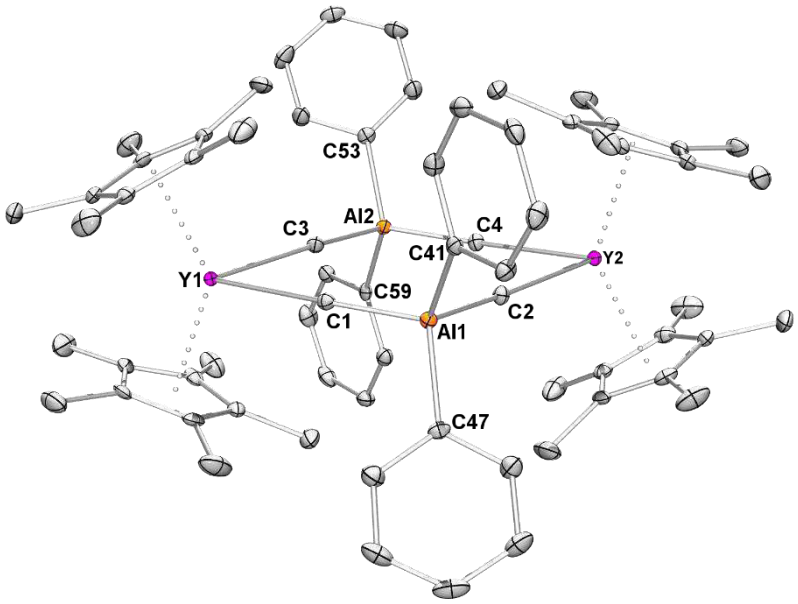

Figure S5. Solid-state structure of $[Cp^*_2Y(Me_2AlPh_2)]$ (**J**).

However, the solid-state structure of **J** (Figure S5) is exclusively represented by the dimer exhibiting a characteristic eight-membered heterobimetallic ring.

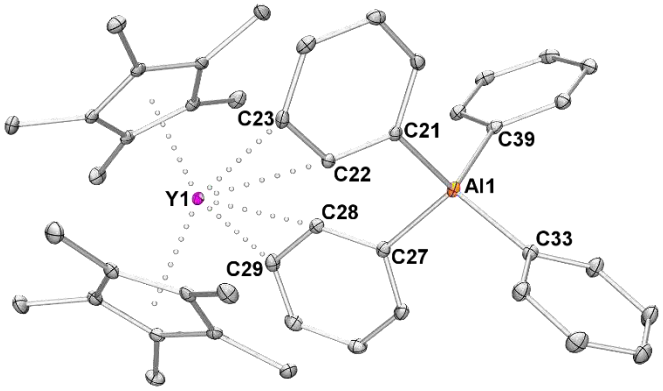

Figure S6. Solid-state structure of [Cp*$_2$Y(AlPh$_4$)] (**K**).

Further thermal treatment at 120 °C pushed the reaction to the perphenylated product with complete methyl/phenyl exchange after 6 days and hence, [Cp*$_2$Y(AlPh$_4$)] (**K**) was isolated as bright yellow powder in 16% yields (Scheme S4). The ^{1}H NMR spectrum clearly corroborates the absence of any Al–Me functionalities and shows instead a set of signals attributed to the phenyl groups, indicating fast dynamic exchange processes in solution. The solid-state structure of **K** (Figure S6) is reminiscent of the tetraphenylborate complex [Cp*$_2$Y(BPh$_4$)].[20] However, the [AlPh$_4$]$^-$ anion is sterically more demanding than [BPh$_4$]$^-$ due to elongated M–C(phenyl) atom distances (M = Al, av 2.007 Å; B, av 1.638 Å).

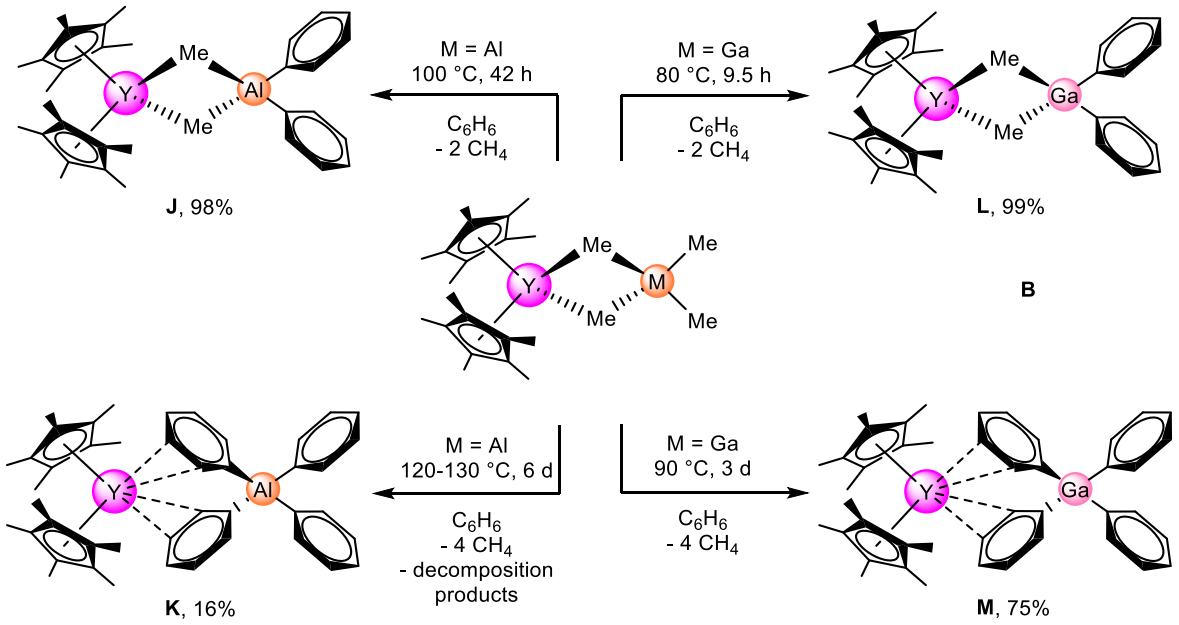

Scheme S4. Multiple methyl/phenyl exchange by [Cp*$_2$Y(MMe$_4$)] (M = Al, Ga) at elevated temperatures in benzene.

A similar reactivity was observed for the corresponding tetramethylgallate complex [Cp*$_2$Y(GaMe$_4$)], but C–H-bond activation took place already at 80 °C in benzene solutions (Scheme S4). Hence, thermal treatment of [Cp*$_2$Y(GaMe$_4$)] for 9.5 hours in benzene solutions

produced [Cp*$_2$Y(Me$_2$GaPh$_2$)] (**L**) and [Cp*$_2$Y(GaPh$_4$)] (**M**) after heating [Cp*$_2$Y(GaMe$_4$)] for 3 days at 90 °C, respectively, in high yields. Not surprising, the ^{1}H NMR spectra of compounds **L** and **M** resemble those of the aluminum counterparts and the solid-state constitution of **L** and **M** represent structural analogs of the aluminum congeners with similar metrical parameters.

For deeper insights in the dynamic behavior of **J**, **K**, **L**, and **M** variable-temperature (VT) ^{1}H NMR studies in toluene-d_8 were performed. At elevated temperatures, the mixed methyl/phenyl compounds [Cp*$_2$Y(Me$_2$MPh$_2$)] shift to the monomeric species, which is in line with reports on the starting material [Cp*$_2$Y(MMe$_4$)].[5, 6c, 36] Strikingly, the required temperature for benzene activation matches the temperatures where the monomer is exclusively present (M = Al, 100 °C; Ga, 80 °C). Unexpectedly, the VT ^{1}H NMR experiment of the tetraphenylgallate [Cp*$_2$Y(GaPh$_4$)] (**M**) is indicative of a pronounced equilibrium of **M** with [Cp*$_2$YPh] and [GaPh$_3$]. At temperatures above 40 °C the singlet resonance at 1.78 ppm is attributed to [Cp*$_2$YPh], merging to a broad signal (1.67 ppm) at 10 °C. Further cooling led to splitting to a minor signal at 1.78 ppm and a dominant singlet at 1.48 ppm, attributed to **M**. Apparently, **M** is labile in solution and dissociates to [Cp*$_2$YPh] and [GaPh$_3$]. A similar behavior was observed at variable temperatures for the tetraphenylaluminate [Cp*$_2$Y(AlPh$_4$)] (**K**). Hence, at temperatures below –10 °C a minor singlet at 1.78 ppm is detected, indicative for traces of [Cp*$_2$YPh], and a dominant resonance signal at 1.48 ppm, in accord with **K**. However, at elevated temperatures no further dissociation was observed. Probably, temperatures higher than 80 °C are necessary to dissociate the [AlPh$_4$]$^-$ anion.

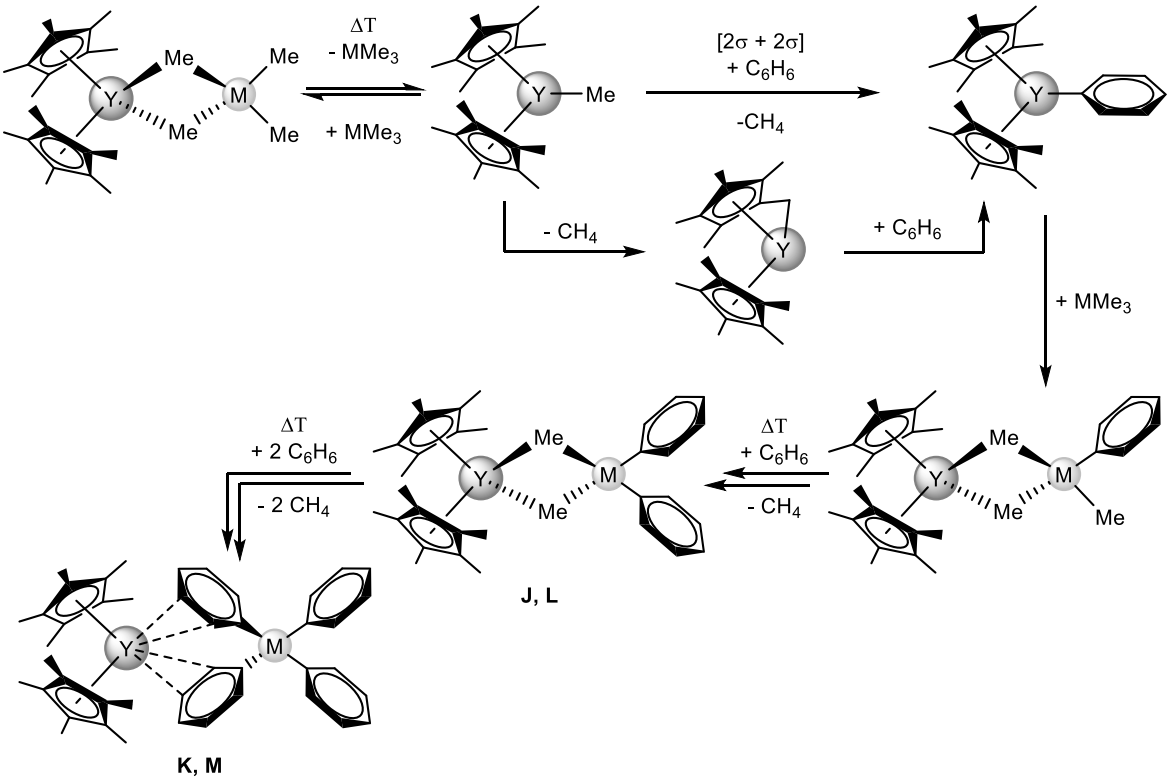

Scheme S5. Possible scenario for benzene activation by [Cp*$_2$Y(MMe$_4$)] (M = Al, Ga).

The reactivity of [Cp*$_2$Y(AlMe$_4$)] revealed striking parallels to metallocenes [Cp*$_2$LnMe]$_x$.[6a, 7, 9b, 11c] Hence, a rational reaction sequence involves the liberation of [Cp*$_2$YMe] by initial dissociation of the Lewis acid [MMe$_3$] from the starting material [Cp*$_2$Y(MMe$_4$)] (Scheme S5). This scenario is indicated by (a) enhanced reactivity of the tetramethyl gallate compound [Cp*$_2$Y(GaMe$_4$)] due to reduced bond strength of the associated Lewis acid GaMe$_3$, (b) a substantial H/D kinetic isotope effect, diagnostic for σ-bond metathesis and (c) extrusion of CH$_4$ and CDH$_3$ concomitant with the activation of C$_6$D$_6$, accounting for two competing reaction pathways, namely, four-centered transition state vs. “tuck-in” complex, resembling the benzene activation by [Cp*$_2$LnMe] (Ln = Sc, Y, Lu, Sm).

To underpin a dissociative scenario the sterically demanding boryl moiety $\{B(NDippCH)_2\}^-$ was utilized to achieve a kinetically more labile yttrocene derivative. As such, $[Cp^*_2Y(Me_3Al\{B(NDippCH)_2\})]$ (**N**) was synthesized by a salt-metathesis protocol employing half-sandwich complex $[Cp^*Y(Me_3Al\{B(NDippCH)_2\})_2]$ and KCp* (Scheme S6). Strikingly, **N** slowly activates benzene already at ambient temperatures, and hence, the corresponding complexes $[Cp^*_2Y(Me_2AlPh\{B(NDippCH)_2\}]$ (**O**) and $[Cp^*_2Y(Ph_3Al\{B(NDippCH)_2\}]$ (**P**) were readily accessed at 60 - 80 °C in high yields (Scheme S6). The pivotal role of the $[Cp^*_2Y]$ functionality for C–H bond activation was elucidated by investigations on the less congested compound $[Cp_2Y(Me_3Al\{B(NDippCH)_2\})]$ (**Q**), displaying a structural analog to that of **N** (Figure S8). However, **Q** is stable in benzene solutions up to 130 °C and hence, no benzene activation was observed. Moreover, $AlMe_3$, $GaMe_3$, and $[Me_2Al\{B(NDippCH)_2\}]$, respectively, are inert in benzene solutions at 110 °C. Thus, a dissociative scenario to liberate highly reactive $[Cp^*_2YMe]$ is straight in line with these findings.

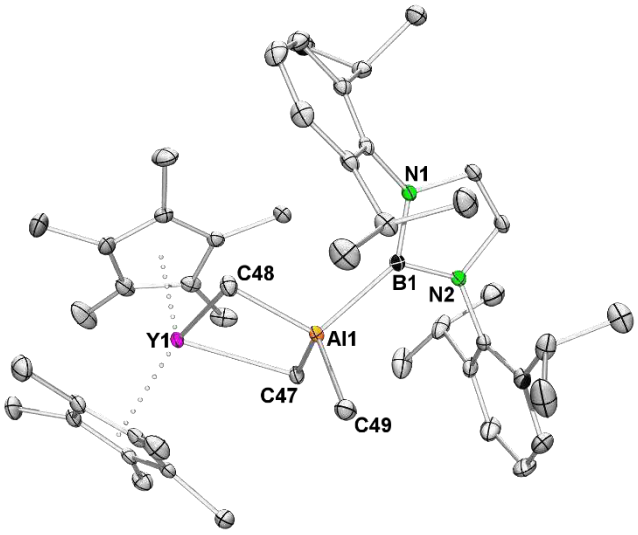

Figure S7. Solid-state structure of $[Cp^*_2Y(Me_3Al\{B(NDippCH)_2\})]$ (**N**).

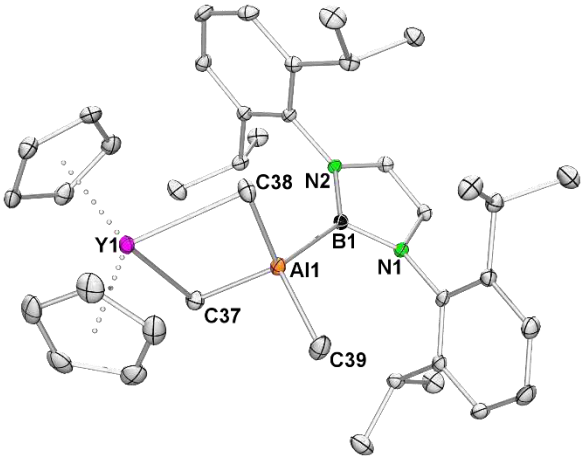

Figure S8. Solid-state structure of $[Cp_2Y(Me_3Al\{B(NDippCH)_2\})]$ (**Q**).

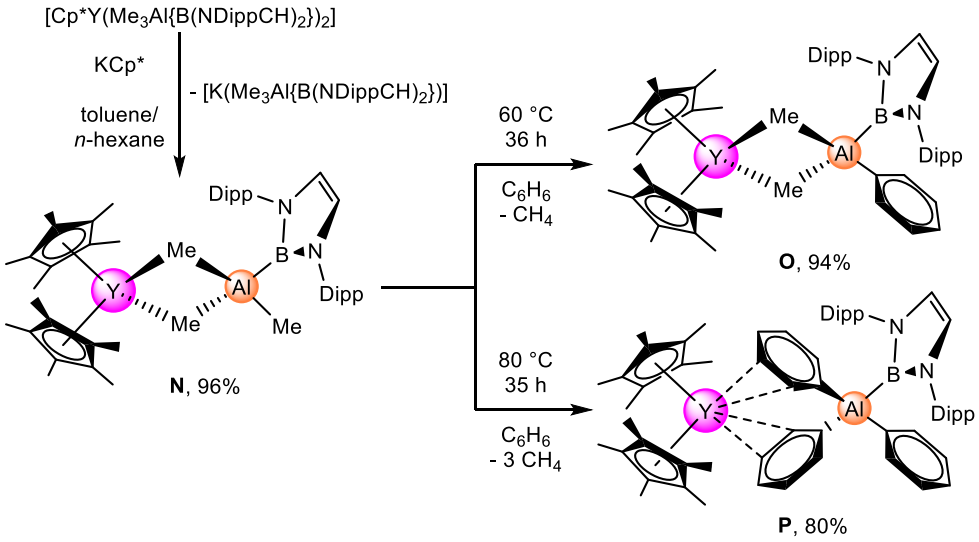

Scheme S6. Synthesis of [Cp*$_2$Y(Me$_3$Al{B(NDippCH)$_2$}] (**N**) and reactivity toward benzene.

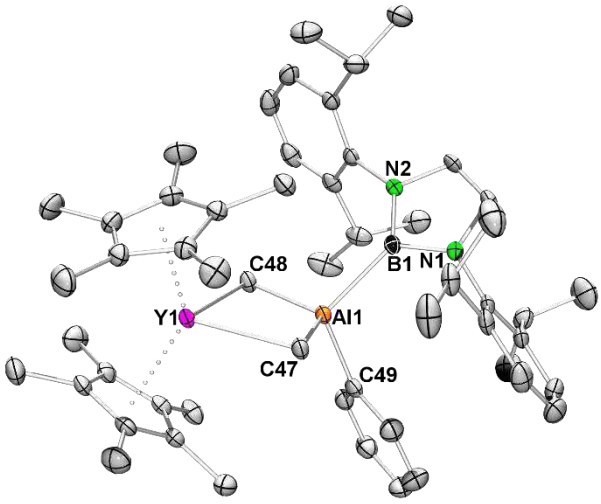

Figure S9. Solid-state structure of [Cp*$_2$Y(Me$_2$AlPh{B(NDippCH)$_2$})] (**O**).

VT ^{1}H NMR experiments of **N** in the range of –80 °C to 80 °C in toluene disclosed that **N** does neither form dimers in solution, nor dissociates into [Cp*$_2$YMe] and [Me$_2$Al{B(NDippCH)$_2$}] at elevated temperatures. Consequently, the solid-state constitution of **N** is represented by a monomer (Figure S7). In complete accordance, **O** forms monomers in solution and in the solid state (Figure S9) and no dissociation can be documented by VT ^{1}H NMR measurements up to 100 °C.

However, fully exchanged **P** displace an equilibrium in benzene solutions at ambient temperature, dissociating into [Cp*$_2$YPh] and [Ph$_2$Al{B(NDippCH)$_2$}]. This dissociation is complete at 80 °C. This is in good agreement with the dynamic behavior of **K** and **M** revealed by ^{1}H NMR spectroscopy at variable temperatures. Moreover, the solid-state constitution of **P** (Figure S10) is reminiscent to those found for **K** and **M**.

The high propensity of weakly coordinating anions $[MPh_4]^-$ (M = Al, Ga) and $[Ph_3Al\{B(NDippCH)_2\}]^-$, respectively, for phenyl transfer to form $[Cp^*_2YPh]$ was investigated by THF adduct formation. As such, addition of THF to a solution of **K** and **M**, respectively, in C_6D_6 at ambient temperatures resulted in formation of the solvent-separated ion pairs $[Cp^*_2Y(THF)_2][MPh_4]$ (M = Al, Ga), evidenced by ^1H NMR spectroscopy. At elevated temperatures formation of $[Cp^*_2YPh(THF)]$ (**R**) is observed, accompanied by $AlPh_3(THF)$ and $GaPh_3$, respectively. However, all attempts to determine the solid-state structures of $[Cp^*_2Y(THF)_2][MPh_4]$ failed. While conversion of $[Cp^*_2Y(THF)_2][AlPh_4]$ to **R** and $AlPh_3(THF)$ is irreversible in benzene solutions, $[Cp^*_2Y(THF)_2][GaPh_4]$ gradually recovers from **R** and $GaPh_3$ upon cooling to ambient temperatures. Since **P** is in pronounced equilibrium with $[Cp^*_2YPh]$ and $[Ph_2Al\{B(NDippCH)_2\}]$ in benzene solutions addition of THF resulted in simultaneous formation of $[Cp^*_2Y(THF)_2][Ph_3Al\{B(NDippCH)_2\}]$ (**S**), **R**, and $[Ph_2Al\{B(NDippCH)_2\}(THF)]$. Most fortunately, the concomitant crystallization of compounds **R** and **S** as colorless and pale-yellow crystals, respectively, allowed for solid-state structure analysis. As such, the solid-state structures of **R** (Figure S11) and **S** (Figure S12) emphasize the presence of a dissociative equilibrium of **P** with $[Cp^*_2YPh]$ and $[Ph_2Al\{B(NDippCH)_2\}]$ in benzene solutions.

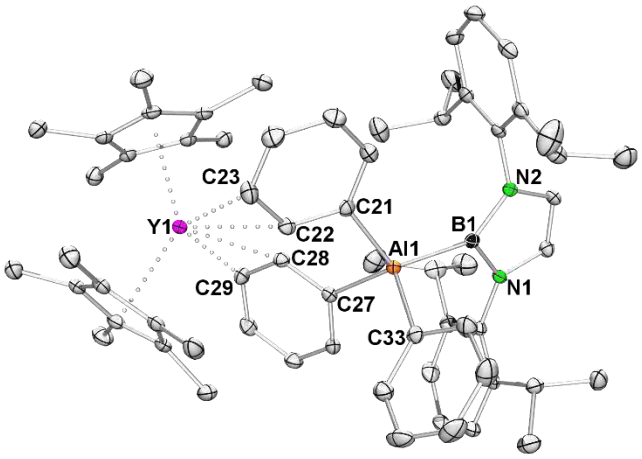

Figure S10. Solid-state structure of $[Cp^*_2Y(Ph_3Al\{B(NDippCH)_2\})]$ (**P**).

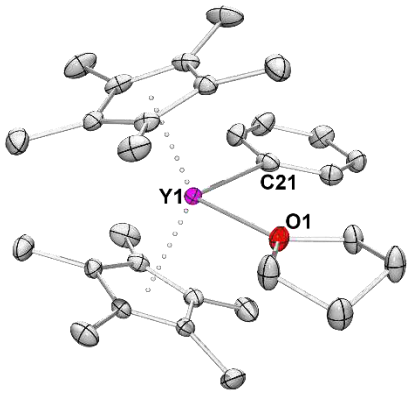

Figure S11. Solid-state structure of $[Cp^*_2YPh(THF)]$ (**R**).

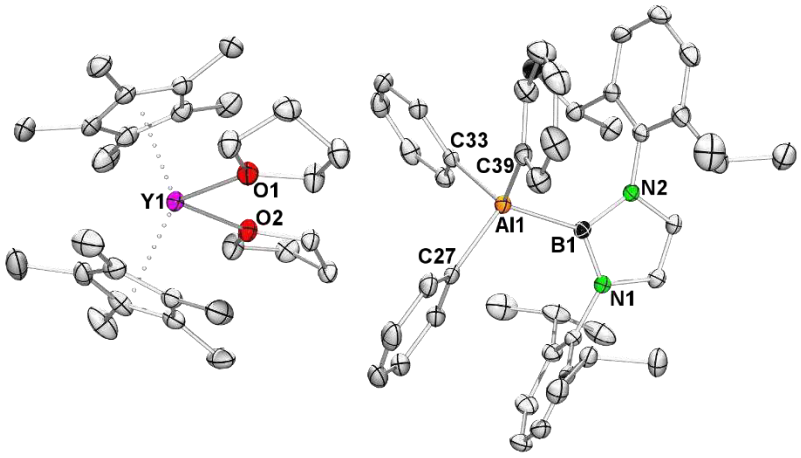

Figure S12. Solid-state structure of $[Cp^*_2Y(THF)_2][(Ph_3Al\{B(NDippCH)_2\})]$ (**S**).

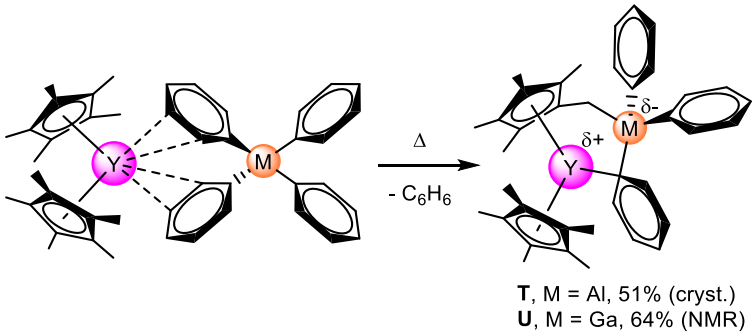

Scheme S7. Metalation of the ancillary ligand Cp* in [Cp*$_2$Y(MPh$_4$)] to form zwitterionic compounds [Cp*Y{C$_5$Me$_4$[μ-CH$_2$]MPh$_2$}] (M = Al, **T**; Ga, **U**).

Prolonged thermal treatment of [Cp*$_2$Y(MPh$_4$)] (M = Al, **K**; Ga, **M**) led to C–H bond activation of the Cp* ligand under elimination of benzene to afford zwitterionic complexes [Cp*Y{C$_5$Me$_4$(μ-CH$_2$)MPh$_3$}] (M = Al, **T**; Ga, **U**; Scheme S7; **Paper V**). In the solid state, **T** and **U** feature almost identical metrical parameters with one phenyl group in bridging position between the metal atoms (Figure S13). At ambient temperatures complex **T** is stable in deuterated benzene solutions. Hence, C_6H_5/C_6D_5 exchange was not observed. According to previous findings, a rational reaction sequence involves dissociation of **K** and **M**, respectively, to form [Cp*$_2$YPh] and MPh$_3$ (Scheme S8). [Cp*$_2$YPh] possibly undergoes intramolecular σ-bond metathesis to eliminate benzene and form the "tuck in" complex [Cp*Y{C$_5$Me$_4$(μ-CH$_2$)}] followed by insertion of MPh$_3$ to generate **T** and **U**. As such, compounds **T** and **U** can be considered as Lewis-acid stabilized "tuck in" complexes of [Cp*Y{C$_5$Me$_4$(μ-CH$_2$)}].

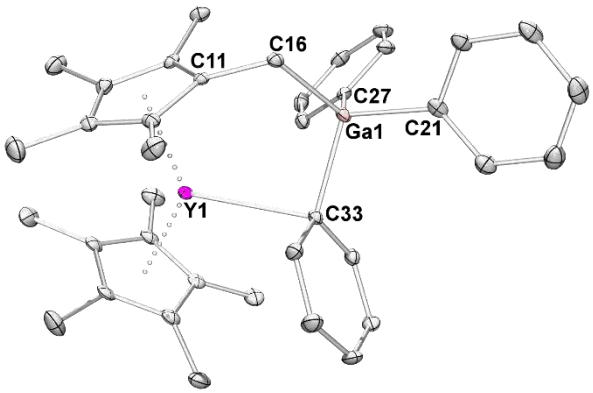

Figure S13. Solid-state structure of [Cp*Y{C$_5$Me$_4$(μ-CH$_2$)GaPh$_3$}] (**U**).

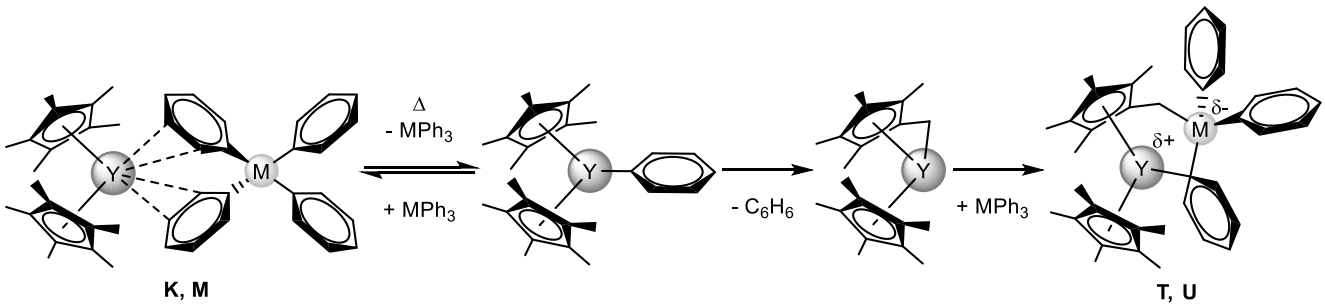

Scheme S8. Possible scenario for the activation of the ancillary ligand Cp* by [Cp*$_2$Y(MPh$_4$)] (M = Al, Ga).

3.2 Lutetacene Derivatives

Having demonstrated the powerful deprotonating capability of [Cp*$_2$Y(AlMe$_4$)] at elevated temperatures we decided to extend our research to the lutetium analog [Cp*$_2$Lu(AlMe$_4$)] since C–H-bond activation of benzene was demonstrated for [Cp*$_2$LuMe] in the original reports on this topic by WATSON et al.[6a, 7]

As such, [Cp*$_2$Lu(AlMe$_4$)] was heated in benzene solutions to generate [Cp*$_2$Lu(Me$_2$AlPh$_2$)] (**V**). However, no reaction was observed at temperatures below 120 °C and hence, heating to 130 °C for 62 hours was necessary to access **V** in 57% yield aside other products (Scheme S9). Apparently, [Cp*$_2$Lu(AlMe$_4$)] is kinetically more stable than the yttrium analog. Probably, the stronger Lewis acid Lu^{3+} hampers the dissociation of AlMe$_3$. Moreover, [Cp*$_2$LuMe] is considerably less reactive in C–H bond activation reactions compared to [Cp*$_2$YMe][6a, 9b] most likely owing to the different ionic radii of the rare-earth-metal ions.

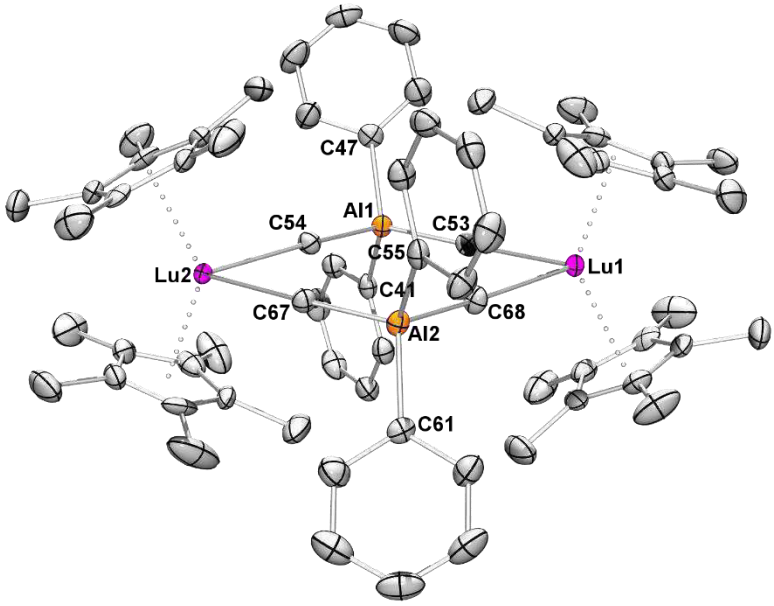

Figure S14. Solid-state structure of [Cp*$_2$Lu(Me$_2$AlPh$_2$)] (**V**).

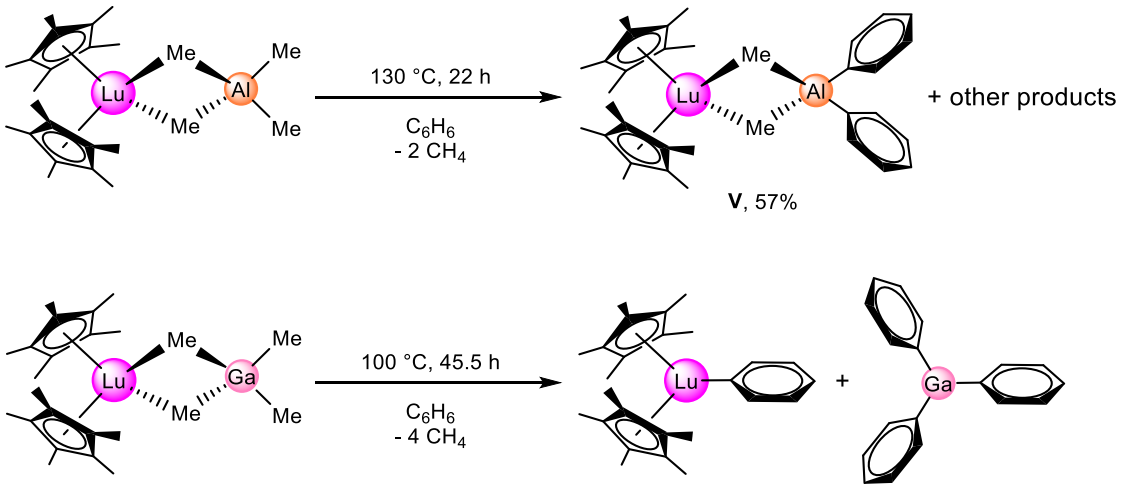

Scheme S9. Multiple methyl/phenyl exchange by [Cp*$_2$Lu(MMe$_4$)] (M = Al, Ga) at elevated temperatures in benzene.

According to ^{1}H NMR measurements compound **V** features a characteristic monomer-dimer equilibrium in C_6D_6 solutions and the solid-state structure (Figure S14) displays a structural analog of the yttrium congeners **J** and **L**.

In accordance with previous findings, the respective gallate compound [Cp*$_2$Lu(GaMe$_4$)] requires less forcing conditions to activate benzene, and hence, shows methyl/phenyl exchange already at 100 °C (Scheme S9). According to ^{1}H NMR experiments heteroaluminate compound [Cp*$_2$Lu(MeAlPh$_3$)] is formed after 15 hours and complete methyl/phenyl exchange occurred after 45.5 hours. However, no lutetacene derivatives could be crystallized from the reaction mixture. Instead GaPh$_3$ was isolated, repeatedly, as confirmed by X-ray diffraction measurements. Moreover, the ^{1}H NMR spectral data indicates the exclusive presence of [Cp*$_2$LuPh] and GaPh$_3$ by a characteristic singlet at 1.79 ppm and multiplets in the aromatic region at 7.76 (6 H, GaPh$_3$), 7.41 (2 H, LuPh), 7.31 (9 H, GaPh$_3$), 7.24 (1 H, LuPh), and 7.05 ppm (2 H, LuPh).[19b] Apparently, elusive [Cp*$_2$Lu(GaPh$_4$)] is not stable in solution at ambient temperatures and dissociates to form [Cp*$_2$LuPh] and GaPh$_3$, what is in line with previous findings for the yttrium analogs **K** and **M**.

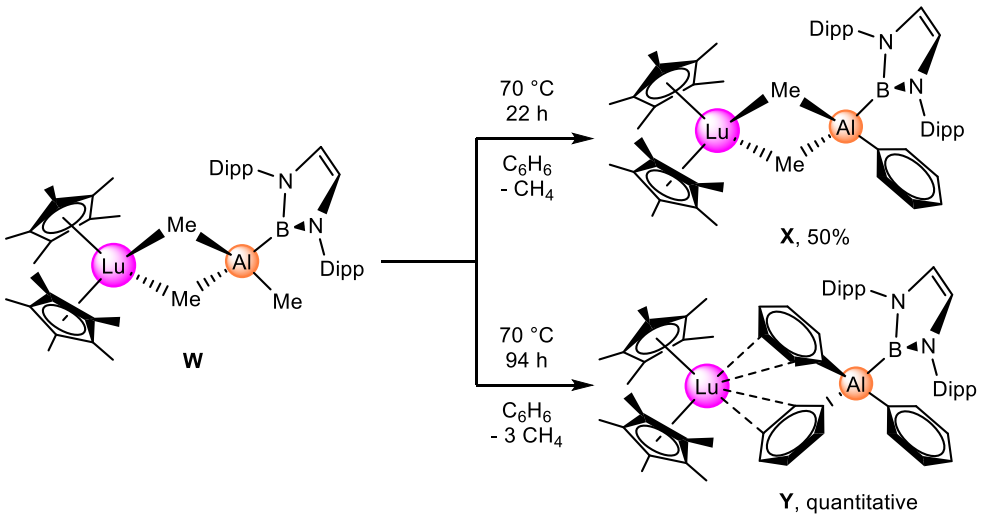

Scheme S10. Reactivity of [Cp*$_2$Lu(Me$_3$Al{B(NDippCH)$_2$}] (**W**) toward benzene.

For further comparative studies, [Cp*$_2$Lu(Me$_3$Al{B(NDippCH)$_2$})] (**W**) was synthesized in analogy to the yttrium compound **N**. In complete accordance to the yttrium analogs, utilizing the boryl moiety {B(NDippCH)$_2$}$^-$ led to a tremendous decrease of the activation temperature. As such, **W** formed [Cp*$_2$Lu(MeAlPh{B(NDippCH)$_2$})] (**X**) within 22 hours at 70 °C and complete methyl/phenyl exchange was confirmed after 94 hours to afford [Cp*$_2$Lu(Ph$_3$Al{B(NDippCH)$_2$})] (**Y**, Scheme S10). The ^{1}H NMR spectrum of **Y** revealed

complete dissociation of **Y** to [Cp*$_2$LuPh] and [Ph$_2$Al{B(NDippCH)$_2$}] at ambient temperature in C_6D_6 solutions, featuring a characteristic singlet resonance at 1.79 ppm. In the solid state, compounds **W** (Figure S15), **X** (Figure S16), and **Y** (Figure S17) are monomeric and display structural analogs of the respective yttrium complexes.

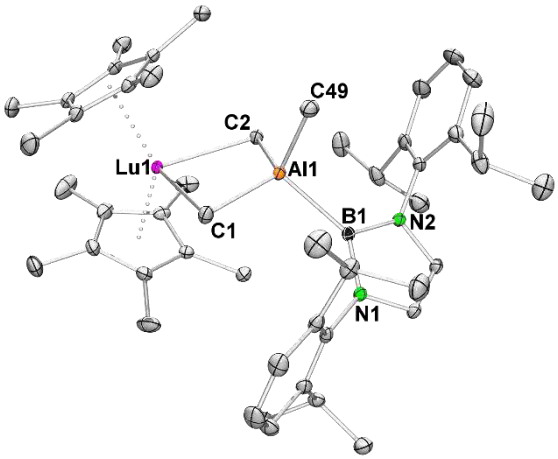

Figure S15. Solid-state structure of [Cp*$_2$Lu(Me$_3$Al{B(NDippCH)$_2$})] (**W**).

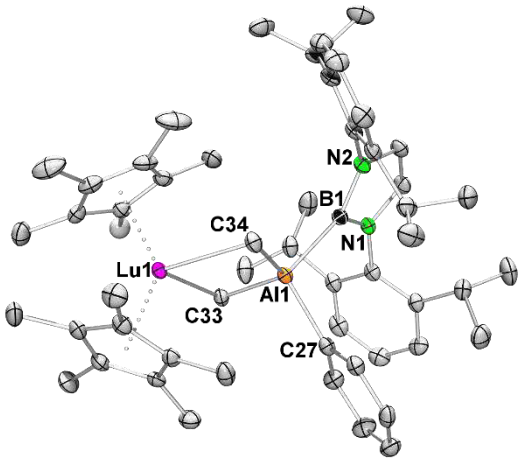

Figure S16. Solid-state structure of [Cp*$_2$Lu(Me$_2$AlPh{B(NDippCH)$_2$})] (**X**).

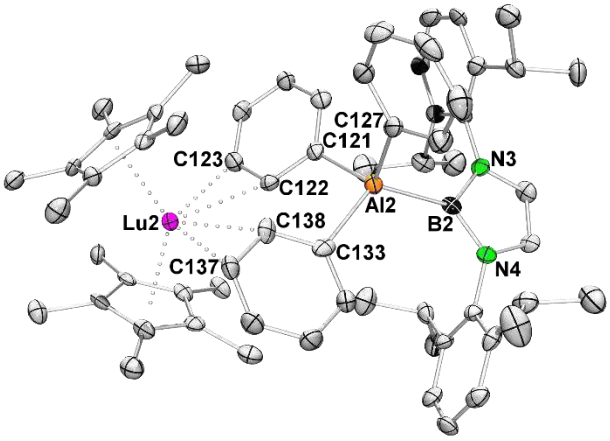

Figure S17. Solid-state structure of [Cp*$_2$Lu(Ph$_3$Al{B(NDippCH)$_2$})] (**Y**).

3.3 Lanthanocene Derivatives

Encouraged by the previous findings on benzene C–H-bond activation by metallocene derivatives of the smaller rare-earth metals yttrium and lutetium we wondered about the reactivity of [Cp*$_2$La(MMe$_4$) (M = Al, Ga), featuring the largest rare-earth metal congeners. The supposed reactive intermediate [Cp*$_2$LaMe] was synthesized previously by adding MeLi to tetraphenylborate [Cp*$_2$La(BPh$_4$)].[11c] So far, [Cp*$_2$LaMe] defied from structural characterization owing to its high reactivity. However, generation of the hydride [Cp*$_2$LaH] by reaction with hydrogen implied its existence. Accordingly, it is of interest if heated samples of [Cp*$_2$La(MMe$_4$)] would offer another route to study lanthanum-based C–H activation chemistry.

A sample of [Cp*$_2$La(AlMe$_4$)] was heated in C_6D_6 at 130 °C since temperatures below 120 °C did not result in C_6D_6 activation. After 6 days ^{1}H NMR measurements indicated formation of [Cp*$_2$La(MeAlPh$_3$)] and [Cp*$_2$La(AlPh$_4$)] (**Z**) in an approximate ratio of 2:1. However, crystals suitable for X-ray diffraction analysis were only achieved for **Z**. The crystal structure of **Z** (Figure S18) is reminiscent to that of tetraphenylborate [Cp*$_2$La(BPh$_4$)]. However, the longer Al–C bonds (av. 2.010 Å) compared to the B–C bonds (av. 1.647 Å) effect some deviations. As such, the closest La···C(Ph) distances in **Z** are found for C_{ortho} and C_{ipso} (C_{ortho} and C_{meta} in [Cp*$_2$La(BPh$_4$)]) and the La···Al distance (4.046 Å) is considerably shorter than found for the Y···Al distance in the yttrocene analog **K** (4.786 Å) and the La···B distance in [Cp*$_2$La(BPh$_4$)] (4.406 Å), respectively. Moreover, the phenyl rings in the closer proximity to the lanthanocene unit are somewhat bent away from the Al–C axis. Beside steric reasons this might be also indicative for stronger interactions between the phenyl moieties and the rare-earth metal in comparison to the yttrocene congener **K**.

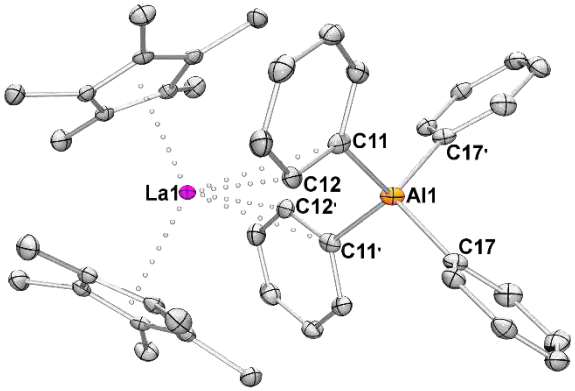

Figure S18. Solid-state structure of [Cp*$_2$La(AlPh$_4$)] (**Z**).

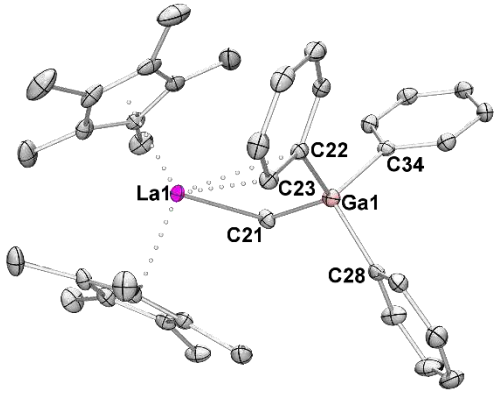

Figure S19. Solid-state structure of [Cp*$_2$La(MeGaPh$_3$)] (**AA**).

Similarly, a sample of [Cp*$_2$La(GaMe$_4$)] in C_6D_6 was heated to 100 °C for 3 days. The ^{1}H NMR

spectrum documented complete consumption of the starting material and formation of [Cp*$_2$La(MeGaPh$_3$)] (**AA**) as the main product. The crystal structure of **AA** (Figure S19) confirmed an odd substitution pattern which was not accessible for the smaller rare-earth metals. This is most likely a consequence of the less congested rare-earth metal center. In good agreement to the starting material **AA** is a monomer in the solid state with the methyl group in bridging position between lanthanum and gallium. The La–C(Me) distance (2.801(2) Å) is somewhat elongated compared to that in [Cp*$_2$La(GaMe$_4$)] (2.724(4) Å). Similar to **Z**, the phenyl moiety aside the lanthanum center is slightly tilt from the Ga–C axis.

4 Activation of Trimethylgallium and Formation of Gallium Methylene

In order to investigate potential reactivity of tetramethylgallate rare-earth metallocene complexes toward other substrates we decided to heat samples of [Cp*$_2$Ln(GaMe$_4$)] (Ln = Y, Lu) in the presence of excess GaMe$_3$.

As such, [Cp*$_2$Ln(GaMe$_4$)] (Ln = Y, Lu) was treated with an eightfold excess of GaMe$_3$ at 130 °C in aromatic solvents for three days. This resulted in the generation of methane and formation of molecular homoleptic gallium methylene [Ga$_8$(CH$_2$)$_{12}$] (**BB**) as pale yellow crystalline material in good yields (Scheme S11; **Paper II**). In contrast to previous findings, no activation of the aromatic solvent could be observed under these conditions. X-ray diffraction analysis of **BB** disclosed a cage-like structural motif were each gallium atom of the "[Ga$_8$] cube" binds to three methylene bridges ("edges"; Figure S20).

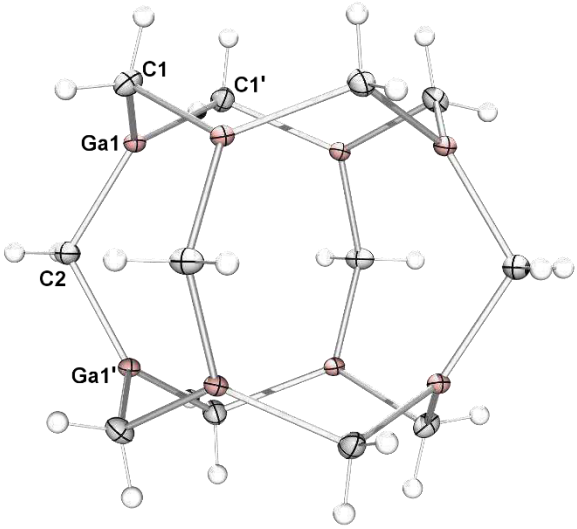

Figure S20. Solid-state structure of [Ga$_8$(CH$_2$)$_{12}$] (**BB**).

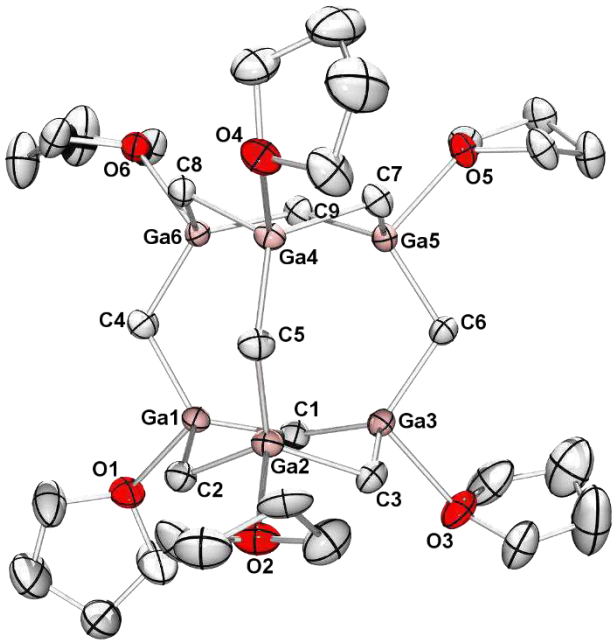

Figure S21. Solid-state structure of [Ga$_6$(CH$_2$)$_9$(THF)$_6$] (**CC**).

The ^{1}H NMR spectrum of **BB** in THF-d_8 revealed the presence of equivalent methylene protones by one singlet resonance at 0.19 ppm. However, in THF-d_8 solution **BB** converts to a smaller gallium methylene oligomer [Ga$_6$(CH$_2$)$_9$(THF)$_6$] (**CC**) within 24 hours, giving rise to a set of signals at 0.12 ppm (doublet), 0.10 ppm (singlet), and –0.49 pmm (doublet) acounting for three magnetically nonequivalent hydrogen atoms. Variable temperature NMR studies revealed that the [Ga$_8$(CH$_2$)$_{12}$]/[Ga$_6$(CH$_2$)$_9$] oligomer switch is suppressed at temperatures below –40 °C and reveresed at

temperatures above 80 °C. In **CC** all gallium atoms are coordinated by a THF molecule and the solid-state structure features two six-membered $[Ga_3(CH_2)_3]$ rings in chair conformation, which are in co-facial orientation connected by three Ga–CH_2–Ga bridges (Figure S21). While crystals of **CC** were obtained from saturated THF solutions at –40 °C, crystallization of gallium methylene at ambient temperatures by slowly condensing *n*-pentane to saturated THF solutions reproducibly triggered the rearrangement of the $[Ga_8(CH_2)_{12}]$ cage. The obtained solid-state structures of $[Ga_8(CH_2)_{12}(THF)_4]$ (**DD**) and $[Ga_8(CH_2)_{12}(THF)_5]$ (**EE**) (Figure S22) point to a rather weak Ga–O(THF) interaction based on solely partial THF coordinaton of the gallium atoms. Strikingly, the coordinated THF molecules in **CC**, **DD**, and **EE** are slowly lost at glovebox atmosphere and can be removed completely under reduced pressure.

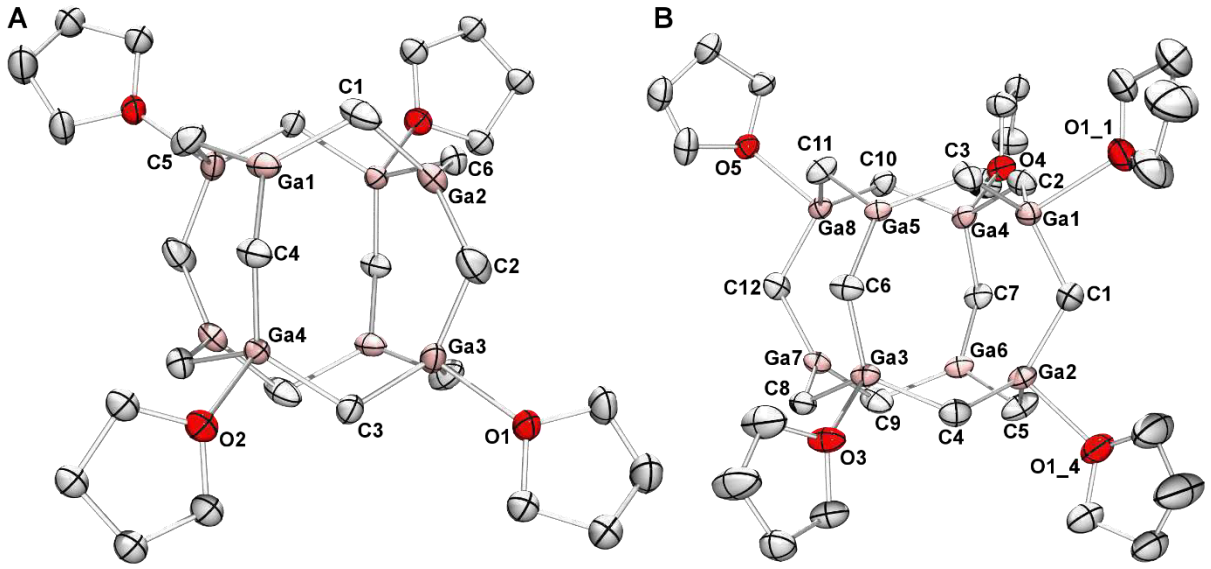

Figure S22. A: Solid-state structure of $[Ga_8(CH_2)_{12}(THF)_4]$ (**DD**); B: Solid-state structure of $[Ga_8(CH_2)_{12}(THF)_5]$ (**EE**).

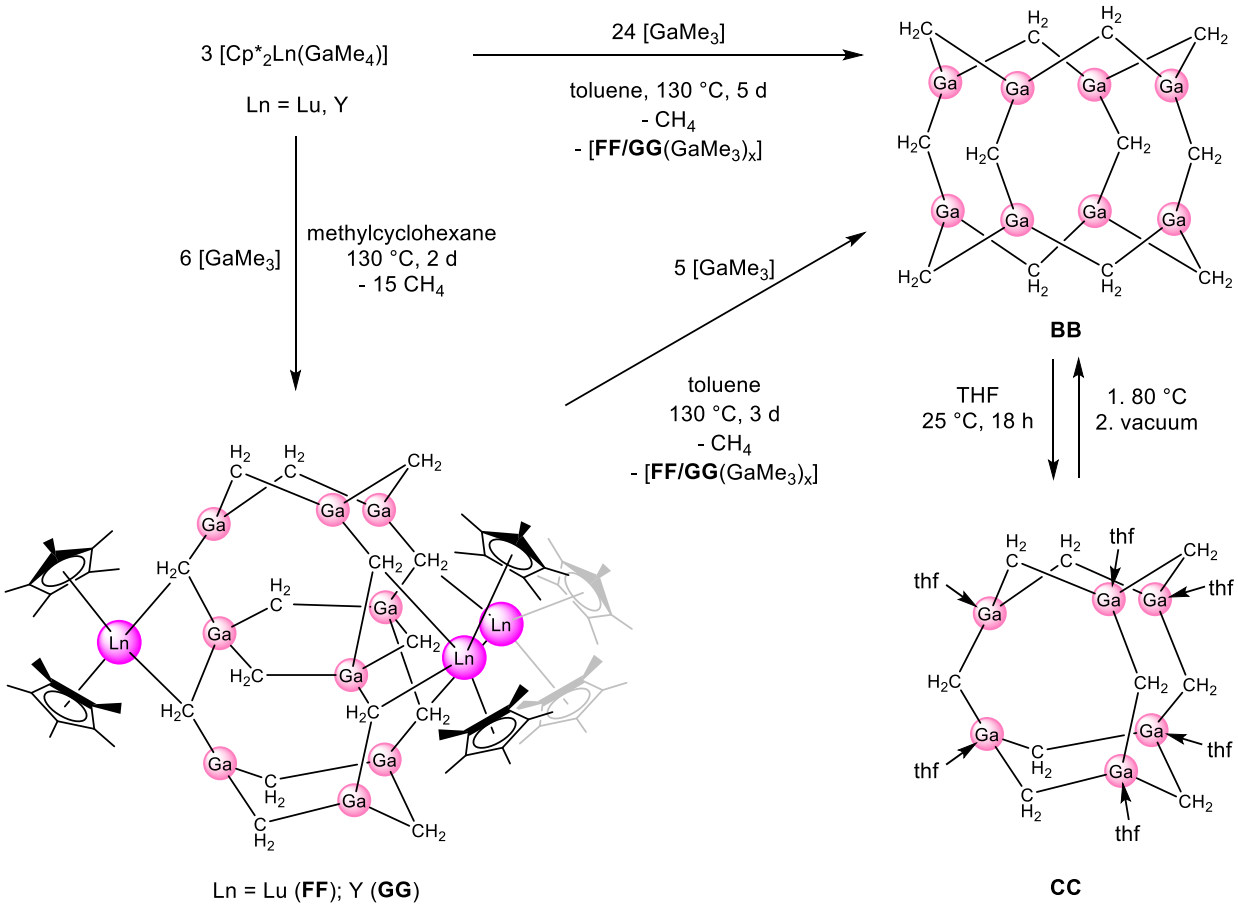

Scheme S11. Synthesis of $[Ga_8(CH_2)_{12}]$ (**BB**), $[Ga_6(CH_2)_9(THF)_6]$ (**CC**), $[Cp^*_6Lu_3Ga_9(CH_2)_{15}]$ (**FF**), and $[Cp^*_6Y_3Ga_9(CH_2)_{15}]$ (**GG**).

Interestingly, the supernatant of the initial reaction mixture produced additional **BB** in several cycles when treated with another eight equivalents of $GaMe_3$ at 130 °C in about the same yields. Hence, an elusive intermediate had to persist after each cycle, capable of promoting the "pseudocatalytic" transformation of $GaMe_3$ into **BB**. Heating the supernatant without addition of $GaMe_3$ or starting the reaction with $[Cp^*_2Ln(GaMe_4)]$ (Ln = Y, Lu) and two equivalents $GaMe_3$ reproducibly afforded colorless crystals of the bimetallic rare-earth metallocene gallium methylene complexes $[Cp^*_6Ln_3Ga_9(CH_2)_{15}]$ (Ln = Lu (**FF**); Y (**GG**); Scheme S11). Compounds **FF** and **GG** efficiently promote the conversion of excess $GaMe_3$ to **BB** at 130 °C. Even at ambient temperatures compound **FF** slowly transformed $GaMe_3$ to **BB** along with the regeneration of the starting material $[Cp^*_2Lu(GaMe_4)]$, as evidenced by NMR spectroscopy. Accordingly, addition products of **FF** and **GG**, respectively, and $GaMe_3$ are suggested as rational reactive intermediates in the reaction sequence leading to the formation of gallium methylene **BB** (Scheme S11). In the solid state **FF** and **GG** feature an identical structural motif,

which can be described as a highly aggregated anionic $[(\mu_3\text{-}CH_2)_6Ga_9(\mu\text{-}CH_2)_9]^{3-}$ core stabilized by three cationic $[Cp^*Ln]^+$ entities (Figure S23).

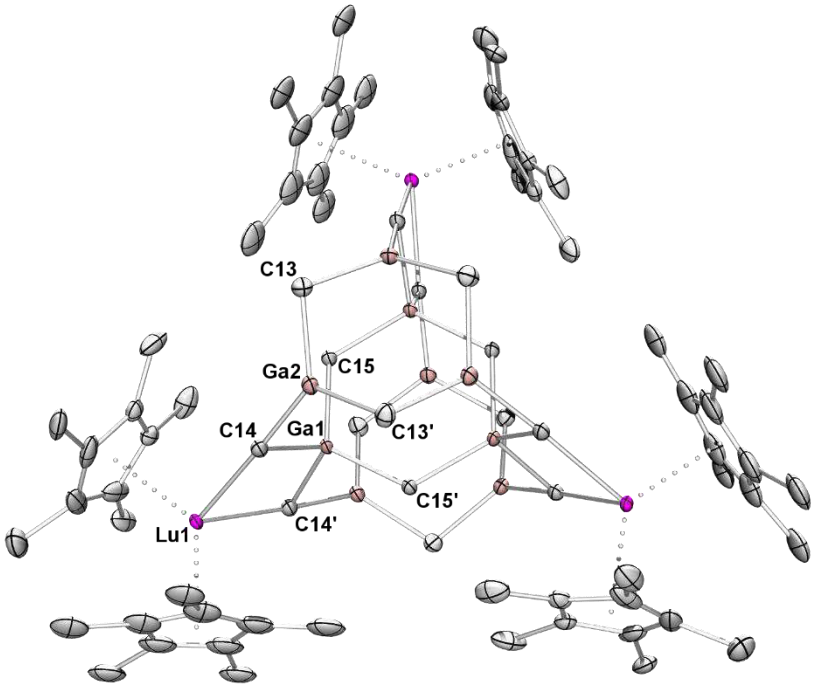

Figure S23. Solid-state structure of $[Cp^*_6Lu_3Ga_9(CH_2)_{15}]$ (**FF**).

The reactivity of the gallium methylene compounds **BB**, **FF**, and **GG** toward 9-fluorenone was assessed in THF-d_8 solutions to elucidate a potential Schrock-type metal-alkylidene behavior. As such, at 80 °C **BB** converted two equivalents of 9-fluorenone within two hours completely to 9-methylene-fluorene, while the insoluble compounds **FF** and **GG** required temperatures above 130 °C to initiate olefination of 9-fluorenone.

5 C–H-Bond Activation by Lutetium Alkylaluminate/gallate Complexes

Our group previously utilized the bulky hydrotris(pyrazolyl)borate ligand $Tp^{tBu,Me}$ to stabilize the unsolvated rare-earth-metal dimethyl complexes $[(Tp^{tBu,Me})LnMe_2]$ (Ln = Lu, Y, Ho).[37] While the yttrium and holmium derivatives rapidly decompose in aromatic solvents, lutetium complex $[(Tp^{tBu,Me})LuMe_2]$ shows a high thermal stability. Interestingly, $[(Tp^{tBu,Me})Lu(Me)(AlMe_4)]$, the formal addition product of $[(Tp^{tBu,Me})LuMe_2]$ and $AlMe_3$, is labile in solution and reacts with aromatic solvents like toluene and benzene.[38] For further investigations on this topic we targeted the synthesis of an heteroalkylaluminato lutetium-$Tp^{tBu,Me}$ complex with a peripheral boryl ligand.

Thus, addition of one equivalent of $[Me_2Al\{B(NDippCH)_2\}]$ to $[(Tp^{tBu,Me})LuMe_2]$ in *n*-hexane solutions resulted in quantitative formation of $[(Tp^{tBu,Me})Lu(Me)(Me_3Al\{B(NDippCH)_2\})]$ (**HH**; Scheme S12; **Paper I**). However, **HH** is labile in solution at ambient temperatures and slowly decomposes to form a new complex $[(Tp^{(tBu\text{-}H)_2/tBu,Me})Lu(Me_2Al\{B(NDippCH)_2\})]$ (**II**) under release of methane. This process is complete at 60 °C after three days. Interestingly, the starting material $[(Tp^{tBu,Me})LuMe_2]$ shows a high thermal stability, while crystallization of the respective homoaluminate derivative $[(Tp^{tBu,Me})Lu(Me)(AlMe_4)]$ was hampered by its reactivity toward aromatic solvents.[37a, 38] Hence, a reasonable mechanistic scenario of the process of C–H-bond activation involves the terminal Lu–CH_3 moiety in a σ-bond metathesis reaction. Apparently, coordination of the organoaluminum compounds $AlMe_3$ and $[Me_2Al\{B(NDippCH)_2\}]$, respectively, forces the methyl group into close proximity with a *tert*-butyl group to initiate a σ-bond metathesis reaction and formation of a methylene moiety. In contrast to $AlMe_3$, the bulky heteroaluminato entity seems to effectively shield the inner coordination sphere at the lutetium center to avoid any further reactions with solvent molecules. Instead, the heteroaluminato entity may switch positions from the methyl to the methylene moiety and stays locked in this position.

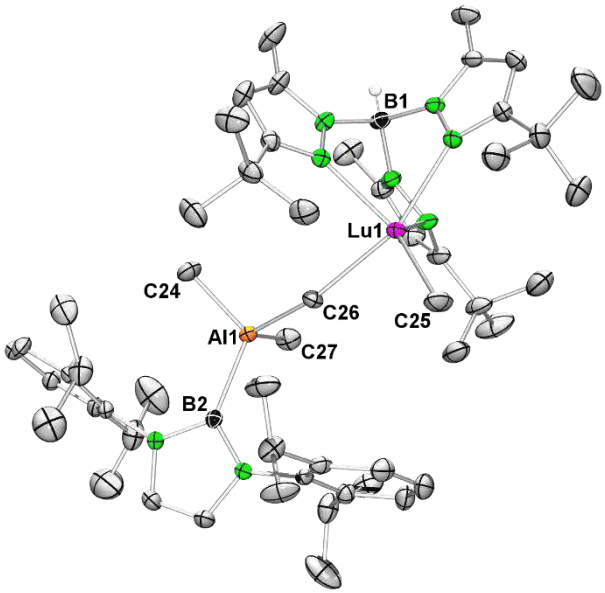

Figure S24. Solid-state structure of $[(Tp^{tBu,Me})Lu(Me)(Me_3Al\{B(NDippCH)_2\})]$ (**HH**).

In the following, the "second" terminal Lu–CH_3 moiety engages in σ-bond metathesis to form compound **II** quantitatively.

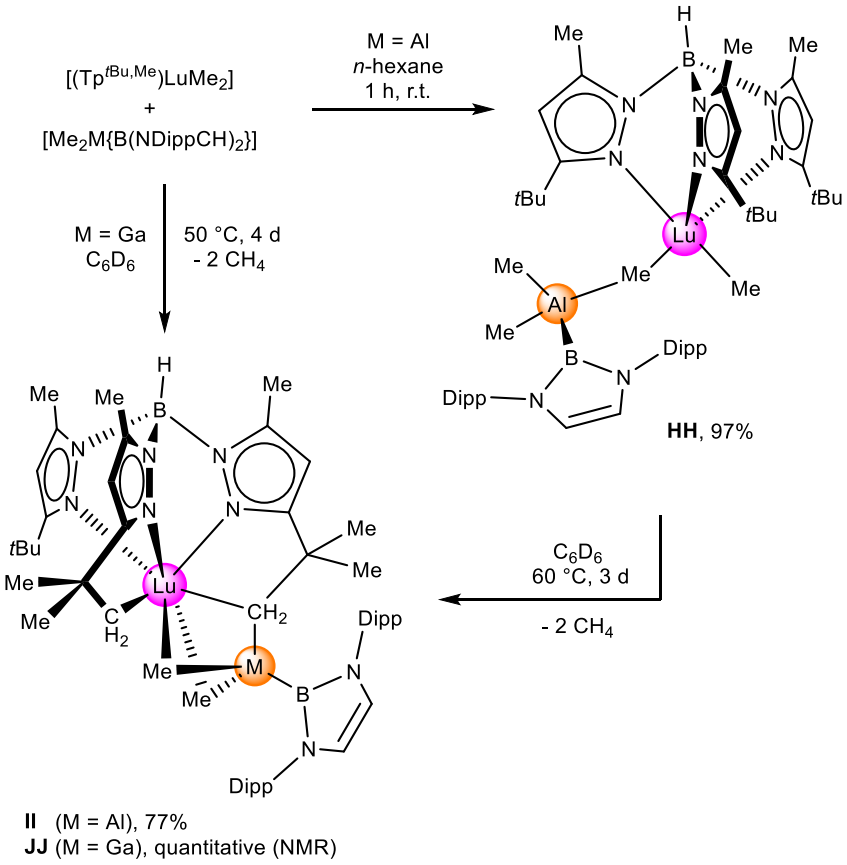

Scheme S12. Synthesis of [(Tp^{tBu,Me})Lu(Me)(Me$_3$Al{B(NDippCH)$_2$})] (**HH**), [(Tp$^{(tBu\text{-}H)_2/tBu,Me}$)Lu(Me$_2$Al{B(NDippCH)$_2$})] (**II**), and [(Tp$^{(tBu\text{-}H)_2/tBu,Me}$)Lu(Me$_2$Ga{B(NDippCH)$_2$})] (**JJ**).

The solid-state structure of **HH** (Figure S24) features a terminal methyl group and a [μ$_2$-MeAlMe$_2${B(NDippCH)$_2$}] moiety, where the bridging methyl group almost linearly connects the lutetium and aluminum centers. As such, **HH** displays a structural analog to that of the respective homoaluminate derivatives [(Tp^{tBu,Me})Ln(Me)(AlMe$_4$)] (Ln = Lu, Y, Ho).[37b, 39] The conversion of **HH** to **II** is nicely reflected by the respective ^{1}H NMR spectra. The ^{1}H NMR spectrum of **HH** is characterized by the high mobility of the heteroaluminato entity, and hence one set of signals for the pyrazolyl moieties and broad singlets assignable to the terminal Lu–CH_3 moieties are detected. On the other hand, the ^{1}H NMR spectrum of **II** revealed a very rigid coordination environment at the lutetium center, since three sets of signals giving evidence of three magnetically different pyrazolyl moieties. Hence, the solid-state structure of **II** (Figure

S25) features a doubly metalated Tp^{tBu,Me} ligand and the rare-earth-metal center is coordinated by the Tp^{tBu,Me} ligand in an unusual κ^5 fashion.

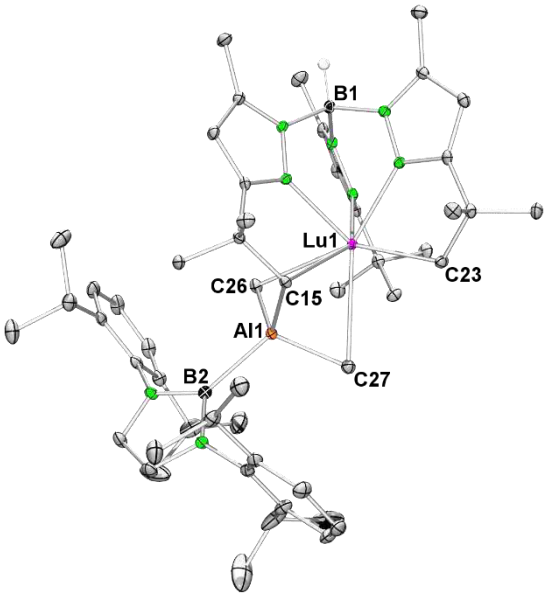

Figure S25. Solid-state structure of [(Tp$^{(tBu-H)2/tBu,Me}$)Lu(Me$_2$Al{B(NDippCH)$_2$})] (**II**).

Any attempts to achieve the corresponding heterogallate compound [(Tp^{tBu,Me})Lu(Me)(Me$_3$Ga{B(NDippCH)$_2$})] by a similar protocol, applying [Me$_2$Ga{B(NDippCH)$_2$}] and [(Tp^{tBu,Me})LuMe$_2$] at ambient temperatures failed (no reaction). However, quantitative formation of [(Tp$^{(tBu-H)_2/tBu,Me}$)Lu(Me$_2$Ga{B(NDippCH)$_2$})] (**JJ**) was observed after four days at 50 °C (Scheme S12). According to ^{1}H NMR spectroscopy, **JJ** displays the same rigid coordination behavior in solution as compound **II**, and hence forms a structural analog to the solid-state structure found for complex **II**.

The reactivity of compound **II** toward excessive THF and AlMe$_3$, respectively, was assessed by ^{1}H NMR spectroscopic studies. Thus, treating **II** with THF in benzene solutions resulted in the formation of [(THF)Me$_2$Al{B(NDippCH)$_2$}] and [(Tp$^{(tBu-H)_2/tBu,Me}$)Lu(THF)$_x$] while upon addition of an excess of AlMe$_3$ exchange of [Me$_2$Al{B(NDippCH)$_2$}] by AlMe$_3$ and formation of the new compound [(Tp$^{(tBu-H)_2/tBu,Me}$)Lu(AlMe$_3$)] (**KK**) was observed (Scheme S13). In the solid state, **KK** adopts a similar structural motif as found for **II** and **JJ**, respectively (Figure S26). However, due to reduced steric hindrance the [AlMe$_3$CH$_2$] unit is in closer proximity to the lutetium center and engages in a η^3 coordination mode.

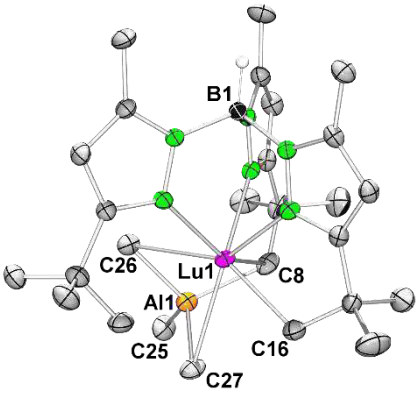

Figure S26. Solid-state structure of [(Tp$^{(tBu-H)2/tBu,Me}$)Lu(AlMe$_3$)] (**KK**).

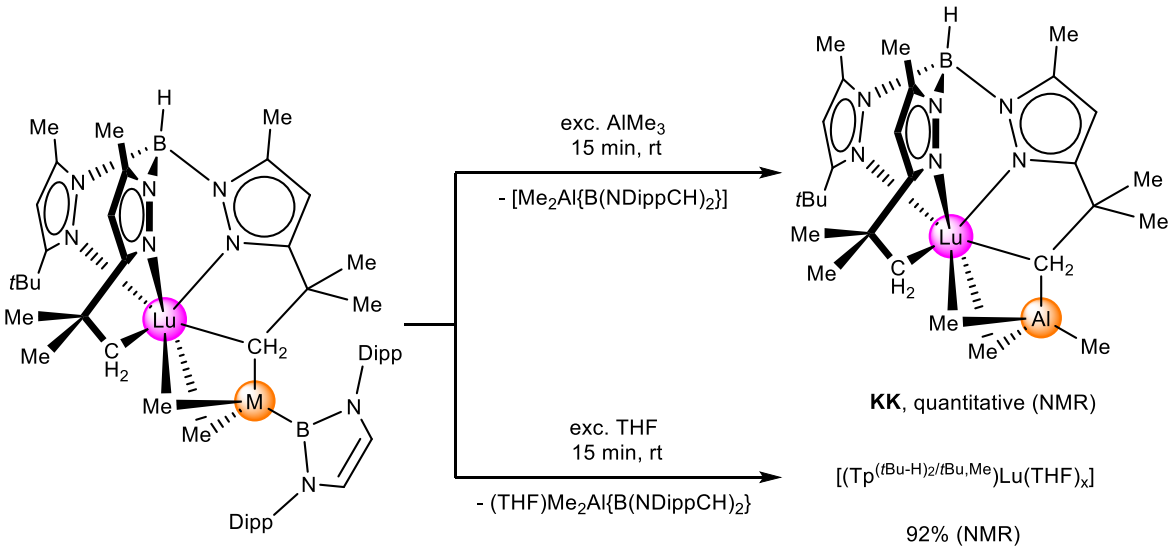

Scheme S13. Reactivity of [(Tp$^{(t\text{Bu-H})_2/t\text{Bu,Me}}$)Lu(Me$_2$Al{B(NDippCH)$_2$})] (**II**) toward an excess of THF and AlMe$_3$, respectively, to form [(Tp$^{(t\text{Bu-H})_2/t\text{Bu,Me}}$)Lu(THF)$_x$] and [(Tp$^{(t\text{Bu-H})_2/t\text{Bu,Me}}$)Lu(AlMe$_3$)] (**KK**).

Compounds **HH** and **II** are active catalysts for the polymerization of isoprene upon activation with borate cocatalysts like [PhNMe$_2$H][B(C$_6$F$_5$)$_4$]. Interestingly, the microstructures of the polyisoprenes achieved after one hour differ markedly for the systems **HH**/[PhNMe$_2$H][B(C$_6$F$_5$)$_4$] and **II**/[PhNMe$_2$H][B(C$_6$F$_5$)$_4$], but after 24 hours rather identical polymers are obtained. This prompted us to investigate into the catalytic species resulting from the binary systems **HH**/[PhNMe$_2$H][B(C$_6$F$_5$)$_4$] and **II**/[PhNMe$_2$H][B(C$_6$F$_5$)$_4$] by ^{1}H NMR spectroscopy.

The ^{1}H NMR spectral data indicate that treatment of **HH** with cocatalyst [PhNMe$_2$H][B(C$_6$F$_5$)$_4$] results in immediate protonation of a methyl group to release CH$_4$ followed by donor cleavage resulting in the formation of [(PhMe$_2$N)Me$_2$Al{B(NDippCH)$_2$}] and [(Tp$^{t\text{Bu,Me}}$)Lu(Me)][B(C$_6$F$_5$)$_4$] (Scheme S14). The latter would represent a rational catalytically active species for the polymerization of isoprene. However, after 16 hours ongoing methane extrusion was observed and sets of signals occurred in the ^{1}H NMR spectrum in good agreement to the formation of cyclometalative C–H-bond activation product [(Tp$^{(t\text{Bu-H})/t\text{Bu}_2\text{,Me}}$)Lu][B(C$_6F_5$)$_4$].

On the other hand, when treating **II** with [PhNMe$_2$H][B(C$_6$F$_5$)$_4$] no methane extrusion was observed, and resonance signal patterns in the ^{1}H NMR spectrum were detected after 10 minutes in good agreement to the formation of [(Tp$^{(t\text{Bu-H})/t\text{Bu}_2\text{,Me}}$)Lu(Me$_2$Al{B(NDippCH)$_2$})][B(C$_6F_5$)$_4$] (Scheme S14), the presumed active species targeted for the system **II**/[PhNMe$_2$H][B(C$_6$F$_5$)$_4$]. Apparently, the final active species of both binary systems show very similar structural motifs.

As such, the observed reactivity of **HH** and **II**, respectively, toward $[PhNMe_2H][B(C_6F_5)_4]$ would be a rational explanation for the observed performances in isoprene polymerization.

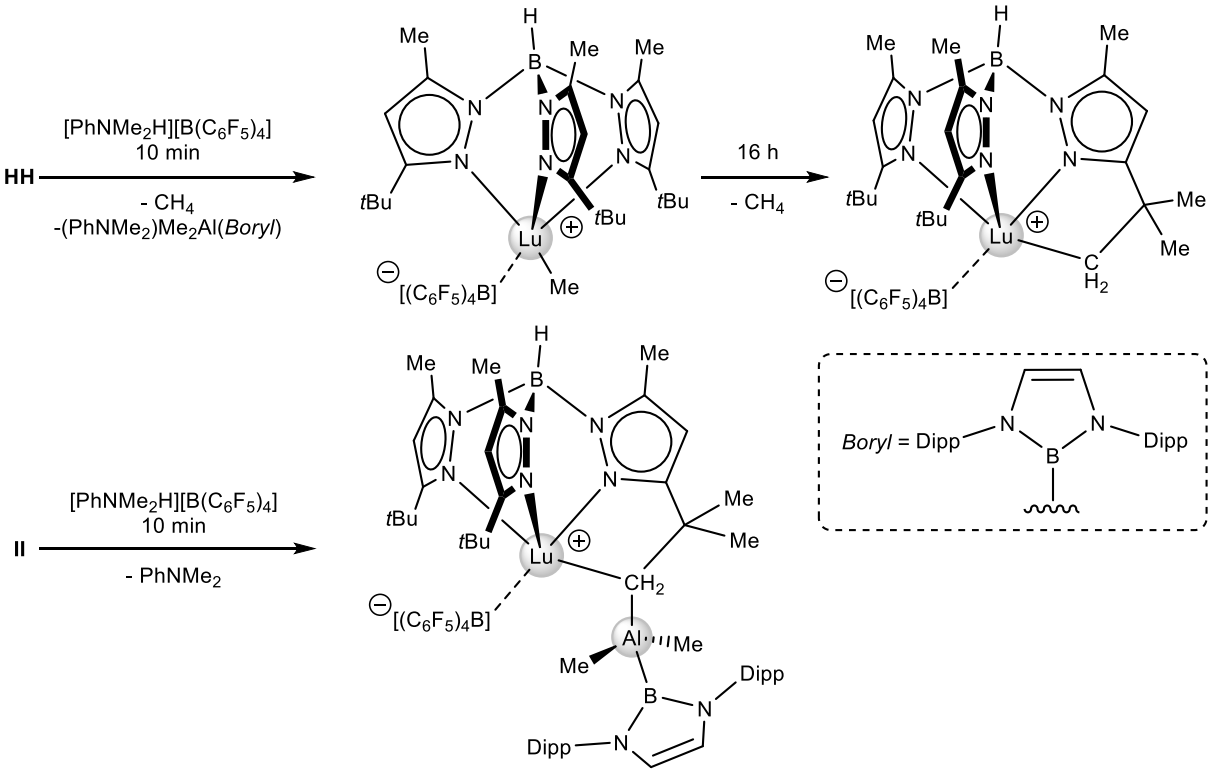

Scheme S14. Proposed activation scenario of $[(Tp^{tBu,Me})Lu(Me)(Me_3Al\{B(NDippCH)_2\})]$ (**HH**) and $[(Tp^{(tBu\text{-}H)_2/tBu,Me})Lu(Me_2Al\{B(NDippCH)_2\})]$ (**II**) with cocatalyst $[PhNMe_2H][B(C_6F_5)_4]$.

C

Bibliography

Bibliography

[1] a) R. H. Crabtree, *Chem. Rev.* **1995**, *95*, 987-1007; b) D. Balcells, E. Clot, O. Eisenstein, *Chem. Rev.* **2010**, *110*, 749-823; c) R. H. Crabtree, A. Lei, *Chem. Rev.* **2017**, *117*, 8481-8482; d) P. Gandeepan, T. Müller, D. Zell, G. Cera, S. Warratz, L. Ackermann, *Chem. Rev.* **2019**, *119*, 2192-2452.

[2] G. Wilkinson, J. M. Birmingham, *J. Am. Chem. Soc.* **1954**, *76*, 6210-6210.

[3] J. Holton, M. F. Lappert, D. G. H. Ballard, R. Pearce, J. L. Atwood, W. E. Hunter, *J. Chem. Soc., Chem. Commun.* **1976**, 480-481.

[4] J. Holton, M. F. Lappert, D. G. H. Ballard, R. Pearce, J. L. Atwood, W. E. Hunter, *J. Chem. Soc., Dalton Trans.* **1979**, 54-61.

[5] H. M. Dietrich, K. W. Törnroos, E. Herdtweck, R. Anwander, *Organometallics* **2009**, *28*, 6739-6749.

[6] a) P. L. Watson, *J. Am. Chem. Soc.* **1983**, *105*, 6491-6493; b) P. L. Watson, T. Herskovitz, *ACS Symp. Ser.* **1983**, *212*, 459-479; c) M. A. Busch, R. Harlow, P. L. Watson, *Inorg. Chim. Acta* **1987**, *140*, 15-20; d) P. L. Watson, D. C. Roe, *J. Am. Chem. Soc.* **1982**, *104*, 6471-6473.

[7] P. L. Watson, *J. Chem. Soc., Chem. Commun.* **1983**, 276-277.

[8] P. L. Watson, *Acc. Chem. Res.* **1985**, *18*, 51-56.

[9] a) M. E. Thompson, J. E. Bercaw, *Pure Appl. Chem.* **1984**, *56*, 1; b) M. E. Thompson, S. M. Baxter, A. R. Bulls, B. J. Burger, M. C. Nolan, B. D. Santarsiero, W. P. Schaefer, J. E. Bercaw, *J. Am. Chem. Soc.* **1987**, *109*, 203-219.

[10] M. D. Walter, P. T. Matsunaga, C. J. Burns, L. Maron, R. A. Andersen, *Organometallics* **2017**, *36*, 4564-4578.

[11] a) V. Jahns, S. Köstlmeier, M. Kotzian, N. Rösch, P. L. Watson, *Int. J. Quantum Chem.* **1992**, *44*, 853-867; b) S. G. Minasian, J. D. Rinehart, P. Bazinet, M. Seitz, *Acta Cryst. Sect. E* **2006**, *62*, 1823-1824; c) W. J. Evans, J. M. Perotti, J. W. Ziller, *J. Am. Chem. Soc.* **2005**, *127*, 3894-3909; d) W. J. Evans, I. Bloom, W. E. Hunter, J. L. Atwood, *J. Am. Chem. Soc.* **1983**, *105*, 1401-1403; e) I. Castillo, T. D. Tilley, *J. Am. Chem. Soc.* **2001**, *123*, 10526-10534; f) A. D. Sadow, T. D. Tilley, *Angew. Chem.* **2003**, *115*, 827-829; g) A. D. Sadow, T. D. Tilley, *J. Am. Chem. Soc.* **2005**, *127*, 643-656.

[12] S. Hajela, W. P. Schaefer, J. E. Bercaw, *Acta Cryst. Sect. C* **1992**, *48*, 1771-1773.

[13] A. D. Sadow, T. D. Tilley, *J. Am. Chem. Soc.* **2003**, *125*, 7971-7977.

[14] W. J. Evans, *Polyhedron* **1987**, *6*, 803-835.

[15] M. R. MacDonald, R. R. Langeslay, J. W. Ziller, W. J. Evans, *J. Am. Chem. Soc.* **2015**, *137*, 14716-14725.

[16] D. B. Culver, W. Huynh, H. Tafazolian, T.-C. Ong, M. P. Conley, *Angew. Chem.* **2018**, *130*, 1-5.

[17] C. L. Webster, J. W. Ziller, W. J. Evans, *Organometallics* **2014**, *33*, 433-436.

[18] a) A. R. Bulls, J. E. Bercaw, J. M. Manriquez, M. E. Thompson, *Polyhedron* **1988**, *7*, 1409-1428; b) K. H. d. Haan, J. H. Teuben, *Recl. Trav. Chim. Pays-Bas* **1984**, *103*, 333-334; c) M. Booij, B. J. Deelman, R. Duchateau, D. S. Postma, A. Meetsma, J. H. Teuben, *Organometallics* **1993**, *12*, 3531-3540.

[19] a) I. Castillo, T. D. Tilley, *Organometallics* **2000**, *19*, 4733-4739; b) I. Castillo, T. D. Tilley, *Organometallics* **2001**, *20*, 5598-5605.

[20] W. J. Evans, B. L. Davis, A. L. Kenward, J. W. Ziller, *Proc. Natl. Acad. Sci.* **2006**, *103*, 12678-12683.

[21] E. Y. J. Min, J. E. Bercaw, A. L. Kenward, W. Piers, *Inorganic Syntheses: Volume 36* **2014**, 42-46.

[22] G. Jeske, H. Lauke, H. Mauermann, P. N. Swepston, H. Schumann, T. J. Marks, *J. Am. Chem. Soc.* **1985**, *107*, 8091-8103.

[23] K. H. Den Haan, J. L. De Boer, J. H. Teuben, A. L. Spek, B. Kojic-Prodic, G. R. Hays, R. Huis, *Organometallics* **1986**, *5*, 1726-1733.

[24] H. J. Heeres, J. Renkema, M. Booij, A. Meetsma, J. H. Teuben, *Organometallics* **1988**, *7*, 2495-2502.

[25] K. H. Den Haan, Y. Wielstra, J. H. Teuben, *Organometallics* **1987**, *6*, 2053-2060.

[26] M. Booij, A. Meetsma, J. H. Teuben, *Organometallics* **1991**, *10*, 3246-3252.

[27] a) H. Heeres, J. Teuben, *Organometallics* **1991**, *10*, 1980-1986; b) N. S. Radu, T. D. Tilley, A. L. Rheingold, *J. Am. Chem. Soc.* **1992**, *114*, 8293-8295; c) N. S. Radu, T. D. Tilley, *Phosphorus, Sulfur, and Silicon and the Related Elements* **1994**, *87*, 209-2; d) N. S. Radu, T. D. Tilley, *J. Am. Chem. Soc.* **1995**, *117*, 5863-5864.

[28] W. J. Evans, J. M. Perotti, J. W. Ziller, *J. Am. Chem. Soc.* **2005**, *127*, 1068-1069.

[29] H. Schumann, *Angew. Chem.* **1984**, *96*, 475-493.

[30] a) W. J. Evans, C. A. Seibel, J. W. Ziller, *J. Am. Chem. Soc.* **1998**, *120*, 6745-6752; b) S.-S. Liu, S. Gao, J. W. Ziller, W. J. Evans, *Dalton Trans.* **2014**, *43*, 15526-15531; c) M. E. Fieser, T. J. Mueller, J. E. Bates, J. W. Ziller, F. Furche, W. J. Evans, *Organometallics* **2014**, *33*, 3882-3890.

[31] B.-J. Deelman, W. M. Stevels, J. H. Teuben, M. T. Lakin, A. L. Spek, *Organometallics* **1994**, *13*, 3881-3891.

[32] a) K. H. den Haan, J. H. Teuben, *J. Chem. Soc., Chem. Commun.* **1986**, 682-683; b) W. J. Evans, T. A. Ulibarri, J. W. Ziller, *Organometallics* **1991**, *10*, 134-142; c) W. J. Evans, J. M. Perotti, J. W. Ziller, *Inorg. Chem.* **2005**, *44*, 5820-5825; d) W. J. Evans, T. M. Champagne, J. W. Ziller, *J. Am. Chem. Soc.* **2006**, *128*, 14270-14271; e) D. H. Woen, J. R. White, J. W. Ziller, W. J. Evans, *J. Organomet. Chem.* **2019**, *899*, 120885.

[33] a) P. L. Watson, *J. Am. Chem. Soc.* **1982**, *104*, 337-339; b) B. J. Burger, M. E. Thompson, W. D. Cotter, J. E. Bercaw, *J. Am. Chem. Soc.* **1990**, *112*, 1566-1577; c) G. Jeske, L. E. Schock, P. N. Swepston, H. Schumann, T. J. Marks, *J. Am. Chem. Soc.* **1985**, *107*, 8103-8110.

[34] a) R. Bates, L. Kroposki, D. Potter, *The Journal of Organic Chemistry* **1972**, *37*, 560-562; b) W. J. Evans, T. A. Ulibarri, L. R. Chamberlain, J. W. Ziller, D. Alvarez, *Organometallics* **1990**, *9*, 2124-2130.

[35] a) R. Thim, H. M. Dietrich, M. Bonath, C. Maichle-Mössmer, R. Anwander, *Organometallics* **2018**, *37*, 2769-2777; b) D. A. Buschmann, H. M. Dietrich, D. Schneider, V. M. Birkelbach, C. Stuhl, K. W. Törnroos, C. Maichle-Mössmer, R. Anwander, *Chem. Eur. J.* **2020**, *26*, 10834-10840.

[36] K. H. Den Haan, Y. Wielstra, J. J. W. Eshuis, J. H. Teuben, *J. Organomet. Chem.* **1987**, *323*, 181-192.

[37] a) M. Zimmermann, R. Litlabø, K. W. Törnroos, R. Anwander, *Organometallics* **2009**, *28*, 6646-6649; b) D. Schädle, C. Maichle-Mössmer, C. Schädle, R. Anwander, *Chem. Eur. J.* **2015**, *21*, 662-670.

[38] M. Zimmermann, J. Takats, G. Kiel, K. W. Törnroos, R. Anwander, *Chem. Commun.* **2008**, 612-614.

[39] R. Litlabø, M. Zimmermann, K. Saliu, J. Takats, K. W. Törnroos, R. Anwander, *Angew. Chem. Int. Ed.* **2008**, *47*, 9560-9564.

D

Appendix

Appendix

X-ray data of compounds not included in the published papers or manuscripts.

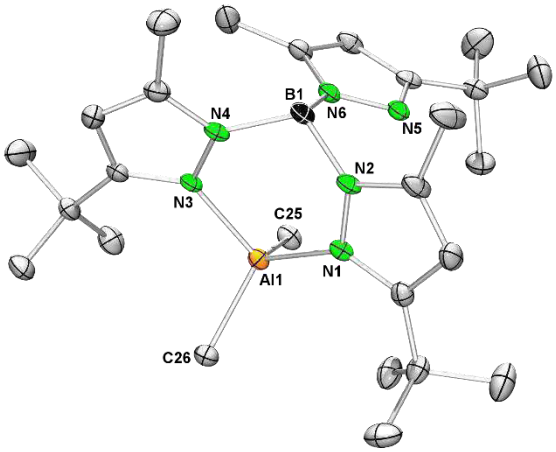

[(Tp^{tBu,Me})AlMe$_2$] (**mb145**)

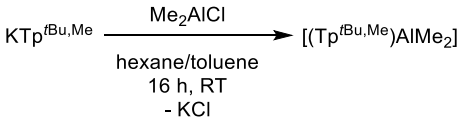

R_1[I>2Sigma(I)] 4.7%, wR_2(all data) 12.1%

Additional analysis: ^{1}H NMR

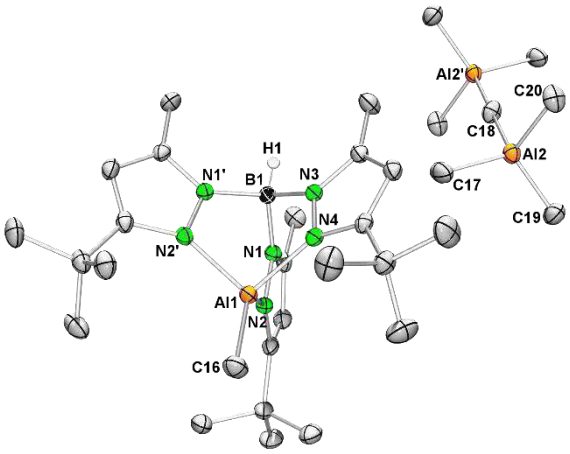

[(Tp^{tBu,Me})AlMe][Al$_2$Me$_7$] (**mb151**)

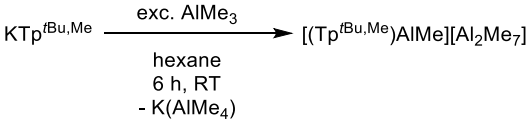

R_1[I>2Sigma(I)] 4.0%, wR_2(all data) 11.3%

Additional analysis: ^{1}H NMR

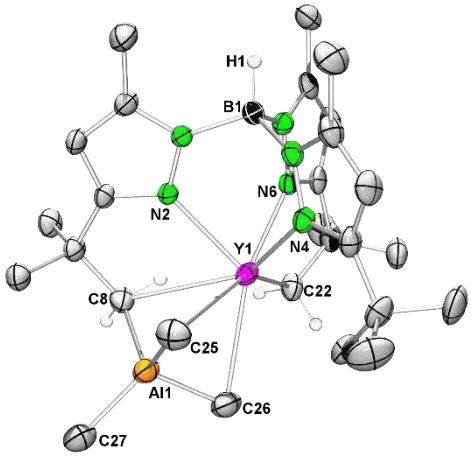

[(Tp$^{(tBu-H)_2/tBu,Me}$)Y(AlMe$_3$)] (**mb276**)

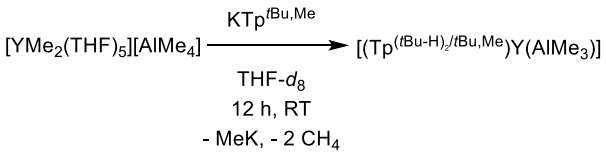

R_1[I>2Sigma(I)] 4.1%, wR_2(all data) 10.3%

Additional analysis: ^{1}H NMR

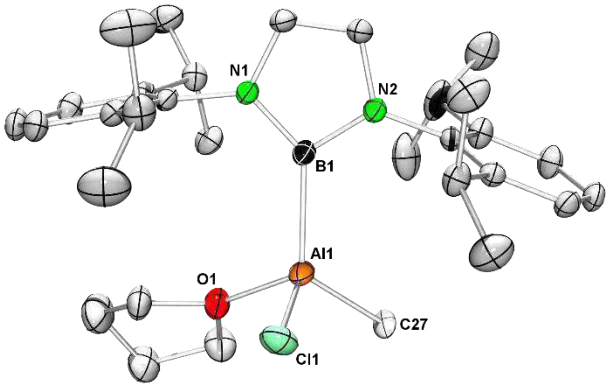

[MeAlCl(THF){B(NDippCH)$_2$}] (**mb109**)

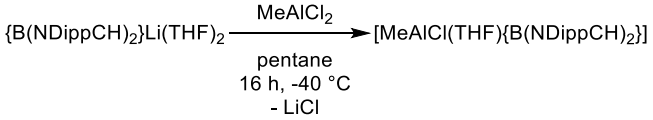

R_1[I>2Sigma(I)] 5.1%, wR_2(all data) 14.6%

Additional analysis: ^{1}H NMR

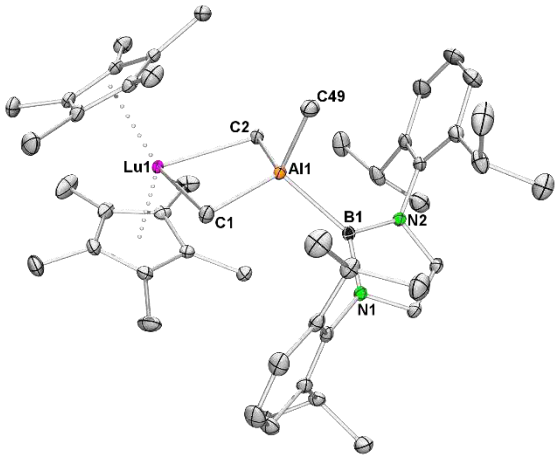

[Cp*$_2$Lu(Me$_3$Al{B(NDippCH)$_2$})] (**mb155**)

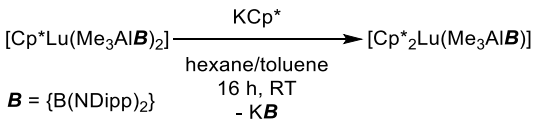

R_1[I>2Sigma(I)] 1.5%, *w*R_2(all data) 3.7%

Additional analysis: ^{1}H NMR, ^{13}C NMR, VT NMR, EA

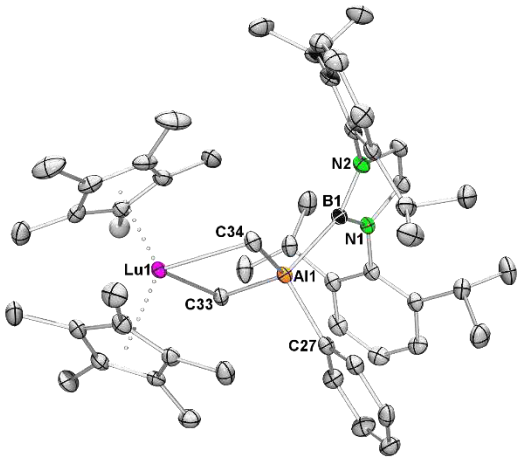

[Cp*$_2$Lu(Me$_2$AlPh{B(NDippCH)$_2$})] (**mb206_2**)

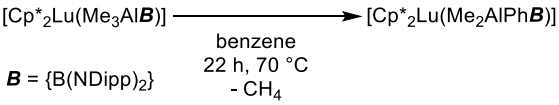

R_1[I>2Sigma(I)] 3.5%, *w*R_2(all data) 9.8%

Additional analysis: ^{1}H NMR

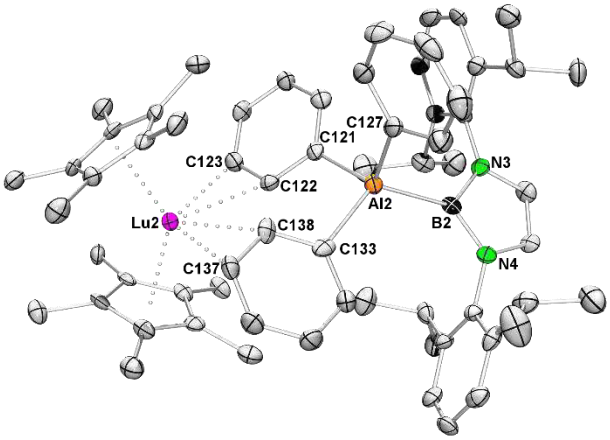

[Cp*$_2$Lu(Ph$_3$Al{B(NDippCH)$_2$})] (**mb206**)

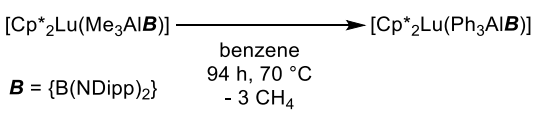

R_1[I>2Sigma(I)] 4.7%, *w*R_2(all data) 11.8%

Additional analysis: ^{1}H NMR

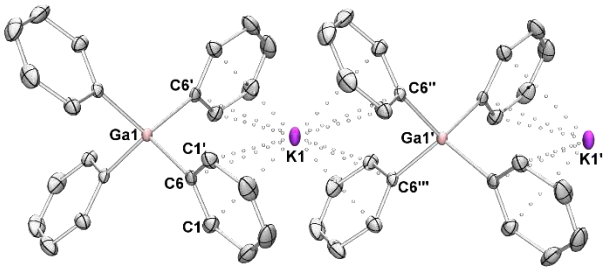

[(K(GaPh$_4$)]$_n$ (**mb224**)

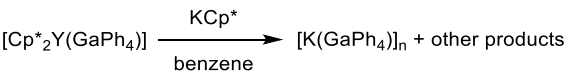

R_1[I>2Sigma(I)] 1.3%, *w*R_2(all data) 3.6%

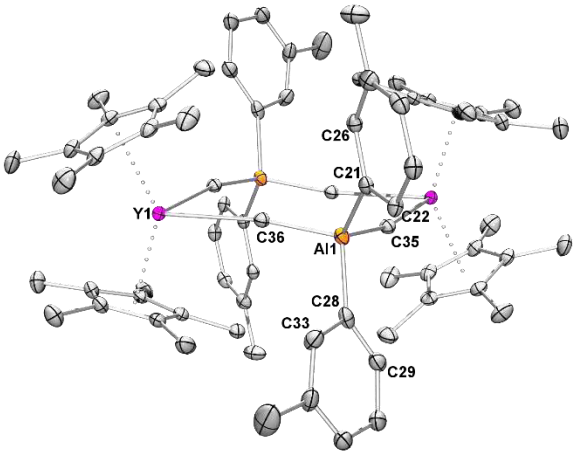

[Cp*$_2$Y(Me$_2$Al{*m*-tol}$_2$)] (**mb186**)

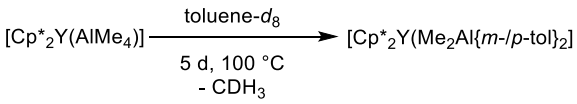

R_1[I>2Sigma(I)] 3.0%, *w*R_2(all data) 7.7%

Additional analysis: ^{1}H NMR

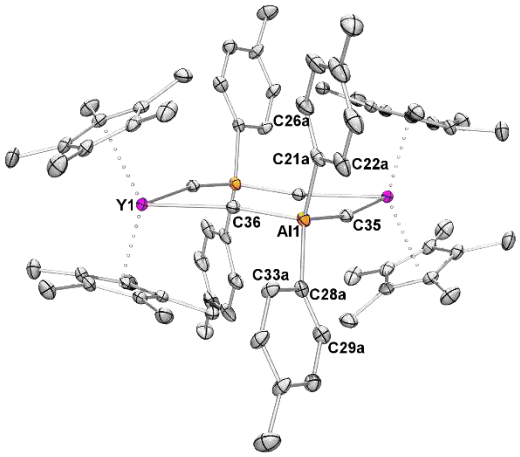

[Cp*$_2$Y(Me$_2$Al{*p*-tol}$_2$)] (**mb186**)

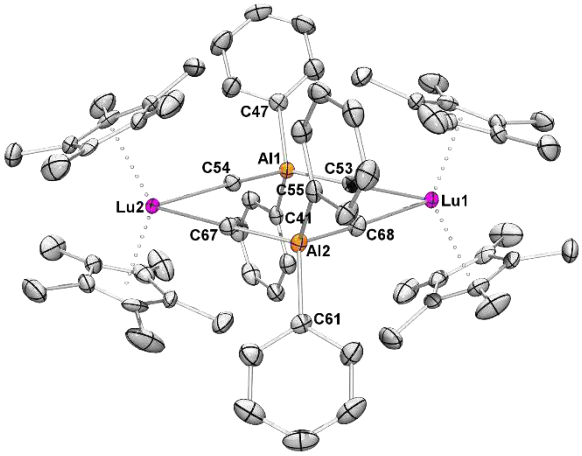

[Cp*$_2$Lu(Me$_2$AlPh$_2$)] (**mb269**)

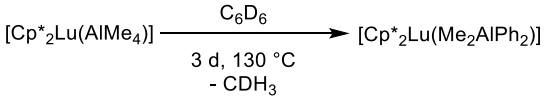

R_1[I>2Sigma(I)] 3.5%, *w*R_2(all data) 6.7%

Additional analysis: ^{1}H NMR, ^{13}C NMR, EA, DRIFT

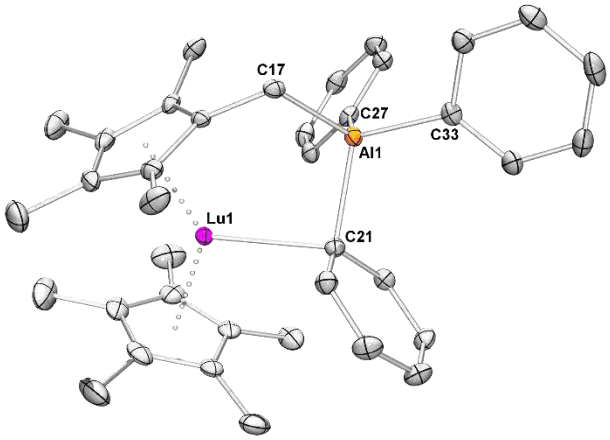

[Cp*Lu{C$_5$Me$_4$(μ-CH$_2$)AlPh$_3$}] (**gz03b**)

Cf. Gernot Zug, *Bachelor Thesis*, Eberhard Karls Universität Tübingen **2017**.

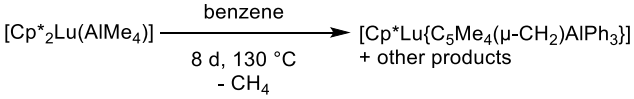

R_1[I>2Sigma(I)] 2.5%, *w*R_2(all data) 6.1%

Additional analysis: ^{1}H NMR, ^{13}C NMR, EA, DRIFT

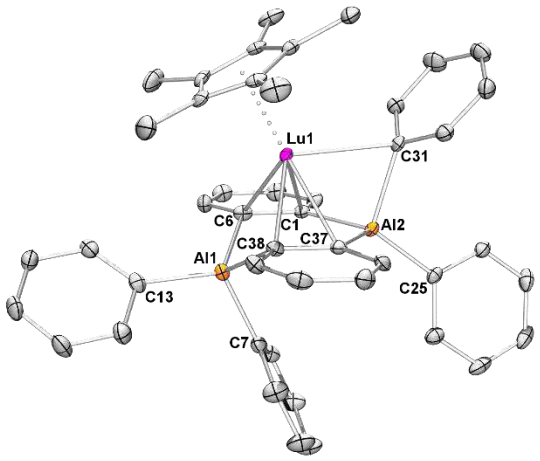

[Cp*Lu(Ph$_2$Al{1,2-C$_6$H$_4$}$_2$AlPh$_2$)] (**gz03a**)

Cf. Gernot Zug, *Bachelor Thesis*, Eberhard Karls Universität Tübingen **2017**.

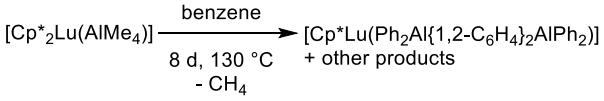

R_1[I>2Sigma(I)] 2.1%, *w*R_2(all data) 4.3%

Additional analysis: ^{1}H NMR

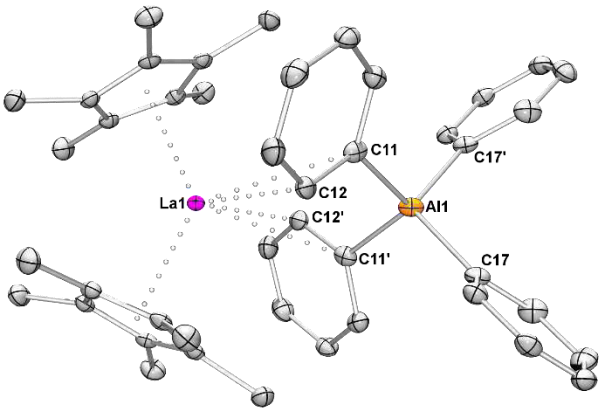

[Cp*$_2$La(AlPh$_4$)] (**mb270**)

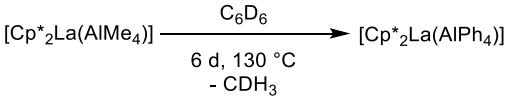

R_1[I>2Sigma(I)] 1.9%, *w*R_2(all data) 4.3%

Additional analysis: ^{1}H NMR

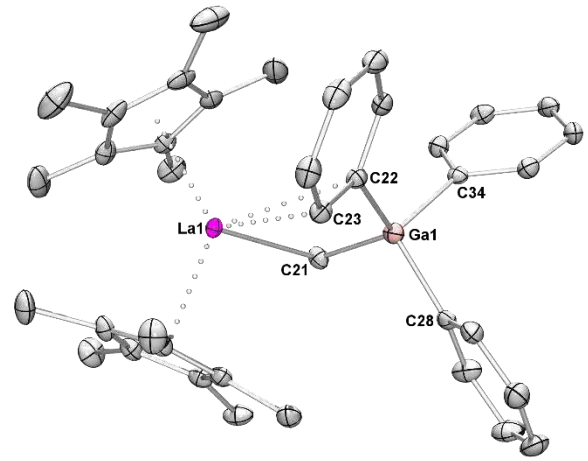

[Cp*$_2$La(MeGaPh$_3$)] (**mb277**)

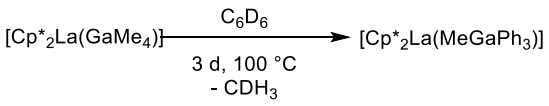

R_1[I>2Sigma(I)] 2.7%, *w*R_2(all data) 7.3%

Additional analysis: ^{1}H NMR

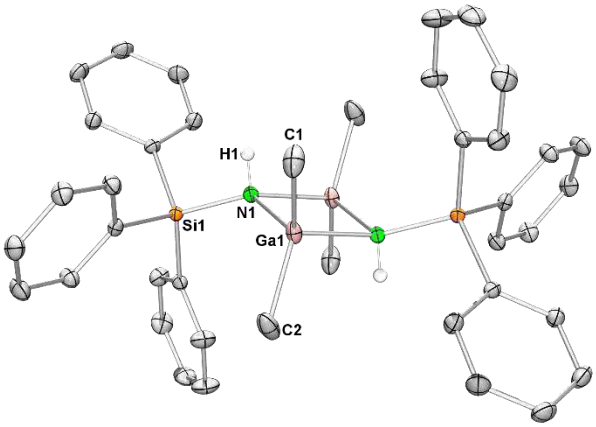

[Me$_2$Ga(NHSiPh$_3$)]$_2$ (**mb359**)

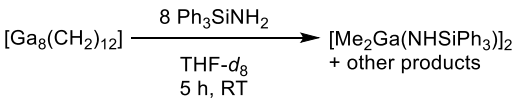

R_1[I>2Sigma(I)] 2.3%, *w*R_2(all data) 6.0%

Additional analysis: ^{1}H NMR

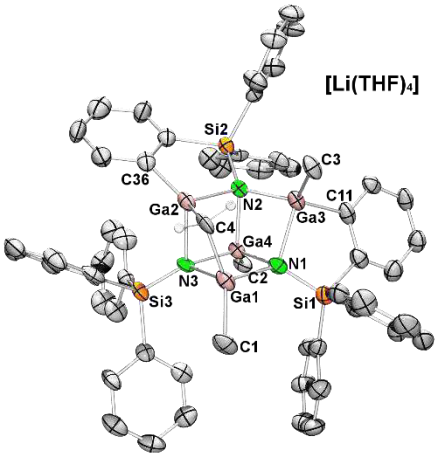

$[Ga_4Me_3(CH_2)(NSiPh_3)(NSiPh_2\{C_6H_4\})_2][Li(THF)_4]$ (**mb359**)

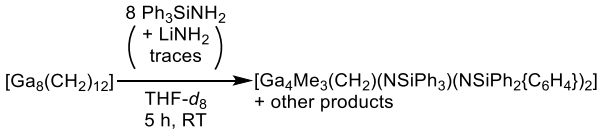

R_1[I>2Sigma(I)] 4.9%, *w*R_2(all data) 11.2%

Additional analysis: ^{1}H NMR

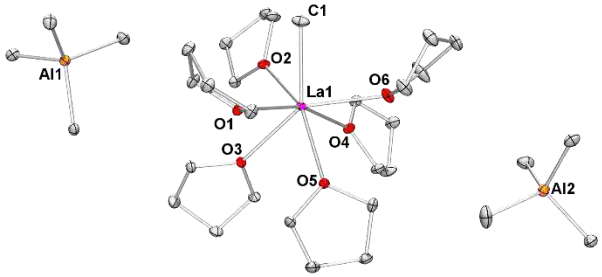

$[LaMe(THF)_6][AlMe_4]_2$ (**mb252**)

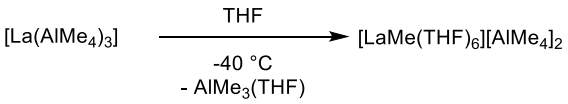

R_1[I>2Sigma(I)] 2.2%, *w*R_2(all data) 5.1%

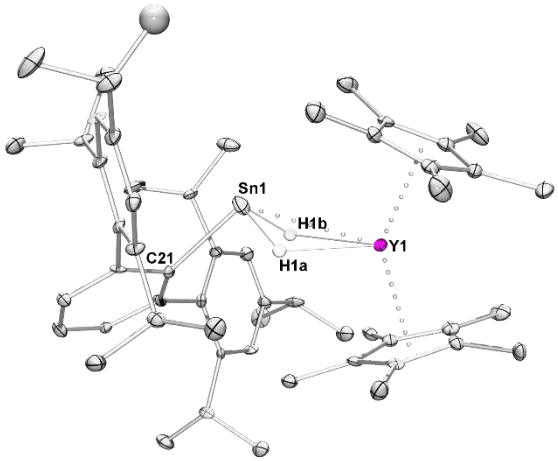

$[Cp^*_2Y(\mu\text{-}H)_2SnAr^{iPr_6}]$ (**mb253_fa268**)

Ar^{iPr_6} = C_6H_3-2,6(C_6H_2-2,4,6-*i*Pr_3)$_2$

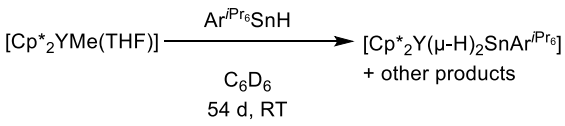

connectivity

Additional analysis: ^{1}H NMR

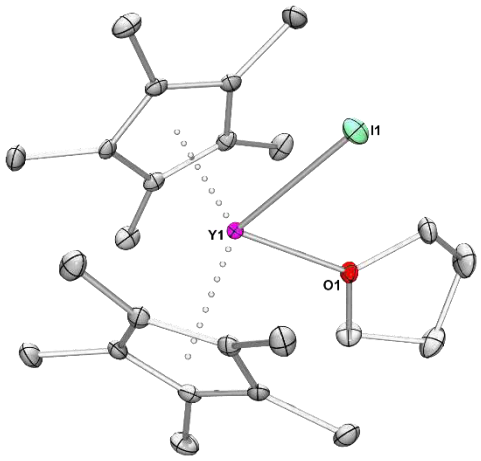

$[Cp^*_2YI(THF)]$ (**DAT20**)

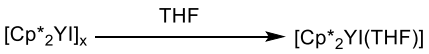

R_1[I>2Sigma(I)] 2.0%, *w*R_2(all data) 4.1%

Additional analysis: ^{1}H NMR, ^{13}C NMR, DRIFT, EA

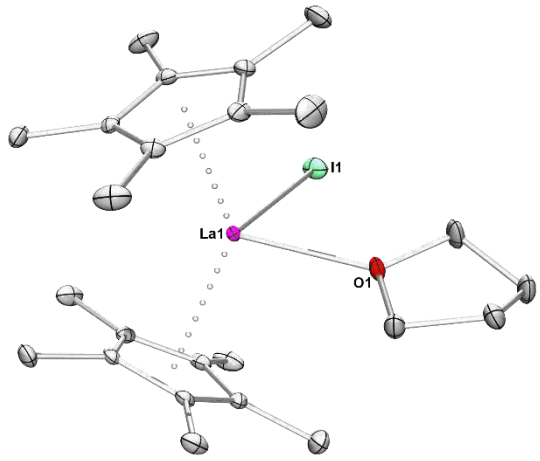

[Cp*$_2$LaI(THF)] (**mb195_thf**)

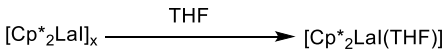

R_1[I>2Sigma(I)] 2.6%, *w*R_2(all data) 5.9%

Additional analysis: ^{1}H NMR, ^{13}C NMR, DRIFT, EA

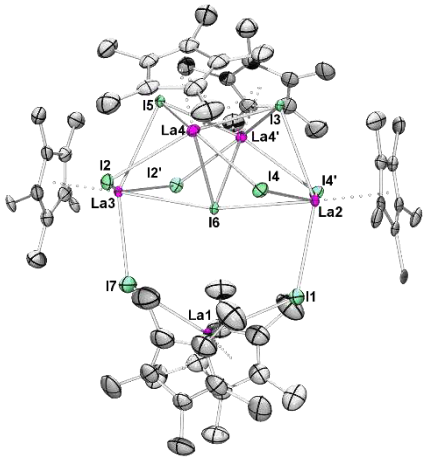

[{Cp*$_4$La$_4$(μ$_4$-I)(μ$_3$-I)$_2$(μ-I)$_6$}LaCp*2] (**mb398**)

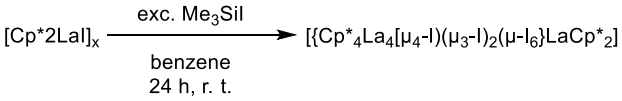

Connectivity

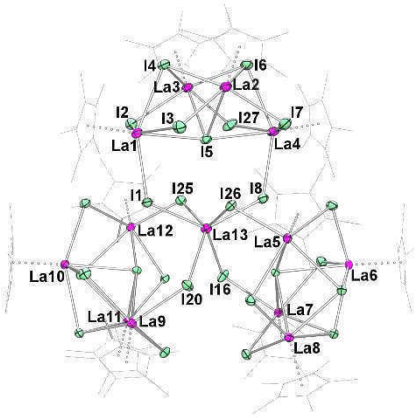

[{Cp*$_4$La$_4$(μ$_4$-I)(μ$_3$-I)$_2$(μ-I)$_6$}$_3$La] (**mb194**)

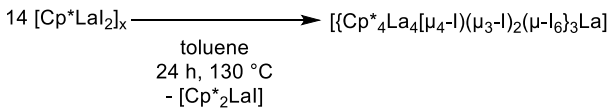

R_1[I>2Sigma(I)] 8.6%, *w*R_2(all data) 17.8%

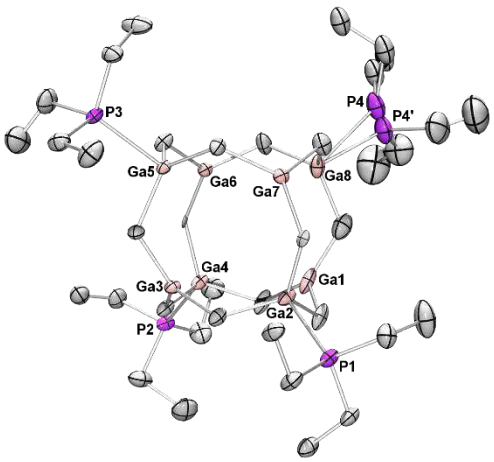

[Ga$_8$(CH$_2$)$_{12}$](PEt$_3$)$_4$ (**mb358b**)

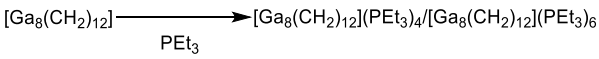

connectivity

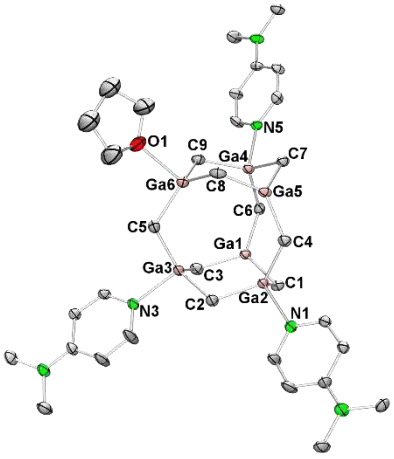

$[Ga_6(CH_2)_9](DMAP)_3(thf)$ (**mb369**)

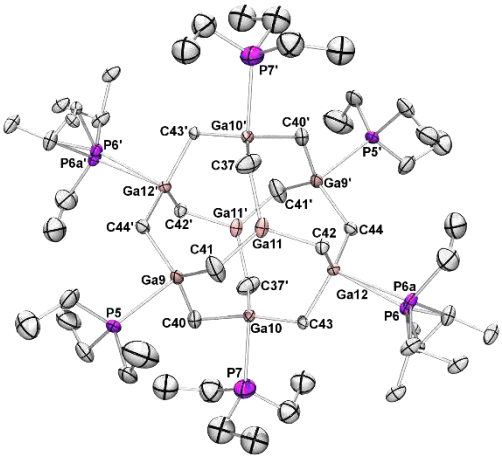

$[Ga_8(CH_2)_{12}](PEt_3)_6$ (**mb358b**)

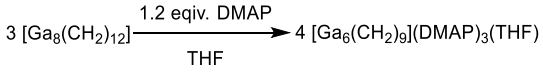

R_1[I>2Sigma(I)] 4.6%, *w*R_2(all data) 9.9%

Additional analysis: ^{1}H NMR

E

Publications and Manuscripts

C–H-Bond Activation and Isoprene Polymerization by Lutetium Alkylaluminate/gallate Complexes Bearing a Peripheral Boryl and a Bulky Hydrotris(pyrazolyl)borate Ligand

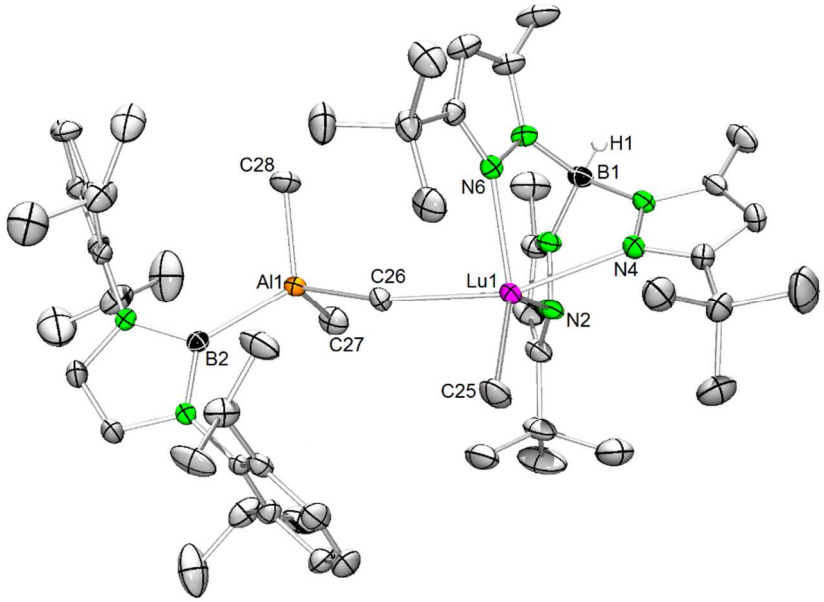

Paper I

ChemPubSoc Europe

DOI: 10.1002/ejic.201700730

EurJIC European Journal of Inorganic Chemistry

Full Paper

Polymerization Precatalysts | *Very Important Paper* |

CLUSTER ISSUE

VIP

C–H Bond Activation and Isoprene Polymerization by Lutetium Alkylaluminate/gallate Complexes Bearing a Peripheral Boryl and a Bulky Hydrotris(pyrazolyl)borate Ligand

Martin Bonath,[a][‡] Christoph O. Hollfelder,[a][‡] Dorothea Schädle,[a] Cäcilia Maichle-Mössmer,[a] Peter Sirsch,*[a] and Reiner Anwander*[a]

Abstract: The bimetallic lutetium alkylaluminate complex [(Tp^{tBu,Me})Lu(Me)(AlMe$_3${B(NDippCH)$_2$})] {Tp^{tBu,Me} = hydrotris(3-Me-5-*t*Bu-pyrazolyl)borate} formed readily upon addition of 0.5 equivalents of the organoaluminum boryl compound [Me$_2$Al{B(NDippCH)$_2$}]$_2$ (Dipp = C$_6$H$_3$*i*Pr$_2$-2,6) to [(Tp^{tBu,Me})LuMe$_2$] in *n*-hexane solution. Thermally induced cyclometalative C–H bond activation of this compound led to the formation of [(Tp$^{(tBu-H)}_2$/*t*Bu,Me)Lu(AlMe$_2${B(NDippCH)$_2$})] {Tp$^{(tBu-H)}_2$/*t*Bu,Me = hydro(3-Me-5-*t*Bu-pyrazolyl)bis[μ-(3-Me-5-Me$_2$CCH$_2$-pyrazolyl)]-borate} in quantitative yields. The latter complex bears an unusual κ^5 coordination mode of the activated tris(pyrazolyl)-borate ligand. Additionally, one Lu–CH$_2$(R) moiety is coordinated by a "neutral" [Me$_2$Al{B(NDippCH)$_2$}] unit, which can be separated off by addition of THF or trimethylaluminum. The gallium analogue of complex [(Tp^{tBu,Me})Lu(Me)(AlMe$_3$-{B(NDippCH)$_2$})] could not be isolated from the respective reaction of monomeric [Me$_2$Ga{B(NDippCH)$_2$}] with [(Tp^{tBu,Me})-LuMe$_2$], but the C–H bond activated gallate complex [(Tp$^{(tBu-H)}_2$/*t*Bu,Me)Lu(GaMe$_2${B(NDippCH)$_2$})] was obtained instead following a prolonged mild thermal treatment. The performance of the new lutetium complexes as precatalysts in the polymerization of isoprene was assessed and possible activation and deactivation scenarios were studied by NMR spectroscopy.

Introduction

Bis(hydrocarbyl) rare-earth-metal complexes supported by a monoanionic ancillary ligand (**L**) of the type [**L**LnR$_2$(Do)] (R = CH$_2$SiMe$_3$, *o*-CH$_2$PhNMe$_2$, η^3-C$_3$H$_5$; Do = neutral donor ligand) have been studied extensively for their exceptional performance in olefin polymerization reactions.[1] Given the importance of organoaluminum cocatalysts in rare-earth-metal-based 1,3-diene polymerization, we set out to develop a bis(hydrocarbylaluminate) postmetallocene library to better understand any potential Ln–Al bimetallic cooperativity as well as ancillary ligand effects.[2] Initially, we and others introduced half-sandwich bis(tetramethylaluminate) rare-earth-metal complexes of the general type [Cp$^R_5$Ln(AlMe$_4$)$_2$] [R$_5$ = HMe$_4$,[3] Me$_5$,[4] H$_2$*t*Bu$_3$,[5] Me$_4$SiMe$_3$,[5,6] H$_3$(SiMe$_3$)$_2$,[5] Me$_4$(quinolyl),[7] Me$_4$(*N*,*N*-dimethylanilyl),[8] Me$_4$(C$_2$H$_4$NMe$_2$)[8]] as donor-solvent free derivatives and established them as versatile precatalysts for the synthesis of highly stereoregular polyisoprene, when pretreated with borane/borate cocatalysts (Figure 1). Varying the substitution pattern of the cyclopentadienyl (Cp) ligand allowed for a comprehensive assessment of the electronic and steric implications of the ancillary ligand for the catalytic performance.[3,4b,5,7–9] In the course of these studies, the bulky carbanion-like boryl ligand {B(NDippCH)$_2$} (Dipp = C$_6$H$_3$*i*Pr$_2$-2,6)[10] was utilized to implement a heterosubstituted aluminato actor ligand which significantly affected the polymerization as well.[11] The microstructure of the polymers resulting from those heteroaluminate precatalysts, [Cp*Ln(AlMe$_3${B(NDippCH)$_2$})$_2$] (Ln = Lu, Y; Cp* = C$_5$Me$_5$), are of special interest as the corresponding active species add the monomers in a predominantly vinylic fashion.

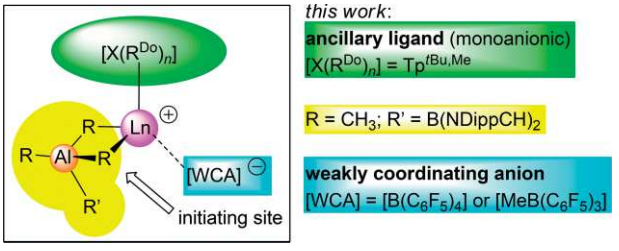

Figure 1. Active species of polymerization reactions previously proposed for the rare-earth-metal (Ln)-based bis(hydrocarbylaluminate) postmetallocene/half-sandwich library. [X(R^{Do})$_n$] = ancillary ligand like cyclopentadienyl, amido, or alkoxy featuring intraligand donor functionalities.

Over the past few years, a variety of rare-earth-metal tetramethylaluminate complexes bearing N-coordinating monoanionic ancillary ligands has been added to this postmetallocene library, including imino-amido-pyridinate,[12] benzamidinate,[13] triazenide,[14] diketiminate,[15] and formamidinate de-

[a] *Institut für Anorganische Chemie, Universität Tübingen, Auf der Morgenstelle 18, 72076 Tübingen Germany*
E-mail: reiner.anwander@uni-tuebingen.de
http://uni-tuebingen.de/syncat-anwander
http://www.mnf.uni-tuebingen.de/fachbereiche/chemie/institute/anorganische-chemie/institut/ag-sirsch.html
[‡] These authors contributed equally to this publication.
Supporting information and ORCID(s) from the author(s) for this article are available on the WWW under https://doi.org/10.1002/ejic.201700730.

rivatives,[16] considerably enhancing the opportunities for further manipulations of the electronic and steric situation at the rare-earth-metal center. Accordingly, the performance in isoprene polymerization of such systems is significantly altered as well.[13a,13c,14–16] Occasional shortcomings observed for such highly reactive bimetallic complexes are Ln-to-Al *N*-coordinating ancillary ligand transfer[14] and C–H bond activation of the ancillary ligand,[8,16,17] the latter displaying a recurrent phenomenon in the field of organometallic chemistry.[18] Interestingly, Jende et al. demonstrated that complexes resulting from ancillary ligand activation can still be active precatalysts.[8]

Previously, our group reported on the synthesis of [(Tp^{tBu,Me})Ln(Me)(AlMe$_4$)] compounds (Ln = Y,[19] Ho,[20] Lu[19]) as yet another class of donor-solvent free Lewis-acid stabilized compounds of the general type [**L**LnR$_2$] (**L** = ancillary ligand, R = hydrocarbyl). We anticipated that these complexes would be suitable precatalysts for isoprene polymerization, as well. For further comprehensive studies of the effect of heteroaluminato actor ligands we targeted the synthesis and characterization of lutetium-Tp^{tBu,Me} complexes bearing an alkylaluminato ligand with a peripheral boryl ligand.

Results and Discussion

Synthesis and Degradation of Heteroaluminate Complex [(Tp^{tBu,Me})Lu(Me)(AlMe$_3${B(NDippCH)$_2$})] (1)

Addition of 0.5 equivalents of [Me$_2$Al{B(NDippCH)$_2$}]$_2$[21] to [(Tp^{tBu,Me})LuMe$_2$][20] formed a new rare-earth-metal alkyl complex, [(Tp^{tBu,Me})Lu(Me)(AlMe$_3${B(NDippCH)$_2$})] (**1**), in almost quantitative yield (Scheme 1). Similar to previously reported [(Tp^{tBu,Me})Lu(Me)(AlMe$_4$)] (**I^{Lu}**), the ^{1}H NMR spectrum of **1** recorded in [D$_6$]benzene revealed a highly fluxional behavior of the metal-bonded methyl groups.

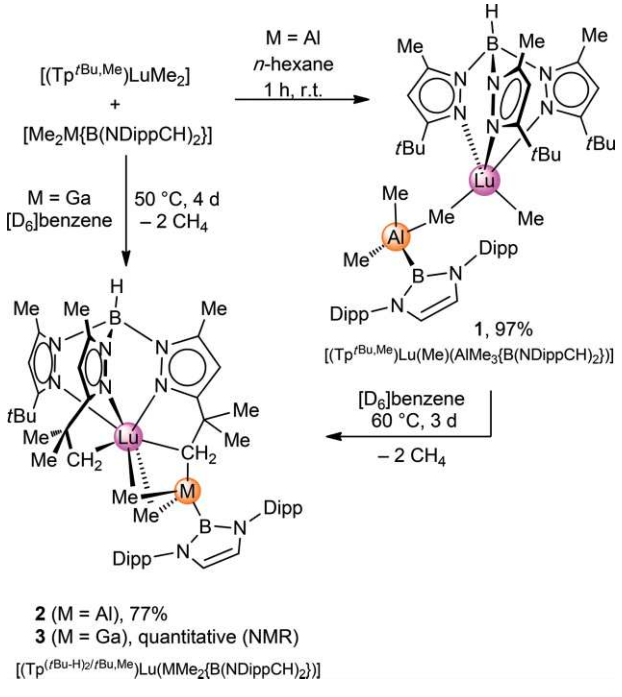

Scheme 1. Reaction of [(Tp^{tBu,Me})LuMe$_2$] with 1/2 [Me$_2$M{B(NDippCH)$_2$}]$_2$ (M = Al, Ga) and thermally induced C–H bond activation.

At ambient temperature two broad singlets were detected at δ = –0.14 ppm [6 H, Lu(C*H*$_3$)$_2$] and –1.20 ppm [6 H, Al(C*H*$_3$)$_2$], indicating that under these conditions the [Me$_2$Al{B(NDippCH)$_2$}] unit rapidly exchanges between the two Lu-bonded methyl groups, while exchange between Al- and Lu-bonded methyl groups is markedly slowed down. This suggests that the sterically demanding {B(NDippCH)$_2$} moiety keeps the Al-bonded methyl groups outside the inner coordination sphere of the Lu center thus impeding a fast methyl exchange process. A ^{1}H-^{1}H EXSY NMR spectroscopic experiment revealed that indeed slow exchange of the Al- and Lu-bonded methyl groups occurs at ambient temperature (Figure S5). Variable-temperature (VT) ^{1}H NMR spectroscopic studies in [D$_8$]toluene were performed for obtaining deeper insights into the dynamic behavior of complex **1** (Figure 2 and S3, Supporting Information). At the coalescence temperature of 70 °C the resonances of the metal alkyl groups merge to a broad singlet at δ = –0.77 ppm besides minor signals of a particular decomposition product (vide infra). Upon cooling to –10 °C the signal of the Lu–CH$_3$ moieties separates into two broad singlets at δ = 0.14 ppm (3 H) and –0.55 ppm (3 H). At –30 °C all of the CH and CH$_3$ pyrazolyl proton signals have decoalesced in a 2:1 ratio, indicating different environments for the pyrazolyl moieties.

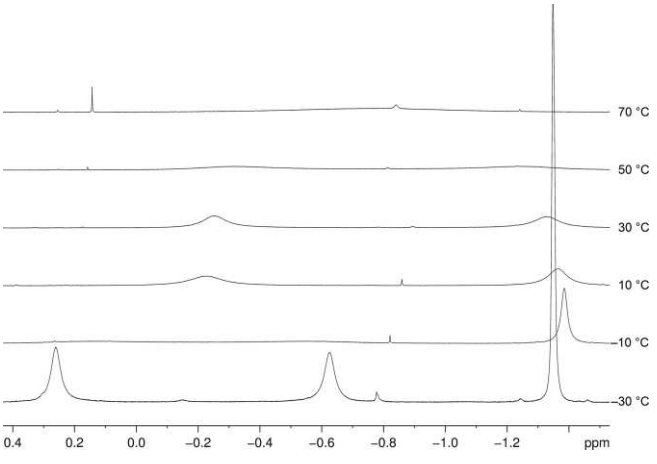

Figure 2. Variable-temperature ^{1}H NMR spectra (500 MHz) of **1**, in the region of metal-bonded C*H*, in [D$_8$]toluene.

In good agreement with the respective homoaluminate derivatives [(Tp^{tBu,Me})Ln(Me)(AlMe$_4$)] [Ln = Y (**I^{Y}**),[19] Ho (**I^{Ho}**)[20]] complex **1** adopts a distorted trigonal bipyramidal coordination geometry (Figure 3). The Lu–C bond lengths of **1** [Lu1–C25 = 2.321(1) Å, Lu1–C26 2.613(3) Å] are similar to those in **I^{Y}** [2.382(3) Å, 2.715(3) Å] and **I^{Ho}** [2.376(3) Å, 2.696(3) Å] considering the differences in the ionic radii.[22] In analogy to **I^{Y}** and **I^{Ho}** the [μ_2-MeAlMe$_2${B(NDippCH)$_2$}$_2$] unit coordinates in an η^1 fashion where the bridging methyl group almost linearly connects the two metal atoms ($\measuredangle$ Lu1C26Al1 = 164.6°). Relating to the Lu–methyl–Al axis the {B(NDippCH)$_2$} moiety captures a diagonal position relative to the Tp^{tBu,Me} ligand to minimize steric strain. Consequently, the Al-bonded methyl groups and the two pyrazolyl rings are located opposite each other.

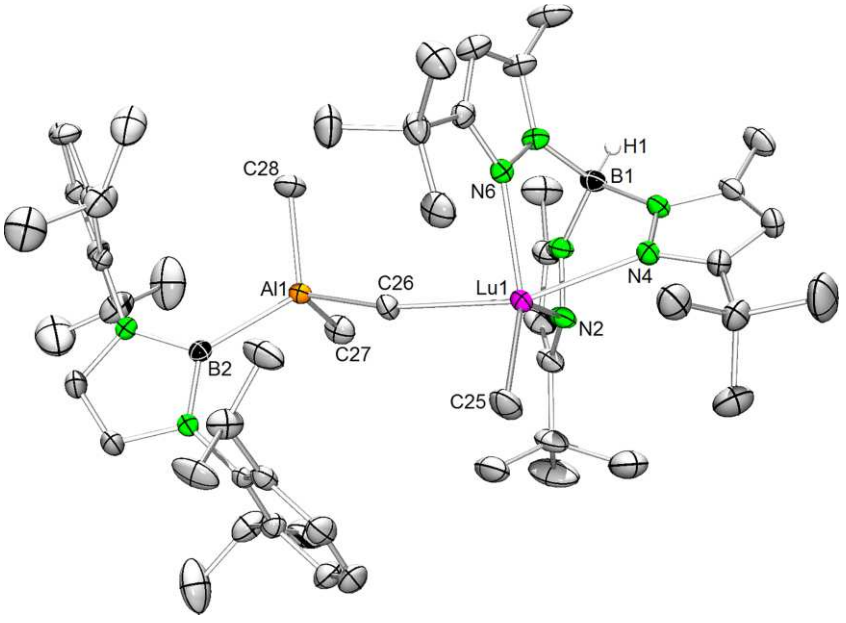

Figure 3. Solid-state structure of **1**; atomic displacement ellipsoids are set at the 50 % probability level. Cocrystallized *n*-hexane, the disorder in the Dipp moieties and one *tert*-butyl group of the $Tp^{tBu,Me}$ ligand and hydrogen atoms except for B–H are omitted for clarity. Selected bond lengths (Å) and angles (°): Lu1–C25 2.321(1), Lu1–C26 2.613(3), Lu1–N2 2.286(2), Lu1–N4 2.369(2), Lu1–N6 2.307(2), Al1–C26 2.092(3), Al1–C27 1.993(3), Al1–C28 2.002(3), Al1–B2 2.171(3), C25–Lu1–C26 96.5(1), Lu1–C26–Al1 164.5(2), N4–Lu1–C26 153.62(9).

Complex **1** dissolves readily in benzene but decomposes slowly at ambient temperature. While decomposition of $\mathbf{I^{Lu}}$ results in a variety of undefined products,[19] decomposition of **1** yielded exclusively [$(Tp^{(tBu-H)}_2/tBu,Me)Lu(AlMe_2\{B(NDippCH)_2\})$] (**2**) with concomitant formation of two equivalents of methane {Scheme 1; $Tp^{(tBu-H)}_2/tBu,Me$ = hydro(3-Me-5-*t*Bu-pyrazolyl)bis-[μ-(3-Me-5-Me_2C-CH_2-pyrazolyl)]borate}. The reaction is driven to completeness at 60 °C after three days according to ^{1}H NMR spectroscopy.

The solid-state structure of **2** revealed a doubly metalated $Tp^{tBu,Me}$ ligand resulting from σ-bond metathesis between the C–H bonds of two *t*Bu groups and the Lu–CH_3 bonds (Figure 4).

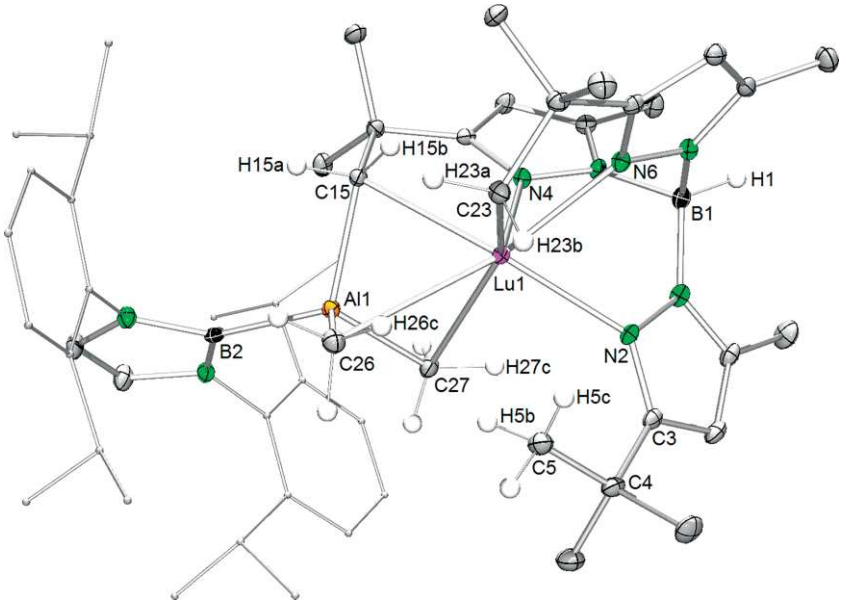

Figure 4. Solid-state structure of **2**; atomic displacement ellipsoids are set at the 50 % probability level. The carbon atoms of the Dipp moieties are shown with reduced radii. Cocrystallized *n*-hexane, the disorder in one Dipp moiety and hydrogen atoms except for B–H, C5–H, methyl and methylene groups are omitted for clarity. Selected bond lengths (Å) and angles (°): Lu1–C15 2.666(3), Lu1–C23 2.391(3), Lu1–C26 2.961(3), Lu1–C27 2.858(3), Lu1···H5b 2.57(3), Lu1···H5c 2.78(3), Lu1···H15b 2.36(3), Lu1···H23a 2.92(4), Lu1···H23b 2.79(3), Lu1···H26c 2.59(3), Lu1···H27c 2.58(3), Lu1–N2 2.409(3), Lu1–N4 2.322(3), Lu1–N6 2.300(2), Al1–C15 2.085(3), Al1–C26 2.024(4), Al1–C27 2.020(3), Al1–B2 2.142(4), C15–Lu1–C23 97.7(1), Lu1–C15–Al1 74.6(1), Lu1–C26–Al1 68.7(1), Lu1–C27–Al1 71.1(1); selected bond lengths (Å) and angles (°) of isostructural complex **3**: Lu1–C15 2.769(3), Lu1–C23 2.386(3), Lu1–C26 2.911(4), Lu1–C27 2.813(4), Ga1–C15 2.091(3), Ga1–C26 2.072(3), Ga1–C27 2.055(4), Ga1–B2 2.099(4), C15–Lu1–C23 97.0(1), Lu1–C15–Ga1 71.7(1), Lu1–C26–Ga1 68.8(1), Lu1–C27–Ga1 71.2(1).

As a consequence, the rare-earth-metal center is coordinated by the Tp^{tBu,Me} ligand in a κ^5 fashion via three nitrogen atoms and two methylene groups. Metalation of the Tp^{tBu,Me} ligand at one *tert*-butyl group was reported previously by the group of Takats for the decomposition of lanthanide dialkyl complex [(Tp^{tBu,Me})Y(CH_2SiMe_3)$_2$], to yield a mixture of products[23] while a similar structural motif was reported by our group for a side product resulting from the salt metathesis reaction of [La($AlMe_4$)$_3$] and K(Tp^{tBu,Me}).[24] The Lu–C(methylene) bond lengths in **2** differ considerably involving a longer Lu–C15 [2.666(3) Å] and a shorter Lu–C23 bond of 2.391(3) Å. While the closer methylene group displays a metal interaction with the lutetium center only, the other methylene moiety additionally connects to the [Me_2Al{B(NDippCH)$_2$}] unit.

In contrast to **1**, there are two methyl groups (C26 and C27) in **2** bridging between the Al atom and the rare-earth-metal center. As a consequence, the Al–Me distances in **2** are somewhat shorter than for the singly bridging methyl group in **1**, whereas the Lu–Me distances in **2** are clearly larger. In the X-ray structure analysis of **2**, a number of H atoms were located in close proximity to the Lu center, including two H atoms of the uncoordinated *tert*-butyl substituent at C3 (Figure 4). As H atom positions are only approximate in X-ray diffraction studies, a DFT geometry optimization of **2** (model system **2a**) was carried out in order to obtain accurate positions and to identify potential agostic interactions in **2**. The geometry obtained for **2a** was in excellent agreement with the solid-state structure of **2** (for details, see the Supporting information). Six H atoms were confirmed to display short contacts to the Lu center, ranging between 2.37 and 2.81 Å (Figure 5; for further details, see the Supporting Information). However, no significant elongation of the respective C–H bonds was observed in the case of the methyl groups, and only very small differences in C–H bond lengths for the two methylene groups (for further details, see the Supporting Information). It is interesting to note, that on C15, C26 and C27 only a single H atom is directed at the Lu atom, instead of two, as commonly observed for bridging alkyl groups.[25] In order to quantify the extent of interaction, if any, between the aforementioned C–H bonds and the Lu center, the natural bond orbital (NBO) approach was employed.[26] The calculated set of natural localized molecular orbitals (NLMOs) revealed that between 1.9 and 2.7 % of the C–H bonding electron pairs are delocalized onto the Lu atom (for details, see the Supporting Information).[27]

While this electronic effect almost appears negligible, a total of six such interactions might represent a small, but significant extra contribution to the stabilization of this complex. Based on our findings, strong agostic interactions, however, can be safely ruled out for **2**.

Finally, we investigated whether the coordination mode of the aluminate ligand would change, when the sterics of the bulky Tp^{tBu,Me} ligand was altered. Optimized model systems, in which the *tert*-butyl moiety at C3 was replaced by a methyl group (model system **2b**) and by a hydrogen atom (model system **2c**), displayed, indeed, a stepwise transition from η^3- to η^2-bridging of the aluminato ligand (for details, see the Supporting information). The distance between the Lu atom and the methyl

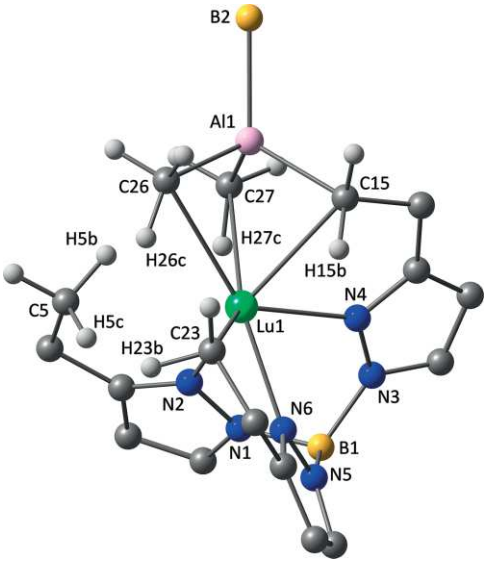

Figure 5. Coordination environment of the Lu center in the DFT-optimized model system of **2**; all further atoms are omitted for clarity. All hydrogen atoms with Lu···H distances shorter than 3 Å are labelled; the distances to Lu1 are as follows (Å): H15b 2.367, H26c 2.481, H27c 2.566, H5b 2.719, H5c 2.778, H23b 2.811.

group on C27 increased from 2.955 in **2a** to 3.381 (**2b**) and 3.678 Å (**2c**), signaling that this methyl group was moving out of the bridging position. At the same time, the interaction between Lu and the bridging methyl group on C26 increased in strength; the Lu–C26 distance shortened notably from 2.808 (**2a**) to 2.571 (**2b**) and 2.477 Å (**2c**). By fixing the angle Lu1–Al1–B2 in **2c** at the value observed in **2a** (174°) and re-optimizing the geometry (model system **2d**), we obtained a good estimate of the energy difference between the two coordination modes: Therefore, the η^2-coordination is about 12 kJ/mol lower in energy, which is outside the typical error range in DFT calculations.

These findings suggest that in **2**, the observed η^3-coordination is only adopted, since a more favorable coordination by two bridging C atoms is prevented by the bulky Tp^{tBu,Me} ligand. The latter seems to be more favorable, as it brings two carbon atoms in closer proximity to the Lu atom compared to the η^3 mode. Once the steric restraint is removed, as in **2b** and **2c**, the coordination mode changes accordingly to η^2.

The ^{1}H NMR spectrum of **2** recorded in [D_6]benzene revealed a very rigid coordination environment at the rare-earth-metal center, as clearly indicated by three sets of signals for the pyrazolyl moieties. Also, two sharp singlets at 0.36 (3 H) and –1.13 ppm (3 H) could be assigned to the Al-Me groups and the resonances attributed to the {B(NDippCH)$_2$} unit split in two sets of signals, indicating a rotational barrier around the Al–B bond. According to ^{1}H,^{1}H-COSY and ^{1}H,^{13}C-HMBC NMR spectroscopic experiments, the protons of the bridging methylene moiety Lu–CH_2(pyrazolyl)–Al resonate as doublets at δ = 1.89 and 1.08 ppm with geminal coupling constants of ^2J(H,H) = 16.9 and 17.2 Hz, respectively, while the remaining two doublets of the non-bridging methylene group are located at δ = 1.07 and 0.75 ppm [^2J(H,H) = 13.6 and 13.7 Hz]. Hence, the doublets at δ = 1.08 and 1.07 ppm are mutually overlapped and addition-

ally interfered by a singlet at δ = 1.11 ppm (Figures S10 and S11). However, for those protons four well resolved doublets are found in the ^{1}H NMR spectrum recorded in [D$_8$]toluene at 1.80 [^2J(H,H) = 17.0 Hz], 0.98 [^2J(H,H) = 17.1 Hz], 0.96 [^2J(H,H) = 13.6 Hz] and 0.62 ppm [^2J(H,H) = 13.7 Hz], unequivocally corroborating the asymmetric environment for the methylene protons (Figure S7). The differences of the chemical shifts is a consequence of the different binding situations at the methylene groups. The signal of the CH_2(pyrazolyl) moiety coordinating exclusively to the rare-earth-metal center is shifted to lower field. In contrast, coordination of the [Me$_2$Al{B(NDippCH)$_2$}] unit would decrease electron density at the respective methylene group and shift the proton signals to higher fields.

The high mobility of the [Me$_2$Al{B(NDippCH)$_2$}] unit in methyl complex **1** vs. its apparent immobility in methylene complex **2** points at a likely mechanistic scenario of the process of C–H bond activation. The four-center-transposition required for σ-bond metathesis seems to involve the terminal Lu–CH_3 moiety, which is forced into close proximity with a *t*Bu group by the bulky heteroaluminato entity. Tallying with this, precursor [(Tp^{tBu,Me})LuMe$_2$] featuring two terminal methyl ligands was ascribed a remarkable thermal stability.[28] Following this first C–H bond activation and formation of the first methylene moiety, the [Me$_2$Al{B(NDippCH)$_2$}] unit switches positions from methyl to methylene and stays locked in this position (adopting a η^3-heteroaluminato coordination). Subsequently, the now available "second" terminal Lu–CH_3 moiety can engage in σ-bond metathesis and formation of the second methylene group.

A Gallate Variant of Complex [(Tp$^{(tBu–H)}_2$/*t*Bu,Me)Lu(AlMe$_2${B(NDippCH)$_2$})] (2) and Reactivity of 2 with THF and AlMe$_3$

Treating [(Tp^{tBu,Me})LuMe$_2$] with one equivalent of [Me$_2$Ga{B(NDippCH)$_2$}][29] in [D$_6$]benzene at ambient temperature did not result in any reaction. However, the gallium analogue of compound **2**, [(Tp$^{(tBu–H)}_2$/*t*Bu,Me)Lu(GaMe$_2${B(NDippCH)$_2$})] (**3**), formed quantitatively within four days at 50 °C according to ^{1}H NMR spectroscopy (Scheme 1) and crystallized isostructurally to **2** (Figure S15). Moreover, complex **3** displays the same rigid coordination behavior in solution as complex **2** (Figure S13). This reactivity is in accordance with the aforementioned mechanistic scenario, that increased steric pressure exerted by even a weakly coordinating [Me$_2$Ga{B(NDippCH)$_2$}] unit enforces C–H bond activation and that the methylene moiety engages in a stronger interaction with the [Me$_2$Ga{B(NDippCH)$_2$}] unit than a terminal methyl group does.

The reaction of complex **2** with an excess of THF and AlMe$_3$, respectively, was monitored by ^{1}H NMR spectroscopy in [D$_6$]benzene. Thus, in the presence of THF separation of the [Me$_2$Al{B(NDippCH)$_2$}] unit occurred via formation of THF adduct [(THF)Me$_2$Al{B(NDippCH)$_2$}] (about 92 %) and a new lutetium compound, presumably [(Tp$^{(tBu–H)}_2$/*t*Bu,Me)Lu(THF)$_x$] (Scheme 2), indicated by a new set of signals assigned to two different pyrazolyl moieties in a 2:1 ratio. The increased symmetry of the new complex is further evidenced by two doublets assigned to the methylene protons at 0.82 [2 H, ^2J(H,H) = 12.5 Hz] and 0.64 ppm [2 H, ^2J(H,H) = 12.4 Hz] (Figure S17). However, crystallization at –40 °C seemed to favor the back reaction, since chilled solutions of **2** in *n*-pentane/THF generated only crystals of **2**.

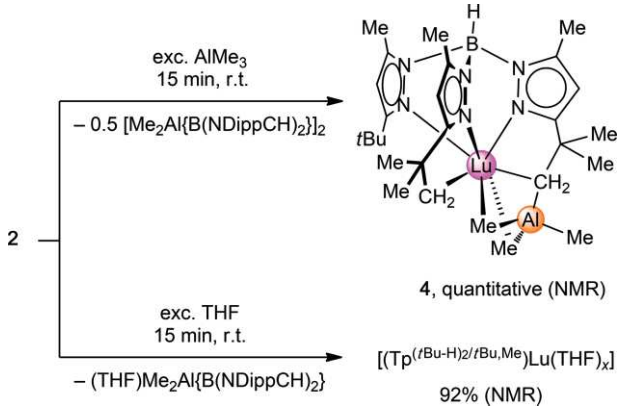

Scheme 2. Reaction of [(Tp$^{(tBu–H)}_2$/*t*Bu,Me)Lu(AlMe$_2${B(NDippCH)$_2$})] (**2**) with an excess of AlMe$_3$ and THF, respectively, in [D$_6$]benzene.

The AlMe$_3$-reaction led to the exchange of [Me$_2$Al{B(NDippCH)$_2$}]$_2$ through AlMe$_3$ and formation of the new complex [(Tp$^{(tBu–H)}_2$/*t*Bu,Me)Lu(AlMe$_3$)] (**4**) (Scheme 2), which was identified by X-ray diffraction analysis (Figure 6).

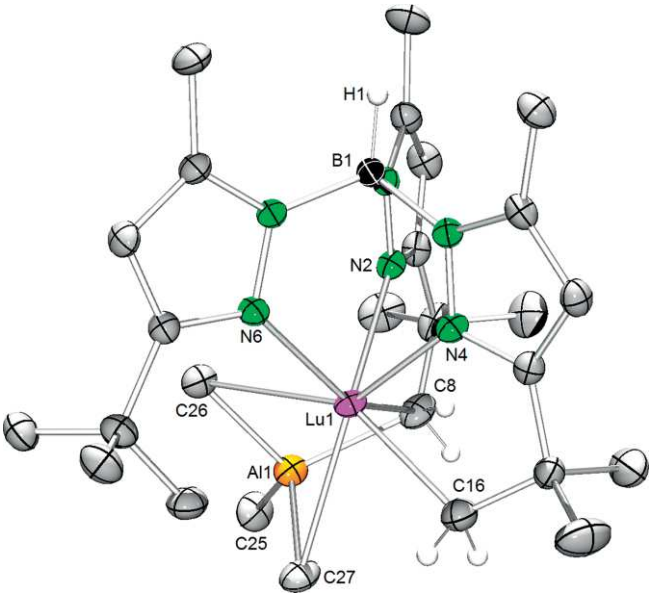

Figure 6. Solid-state structure of **4**; atomic displacement ellipsoids are set at the 50 % probability level. The second molecule of the asymmetric unit and the hydrogen atoms except for B–H and methylene groups are omitted for clarity. Selected bond lengths (Å) and angles (°): Lu1–C8 2.823(6), Lu1–C16 2.418(5), Lu1–C26 2.824(6), Lu1–C27 2.870(6), Lu1–N2 2.487(3), Lu1–N4 2.197(3), Lu1–N6 2.320(3), Al1–C8 2.203(6), Al1–C25 1.85(1), Al1–C26 2.096(7), Al1–C27 2.057(6), C8–Lu1–C16 96.0(2), Lu1–C8–Al1 64.4(2), Lu1–C26–Al1 65.4(2), Lu1–C27–Al1 64.8(2).

Compound **4** adopts a similar crystal structure as complex **2**. However, due to less steric hindrance at the [AlMe$_3$CH$_2$] unit,

the Lu1···Al1 distance [2.729(3) Å] is shorter than in **2** [2.917(1) Å] and the Lu1–CH_2 bond to the bridging methylene group is elongated [2.823(6) vs. 2.673(3) Å]. As a consequence the [$AlMe_3CH_2$] unit engages in a η^3 coordination mode and the aluminum carbon bonds to the coordinating methyl/methylene groups are elongated [2.203(6), 2.096(7), 2.057(6) Å] compared to compound **2**.

Polymerization of Isoprene

The performance of complexes **1** and **2** was assessed in the polymerization of isoprene. While none of the complexes served as a single-component catalyst, in situ activation with borate and borane cocatalysts, respectively, led to the fabrication of polyisoprene within one hour (Table 1, Figure 7).

Applying **1** in combination with the borate cocatalysts [Ph_3C][$B(C_6F_5)_4$] (**A**) or [$PhNMe_2H$][$B(C_6F_5)_4$] (**B**) polyisoprenes with predominant *cis*-1,4 units in low to moderate yields were obtained (runs 1–4), while for the borane cocatalyst [$B(C_6F_5)_3$] (**C**) an unselective microstructure was found (run 5). The binary systems **1**/**A** and **1**/**C** gave multimodal molecular weight distributions (MWDs) with a main mode at 67 and 33 kg/mol, respectively, which revealed polydispersity indices (PDIs) of 1.91 and 1.80, representing 85 and 78 mol-% of the polymer, respectively. For cocatalyst **B** a monomodal MWD with a PDI as high as 2.98 was obtained (run 4). These findings and ^{1}H NMR spectroscopic studies of the active species (Figures S19, S20, and S21) led us to conclude that the catalyst has altered (degraded) during the catalytic process. Such "degradation" products display active catalysts in combination with cocatalysts **A** and **C**, initiating new polymerizations responsible for the MWD side modes in these products. However, in combination with cocatalyst **B**, the "degradation" products seem to be inactive, in the first place. This means that the number of active centers changes during the polymerization causing the augmented polydispersity of the polymer (vide infra).

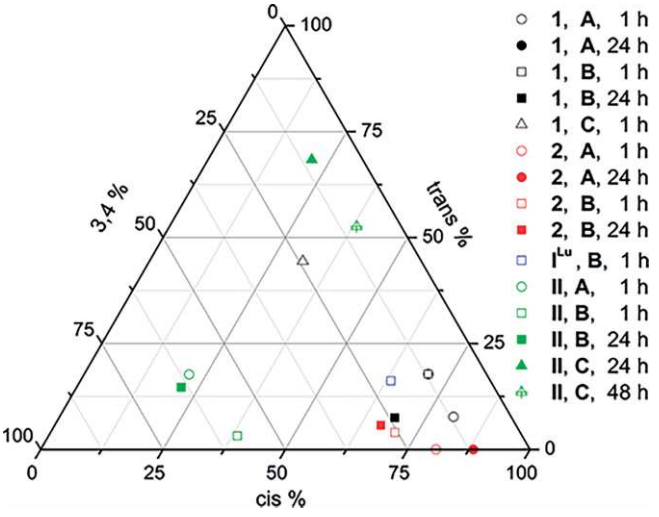

Figure 7. Ternary plot of the microstructures of the polyisoprenes obtained from precatalysts **1**, **2**, $\mathbf{I^{Lu}}$ and **II** upon activation with **A** (●), **B** (■) and **C** (▲) (see Table 1).

If the thermolytic product **2** is applied as a precatalyst in combination with cocatalysts **A**–**C**, in in situ activation reactions, polyisoprenes were obtained only for the borate cocatalysts **A** and **B** (runs 6–9). With these binary systems higher *cis*-1,4 selectivities were observed [up to 88 % (**2**/**A**), Table 1, run 7]. Multimodal MWDs were found with **2**/**A** and **2**/**B**, as well, while in case of cocatalyst **A** only 24 % of the obtained blend was THF soluble and could therefore be analyzed (run 7). With cocatalyst **B**, which produced a less active initiator compared

Table 1. Selected examples for isoprene homopolymerization applying precatalysts **1** and **2**.

Entry[a]	Pre-catalyst	Co-catalyst[b]	Time (h)	Yield (%)	*cis*-1,4[c]	*trans*-1,4[c]	3,4[c]	M_n[d] (× 10^4 g/mol)	M_w/M_n[d]	T_g[e] (°C)
1	**1**	**A**	1	14	80.6	7.7	11.8	6.7[f]	1.91[f]	–56.9
2	**1**	**A**	24	90	70.3	17.8	11.9	14.0	2.63	–56.1
3	**1**	**B**	1	47	72.5	2.6	24.9	11.9	3.72	–47.5
4	**1**	**B**	24	89	68.7	7.5	23.9	14.0	2.98	–48.2
5	**1**	**C**	1	31	31.4	44.4	24.2	3.3[f]	1.80[f]	–38.6
6	**2**	**A**	1	32	80.8	0.0	19.2	26.4	1.77	–52.8
7	**2**	**A**	24	> 99	88.4	0.0	11.6	5.6[g]	2.41[g]	–54.6
8	**2**	**B**	1	2	70.4	4.0	25.6	36.1[f]	1.81[f]	–46.0
9	**2**	**B**	24	90	66.7	5.7	27.6	27.9[f]	2.60[f]	–45.9
10	$\mathbf{I^{Lu}}$	**A**	1	0	–	–	–	–	–	–
11	$\mathbf{I^{Lu}}$	**B**	1	90	63.5	16.2	20.3	15.3	2.40	–51.5
12[h]	**II**	**A**	1	> 99	21.5	17.7	60.8	4.7	1.44	n.d.
13[h]	**II**	**B**	1	5.5	38.6	3.2	58.2	n.d.[i]	n.d.[i]	n.d.
14[h]	**II**	**B**	24	> 99	21.4	14.7	63.9	6.0	1.23	n.d.
15[h]	**II**	**C**	1	traces	n.d.[j]	n.d.[j]	n.d.[j]	n.d.[j]	n.d.[j]	n.d.
16[h]	**II**	**C**	24	34.1	21.2	68.4	10.4	3.0	1.97	n.d.
17[h]	**II**	**C**	48	65.9	38.3	52.6	9.1	3.2	2.07	n.d.

[a] Conditions: 0.02 mmol precatalyst, 8 mL of toluene, 20 mmol isoprene, ambient temperature. [b] Aged with cocatalyst at ambient temperature for 5 min: **A** = [Ph_3C][$B(C_6F_5)_4$], **B** = [$PhNMe_2H$][$B(C_6F_5)_4$], **C** = [$B(C_6F_5)_3$]. [c] Determined by ^{1}H and ^{13}C NMR spectroscopy in $CDCl_3$. [d] Determined by means of size-exclusion chromatography (SEC) against polystyrene standards. [e] Determined on a Perkin–Elmer DSC 8000; heat rate: 20 K/min, cooling rate: 60 K/min. [f] MWD contains more than one mode. The data of the main mode is given here; it represents 85 mol-% (run 1), 78 mol-% (run 5), 98 mol-% (run 8), and > 99 mol-% (run 9) of the polymer. [g] The polymers are not fully soluble in THF. The data of the soluble part is given here; it represents 24 mol-% of the actual polymer mixture. [h] Taken from ref.[11] [i] Not determined due to low polymer solubility in THF. [j] Not determined due to low yield.

to **1**/**B**, the formed polyisoprene is completely soluble, but bimodal MWDs were observed in GPC analysis. For **2**/**B** the content of the smaller mode at M_n of about 1200 kg/mol was at 2 mol-% of the polymer after 1 h and <0.1 mol-% after 24 h (Table 1, runs 8 and 9), which implies that the production of the polymer with high M_n ceased already in the beginning of the polymerization reaction. Thereafter, the main part of the polymer was produced with a higher PDI but a shorter average chain length. The corresponding active species resulting from the binary system **2**/**B** was stable in solution over several days and was investigated by ^{1}H NMR spectroscopy (Figure S23). These findings can be interpreted by a continuous, slow initiation process, taking place over a long period upon monomer addition. As the active species is formed quantitatively within five minutes in the prereaction, according to NMR spectroscopic data, this is probably due to a low affinity of this active species to coordinate the first monomer.

Comparing the performance of **1** with its [$AlMe_4$] analogue [($Tp^{tBu,Me}$)Lu(Me)($AlMe_4$)] (**I^{Lu}**), (Table 1, runs 10 and 11) revealed that **I^{Lu}** is only active, when activated by a Brønsted acid, that is, cocatalyst **B** under the given conditions. Binary system **I^{Lu}**/**B** produced polymers with higher *trans* contents compared to the boryl-implemented system **1**/**B**, which is in analogy the polymers fabricated by similar Cp*-supported systems.[5,9] Furthermore, complex [Cp*Lu($AlMe_3${B(NDippCH)$_2$})$_2$] (**II**) has been investigated previously by us (Table 1, runs 12–17).[11] Based on a ^{1}H NMR spectroscopic study, the active species of the binary system **II**/**A** was described as a weakly coordinated (via Lu···F) cation/anion pair with the lutetium center surrounded by a Cp* and a heteroaluminato ligand, the latter of which forming two Lu–CH_3-linkages and a Lu···arene contact involving the peripheral boryl moiety. This catalytic system produced a polymer that contains mainly monomer units, added in vinylic 3,4-fashion, as a consequence of the crowded coordination sphere at the lutetium center. The low vinyl content of the polyisoprenes detected in the present study applying **1** suggests a sterically less saturated active lutetium species (vide infra). Interestingly, for both binary systems **1**/**C** and **II**/**C** a large shift toward *trans*-selectivity was observed.

Investigation of the catalytic species resulting from the binary system **1**/**B** by ^{1}H NMR spectroscopy did indicate a different activation process compared to the binary system **II**/**A**.[11,30] Although a comprehensive/accurate peak assignment of the active species was hampered by signal overlapping (Figure S19, Supporting Information), some approximations were possible. The sharpening of the [Me_2Al{B(NDippCH)$_2$}] proton signal that occurred, is characteristic of donor-coordinated monomer species of the [(Do)Me_2Al{B(NDippCH)$_2$}] structural motif. This indicated the formation of [(NMe_2Ph)Me_2Al{B(NDippCH)$_2$}], which implied the concomitant formation of [($Tp^{tBu,Me}$)LuMe][$B(C_6F_5)_4$] (**5a**) (Scheme 3). Species **5a** could react further to [($Tp^{(tBu-H)/tBu}_2$,Me)Lu][$B(C_6F_5)_4$] (**5b**) [$Tp^{(tBu-H)/tBu}_2$,Me = hydrobis(3-Me-5-*t*Bu-pyrazolyl){μ-(3-Me-5-Me_2CCH_2-pyrazolyl)}borate], which would explain the ongoing methane formation monitored by ^{1}H NMR spectroscopy. If the formation of the C–H bond activated complex **5b** would occur after initiation, this would have terminated the growing polymer chain and therewith caused the high polydispersity. Complex **5b** shows a similar structural motif as the active species [($Tp^{(tBu-H)/tBu}_2$,Me)-Lu(Me_2Al{B(NDippCH)$_2$})][$B(C_6F_5)_4$] (**6**) targeted for the system **2**/**B** (Scheme 3).

Monitoring the activation of **2** with cocatalyst **B** (only benzene soluble part) by ^{1}H NMR spectroscopy (Figure S23) showed neither the abovementioned sharpening of the [Me_2Al{B(NDippCH)$_2$}] signal of the main product nor the occurrence of free $PhNMe_2$. Moreover, the signal pattern observed for the

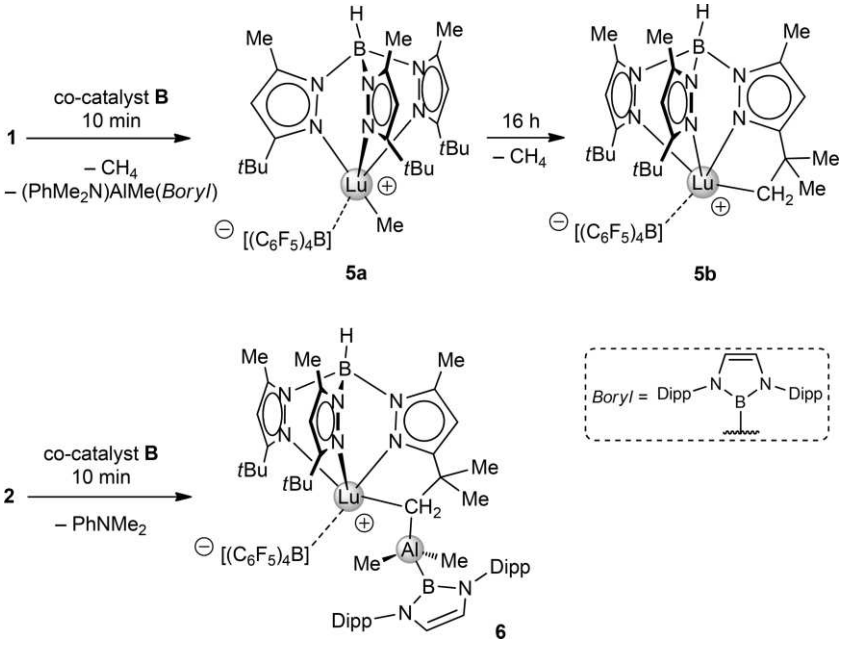

Scheme 3. Proposed activation scenario of [($Tp^{tBu,Me}$)Lu(Me)($AlMe_3${B(NDippCH)$_2$})] (**1**) and [($Tp^{(tBu-H)}_2$/*t*Bu,Me)Lu($AlMe_2${B(NDippCH)$_2$})] (**2**) with cocatalyst [$PhNMe_2H$][$B(C_6F_5)_4$] (**B**).

tris(pyrazolyl)borato ligand was in agreement with the formation of complex **6**, requiring the re-protonation of one [μ-CH_2(R)] moiety. Hence, **6** differs from **5b** through the [μ-CH_2(R)] moiety which is linked to a [Me_2Al{B(NDippCH)$_2$}] unit. Preservation of the Lu–CH_2(R)–Al linkage further proved the high stability of this moiety and also underpinned the mechanistic C–H bond activation scenario considered vide supra. In contrast to the arene-stabilized active species obtained from **II**/**A**, the steric encumbrance of the Tp system in **5b** or **6** disfavors a similar π-interaction with the peripheral boryl, as suggested by NMR spectroscopy. Since, both in **5b** and **6**, the Lu–CH_2(R)–Al linkage features supposedly the initiating site chain propagation will accomplish Lu centers of almost identical environment (off-migration of the bulky boryl moiety). This explains, why the polymerization results applying **1**/**B** and **2**/**B** differed after one hour (Table 1, runs 3 and 8), but after 24 h, a rather identical polymer was observed (Table 1, runs 4 and 9).

The ^{19}F NMR spectroscopic analysis (Figures S22 and S24) according to Horton et al.[31] indicated weak interactions between the [B(C_6F_5)$_4$] anion and the respective cationic entity in both catalyst mixtures (**1**/**B** and **2**/**B**).[32]

Conclusions

The terminal lutetium methyl complex [(Tp^{tBu,Me})LuMe_2] adds selectively one equivalent of the bulky organoaluminum boryl moiety [Me_2Al{B(NDippCH)$_2$}] (Dipp = C_6H_3iPr$_2$-2,6) to afford [(Tp^{tBu,Me})Lu(Me)(AlMe$_3${B(NDippCH)$_2$})] featuring a Lu–CH_3–Al linkage (η^1-heteroaluminato coordination). This nicely reflects the enhanced steric demand of the Tp^{tBu,Me} vs. the C_5Me_5 ancillary ligand, since it has been shown previously that [(C_5Me_5)LuMe_2]$_3$ does form a twofold addition compound.[11] [(Tp^{tBu,Me})Lu(Me)(AlMe$_3${B(NDippCH)$_2$})] was found to undergo a thermally induced intramolecular cyclometalative C–H bond activation (Tp^{tBu,Me} ligand degradation) giving complex [(Tp$^{(tBu-H)}_2$/*t*Bu,Me)Lu(AlMe$_2${B(NDippCH)$_2$})] by releasing two equivalents of methane. The increased steric unsaturation implied by the twofold cyclometalation effects a η^3-heteroaluminato coordination of the organoaluminum boryl fragment. In contrast to the highly fluxional η^1-heteroaluminato coordination, the latter η^3-mode stays locked at ambient temperature as shown by VT NMR spectroscopy. Nevertheless, the [Me_2Al{B(NDippCH)$_2$}] unit can be fully separated off/displaced by addition of THF or trimethylaluminum. The gallium analogue of complex [(Tp^{tBu,Me})Lu(Me)(AlMe$_3${B(NDippCH)$_2$})] was found not isolable but the C–H bond activated gallate complex [(Tp$^{(tBu-H)}_2$/*t*Bu,Me)Lu(GaMe$_2${B(NDippCH)$_2$})] could be obtained quantitatively following prolonged mild thermal treatment. Such distinct aluminate/gallate reactivity is in line with our previous findings of a weaker gallate bonding.[28] Applying [(Tp^{tBu,Me})Lu(Me)(AlMe$_3${B(NDippCH)$_2$})] and cyclometalated [(Tp$^{(tBu-H)}_2$/*t*Bu,Me)Lu(AlMe$_2${B(NDippCH)$_2$})] in the presence of fluorinated borate cocatalysts in isoprene polymerization resulted in moderately *cis*-selective monomer addition. The resulting polymers are mainly bimodal and of augmented polydispersity due to active species degradation, which could be corroborated by ^{1}H NMR spectroscopy. A most likely active (and degraded) species is featured by [(Tp$^{(tBu-H)/tBu}_2$,Me)Lu(Me_2Al{B(NDippCH)$_2$})][B(C_6F_5)$_4$] comprising three distinct boron sites.

Experimental Section

General Considerations: Syntheses and manipulations of all organometallic compounds were carried out under dry argon by using standard *Schlenk*, high-vacuum, and glovebox techniques (MBraun MB 200B; <1 ppm O_2, <1 ppm $H_2$0). *n*-Pentane, *n*-hexane, toluene, and THF were purified by using *Grubbs* columns (MBraun SPS-800, solvent purification system) and stored in a glovebox. [D_6]benzene and [D_8]toluene were obtained from Aldrich, dried with sodium for 24 h, and filtered prior to use. [D]Chloroform and $AlMe_3$ were purchased from Aldrich and used as received. Isoprene was obtained from Aldrich, dried with trioctylaluminum, and vacuum transferred prior to use. [Ph_3C][B(C_6F_5)$_4$] (**A**) [PhNMe_2H][B(C_6F_5)$_4$] (**B**), and B(C_6F_5)$_3$ (**C**) were purchased from Boulder Scientific Company and used without any further purification. [(Tp^{tBu,Me})LuMe_2],[20] [(Tp^{tBu,Me})Lu(Me)AlMe_4],[19] [Me_2Al{B(NDippCH)$_2$}]$_2$[21] (Dipp = C_6H_3iPr$_2$-2,6) and [Me_2Ga{B(NDippCH)$_2$}][29] were synthesized according to literature procedures. NMR spectra of air- and moisture-sensitive compounds were recorded by using *J. Young* valve NMR tubes at 26 °C with a *Bruker* DMX-400 Avance (^{1}H: 400.13 Hz; ^{13}C: 100.61 MHz). ^{1}H and ^{13}C shifts are referenced to internal solvent resonances and reported in parts per million (ppm) relative to TMS. IR spectra were recorded with a NICOLET 6700 FTIR spectrometer using a DRIFT chamber with dry KBr/sample mixtures and KBr windows. For the latter the collected data were converted using the Kubelka–Munk refinement. Elemental analyses were performed with an *Elementar Vario MICRO cube*. Single crystals suitable for X-ray structure analyses were selected in a glovebox, coated with Paratone-N (Hampton Research). X-ray data were collected with a Bruker APEX II DUO diffractometer by using QUAZAR optics and Mo-K_α radiation (λ = 0.71073 Å) with ω and φ scans. Raw data were processed by using APEX2[33] and SAINT[34] software; structure solution and final model refinement were performed by using SHELXTL and SHELXLE.[35] Corrections for absorption effects were applied by using SADABS.[36] All plots were generated utilizing the programs ORTEP-3[37] and POV-Ray.[38] The molar masses (M_W and M_n) of the polymers were determined by size-exclusion chromatography (SEC). Sample solutions (1.0 mg of polymer per mL THF) were filtered through a 0.45 μm syringe filter prior to injection. SEC was performed with a pump supplied by Viscotek (GPCmax VE 2001), employing ViscoGEL columns. Signals were detected by means of a triple detection array (TDA 305) and calibrated against polystyrene standards (M_W/M_n < 1.15). The flowrate was set to 1.0 mL min^{-1}. The microstructures of the polyisoprenes were examined by means of ^{1}H and ^{13}C NMR spectroscopic experiments with AV400 spectrometers at ambient temperature, using [D]chloroform as a solvent. Glass transition temperatures of the polyisoprenes (T_g) were recorded with a Perkin–Elmer DSC 8000 calibrated with indium and cyclohexane standards, scanning from –100 °C up to +100 °C with heating rates of 20 K/min and cooling rates of 60 K/min in N_2 atmosphere.

[(Tp^{tBu,Me})Lu(Me)(AlMe$_3${B(NDippCH)$_2$})] (1): A solution of [Me_2Al{B(NDippCH)$_2$}]$_2$ (106 mg, 0.12 mmol) in *n*-hexane (5 mL) was stirred into a suspension of [(Tp^{tBu,Me})LuMe_2] (150 mg, 0.24 mmol) in *n*-hexane (4 mL). The white suspension turned into an almost clear solution within 30 minutes. The reaction mixture was stirred for 1 h at ambient temperature and then cooled to –40 °C for 16 h. Clear, colorless crystals formed. The supernatant was decanted, and

the product was concentrated to dryness in vacuo to yield **1** as a white powder (253 mg, 0.24 mmol, 97 %). Single crystals suitable for X-ray crystallography were grown from a saturated *n*-hexane solution at –40 °C. ^{1}H NMR ([D$_6$]benzene, 400 MHz, 26 °C): δ = 7.29 (s, 6 H, H_{Ar}), 6.47 (s, 2 H, NC*H*), 5.59 (s, 3 H, 4-pz-*H*), 4.40 (br. s, 1 H, B*H*), 3.65 [sept, ^3J(H,H) = 6.8 Hz, 4 H, C*H*(CH$_3$)$_2$], 1.91 (s, 9 H, pz-CH_3), 1.47 [d, ^3J(H,H) = 6.8 Hz, 12 H, CH(CH_3)$_2$], 1.33 [d, ^3J(H,H) = 6.8 Hz, 12 H, CH(CH_3)$_2$, overlapping with peak 1.32], 1.32 [s, 27 H, pz-C(CH_3)$_3$], –0.14 [br. s, 6 H, Lu(CH_3)$_2$], –1.20 [br. s, 6 H, Al(CH_3)$_2$] ppm. ^{13}C{^{1}H} NMR ([D$_6$]benzene, 101 MHz, 26 °C): δ = 166.0 (3-pz-*C*), 148.3 (5-pz-*C*), 146.5 (Ar, C_{ortho}), 144.0 (Ar, C_{ipso}), 126.4 (Ar, C_{para}), 123.0 (Ar, C_{meta}), 120.7 (NCH), 105.0 (4-pz-*C*), 32.3 [*C*(CH$_3$)$_3$], 31.4 [C(*C*H$_3$)$_3$], 28.6 [*C*H(CH$_3$)$_2$], 25.7 [CH(*C*H$_3$)$_2$], 24.2 [CH(*C*H$_3$)$_2$], 12.9 (pz-*C*H$_3$), –4.5 [Lu(*C*H$_3$)$_2$ or Al(*C*H$_3$)$_2$] ppm; for the carbon atoms of the Lu(CH$_3$)$_2$ or Al(CH$_3$)$_2$ groups, respectively, only one very broad signal could be detected. ^{11}B{^{1}H} NMR ([D$_6$]benzene, 80 MHz, 26 °C): δ = 39.3 (*B*Al), –8.8 (*B*H) ppm. DRIFT (KBr): $\tilde{\nu}$ = 2562 (m, B–H) cm^{-1}. $C_{54}H_{88}AlB_2LuN_8$ (1072.92 g mol^{-1}): calcd. C 60.45, H 8.27, N 10.44; found C 60.67, H 8.11, N 10.40.

[(Tp$^{(tBu–H)}$$_2$/*t*Bu,Me)Lu(AlMe$_2${B(NDippCH)$_2$})] (2): A solution of **1** (261 mg, 0.24 mmol) in benzene (4 mL) was stirred in a pressure tube for 72 h at 60 °C. The solvent was removed in vacuo and the resulting yellow, sticky residue triturated with *n*-pentane (1.5 mL). The resulting white precipitate was washed with *n*-pentane (2 × 1 mL) and concentrated to dryness in vacuo to yield a white powder (194 mg, 0.19 mmol, 77 %). Single crystals suitable for X-ray crystallography were grown from a saturated *n*-hexane solution at –40 °C. ^{1}H NMR ([D$_6$]benzene, 400 MHz, 26 °C): δ = 7.19 (m, 4 H, H_{Ar}), 7.12 (m, 2 H, H_{Ar}), 6.48 (s, 2 H, NC*H*), 5.55 [d, ^4J(H,H) = 0.5 Hz, 1 H, 4-pz-*H*], 5.53 [d, ^4J(H,H) = 0.6 Hz, 1 H, 4-pz-*H*], 5.49 [d, ^4J(H,H) = 0.5 Hz, 1 H, 4-pz-*H*], 4.57 (br. s, 1 H, B*H*), 3.59 [sept, ^3J(H,H) = 6.8 Hz, 2 H, C*H*(CH$_3$)$_2$], 3.48 [sept, ^3J(H,H) = 6.8 Hz, 2 H, C*H*(CH$_3$)$_2$], 2.11 (s, 3 H, pz-CH_3), 2.07 (s, 3 H, pz-CH_3), 1.89 (s, 3 H, pz-CH_3), 1.89 [d, ^2J(H,H) = 16.9 Hz, 1 H, C(CH$_3$)$_2$CH_2], 1.54 [s, 3 H, C(CH_3)$_2$CH$_2$], 1.45 [d, ^3J(H,H) = 6.9 Hz, 6 H, CH(CH_3)$_2$], 1.40 [s, 3 H, C(CH_3)$_2$CH$_2$], 1.37 [d, ^3J(H,H) = 6.9 Hz, 6 H, CH(CH_3)$_2$], 1.31 [s, 3 H, C(CH_3)$_2$CH$_2$], 1.28 [d, ^3J(H,H) = 6.8 Hz, 6 H, CH(CH_3)$_2$], 1.21 [d, ^3J(H,H) = 6.8 Hz, 6 H, CH(CH_3)$_2$], 1.17 [s, 9 H, pz-C(CH_3)$_3$], 1.11 [s, 3 H, C(CH_3)$_2$CH$_2$], 1.08 [d, ^2J(H,H) = 17.2 Hz, 1 H, C(CH$_3$)$_2$CH_2], 1.07 [d, ^2J(H,H) = 13.6 Hz, 1 H, C(CH$_3$)$_2$CH_2], 0.75 [d, ^2J(H,H) = 13.7 Hz, 1 H, C(CH$_3$)$_2$CH_2], 0.36 (s, 3 H, AlCH_3), –1.13 (s, 3 H, AlCH_3) ppm. ^{13}C{^{1}H} NMR ([D$_6$]benzene, 101 MHz, 26 °C): δ = 173.1 (3-pz-*C*), 167.4 (3-pz-*C*), 164.5 (3-pz-*C*), 146.8 (5-pz-*C*), 146.4 (Ar, C_{ortho}), 146.4 (Ar, C_{ortho}), 145.4 (5-pz-*C*), 144.6 (5-pz-*C*), 142.5 (Ar, C_{ipso}), 127.2 (Ar, C_{para}), 123.4 (Ar, C_{meta}), 123.3 (Ar, C_{meta}), 121.8 (NCH), 103.5 (4-pz-*C*), 101.9 (4-pz-*C*), 101.1 (4-pz-*C*), 68.4 [C(CH$_3$)$_2$CH$_2$], 40.0 [*C*(CH$_3$)$_2$CH$_2$], 38.6 [C(*C*H$_3$)$_2$CH$_2$], 37.6 [C(CH$_3$)$_2$CH$_2$], 35.9 [C(CH$_3$)$_2$CH$_2$], 35.6 [C(CH$_3$)$_2$CH$_2$], 35.5 [C(CH$_3$)$_2$CH$_2$], 32.3 [*C*(CH$_3$)$_3$], 31.0 [C(*C*H$_3$)$_3$], 30.2 [C(CH$_3$)$_2$CH$_2$], 28.9 [*C*H(CH$_3$)$_2$], 28.5 [CH(*C*H$_3$)$_2$], 27.0 [CH(*C*H$_3$)$_2$], 26.8 [CH(*C*H$_3$)$_2$], 23.6 [CH(*C*H$_3$)$_2$], 22.8 [CH(*C*H$_3$)$_2$], 13.5 (pz-*C*H$_3$), 12.6 (pz-*C*H$_3$), 11.8 (pz-*C*H$_3$), –3.5 (AlCH$_3$), –7.5 (AlCH$_3$) ppm. ^{11}B{^{1}H} NMR ([D$_6$]benzene, 80 MHz, 26 °C): δ = 34.8 (*B*Al), –8.8 (*B*H) ppm. DRIFT (KBr): $\tilde{\nu}$ = 2509 (m, B–H) cm^{-1}. $C_{52}H_{80}AlB_2LuN_8$ (1040.84 g mol^{-1}): calcd. C 60.01, H 7.75, N 10.77; found C 60.32, H 7.48, N 10.45.

[(Tp$^{(tBu–H)}$$_2$/*t*Bu,Me)Lu(GaMe$_2${B(NDippCH)$_2$})] (3): In a *J. Young* valved NMR tube, [(Tp^{tBu,Me})LuMe$_2$] (16.8 mg, 0.027 mmol) in 0.5 mL [D$_6$]benzene was treated with Me$_2$Ga{B(NDippCH)$_2$} (13.0 mg, 0.027 mmol) and heated up to 50 °C for 96 h. The reaction was monitored by ^{1}H NMR spectroscopy. Complete conversion was indicated by the evolution of methane and quantitative formation of **3**. Single crystals suitable for X-ray crystallography were grown from a saturated *n*-pentane solution at –40 °C. ^{1}H NMR ([D$_6$]benzene, 400 MHz, 26 °C): δ = 7.18 (m, 4 H, H_{Ar}), 7.12 (m, 2 H, H_{Ar}), 6.47 (s, 2 H, NC*H*), 5.56 (s, 1 H, 4-pz-*H*), 5.53 (s, 1 H, 4-pz-*H*), 5.50 (s, 1 H, 4-pz-*H*), 4.58 (br. s, 1 H, B*H*), 3.58 [sept, ^3J(H,H) = 6.9 Hz, 2 H, C*H*(CH$_3$)$_2$], 3.46 [sept, ^3J(H,H) = 6.9 Hz, 2 H, C*H*(CH$_3$)$_2$], 2.12 (s, 3 H, pz-CH_3), 2.08 [d, ^2J(H,H) = 16.8 Hz, 1 H, C(CH$_3$)$_2$CH_2], 2.08 (s, 3 H, pz-CH_3), 1.89 (s, 3 H, pz-CH_3), 1.54 [s, 3 H, C(CH_3)$_2$CH$_2$], 1.44 [d, ^3J(H,H) = 6.9 Hz, 6 H, CH(CH_3)$_2$], 1.40 [s, 3 H, C(CH_3)$_2$CH$_2$], 1.37 [d, ^3J(H,H) = 6.9 Hz, 6 H, CH(CH_3)$_2$], 1.28 [s, 3 H, C(CH_3)$_2$CH$_2$], 1.27 [d, ^3J(H,H) = 6.8 Hz, 6 H, CH(CH_3)$_2$], 1.20 [d, ^3J(H,H) = 6.8 Hz, 6 H, CH(CH_3)$_2$], 1.16 [s, 9 H, pz-C(CH_3)$_3$], 1.12 [s, 3 H, C(CH_3)$_2$CH$_2$], 1.10 [d, ^2J(H,H) = 13.6 Hz, 1 H, C(CH$_3$)$_2$CH_2], 1.01 [d, ^2J(H,H) = 16.6 Hz, 1 H, C(CH$_3$)$_2$CH_2], 0.74 [d, ^2J(H,H) = 13.6 Hz, 1 H, C(CH$_3$)$_2$CH_2], 0.44 (s, 3 H, GaCH_3), –1.08 (s, 3 H, GaCH_3) ppm. ^{11}B{^{1}H} NMR ([D$_6$]benzene, 80 MHz, 26 °C): δ = 30.2 (*B*Ga), –9.6 (*B*H) ppm.

Homopolymerization of Isoprene: A detailed polymerization procedure is described as a typical example (Table 1, run 1). [Ph$_3$C][B(C$_6$F$_5$)$_4$] (**A**) (18 mg, 0.02 mmol, 1 equiv.) was added to a solution of **1** (21.5 mg, 0.02 mmol) in toluene (8 mL) and the mixture was aged at ambient temperature for 5 min. After the addition of isoprene (1.36 g, 20 mmol), the polymerization was carried out at 25 °C for 1 h. The reaction was terminated by pouring the polymerization mixture into 25 mL of methanol containing 0.1 % (w/w) 2,6-di-*tert*-butyl-4-methylphenol as a stabilizer and stirred for 1 h. The polymer was washed with methanol and dried under vacuum at ambient temperature to constant weight.

Computational Details: DFT calculations were carried out with the Gaussian 09 program suite[39] using the BP86 density functional,[40] along with the implemented cc-pVTZ basis set for the p block elements and the cc-pVDZ basis set for all H atoms.[41] For the Lu center, a Stuttgart/Dresden effective core potential for 28 core electrons (MWB28) was employed,[42] in combination with the optimized valence basis set as implemented in Gaussian 09. All geometry optimizations were performed without imposing any symmetry constraints, and the structures obtained were confirmed as true minima by calculating analytical frequencies. NBO analyses were carried out by using the NBO 6.0 software.[43] Plots were generated with the software Chemcraft.[44]

Acknowledgments

The authors are grateful to the German Science Foundation (Grant: An238/14-2) and Bridgestone Japan for support, as well as for the computational resources provided by the bwForCluster JUSTUS, funded by the State of Baden-Württemberg, Germany, through the bwHPC project, and by the Deutsche Forschungsgemeinschaft (DFG). We thank Cornelius Knappe for assistance with the DFT calculations.

Keywords: Aluminum · C–H activation · Borates · Gallium · Lutetium

[1] For recent review articles, see: a) M. Nishiura, Z. Hou, *Nat. Chem.* **2010**, *2*, 257–268; b) Z. Zhang, D. Cui, B. Wang, B. Liu, Y. Yang, *Struct. Bonding (Berlin)* **2010**, *137*, 49–108; c) M. Nishiura, F. Guo, Z. Hou, *Acc. Chem. Res.* **2015**, *48*, 2209–2220; d) R. P. Kelly, P. W. Roesky, *Struct. Bonding (Berlin)* **2015**, *172*, 85–118; e) A. A. Trifonov, D. M. Lyobov, *Coord. Chem. Rev.* **2017**, *340*, 10–61; f) F. Yang, X. Li, *J. Polym. Sci., Part A* **2017**, *55*, 000–000.

[2] a) A. Fischbach, R. Anwander, *Adv. Polym. Sci.* **2006**, *204*, 155–281; b) M. Zimmermann, R. Anwander, *Chem. Rev.* **2010**, *110*, 6194–6259.

[3] M. Zimmermann, J. Volbeda, K. W. Törnroos, R. Anwander, *C. R. Chim.* **2010**, *13*, 651–660.

[4] a) R. Anwander, M. G. Klimpel, H. M. Dietrich, D. J. Shorokhov, W. Scherer, *Chem. Commun.* **2003**, 1008–1009; b) H. M. Dietrich, C. Zapilko, E. Herdtweck, R. Anwander, *Organometallics* **2005**, *24*, 5767–5771.

[5] M. Zimmermann, K. W. Törnroos, H. Sitzmann, R. Anwander, *Chem. Eur. J.* **2008**, *14*, 7266–7277.

[6] D. Robert, T. P. Spaniol, J. Okuda, *Eur. J. Inorg. Chem.* **2008**, 2801–2809.

[7] R. Litlabø, M. Enders, K. W. Törnroos, R. Anwander, *Organometallics* **2010**, *29*, 2588–2595.

[8] L. N. Jende, C. Maichle-Mössmer, R. Anwander, *Chem. Eur. J.* **2013**, *19*, 16321–16333.

[9] M. Zimmermann, K. W. Törnroos, R. Anwander, *Angew. Chem. Int. Ed.* **2008**, *47*, 775–778; *Angew. Chem.* **2008**, *120*, 787–790.

[10] a) Y. Segawa, M. Yamashita, K. Nozaki, *Science* **2006**, *314*, 113–115; b) Y. Segawa, Y. Suzuki, M. Yamashita, K. Nozaki, *J. Am. Chem. Soc.* **2008**, *130*, 16069–16079.

[11] N. Dettenrieder, C. O. Hollfelder, L. N. Jende, C. Maichle-Mössmer, R. Anwander, *Organometallics* **2014**, *33*, 1528–1531.

[12] M. Zimmermann, K. W. Törnroos, R. Anwander, *Angew. Chem. Int. Ed.* **2007**, *46*, 3126–3130; *Angew. Chem.* **2007**, *119*, 3187–3191.

[13] a) L. Zhang, M. Nishiura, M. Yuki, Y. Luo, Z. Hou, *Angew. Chem. Int. Ed.* **2008**, *47*, 2642–2645; *Angew. Chem.* **2008**, *120*, 2682–2685; b) J. Hong, L. Zhang, X. Yu, M. Li, Z. Zhang, P. Zheng, M. Nishiura, Z. Hou, X. Zhou, *Chem. Eur. J.* **2011**, *17*, 2130–2137; c) Y. Luo, Y. Lei, S. Fan, Y. Wang, J. Chen, *Dalton Trans.* **2013**, *42*, 4040–4051.

[14] a) R. Litlabø, H. S. Lee, M. Niemeyer, K. W. Törnroos, R. Anwander, *Dalton Trans.* **2010**, *39*, 6815–6825; b) H. Kaneko, H. Martin Dietrich, C. Schädle, C. Maichle-Mössmer, H. Tsurugi, K. W. Törnroos, K. Mashima, R. Anwander, *Organometallics* **2013**, *32*, 1199–1208.

[15] S. Sun, H. Ouyang, Y. Luo, Y. Zhang, Q. Shen, Y. Yao, *Dalton Trans.* **2013**, *42*, 16355–16364.

[16] S. Hamidi, L. N. Jende, H. Martin Dietrich, C. Maichle-Mössmer, K. W. Törnroos, G. B. Deacon, P. C. Junk, R. Anwander, *Organometallics* **2013**, *32*, 1209–1223.

[17] M. Zimmermann, F. Estler, E. Herdtweck, K. W. Törnroos, R. Anwander, *Organometallics* **2007**, *26*, 6029–6041.

[18] a) M. I. Bruce, *Angew. Chem. Int. Ed. Engl.* **1977**, *16*, 73–86; *Angew. Chem.* **1977**, *89*, 75–89; b) K. R. D. Johnson, P. G. Hayes, *Chem. Soc. Rev.* **2013**, *42*, 1947–1960.

[19] M. Zimmermann, J. Takats, G. Kiel, K. W. Törnroos, R. Anwander, *Chem. Commun.* **2008**, 612–614.

[20] D. Schädle, C. Maichle-Mössmer, C. Schädle, R. Anwander, *Chem. Eur. J.* **2015**, *21*, 662–670.

[21] N. Dettenrieder, H. M. Dietrich, C. Schädle, C. Maichle-Mössmer, K. W. Törnroos, R. Anwander, *Angew. Chem. Int. Ed.* **2012**, *51*, 4461–4465; *Angew. Chem.* **2012**, *124*, 4537–4541.

[22] R. Shannon, *Acta Crystallogr., Sect. A: Found. Crystallogr.* **1976**, *32*, 751–767.

[23] J. Cheng, K. Saliu, M. J. Ferguson, R. McDonald, J. Takats, *J. Organomet. Chem.* **2010**, *695*, 2696–2702.

[24] R. Litlabø, PhD Thesis, University of Bergen, **2010**.

[25] W. T. Klooster, R. S. Lu, R. Anwander, W. J. Evans, T. F. Koetzle, R. Bau, *Angew. Chem. Int. Ed.* **1998**, *37*, 1268–1270; *Angew. Chem.* **1998**, *110*, 1326–1329.

[26] E. D. Glendening, C. R. Landis, F. Weinhold, *Wiley Interdiscip. Rev.: Comput. Mol. Sci.* **2012**, *2*, 1–42.

[27] For comparison, in a typical Lu hydride bond, more than 20 % of the bonding electrons of the respective NBO are assigned to the Lu center (for details, see the Supporting Information).

[28] M. Zimmermann, R. Litlabø, K. W. Törnroos, R. Anwander, *Organometallics* **2009**, *28*, 6646–6649.

[29] N. Dettenrieder, C. Schädle, C. Maichle-Mössmer, P. Sirsch, R. Anwander, *J. Am. Chem. Soc.* **2014**, *136*, 886–889.

[30] Neither arene coordination as found for complex **II**, nor free $[Me_2Al\{B(NDippCH)_2\}]_2$ was observed (Figures S20 and S21; c. f., ref.[11]).

[31] a) A. D. Horton, *Organometallics* **1996**, *15*, 2675–2677; b) A. D. Horton, J. de With, A. J. van der Linden, H. van de Weg, *Organometallics* **1996**, *15*, 2672–2674.

[32] The chemical shifts of the resonances of *meta*- and *para*-fluorine atoms differ by 3.73 (**1**/**B**) and 3.70 (**2**/**B**) ppm, respectively, while tight ion pairs show differences in the range of 5.4 ppm and completely free anions in the range of 2.5 ppm, according to ref.[31]

[33] APEX v. **2008**.5–0, Madison, 2008.

[34] Bruker Saint v. 756A, Madison, **2009**.

[35] a) G. M. Sheldrick, *Acta Crystallogr., Sect. A* **2008**, *64*, 112–122; b) C. B. Hubschle, G. M. Sheldrick, B. Dittrich, *J. Appl. Crystallogr.* **2011**, *44*, 1281–1284.

[36] SADABS v. **2008**/1 (SADABS v. 2008/1), University of Göttingen, Göttingen, 2008.

[37] L. J. Farrugia, *J. Appl. Crystallogr.* **1997**, *30*, 565.

[38] POV-Ray v. 3.6, Williamstown, Victoria, Australia, **2004** (http://www.povray.org).

[39] M. J. Frisch, G. W. Trucks, H. B. Schlegel, G. E. Scuseria, M. A. Robb, J. R. Cheeseman, G. Scalmani, V. Barone, B. Mennucci, G. A. Petersson, H. Nakatsuji, M. Caricato, X. Li, H. P. Hratchian, A. F. Izmaylov, J. Bloino, G. Zheng, J. L. Sonnenberg, M. Hada, M. Ehara, K. Toyota, R. Fukuda, J. Hasegawa, M. Ishida, T. Nakajima, Y. Honda, O. Kitao, H. Nakai, T. Vreven, J. A. Montgomery Jr., J. E. Peralta, F. Ogliaro, M. Bearpark, J. J. Heyd, E. Brothers, K. N. Kudin, V. N. Staroverov, R. Kobayashi, J. Normand, K. Raghavachari, A. Rendell, J. C. Burant, S. S. Iyengar, J. Tomasi, M. Cossi, N. Rega, J. M. Millam, M. Klene, J. E. Knox, J. B. Cross, V. Bakken, C. Adamo, J. Jaramillo, R. Gomperts, R. E. Stratmann, O. Yazyev, A. J. Austin, R. Cammi, C. Pomelli, J. W. Ochterski, R. L. Martin, K. Morokuma, V. G. Zakrzewski, G. A. Voth, P. Salvador, J. J. Dannenberg, S. Dapprich, A. D. Daniels, Ö. Farkas, J. B. Foresman, J. V. Ortiz, J. Cioslowski, D. J. Fox, *Gaussian 09, Revision D.01*, Gaussian, Inc., Wallingford CT, **2013**.

[40] a) A. D. Becke, *Phys. Rev. A* **1988**, *38*, 3098–3100; b) J. P. Perdew, *Phys. Rev. B* **1986**, *33*, 8822–8824.

[41] a) T. H. Dunning Jr., *J. Chem. Phys.* **1989**, *90*, 1007–1023; b) R. A. Kendall, T. H. Dunning Jr., R. J. Harrison, *J. Chem. Phys.* **1992**, *96*, 6796–6806; c) D. E. Woon, T. H. Dunning Jr., *J. Chem. Phys.* **1993**, *98*, 1358–1371.

[42] a) X. Cao, M. Dolg, *J. Chem. Phys.* **2001**, *115*, 7348–7355; b) X. Cao, M. Dolg, *THEOCHEM* **2002**, *581*, 139–147.

[43] E. D. Glendening, J. K. Badenhoop, A. E. Reed, J. E. Carpenter, J. A. Bohmann, C. M. Morales, C. R. Landis, F. Weinhold, NBO 6.0, University of Wisconsin, Madison, WI, USA, **2013**.

[44] G. A. Zhurko, CHEMCRAFT (http://www.chemcraftprog.com).

Received: June 20, 2017

Eur. J. Inorg. Chem. **2017** · ISSN 1099–0682

https://doi.org/10.1002/ejic.201700730

SUPPORTING INFORMATION

Title: C–H Bond Activation and Isoprene Polymerization by Lutetium Alkylaluminate/gallate Complexes Bearing a Peripheral Boryl and a Bulky Hydrotris(pyrazolyl)borate Ligand

Author(s): Martin Bonath, Christoph O. Hollfelder, Dorothea Schädle, Cäcilia Maichle-Mössmer, Peter Sirsch,* Reiner Anwander*

Table of Contents

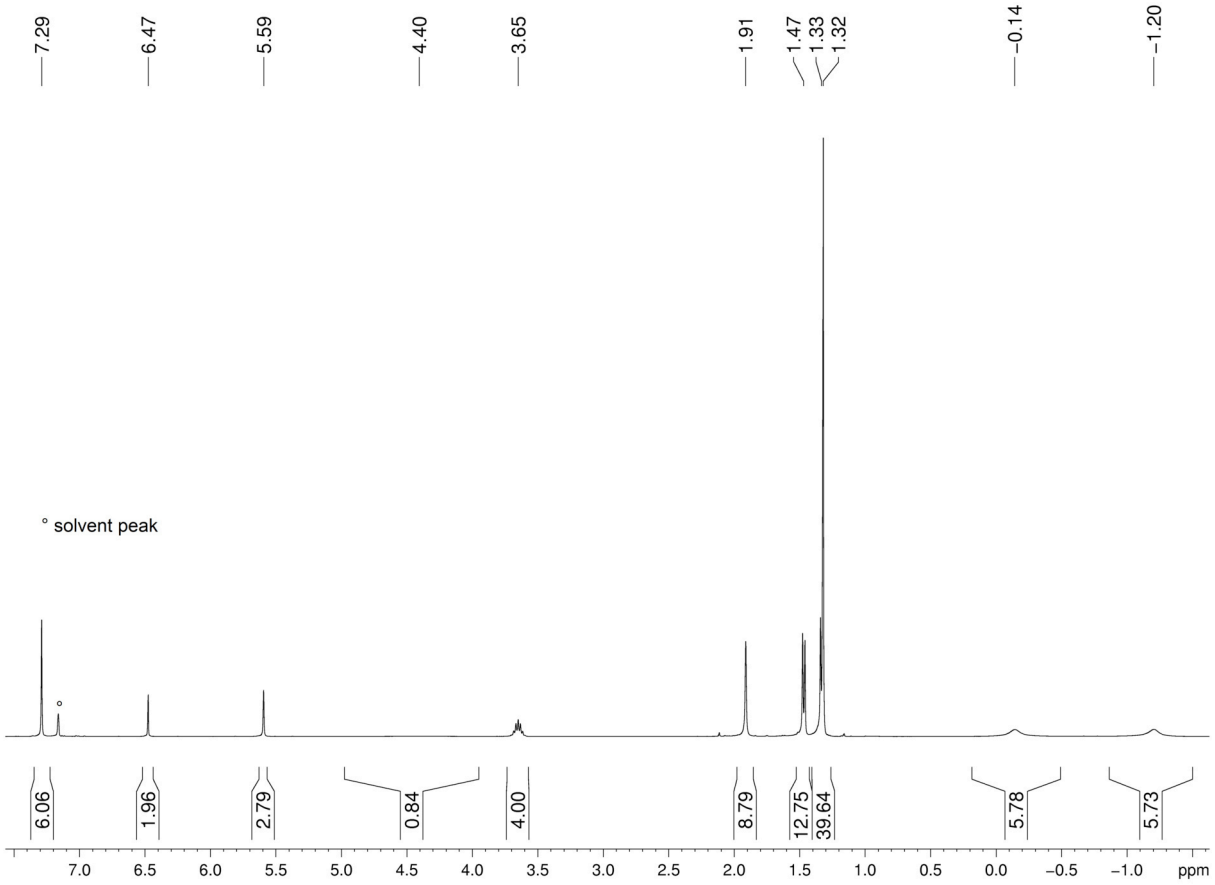

Figure S1. ^{1}H NMR spectrum (400 MHz) of **1** in [D_6]benzene at 26 °C.

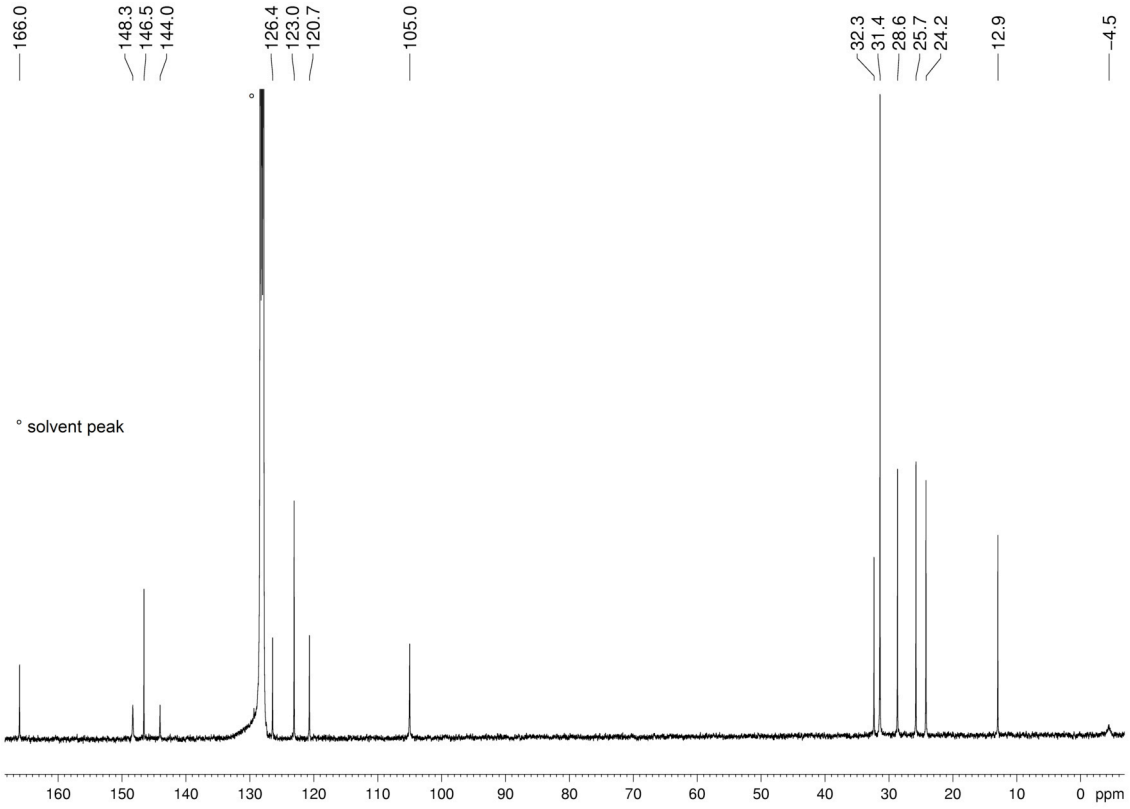

Figure S2. ^{13}C{^{1}H} NMR spectrum (101 MHz) of **1** in [D_6]benzene at 26 °C.

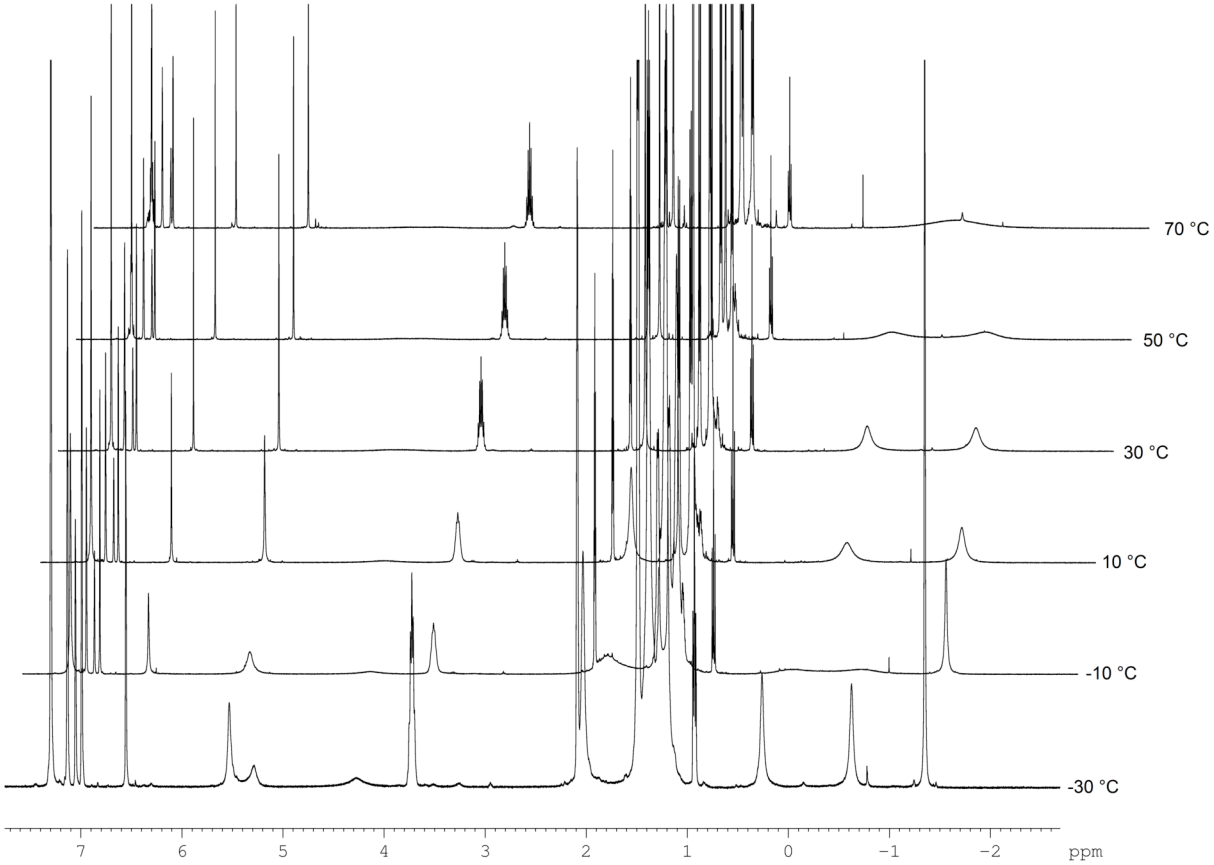

Figure S3. Variable-temperature ^{1}H NMR spectra (500 MHz) of **1** in [D_8]toluene.

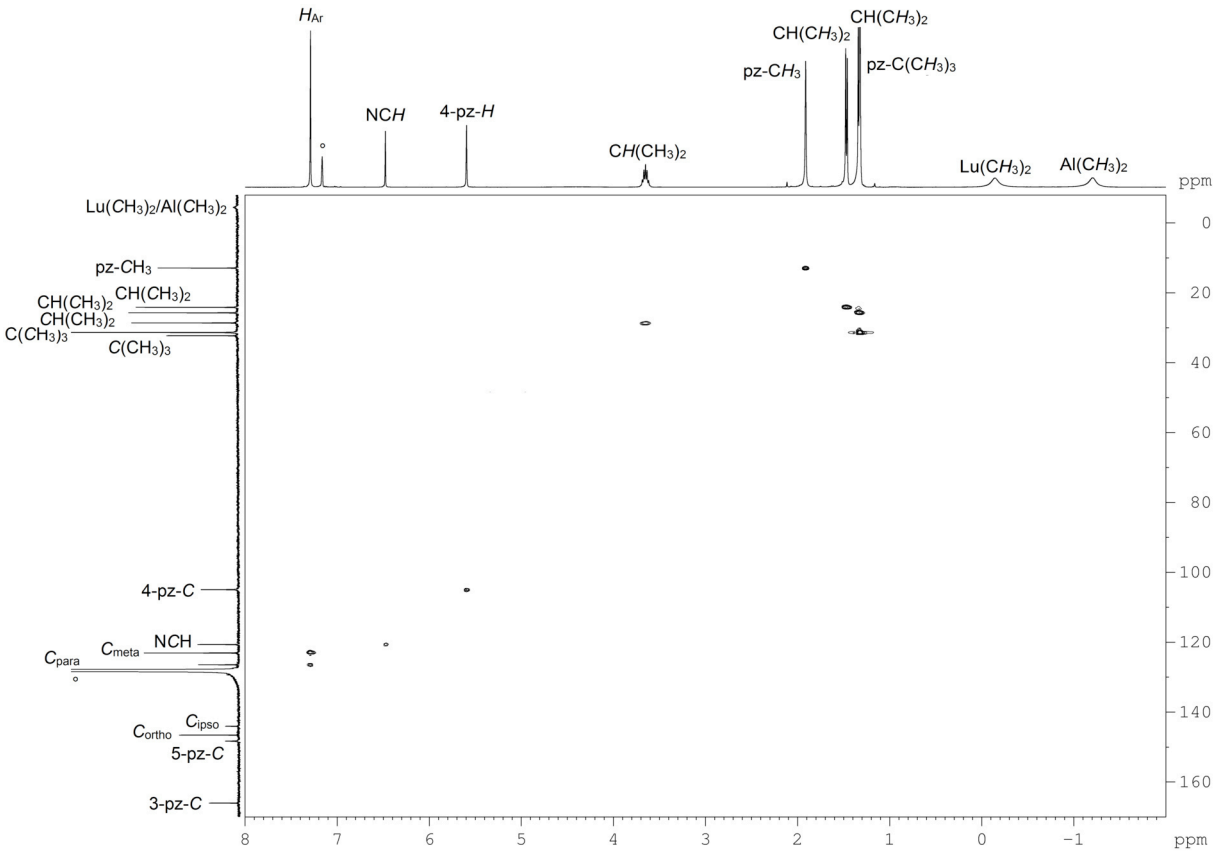

Figure S4. ^{1}H-^{13}C HSQC NMR spectrum (400 MHz, 101 MHz) of **1** in [D_6]benzene at 26 °C.

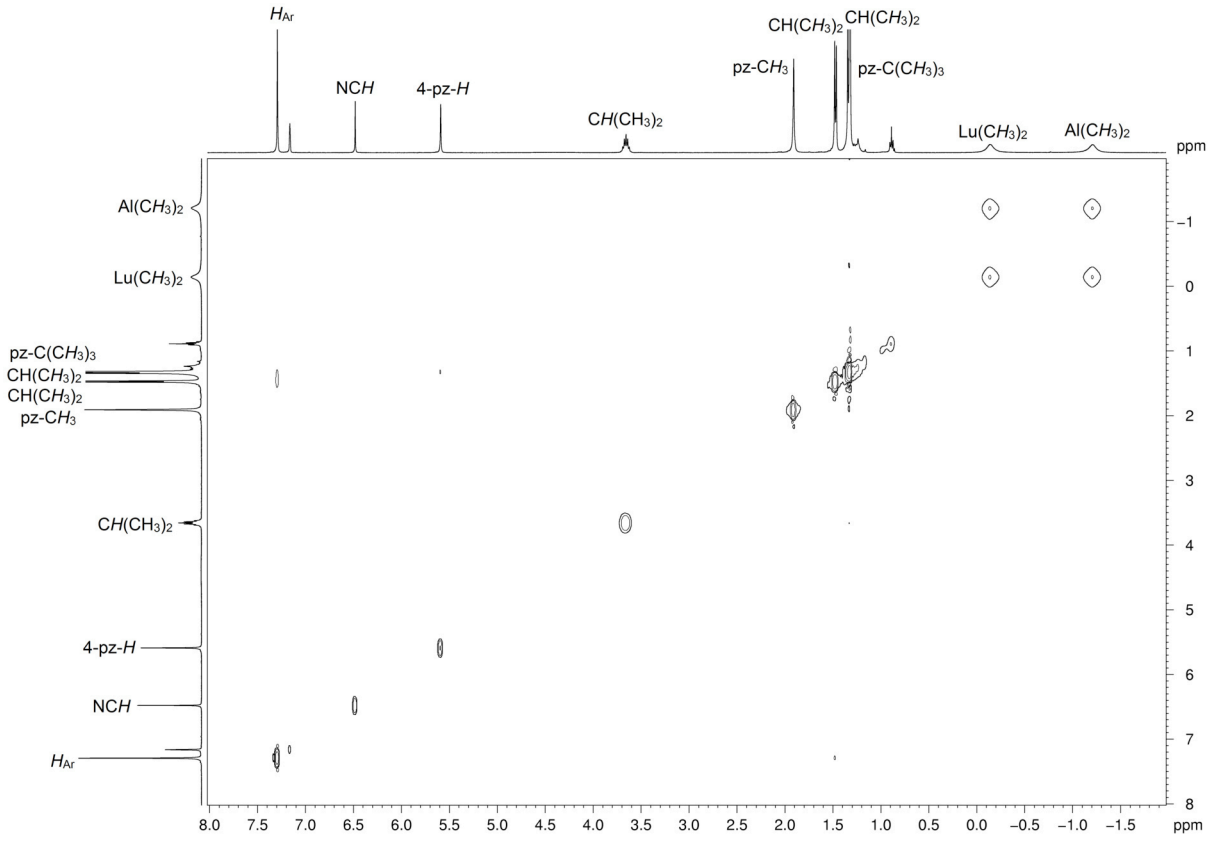

Figure S5. ^{1}H-^{1}H EXSY NMR spectrum (400 MHz) of **1** in [D_6]benzene at 26 °C.

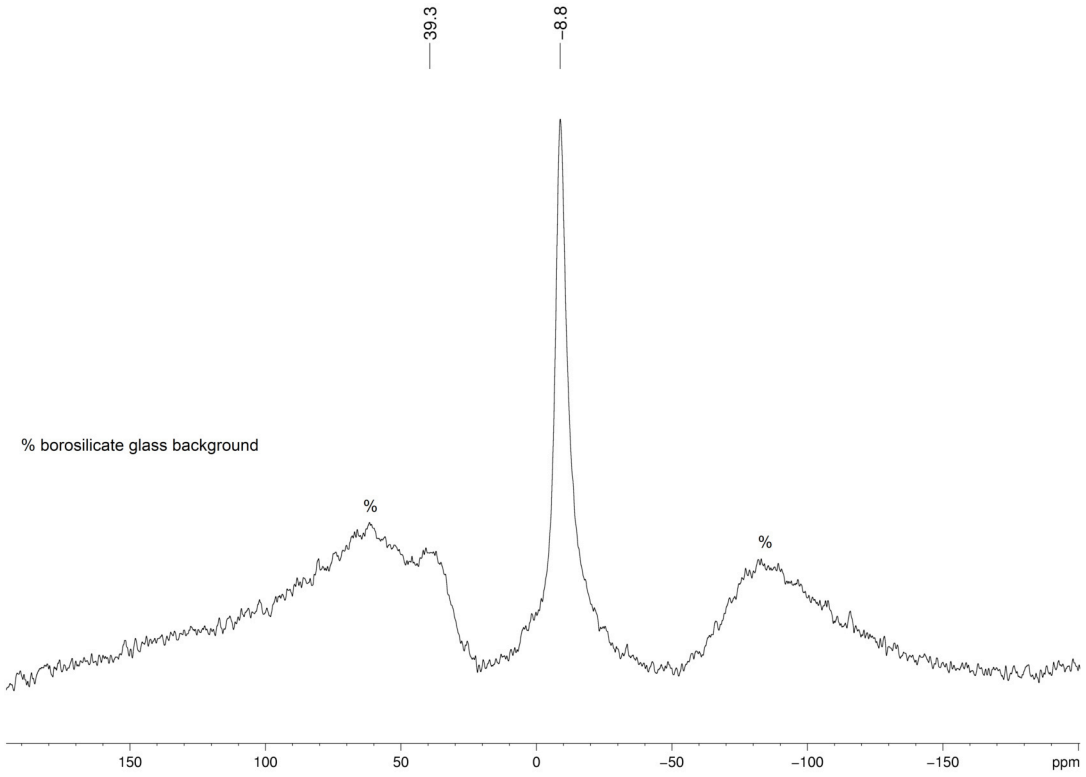

Figure S6. $^{11}B\{^{1}H\}$ NMR spectrum (80 MHz) of **1** in [D_6]benzene at 26 °C.

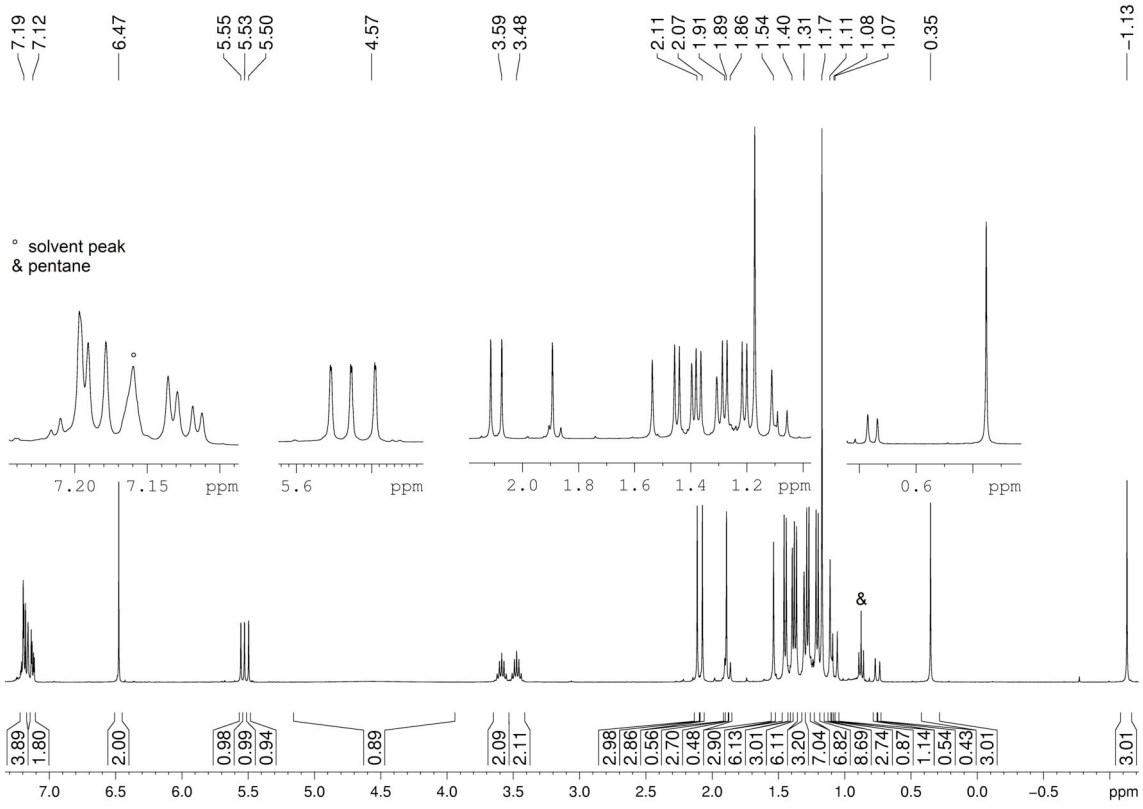

Figure S7. ^{1}H NMR spectrum (400 MHz) of **2** in [D_6]benzene at 26 °C.

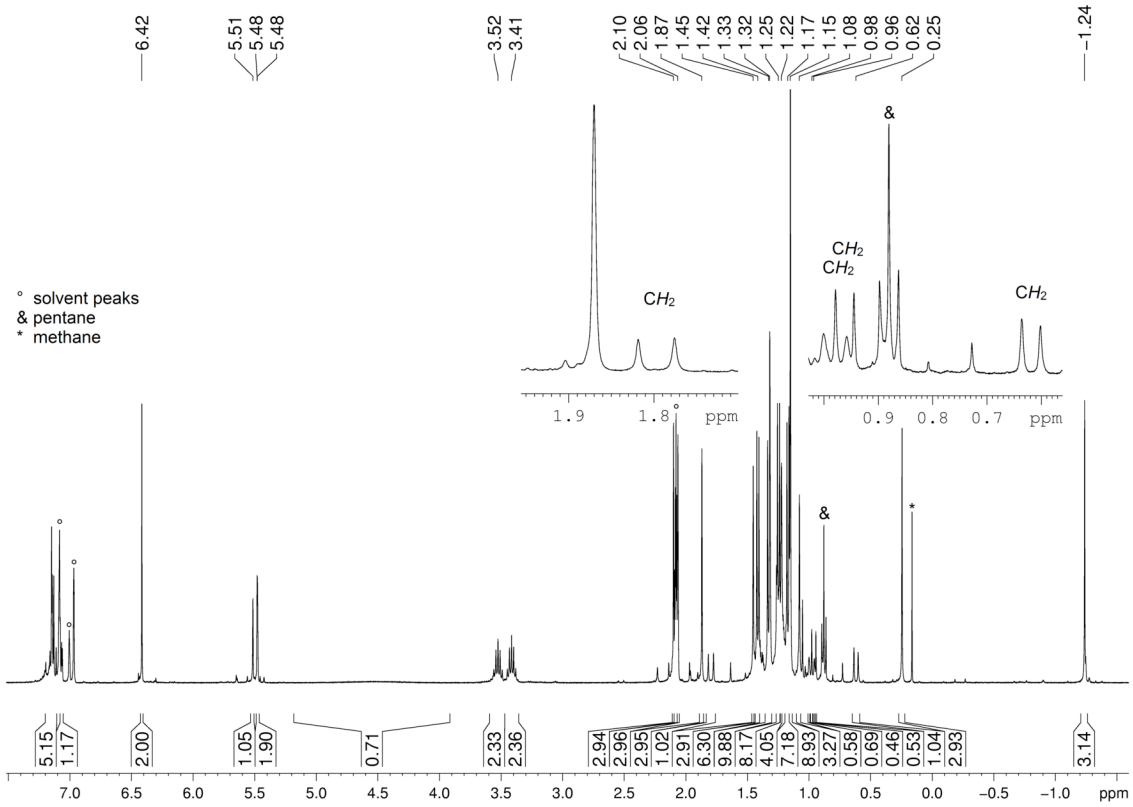

Figure S8. ^{1}H NMR spectrum (400 MHz) of **2** in [D_8]toluene at 26 °C. Recorded after heating **1** to 60 °C for 4 d in a sealed *J. Young* valved NMR tube.

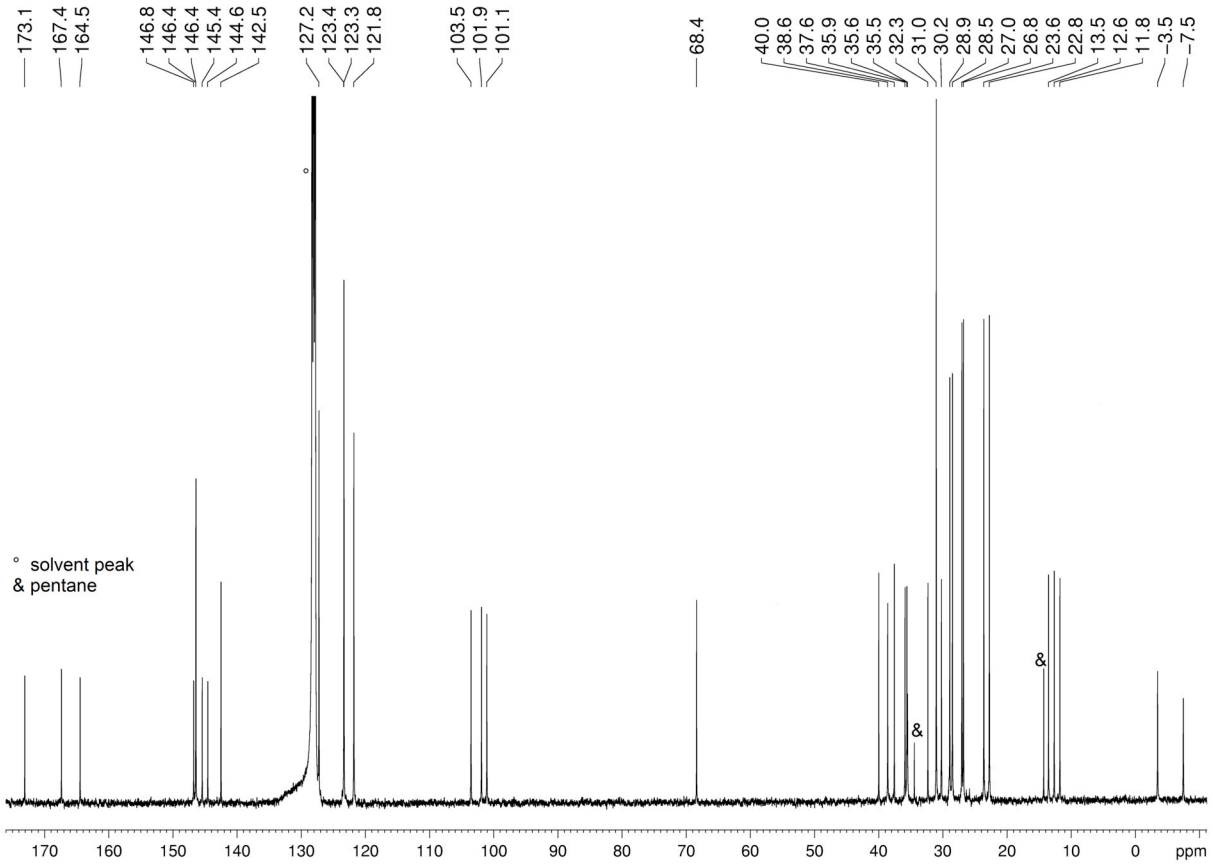

Figure S9. ^{13}C{^{1}H} NMR spectrum (101 MHz) of **2** in [D_6]benzene at 26 °C.

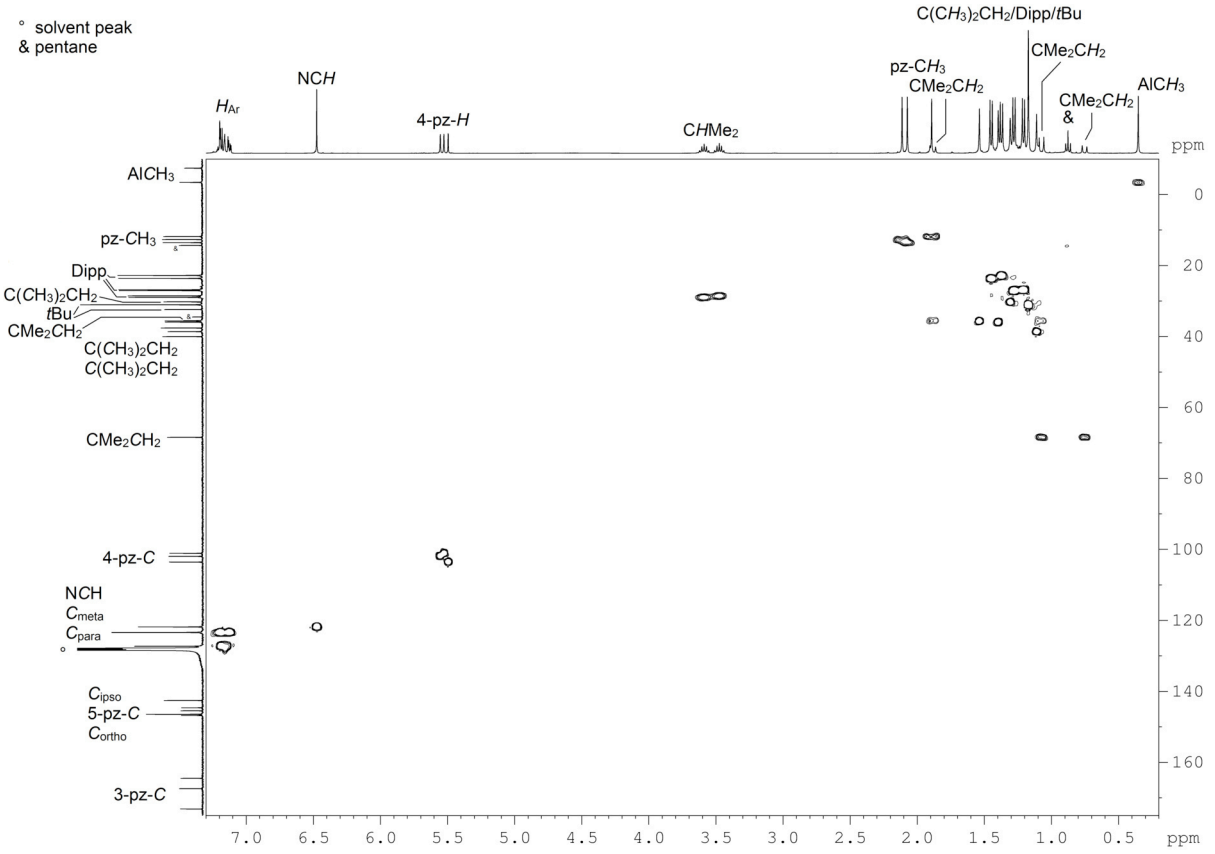

Figure S10. ^{1}H-^{13}C HSQC NMR spectrum (400 MHz, 101 MHz) of **2** in [D_6]benzene at 26 °C.

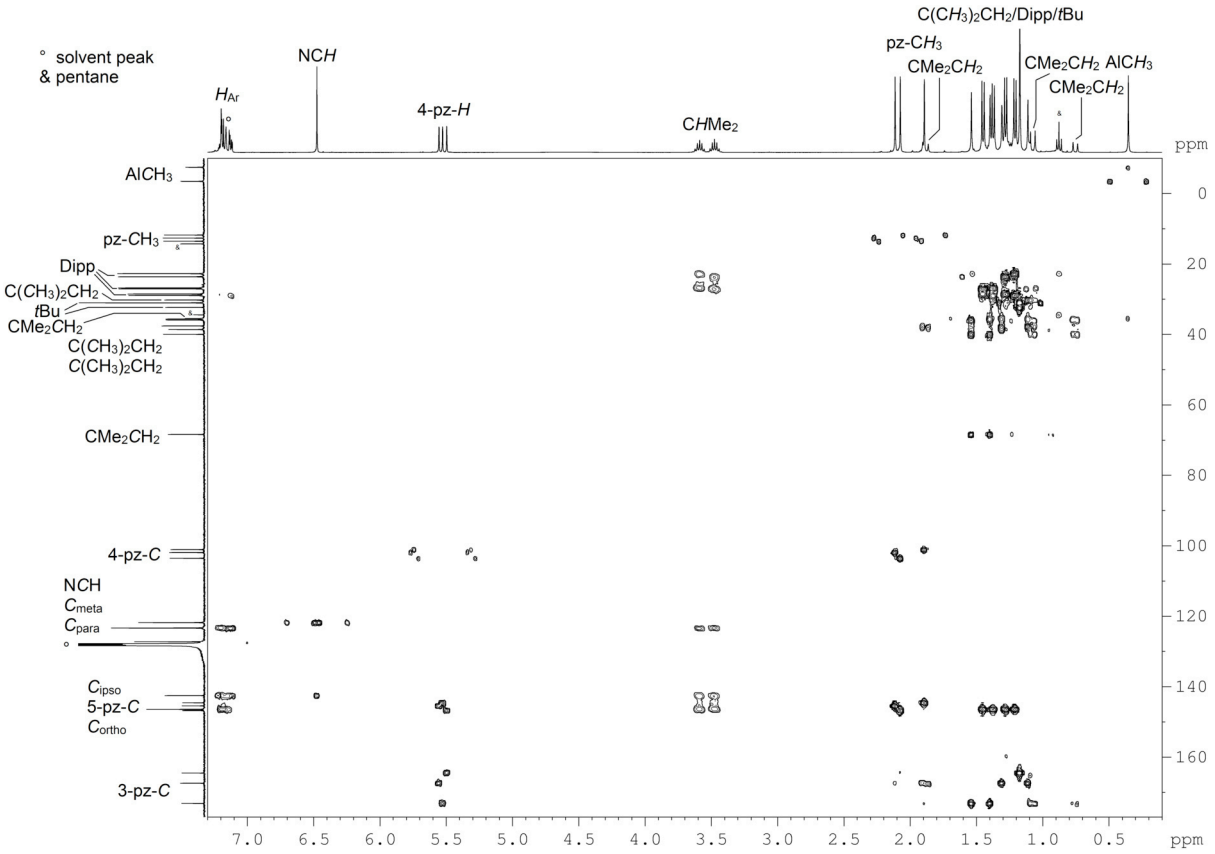

Figure S11. ^{1}H-^{13}C HMBC NMR spectrum (400 MHz, 101 MHz) of **2** in [D_6]benzene at 26 °C.

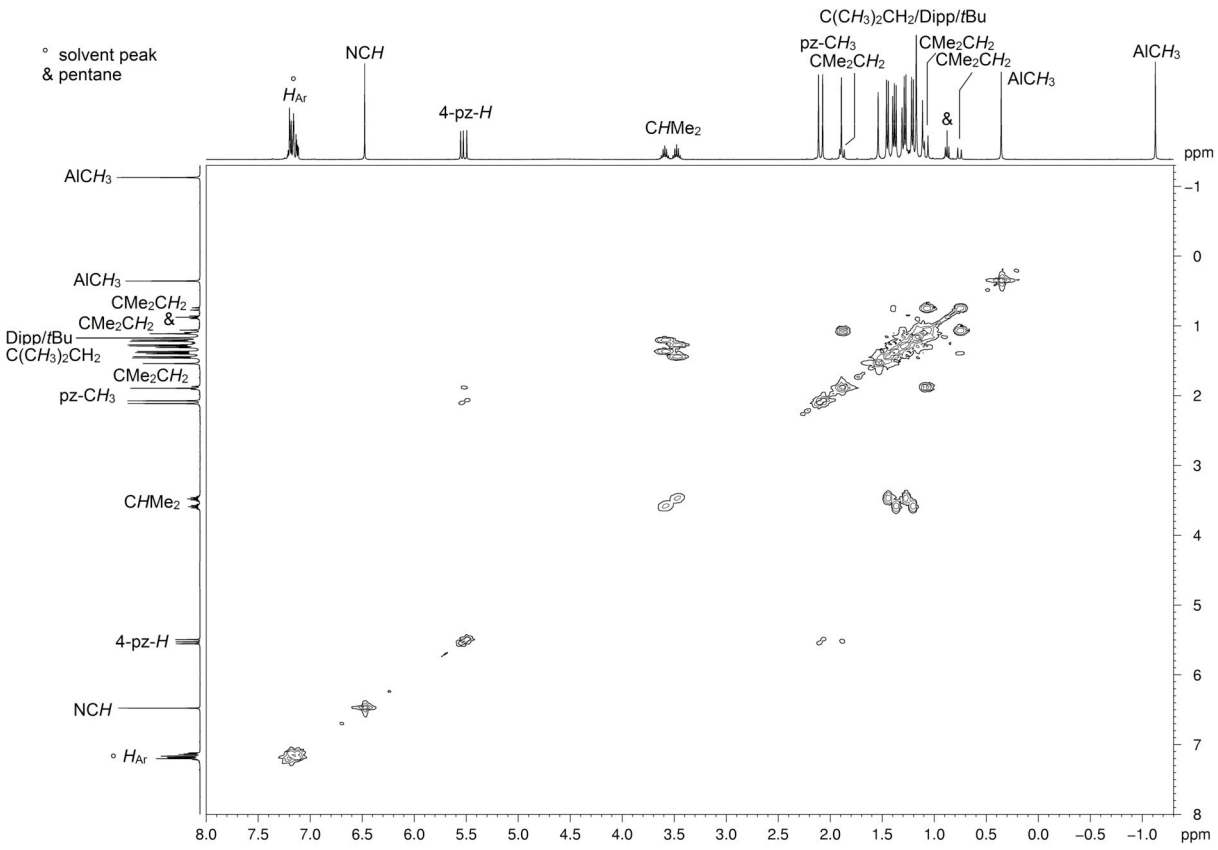

Figure S12. ^{1}H-^{1}H COSY NMR spectrum (400 MHz) of **2** in [D_6]benzene at 26 °C.

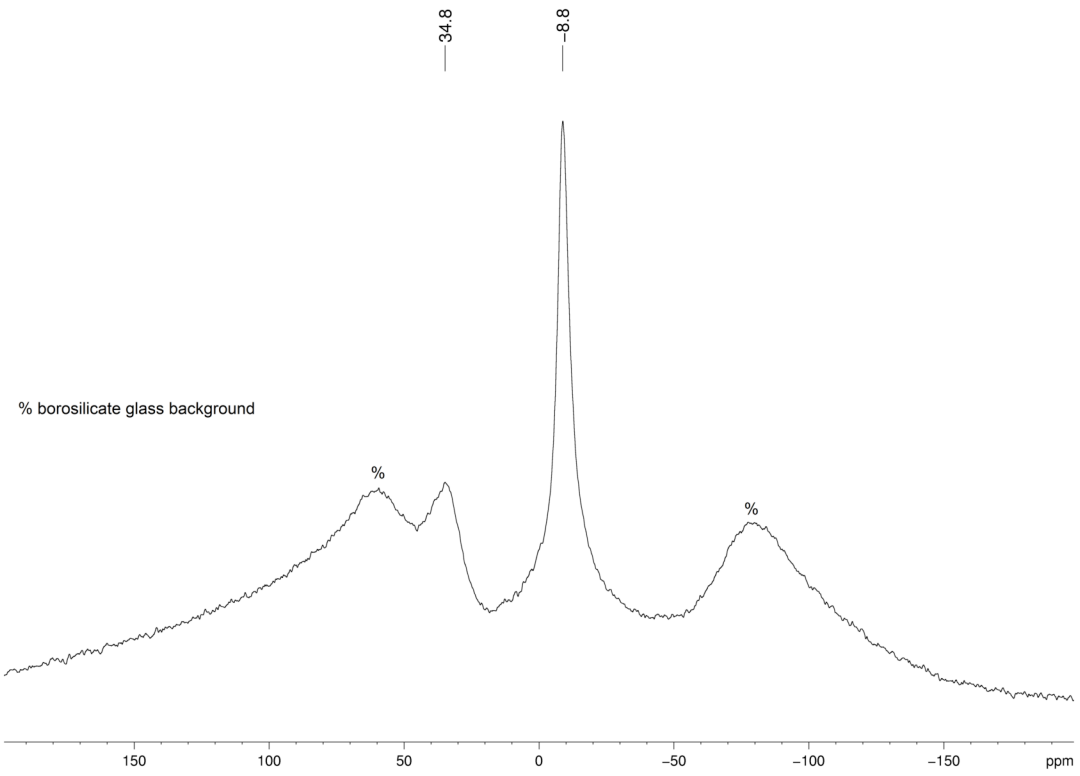

Figure S13. ^{11}B{^{1}H} NMR spectrum (80 MHz) of **2** in [D_6]benzene at 26 °C.

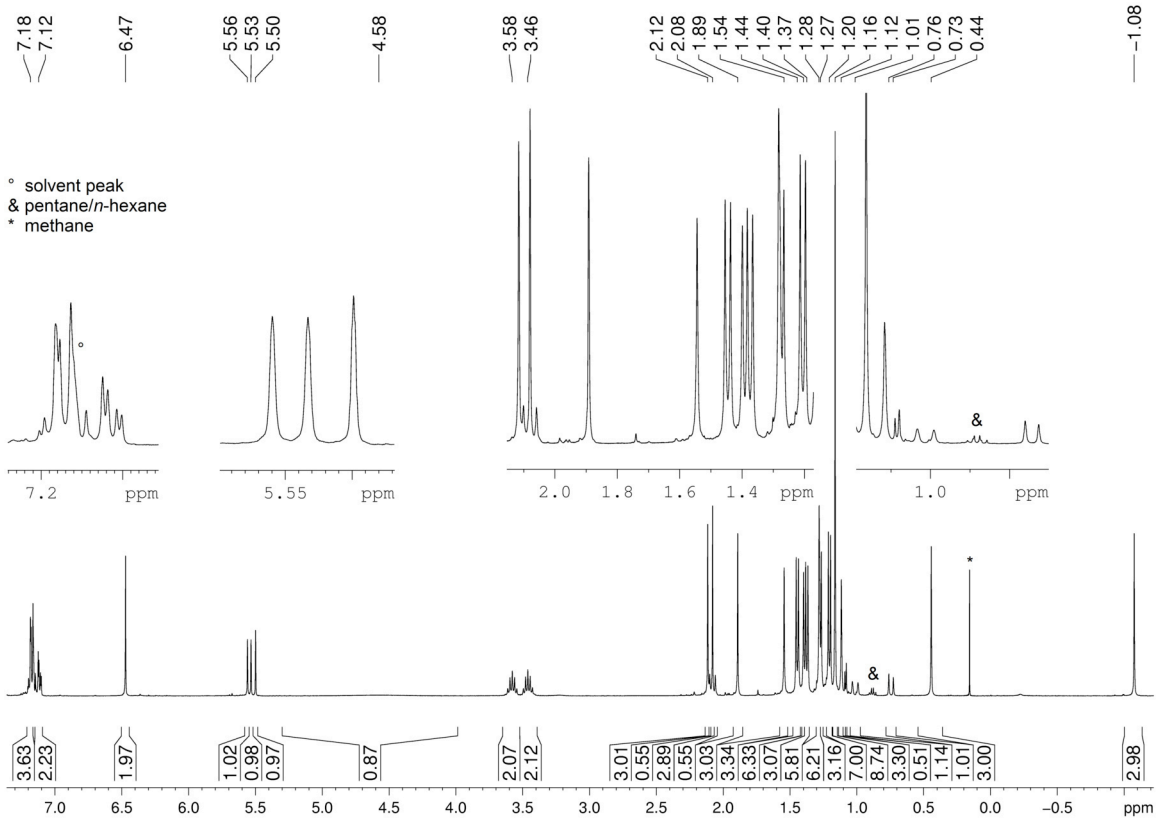

Figure S14. ^{1}H NMR spectrum (400 MHz) in [D_6]benzene at 26 °C of the reaction of [($Tp^{tBu,Me}$)$LuMe_2$] with [$Me_2Ga\{B(NDippCH)_2\}$] after heating for 96 h to 50 °C in a sealed *J.-Young* valved NMR tube.

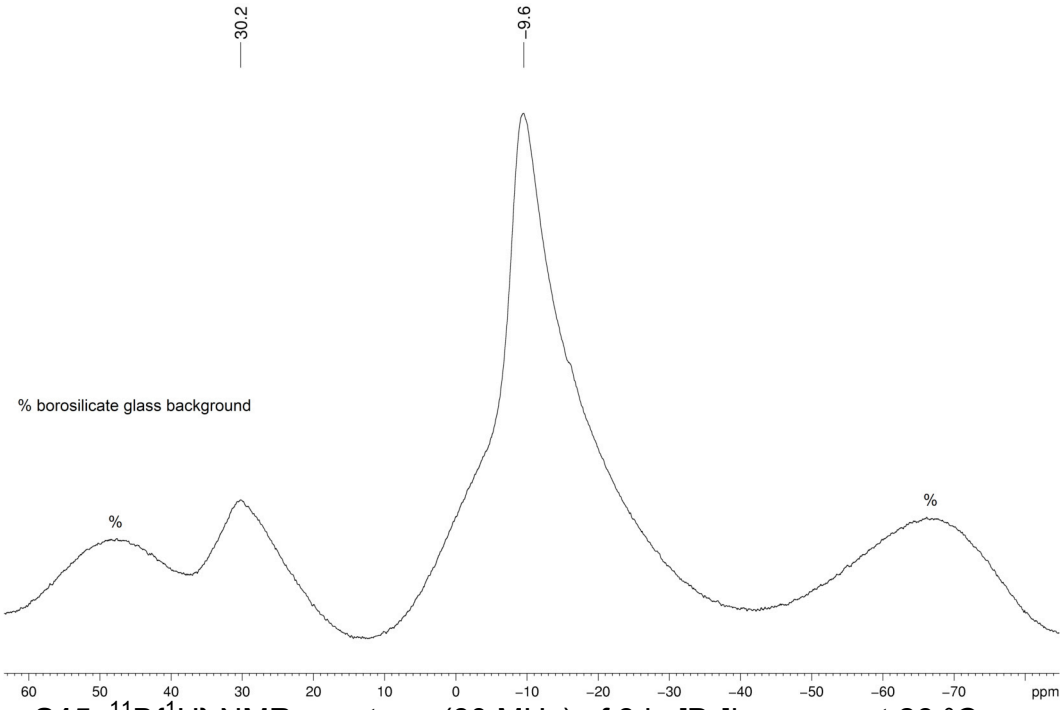

Figure S15. $^{11}B\{^{1}H\}$ NMR spectrum (80 MHz) of **3** in [D_6]benzene at 26 °C.

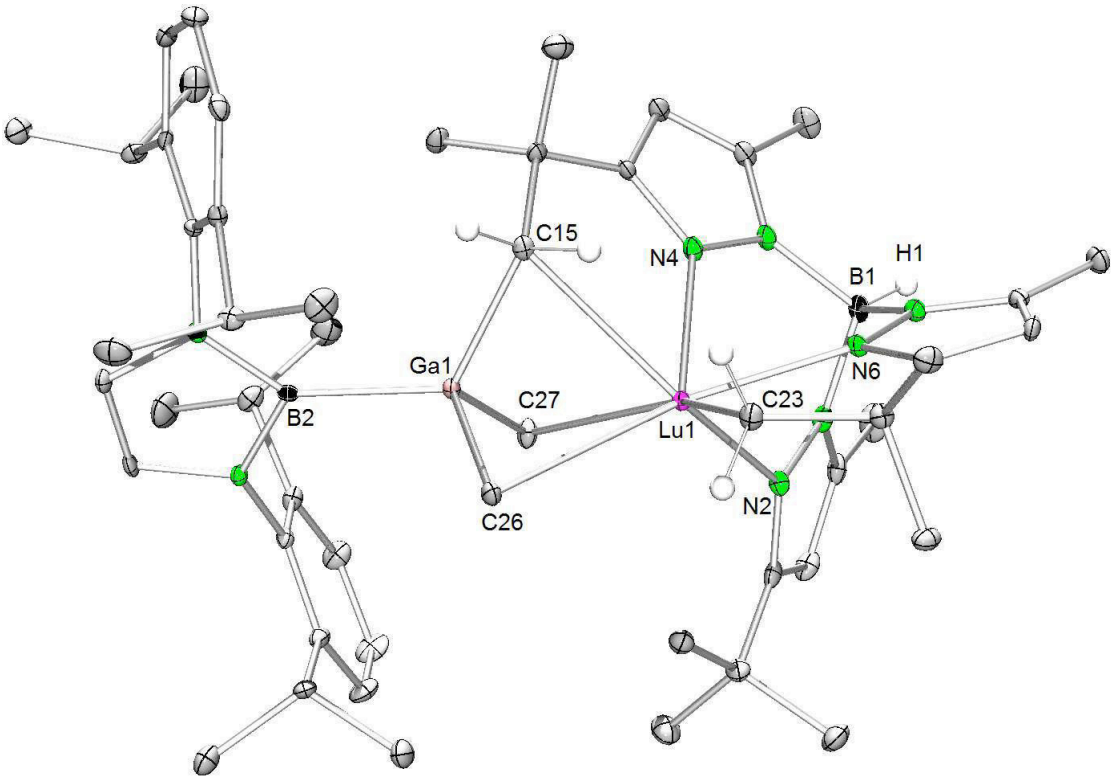

Figure S16. Solid-state structure of [(Tp$^{(t\text{Bu-H})2/t\text{Bu,Me}}$)Lu(GaMe$_2${B(NDippCH)$_2$})] (**3**); thermal ellipsoids are set at the 50% probability level. Hydrogen atoms except for B–H and methylene groups are omitted for clarity. Selected bond lengths [Å] and angles [°]: Lu1–C23 2.386(3), Lu1–C15 2.769(3), Lu1–C26 2.911(4), Lu1–C27 2.813(4), Lu1–N2 2.397(3), Lu1–N4 2.335(3), Lu1–N6 2.306(3), Ga1–C15 2.091(3), Ga1–C27 2.055(4), Ga1–C26 2.072(3), Ga1–B2 2.099(4), Lu1–N2 2.397(3), Lu1–N4 2.335(3), Lu1–N6 2.306(3), C15-Lu1-C23 97.0(1), Lu1-C15-Ga1 71.7(1), Lu1-C26-Ga1 68.8(1), Lu1-C27-Ga1 71.2(1).

Reactivity of 2 toward excess AlMe$_3$ - [(Tp$^{(t\text{Bu-H})2/t\text{Bu,Me}}$)Lu(AlMe$_3$)] (4)

A [D$_6$]benzene solution of **2** (23.2 mg, 0.022 mmol) was treated with an excess of AlMe$_3$ at ambient temperature. The ^{1}H NMR spectrum indicates instant separation of unsolvated [Me$_2$Al{B(NDippCH)$_2$}$_2$]$_2$ and formation of the new complex **4**. Single crystals suitable for X-ray crystallography could be obtained from the reaction mixture after drying *in vacuo*, redissolving in *n*-pentane and storing at –40 °C.

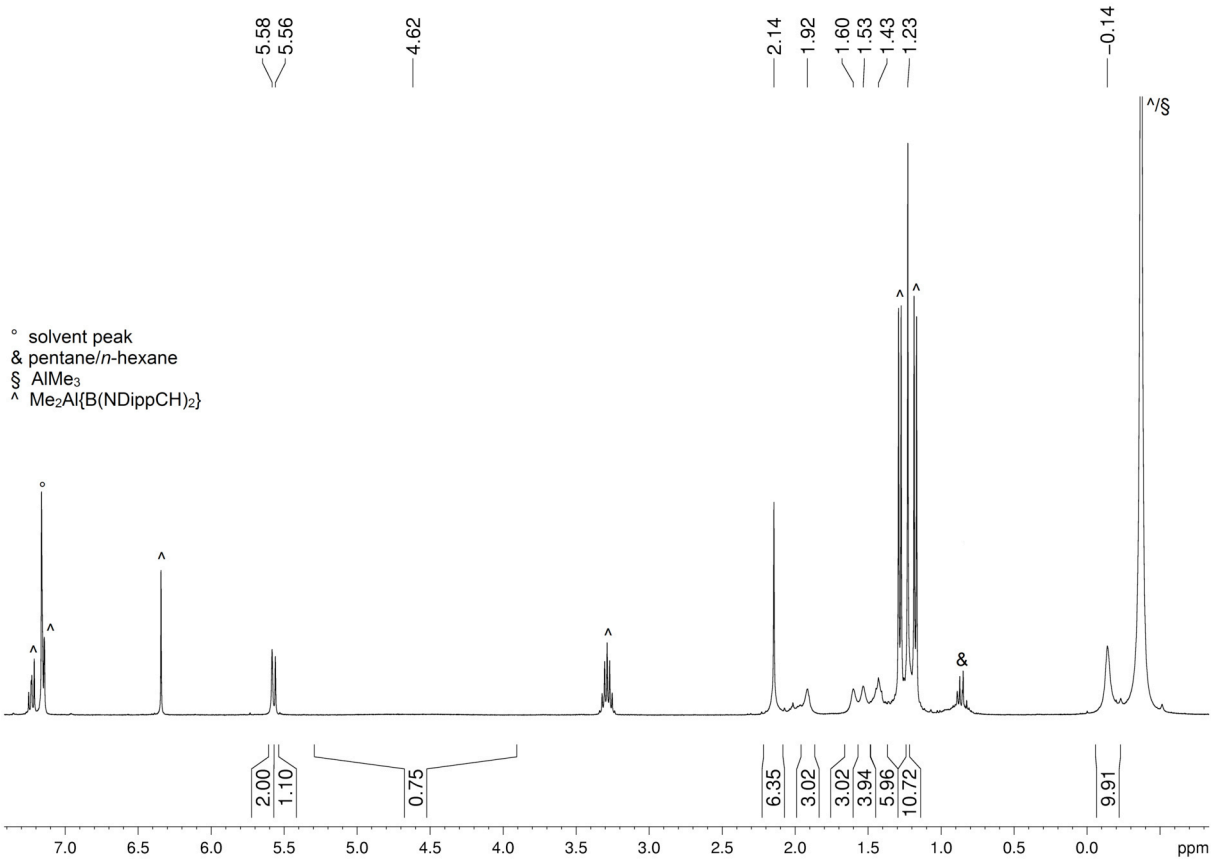

Figure S17. ^{1}H NMR spectrum (400 MHz) in [D_6]benzene of the reaction of **2** with an excess of $AlMe_3$ after 15 min in a sealed *J.-Young* valved NMR tube at 26 °C.

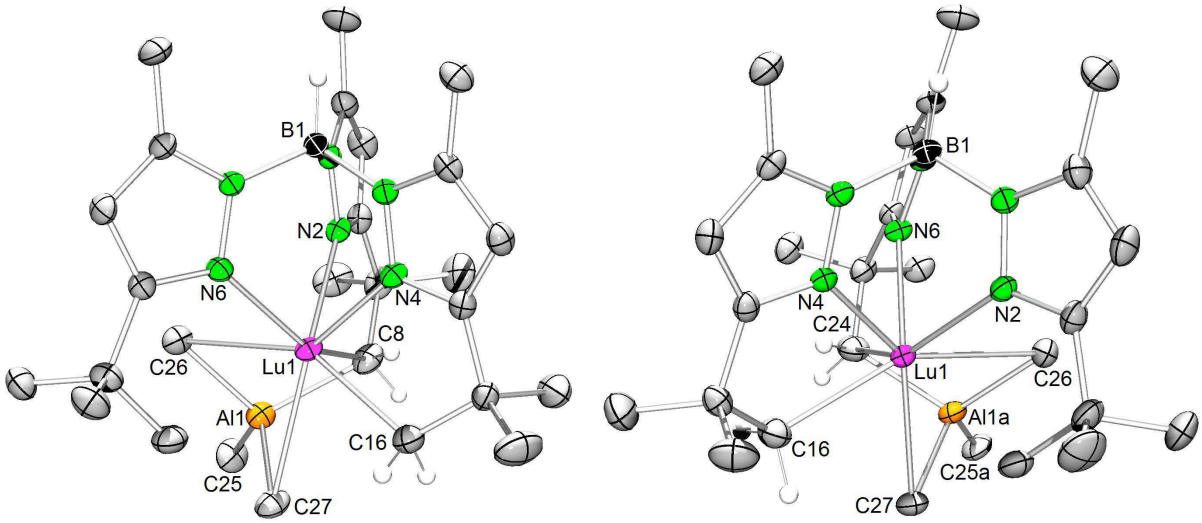

Figure S18. Solid-state structure of **4** showing the two molecules in the asymmetric unit; thermal ellipsoids are set at the 50% probability level. The hydrogen atoms except for B–H and methylene groups are omitted for clarity. Selected bond lengths [Å] and angles [°]: Lu1–C16 2.418(5), Lu1–C8 2.823(6), Lu1–C24 3.070(6), Lu1–C26 2.824(6), Lu1–C27 2.870(6), Al1–C8 2.203(6), Al1–C25 1.85(1), Al1–C26 2.096(7), Al1–C27 2.057(6), Lu1–N2 2.487(3), Lu1–N4 2.197(3), Lu1–N6 2.320(3), Al1–C8 2.203(6), Al1–C25 1.85(1), Al1–C26 2.096(7), Al1–C27 2.057(6), Al1a–C24 2.074(6), Al1a–C25a 1.95(1), Al1a–C26 2.146(6), Al1a–C27 2.013(7), C8-Lu1-C16 96.0(2), C24-Lu1-C16 89.2(2), Lu1-C8-Al1 64.4(2), Lu1-C26-Al1 65.4(2), Lu1-C27-Al1 64.8(2), Lu1-C24-Al1a 66.0(2), Lu1-C26-Al1a 70.5(2), Lu1-C27-Al1a 71.1(2).

Reactivity of 2 toward THF

A [D_6]benzene solution of **2** (9.7 mg, 0.009 mmol) was treated with an excess of THF at ambient temperature. The ^{1}H NMR spectrum indicated separation of the [$Me_2Al\{B(NDippCH)_2\}_2$] unit in about 92% by forming the THF adduct [$(THF)Me_2Al\{B(NDippCH)_2\}_2$] and a new compound, tentatively assigned as [$(Tp^{(t\text{Bu-H})2/t\text{Bu,Me}})Lu(THF)_x$].

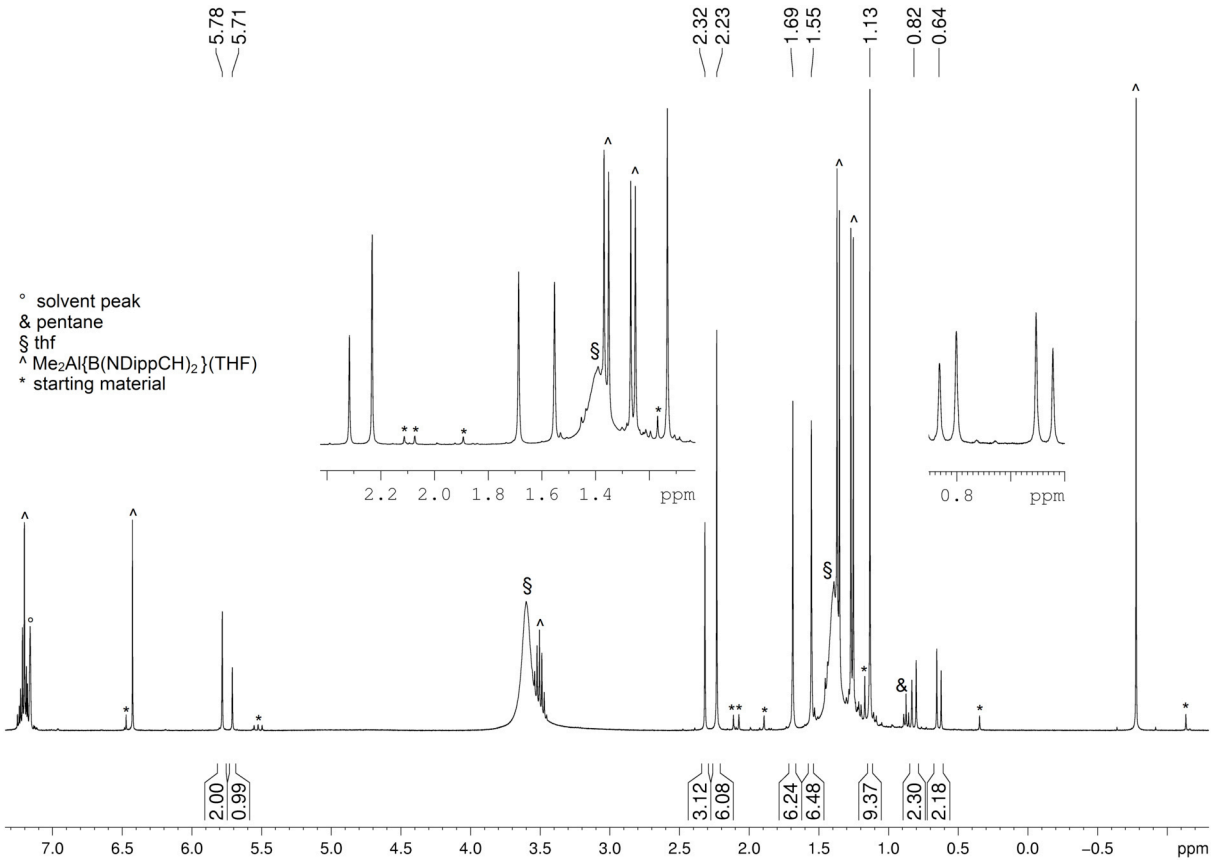

Figure S19. ^{1}H NMR spectrum (400 MHz) in [D_6]benzene of the reaction of **2** with an excess of THF after 1 h in a sealed *J.-Young* valved NMR tube at 26 °C.

Investigations into the active species of the system 1/B

A solution of **1** (21.5 mg, 0.02 mmol) in 0.5 mL [D_6]benzene was treated with [$PhNMe_2H$][$B(C_6F_5)_4$] (**B**) (18 mg, 0.02 mmol) in a *J.-Young* valved NMR tube. After 10 min a first ^{1}H NMR spectrum was recorded (Figure S19) showing complete consumption of the starting materials, the formation of methane, and separation of the [$Me_2Al\{B(NDippCH)_2\}_2$] unit forming [$(PhNMe_2)Me_2Al\{B(NDippCH)_2\}_2$]. Besides, signals matching the assumed ion pair [$Tp^{tBu,Me}LuMe$][$B(C_6F_5)_4$] (**5a**) were found at 5.62, 1.95, 1.11 and 0.25 ppm in a 3:9:27:3 ratio accompanied by minor side products. After 16 h a second ^{1}H NMR spectrum was recorded (Figure S20) of the same sample in a sealed *J.-Young* valved NMR tube. While the signals for [$(PhNMe_2)Me_2Al\{B(NDippCH)_2\}_2$] and the side product were still present signals attributed to **5a** had vanished and the methane peak showed increased intensity. However, new signals appeared and can be assigned to the CH-actived product [$(Tp^{(tBu-H)/tBu2,Me})Lu$][$B(C_6F_5)_4$] (**5b**) revealing two different pyrazolyl moieties in a 2:1 ratio.

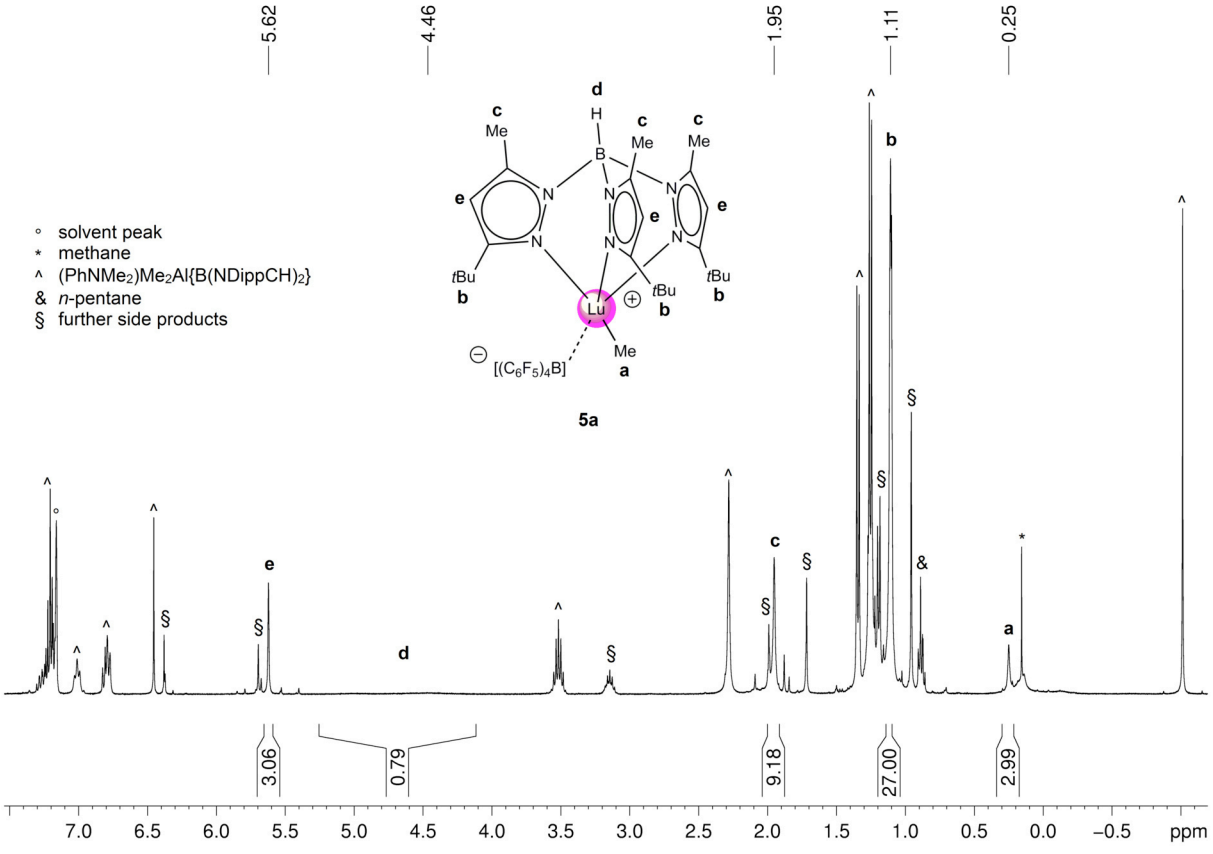

Figure S20. ^{1}H NMR spectrum (400 MHz) in [D_6]benzene of the reaction of **1** with co-catalyst **B** after 10 min in a sealed *J.-Young* valved NMR tube at 26 °C.

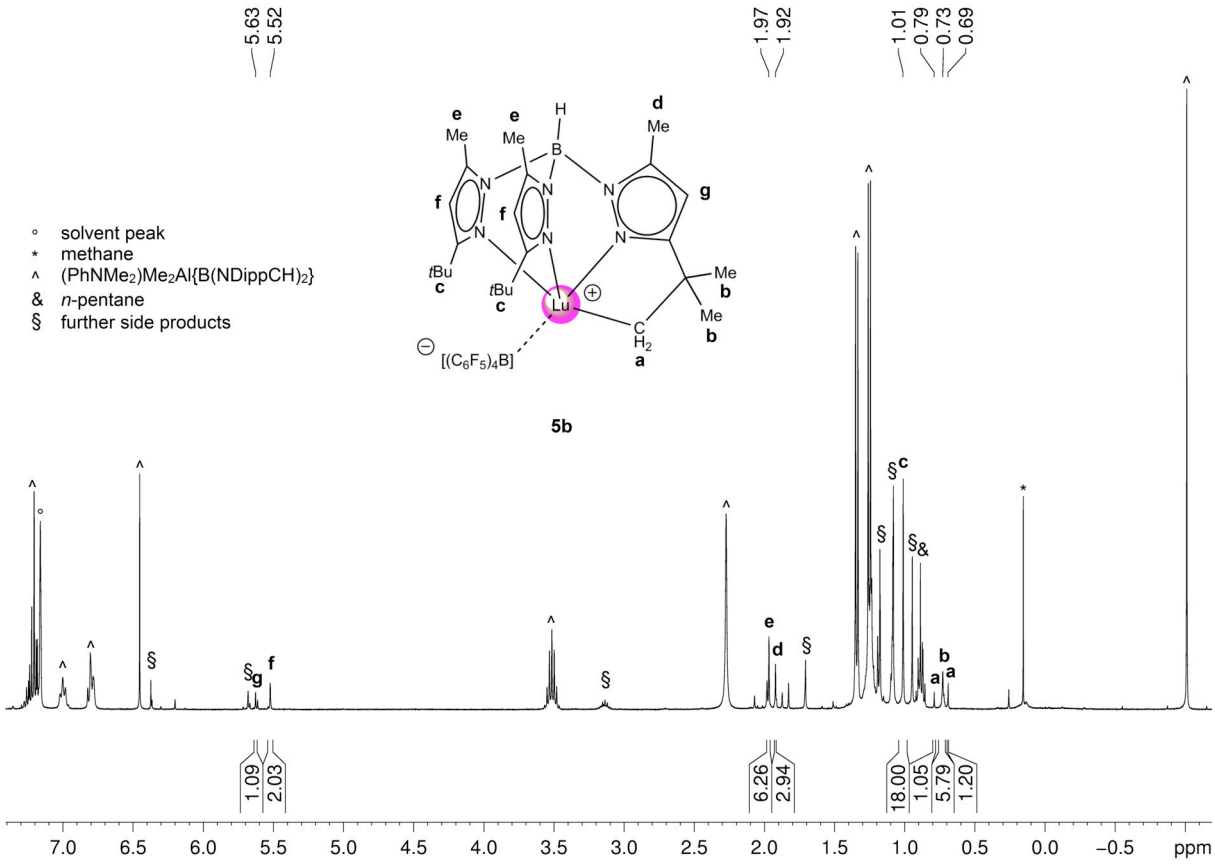

Figure S21. ^{1}H NMR spectrum (400 MHz) in [D_6]benzene of the reaction of **1** with co-catalyst **B** after 16 h in a sealed *J.-Young* valved NMR tube at 26 °C.

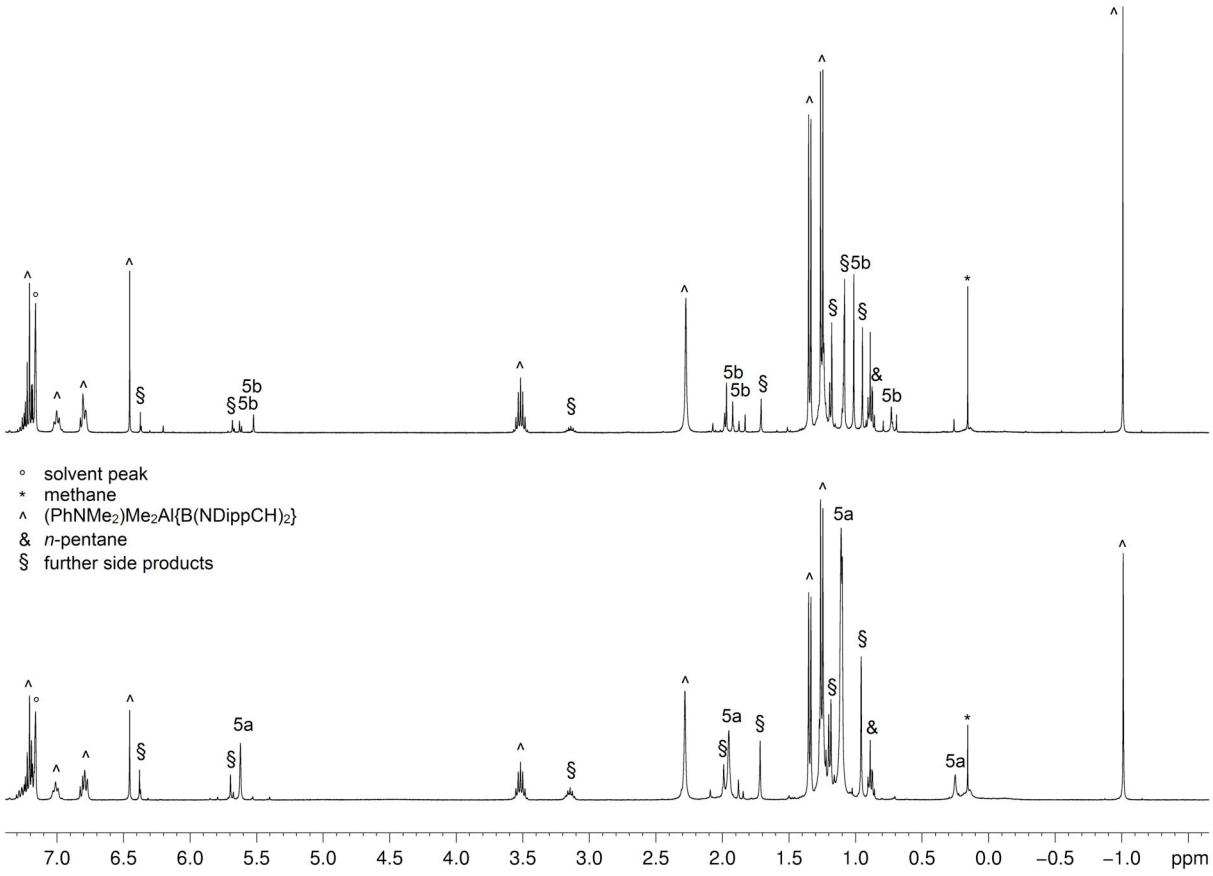

Figure S22. Comparing ^{1}H NMR spectra (400 MHz) in [D_6]benzene of the reaction of **1** with co-catalyst **B** after 10 min and 16 h at 26 °C.

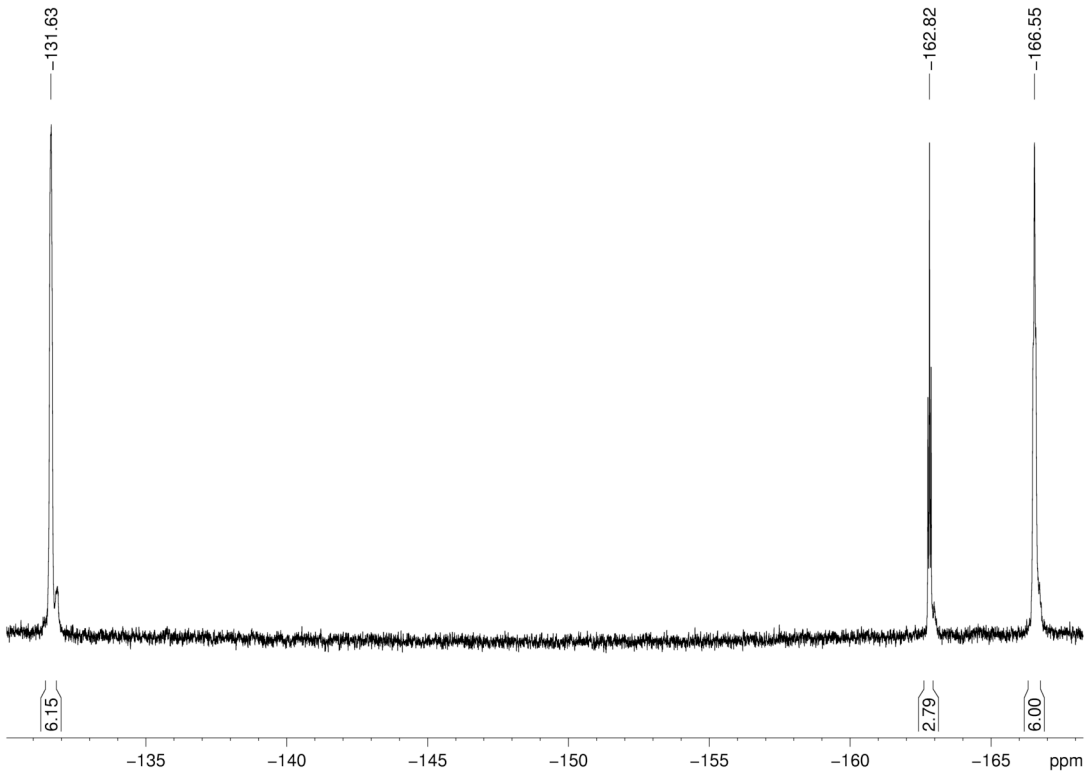

Figure S23. ^{19}F{^{1}H} NMR spectrum (400 MHz) in [D_6]benzene of the reaction of **1** with co-catalyst **B** after 10 min in a sealed *J.-Young* valved NMR tube at 26 °C.

Investigations into the active species of the system 2/B

In a *J.-Young* valved NMR tube, **2** (20.9 mg, 0.02 mmol) in 0.5 mL [D_6]benzene was treated with [$PhNMe_2H$][$B(C_6F_5)_4$] (**B**) (18 mg, 0.02 mmol) and aged for 5 min. The ^{1}H NMR spectrum showed almost complete conversion, release of methane and formation of a species assignable to [$(Tp^{(tBu\text{-}H)/tBu2,Me})LuMe_2Al(boryl)$][$B(C_6F_5)_4$] (**6**). The formation of a yellow oil phase was observed in the course of the reaction, which implied the non-equimolar integrals of main and side-product ($PhNMe_2$) in the ^{1}H NMR spectrum to be due to different solubility of product and side product in [D_6]benzene. ^{1}H NMR (400 MHz, [D_6]benzene, 26 °C): δ = 7.24 (m, 2 H, $H_{Ar(m)}$ of $PhNMe_2$), 7.20 (m, 2 H, $H_{Ar(p)}$ of $C_6H_3(CH(CH_3)_2)_2$), 7.14 (d, 4 H, ^3J(HH) = 7.3 Hz, $H_{Ar(m)}$ of $C_6H_3(CH(CH_3)_2)_2$), 6.80 (t, 1 H, ^3J(HH) = 7.3 Hz, $H_{Ar(p)}$ of $PhNMe_2$), 6.64 (d, 2 H, ^3J(HH) = 8.2 Hz, $H_{Ar(o)}$ of $PhN(CH_3)_2$), 6.37 (s, 2 H, NC*H*) 5.43 (s, 1 H, 4-pz-*H*), 5.41 (s, 2 H, 4-pz-*H*), 4.3 (bs, 1 H, B*H*), 3.20 (sep, 4 H, ^3J = 6.8 Hz, $CH(CH_3)_2$), 2.51 (s, 6 H, $PhNMe_2$) 2.01 (s, 3 H, pz-CH_3), 1.90 (s, 6 H, pz-CH_3), 1.27 (d, 12 H, ^3J(HH) = 6.8 Hz, $CH(CH_3)_2$), 1.17 (d, 12 H, ^3J(HH) = 6.8 Hz, $CH(CH_3)_2$) 1.03 (s, 18 H, pz-$C(CH_3)_3$), 0.94 (s, 8 H, pz-$C(CH_3)_2CH_2$)), 0.00 (bs, 6 H, $Al(CH_3)_2$) ppm. ^{19}F{^{1}H} NMR (376.5 MHz, [D_6]benzene, 26 °C): δ = –131.7 (d, 8 F, ^3J(FF) = 9.5 Hz $F_{Ar(o)}$), –162.8 (t, 4 F, ^3J(FF) = 20.8 Hz, $F_{Ar(p)}$), –166.5 (m, 8 F, $F_{Ar(m)}$) ppm.

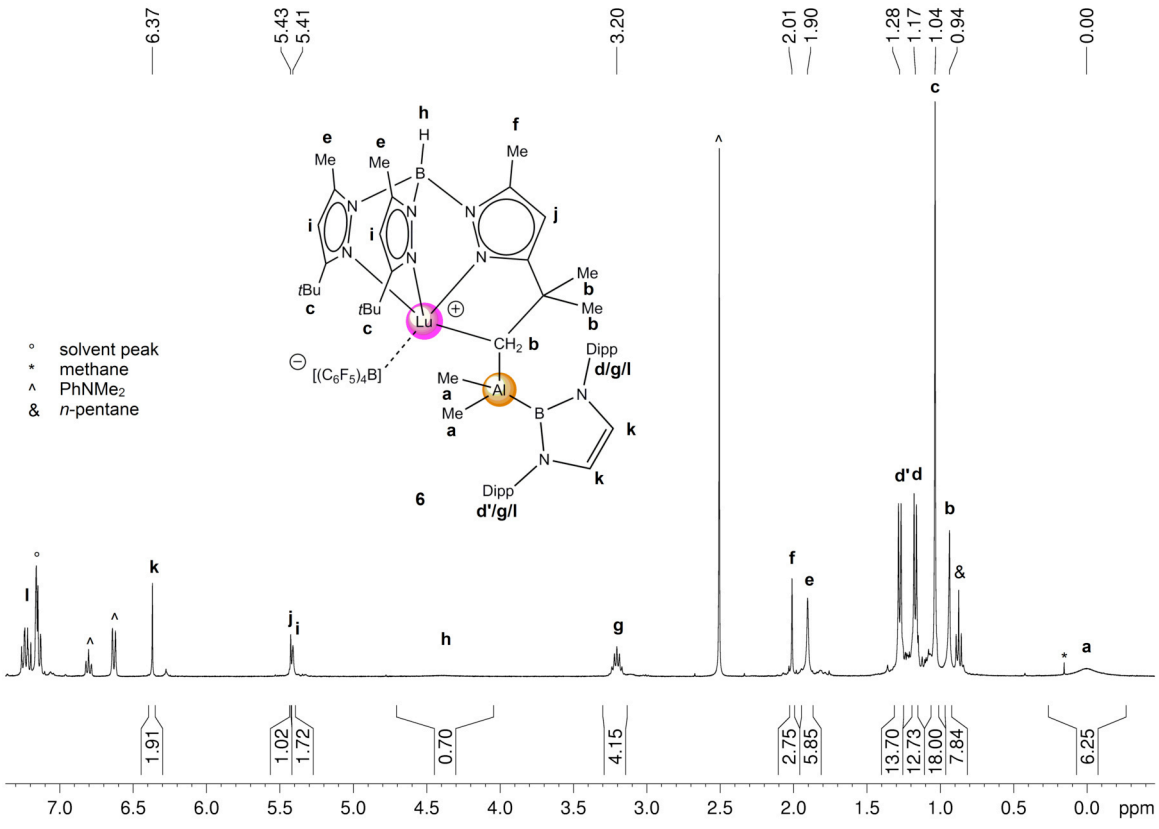

Figure S24. ^{1}H NMR spectrum (400 MHz) in [D_6]benzene of the reaction of **2** with co-catalyst **B** after 10 min in a sealed *J.-Young* valved NMR tube at 26 °C.

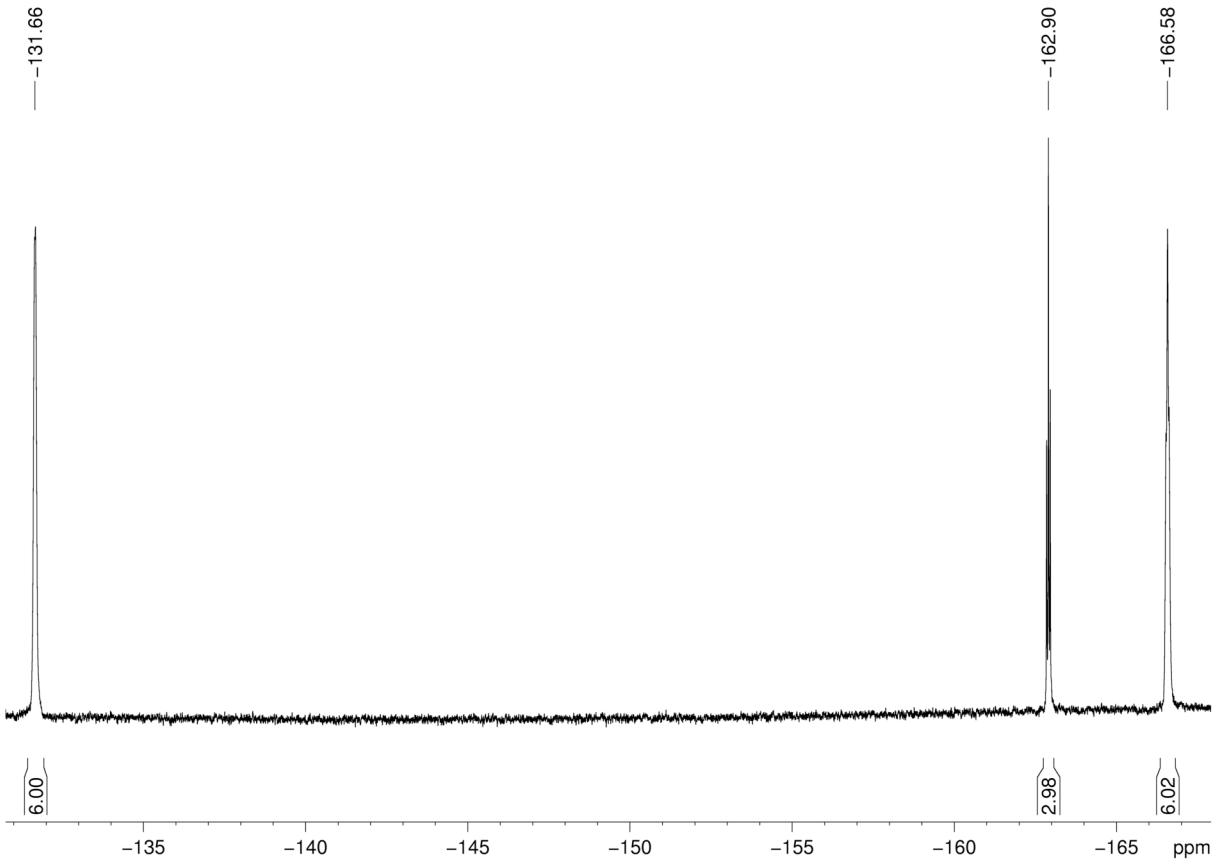

Figure S25. $^{19}F\{^{1}H\}$ NMR spectrum (400 MHz) in [D_6]benzene of the reaction of **2** with co-catalyst **B** after 10 min in a sealed *J.-Young* valved NMR tube at 26 °C.

Crystallographic Data

Table S1. Crystallographic data information of complexes **1**, **2**, **3** and **4**

	1	**2**	**3**	**4**
Formula	$C_{57}H_{95}AlB_2LuN_8$	$C_{58}H_{94}AlB_2LuN_8$	$C_{52}H_{80}B_2GaLuN_8$	$C_{27}H_{47}AlBLuN_6$
Fw	1115.97	1126.98	1083.55	668.46
temp (K)	180(2)	121(2)	100(2)	100(2)
cryst syst	Triclinic	Orthorhombic	Monoclinic	Triclinic
space group	$P\bar{1}$	$P2_12_12_1$	$P2_1/n$	$P\bar{1}$
a (Å)	13.0103(4)	16.116(1)	11.182(1)	12.207(6)
b (Å)	13.9770(4)	18.866(1)	39.772(4)	12.210(8)
c (Å)	18.1287(5)	19.800(1)	11.648(1)	12.954(6)
α (deg)	92.076(2)	90	90	71.94(2)
β (deg)	102.072(2)	90	96.389(2)	75.156(5)
γ (deg)	101.852(1)	90	90	60.47(1)
V (Å^3)	3144.2(2)	6020.0(8)	5148.0(9)	1585(2)
Z	2	4	4	2
ρ_{calcd} (mg/mm^3)	1.179	1.243	1.398	1.401
μ (mm^{-1})	1.623	1.696	2.472	3.167
R1[a] ($I > 2.0\sigma(I)$)	0.0328	0.0234	0.0361	0.0344
wR2[b] (all data)	0.0743	0.0498	0.0672	0.0903
solvent	*n*-hexane	*n*-hexane	*n*-pentane	*n*-pentane

[a] $R1 = \Sigma(||F0|-|Fc||)/\Sigma|F0|$. [b] $wR2 = \{\Sigma[w(F0^2-Fc^2)^2/\Sigma[w(F0^2)^2]\}^{1/2}$.

DFT Calculations

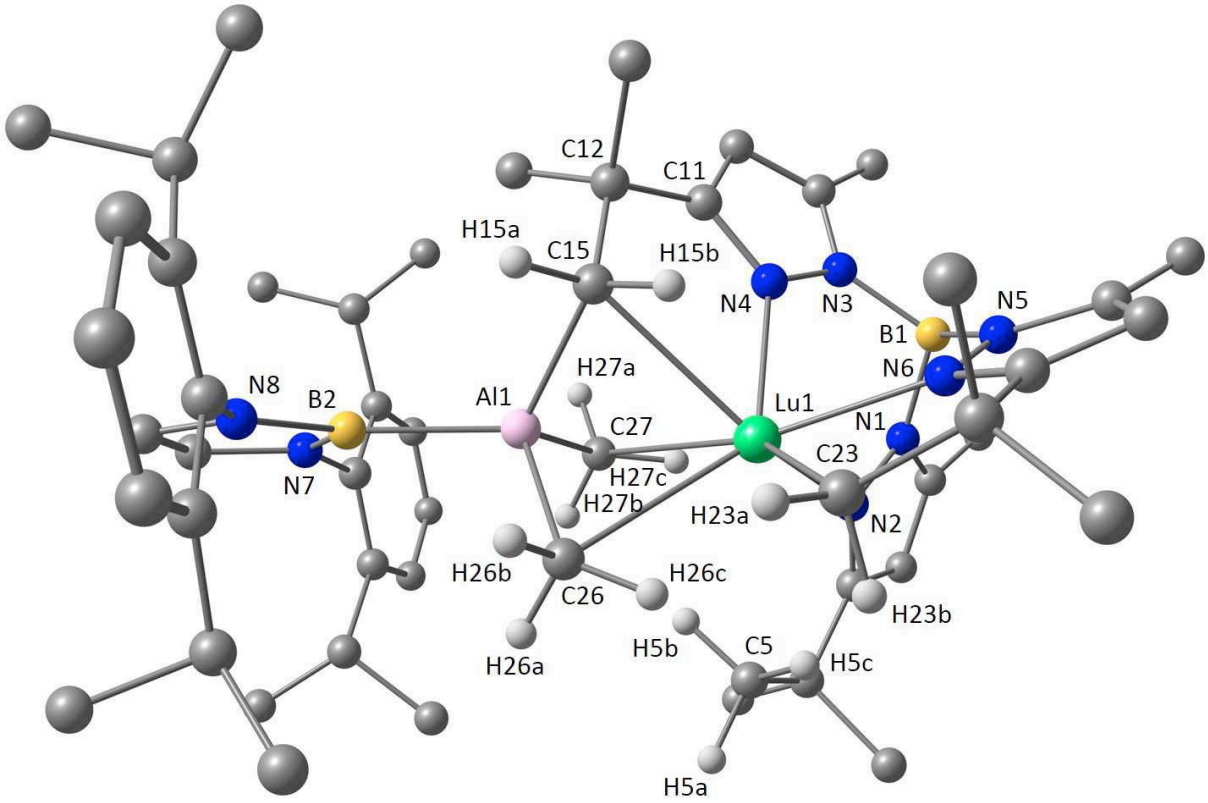

Figure S26. Optimized geometry for the DFT-optimized model system **2a**.

Table S2. Selected geometrical parameters for **2a** (distances in Å, angles in deg); deviations with respect to the X-ray parameters of **2** are given in square brackets

Lu1−C15	2.716 [+1.8 %]	C26−H26a	1.106	B1−N1	1.561 [+0.7 %]
Lu1−C23	2.395 [+0.2 %]	C26−H26b	1.105	B1−N3	1.555 [+0.1 %]
Lu1−C26	2.808 [-5.2 %]	C26−H26c	1.106	B1−N5	1.548 [+0.1 %]
Lu1−C27	2.955 [+3.4 %]	Lu1···H26c	2.481	N1−N2	1.383 [+0.1 %]
Lu1−N4	2.330 [+0.3 %]	C27−H27a	1.105	N3−N4	1.373 [-0.1 %]
Lu1−N6	2.315 [+0.7 %]	C27−H27b	1.106	N5−N6	1.367 [+0.3 %]
Lu1···Al1	2.918 [+0.1 %]	C27−H27c	1.108	B2−Al1−C15	117.5 [+4.2 %]
C15−H15a	1.111	Lu1···H27c	2.566	B2−Al1−C26	108.3 [-6.2 %]
C15−H15b	1.121	Al1−C15	2.114 [+1.4 %]	B2−Al1−C27	114.1 [+3.6 %]
Lu1···H15b	2.367	Al1−C26	2.059 [+1.7 %]	C26−Al1−C27	108.2 [-0.2 %]
C23−H23a	1.107	Al1−C27	2.050 [+1.5 %]	C15−Al1−C26	99.6 [-0.3 %]
C23−H23b	1.118	Al1−B2	2.165 [+1.1 %]	C15−Al1−C27	107.9 [-0.5 %]
Lu1···H23a	3.064	B2−N7	1.468 [+1.4 %]	C26−Lu1−C27	70.5 [+2.8 %]
Lu1···H23b	2.811	B2−N8	1.470 [+1.6 %]	C11−C12−C15	110.4 [0 %]

Table S3. Lu occupancy for selected C−H NLMOs

NLMO	Percent from parent NBO	Percent Lu
C5−H5a	99.2	0.1
C5−H5b	97.2	1.9
C5−H5c	97.6	1.6
C15−H15a	98.2	0.2
C15−H15b	96.1	2.7
C23−H23a	98.1	0.9
C23−H23b	97.0	1.9
C26−H26a	99.0	0.2
C26−H26b	98.9	0.3
C26−H26c	97.0	2.3
C27−H27a	99.0	0.2
C27−H27b	99.1	0.2
C27−H27c	97.5	1.8

Cartesian Coordinates for **2a**:

6	-5.016861000	3.594118000	-2.659690000
6	-2.550129000	3.182182000	-3.054669000
6	1.878609000	3.872720000	-2.980544000
6	-3.054591000	4.869645000	-0.545514000
6	-3.726250000	2.979222000	-2.085092000
6	3.634951000	2.516720000	-4.181499000
6	-2.828902000	5.421288000	0.712713000
6	-3.434938000	3.527840000	-0.692770000
6	-5.609147000	-1.314085000	-3.365139000
6	-3.329234000	-2.011457000	-4.168207000
6	2.663425000	2.541971000	-2.978402000
6	4.474573000	3.309591000	-1.264777000
6	-2.987767000	4.634803000	1.851937000
6	-4.154448000	-1.603643000	-2.937653000
6	1.681347000	1.374669000	-3.102480000
6	-3.575020000	2.737445000	0.472790000
6	3.467612000	2.430005000	-1.698159000
6	-3.365588000	3.287876000	1.759520000
6	-5.362631000	1.081267000	0.276029000
6	4.963467000	2.777594000	-0.077963000
6	6.055287000	3.310849000	0.792935000
6	-0.042696000	1.716849000	0.213052000
6	-5.527710000	-0.241824000	0.015618000
6	-4.121256000	-2.629379000	-1.808035000
6	-5.010203000	2.676136000	3.574812000
6	-0.617535000	-0.746890000	-1.947813000
6	-4.077238000	-3.997816000	-2.110282000
6	-3.584388000	2.467152000	3.024736000
6	-4.201121000	-2.247379000	-0.444283000
6	-2.547433000	2.758100000	4.121081000
6	-4.128161000	-4.964016000	-1.108036000
6	-4.282297000	-3.218791000	0.582318000
6	2.215900000	-2.411965000	-1.877775000
6	-4.236413000	-4.574200000	0.223601000
6	-0.119482000	-1.530638000	1.103238000
6	-1.005427000	-0.618127000	3.303401000
6	-5.972902000	-2.915644000	2.432711000

6	-4.482505000	-2.831888000	2.043438000
6	1.438129000	-0.519990000	2.800762000
6	3.268005000	0.500382000	3.584863000
6	4.368057000	-2.495262000	-0.655548000
6	4.150880000	-3.900702000	-2.713847000
6	3.412047000	-3.321330000	-1.486498000
6	4.326807000	1.133025000	4.429014000
6	0.174762000	-1.328540000	2.612776000
6	5.991207000	-1.585531000	0.594253000
6	2.052526000	-0.053831000	3.979770000
6	7.252207000	-1.266498000	1.331000000
6	5.688002000	-2.693780000	-0.199441000
6	-3.644468000	-3.681440000	3.011626000
6	2.907511000	-4.498405000	-0.617870000
6	0.406331000	-2.697647000	3.305822000
5	-3.211527000	0.148744000	0.099953000
5	4.581915000	0.577990000	1.288290000
13	-1.060665000	-0.040218000	-0.065494000
71	1.787366000	-0.483770000	-0.522875000
7	-3.993405000	1.367709000	0.339147000
7	3.335166000	1.414362000	-0.813453000
7	-4.271582000	-0.849808000	-0.103489000
7	4.271384000	1.633751000	0.181037000
7	2.230608000	-0.240399000	1.751533000
7	3.361719000	0.373075000	2.230523000
7	3.912920000	-1.328967000	-0.167612000
7	4.896807000	-0.772509000	0.600762000
1	-4.913205000	4.684955000	-2.790039000
1	-2.348469000	4.251787000	-3.233826000
1	-5.248321000	3.155893000	-3.644945000
1	-2.775409000	2.719793000	-4.030171000
1	-2.938908000	5.495156000	-1.434927000
1	1.298781000	3.972470000	-3.913421000
1	2.559832000	4.735358000	-2.910082000
1	-5.876332000	3.413574000	-1.995229000
1	3.071699000	2.602235000	-5.126076000
1	-2.530918000	6.468647000	0.807197000
1	4.350158000	3.352892000	-4.134830000
1	-5.629444000	-0.562262000	-4.172090000
1	-1.628053000	2.724549000	-2.663060000
1	-3.284463000	-1.171359000	-4.880516000
1	1.179863000	3.920382000	-2.130312000
1	4.816995000	4.218186000	-1.750901000
1	-3.889348000	1.894563000	-1.983882000
1	-6.090195000	-2.232485000	-3.743550000
1	-3.784450000	-2.862471000	-4.702512000
1	4.211252000	1.577748000	-4.205151000
1	1.110209000	1.434368000	-4.042376000
1	-6.210544000	-0.929705000	-2.528244000
1	-2.297600000	-2.284340000	-3.899279000
1	-3.728413000	-0.667230000	-2.539672000
1	6.399231000	4.276114000	0.394268000
1	-2.815857000	5.077816000	2.835536000
1	-0.520133000	2.473297000	-0.437062000
1	-6.116571000	1.851313000	0.412870000
1	0.935477000	1.400089000	-2.289081000
1	-1.145586000	-0.044980000	-2.619189000
1	-5.169141000	3.732307000	3.853047000
1	2.211192000	0.403980000	-3.121306000
1	-5.773583000	2.399775000	2.831587000
1	-4.006781000	-4.314339000	-3.152997000
1	-6.449362000	-0.805366000	-0.096673000
1	-0.254973000	2.028264000	1.252317000
1	5.715417000	3.468678000	1.828716000
1	1.046200000	1.891062000	0.107186000
1	6.919766000	2.628534000	0.831806000
1	-2.675946000	3.766615000	4.549181000
1	0.329625000	-0.985475000	-2.466698000
1	-1.167986000	-1.704668000	-1.979755000

1	-5.172038000	2.058350000	4.474288000
1	-3.491421000	1.406036000	2.739927000
1	-1.517173000	2.682322000	3.739165000
1	2.482456000	-1.913039000	-2.841856000
1	-4.089590000	-6.025017000	-1.367681000
1	-2.660979000	2.038174000	4.947996000
1	-1.177048000	0.379637000	2.871601000
1	5.525363000	0.954000000	1.935297000
1	-6.594235000	-2.259567000	1.804951000
1	1.351109000	-3.052125000	-2.136038000
1	4.535613000	2.168425000	4.114120000
1	4.557885000	-3.091827000	-3.342742000
1	0.679723000	-2.193972000	0.682103000
1	7.708367000	-0.328162000	0.974213000
1	-1.929046000	-1.206389000	3.184685000
1	-4.167330000	-1.780333000	2.149097000
1	-0.984791000	-2.222361000	1.025829000
1	-0.817968000	-0.492645000	4.382557000
1	-4.290907000	-5.337976000	1.002868000
1	3.448368000	-4.489379000	-3.326676000
1	-6.344266000	-3.948675000	2.319698000
1	-6.114903000	-2.614599000	3.484363000
1	3.995887000	1.155644000	5.477152000
1	5.277523000	0.577413000	4.381449000
1	7.076921000	-1.155801000	2.413707000
1	4.987448000	-4.563074000	-2.424872000
1	1.677139000	-0.118250000	4.996777000
1	7.981065000	-2.076366000	1.184761000
1	6.347207000	-3.531084000	-0.409322000
1	-2.584420000	-3.705373000	2.715126000
1	2.356878000	-4.128900000	0.262639000
1	2.223490000	-5.132403000	-1.206488000
1	-4.003087000	-4.723303000	3.058743000
1	-0.488414000	-3.331994000	3.199425000
1	-3.708235000	-3.269752000	4.032336000
1	1.258350000	-3.226833000	2.849268000
1	0.616513000	-2.578236000	4.382134000
1	3.741836000	-5.126524000	-0.262234000

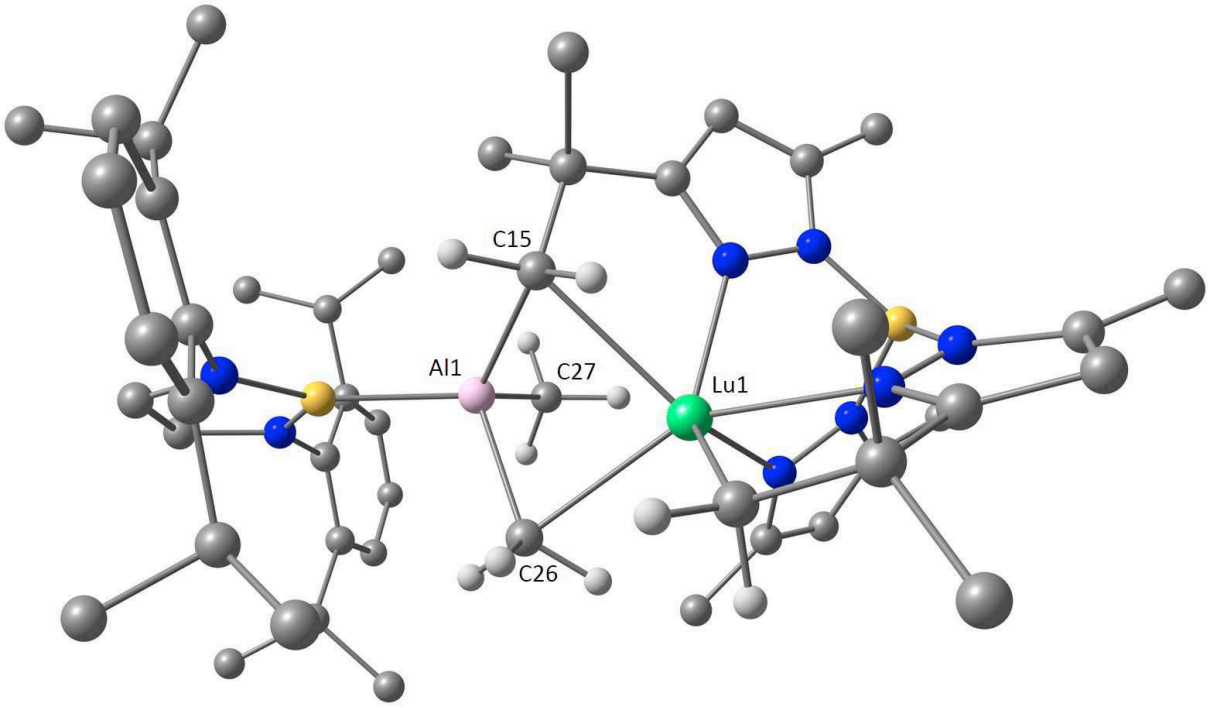

Figure S27. Optimized geometry for the DFT-optimized model system **2b**.

Table S4. Selected geometrical parameters for **2b** (distances in Å)

Lu1−C15	2.627	Al1−C15	2.142
Lu1−C23	2.371	Al1−C26	2.121
Lu1−C26	2.571	Al1−C27	2.019
Lu1···C27	3.381	Lu1···Al1	2.943

Cartesian Coordinates for **2b**:

6	-5.276942000	2.616198000	-3.487126000
6	-2.785715000	2.892393000	-3.806162000
6	-3.709239000	4.600037000	-1.492126000
6	-3.891754000	2.457630000	-2.829828000
6	-3.685531000	5.314521000	-0.297354000
6	-3.828057000	3.202327000	-1.500716000
6	-4.363181000	-2.708661000	-3.271797000
6	-1.879874000	-3.141281000	-3.377738000
6	3.912157000	3.913345000	-1.285960000
6	-3.781749000	4.637723000	0.916942000
6	-3.024568000	-2.594909000	-2.512252000
6	-3.922928000	2.529995000	-0.259785000
6	2.945549000	2.959337000	-1.631311000
6	-3.905747000	3.242494000	0.963951000
6	-5.375437000	0.558034000	-0.352041000
6	4.676501000	3.336421000	-0.274057000
6	5.839775000	3.925941000	0.457336000
6	-0.277034000	2.149699000	0.475736000
6	-5.290394000	-0.796604000	-0.286404000
6	-3.131803000	-3.263108000	-1.146008000
6	-5.543919000	2.525312000	2.743502000
6	-0.246090000	0.117166000	-2.030925000
6	-2.818571000	-4.622160000	-1.003325000
6	-4.065628000	2.532512000	2.303392000

6	-3.612318000	-2.562516000	-0.011527000
6	-3.182873000	3.122549000	3.414029000
6	-2.994766000	-5.282169000	0.210855000
6	-3.820616000	-3.226489000	1.223083000
6	2.309066000	-2.028161000	-2.084855000
6	-3.499529000	-4.589417000	1.307613000
6	0.090168000	-1.211793000	1.025347000
6	-0.655104000	-0.272523000	3.272129000
6	-5.924458000	-2.854481000	2.573810000
6	-4.424610000	-2.521224000	2.433490000
6	1.764508000	-0.285372000	2.678943000
6	3.644651000	0.714066000	3.369397000
6	4.587642000	-1.963840000	-1.118433000
6	4.251516000	-3.304130000	-3.207088000
6	3.614053000	-2.840500000	-1.877963000
6	4.757467000	1.323653000	4.159465000
6	0.460281000	-1.038228000	2.528986000
6	6.255587000	-0.961015000	-0.004727000
6	2.464514000	0.129600000	3.828947000
6	7.557796000	-0.559738000	0.609797000
6	5.962821000	-2.058240000	-0.818215000
6	-3.701936000	-2.855017000	3.749514000
6	3.314350000	-4.089737000	-1.014955000
6	0.636789000	-2.429114000	3.190456000
5	-3.099604000	0.029904000	-0.097899000
5	4.732675000	1.019476000	0.959547000
13	-0.958322000	0.321250000	-0.043355000
71	1.878148000	-0.213924000	-0.620097000
7	-4.090827000	1.101868000	-0.240281000
7	3.104916000	1.849299000	-0.873979000
7	-3.948998000	-1.168399000	-0.128669000
7	4.180217000	2.092110000	-0.037498000
7	2.482741000	0.040160000	1.590980000
7	3.639992000	0.646243000	2.007930000
7	4.092490000	-0.864640000	-0.525386000
7	5.102428000	-0.252957000	0.160931000
1	-5.482459000	3.675687000	-3.717691000
1	-2.923445000	3.933755000	-4.142712000
1	-5.324681000	2.047149000	-4.430694000
1	-2.796881000	2.253296000	-4.704546000
1	-3.636927000	5.137917000	-2.440807000
1	-6.079592000	2.250917000	-2.828014000
1	-3.591826000	6.403418000	-0.311436000
1	-4.296452000	-2.202260000	-4.249573000
1	-1.787988000	2.818180000	-3.344925000
1	-1.759500000	-2.517152000	-4.278014000
1	4.040656000	4.902765000	-1.715187000
1	-3.747292000	1.386698000	-2.611771000
1	-4.616165000	-3.767627000	-3.452665000
1	-2.079767000	-4.169917000	-3.722806000
1	-5.188266000	-2.249397000	-2.706239000
1	-0.921084000	-3.146901000	-2.835131000
1	-2.834633000	-1.522785000	-2.338719000
1	6.024071000	4.944239000	0.085980000
1	-3.762671000	5.206283000	1.849485000
1	-0.704575000	2.898459000	-0.216497000
1	-6.255999000	1.182979000	-0.470757000
1	-1.066180000	0.729973000	-2.447613000
1	-5.910916000	3.555817000	2.890875000
1	-6.184504000	2.038006000	1.992504000
1	-2.436302000	-5.177580000	-1.862122000
1	-6.085903000	-1.533242000	-0.347409000
1	-0.610783000	2.440406000	1.487015000
1	5.654677000	3.985365000	1.541858000
1	0.818631000	2.301821000	0.472017000
1	6.759453000	3.336422000	0.313424000
1	-3.515012000	4.131215000	3.712727000
1	0.641717000	0.568556000	-2.533888000
1	-0.356458000	-0.884924000	-2.476983000

1	-5.661450000	1.982569000	3.696628000
1	-3.757503000	1.484338000	2.151916000
1	-2.129157000	3.192345000	3.100872000
1	2.434412000	-1.415978000	-3.013040000
1	-2.742301000	-6.341813000	0.299969000
1	-3.233510000	2.486212000	4.312803000
1	-0.746638000	0.757120000	2.896831000
1	5.698592000	1.464597000	1.524006000
1	-6.491893000	-2.575253000	1.673718000
1	1.485165000	-2.726264000	-2.329077000
1	4.912587000	2.382855000	3.896752000
1	4.511394000	-2.439307000	-3.839296000
1	0.834132000	-1.917757000	0.569489000
1	7.884949000	0.434510000	0.262813000
1	-1.623664000	-0.779060000	3.136640000
1	-4.335712000	-1.435842000	2.260093000
1	-0.802159000	-1.870354000	0.996114000
1	-0.446552000	-0.222469000	4.353478000
1	-3.648504000	-5.118241000	2.252209000
1	3.534941000	-3.930478000	-3.763477000
1	-6.066763000	-3.935742000	2.743173000
1	-6.360334000	-2.315464000	3.431687000
1	4.520049000	1.269950000	5.231493000
1	5.713338000	0.800852000	3.993074000
1	7.496758000	-0.520029000	1.709913000
1	5.169479000	-3.898804000	-3.046190000
1	2.167014000	0.020855000	4.867616000
1	8.335297000	-1.287688000	0.337712000
1	6.665808000	-2.820822000	-1.140340000
1	-2.615771000	-2.695284000	3.672230000
1	2.839849000	-3.804010000	-0.061844000
1	2.622888000	-4.759438000	-1.553293000
1	-3.866851000	-3.902928000	4.050912000
1	-0.295701000	-3.010678000	3.103358000
1	-4.084691000	-2.218208000	4.564041000
1	1.440635000	-2.998279000	2.695932000
1	0.891184000	-2.340245000	4.260092000
1	4.233488000	-4.654571000	-0.785290000
6	1.870386000	3.087823000	-2.663389000
1	1.953629000	4.060444000	-3.168761000
1	1.945061000	2.303146000	-3.435001000
1	0.867945000	3.027252000	-2.209496000

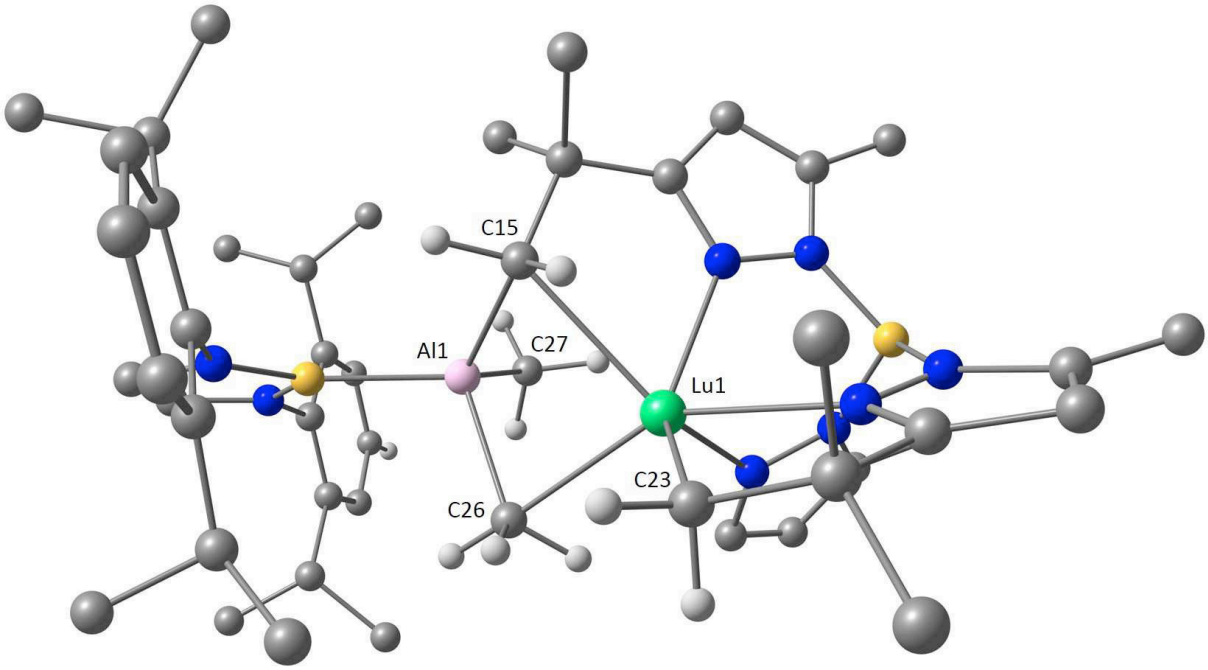

Figure S28. Optimized geometry for the DFT-optimized model system **2c**.

Table S5. Selected geometrical parameters for **2c** (distances in Å)

Lu1−C15	2.603	Al1−C15	2.166
Lu1−C23	2.373	Al1−C26	2.135
Lu1−C26	2.477	Al1−C27	2.011
Lu1···C27	3.678	Lu1···Al1	2.985

Cartesian Coordinates for **2c**:

6	-5.161503000	2.066689000	-3.782313000
6	-2.698362000	2.628352000	-3.909968000
6	-4.013334000	4.348230000	-1.809509000
6	-3.832789000	2.122628000	-3.003082000
6	-4.190970000	5.131250000	-0.671498000
6	-3.981548000	2.948692000	-1.730689000
6	-4.012152000	-3.033847000	-3.171517000
6	-1.507454000	-3.296010000	-3.266144000
6	3.496107000	3.837796000	-1.974323000
6	-4.337081000	4.521535000	0.572320000
6	-2.685020000	-2.785379000	-2.423817000
6	-4.129763000	2.344732000	-0.459813000
6	2.601279000	2.767999000	-2.055667000
6	-4.310376000	3.126503000	0.706229000
6	-5.374788000	0.238160000	-0.454485000
6	4.391964000	3.488947000	-0.962348000
6	5.556875000	4.268611000	-0.443042000
6	-0.500702000	2.378818000	0.330258000
6	-5.158896000	-1.097277000	-0.323374000
6	-2.745505000	-3.382524000	-1.021758000
6	-6.002645000	2.490927000	2.469975000
6	-0.123470000	0.108760000	-1.972215000
6	-2.297173000	-4.690473000	-0.792330000
6	-4.511648000	2.492258000	2.077493000
6	-3.317562000	-2.670078000	0.062088000
6	-3.670715000	3.163117000	3.176057000

6	-2.428743000	-5.292425000	0.457848000
6	-3.480016000	-3.277499000	1.331353000
6	2.394198000	-2.290669000	-1.709317000
6	-3.023901000	-4.592788000	1.503419000
6	0.134155000	-0.905062000	1.243387000
6	-0.543113000	0.333988000	3.361167000
6	-5.612387000	-3.084515000	2.673958000
6	-4.172120000	-2.564939000	2.488817000
6	1.851386000	0.306516000	2.664361000
6	3.705993000	1.479538000	3.106295000
6	4.698995000	-1.892147000	-0.879130000
6	4.384683000	-3.634232000	-2.651892000
6	3.762259000	-2.958441000	-1.409455000
6	4.806444000	2.269590000	3.737759000
6	0.568626000	-0.496811000	2.685954000
6	6.332137000	-0.603358000	-0.041850000
6	2.556041000	0.955721000	3.697117000
6	7.622405000	-0.021460000	0.438559000
6	6.086537000	-1.847800000	-0.626853000
6	-3.401300000	-2.684905000	3.813726000
6	3.581406000	-4.027861000	-0.305261000
6	0.827150000	-1.767342000	3.536459000
5	-3.061117000	-0.050889000	-0.156214000
5	4.709377000	1.413534000	0.639754000
13	-0.958802000	0.455924000	-0.038452000
71	1.886407000	-0.269254000	-0.574487000
7	-4.150896000	0.910138000	-0.358037000
7	2.917340000	1.812397000	-1.161204000
7	-3.789308000	-1.326745000	-0.140295000
7	4.027732000	2.265784000	-0.485604000
7	2.542286000	0.434799000	1.519202000
7	3.681998000	1.150166000	1.783761000
7	4.152018000	-0.731791000	-0.480243000
7	5.140934000	0.055092000	0.038350000
1	-5.470226000	3.076332000	-4.103854000
1	-2.928167000	3.617478000	-4.340457000
1	-5.056421000	1.439701000	-4.683721000
1	-2.545515000	1.933160000	-4.752049000
1	-3.901581000	4.834168000	-2.782063000
1	-5.969872000	1.644237000	-3.165452000
1	-4.213511000	6.220892000	-0.753803000
1	-3.978500000	-2.581089000	-4.176878000
1	-1.749759000	2.716000000	-3.356660000
1	-1.430146000	-2.709154000	-4.195839000
1	3.499131000	4.750655000	-2.561571000
1	-3.585776000	1.092903000	-2.695948000
1	-4.190205000	-4.116492000	-3.290595000
1	-1.640795000	-4.350571000	-3.561621000
1	-4.867836000	-2.600984000	-2.631743000
1	-0.548465000	-3.214830000	-2.730137000
1	-2.571340000	-1.694620000	-2.307813000
1	5.632173000	5.219771000	-0.989015000
1	-4.476084000	5.142959000	1.460374000
1	-0.804714000	3.000518000	-0.532367000
1	-6.309686000	0.767720000	-0.614793000
1	-1.009664000	0.501294000	-2.496183000
1	-6.387411000	3.522426000	2.548965000
1	-6.614853000	1.956211000	1.727344000
1	-1.843093000	-5.253935000	-1.609861000
1	-5.877921000	-1.910773000	-0.352010000
1	-1.041971000	2.785842000	1.202131000
1	5.450846000	4.496670000	0.629742000
1	0.572414000	2.575415000	0.503891000
1	6.505470000	3.722671000	-0.570367000
1	-4.005447000	4.194628000	3.377983000
1	0.702787000	0.695827000	-2.442066000
1	-0.010267000	-0.931990000	-2.333654000
1	-6.145570000	1.999827000	3.447347000
1	-4.183672000	1.442831000	2.000300000

1	-2.605081000	3.202040000	2.900943000
1	2.446260000	-1.858878000	-2.739511000
1	-2.072517000	-6.313884000	0.613657000
1	-3.762269000	2.599932000	4.119540000
1	-0.717300000	1.277201000	2.823023000
1	5.659002000	2.012793000	1.075168000
1	-6.210317000	-2.959253000	1.758592000
1	1.620451000	-3.079818000	-1.779429000
1	4.904677000	3.268918000	3.283081000
1	4.550244000	-2.898473000	-3.455807000
1	0.835450000	-1.711959000	0.895838000
1	7.857782000	0.928157000	-0.069593000
1	-1.486466000	-0.235135000	3.381196000
1	-4.231291000	-1.495393000	2.228877000
1	-0.775742000	-1.528188000	1.360811000
1	-0.275974000	0.579161000	4.402107000
1	-3.138512000	-5.077221000	2.476376000
1	3.701527000	-4.410094000	-3.034878000
1	-5.610612000	-4.157137000	2.933237000
1	-6.117881000	-2.538970000	3.488413000
1	4.596683000	2.401703000	4.808716000
1	5.781747000	1.765942000	3.638839000
1	7.600553000	0.182112000	1.522035000
1	5.353266000	-4.116018000	-2.424799000
1	2.279294000	1.041336000	4.743616000
1	8.442663000	-0.726188000	0.241254000
1	6.827668000	-2.614393000	-0.833256000
1	-2.357391000	-2.352227000	3.706895000
1	3.124065000	-3.586177000	0.595418000
1	2.917653000	-4.830905000	-0.667094000
1	-3.386770000	-3.722544000	4.187484000
1	-0.083143000	-2.387110000	3.585211000
1	-3.880061000	-2.064801000	4.589564000
1	1.631490000	-2.377799000	3.094543000
1	1.123643000	-1.508588000	4.566825000
1	4.544992000	-4.479580000	-0.015423000
1	1.739792000	2.644525000	-2.707451000

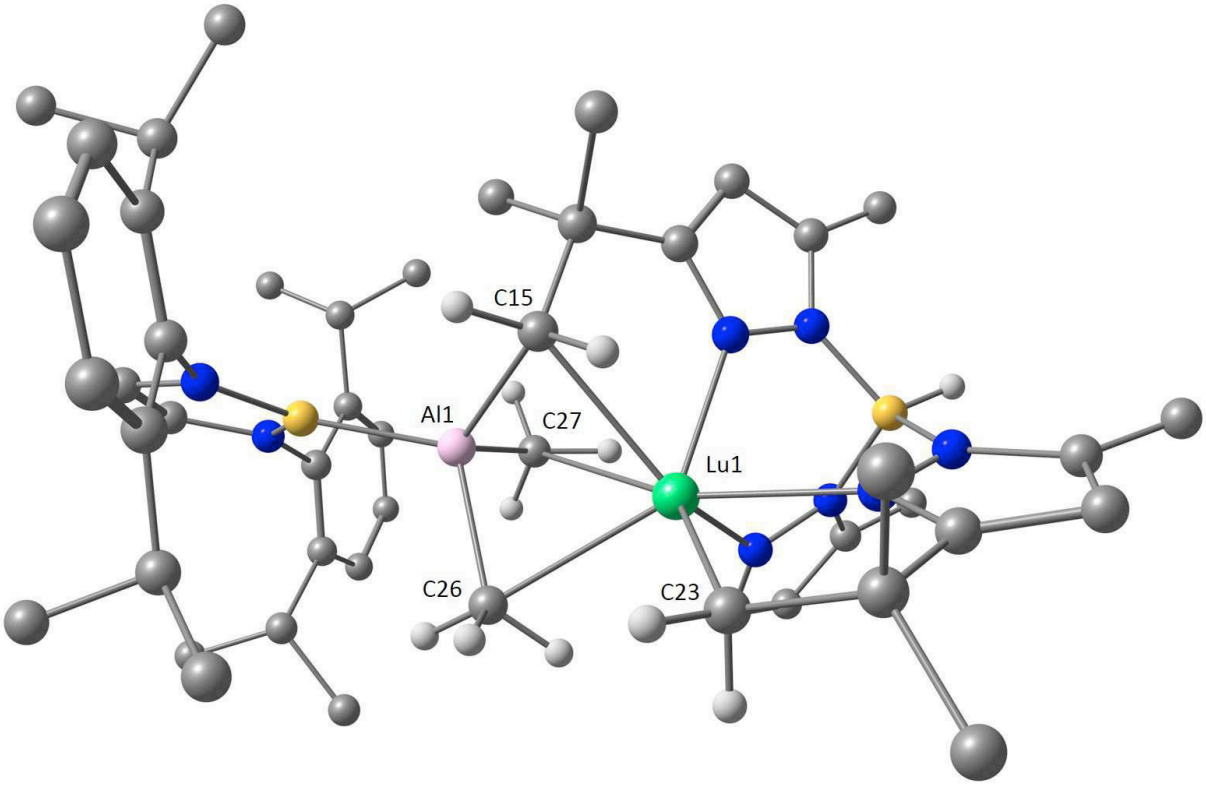

Figure S29. Optimized geometry for the DFT-optimized model system **2d** (partial optimization of **2c** with a fixed Lu-Al-B-angle of 174.0°).

Cartesian Coordinates for **2d**:

6	-4.996626000	2.527710000	-3.576405000
6	-2.515391000	2.603754000	-4.055498000
6	-3.119018000	4.583670000	-1.886265000
6	-3.585605000	2.348211000	-2.981707000
6	-2.993228000	5.415781000	-0.776476000
6	-3.404879000	3.218411000	-1.742918000
6	-4.782258000	-2.472692000	-3.047572000
6	-2.403710000	-3.290879000	-3.259515000
6	3.931927000	3.722554000	-1.671803000
6	-3.152259000	4.891276000	0.503748000
6	-3.403363000	-2.550585000	-2.359271000
6	-3.559360000	2.700005000	-0.435066000
6	3.008509000	2.708037000	-1.938829000
6	-3.439032000	3.533432000	0.702410000
6	-5.249437000	0.946171000	-0.192535000
6	4.656688000	3.276291000	-0.565058000
6	5.773067000	3.965596000	0.150940000
6	-0.076248000	1.886456000	0.018534000
6	-5.339026000	-0.400467000	-0.035524000
6	-3.541897000	-3.157585000	-0.966979000
6	-5.066287000	3.345825000	2.623101000
6	-0.200575000	-0.301125000	-2.266683000
6	-3.404686000	-4.541521000	-0.792252000
6	-3.651440000	3.002689000	2.115455000
6	-3.886182000	-2.368173000	0.160112000
6	-2.594087000	3.506818000	3.111588000
6	-3.622252000	-5.141428000	0.446064000
6	-4.124994000	-2.967098000	1.422742000
6	2.448077000	-2.209728000	-2.023903000
6	-3.985945000	-4.358504000	1.537077000
6	0.114050000	-1.337264000	0.933400000

6	-0.778008000	-0.202410000	3.031981000
6	-6.079567000	-2.305371000	2.889110000
6	-4.563507000	-2.162269000	2.642936000
6	1.671762000	-0.190748000	2.582310000
6	3.474050000	0.942004000	3.280085000
6	4.675617000	-2.046600000	-0.952428000
6	4.467778000	-3.508320000	-2.972087000
6	3.754800000	-2.983689000	-1.705143000
6	4.521300000	1.658436000	4.069827000
6	0.398946000	-0.999741000	2.431042000
6	6.274675000	-0.944722000	0.170174000
6	2.297070000	0.342300000	3.728031000
6	7.539657000	-0.480547000	0.817093000
6	6.036575000	-2.097298000	-0.581786000
6	-3.802227000	-2.550907000	3.922566000
6	3.434138000	-4.187753000	-0.787500000
6	0.573507000	-2.312653000	3.236432000
5	-3.052602000	0.121587000	-0.146998000
5	4.683942000	1.078896000	0.910081000
13	-0.904883000	0.051003000	-0.324199000
71	1.918652000	-0.310203000	-0.692724000
7	-3.899248000	1.312548000	-0.260198000
7	3.150162000	1.696278000	-1.063520000
7	-4.050272000	-0.947015000	0.004541000
7	4.171705000	2.052236000	-0.212561000
7	2.431888000	0.081020000	1.509895000
7	3.540945000	0.770824000	1.928331000
7	4.136485000	-0.921443000	-0.455593000
7	5.104306000	-0.247808000	0.235081000
1	-5.153010000	3.570483000	-3.902329000
1	-2.620368000	3.603157000	-4.510081000
1	-5.133973000	1.872182000	-4.452734000
1	-2.609902000	1.864907000	-4.868233000
1	-2.995475000	5.004212000	-2.887254000
1	-5.776679000	2.279787000	-2.840077000
1	-2.769299000	6.477216000	-0.910143000
1	-4.690096000	-2.014054000	-4.046525000
1	-1.498739000	2.527574000	-3.638247000
1	-2.239514000	-2.718630000	-4.186883000
1	4.063242000	4.660794000	-2.201634000
1	-3.493058000	1.298169000	-2.658693000
1	-5.207928000	-3.483092000	-3.173567000
1	-2.775017000	-4.286464000	-3.556384000
1	-5.492498000	-1.871093000	-2.460082000
1	-1.428858000	-3.426231000	-2.764575000
1	-3.039189000	-1.517431000	-2.232920000
1	5.955384000	4.944592000	-0.314734000
1	-3.051715000	5.550846000	1.369176000
1	-0.389271000	2.574884000	-0.787685000
1	-6.046841000	1.680086000	-0.267669000
1	-1.026776000	0.254007000	-2.750536000
1	-5.205832000	4.439294000	2.676861000
1	-5.843577000	2.936460000	1.959762000
1	-3.133048000	-5.165208000	-1.646038000
1	-6.227999000	-1.019474000	0.038454000
1	-0.539975000	2.271113000	0.944486000
1	5.537697000	4.130254000	1.214637000
1	1.005034000	2.057444000	0.164346000
1	6.708926000	3.385534000	0.107626000
1	-2.690844000	4.589683000	3.298385000
1	0.691260000	0.179391000	-2.737830000
1	-0.231408000	-1.324413000	-2.671227000
1	-5.226771000	2.932170000	3.633053000
1	-3.570066000	1.904520000	2.064640000
1	-1.571191000	3.317774000	2.749149000
1	2.607398000	-1.657840000	-2.983885000
1	-3.512934000	-6.223098000	0.557985000
1	-2.715133000	2.996828000	4.081481000
1	-0.885911000	0.777708000	2.544478000

1	5.612209000	1.589275000	1.482795000
1	-6.669680000	-1.985012000	2.017808000
1	1.647774000	-2.937476000	-2.258814000
1	4.651777000	2.697464000	3.725720000
1	4.739508000	-2.675309000	-3.640972000
1	0.919259000	-2.029933000	0.576245000
1	7.871078000	0.492371000	0.417630000
1	-1.720100000	-0.756472000	2.900042000
1	-4.354629000	-1.100716000	2.430535000
1	-0.739953000	-2.045804000	0.933641000
1	-0.630034000	-0.030599000	4.110921000
1	-4.164586000	-4.836485000	2.503260000
1	3.793956000	-4.183466000	-3.524903000
1	-6.339300000	-3.355666000	3.106299000
1	-6.389216000	-1.693520000	3.753009000
1	4.230639000	1.684452000	5.129663000
1	5.502489000	1.161936000	3.994940000
1	7.423578000	-0.366005000	1.907436000
1	5.390375000	-4.068525000	-2.732795000
1	1.952656000	0.300698000	4.757129000
1	8.338952000	-1.212841000	0.634685000
1	6.764862000	-2.866866000	-0.820547000
1	-2.711961000	-2.528869000	3.774529000
1	2.911599000	-3.857923000	0.125517000
1	2.778226000	-4.898145000	-1.318135000
1	-4.074523000	-3.562488000	4.267058000
1	-0.340254000	-2.925301000	3.162993000
1	-4.051192000	-1.851579000	4.737751000
1	1.414031000	-2.906236000	2.841608000
1	0.769385000	-2.111802000	4.303237000
1	4.349526000	-4.723402000	-0.484168000
1	2.241585000	2.660588000	-2.709199000

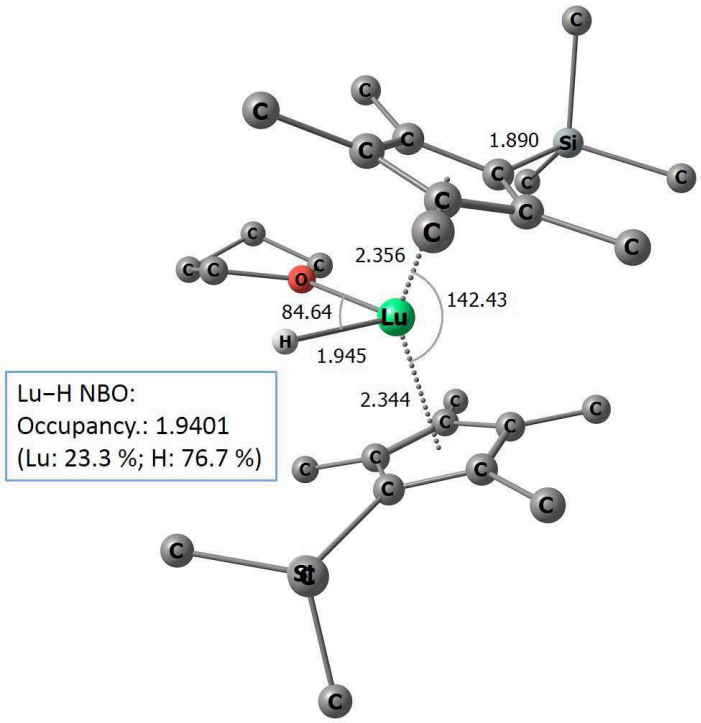

Figure S30. Optimized geometry, salient geometrical parameters, and Lu−H NBO composition for the DFT-optimized model system [$(C_5Me_4SiMe_3)_2LuH(THF)$] (starting coordinates were taken from the X-ray structure determination, published in the following reference: Y. Takenaka, Z. Hou, *Organometallics* **2009**, *28*, 5196).

Cartesian Coordinates for the DFT-optimized model system $[(C_5Me_4SiMe_3)_2LuH(THF)]$ from Figure S30:

6	1.589470000	-3.215978000	0.592630000
6	4.020655000	-2.481533000	-1.553944000
6	-1.818673000	-3.120909000	-0.498476000
6	0.251058000	-2.231790000	-2.773786000
6	1.578419000	-1.781397000	1.046681000
6	-1.629647000	-1.718289000	-1.015640000
6	0.046939000	-2.140984000	3.137068000
6	-0.671821000	-1.335018000	-1.999113000
6	5.455427000	-0.566210000	0.298528000
6	-3.946538000	-1.771610000	1.818477000
6	0.913763000	-1.328814000	2.218019000
6	-5.460664000	-1.276025000	-0.808565000
6	2.377963000	-0.693096000	0.516394000
6	3.795163000	0.505507000	-2.057408000
6	-2.477805000	-0.585789000	-0.729715000
6	-0.919371000	0.032131000	-2.347867000
6	-0.255853000	0.734217000	-3.501732000
6	1.301393000	0.028160000	2.459483000
6	2.201104000	0.414270000	1.434112000
6	-2.030759000	0.486584000	-1.581888000
6	0.936846000	0.820700000	3.682014000
6	2.965072000	1.711629000	1.430954000
6	-4.596010000	1.069493000	0.970957000
6	-2.690222000	1.831254000	-1.732773000
6	0.794718000	3.173306000	-1.036751000
6	-0.496037000	3.315291000	0.978679000
6	0.865662000	4.598062000	-0.498079000
6	-0.424589000	4.692073000	0.329800000
1	4.159419000	-3.310502000	-0.842867000
1	2.468514000	-3.749336000	1.000279000
1	-1.051623000	-3.800111000	-0.898101000
1	0.700029000	-3.757155000	0.948372000
1	4.923770000	-2.432602000	-2.187428000
1	1.628884000	-3.317190000	-0.500140000
1	0.442439000	-3.183590000	-2.257771000
1	3.170532000	-2.729000000	-2.208033000
1	-2.799774000	-3.525751000	-0.804480000
1	-1.776187000	-3.185608000	0.600515000
1	-0.187004000	-2.482742000	-3.758933000
1	1.225592000	-1.757205000	-2.972407000
1	-0.419027000	-2.996431000	2.623498000
1	0.632200000	-2.551649000	3.981429000
1	-3.867137000	-2.836112000	1.549744000
1	5.545517000	-1.328485000	1.090217000
1	-5.234381000	-2.287133000	-1.186267000
1	6.326745000	-0.669424000	-0.371246000
1	-4.862252000	-1.649494000	2.422832000
1	-6.415542000	-1.327328000	-0.257542000
1	-0.763077000	-1.528863000	3.564486000
1	-3.084898000	-1.500035000	2.448940000
1	4.661600000	0.369831000	-2.727408000
1	-0.495167000	0.230205000	-4.456551000
1	5.516102000	0.422921000	0.778881000
1	2.883162000	0.411783000	-2.670664000
1	-5.609406000	-0.621459000	-1.683615000
1	0.845258000	0.750141000	-3.425780000
1	3.841785000	1.537030000	-1.670561000
1	1.518117000	0.483572000	4.561256000
1	-1.368094000	0.488012000	1.637989000
1	-0.595206000	1.776513000	-3.601143000
1	-0.132040000	0.719327000	3.926258000
1	3.807339000	1.677086000	2.146518000
1	3.394784000	1.943081000	0.444890000
1	-5.467961000	0.926867000	1.632895000
1	-3.684337000	1.737896000	-2.206532000

1	-3.787539000	1.521751000	1.567903000
1	-4.893948000	1.771331000	0.177070000
1	1.148913000	1.894230000	3.554315000
1	-2.099651000	2.504684000	-2.373854000
1	1.776859000	2.708254000	-1.208740000
1	2.338853000	2.568571000	1.730358000
1	-2.846525000	2.337825000	-0.767584000
1	0.200334000	3.116758000	-1.963760000
1	0.104713000	3.260146000	1.902735000
1	-1.507825000	2.948589000	1.195765000
1	1.750198000	4.725367000	0.147663000
1	0.919091000	5.340599000	-1.307812000
1	-1.294380000	4.855659000	-0.327613000
1	-0.400513000	5.497025000	1.078792000
8	0.102007000	2.400322000	-0.006041000
14	3.839402000	-0.807807000	-0.676577000
14	-4.059695000	-0.627582000	0.307962000
71	-0.127791000	0.054980000	0.203716000

Paper II

Gallium Methylene

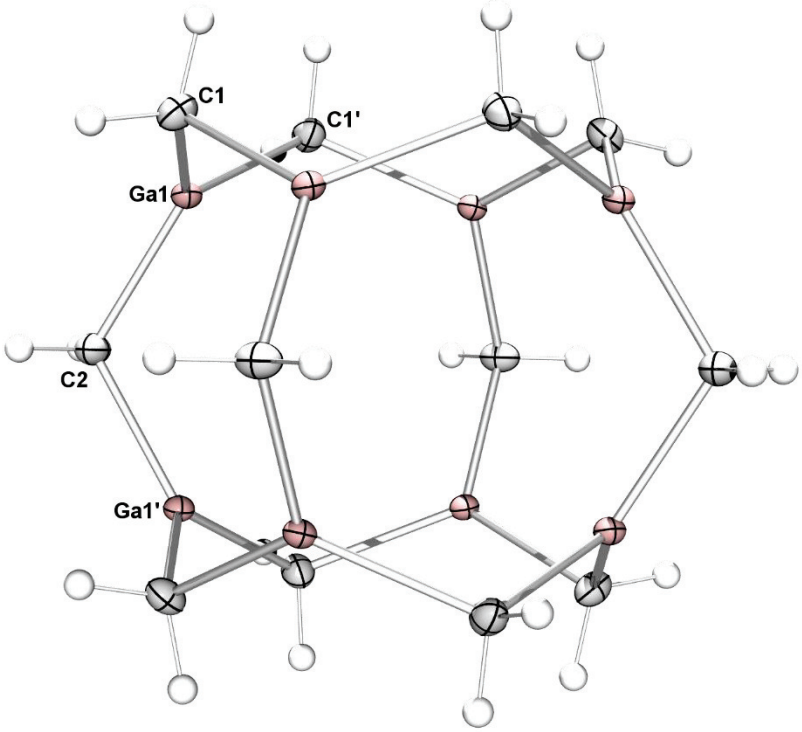

Metal Alkylidenes

International Edition: DOI: 10.1002/anie.201902063
German Edition: DOI: 10.1002/ange.201902063

Gallium Methylene

Martin Bonath, Cäcilia Maichle-Mössmer, Peter Sirsch, and Reiner Anwander**

Abstract: *Despite the eminent importance of metal alkylidene species for organic synthesis and industrial catalytic processes, molecular homoleptic metal methylene compounds $[M(CH_2)_n]$ as the simplest representatives, have remained elusive. Reports on this topic date back to 1955 when polymeric $[Li_2(CH_2)]_n$ and $[Mg(CH_2)]_n$ were accessed by pyrolysis of methyllithium and dimethylmagnesium, respectively. However, the insoluble salt-like composition of these compounds has impeded their application as valuable reagents. We report that rare-earth metallocene methyl complexes $[(C_5Me_5)_2Ln\{(\mu\text{-}Me)_2GaMe_2\}]$ (Ln = Lu, Y) trigger the formation of homoleptic gallium methylene $[Ga_8(\mu\text{-}CH_2)_{12}]$ from trimethylgallium $[GaMe_3]$ (Me = methyl) via a cascade C–H bond activation involving the dodecametallic clusters $[(C_5Me_5)_6Ln_3(\mu_3\text{-}CH_2)_6Ga_9(\mu\text{-}CH_2)_9]$ as crucial intermediates. Such gallium methylene compounds feature a reversible $[Ga_8(\mu\text{-}CH_2)_{12}]/[Ga_6(\mu\text{-}CH_2)_9]$ oligomer switch in donor solvents and act as Schrock-type methylene-transfer reagents.*

Metal methylene/methylidene moieties are key components of both carbonyl olefination reactions for natural product synthesis[1] and also major industrial catalytic processes such as olefin metathesis[2] and Fischer–Tropsch synthesis.[3] In particular, the discovery and structural elucidation of transition-metal methylidene species has triggered tremendous research in these emerging fields.[4] Seminal works comprise Schrock's terminal methylidene $[Cp_2Ta(=CH_2)(CH_3)]$ (**I**, Cp = cyclopentadienyl; Figure 1),[4a,b] Herrmann's bridging methylene $[Cp(CO)_2Mn(\mu\text{-}CH_2)MnCp(CO)_2]$ (**II**),[4c,d] and Tebbe's reagent $[Cp_2Ti(\mu\text{-}CH_2)(\mu\text{-}Cl)Al(CH_3)_2]$ (**III**),[4e–g] which have crucially contributed to a fundamental understanding of the processes involved as well as their successful further development. d/f-Transition-metal methylidene/alkylidene chemistry is still a hot topic, e.g., the isolation of terminal methylidene complexes of the Group 4 metals, and more specifically complexes $[(PNP)M(=CH_2)(OAr)]$ (M = Zr, Hf, PNP = N[2-P(*i*Pr)$_2$-4-CH$_3$-C$_6$H$_3$]$_2$, Ar = C$_6$H$_3$*i*Pr$_2$-2,6)[5] and $[(PN)Ti{=}CH_2]$ (PN = N[2-P(*i*Pr)$_2$-4-CH$_3$-C$_6$H$_3$]$_2$(C$_6$H$_2$Me$_3$-2,4,6)).[6] These achievements were made possible mainly by tailor-made ligand environments and the emergence of new synthesis strategies. In stark contrast, and despite the great importance of the Wittig reagent Ph_3PCH_2 for olefination chemistry,[1,7] main-group-metal methylene chemistry has remained underdeveloped. Remarkably, the syntheses of dilithium methylene $[Li_2CH_2]_n$ and magnesium methylene $[MgCH_2]_n$ were described by Ziegler already in 1955 via pyrolysis of the respective methyl compounds,[8] but it was only in 1990 that the solid-state structure of salt-like $[Li_2CD_2]_n$ was examined by X-ray and neutron powder diffraction techniques.[9] Methylene-bridged aluminum centers of the type $[R_2Al{-}CH_2{-}AlR_2]$ (**IV**)[10] have been made accessible via derivatization of the halogenido derivatives $[X_2Al{-}CH_2{-}AlX_2]$ (available from Al and CH_2X_2)[11] and degradation/deprotonation of methyl and tetramethylaluminato ligands as found in, e.g., $[(tBu_3PN)_2TiAl_3(CH_2)_2(CH_3)_7]$[12] or $[La_4Al_8(C)(CH)_2(CH_2)_2(CH_3)_{22}(toluene)]$.[13]

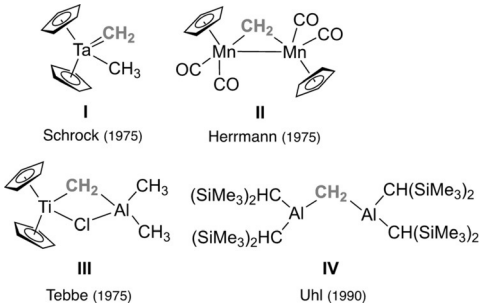

Figure 1. Milestones in metal methylene/methylidene chemistry.

Methane activation via solvent-free rare-earth-metallocene derivatives $[(C_5Me_5)_2LnMe]$ (Ln = Sc, Lu) represents one of the major discoveries in organolanthanide chemistry.[14] We have shown that such highly reactive Ln–CH$_3$ moieties can engage in multiple C–H bond activations, preferably in the presence of trimethylaluminum even at ambient temperature.[13] Crucially, such methyl group degradation can be controlled in the presence of sterically demanding ancillary ligands, affording, e.g., methylidene complex $[(C_5Me_5)_3Y_3(\mu\text{-}Cl)_3(\mu_3\text{-}Cl)(\mu_3\text{-}CH_2)(thf)_3]$[15] and Tebbe-like $[(Tp^{tBu,Me})La[(\mu\text{-}CH_2)\{(\mu\text{-}Me)AlMe_2\}_2]]$ ($Tp^{tBu,Me}$ = hydrotris(3-*tert*-butyl-5-methylpyrazolyl)borato).[16] By studying the reaction of $[(C_5Me_5)_2LnMe]$ (Ln = Y, Lu) with an excess of trimethylgallium we have now obtained oligomeric gallium methylene $[Ga_8(\mu\text{-}CH_2)_{12}]$. Herein we describe the organo-rare-earth metal-promoted formation and full characterization of $[Ga_8(\mu\text{-}CH_2)_{12}]$, which represents the first molecular homoleptic metal methylene complex.

Treatment of $[(C_5Me_5)_2Ln\{(\mu\text{-}Me)_2GaMe_2\}]$ (Ln = Lu ($\mathbf{1}^{Lu}$),[17] Y ($\mathbf{1}^{Y}$);[18] see the Supporting Information) with an eightfold excess of $[GaMe_3]$ at 130 °C in aromatic solvents like C_6D_6 generates methane and provides access to $[Ga_8(\mu\text{-}CH_2)_{12}]$ (**2**) as a pale yellow crystalline material in 80% yield (Scheme 1).[19] The solid-state structure of oligomeric compound **2** was determined by single-crystal X-ray diffraction

[*] M. Bonath, Dr. C. Maichle-Mössmer, Dr. P. Sirsch, Prof. Dr. R. Anwander
Institut für Anorganische Chemie
Eberhard Karls Universität Tübingen
Auf der Morgenstelle 18, 72076 Tübingen (Germany)
E-mail: peter.sirsch@uni-tuebingen.de
reiner.anwander@uni-tuebingen.de
Supporting information and the ORCID identification number(s) for the author(s) of this article can be found under: https://doi.org/10.1002/anie.201902063.

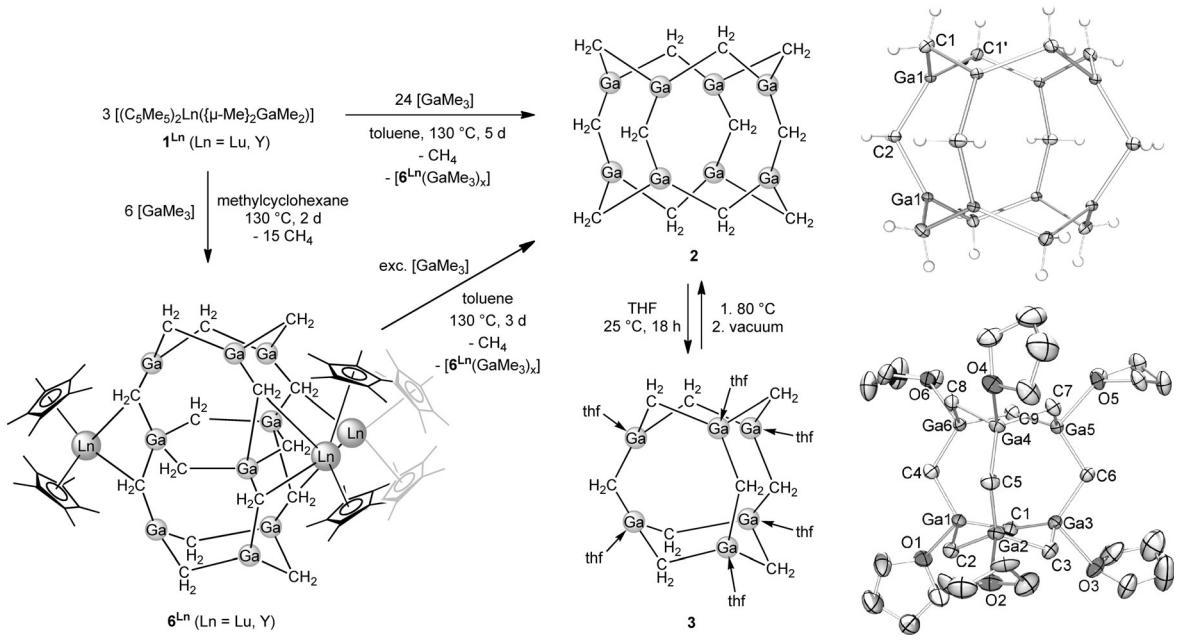

Scheme 1. Synthesis of compounds **2**, **3**, and **6**, including the crystal structures of gallium methylenes **2** and **3**.[31] d = Days.

(XRD) analysis (Scheme 1), revealing a cage-like structural motif closely related to silsesquioxanes of the general formula $[\{Si_8(\mu\text{-}O)_{12}\}R_8]$.[20] Each gallium atom of the "$[Ga_8]$ cube" binds to three methylene bridges ("edges"), thus adopting a trigonal-planar geometry (sum of angles about Ga 359.2°) with bond lengths (1.960(2) Å, 1.961(1) Å, 1.972(2) Å) in the same range as those reported for $[GaMe_3]$.[21] For comparison, galloxane clusters like $[Ga_{12}tBu_{12}(\mu_3\text{-}O)_8(\mu\text{-}O)_2(\mu\text{-}OH)_4]$ obtained via alkyl hydrolysis tend to adopt an icosahedral arrangement of the alkylgallium(III) moieties,[22] while silicon methylene derivatives favor ring structures.[23]

Analysis of **2** by NMR spectroscopy at ambient temperature in [D$_8$]THF solution provided data consistent with homoleptic gallium methylene **2**. The ^{1}H NMR spectrum of **2** shows a singlet resonance at $\delta = 0.19$ ppm assignable to equivalent methylene protons. However, at ambient temperature in [D$_8$]THF solution compound **2** converted within 24 hours to the smaller gallium methylene oligomer $[Ga_6(\mu\text{-}CH_2)_9(thf)_6]$ (**3**), giving rise to a set of signals at $\delta = 0.12$ (d, $^2J_{H,H} = 9.1$ Hz, 6H), 0.10 (s, 6H), and -0.49 ppm (d, $^2J_{H,H} = 8.8$ Hz, 6H) consistent with three magnetically nonequivalent protons. Tracking this process at variable temperatures by NMR spectroscopy revealed that the $[Ga_8(\mu\text{-}CH_2)_{12}]$/$[Ga_6(\mu\text{-}CH_2)_9]$ oligomer switch in THF solution is suppressed at temperatures below -40 °C and reversed at temperatures above 80 °C (Figures S2 and S3). Single crystals of compound **3** could be grown from saturated THF solutions at -40 °C and were subjected to XRD analysis. The solid-state structure of hexagallium methylene **3** (Scheme 1) features two six-membered $[Ga_3(\mu\text{-}CH_2)_3]$ rings in chair conformation. The two $[Ga_3(\mu\text{-}CH_2)_3]$ subunits are co-facially oriented and connected by three Ga–CH_2–Ga bridges; overall, the structure is reminiscent of silsesquioxanes of the general formula $[\{Si_6(\mu\text{-}O)_9\}R_6]$.[24] All gallium atoms in compound **3** are coordinated additionally by a THF molecule and therefore display distorted tetrahedral geometry with slightly elongated average Ga–C bond lengths (av. 1.982 Å) compared to **2**.

Crystallization of gallium methylene **2** from THF solution at ambient temperature by slowly condensing *n*-pentane into the solution triggers the rearrangement of the $[Ga_8(\mu\text{-}CH_2)_{12}]$ cage as confirmed by ^{1}H NMR spectroscopy. Single-crystal XRD analysis corroborates a rather weak Ga–O(THF) interaction since the solid-state structures of $[Ga_8(\mu\text{-}CH_2)_{12}(thf)_4]$ (**4**) and $[Ga_8(\mu\text{-}CH_2)_{12}(thf)_5]$ (**5**) display only partial THF coordination (Figure 2).

THF coordination leads to structural distortions of the cage motif disclosed for unsolvated compound **2**. The coordinated THF molecules in **3**, **4**, and **5** are slowly lost at glovebox atmosphere and can be removed completely under reduced pressure (Figure S13).

The ease of the donor-mediated interconversion of Ga_6 and Ga_8 methylene cages involving Ga–C bond disruption and formation, respectively, seems remarkable. To gain further insight into this process and the relative stabilities of the different oligomers depending on donor solvent coordination, density functional theory (DFT) calculations were carried out. They revealed that in the absence of THF, the larger Ga_8 oligomers are clearly more stable than the Ga_6 cages: $\Delta E = +226$ kJ mol^{-1} and $\Delta G(298\text{ K}) = +174$ kJ mol^{-1} for the conversion of three Ga_8 into four Ga_6 oligomers (in the gas phase). However, the smaller cages should become more favorable in the case of THF coordination, as more donor molecules in total can now be bound by gallium atoms: whereas in **3** all gallium atoms were coordinated by THF, only partial coordination was observed for the larger cages **4** and **5**. Interestingly, the additional bonds formed and the concomitant loss in entropy balance each other out, and the computed value of ΔG ($+4$ kJ mol^{-1} at 298 K) for the conversion of **5** into **3** (for comparison, $\Delta E = -400$ kJ mol^{-1}) points to an equilibrium at ambient temperature. At lower temperature,

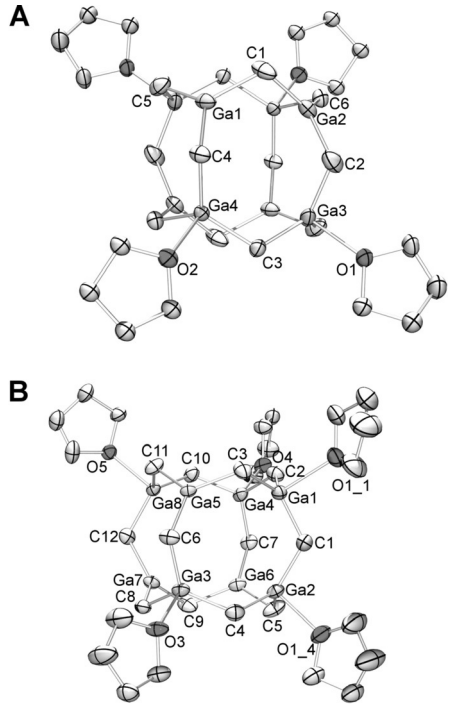

Figure 2. Crystal structures of **4** (A) and **5** (B).[31]

the equilibrium shifts towards the smaller cage (e.g., $\Delta G = -129\ \mathrm{kJ\,mol^{-1}}$ at 200 K), which is in line with the findings from low-temperature NMR spectroscopy. Replacing THF by the stronger donor pyridine renders the Ga_6 cage the preferred species at room temperature (see the NMR spectra and solid-state structures of the pyridine adduct $[Ga_6(\mu\text{-}CH_2)_9(py)_6]$ (**7**) and its partial decomposition product $[Ga_5(\mu\text{-}CH_2)_7(CH_3)(py)_5]$ (**8**) in the Supporting Information). It is noteworthy that the calculated thermochemical data ($\Delta E = -464\ \mathrm{kJ\,mol^{-1}}$, $\Delta G(298\ \mathrm{K}) = -111\ \mathrm{kJ\,mol^{-1}}$) suggest that this is only partly due to stronger bonds forming between the solvent molecules and the gallium atoms. To a larger extent, it is a consequence of a lower entropy contribution of the free pyridine ligands, which are more rigid than their THF counterparts. Finally, in order to understand the observed partial coordination of the Ga_8 oligomer, we computed the changes in energy and free enthalpy for the successive coordination of **2** by THF. The values for ΔE range from -70 to $-45\ \mathrm{kJ\,mol^{-1}}$ (coordination of the first and last THF molecule, respectively). Due to entropy losses, the differences in free enthalpy at 298 K, however, are considerably lower (-27 and $+11\ \mathrm{kJ\,mol^{-1}}$, respectively). ΔG for binding a sixth or seventh THF donor amounts to less than $-2\ \mathrm{kJ\,mol^{-1}}$ and explains the partial coordination pattern observed for the crystal structures of **4** and **5**. Packing effects can therefore be ruled out as a potential cause and partial coordination might also be prevalent in solution.

Treating the supernatant of the initial reaction mixture with another eight equivalents of $[GaMe_3]$ at 130 °C generated additional **2** in about the same yield. Since this procedure can be repeated several times, an elusive intermediate capable of promoting the "pseudocatalytic" transformation of $[GaMe_3]$ into **2** persists after each cycle. Fortunately, prolonged thermal treatment of the supernatant without addition of $[GaMe_3]$ afforded reproducibly colorless crystals of the bimetallic rare-earth metallocene gallium methylene complexes $[(C_5Me_5)_6Ln_3(\mu_3\text{-}CH_2)_6Ga_9(\mu\text{-}CH_2)_9]$ (Ln = Lu (**6^{Lu}**); Y (**6^{Y}**); Figure 3; compound **6^{Y}** behaves in complete

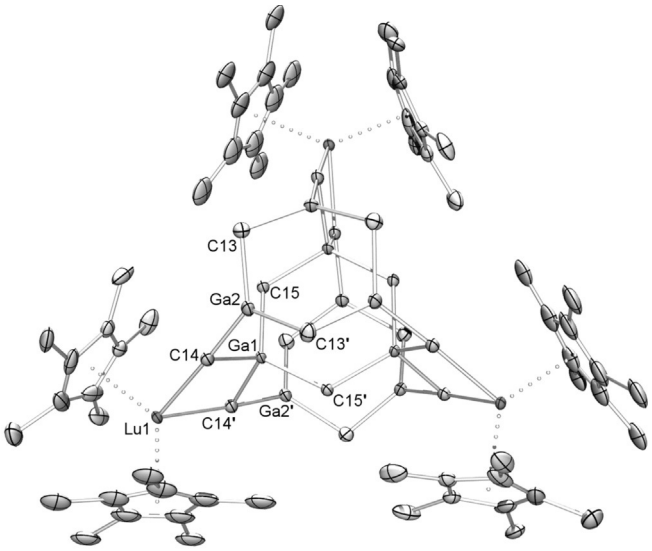

Figure 3. Crystal structure of **6^{Lu}**.[31]

analogy to **6^{Lu}**, see the Supporting Information). Compound **6^{Lu}** was identified as a crucial intermediate in the formation of **2**, since it converts excess $[GaMe_3]$ to **2** at 130 °C within 3 days (87 %, Scheme 1). Even at ambient temperature, compound **6^{Lu}** slowly extrudes **2** in the presence of $[GaMe_3]$, accompanied by the release of starting material $[(C_5Me_5)_2Lu\{(\mu\text{-}Me)_2GaMe_2\}]$ (**1^{Lu}**), as evidenced by NMR spectroscopy (Figure S6). Monitoring compound **6^{Lu}** in the presence of excess $[GaMe_3]$ by NMR spectroscopy revealed spectral data very similar to those observed for the transformation of $[GaMe_3]$ to compound **2** promoted by $[(C_5Me_5)_2Lu\{(\mu\text{-}Me)_2GaMe_2\})]$ (**1^{Lu}**). This suggests that the reactive intermediate is in fact an addition product of **6^{Lu}** and $[GaMe_3]$ (Scheme 1).

Single-crystal XRD analysis of complex **6^{Lu}** disclosed its solid-state structure (Figure 3), which can be described as a highly aggregated anionic $[(\mu_3\text{-}CH_2)_6Ga_9(\mu\text{-}CH_2)_9]^{3-}$ core stabilized by three cationic $[(C_5Me_5)_2Lu]^{+}$ entities. The $[(\mu_3\text{-}CH_2)_6Ga_9(\mu\text{-}CH_2)_9]^{3-}$ core unit comprises three staggered six-membered $[Ga_3(\mu\text{-}CH_2)_3]$ rings interconnected by μ_3-Ga_2Lu-bridging methylene units involving the flanking rare-earth metallocene entities. Comparable to **3**, the outer rings adopt a chair conformation with gallium atoms in distorted trigonal-planar geometry. In contrast, the central ring system exhibits a planar arrangement with gallium atoms in a distorted tetrahedral coordination environment. Consequently, the three-coordinate gallium atoms display Ga–C bond lengths (1.961(6), 1.973(6), 1.972(6) Å) comparable to those in compound **2**, whereas all four-coordinate gallium atoms exhibit longer Ga–C distances (Ga–(μ-CH_2) = 2.008(7), Ga–(μ_3-CH_2) = 2.125(6) Å) similar to those reported for

$[GaMe_4]^-$ moieties.[25] The Lu–C(methylene) distances of 2.510(6) Å are considerably shorter than the Lu–C(Me) bond lengths of the starting material $[(C_5Me_5)_2Lu\{(\mu\text{-}Me)_2GaMe_2\}]$ ($\mathbf{1^{Lu}}$) (av. 2.614 Å) (Figure S35) which is attributable to the increased negative charge at the methylene carbon atoms.

In contrast to homoleptic gallium methylene **2**, compound $\mathbf{6^{Lu}}$ is insoluble in $[D_8]$THF but dissolved to a minor extent when 4-dimethylaminopyridine (DMAP) was added to the corresponding suspension in $[D_8]$THF. The NMR data for $\mathbf{6^{Lu}}$ in $[D_8]$THF are consistent with the composition in the solid state (Figure S14). The $[(\mu_3\text{-}CH_2)_6Ga_9(\mu\text{-}CH_2)_9]$ core structure of $\mathbf{6^{Lu}}$ is evidenced by ^{1}H NMR resonances at $\delta = 0.25$ (d, $^2J_{H,H} = 9.3$ Hz, 6H), −0.75 (d, $^2J_{H,H} = 9.3$ Hz, 6H), −0.99 (s, 12H), and −1.35 ppm (s, 6H). As in compound **3**, the equatorial and axial arrangements of the protons at C13 give rise to doublet resonance signals while the protons at C14 and C15 perceive a symmetrical environment and show singlet resonance signals. However, compound $\mathbf{6^{Lu}}$ is not stable in solution and decomposes slowly by forming **3** and other products (Figure S15). Further analysis of compounds **2** and $\mathbf{6^{Lu}}$ in the solid state was performed by means of cross-polarization magic-angle-spinning (CP/MAS) NMR spectroscopy. The ^{13}C CP/MAS NMR spectrum of **2** exhibits a very broad singlet at $\delta = 28$ ppm assigned to the methylene carbon atoms (Figure S12). The line broadening may originate from a strong quadrupolar coupling caused by the two NMR-active isotopes of gallium (^{69}Ga and ^{71}Ga).[26] In a similar vein, the ^{13}C CP/MAS NMR spectrum of $\mathbf{6^{Lu}}$ revealed very broad methylene resonances at $\delta = 18$ and −4 ppm in addition to the signals of the C_5Me_5 ligands at $\delta = 116$ and 12 ppm (Figure S16). The absence of gallium methyl moieties was verified by deuterolysis experiments of compounds **2** and $\mathbf{6^{Lu}}$ (Figure S28).

The olefination of carbonyl moieties is a characteristic reaction of Schrock-type metal alkylidene compounds. This prompted us to study the reactivity of gallium methylene compounds **2** and $\mathbf{6^{Lu}}$ toward 9-fluorenone. Treating **2** with two equivalents 9-fluorenone at ambient temperatures in D_8[THF] solution resulted in complete conversion to 9-methylene-fluorene within 5 days (Figure S29), while at 80 °C the reaction was nearly complete after two hours (Figure S30). Due to the insolubility of compound $\mathbf{6^{Lu}}$ in $[D_8]$THF, olefination of 9-fluorenone required more forcing conditions. Hence, 9-methylene-fluorene could be detected, in addition to other products (Figure S31), in the corresponding ^{1}H NMR spectra only after the sample had been heated to 130 °C for three days. Clearly, gallium methylene compounds are prone to olefination reactions.

Encouraged by the existence of **2** we wondered whether the original pyrolysis protocol described by Ziegler et al.[8] would also be viable to transfer $[GaMe_3]$ directly into **2**. Indeed, heating neat $[GaMe_3]$ to 280 °C for 42 hours led to the formation of trackable amounts of **2** (≈1%) next to unreacted $[GaMe_3]$, according to ^{1}H NMR measurements [Figure S4]. In contrast, Ziegler et al. could not isolate the analogous aluminum compound upon heating $[AlMe_3]_2$ to temperatures up to 235 °C. Instead mixed aluminum [methyl-methylene-methine-carbide] compounds or aluminum carbide $[Al_4C_3]$ were achieved.[27] Certainly, $[Al_2(CH_2)_3]_n$ would be a plausible intermediate but it is prone to further degradation under these harsh conditions.[28] Since gallium carbide is presumed to be thermodynamically unstable,[29] pyrolysis of $[Ga_8(\mu\text{-}CH_2)_{12}]$ is, therefore, much more disfavored. Additionally, formation of **2** may benefit from the increased covalent character of the Ga–C bond compared to the Al–C bond owing to a decreased difference of the electronegativities.

The present findings on oligomeric gallium methylenes show that rare-earth-metal alkyl complexes serve as efficient promotors for methyl group deprotonation since they are capable of both stabilizing and transferring methylene moieties. The ease of Ga–C(methylene) bond disruption and formation might contribute to a better understanding of the occurrence of multiple methylene insertions on gallium-rich GaAs(100) surfaces and open new avenues for gallium as a promotor metal in Fischer–Tropsch catalysis.[30]

Acknowledgements

We thank the German Science Foundation (Grant AN 238/15-2) for funding and for access to the computational resources of the bwFor cluster JUSTUS, which is supported by the State of Baden-Württemberg and the German Science Foundation.

Conflict of interest

The authors declare no conflict of interest.

Keywords: C–H bond activation · gallium · lutetium · methylidene · yttrium

How to cite: *Angew. Chem. Int. Ed.* **2019**, *58*, 8206–8210
Angew. Chem. **2019**, *131*, 8289–8293

[1] *Modern Carbonyl Olefination* (Ed.: T. Takeda), Wiley-VCH, Weinheim, **2004**.
[2] a) N. Calderon, *Acc. Chem. Res.* **1972**, *5*, 127–132; b) Y. Chauvin, *Angew. Chem. Int. Ed.* **2006**, *45*, 3740–3747; *Angew. Chem.* **2006**, *118*, 3824–3831; c) *Handbook on Metathesis* (Ed.: R. H. Grubbs), Wiley-VCH, Weinheim, **2003**; d) R. R. Schrock, *Acc. Chem. Res.* **1979**, *12*, 98–104.
[3] a) W. A. Herrmann, *Angew. Chem. Int. Ed. Engl.* **1982**, *21*, 117–130; *Angew. Chem.* **1982**, *94*, 118–131; b) "Fischer–Tropsch Synthesis: Catalysts and Chemistry": J. van de Loosdrecht, F. G. Botes, I. M. Ciobica, A. Ferreira, P. Gibson, D. J. Miidley, A. M. Salb, J. L. Visagie, C. J. Weststate, J. W. Niemantsverdriet, *in Comprehensive Inorganic Chemistry II*, 2nd Ed. (Eds.: J. Reedijk, K. Poeppelmeier), Elsevier, Amsterdam, **2013**, Chap. 7.20.
[4] a) R. R. Schrock, *J. Am. Chem. Soc.* **1975**, *97*, 6577–6578; b) L. J. Guggenberger, R. R. Schrock, *J. Am. Chem. Soc.* **1975**, *97*, 6578–6579; c) W. A. Herrmann, B. Reiter, H. Biersack, *J. Organomet. Chem.* **1975**, *97*, 245–251; d) D. A. Clemente, B. Rees, G. Bandoli, M. C. Biagini, B. Reiter, W. A. Herrmann, *Angew. Chem. Int. Ed. Engl.* **1981**, *20*, 887–888; *Angew. Chem.* **1981**, *93*, 920–922; e) F. N. Tebbe, G. W. Parshall, G. D. Reddy, *J. Am. Chem. Soc.* **1978**, *100*, 3611–3613; f) F. N. Tebbe, G. W. Parshall, D. W. Ovenall, *J. Am. Chem. Soc.* **1979**, *101*, 5074–

5075; g) R. Thompson, E. Nakamaru-Ogiso, C.-H. Chen, M. Pink, D. J. Mindiola, *Organometallics* **2014**, *33*, 429 – 432.
[5] M. Kamitani, B. Pinter, C. H. Chen, M. Pink, D. J. Mindiola, *Angew. Chem. Int. Ed.* **2014**, *53*, 10913 – 10915; *Angew. Chem.* **2014**, *126*, 11093 – 11095.
[6] L. N. Grant, S. Ahn, B. C. Manor, M.-H. Baik, D. J. Mindiola, *Chem. Commun.* **2017**, *53*, 3415 – 3417.
[7] a) G. Wittig, M. Rieber, *Liebigs Ann.* **1949**, *562*, 177 – 186; b) G. Wittig, U. Schöllkopf, *Chem. Ber.* **1954**, *87*, 1318 – 1330.
[8] K. Ziegler, K. Nagel, M. Patheiger, *Z. Anorg. Allg. Chem.* **1955**, *282*, 345 – 351.
[9] G. Stucky, M. Eddy, W. Harrison, R. Lagow, H. Kawa, D. Cox, *J. Am. Chem. Soc.* **1990**, *112*, 2425 – 2427.
[10] M. Layh, W. Uhl, *Polyhedron* **1990**, *9*, 277 – 282.
[11] H. Lehmkuhl, R. Schäfer, *Tetrahedron Lett.* **1966**, *7*, 2315 – 2320.
[12] J. E. Kickham, F. Guérin, D. W. Stephan, *J. Am. Chem. Soc.* **2002**, *124*, 11486 – 11494.
[13] L. C. H. Gerber, E. Le Roux, K. W. Törnroos, R. Anwander, *Chem. Eur. J.* **2008**, *14*, 9555 – 9564.
[14] a) P. L. Watson, *J. Am. Chem. Soc.* **1983**, *105*, 6491 – 6493; b) M. E. Thompson, S. M. Baxter, A. R. Bulls, B. J. Burger, M. C. Nolan, B. D. Santarsiero, W. P. Schaefer, J. E. Bercaw, *J. Am. Chem. Soc.* **1987**, *109*, 203 – 219.
[15] H. M. Dietrich, K. W. Törnroos, R. Anwander, *J. Am. Chem. Soc.* **2006**, *128*, 9298 – 9299.
[16] R. Litlabø, M. Zimmermann, K. Saliu, J. Takats, K. W. Törnroos, R. Anwander, *Angew. Chem. Int. Ed.* **2008**, *47*, 9560 – 9564; *Angew. Chem.* **2008**, *120*, 9702 – 9706.
[17] M. A. Busch, R. Harlow, P. L. Watson, *Inorg. Chim. Acta* **1987**, *140*, 15 – 20.
[18] a) H. M. Dietrich, C. Maichle-Mössmer, R. Anwander, *Dalton Trans.* **2010**, *39*, 5783 – 5785; b) H. M. Dietrich, K. W. Törnroos, E. Herdtweck, R. Anwander, *Organometallics* **2009**, *28*, 6739 – 6749.
[19] At low [$GaMe_3$] concentrations gallium methylene formation competes with the activation of C_6D_6, cf., Figures S21–S27. Compound **2** decomposes $>280\,^{\circ}C$ under high vacuum (ca. 10^{-5} mbar).
[20] a) K. Larsson, *Arkiv För Kemi*, Almquist & Wiksells Boktryckeri, **1960**; b) T. P. E. auf der Heyde, H.-B. Bürgi, H. Bürgy, K. W. Törnroos, *CHIMIA* **1991**, *45*, 38 – 40.
[21] N. W. Mitzel, C. Lustig, R. J. F. Berger, N. Runeberg, *Angew. Chem. Int. Ed.* **2002**, *41*, 2519 – 2522; *Angew. Chem.* **2002**, *114*, 2629 – 2632.
[22] C. C. Landry, C. J. Harlan, S. G. Bott, A. R. Barron, *Angew. Chem. Int. Ed. Engl.* **1995**, *34*, 1201 – 1202; *Angew. Chem.* **1995**, *107*, 1315 – 1317.
[23] a) G. Fritz, B. Raabe, *Z. Anorg. Allg. Chem.* **1956**, *286*, 149 – 167; b) W. A. Kriner, *J. Org. Chem.* **1964**, *29*, 1601 – 1606.
[24] a) Y. I. Smolin, *Kristallografiya* **1970**, *15*, 31 – 37; b) D. Hoebbel, G. Engelhardt, A. Samoson, K. Ujszaszy, Y. I. Smolin, *Z. Anorg. Allg. Chem.* **1987**, *552*, 236 – 240.
[25] W. J. Evans, R. Anwander, R. J. Doedens, J. W. Ziller, *Angew. Chem. Int. Ed. Engl.* **1994**, *33*, 1641 – 1644; *Angew. Chem.* **1994**, *106*, 1725 – 1728.
[26] F. Fredoueil, B. Bujoli, F. Fredoueil, D. Massiot, D. Poojary, A. Clearfield, M. Bujoli-Doeuff, *Chem. Commun.* **1998**, 175 – 176.
[27] K. Ziegler, K. Nagel, W. Phohl, *Liebigs Ann.* **1960**, *629*, 210 – 221.
[28] Preliminary DFT calculations revealed that putative aluminum methylene forms stable [$Al_6(CH_2)_9$] hexamers, while octamers [$Al_8(CH_2)_{12}$] seem to be unstable.
[29] a) B. Hájek, V. Kohout, V. Flemr, *Monatsh. Chem.* **1986**, *117*, 1157 – 1164; b) V. B. Kumar, M. Monte, O. Mathon, S. Pascarelli, Z. e. Porat, A. Gedanken, *J. Am. Ceram. Soc.* **2017**, *100*, 3305 – 3315.
[30] N. T. Kemp, N. K. Singh, *Chem. Commun.* **2005**, 4348 – 4350.
[31] CCDC 1890815 (**2**), 1890816 (**3**), 1890819 (**4**), 1890820 (**5**), 1890824 (**6^{Lu}**), 1890821 (**6^{Y}**), 1890817 (**7**), and 1890818 (**8**) contain the supplementary crystallographic data for this paper. These data are provided free of charge by Cambridge Crystallographic Data Centre. Atomic displacement parameters set at 50% probability. Hydrogen atoms and the disorder in coordinated THF molecules in **3** have been omitted for clarity. For selected interatomic distances and angles, see the Supporting Information.

Manuscript received: February 16, 2019
Revised manuscript received: April 1, 2019
Accepted manuscript online: April 3, 2019
Version of record online: May 9, 2019

Metallalkylidene

Deutsche Ausgabe: DOI: 10.1002/ange.201902063
Internationale Ausgabe: DOI: 10.1002/anie.201902063

Galliummethylen

Martin Bonath, Cäcilia Maichle-Mössmer, Peter Sirsch und Reiner Anwander**

Abstract: *Ungeachtet der herausragenden Bedeutung von Metallalkyliden-Verbindungen für die organische Synthese und industrielle katalytische Prozesse sind molekulare homoleptische Metallmethylen-Verbindungen $[M(CH_2)_n]$ als deren einfachste Vertreter bislang nicht beschrieben worden. Erstmals wurde 1955 berichtet, dass polymeres $[Li_2(CH_2)]_n$ und $[Mg(CH_2)]_n$ durch Pyrolyse von Methyllithium bzw. Dimethylmagnesium erhalten werden kann. Die unlösliche, salzartige Beschaffenheit dieser Verbindungen erschwerte jedoch die Verwendung als nützliche Reagenzien. Wir berichten nun, dass homoleptisches Galliummethylen $[Ga_8(\mu\text{-}CH_2)_{12}]$ ausgehend von Trimethylgallium $[GaMe_3]$ über eine Kaskade von C-H-Bindungsaktivierungen erhalten werden kann. Seine Bildung wird durch Seltenerdmetallocen-Methyl-Komplexe $[(C_5Me_5)_2Ln\{(\mu\text{-}Me)_2GaMe_2\}]$ (Ln = Lu, Y) vermittelt, wobei dodekametallische Cluster des Typs $[(C_5Me_5)_6Ln_3(\mu_3\text{-}CH_2)_6Ga_9(\mu\text{-}CH_2)_9]$ als entscheidende Zwischenstufen auftreten. Galliummethylen zeigt eine charakteristische, reversible $[Ga_8(\mu\text{-}CH_2)_{12}]/[Ga_6(\mu\text{-}CH_2)_9]$-Isomerenumwandlung in Donorlösungsmitteln und erweist sich als Methylen-Transferreagenz vom Schrock-Typ.*

Metallmethylen/-methyliden-Gruppen sind gleichermaßen Schlüsselkomponenten sowohl in Carbonyl-Olefinierungen für die Naturstoffsynthese[1] als auch in wichtigen industriellen Katalyseprozessen wie der Olefin-Metathese[2] oder der Fischer-Tropsch-Synthese.[3] Die Entdeckung und Strukturaufklärung von Übergangsmetallmethyliden-Spezies zogen immense Forschungsaktivitäten auf diesen neuen Gebieten nach sich.[4] Wegweisende Arbeiten umfassen Schrocks terminales Methyliden $[Cp_2Ta(=CH_2)(CH_3)]$ (**I**, Cp = Cyclopentadienyl; Abbildung 1),[4a,b] Herrmanns verbrückendes Methylen $[Cp(CO)_2Mn(\mu\text{-}CH_2)MnCp(CO)_2]$ (**II**)[4c,d] und das Tebbe-Reagenz $[Cp_2Ti(\mu\text{-}CH_2)(\mu\text{-}Cl)Al(CH_3)_2]$ (**III**).[4e–g] Diese Verbindungen haben wesentlich zu einem fundamentalen Verständnis der beteiligten Prozesse beigetragen und die weitere Forschung vorangetrieben. Auch weiterhin werden im Bereich der d/f-Übergangsmetallmethyliden/-alkyliden-Chemie wichtige Ergebnisse erzielt, so z. B. die Isolierung terminaler Methyliden-Komplexe der 4. Gruppe (Titangruppe) wie $[(PNP)M(=CH_2)(OAr)]$ (M = Zr, Hf, PNP = $N[2\text{-}P(i\text{Pr})_2\text{-}4\text{-}CH_3C_6H_3]_2$, Ar = $C_6H_3i\text{Pr}_2\text{-}2,6$)[5] und $[(PN)Ti{=}CH_2]$ (PN = $N[2\text{-}P(i\text{Pr})_2\text{-}4\text{-}CH_3C_6H_3]_2(C_6H_2Me_3\text{-}2,4,6)$).[6] Die letztgenannten Fortschritte wurden hauptsächlich aufgrund maßgeschneiderter Ligandenumgebungen und des Aufkommens neuer Synthesestrategien ermöglicht. Trotz der großen Bedeutung des Wittig-Reagenzes Ph_3PCH_2 für die Olefinierungschemie[1,7] wurde die Hauptgruppenmetall-Methylenchemie bislang nur wenig erforscht. Erstaunlicherweise berichteten Ziegler et al. bereits 1955 über die Synthese von Dilithiummethylen, $[Li_2CH_2]_n$, und Magnesiummethylen, $[MgCH_2]_n$, durch Pyrolyse der entsprechenden Methylverbindungen.[8] Dennoch konnte die Festkörperstruktur des salzähnlichen $[Li_2CD_2]_n$ erst 1990 durch Röntgen- und Neutronen-Pulver-Diffraktometrie-Analysen aufgeklärt werden.[9] Methylenverbrückte Aluminiumzentren vom Typ $[R_2Al\text{-}CH_2\text{-}AlR_2]$ (**IV**)[10] konnten durch Derivatisierung der Halogenidoderivate $[X_2Al\text{-}CH_2\text{-}AlX_2]$ (zugänglich aus Al und CH_2X_2)[11] und Zersetzung/Deprotonierung von Methyl- und Tetramethylaluminato-Liganden, wie beispielsweise vorhanden in $[(t\text{Bu}_3\text{PN})_2\text{TiAl}_3(CH_2)_2(CH_3)_7]$[12] oder $[La_4Al_8(C)(CH)_2(CH_2)_2(CH_3)_{22}(\text{Toluol})]$,[13] erhalten werden.

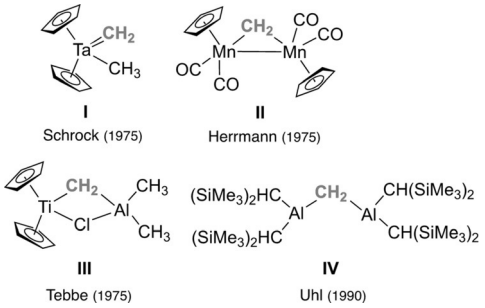

Abbildung 1. Meilensteine der Metallmethylen/-methyliden-Chemie.

Die Aktivierung von Methan durch unsolvatisierte Seltenerd-Metallocenderivate $[(C_5Me_5)_2LnMe]$ (Ln = Sc, Lu) stellt eine der wichtigsten Entdeckungen in der Organolanthanoid-Chemie dar.[14] Wir konnten zeigen, dass sich solche hochreaktiven Ln-CH_3-Gruppen mehrfach an C-H-Bindungsaktivierungen beteiligen können, bevorzugt in Gegenwart von Trimethylaluminium und sogar bei Raumtemperatur.[13] In entscheidender Weise lässt sich dieser Methylgruppen-Abbau in Gegenwart von sterisch anspruchsvollen Hilfsliganden kontrollieren. So erhielten wir z. B. den Methyliden-Komplex $[(C_5Me_5)_3Y_3(\mu\text{-}Cl)_3(\mu_3\text{-}Cl)(\mu_3\text{-}CH_2)(thf)_3]$[15] und mit $[(Tp^{t\text{Bu,Me}})La[(\mu\text{-}CH_2)\{(\mu\text{-}Me)AlMe_2\}_2]]$ eine Seltenerdvariante des Tebbe-Reagenzes ($Tp^{t\text{Bu,Me}}$ = Hydrotris(3-*tert*-butyl-5-methylpyrazolyl)borato).[16] Im Rahmen weiterer Studien zur Reaktivität von $[(C_5Me_5)_2LnMe]$ (Ln = Y, Lu) gegenüber einem Überschuss an Trimethylgallium erhielten wir nun oligomeres Galliummethylen $[Ga_8(\mu\text{-}CH_2)_{12}]$. Hier beschreiben wir diese Organoseltenerdmetall-getriebene Bildung und die vollständige Charakterisierung von $[Ga_8(\mu\text{-}CH_2)_{12}]$, das

[*] M. Bonath, Dr. C. Maichle-Mössmer, Dr. P. Sirsch, Prof. Dr. R. Anwander
Institut für Anorganische Chemie
Eberhard Karls Universität Tübingen
Auf der Morgenstelle 18, 72076 Tübingen (Deutschland)
E-Mail: peter.sirsch@uni-tuebingen.de
reiner.anwander@uni-tuebingen.de
Hintergrundinformationen und die Identifikationsnummern (ORCIDs) der Autoren sind unter: https://doi.org/10.1002/ange.201902063 zu finden.

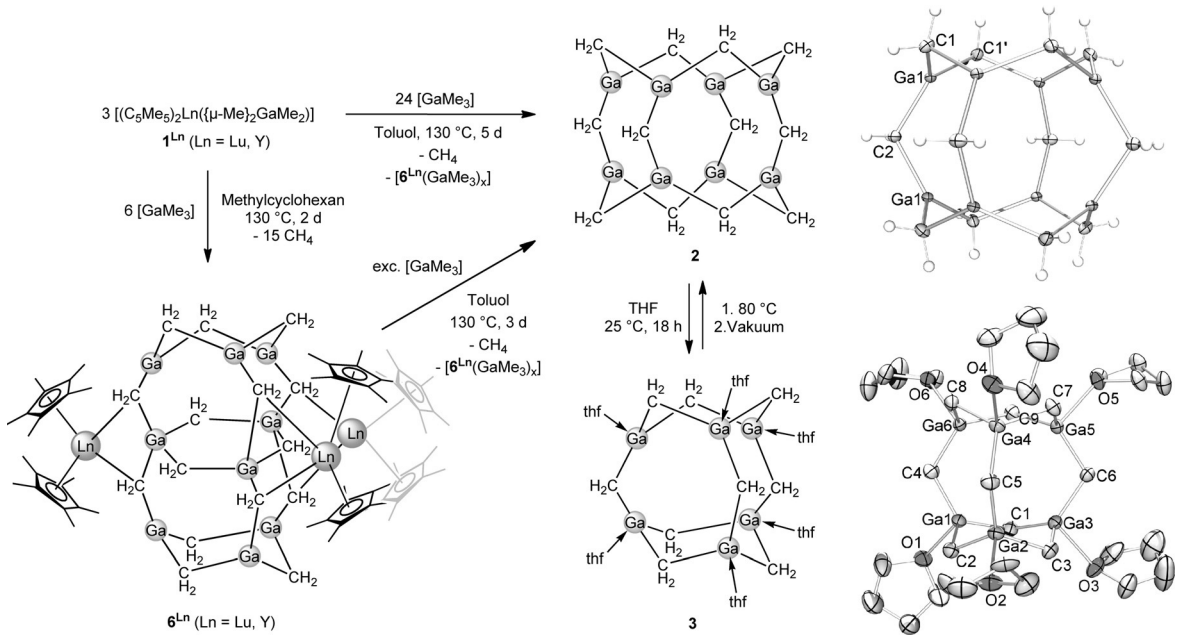

Schema 1. Synthese von **2**, **3** und **6** sowie die Molekülstrukturen der Galliummethylene **2** und **3**.[31] d = Tage; exc. = Überschuss.

den ersten molekularen, homoleptischen Metallmethylen-Komplex repräsentiert.

Wird $[(C_5Me_5)_2Ln\{(\mu\text{-}Me)_2GaMe_2\}]$ (Ln = Lu (**1^{Lu}**),[17] Y (**1^{Y}**);[18] siehe Hintergrundinformationen) mit einem achtfachen Überschuss an $[GaMe_3]$ in aromatischen Lösungsmitteln wie C_6D_6 bei 130 °C gerührt, wird Methan freigesetzt, und man erhält $[Ga_8(\mu\text{-}CH_2)_{12}]$ (**2**) als hellgelben, kristallinen Feststoff in 80 % Ausbeute (Schema 1).[19] Die Festkörperstruktur der oligomeren Verbindung **2** wurde durch Einkristall-Röntgenbeugungsanalyse bestimmt (Schema 1) und zeigt ein käfigartiges Strukturmotiv, das große Ähnlichkeit zu Silsesquioxanen der allgemeinen Formel $[\{Si_8(\mu\text{-}O)_{12}\}R_8]$ aufweist.[20] Die Galliumatome des „$[Ga_8]$-Würfels" binden jeweils zu drei Methylenbrücken („Kanten") und nehmen somit eine trigonal-planare Geometrie ein (Winkelsumme an Ga 359.2°), mit vergleichbaren Ga-C-Bindungslängen (1.960(2), 1.961(1), 1.972(2) Å), wie sie für $[GaMe_3]$ beschrieben sind.[21] Zum Vergleich: Galloxancluster wie $[Ga_{12}tBu_{12}(\mu_3\text{-}O)_8(\mu\text{-}O)_2(\mu\text{-}OH)_4]$, erhältlich durch Hydrolyse von Alkylvorstufen, bilden üblicherweise ikosaedrische Strukturen der Alkylgallium(III)-Einheiten,[22] während Siliciummethylen-Derivate bevorzugt Ringstrukturen aufbauen.[23]

Die Ergebnisse von NMR-spektroskopischen Messungen von **2** bei Raumtemperatur in $[D_8]$THF-Lösung sind in Einklang mit homoleptischem Galliummethylen **2**. Das ^{1}H-NMR-Spektrum von **2** zeigt ein Singulett-Signal bei $\delta =$ 0.19 ppm, das den äquivalenten Protonen zugeordnet werden kann. Bei Raumtemperatur in $[D_8]$THF-Lösung wandelte sich **2** jedoch innerhalb von 24 Stunden in das kleinere Galliummethylen-Oligomer $[Ga_6(\mu\text{-}CH_2)_9(thf)_6]$ (**3**) um, wodurch ein Signalsatz bei $\delta = 0.12$ (d, $^2J_{H,H} = 9.1$ Hz, 6H), 0.10 (s, 6H) und −0.49 ppm (d, $^2J_{H,H} = 8.8$ Hz, 6H) erhalten wurde, vereinbar mit drei magnetisch inäquivalenten CH_2-Gruppen. Dieser Prozess wurde durch NMR-Studien bei variablen Temperaturen genauer untersucht. Dabei zeigte sich, dass die $[Ga_8(\mu\text{-}CH_2)_{12}]$/$[Ga_6(\mu\text{-}CH_2)_9]$-Oligomerenumwandlung in THF-Lösung bei Temperaturen unter −40 °C unterdrückt und bei Temperaturen über 80 °C wieder umgekehrt wird (Abbildungen S2 und S3 der Hintergrundinformationen). Einkristalle von **3** konnten aus einer gesättigten THF-Lösung bei −40 °C erhalten werden und wurden durch Röntgenbeugungsanalyse untersucht. Als auffälliges Strukturelement der Festkörperstruktur von Hexagalliummethylen **3** (Schema 1) findet man zwei $[Ga_3(\mu\text{-}CH_2)_3]$-6-Ringe in Sesselkonformation. Die beiden $[Ga_3(\mu\text{-}CH_2)_3]$-Untereinheiten sind cofacial zueinander orientiert und über drei Ga-CH_2-Ga-Brücken verknüpft, sodass die Struktur insgesamt an Silsesquioxane der allgemeinen Formel $[\{Si_6(\mu\text{-}O)_9\}R_6]$ erinnert.[24] In **3** werden alle Galliumatome zusätzlich durch ein THF-Molekül koordiniert, wodurch sich eine verzerrt tetraedrische Geometrie ergibt und die durchschnittliche Ga-C-Bindungslänge (1.982 Å) gegenüber der in **2** leicht erhöht wird.

Wird der Kristallisationsvorgang von Galliummethylen **2** bei Raumtemperatur durch langsames Eindampfen von *n*-Pentan in eine gesättigte THF-Lösung eingeleitet, erfolgt eine Reorganisation des $[Ga_8(\mu\text{-}CH_2)_{12}]$-Käfigs, was durch ^{1}H-NMR-Spektroskopie bestätigt werden konnte. Einkristall-Röntgenbeugungsanalysen bestätigen eine relativ schwache Ga-THF-Wechselwirkung, da man in den Festkörperstrukturen von $[Ga_8(\mu\text{-}CH_2)_{12}(thf)_4]$ (**4**) und $[Ga_8(\mu\text{-}CH_2)_{12}(thf)_5]$ (**5**) nur eine partielle THF-Koordination findet (Abbildung 2).

Die Koordination durch THF führt zu einer Verzerrung des Käfigmotivs, wie es für das unsolvatisierte **2** gefunden wurde. Die koordinierten THF-Moleküle in **3**–**5** gehen unter Argon langsam verloren und können am Vakuum vollständig entfernt werden (Abbildung S13).

Die Leichtigkeit der Donor-vermittelten gegenseitigen Umwandlung von Ga_6- und Ga_8-Methylenkäfigstrukturen ist bemerkenswert, da Ga-C-Bindungsbruch bzw. -bildung er-

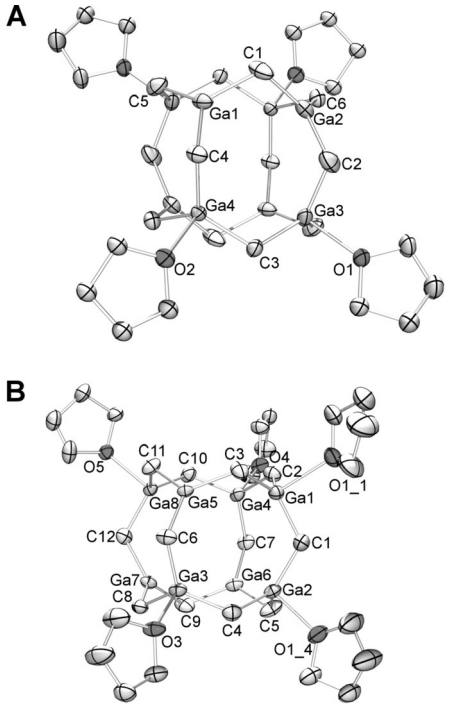

Abbildung 2. Molekülstrukturen von **4** (A) und **5** (B).[31]

folgen muss. Um ein tieferes Verständnis für diesen Prozess und die Abhängigkeit der relativen Stabilitäten der verschiedenen Oligomere von der Koordination durch Donorlösungsmittel zu erhalten, wurden Dichtefunktionalrechnungen durchgeführt. Diese lieferten das Ergebnis, dass die größeren Ga_8-Oligomere in Abwesenheit von THF deutlich stabiler sind als die Ga_6-Käfigstrukturen: $\Delta E = +226\ kJ\,mol^{-1}$ und $\Delta G(298\ K) = +174\ kJ\,mol^{-1}$ für die Umwandlung von drei Ga_8- zu vier Ga_6-Oligomeren (in der Gasphase). Die kleineren Käfige sollten jedoch durch THF-Koordination begünstigt werden, da nun insgesamt mehr Donor-Moleküle an Galliumatome gebunden werden können: Während in **3** alle Galliumatome durch THF koordiniert sind, beobachtet man für die größeren Käfigstrukturen **4** und **5** nur eine unvollständige Koordination. Interessanterweise gleichen sich die zusätzlich gebildeten Bindungen und der damit einhergehende Entropieverlust gegenseitig aus. Dementsprechend deutet der berechnete Wert von ΔG ($+4\ kJ\,mol^{-1}$ bei 298 K) für die Umwandlung von **5** in **3** (zum Vergleich: $\Delta E = -400\ kJ\,mol^{-1}$) auf ein Gleichgewicht bei Raumtemperatur hin. Bei niedrigeren Temperaturen verschiebt sich das Gleichgewicht zugunsten der kleineren Käfigstruktur (z. B. $\Delta G = -129\ kJ\,mol^{-1}$ bei 200 K), was in Einklang mit den Befunden der NMR-Messungen bei niedrigen Temperaturen ist. Ersetzt man THF durch den stärkeren Donor Pyridin, errechnet sich die Ga_6-Struktur zur bevorzugten Spezies bei Raumtemperatur (siehe NMR-Spektren und Festkörperstrukturen des Pyridin-Addukts $[Ga_6(\mu\text{-}CH_2)_9(py)_6]$ (**7**) und seines partiellen Zersetzungsprodukts $[Ga_5(\mu\text{-}CH_2)_7(CH_3)(py)_5]$ (**8**) in den Hintergrundinformationen). Beachtenswert ist, dass die berechneten thermochemischen Daten ($\Delta E = -464\ kJ\,mol^{-1}$, $\Delta G(298\ K) = -111\ kJ\,mol^{-1}$) nahelegen, dass dies nur teilweise auf die stärkeren Bindungen zwischen den Lösungsmittelmolekülen und den Galliumatomen zurückzuführen ist. Im größeren Umfang resultiert dieser Befund aus einem geringeren Entropiebeitrag der freien Pyridin-Liganden, die deutlich rigider sind als die THF-Pendants. Um die beobachtete unvollständige Koordination der Ga_8-Oligomere zu verstehen, berechneten wir abschließend die Energieänderungen und die Änderungen der freien Enthalpie bei sukzessiver Koordination von THF an **2**. Die Werte für ΔE bewegen sich zwischen -70 und $-45\ kJ\,mol^{-1}$ (Koordination des ersten bzw. des letzten THF-Moleküls). Aufgrund von Entropieverlusten sind die Unterschiede der freien Enthalpie bei 298 K jedoch deutlich geringer (-27 bzw. $+11\ kJ\,mol^{-1}$). Die ΔG-Werte für die Bindung eines sechsten oder siebten THF-Donors sind geringer als $-2\ kJ\,mol^{-1}$ und erklären den unvollständigen Koordinationsgrad, wie er in den Kristallstrukturen von **4** und **5** gefunden wurde. Packungseffekte können damit als mögliche Ursache ausgeschlossen werden, und eine partielle Koordination könnte auch in Lösung vorherrschen.

Rührt man den Überstand der ursprünglichen Reaktionsmischung nach Versetzen mit weiteren acht Äquivalenten $[GaMe_3]$ bei 130 °C, bildet sich zusätzliches **2** in vergleichbarer Ausbeute. Da diese Prozedur mehrfach wiederholt werden kann, verbleibt offenbar nach jedem Zyklus ein unbekanntes Intermediat, das diese „pseudokatalytische" Umwandlung von $[GaMe_3]$ zu **2** vorantreibt. Glücklicherweise führt längeres Erhitzen der Überstände ohne Versetzen mit $[GaMe_3]$ reproduzierbar zur Bildung farbloser Kristalle der bimetallischen Seltenerdmetallocen-Galliummethylen-Komplexe $[(C_5Me_5)_6Ln_3(\mu_3\text{-}CH_2)_6Ga_9(\mu\text{-}CH_2)_9]$ (Ln = Lu (**6^{Lu}**); Y (**6^{Y}**); Abbildung 3; **6^{Y}** verhält sich völlig analog zu **6^{Lu}**, siehe Hintergrundinformationen). Komplex **6^{Lu}** wurde als entscheidende Zwischenstufe bei der Bildung von **2** identifiziert, da es überschüssiges $[GaMe_3]$ bei 130 °C innerhalb von drei Tagen in **2** umwandelt (Schema 1). Selbst bei Raumtemperatur setzt **6^{Lu}** in Gegenwart von $[GaMe_3]$ langsam **2** frei, einhergehend mit der Bildung des Startmaterials $[(C_5Me_5)_2Lu\{(\mu\text{-}Me)_2GaMe_2\}]$ (**1^{Lu}**), was durch NMR-Spek-

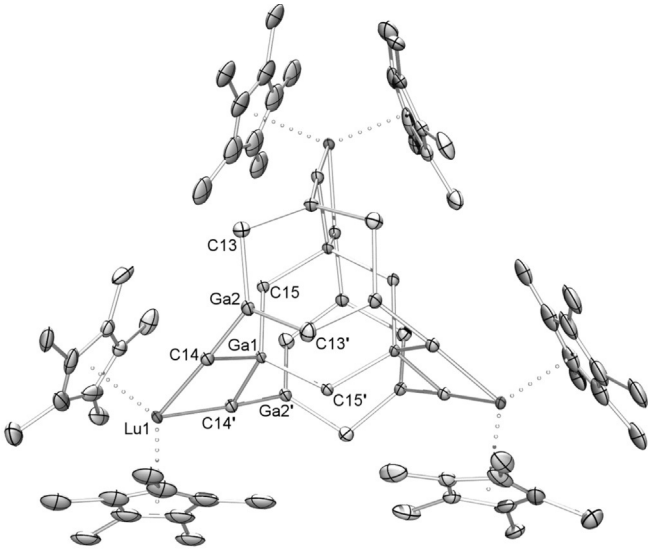

Abbildung 3. Molekülstruktur von **6^{Lu}**.[31]

troskopie belegt wurde (Abbildung S6). Untersucht man $\mathbf{6^{Lu}}$ in Gegenwart eines Überschusses [$GaMe_3$] mittels NMR-Spektroskopie, erhält man spektrale Daten, die denen der Umwandlung von [$GaMe_3$] zu **2** gleichen, wenn diese durch [$(C_5Me_5)_2Lu\{(\mu\text{-}Me)_2GaMe_2\}$] ($\mathbf{1^{Lu}}$) vorangetrieben wird. Dies legt den Schluss nahe, dass es sich bei dem reaktiven Intermediat tatsächlich um ein Additionsprodukt von $\mathbf{6^{Lu}}$ und [$GaMe_3$] handelt (Schema 1).

Die Festkörperstruktur von $\mathbf{6^{Lu}}$ (Abbildung 3) wurde durch Einkristall-Röntgenbeugungsanalyse aufgeklärt und lässt sich am besten als ein hochaggregierter, anionischer $[(\mu_3\text{-}CH_2)_6Ga_9(\mu\text{-}CH_2)_9]^{3-}$-Kern beschreiben, der durch drei kationische $[(C_5Me_5)_2Lu]^+$-Einheiten stabilisiert wird. Der Kern enthält drei gestaffelt angeordnete $[Ga_3(\mu\text{-}CH_2)_3]$-Sechsringe, die über μ_3-Ga_2Lu-verbrückende Methyleneinheiten verknüpft sind, wodurch die flankierenden Seltenerd-Metallocen-Einheiten mit eingebunden sind. Vergleichbar zu **3** nehmen die äußeren Ringe eine Sesselkonformation ein, wodurch die Galliumatome eine verzerrt trigonal-planare Geometrie aufweisen. Im Unterschied dazu liegt die mittlere Ringstruktur als planare Einheit vor, und die Galliumatome weisen eine verzerrt tetraedrische Koordinationsumgebung auf. Infolgedessen findet man für die dreifach-koordinierten Galliumatome Ga-C-Bindungslängen (1.961(6), 1.973(6), 1.972(6) Å) vergleichbar wie in **2**, während die vierfach koordinierten Galliumatome größere Ga-C-Abstände aufweisen ($Ga\text{-}(\mu\text{-}CH_2) = 2.008(7)$, $Ga\text{-}(\mu_3\text{-}CH_2) = 2.125(6)$ Å), ähnlich wie sie für $[GaMe_4]^-$-Einheiten bekannt sind.[25] Die Lu-C(Methylen)-Abstände von 2.510(6) Å sind deutlich kleiner als die Lu-C(Me)-Bindungslängen der Ausgangsverbindung [$(C_5Me_5)_2Lu\{(\mu\text{-}Me)_2GaMe_2\}$] ($\mathbf{1^{Lu}}$; durchschn. 2.614 Å; Abbildung S35), was auf die erhöhte negative Ladung am Methylen-Kohlenstoffatom zurückzuführen ist.

Im Unterschied zu homoleptischem Galliummethylen **2** ist $\mathbf{6^{Lu}}$ in [D_8]THF unlöslich, löst sich aber zu einem geringen Anteil bei der Zugabe von 4-Dimethylaminopyridin (DMAP) zur entsprechenden Suspension in [D_8]THF. Die Ergebnisse der NMR-Spektroskopie von $\mathbf{6^{Lu}}$ in [D_8]THF sind in Einklang mit der Zusammensetzung im Festkörper (Abbildung S14). Die $[(\mu_3\text{-}CH_2)_6Ga_9(\mu\text{-}CH_2)_9]$-Kernstruktur von $\mathbf{6^{Lu}}$ wird durch ^{1}H-NMR-Signale bei $\delta = 0.25$ (d, $^2J_{H,H} = 9.3$ Hz, 6H), -0.75 (d, $^2J_{H,H} = 9.3$ Hz, 6H), -0.99 (s, 12H) und -1.35 ppm (s, 6H) bestätigt. In vergleichbarer Weise wie in **3** ergeben sich für die Protonen in äquatorialer und axialer Position an C13 Dublett-Signale, wogegen sich die Protonen an C14 und C15 in symmetrischer Umgebung befinden und daher Singulett-Signale zeigen. Komplex $\mathbf{6^{Lu}}$ ist in Lösung jedoch nicht stabil und zersetzt sich langsam, wobei sich **3** und andere Produkte bilden (Abbildung S15). Weiterhin wurden **2** und $\mathbf{6^{Lu}}$ im Festkörper durch CP/MAS-NMR-Spektroskopie (Cross-Polarization/Magic-Angle-Spinning) charakterisiert. Das ^{13}C-CP/MAS-NMR-Spektrum von **2** zeigt ein sehr breites Singulett bei $\delta = 28$ ppm, das den Methylen-Kohlenstoffatomen zugeordnet werden kann (Abbildung S12). Die Linienverbreiterung könnte aus dem starken Quadrupolmoment resultieren, das durch die NMR-aktiven Isotope des Galliums (^{69}Ga und ^{71}Ga) erzeugt wird.[26] In vergleichbarer Weise findet man im ^{13}C-CP/MAS-NMR-Spektrum von $\mathbf{6^{Lu}}$ sehr breite Methylen-Signale bei $\delta = 18$ und -4 ppm sowie Signale der C_5Me_5-Liganden bei $\delta = 116$ und 12 ppm (Abbildung S16). Die Abwesenheit von Galliummethyl-Gruppen wurde durch Deuterolyse-Experimente von **2** und $\mathbf{6^{Lu}}$ bestätigt (Abbildung S28).

Die Olefinierung von Carbonylgruppen ist eine charakteristische Reaktion von Metallalkyliden-Verbindungen des Schrock-Typs. Dies bewog uns, die Reaktivität der Galliummethylen-Verbindungen **2** und $\mathbf{6^{Lu}}$ gegenüber 9-Fluorenon zu untersuchen. Bei Raumtemperatur werden zwei Äquivalente 9-Fluorenon in [D_8]THF durch **2** innerhalb von fünf Tagen vollständig zu 9-Methylenfluoren umgesetzt (Abbildung S29), während durch Erhitzen auf 80 °C die Reaktion bereits nach zwei Stunden nahezu vollständig abgelaufen ist (Abbildung S30). Wegen der Unlöslichkeit von $\mathbf{6^{Lu}}$ in [D_8]THF erfordert die Olefinierung von 9-Fluorenon drastischere Bedingungen. Demensprechend lässt sich 9-Methylenfluoren, neben anderen Produkten, in den NMR-Spektren erst nach Erhitzen der Probe für drei Tage auf 130 °C nachweisen (Abbildung S31). Dies zeigt eindeutig, dass Galliummethylen-Verbindungen für Olefinierungen geeignet sind.

Ermutigt durch die Existenz von **2** fragten wir uns, ob das ursprüngliche Pyrolyseexperiment von Ziegler et al.[8] auch dazu geeignet sein könnte, [$GaMe_3$] direkt in **2** zu überführen. Tatsächlich führte das 42-stündige Erhitzen von reinem [$GaMe_3$] auf 280 °C zur Bildung nachweisbarer Mengen von **2** (ca. 1 %) neben nicht umgesetztem [$GaMe_3$], wie durch ^{1}H-NMR-Spektroskopie nachgewiesen wurde (Abbildung S4). Dagegen konnten Ziegler et al. die analoge Aluminiumverbindung durch Heizen von $[AlMe_3]_2$ auf 235 °C nicht isolieren. Stattdessen wurden gemischte [Methyl-Methylen-Methin-Carbid]-Verbindungen oder Aluminiumcarbid, [Al_4C_3], erhalten.[27] Sicherlich wäre $[Al_2(CH_2)_3]_n$ ein plausibles Zwischenprodukt, das jedoch unter solch harschen Bedingungen leicht zur weiteren Zersetzung neigt.[28] Da Galliumcarbid als thermodynamisch instabil gilt,[29] ist die Pyrolyse von $[Ga_8(\mu\text{-}CH_2)_{12}]$ daher deutlich ungünstiger. Die Bildung von **2** könnte zusätzlich durch den höheren kovalenten Charakter der Ga-C-Bindung gegenüber der Al-C-Bindung begünstigt werden, was der geringeren Elektronegativitätsdifferenz geschuldet ist.

Die vorliegenden Ergebnisse zu oligomeren Galliummethylenen zeigen, dass Seltenerdmetall-Alkyl-Komplexe die Deprotonierung von Methylgruppen effizient beschleunigen und dabei Methylengruppen sowohl stabilisieren als auch übertragen können. Die Leichtigkeit der Spaltung und Bildung von Ga-C(Methylen)-Bindungen könnte zu einem besseren Verständnis des Auftretens von mehrfachen Methyleneinschüben auf Gallium-reichen GaAs(100)-Oberflächen beitragen und neue Möglichkeiten für die Verwendung von Gallium als Promotormetall für die Fischer-Tropsch-Katalyse eröffnen.[30]

Danksagung

Wir danken für die großzügige Projektförderung (Sachbeihilfe AN 238/15-2) durch die DFG und für den Zugang zu den Hochleistungsrechnern des bwFor-Clusters JUSTUS, der

durch das Land Baden-Württemberg und die DFG gefördert wird.

Interessenkonflikt

Die Autoren erklären, dass keine Interessenkonflikte vorliegen.

Stichwörter: C-H-Bindungsaktivierung · Gallium · Lutetium · Methyliden · Yttrium

Zitierweise: *Angew. Chem. Int. Ed.* **2019**, *58*, 8206–8210
Angew. Chem. **2019**, *131*, 8289–8293

[1] *Modern Carbonyl Olefination* (Hrsg.: T. Takeda), Wiley-VCH, Weinheim, **2004**.
[2] a) N. Calderon, *Acc. Chem. Res.* **1972**, *5*, 127–132; b) Y. Chauvin, *Angew. Chem. Int. Ed.* **2006**, *45*, 3740–3747; *Angew. Chem.* **2006**, *118*, 3824–3831; c) *Handbook on Metathesis* (Hrsg.: R. H. Grubbs) Wiley-VCH, Weinheim, **2003**; d) R. R. Schrock, *Acc. Chem. Res.* **1979**, *12*, 98–104.
[3] a) W. A. Herrmann, *Angew. Chem. Int. Ed. Engl.* **1982**, *21*, 117–130; *Angew. Chem.* **1982**, *94*, 118–131; b) „Fischer–Tropsch Synthesis: Catalysts and Chemistry": J. van de Loosdrecht, F. G. Botes, I. M. Ciobica, A. Ferreira, P. Gibson, D. J. Miidley, A. M. Salb, J. L. Visagie, C. J. Weststate, J. W. Niemantsverdriet, *in Comprehensive Inorganic Chemistry II*, 2. Aufl. (Hrsg.: J. Reedijk, K. Poeppelmeier), Elsevier, Amsterdam, **2013**, Kapitel 7.20.
[4] a) R. R. Schrock, *J. Am. Chem. Soc.* **1975**, *97*, 6577–6578; b) L. J. Guggenberger, R. R. Schrock, *J. Am. Chem. Soc.* **1975**, *97*, 6578–6579; c) W. A. Herrmann, B. Reiter, H. Biersack, *J. Organomet. Chem.* **1975**, *97*, 245–251; d) D. A. Clemente, B. Rees, G. Bandoli, M. C. Biagini, B. Reiter, W. A. Herrmann, *Angew. Chem. Int. Ed. Engl.* **1981**, *20*, 887–888; *Angew. Chem.* **1981**, *93*, 920–922; e) F. N. Tebbe, G. W. Parshall, G. D. Reddy, *J. Am. Chem. Soc.* **1978**, *100*, 3611–3613; f) F. N. Tebbe, G. W. Parshall, D. W. Ovenall, *J. Am. Chem. Soc.* **1979**, *101*, 5074–5075; g) R. Thompson, E. Nakamaru-Ogiso, C.-H. Chen, M. Pink, D. J. Mindiola, *Organometallics* **2014**, *33*, 429–432.
[5] M. Kamitani, B. Pinter, C. H. Chen, M. Pink, D. J. Mindiola, *Angew. Chem. Int. Ed.* **2014**, *53*, 10913–10915; *Angew. Chem.* **2014**, *126*, 11093–11095.
[6] L. N. Grant, S. Ahn, B. C. Manor, M.-H. Baik, D. J. Mindiola, *Chem. Commun.* **2017**, *53*, 3415–3417.
[7] a) G. Wittig, M. Rieber, *Liebigs Ann.* **1949**, *562*, 177–186; b) G. Wittig, U. Schöllkopf, *Chem. Ber.* **1954**, *87*, 1318–1330.
[8] K. Ziegler, K. Nagel, M. Patheiger, *Z. Anorg. Allg. Chem.* **1955**, *282*, 345–351.
[9] G. Stucky, M. Eddy, W. Harrison, R. Lagow, H. Kawa, D. Cox, *J. Am. Chem. Soc.* **1990**, *112*, 2425–2427.
[10] M. Layh, W. Uhl, *Polyhedron* **1990**, *9*, 277–282.
[11] H. Lehmkuhl, R. Schäfer, *Tetrahedron Lett.* **1966**, *7*, 2315–2320.
[12] J. E. Kickham, F. Guérin, D. W. Stephan, *J. Am. Chem. Soc.* **2002**, *124*, 11486–11494.
[13] L. C. H. Gerber, E. Le Roux, K. W. Törnroos, R. Anwander, *Chem. Eur. J.* **2008**, *14*, 9555–9564.
[14] a) P. L. Watson, *J. Am. Chem. Soc.* **1983**, *105*, 6491–6493; b) M. E. Thompson, S. M. Baxter, A. R. Bulls, B. J. Burger, M. C. Nolan, B. D. Santarsiero, W. P. Schaefer, J. E. Bercaw, *J. Am. Chem. Soc.* **1987**, *109*, 203–219.
[15] H. M. Dietrich, K. W. Törnroos, R. Anwander, *J. Am. Chem. Soc.* **2006**, *128*, 9298–9299.
[16] R. Litlabø, M. Zimmermann, K. Saliu, J. Takats, K. W. Törnroos, R. Anwander, *Angew. Chem. Int. Ed.* **2008**, *47*, 9560–9564; *Angew. Chem.* **2008**, *120*, 9702–9706.
[17] M. A. Busch, R. Harlow, P. L. Watson, *Inorg. Chim. Acta* **1987**, *140*, 15–20.
[18] a) H. M. Dietrich, C. Maichle-Mössmer, R. Anwander, *Dalton Trans.* **2010**, *39*, 5783–5785; b) H. M. Dietrich, K. W. Törnroos, E. Herdtweck, R. Anwander, *Organometallics* **2009**, *28*, 6739–6749.
[19] Bei geringer [$GaMe_3$]-Konzentration konkurriert die Bildung von Galliummethylen mit der Aktivierung von C_6D_6 (Abbildungen S21–S27).
[20] a) K. Larsson, *Arkiv För Kemi*, Almquist & Wiksells Boktryckeri, **1960**; b) T. P. E. auf der Heyde, H.-B. Bürgi, H. Bürgy, K. W. Törnroos, *CHIMIA* **1991**, *45*, 38–40.
[21] N. W. Mitzel, C. Lustig, R. J. F. Berger, N. Runeberg, *Angew. Chem. Int. Ed.* **2002**, *41*, 2519–2522; *Angew. Chem.* **2002**, *114*, 2629–2632.
[22] C. C. Landry, C. J. Harlan, S. G. Bott, A. R. Barron, *Angew. Chem. Int. Ed. Engl.* **1995**, *34*, 1201–1202; *Angew. Chem.* **1995**, *107*, 1315–1317.
[23] a) G. Fritz, B. Raabe, *Z. Anorg. Allg. Chem.* **1956**, *286*, 149–167; b) W. A. Kriner, *J. Org. Chem.* **1964**, *29*, 1601–1606.
[24] a) Y. I. Smolin, *Kristallografiya* **1970**, *15*, 31–37; b) D. Hoebbel, G. Engelhardt, A. Samoson, K. Ujszaszy, Y. I. Smolin, *Z. Anorg. Allg. Chem.* **1987**, *552*, 236–240.
[25] W. J. Evans, R. Anwander, R. J. Doedens, J. W. Ziller, *Angew. Chem. Int. Ed. Engl.* **1994**, *33*, 1641–1644; *Angew. Chem.* **1994**, *106*, 1725–1728.
[26] F. Fredoueil, B. Bujoli, F. Fredoueil, D. Massiot, D. Poojary, A. Clearfield, M. Bujoli-Doeuff, *Chem. Commun.* **1998**, 175–176.
[27] K. Ziegler, K. Nagel, W. Phohl, *Liebigs Ann.* **1960**, *629*, 210–221.
[28] Erste Dichtefunktionalrechnungen deuten darauf hin, dass Aluminiummethylen stabile [$Al_6(CH_2)_9$]-Hexamere zu bilden vermag, während oktameres [$Al_8(CH_2)_{12}$] instabil zu sein scheint.
[29] a) B. Hájek, V. Kohout, V. Flemr, *Monatsh. Chem.* **1986**, *117*, 1157–1164; b) V. B. Kumar, M. Monte, O. Mathon, S. Pascarelli, Z. e. Porat, A. Gedanken, *J. Am. Ceram. Soc.* **2017**, *100*, 3305–3315.
[30] N. T. Kemp, N. K. Singh, *Chem. Commun.* **2005**, 4348–4350.
[31] CCDC 1890815 (**2**), 1890816 (**3**), 1890819 (**4**), 1890820 (**5**), 1890824 ($\mathbf{6^{Lu}}$), 1890821 ($\mathbf{6^{Y}}$), 1890817 (**7**), and 1890818 (**8**) enthalten die ausführlichen kristallographischen Daten zu dieser Veröffentlichung. Die Daten sind kostenlos beim Cambridge Crystallographic Data Centre erhältlich. Ellipsoide beschreiben 50% der atomaren Aufenthaltswahrscheinlichkeit. Wasserstoffatome und Fehlordnungen in koordinierten THF-Molekülen sind weggelassen. Ausgewählte interatomare Abstände und Winkel siehe Hintergrundinformation.

Manuskript erhalten: 16. Februar 2019
Veränderte Fassung erhalten: 1. April 2019
Akzeptierte Fassung online: 3. April 2019
Endgültige Fassung online: 9. Mai 2019

Angewandte Chemie
Eine Zeitschrift der Gesellschaft Deutscher Chemiker

Supporting Information

Gallium Methylene

Martin Bonath, Cäcilia Maichle-Mössmer, Peter Sirsch, and Reiner Anwander**

anie_201902063_sm_miscellaneous_information.pdf

Table of Contents

SUPPORTING INFORMATION

Experimental Section

General Considerations. Syntheses and manipulations of all organometallic compounds were carried out under rigorous exclusion of air and moisture, using standard Schlenk, high-vacuum, and glovebox techniques (MB Braun MB200B; <1 ppm O_2, <1 ppm H_2O, argon atmosphere). The solvents toluene and tetrahydrofuran (thf) were purified using Grubbs-type columns (MBraun SPS, solvent purification system). Methylcyclohexane (99%, Sigma-Aldrich), C_6D_6 (99.6%, Sigma-Aldrich) and d_8-thf (99.5%, Euriso-top) were dried by distillation from Na/K-alloy. All solvents were stored inside a glovebox. Trimethylgallium ($GaMe_3$, Dockweiler Chemicals, optoelectronic grade) was used as received. $[(C_5Me_5)_2Y(\{\mu\text{-}Me\}_2GaMe_2)]$ and $[(C_5Me_5)_2Lu(\{\mu\text{-}Me\}_2GaMe_2)]$ were synthesized according to a slightly modified literature procedure.[1] The NMR spectra of air and moisture sensitive compounds were recorded by using J. Young valve NMR tubes at variable temperatures on a Bruker AVII+400 (^{1}H: 400.13 MHz; ^{13}C: 100.61 MHz) and a Bruker AVII+500 (^{1}H: 500.13 MHz; ^{13}C: 125.76 MHz). ^{1}H and ^{13}C NMR chemical shifts are referenced to solvent residual resonances and reported in parts per million, relative to tetramethylsilane (TMS). Coupling constants are given in Hertz. Solid-state NMR spectra were recorded on a Bruker ASX 300 instrument equipped with MAS (magic angle spinning) hardware and using a ZrO_2 rotor with an inside diameter of 7 mm. IR spectra were recorded on a NICOLET 6700 FTIR spectrometer with a DRIFT cell (KBr window), and the samples were prepared in a glovebox and mixed with KBr powder. Elemental analyses (C, H, N) were performed on an Elementar Vario Micro Cube.

$[(C_5Me_5)_2Lu(\{\mu\text{-}Me\}_2AlMe_2)]$. In a pressure tube, a slurry of $[Lu(\{\mu\text{-}Me\}_2AlMe_2)_3]$ (1018 mg, 2.33 mmol) and an excess of C_5Me_5H (718 mg, 5.27 mmol) in toluene were heated to 130 °C. After stirring for 12 h all volatile parts were removed under reduced pressure to yield a white solid. The solid was washed with *n*-hexane (3 x 2 mL) and evaporated to dryness in vacuo to yield pure $[(C_5Me_5)_2Lu(\{\mu\text{-}Me\}_2AlMe_2)]$ (1056 mg, 1.98 mmol, 85%). ^{1}H NMR (400.11 MHz, C_6D_6, 26 °C): dimer: δ 1.91 (s, 30 H, $C_5(CH_3)_5$), –0.08 (s, 6 H, $Al(CH_3)_2$), –0.83 (s, 6 H, $(\mu\text{-}CH_3)_2Al$); monomer: δ 1.82 (s, 30 H, $C_5(CH_3)_5$), –0.29 (s, 6 H, $Al(CH_3)_2$), –0.29 (s, 6 H, $(\mu\text{-}CH_3)_2Al$) ppm.

$[(C_5Me_5)_2LuMe(thf)]$. In a glovebox, $[(C_5Me_5)_2Lu(\{\mu\text{-}Me\}_2AlMe_2)]$ (515 mg, 0.97 mmol) was dissolved in 2.4 mL of thf and 15 mL of *n*-hexane and immediately filtered. The filtrate was stored at –40 °C for 3 d to afford colorless crystals. The supernatant was decanted and the solid washed with two portions of *n*-hexane (2 mL) to remove any $[AlMe_3(thf)]$ from the crude product. After drying in vacuum a white solid was obtained (393 mg, 76%). ^{1}H NMR (400.11 MHz, C_6D_6, 26 °C): δ 3.24 (m, 4 H, OCH_2CH_2), 2.00 (s, 30 H, $C_5(CH_3)_5$), 1.11 (m, 4 H, OCH_2CH_2), –0.62 (s, 3 H, $Lu(CH_3)$) ppm.

$[(C_5Me_5)_2Lu(\{\mu\text{-}Me\}_2GaMe_2)]$ ($\mathbf{1^{Lu}}$). In a glovebox, a solution of $[(C_5Me_5)_2LuMe(thf)]$ (418 mg, 0.78 mmol) in toluene (8 mL) was treated with $[GaMe_3]$ (270 mg, 2.35 mmol) and stirred for 2 h. Subsequently, all volatiles were evaporated to yield pure $[(C_5Me_5)_2Lu(\{\mu\text{-}Me\}_2GaMe_2)]$ (440 mg, 97%). ^{1}H NMR (400.11 MHz, C_6D_6, 26 °C): dimer: δ 1.92 (s, 30 H, $C_5(CH_3)_5$), 0.23 (s, 6 H, $Ga(CH_3)_2$), –0.71 (s, 6 H, $(\mu\text{-}CH_3)_2Ga$); monomer: δ 1.84 (s, 30 H, $C_5(CH_3)_5$), 0.00 (s, 6 H, $Ga(CH_3)_2$), –0.26 (s, 6 H, $(\mu\text{-}CH_3)_2Ga$) ppm.

$[Ga_8(\mu\text{-}CH_2)_{12}]$ (2), $[Ga_6(\mu\text{-}CH_2)_9(thf)_6]$ (3), $[Ga_8(\mu\text{-}CH_2)_{12}(thf)_4]$ (4), and $[Ga_8(\mu\text{-}CH_2)_{12}(thf)_5]$ (5). a) In a pressure tube, a solution of $[(C_5Me_5)_2Lu(\{\mu\text{-}Me\}_2GaMe_2)]$ ($\mathbf{1^{Lu}}$, 202 mg, 0.35 mmol) and excess $[GaMe_3]$ (315 mg, 2.74 mmol) in toluene were heated at 130 °C under vigorous stirring. After 3 d a pale yellow solid precipitated from the hot toluene solution. The supernatant was decanted, the product was washed with *n*-pentane and evaporated to dryness in vacuo to yield **2** as a pale yellow powder (147 mg, 0.20 mmol, 80%). Crystals of **2** suitable for X-ray crystallography were obtained when $\mathbf{1^{Lu}}$ (19 mg, 0.03 mmol) and $[GaMe_3]$ (30 mg, 0.26 mmol) were diluted in C_6D_6 in a J. Young valve NMR tube and heated at 100 °C for 28 d. Compounds **3**, **4**, and **5** formed instantly when **2** was dissolved in thf. Crystals suitable for X-ray crystallography were either grown from saturated thf solutions at –40 °C (**3**) or by condensing *n*-pentane into saturated thf solutions at ambient temperature (**4** and **5**). b) Following a similar procedure, $[(C_5Me_5)_2Y(\{\mu\text{-}Me\}_2GaMe_2)]$ ($\mathbf{1^{Y}}$, 472 mg, 0.97 mmol) and $[GaMe_3]$ (1209 mg, 10.53 mmol) afforded 277 mg (35%) of **2** after 13 d. ^{1}H NMR (400.1 MHz, d_8-thf, 26 °C): **4**/**5**: δ 0.19 (s, 24 H, $GaCH_2$); **3**: δ 0.12 (d, $^2J_{HH}$ = 9.1 Hz, 6 H, $GaCH_2$), –0.10 (s, 6 H, $GaCH_2$), –0.49 (d, $^2J_{HH}$ = 8.8 Hz, 6 H, $GaCH_2$) ppm. $^{13}C\{^1H\}$ NMR (100.6 MHz, d_8-thf, 26 °C): **4**/**5**: δ 18.9 ($GaCH_2$); **3**: δ 13.0 ($GaCH_2$) ppm. ^{13}C CP/MAS NMR (76 MHz, 26 °C): **2**: δ 28 (s, vbr, $[Ga(\mu\text{-}CH_2)]$) ppm. DRIFT (KBr): ν 2924 (m), 2869 (m), 1340 (m), 871 (m), 840 (s), 671 (m), 641 (s), 484 (vs), 479 (s) cm^{-1}. $C_{12}H_{24}Ga_9Ga_8$ (726.11 g/mol): calcd. C 19.85, H 3.33; found C 19.65, H 3.26.

$[(C_5Me_5)_6Lu_3(\mu_3\text{-}CH_2)_6Ga_9(CH_2)_9]$ ($\mathbf{6^{Lu}}$). In a pressure tube, $[(C_5Me_5)_2Lu(\{\mu\text{-}Me\}_2GaMe_2)]$ ($\mathbf{1^{Lu}}$, 294 mg, 0.51 mmol) and two equivalents $[GaMe_3]$ (117 mg, 1.02 mmol) were stirred in methylcyclohexane (8 mL). At 130 °C the white suspension started to clear up within one minute. After 2 d a white precipitate had formed. The precipitate was washed with *n*-pentane and dried in vacuo to yield $\mathbf{6^{Lu}}\bullet C_7H_{14}$ as a white powder (351 mg, 91%). Single crystals suitable for X-ray crystallography were obtained by heating $\mathbf{1^{Lu}}$ (20 mg, 0.04 mmol) and $[GaMe_3]$ (12 mg, 0.10 mmol) in a J. Young valve NMR tube in C_6D_6 for 10 d at 100 °C. ^{1}H NMR (400.1 MHz, d_8-thf + DMAP, 26 °C): δ 1.93 (s, 90 H, $C_5(CH_3)_5$), 0.25 (d, $^2J_{HH}$ = 9.4 Hz, 6 H, $GaCH_2$), –0.75 (d, $^2J_{HH}$ = 9.4 Hz, 6 H, $GaCH_2$), –0.99 (s, 12 H, $GaCH_2$), –1.35 (s, 6 H, $GaCH_2$) ppm. ^{13}C CP/MAS NMR (76 MHz, 26 °C): δ 116.1 (s, shldr, C_5Me_5), 115.7 (s, C_5Me_5), 114.8 (s, C_5Me_5), 17.8 (s, vbr, $GaCH_2$), 12.4 (s, $C_5(CH_3)_5$), –4.4 (s, vbr, $GaCH_2$) ppm. DRIFT (KBr): ν 2916 (s), 2894 (s), 2855 (s), 2721 (w), 1445 (m), 1436 (m), 929 (m), 774 (s), 630 (vs), 599 (m) cm^{-1}. $C_{75}H_{120}Ga_9Lu_3\bullet C_7H_{14}$ (2272.38 g/mol): calcd. C 43.34, H 5.94; found C 43.01, H 5.95.

SUPPORTING INFORMATION

[(C$_5$Me$_5$)$_6$Y$_3$(μ$_3$-CH$_2$)$_6$Ga$_9$(CH$_2$)$_9$] (6^{Y}). Following the procedure described for synthesis of **6^{Lu}**, [(C$_5$Me$_5$)$_2$Y({μ-Me}$_2$GaMe$_2$)] (**1^{Y}**, 126 mg, 0.26 mmol) afforded **6^{Y}** as a white powder (97 mg, 59%). Single crystals suitable for X-ray crystallography were obtained by heating **1^{Y}** (20 mg, 0.04 mmol) and [GaMe$_3$] (6 mg, 0.05 mmol) in a J. Young valve NMR tube in C$_6$D$_6$ for 45 d at 90 °C. ^{1}H NMR (400.1 MHz, d_8-thf + DMAP, 26 °C): δ 1.96 (s, 90 H, C$_5$(C*H*$_3$)$_5$), 0.27 (d, $^2J_{HH}$ = 9.2 Hz, 6 H, GaC*H*$_2$), –0.68 (d, $^2J_{HH}$ = 9.2 Hz, 6 H, GaC*H*$_2$), –1.13 (d, $^2J_{YH}$ = 3.7 Hz, 12 H, GaC*H*$_2$), –1.32 (s, 6 H, GaC*H*$_2$) ppm. ^{13}C CP/MAS NMR (76 MHz, 26 °C): δ 118.9 (s, *C*$_5$Me$_5$), 117.3 (s, *C*$_5$Me$_5$), 24.1 (s, vbr, Ga*C*H$_2$), 12.1 (s, C$_5$(*C*H$_3$)$_5$), 11.3 (s, C$_5$(*C*H$_3$)$_5$) ppm. DRIFT (KBr): ν 2916 (s), 2855 (s), 1449 (m), 1436 (m), 927 (m), 780 (s), 630 (vs), 598 (m) cm^{-1}. C$_{75}$H$_{120}$Ga$_9$Y$_3$•C$_7$H$_{14}$ (2014.20 g/mol): calcd. C 48.90, H 6.71; found C 48.85, H 6.67.

[Ga$_6$(μ-CH$_2$)$_9$(pyr-*d*$_5$)$_6$] (7) and [Ga$_5$(μ-CH$_2$)$_7$(Me)(pyr-*d*$_5$)$_5$] (8). Compound **2** dissolved slowly in d_5-pyridine and gradually formed **7** and a second compound within several days. In contrast to **3**, reformation of **2** from **7** was not observed when **7** was heated at 80 °C or under dynamic vacuum. However, in d_5-pyridine solutions **7** converted slowly to the methyl/methylidene complex **8**. Crystals suitable for X-ray crystallography were either grown from saturated d_5-pyridine solutions at –40 °C (**7**) or by condensing *n*-pentane into a saturated d_5-pyridine solution at ambient temperature (**8**). ^{1}H NMR (400.1 MHz, pyr-d_5, 26 °C): **7**: δ 0.63 (d, $^2J_{HH}$ = 9.2 Hz, 6 H, GaC*H*$_2$), 0.30 (s, 6 H, GaC*H*$_2$), –0.07 (d, $^2J_{HH}$ = 9.2 Hz, 6 H, GaC*H*$_2$) ppm; **8**: **7**: δ 0.50 (d, $^2J_{HH}$ = 9.3 Hz, 4 H, GaC*H*$_2$), 0.47 (s, 3 H, GaC*H*$_3$), 0.12 (d, $^2J_{HH}$ = 3.9 Hz, 4 H, GaC*H*$_2$), 0.11 (s, 2 H, GaC*H*$_2$), –0.05 (d, $^2J_{HH}$ = 9.5 Hz, 4 H, GaC*H*$_2$) ppm.

General procedure for deuterolysis experiments. A J. Young NMR tube was charged with 0.1 mL D$_2$O, sealed, and transferred into a glovebox. The deuterium oxide was frozen at –40 °C and the atmosphere inside the J. Young NMR tube removed at dynamic vacuum. Subsequently, a sample of **2** (or **6^{Lu}** or **6^{Y}**) in 0.3 mL d_8-thf was added to the frozen D$_2$O and the J. Young tube was sealed immediately to exclude any loss of volatile components. The deuterolysis reaction started instantly when D$_2$O began to melt and gas evolution was observed. After 15 min ^{1}H NMR spectra were taken, proving the exclusive formation of CD$_2$H$_2$ by a characteristic septet resonance at δ 0.13 ppm [Fig. S28].

NMR Spectra

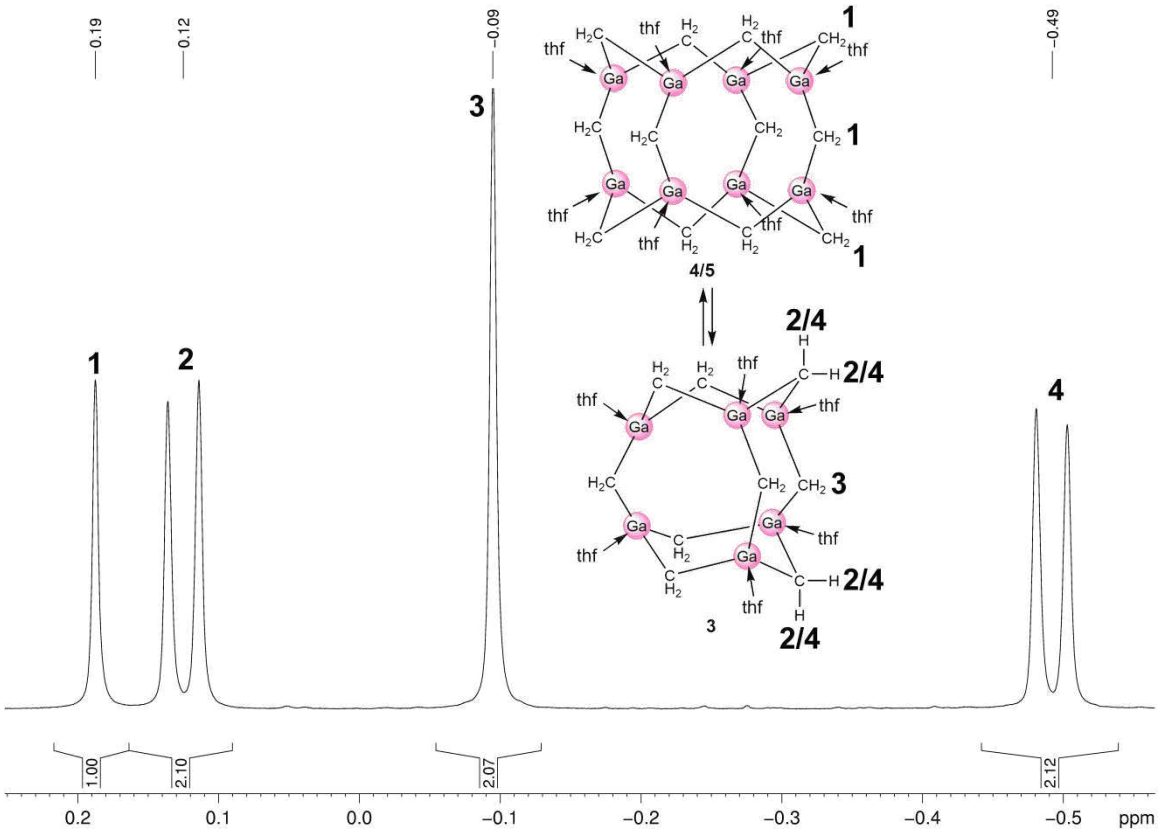

Fig. S1. ^{1}H NMR spectrum (400.1 MHz) of **4**/**5** and **3** recorded after 6 h in d_8-thf solution at 26 °C.

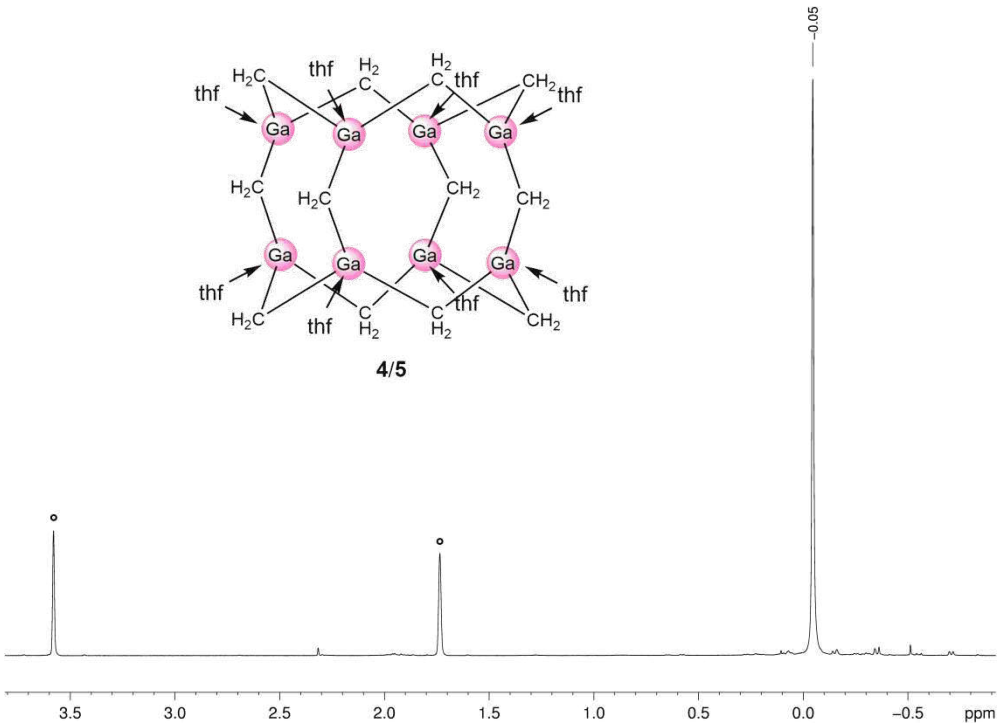

Fig. S2. ^{1}H NMR spectrum (400.1 MHz) of **2(thf)** (structurally characterized as **4** and **5**) in d_8-thf solution at –40 °C.

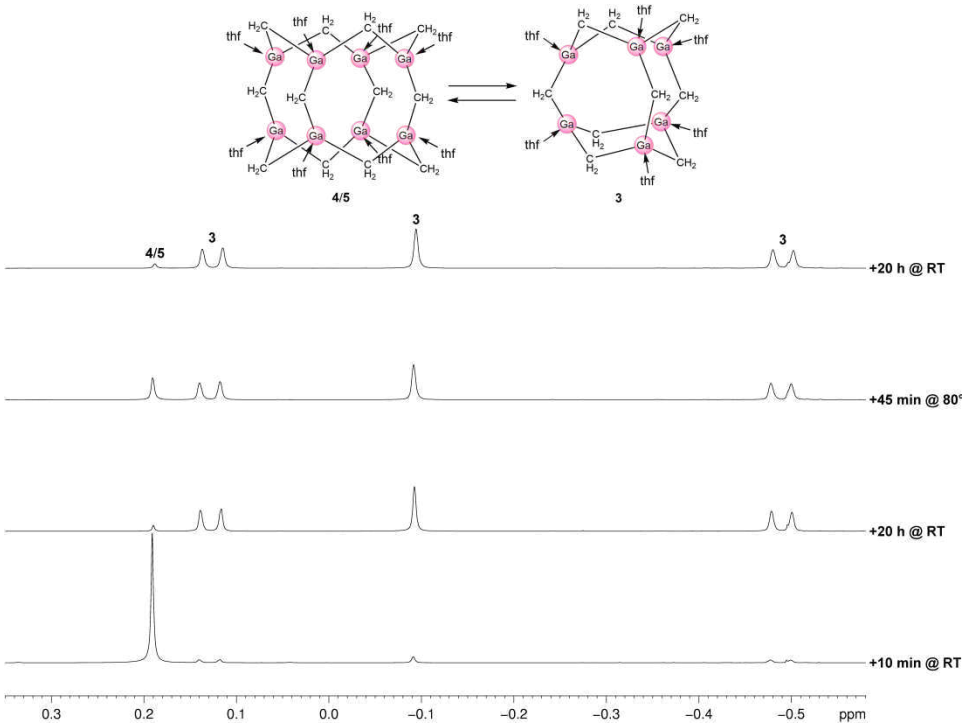

Fig. S3. ^{1}H NMR spectra (400.1 MHz) of gallium methylene in d_8-thf solution monitoring the transformation of **4**/**5** into **3** depending on time and temperature.

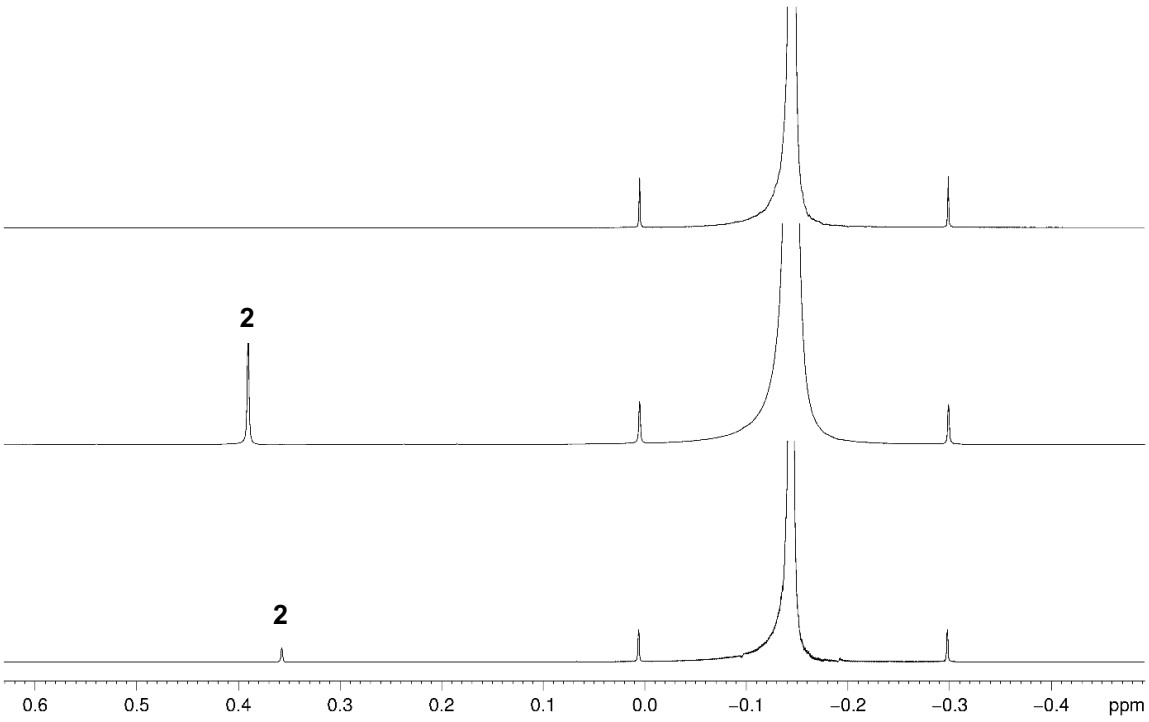

Fig. S4. Section of the ^{1}H NMR spectra (400.1 MHz) of the crude reaction mixture of the pyrolysis reaction of [$GaMe_3$] (bottom), [$Ga_8(CH_2)_{12}$] (**2**) pre-dissolved in [$GaMe_3$] (middle), and neat $GaMe_3$ (top) in C_6D_6 at 26 °C

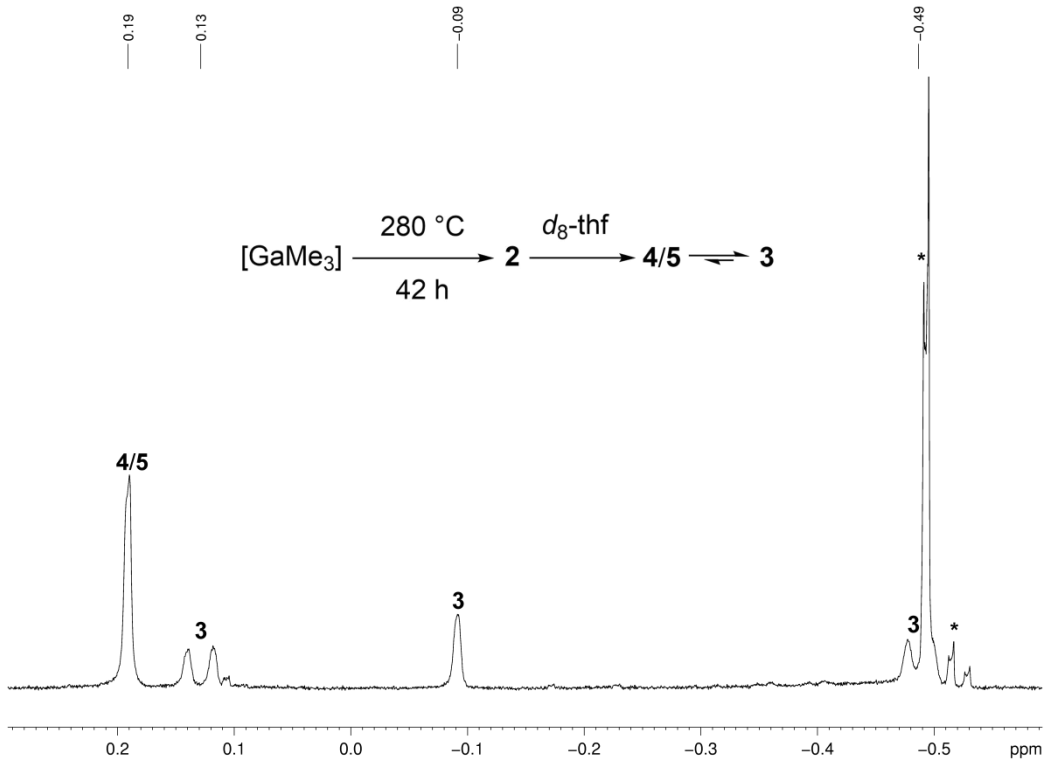

Fig. S5. ^{1}H NMR spectrum (400.1 MHz) of the crude product of the pyrolysis reaction of [$GaMe_3$] in d_8-thf at 26 °C (* unknown side products).

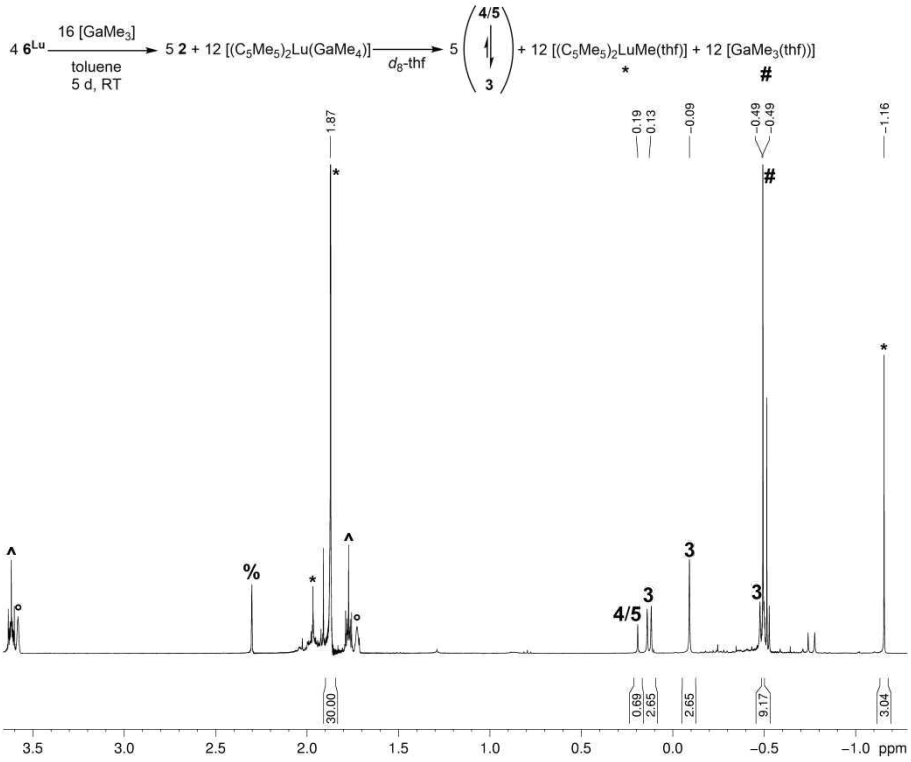

Fig. S6. ^{1}H NMR spectrum (400.1 MHz) of the crude products of reaction of **6^{Lu}** with excessive [GaMe$_3$] at ambient temperature in toluene (^ thf, ° d_8-thf, % toluene).

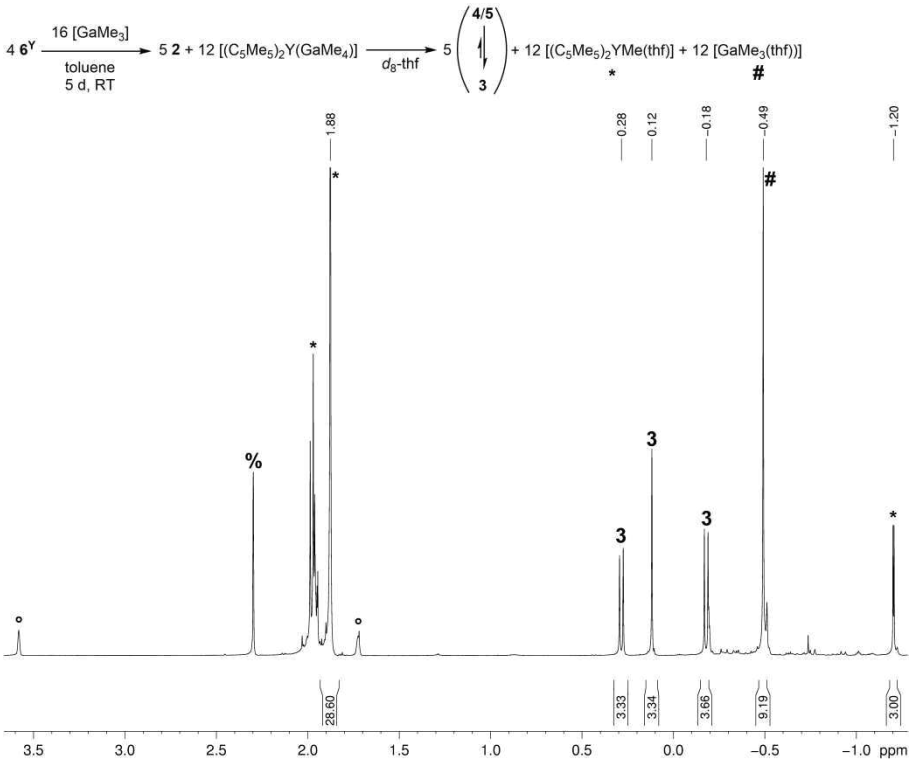

Fig. S7. ^{1}H NMR spectrum (400.1 MHz) of the crude products of the reaction of **6^{Y}** with excessive [GaMe$_3$] at ambient temperature in toluene (° d_8-thf, % toluene).

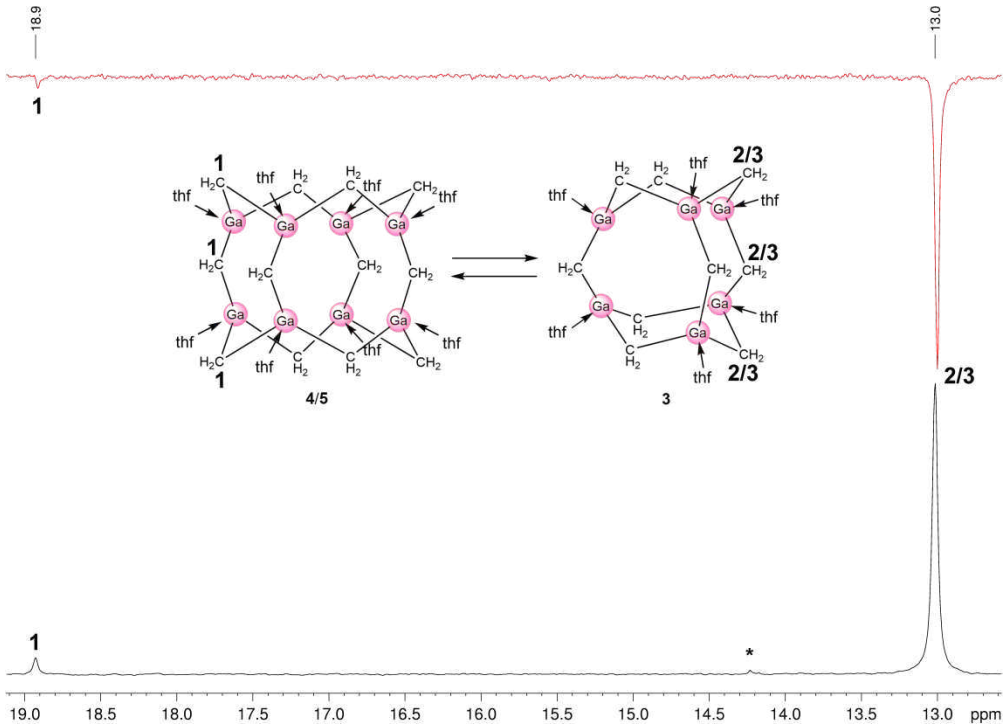

Fig. S8. $^{13}C\{^{1}H\}$ NMR spectrum (black) and DEPT $^{13}C\{^{1}H\}$ spectrum (red; 100.6 MHz) of **2** in d_8-thf at 26 °C (* *n*-pentane).

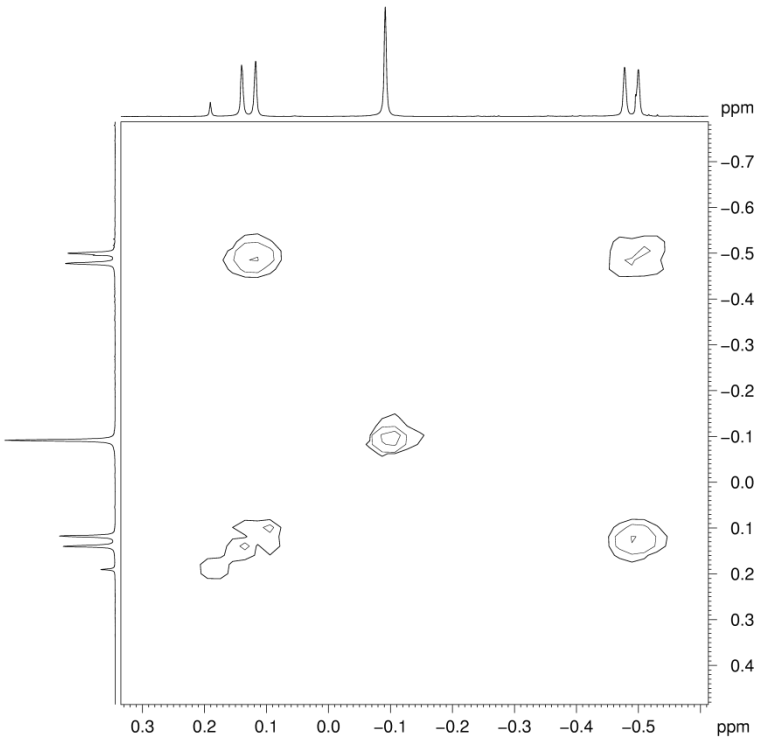

Fig. S9. ^{1}H-^{1}H COSY NMR spectrum (400.1 MHz) of **3** and **4**/**5** in d_8-thf at 26 °C.

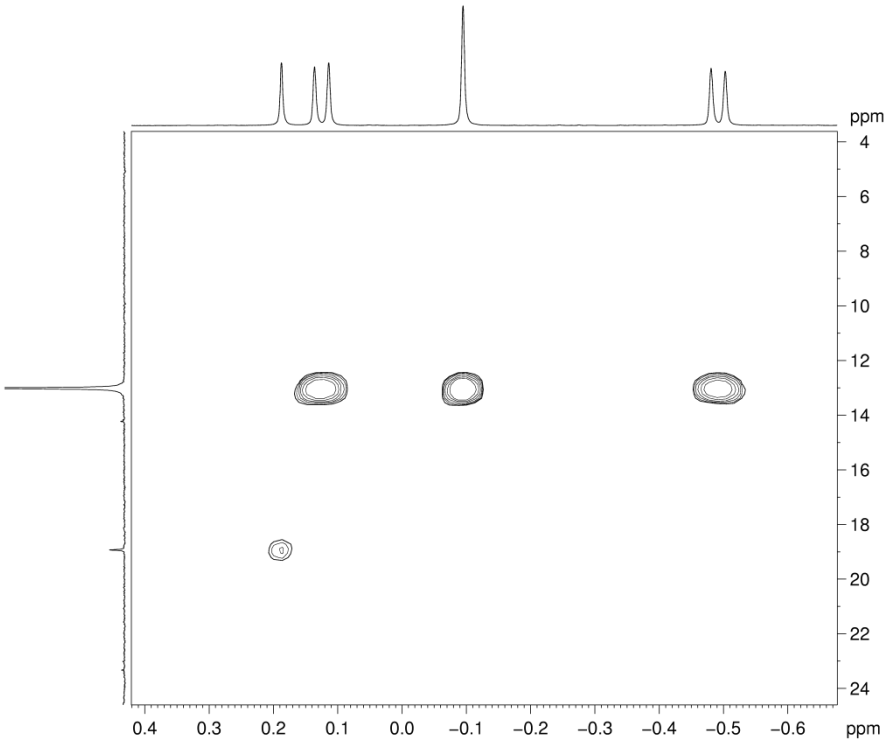

Fig. S10. ^{1}H-^{13}C HSQC NMR spectrum (400.1 MHz, 100.6 MHz) of **3** and **4**/**5** in d_8-thf at 26 °C.

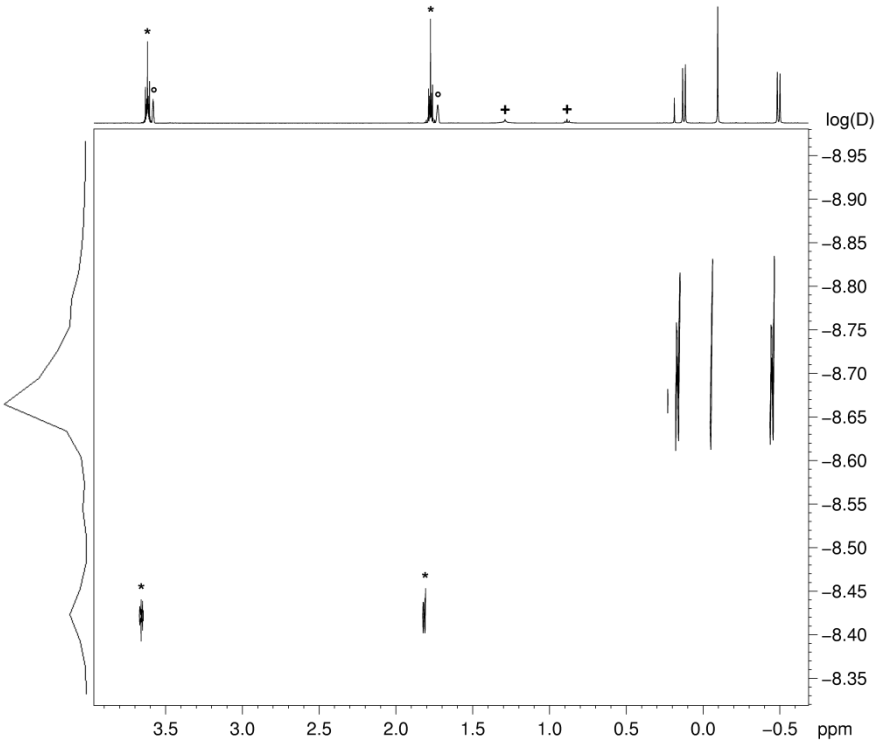

Fig. S11. ^{1}H DOSY NMR spectrum (500.1 MHz, 100.6 MHz) of **3** and **4**/**5** in d_8-thf (°) solutions at 26 °C (* thf, **+** *n*-pentane).

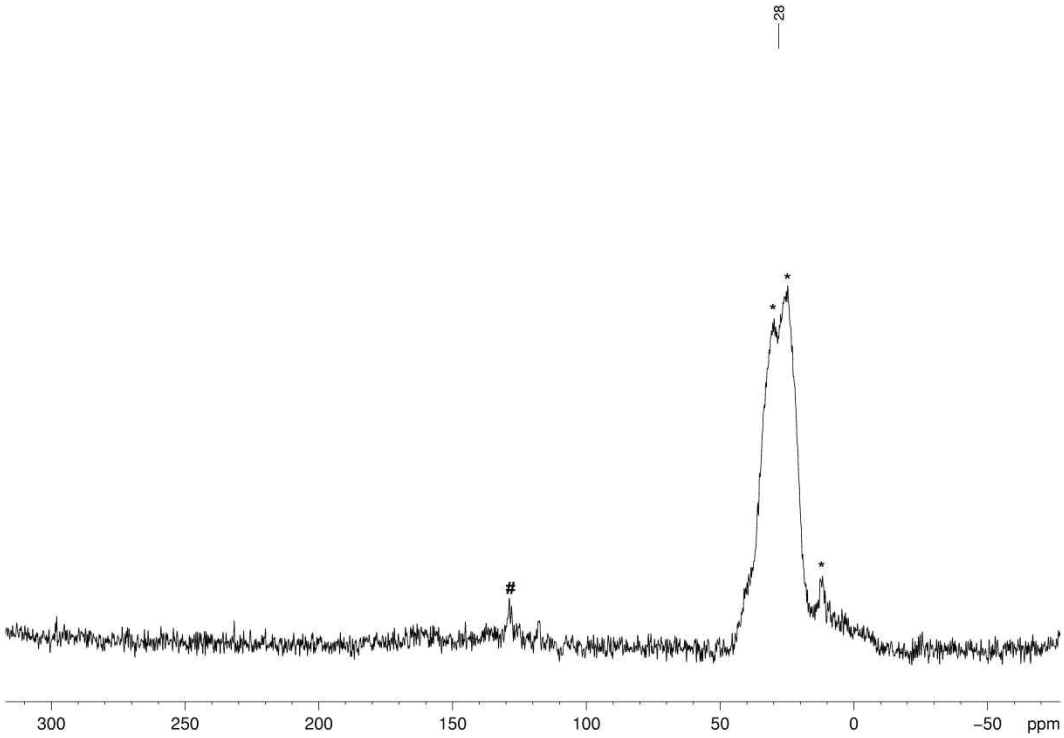

Fig. S12. ^{13}C CP/MAS NMR spectrum (76 MHz) of **2** (# benzene, * *n*-pentane).

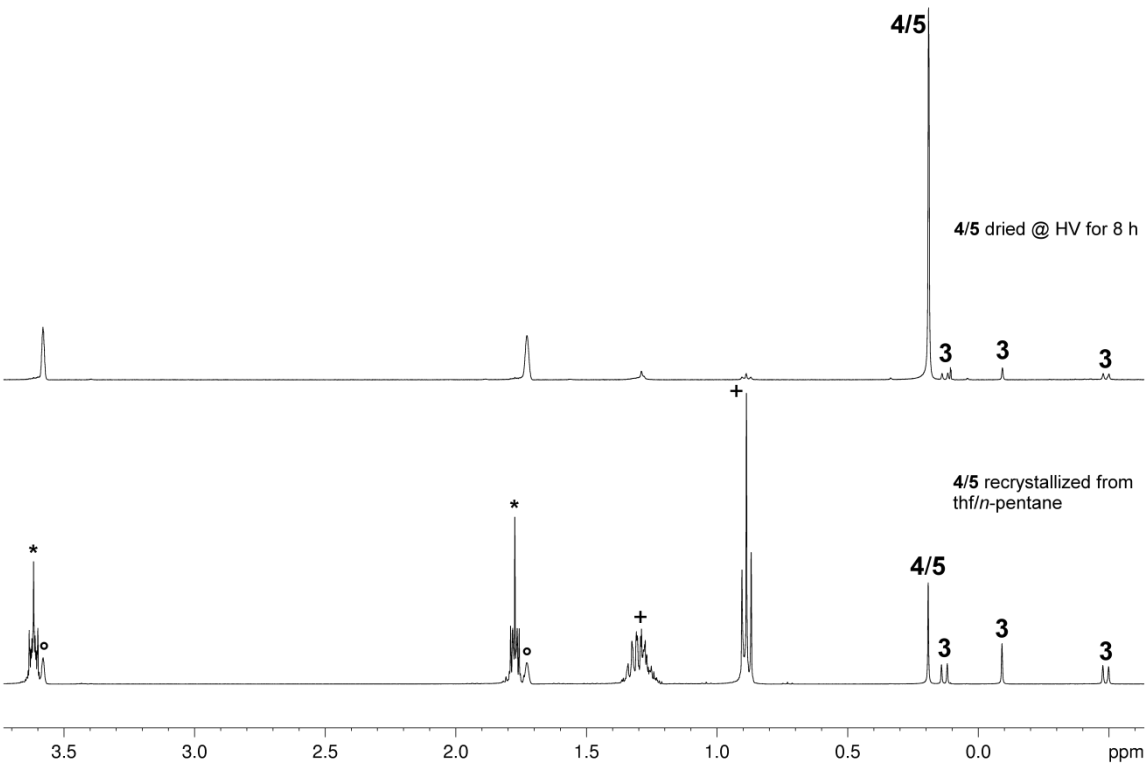

Fig. S13. ^{1}H NMR spectra (400.1 MHz) in d_8-thf demonstrating the removal of thf from **4**/**5** (bottom, recrystallized from thf/*n*-pentane) at high vacuum after 8 h (top) to achieve **2** (° d_8-thf * thf, + *n*-pentane).

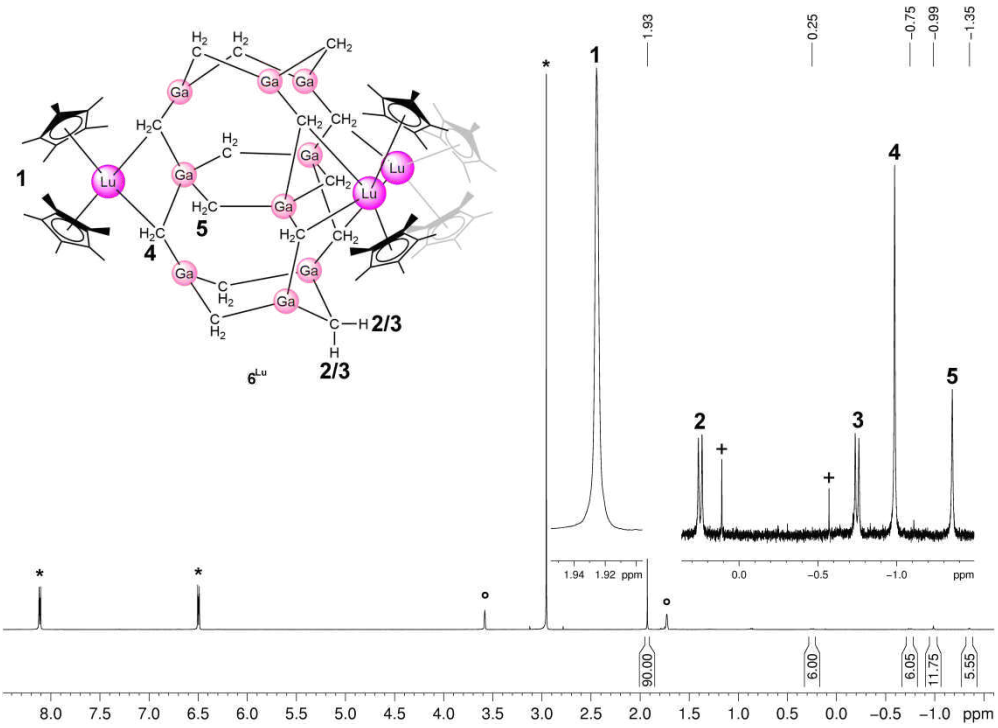

Fig. S14. ^{1}H NMR spectrum (400.1 MHz) of $\mathbf{6^{Lu}}$ + DMAP (*) in d_8-thf (°) at 26 °C (+ minor side products).

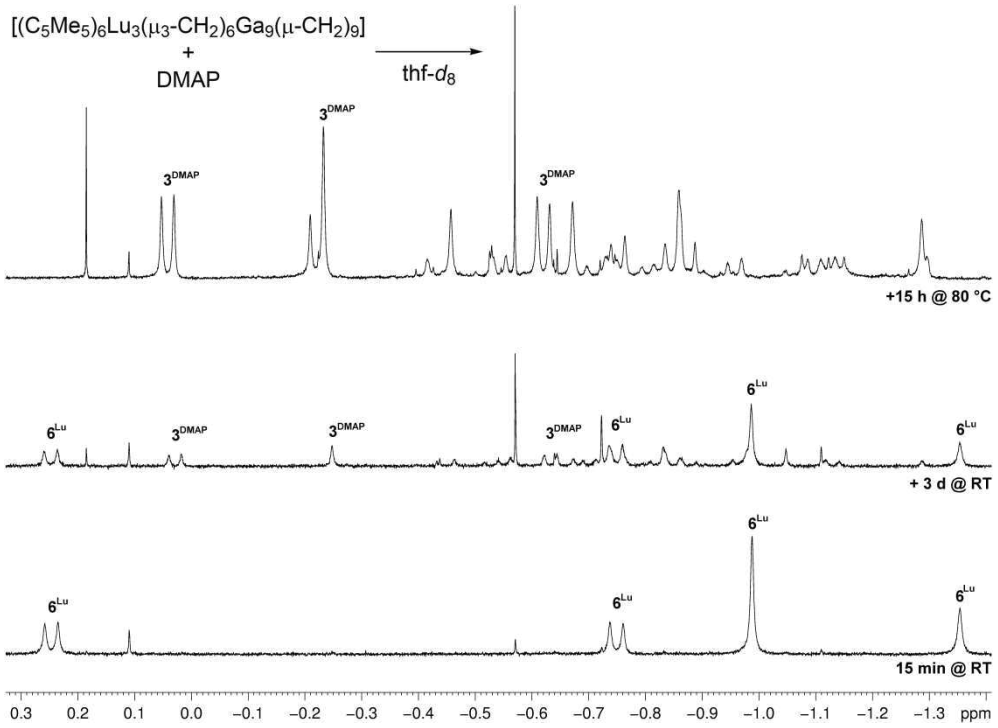

Fig. S15. Section of the ^{1}H NMR spectra (400.1 MHz) in the upfield region, monitoring the decomposition of $\mathbf{6^{Lu}}$ in the presence of DMAP forming $\mathbf{3^{DMAP}}$ and other products.

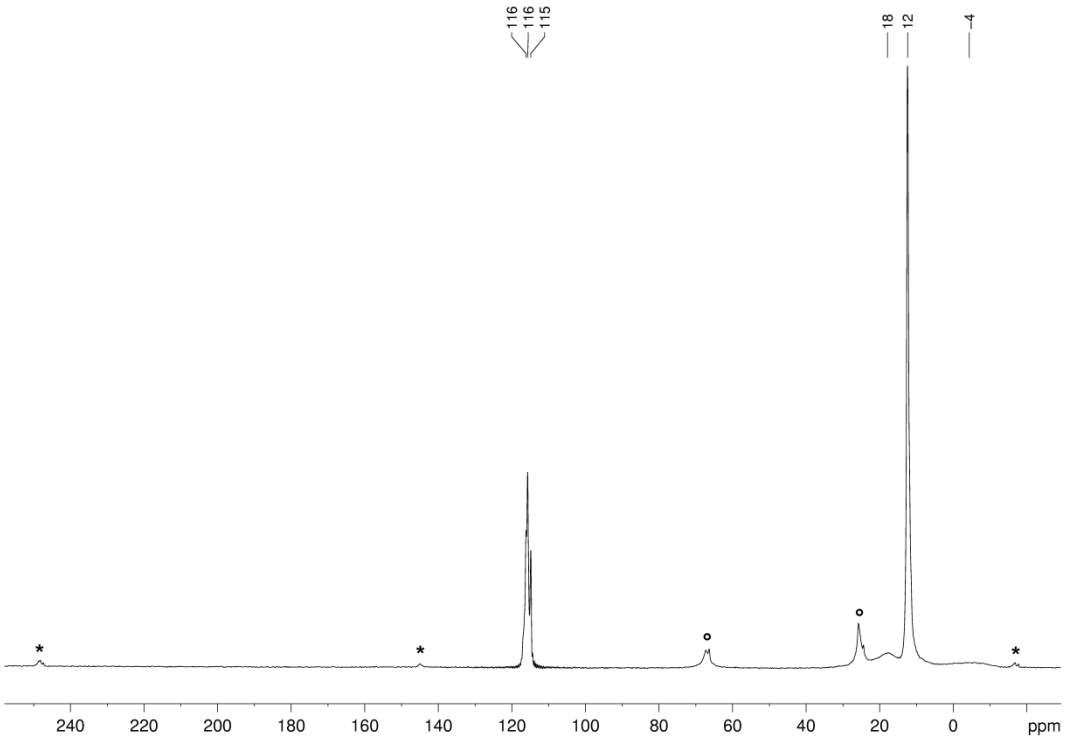

Fig. S16. ^{13}C CP/MAS NMR spectrum (76 MHz) of **6^{Lu}** (* spinning sidebands ±10 kHz, ° thf).

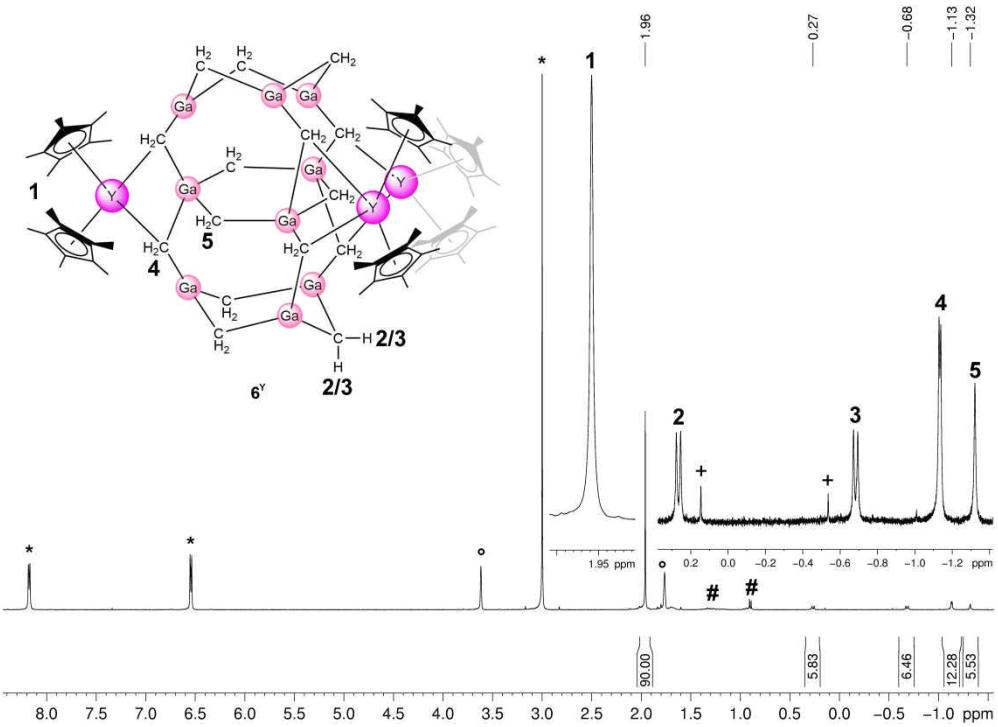

Fig. S17. ^{1}H NMR spectrum (400.1 MHz) of **6^{Y}** + DMAP (*) in d_8-thf (°) at 26 °C (# methylcyclohexane, + minor side products).

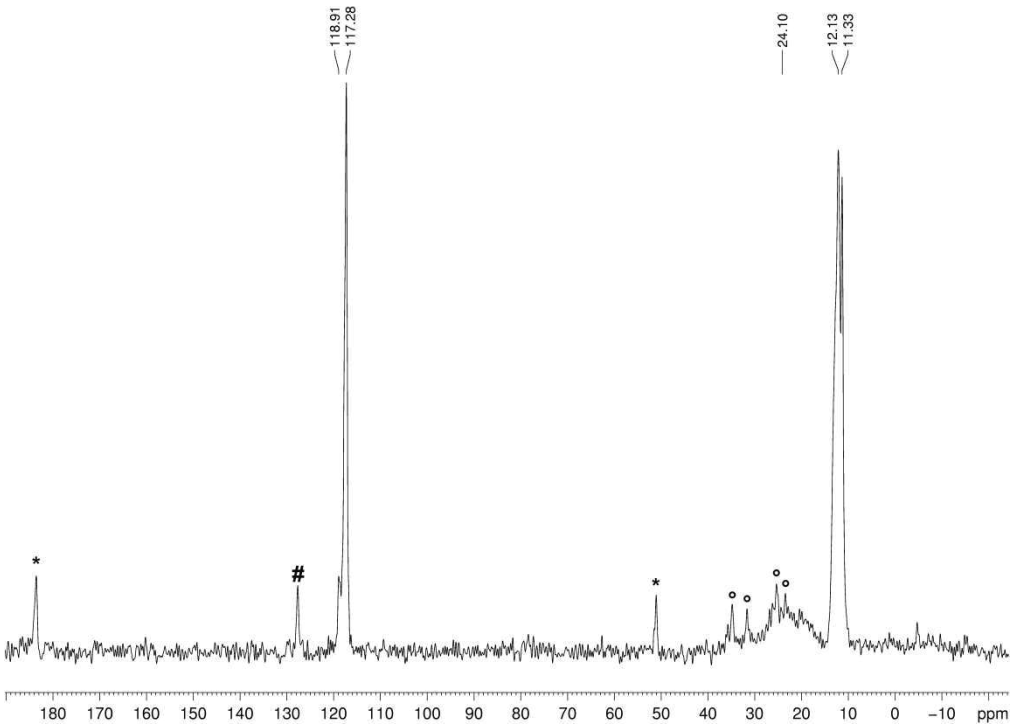

Fig. S18. ^{13}C CP/MAS NMR spectrum (76 MHz) of **6**^{Y} (* spinning sidebands ±5 kHz, # benzene, ° methylcyclohexane).

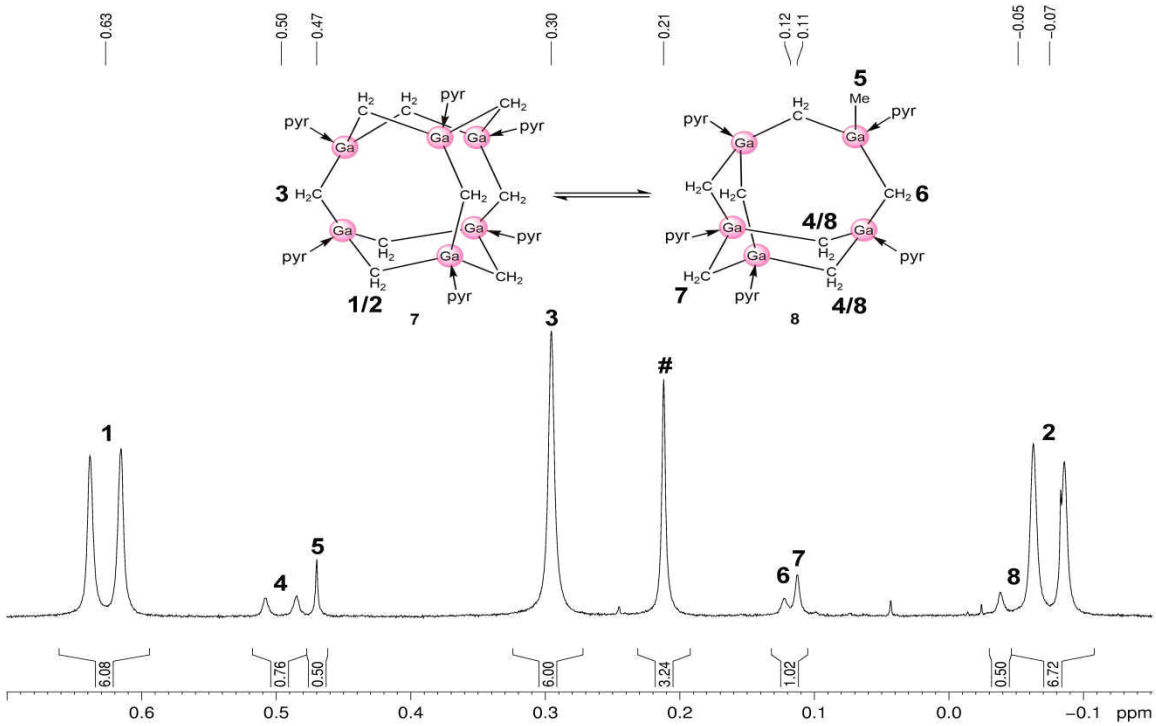

Fig. S19. ^{1}H NMR spectrum (400.1 MHz) of **7** and **8** recorded after thermal treatment (80 °C) for 16 h in d_5-pyr solutions at 26 °C (# unknown side product).

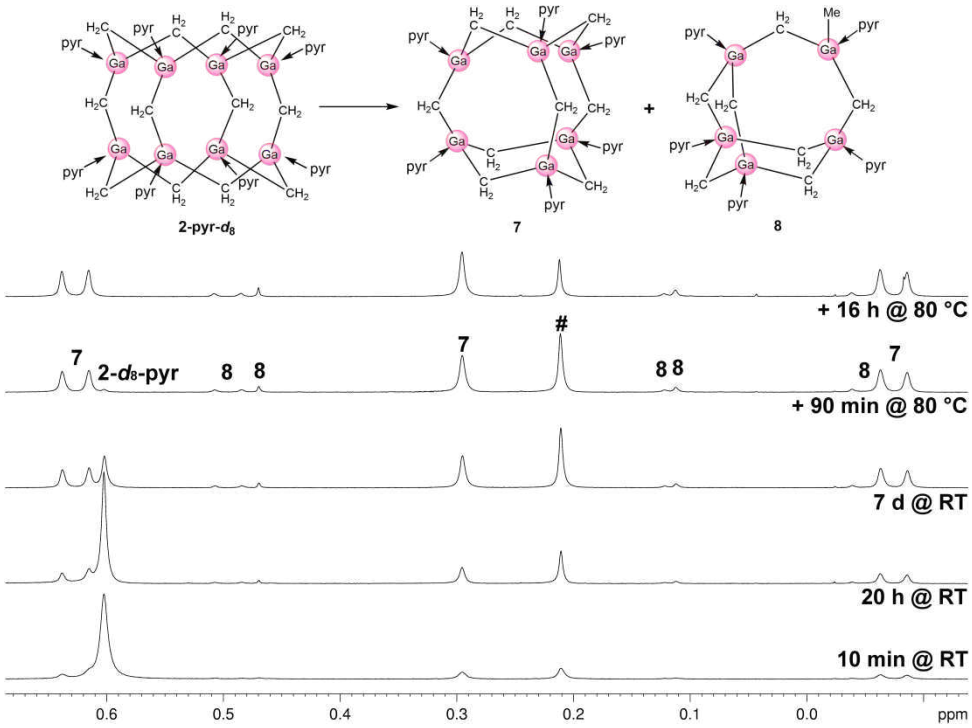

Fig. S20. ^{1}H NMR spectra (400.1 MHz) of **7** and **8** monitoring the decomposition of **2** in d_5-pyr solutions at 26 °C (# unknown side product).

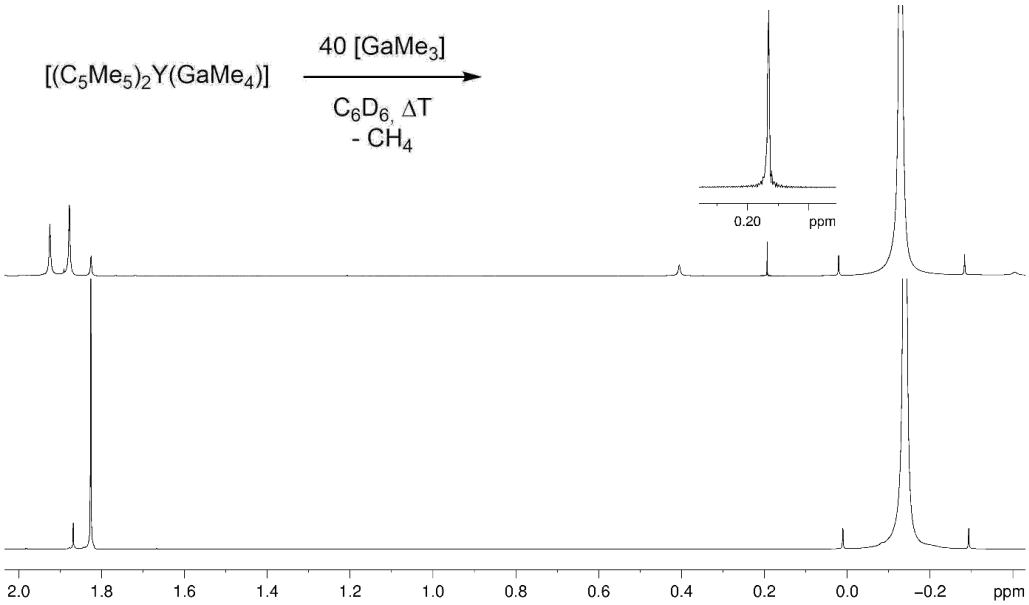

Fig. S21. Section of the ^{1}H NMR spectra (400.1 MHz) of the reaction of $[(C_5Me_5)_2Y(GaMe_4)]$ (**1^Y**) with 40 $[GaMe_3]$ before (bottom) and after thermal treatment (top) in C_6D_6. Note: no crystalline material was obtained in this case.

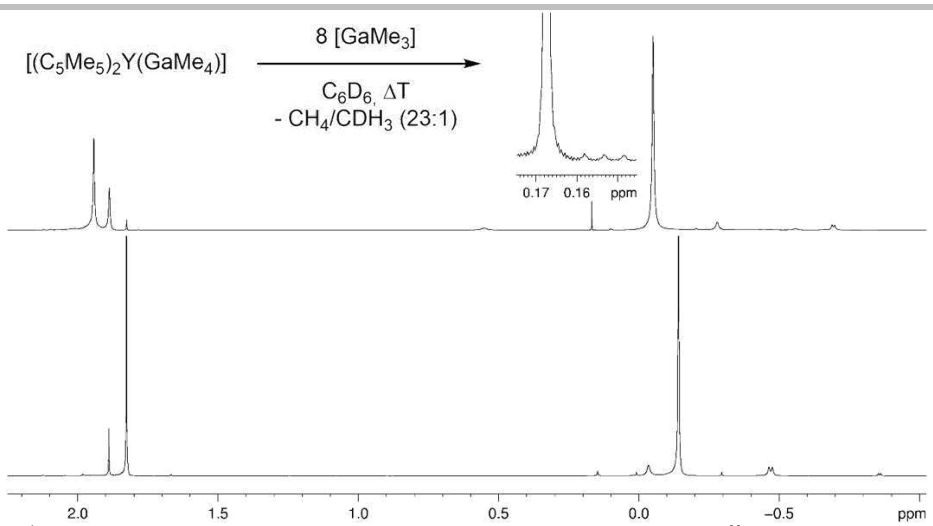

Fig. 22. Section of the ^{1}H NMR spectra (400.1 MHz) of the reaction of $[(C_5Me_5)_2Y(GaMe_4)]$ (**1^Y**) and 8 $[GaMe_3]$ before (bottom) and after thermal treatment (top) in C_6D_6. Note: bright yellow crystals of $[Ga_8(CH_2)_{12}]$ (**2**) were obtained in this case.

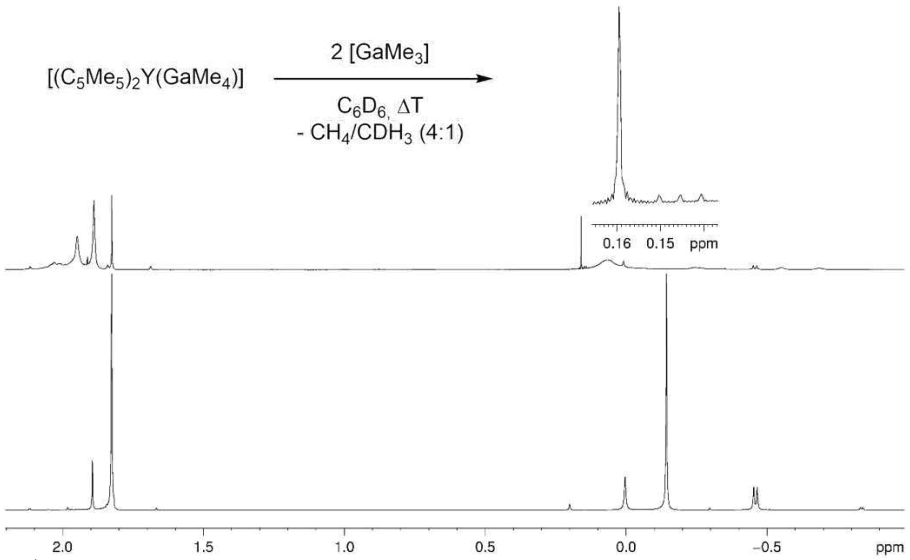

Fig. S23. Section of the ^{1}H NMR spectra (400.1 MHz) of the reaction of $[(C_5Me_5)_2Y(GaMe_4)]$ and 2 $[GaMe_3]$ before (bottom) and after thermal treatment (top) in C_6D_6. Note: colorless crystals of $[(C_5Me_5)_6Y_3(\mu_3\text{-}CH_2)_6Ga_9(CH_2)_9]$ (**6^Y**) were obtained in this case.

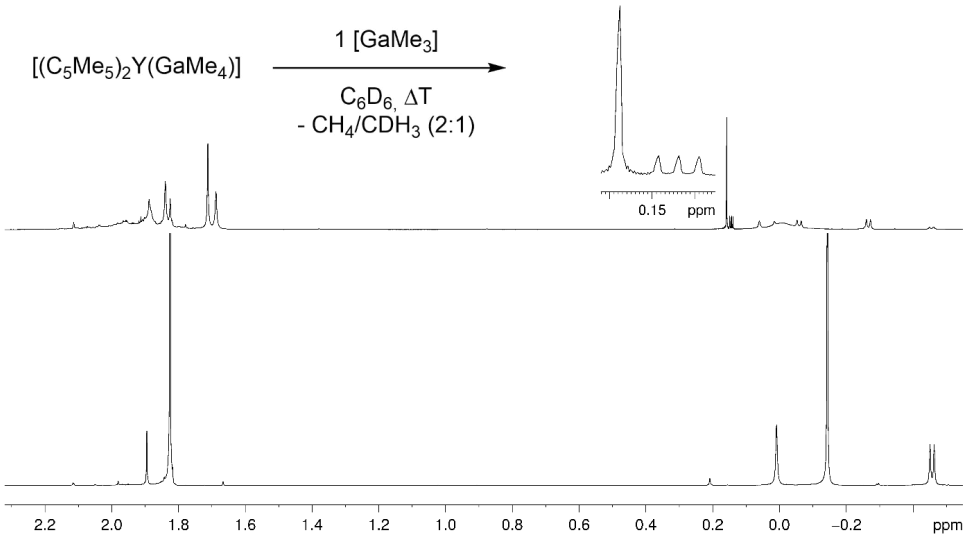

Fig. S24. Section of the ^{1}H NMR spectra (400.1 MHz) of the reaction of $[(C_5Me_5)_2Y(GaMe_4)]$ with1 $[GaMe_3]$ before (bottom) and after thermal treatment (top) in C_6D_6. Note: colorless crystals of $[(C_5Me_5)_6Y_3(\mu_3\text{-}CH_2)_6Ga_9(CH_2)_9]$ (**6^Y**) were obtained in this case.

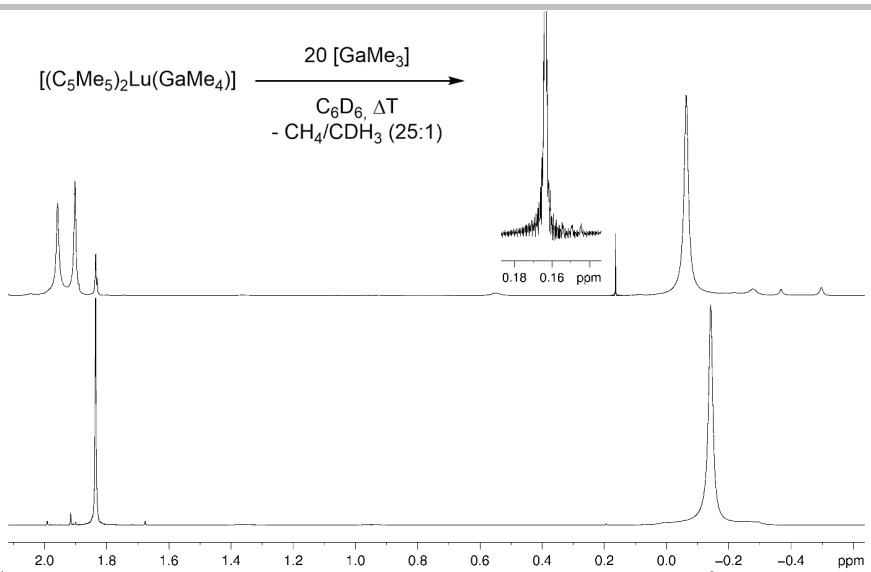

Fig. 25. Section of the ^{1}H NMR spectra (400.1 MHz) of the reaction of $[(C_5Me_5)_2Lu(GaMe_4)]$ (**1^{Lu}**) and 20 $[GaMe_3]$ before (bottom) and after thermal treatment (top) in C_6D_6. Note: no crystalline material was obtained in this case.

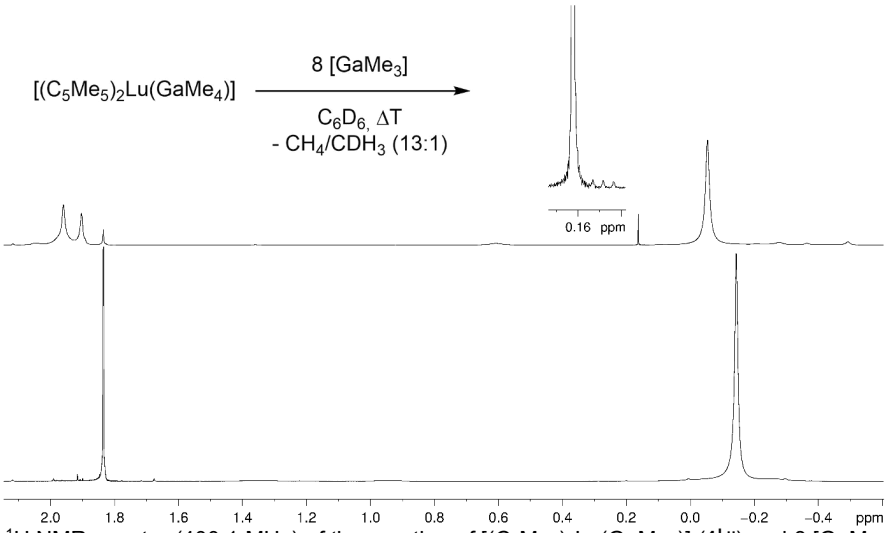

Fig. 26. Section of the ^{1}H NMR spectra (400.1 MHz) of the reaction of $[(C_5Me_5)_2Lu(GaMe_4)]$ (**1^{Lu}**) and 8 $[GaMe_3]$ before (bottom) and after thermal treatment (top) in C_6D_6. Note: bright yellow crystals of $[Ga_8(CH_2)_{12}]$ (**2**) were obtained in this case.

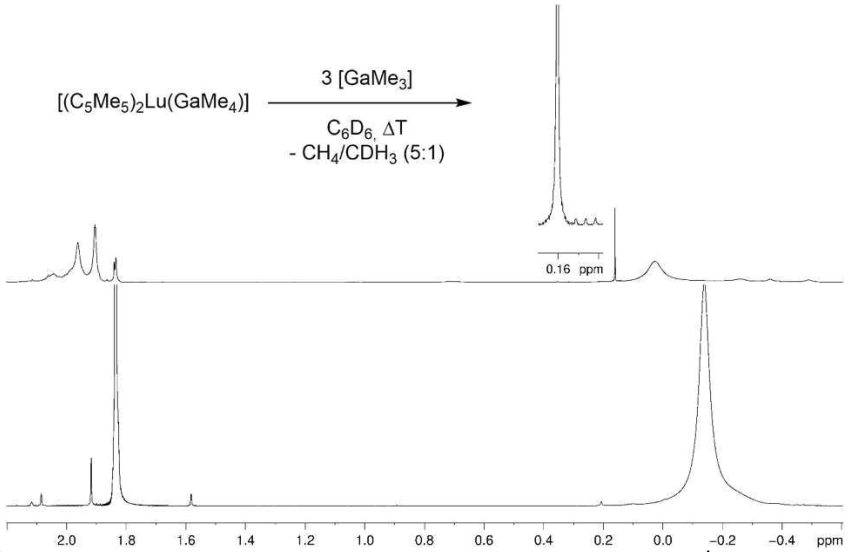

Fig. S27 Section of the ^{1}H NMR spectra (400.1 MHz) of the reaction of $[(C_5Me_5)_2Lu(GaMe_4)]$ (**1^{Lu}**) and 3 $[GaMe_3]$ before (bottom) and after thermal treatment (top) in C_6D_6. Note: colorless crystals of $[(C_5Me_5)_6Lu_3(\mu_3\text{-}CH_2)_6Ga_9(CH_2)_9]$ (**6^{Lu}**) were obtained in this case.

Deuterolysis Reactions of 2, 6^{Y}, and 6^{Lu}

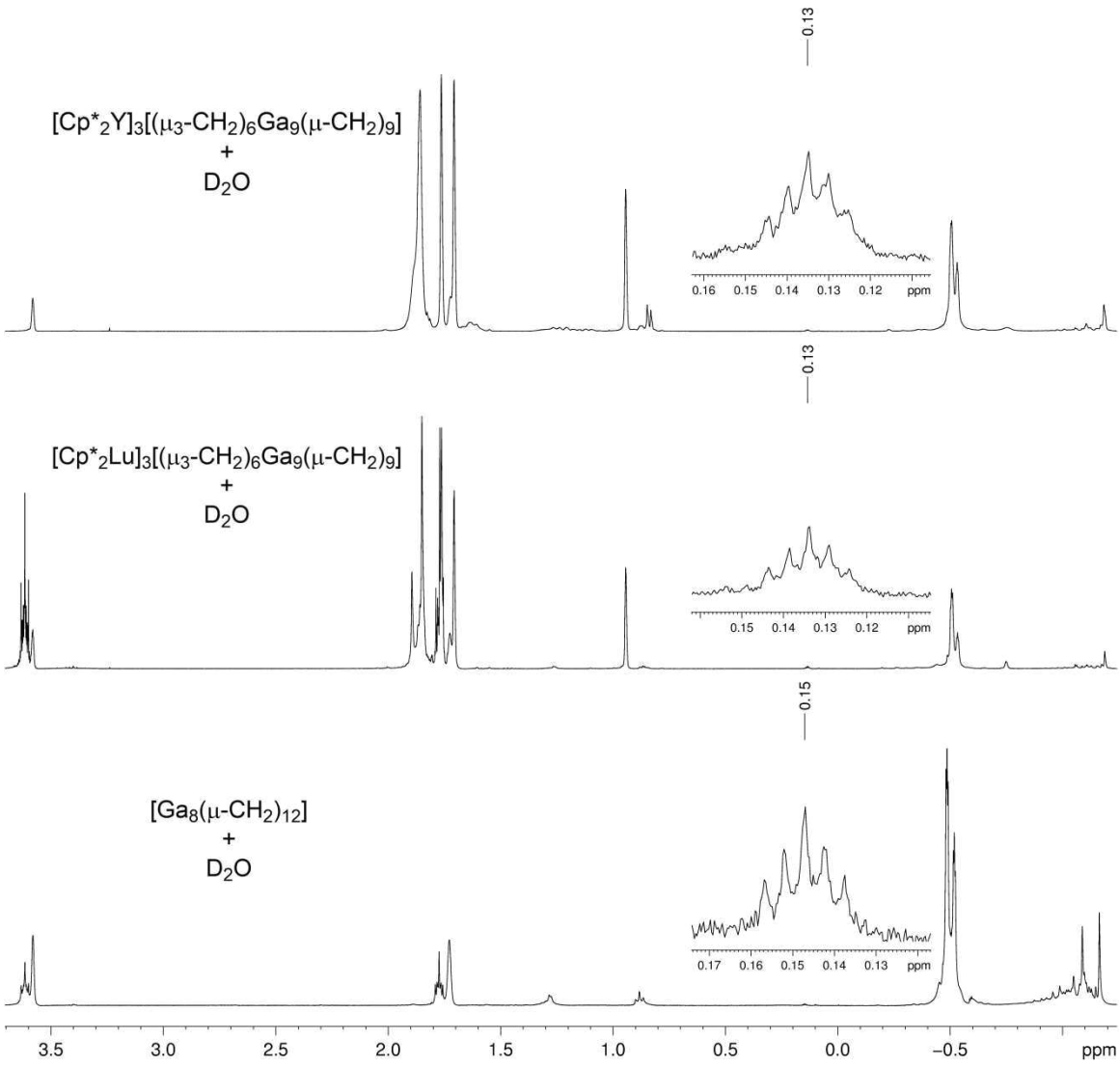

Fig. S28. ^{1}H NMR spectra (400.1 MHz) monitoring deuterolysis reactions of **2**, $\mathbf{6^{Lu}}$, and $\mathbf{6^{Y}}$, respectively, in d_8-thf solutions.

Olefination of Fluorenone with 2, 6^{Lu}, and 6^{Y}

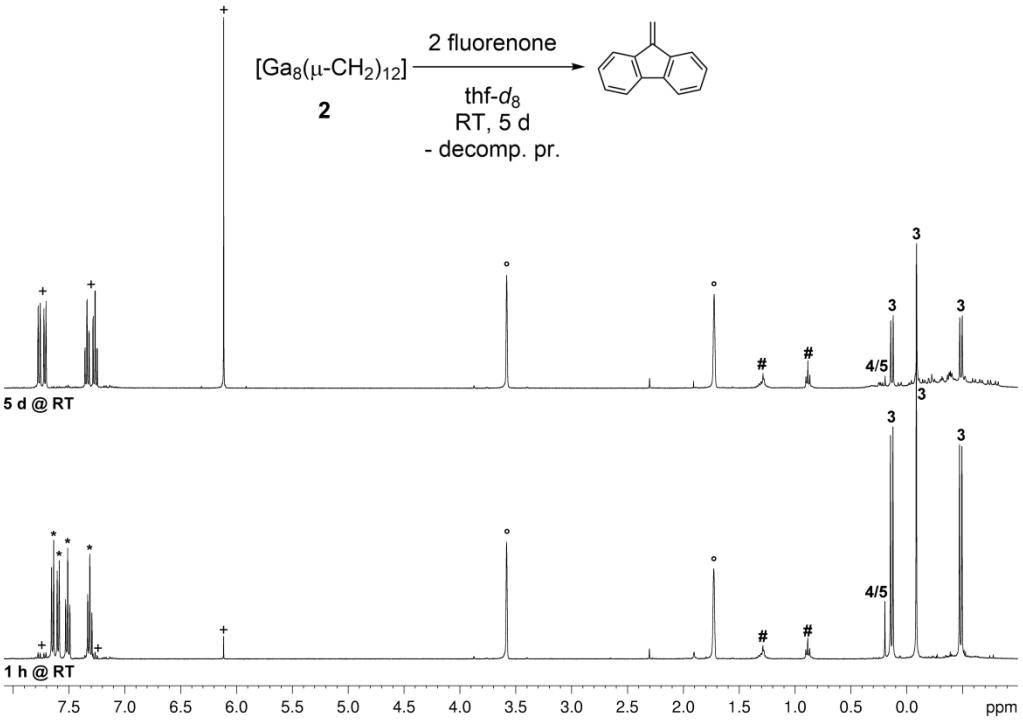

Fig. S29. ^{1}H NMR spectra (400.1 MHz) monitoring olefination of fluorenone with **2** in d_8-thf (°) solutions at 26 °C (+ 9-methylidene-fluorene, * fluorenone, # *n*-pentane).

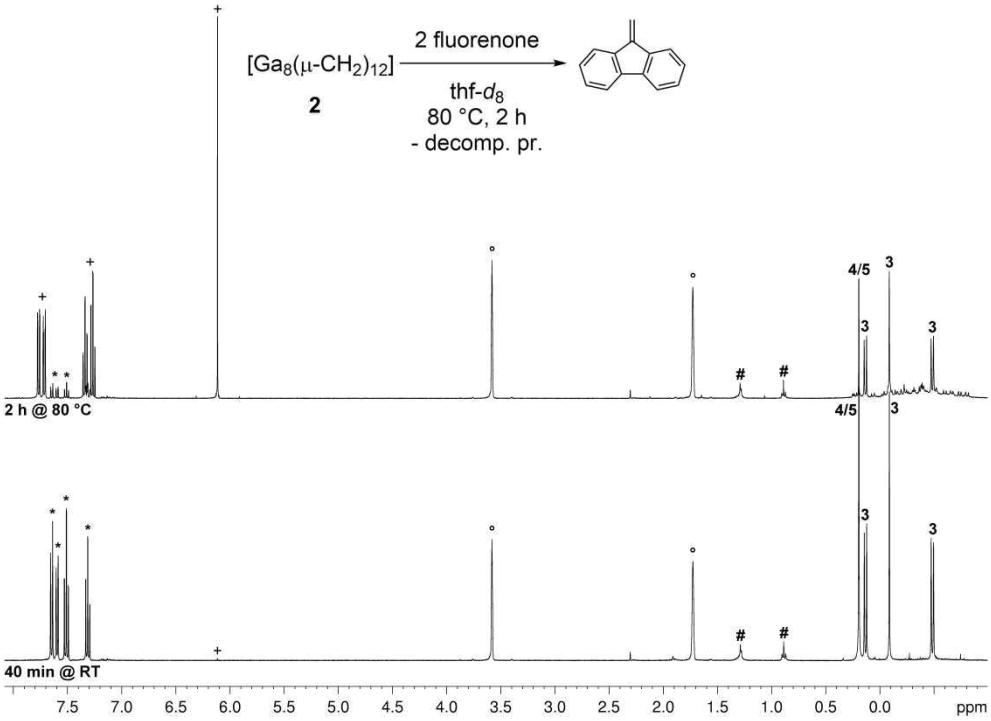

Fig. S30. ^{1}H NMR spectra (400.1 MHz) monitoring olefination of fluorenone with **2** in d_8-thf (°) solutions at 80 °C (+ 9-methylidene-fluorene, * fluorenone, # *n*-pentane).

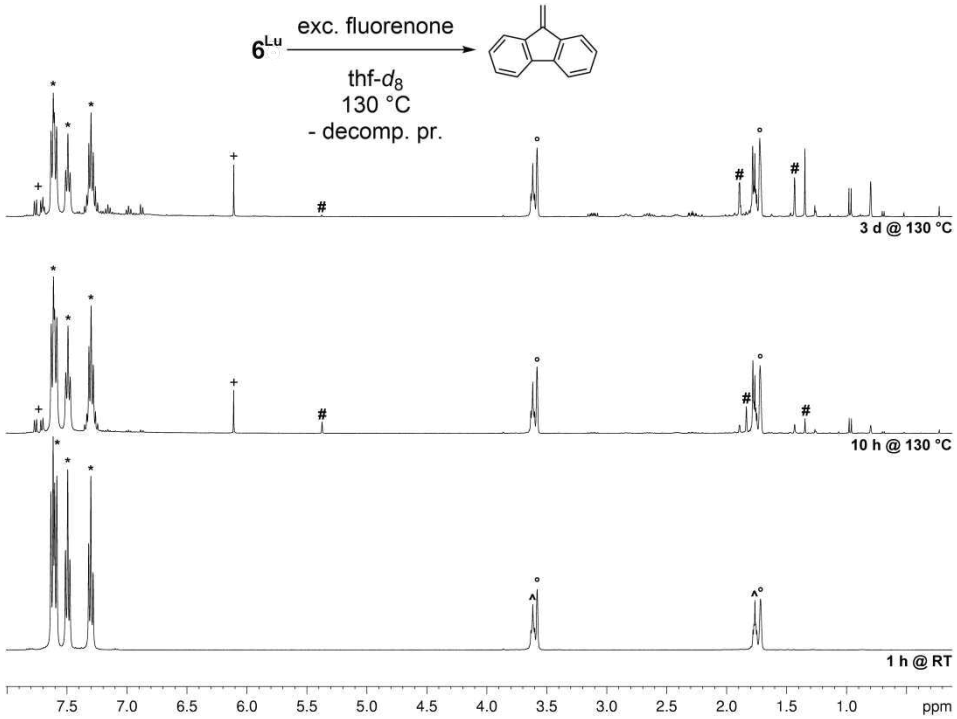

Fig. S31. ^{1}H NMR spectra (400.1 MHz) monitoring olefination of fluorenone with **6^{Lu}** in d_8-thf (°) at 130 °C (+ 9-methylidene-fluorene, * fluorenone, # tetramethylfulvene, ^ thf).

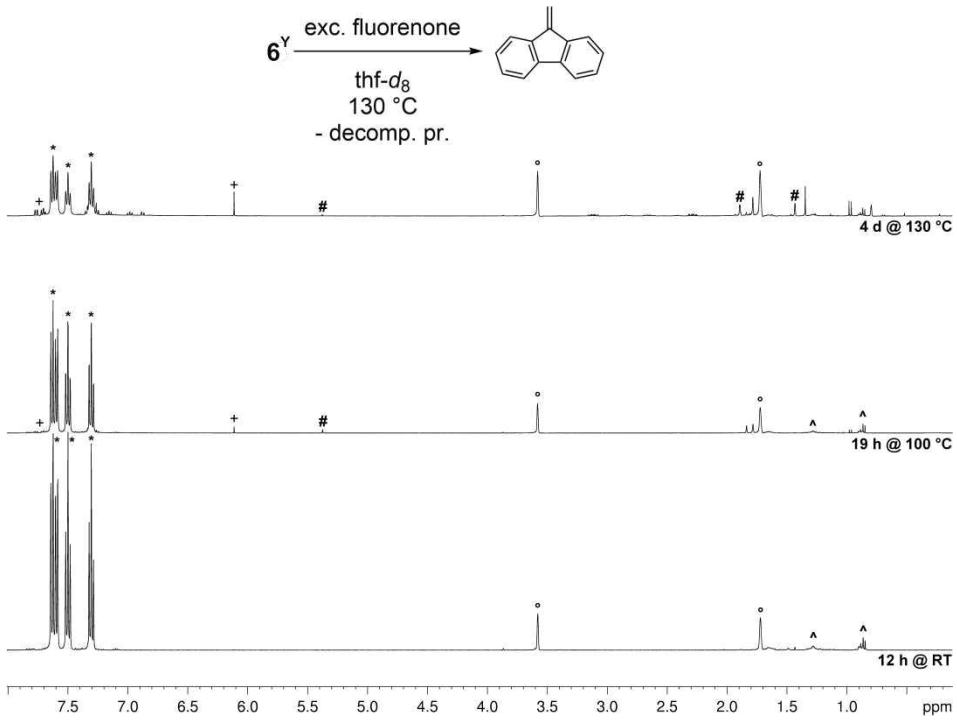

Fig. S32. ^{1}H NMR spectra (400.1 MHz) monitoring olefination of fluorenone with **6^{Y}** in d_8-thf (°) at elevated temperatures (+ 9-methylidene-fluorene, * fluorenone, # tetramethylfulvene, ^ *n*-pentane).

Crystallography

X-Ray Crystallography and Crystal Structure Determinations. Main Single crystals were selected, coated with Parabar 10312 (previously known as Paratone N, Hampton Research) and fixed on a microloop. Crystal mounting has been done under a cold N2 stream to prevent crystals from decomposing. Data for complexes **2**-**5**, **7**, **8**, and $[(C_5Me_5)_2Lu(\{\mu\text{-}Me\}_2AlMe_2)]$, $[(C_5Me_5)_2LuMe(thf)]$ and $[(C_5Me_5)_2Lu(\{\mu\text{-}Me\}_2GaMe_2)]$ (**1**^{Lu}) the three given in the table with formula were collected on a Bruker APEX DUO instrument equipped with an IμS microfocus sealed tube and QUAZAR optics for MoK_α radiation (λ = 0.71073 Å). Data for complexes **6**^{Lu} and **6**^{Y} were collected on a Bruker SMART APEX II instrument equipped with a fine focus sealed tube and TRIUMPH monochromator using MoK_α radiation (λ = 0.71073 Å). The data collection strategy was determined using COSMO[2] employing ω and/or ϕ scans. Raw data were processed using APEX[3] and SAINT,[4] corrections for absorption effects were applied using SADABS[5] or TWINABS.[6] The structures were solved by direct methods[7] and refined against all data by full-matrix least-squares methods on F^2 using SHELXTL[8] and Shelxle.[9] In some cases disorder was modelled using DSR.[10] All graphics were produced by using ORTEP-3[11] and POV-Ray.[12]

Table S1. Crystallographic data information of complexes **2, 3, 4**, and **5**

	2	**3**	**4**	**5**
Formula	$C_{12}H_{24}Ga_8$	$C_{33}H_{66}O_6Ga_6$	$C_{28}H_{56}O_4Ga_8$	$C_{32}H_{64}O_5Ga_8$
CCDC	1890815	1890816	1890819	1890820
M_r [g mol^{-1}]	726.07	976.17	1014.48	1086.59
cryst syst	tetragonal	orthorhombic	triclinic	trigonal
space group	*I4/m*	*Pna*2$_1$	$P\bar{1}$	$R\bar{3}$
a [Å]	9.3772(8)	20.2886(16)	9.2900(7)	47.428(2)
b [Å]	9.3772(8)	10.8625(8)	10.5163(7)	47.428(2)
c [Å]	11.8225(10)	18.8725(14)	11.1877(7)	10.4528(5)
α [°]	90	90	106.3360(10)	90
β [°]	90	90	107.8230(10)	90
γ [°]	90	90	104.2600(10)	120
V [Å^3]	1039.6(2)	4159.2(5)	930.09(11)	20362(2)
Z	2	4	1	18
T [K]	101(2)	180(2)	200(2)	100(2)
ρ_{calcd} [g cm^{-3}]	2.320	1.559	1.811	1.595
μ [mm^{-1}]	10.187	3.868	5.729	4.718
F (000)	688	1988	504	9792
R1/*w*R2 (I>2σ)[a]	0.0158/0.0360	0.0379/0.0713	0.0292/0.0632	0.0383/0.0802
R1/*w*R2 (all data)[a]	0.0194/0.0370	0.0655/0.0795	0.0401/0.0687	0.0676/0.0915
GOF[a]	1.073	0.989	1.034	1.007

[a] $R1 = \Sigma(||F_0|-|F_c||)/\Sigma|F_0|$, $F_0 > 4\sigma(F_0)$. $wR2 = \{\Sigma[w(F_0^2-F_c^2)^2/\Sigma[w(F_0^2)^2]\}^{1/2}$.

Table S2. Crystallographic data information of complexes $\mathbf{6^{Lu}}$, $\mathbf{6^{Y}}$, **7**, and **8**

	$\mathbf{6^{Lu}}$	$\mathbf{6^{Y}}$	**7**	**8**
Formula	$C_{75}H_{120}Ga_9Lu_3 \cdot C_6D_6$	$C_{75}H_{120}Ga_9Y_3 \cdot C_6D_6$	$C_{39}H_{48}N_6Ga_6 \cdot C_5D_5N$	$C_{33}H_{19}D_{25}N_5Ga_5 \cdot C_6D_5N$ $C_{39}H_{18}D_{30}N_6Ga_6$
CCDC	1890824	1890821	1890817	1890818
M_r [g mol^{-1}]	2258.24	2000.06	1098.25	3947.74
cryst syst	hexagonal	hexagonal	monoclinic	triclinic
space group	$P\bar{6}\,2c$	$P\bar{6}\,2c$	$P2_1/c$	$P1$
a [Å]	17.3157(7)	17.4798(9)	18.5672(10)	11.964(8)
b [Å]	17.3157(7)	17.4798(9)	12.4090(7)	17.695(13)
c [Å]	15.5467(8)	15.5945(8)	20.0724(10)	19.616(14)
α [°]	90	90	90	93.478(15)
β [°]	90	90	90.169(3)	90.553(13)
γ [°]	120	120	90	97.216(16)
V [Å^3]	4036.9(4)	4126.4(5)	4624.7(4)	4112(5)
Z	2	2	4	2
T [K]	100(2)	150(2)	150(2)	100(2)
ρ_{calcd} [g cm^{-3}]	1.858	1.610	1.577	1.594
μ [mm^{-1}]	6.619	5.007	3.484	3.587
F (000)	2208	2016	2208	1922
R1/*w*R2 (I>2σ)[a]	0.0239/0.0567	0.0274/0.0658	0.0441/0.1077	0.0585/0.1097
R1/*w*R2 (all data)[a]	0.0270/0.0582	0.0316/0.0679	0.0623/0.1179	0.0886/0.1232
GOF[a]	1.060	1.050	1.082	1.034

[a] $R1 = \Sigma(||F_0|-|F_c||)/\Sigma|F_0|$, $F_0 > 4\sigma(F_0)$. $wR2 = \{\Sigma[w(F_0^2-F_c^2)^2/\Sigma[w(F_0^2)^2]\}^{1/2}$.

SUPPORTING INFORMATION

Table S3. Crystallographic data information of complexes $[(C_5Me_5)_2Lu(\{\mu\text{-}Me\}_2AlMe_2)]$, $[(C_5Me_5)_2LuMe(thf)]$ and $[(C_5Me_5)_2Lu(\{\mu\text{-}Me\}_2GaMe_2)]$ (**1^{Lu}**)

	$[(C_5Me_5)_2Lu(AlMe_4)]$	$[(C_5Me_5)_2LuMe(thf)]$	**1^{Lu}**
Formula	$C_{48}H_{84}Al_2Lu_2 \cdot (C_7H_{13})_4$	$C_{25}H_{41}OLu$	$C_{48}H_{84}Ga_2Lu_2 \cdot (C_7H_{13})_4$
CCDC	1890822	1890825	1890823
cryst syst	triclinic	orthorhombic	triclinic
space group	$P\bar{1}$	*Pnma*	$P\bar{1}$
a [Å]	11.263(7)	17.7477(9)	11.1947(7)
b [Å]	12.443(6)	15.0503(7)	12.5690(7)
c [Å]	14.798(7)	8.6198(4)	14.8320(9)
α [°]	103.587(11)	90	105.155(2)
β [°]	100.167(11)	90	101.112(2)
γ [°]	111.849(14)	90	112.719(2)
V [Å^3]	1789.1(16)	2302.42(19)	1754.07(18)
Z	1	4	1
T [K]	100(2)	100(2)	200(2)
ρ_{calcd} [g cm^{-3}]	1.331	1.536	1.438
μ [mm^{-1}]	2.806	4.299	3.589
F (000)	740	1080	776
R1/*w*R2 (I>2σ)[a]	0.0332/0.0822	0.0577/0.1360	0.0243/0.0586
R1/*w*R2 (all data)[a]	0.0364/0.0843	0.0600/0.1367	0.0292/0.0611
GOF[a]	1.083	1.397	1.028

[a] R1 = $\Sigma(||F_0|-|F_c||)/\Sigma|F_0|$, $F_0 > 4\sigma(F_0)$. *w*R2 = $\{\Sigma[w(F_0^2-F_c^2)^2/\Sigma[w(F_0^2)^2]\}^{1/2}$.

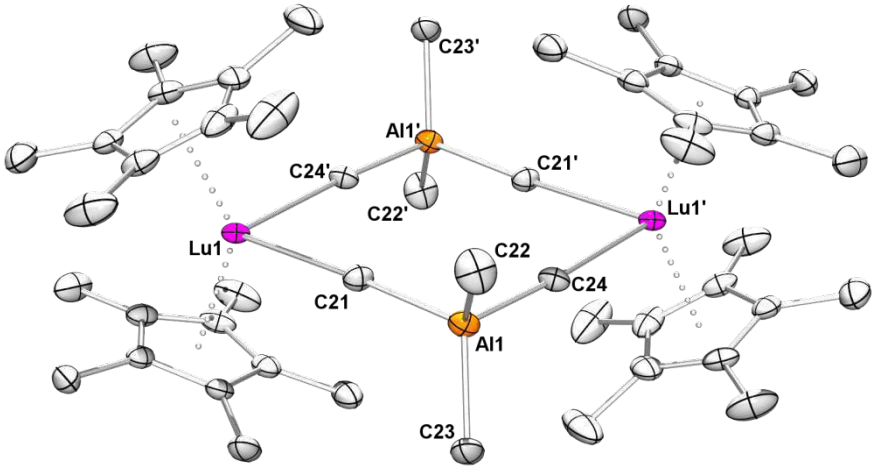

Fig. S33. ORTEP representation (50% probability ellipsoids) of $[(C_5Me_5)_2Lu(\{\mu\text{-}Me\}_2AlMe_2)]$. Hydrogen atoms and co-crystallized solvent molecules (toluene) have been omitted for clarity. Selected bond lengths (Å) and angles (°): Lu1–C21 2.641(4), Lu1–C24' 2.614(3), Al1–C21 2.060(4), Al1–C22 1.985(4), Al1–C23 1.986(4), Al1–C24 2.053(3); Lu1-C21-Al1 173.6(2), Lu1-C24'-Al1' 175.7(2), C21-Al1-C24 100.4(1), C22-Al1-C23 113.9(2).

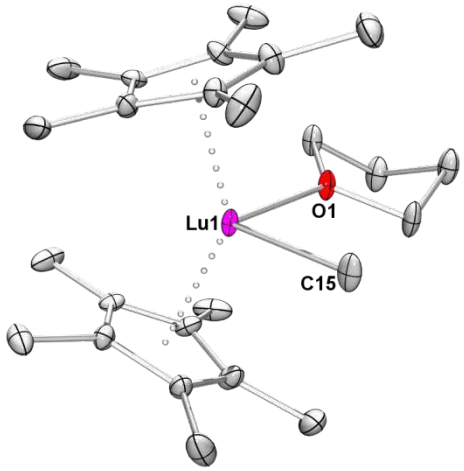

Fig. S34. ORTEP representation (50% probability ellipsoids) of $[(C_5Me_5)_2LuMe(thf)]$. Hydrogen atoms and disorder in the thf and C_5Me_5 ligands have been omitted for clarity. Selected bond lengths (Å) and angles (°): Lu1–C15 2.33(1), Lu1–O1 2.324(9); C15-Lu1-O1 89.1(4).

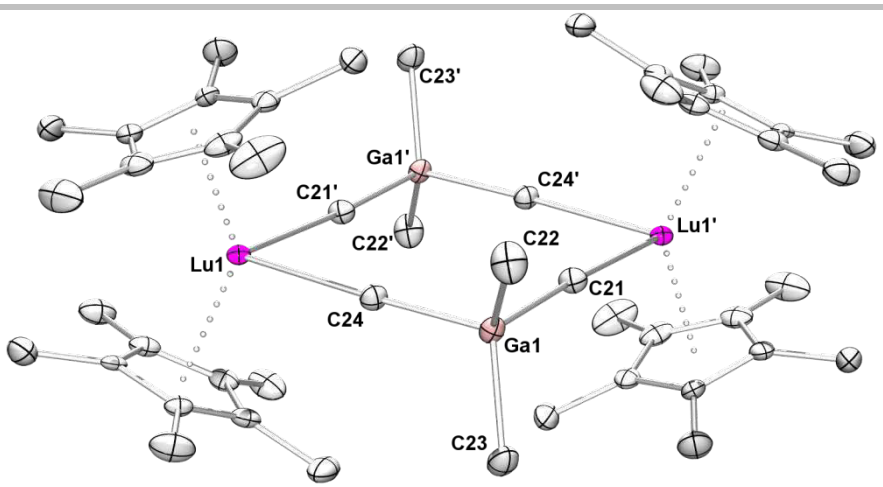

Fig. S35. ORTEP representation (50% probability ellipsoids) of $[(C_5Me_5)_2Lu(\{\mu\text{-}Me\}_2GaMe_2)]$ (**1**^{Lu}). Hydrogen atoms, co-crystallized solvent molecules (toluene) and disorder in one C_5Me_5 ligand have been omitted for clarity. Selected bond lengths (Å) and angles (°): Lu1–C21' 2.633(3), Lu1–C24 2.594(7), Ga1–C21 2.082(3), Ga1–C22 1.990(3), Ga1–C23 1.992(3), Ga1–C24 2.072(3); Lu1-C21'-Ga1' 174.2(1), Lu1-C24-Ga1 175.9(1), C21-Ga1-C24 99.6(1), C22-Ga1-C23 115.4(1).

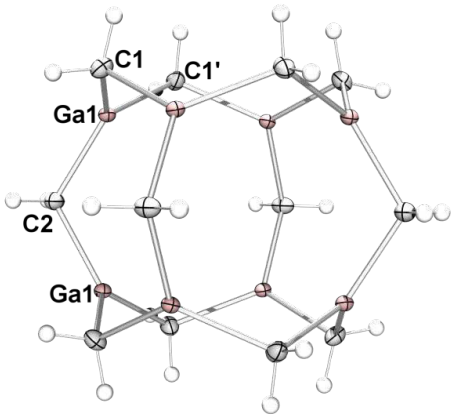

Fig. S36. ORTEP representation (50% probability ellipsoids) of $[Ga_8(\mu\text{-}CH_2)_{12}]$ (**2**). Selected bond lengths (Å) and angles (°): Ga1–C1 1.972(2), Ga1–C1' 1.960(2); C1-Ga1-C1' 118.8(1), C1-Ga1-C2 119.9(1), C1'-Ga1-C2 120.5(1).

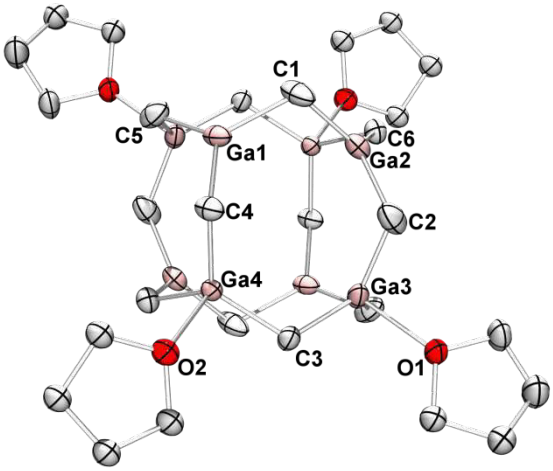

Fig. S37. ORTEP representation (50% probability ellipsoids) of $[Ga_8(\mu\text{-}CH_2)_{12}(thf)_4]$ (**4**). Hydrogen atoms and the disorder in coordinated thf molecules have been omitted for clarity. Selected bond lengths (Å) and angles (°): Ga1–C1 1.968(3), Ga1–C4 1.951(3), Ga1–C5 1.951(4), Ga2–C2 1.942(3), Ga4–C4 1.992(3); Ga1-C1-Ga2 111.6(1), Ga3-C3-Ga4 117.7(1), Ga3–O1 2.226(4), Ga4–O2 2.215(2).

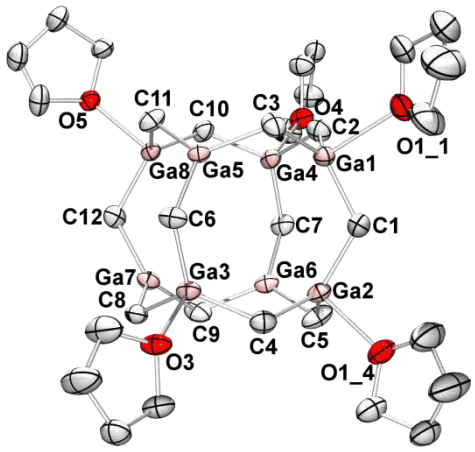

Fig. S38. ORTEP representation (50% probability ellipsoids) of $[Ga_8(\mu\text{-}CH_2)_{12}(thf)_5]$ (**5**). Hydrogen atoms and the disorder in coordinated thf molecules have been omitted for clarity. Selected bond lengths (Å) and angles (°): Ga2–C5 1.984(5), Ga3–C8 1.981(4), Ga4–C7 1.981(4), Ga5–C3 1.946(4), Ga6–C5 1.931(5), Ga6–C7 1.941(4), Ga8–C3 1.986(4), Ga2–O1_4 2.18(3), Ga1–O1_1 2.34(1); Ga1-C3-Ga5 113.7(2), Ga2-C4-Ga3 122.3(2).

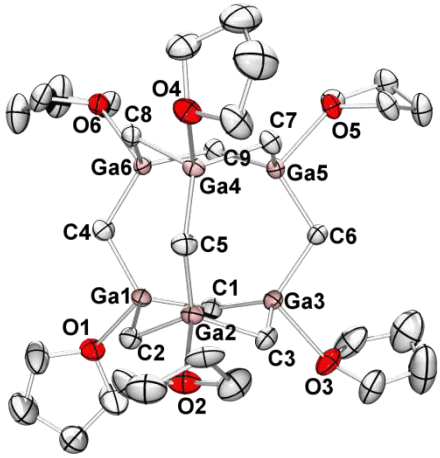

Fig. S39. ORTEP representation (50% probability ellipsoids) of $[Ga_6(\mu\text{-}CH_2)_9(thf)_6]$ (**3**). Hydrogen atoms and the disorder in coordinated thf molecules have been omitted for clarity. Selected bond lengths (Å) and angles (°): Ga1–C1 1.975(8), Ga1–C2 1.977(8), Ga1–C4 1.971(8), Ga1–O1 2.286(5), Ga3–C6 1.961(7), Ga3–C1 1.994(7); C2-Ga2-C3 109.6(3), C5-Ga2-C3 122.4(4), Ga4-C8-Ga6 106.7(3), Ga4-C5-Ga2 119.4(3).

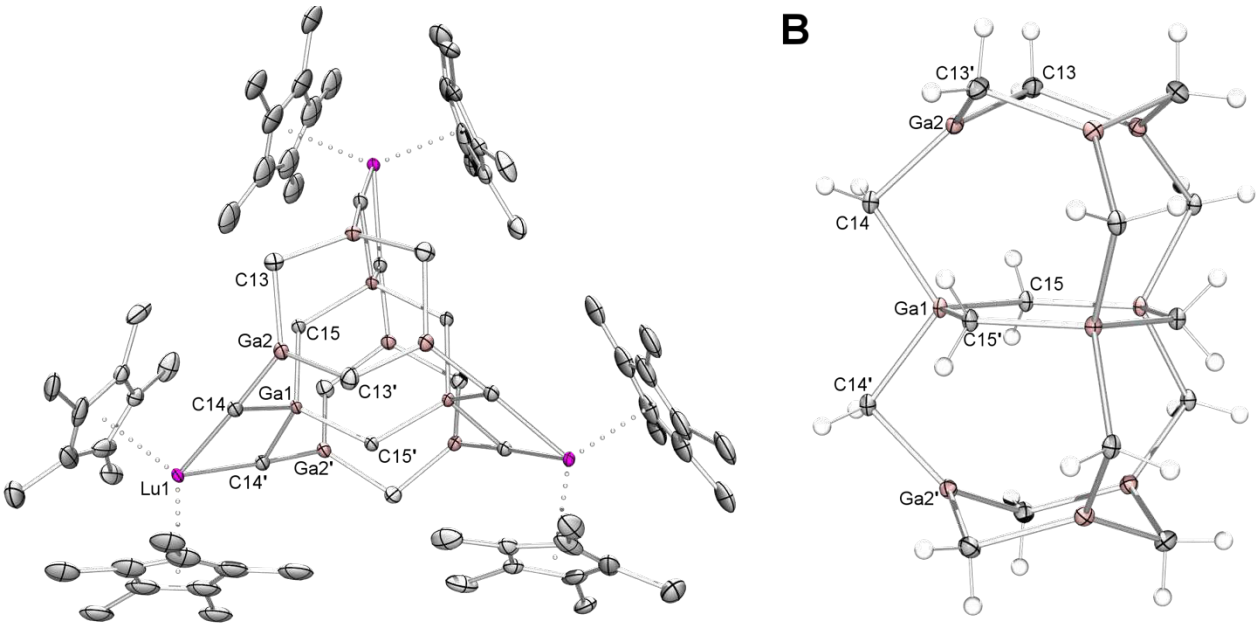

Fig. S40. ORTEP representation (50% probability ellipsoids) of $[(C_5Me_5)_6Lu_3(\mu_3\text{-}CH_2)_6Ga_9(CH_2)_9]$ (**6^{Lu}**, **A**) and its Ga methylene core (**B**). Hydrogen atoms, the disorder in the C_5Me_5 ligands and co-crystallized solvent (benzene) have been omitted for clarity. Selected bond lengths (Å) and angles (°): Lu1–C14 2.510(6), Ga1–C14 2.125(6), Ga1–C15 2.008(7), Ga1–C15' 1.999(7), Ga2–C13 1.961(6), Ga2–C13' 1.973(6), Ga2–C14 1.972(6); Lu1-C14-Ga1 83.8(2), Lu1-C14-Ga2 177.5(3), Ga1-C14-Ga2 95.6(2), C13-Ga2-C13' 114.3(3), C13-Ga2-C14 123.2(2), C13'-Ga2-C14 122.0(2), C14-Ga1-C15 108.8 (2), C14-Ga1-C15' 106.5(2), C14-Ga1-C14', 106.7(3), C15-Ga1-C15', 118.9(4).

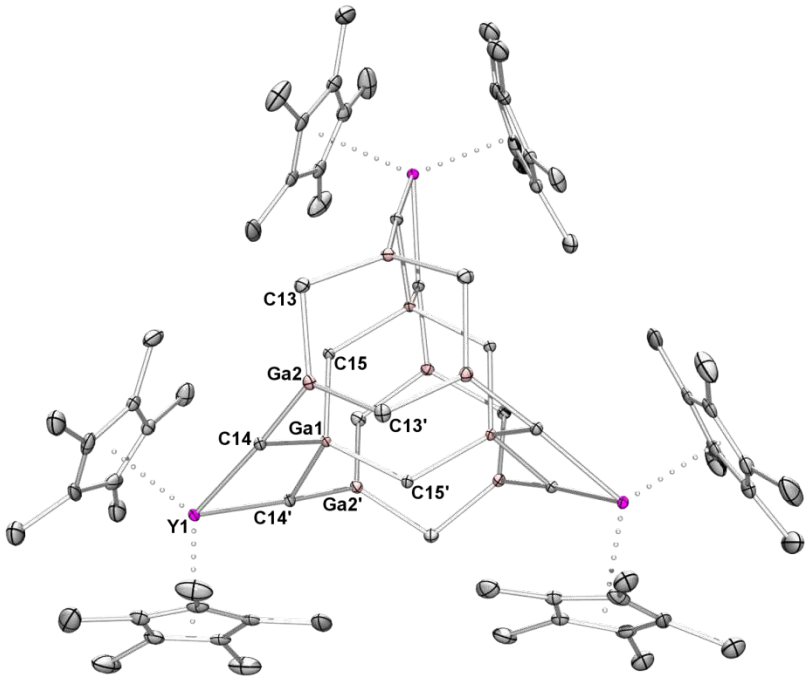

Fig. S41. ORTEP representation (50% probability ellipsoids) of $[(C_5Me_5)_6Y_3(\mu_3\text{-}CH_2)_6Ga_9(CH_2)_9]$ (**6^{Y}**). Hydrogen atoms, the disorder in the C_5Me_5 ligands and co-crystallized solvent (benzene) have been omitted for clarity. Selected bond lengths (Å) and angles (°): Y1–C14 2.565(4), Ga1–C14 2.121(4), Ga1–C15 2.001(5), Ga2–C13 1.967(4), Ga2–C14 1.971(4); Y1-C14-Ga1 84.5(1), Y1-C14-Ga2 176.9(2), Ga1-C14-Ga2 96.4(2), C13-Ga2-C13' 114.2(2), C15-Ga1-C15, 118.7(3).

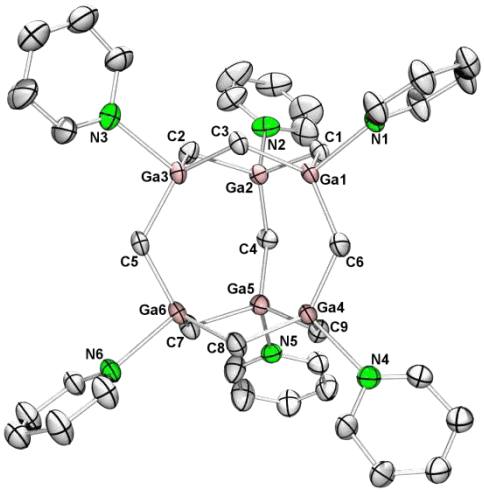

Fig. S42. ORTEP representation (50% probability ellipsoids) of $[Ga_6(\mu\text{-}CH_2)_9(pyr\text{-}d_5)_6]$ (**7**). Hydrogen atoms, the disorder in four of the coordinated pyridine molecules and co-crystallized pyridine have been omitted for clarity. Selected bond lengths (Å) and angles (°): Ga1–C1 1.989(4), Ga1–C3 1.984(4), Ga1–C6 1.987(4), Ga1–N1 2.209(3), Ga2–C4 1.970(4), Ga2–C2 1.990(4); Ga1-C1-Ga2 109.9(1), Ga1-C3-Ga3 109.1(1), Ga1-C6-Ga4 120.2(2).

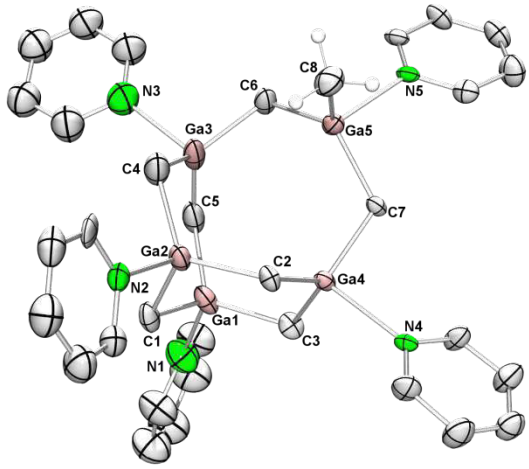

Fig. S43. ORTEP representation (50% probability ellipsoids) of $[Ga_5(\mu\text{-}CH_2)_7(Me)(pyr\text{-}d_5)_5]$ (**8**). Hydrogen atoms, a second molecule of **8**, two co-crystallized molecules of **7** and co-crystallized pyridine have been omitted for clarity. Selected bond lengths (Å) and angles (°): Ga1–C1 1.97(2), Ga1–C3 2.02(2), Ga1–C5 2.04(2), Ga1–N1 2.14(2), Ga3–C4 1.98(2), Ga3–C5 1.90(2), Ga3–C6 1.99(2), Ga3–N3 2.22(2), Ga5–C6 1.97(2), Ga5–C7 2.01(2), Ga5–C8 2.04(2), Ga5–N5 2.01(2); Ga1-C1-Ga2 101.3(8), Ga1-C5-Ga3 114(1), Ga3-C6-Ga5 110.4(9).

DFT Model Systems and Thermochemical Data

Computational Details. DFT calculations were carried out in the gas phase with the Gaussian 09 program suite[13] using the M06-2X density functional.[14] All geometry optimizations were performed with the implemented 6-311G(d,p) basis set[15] and without imposing any symmetry constraints, except for the following model systems, which were optimized within the symmetries given: $[Ga_8(\mu\text{-}CH_2)_{12}]$ (**2**) *T*, $[Ga_6(\mu\text{-}CH_2)_9]$ D_{3h}, $[Ga_6(\mu\text{-}CH_2)_9(pyr)_6]$ C_s, pyridine C_{2v}. All structures obtained were confirmed as true minima by calculating analytical frequencies. For the thermal energy corrections and the zero-point energies a scale factor of 0.970 was applied.[16] The larger basis set 6-311G(2df,2p) was employed for the energy calculations. Plots were generated with the software Chemcraft.[17]

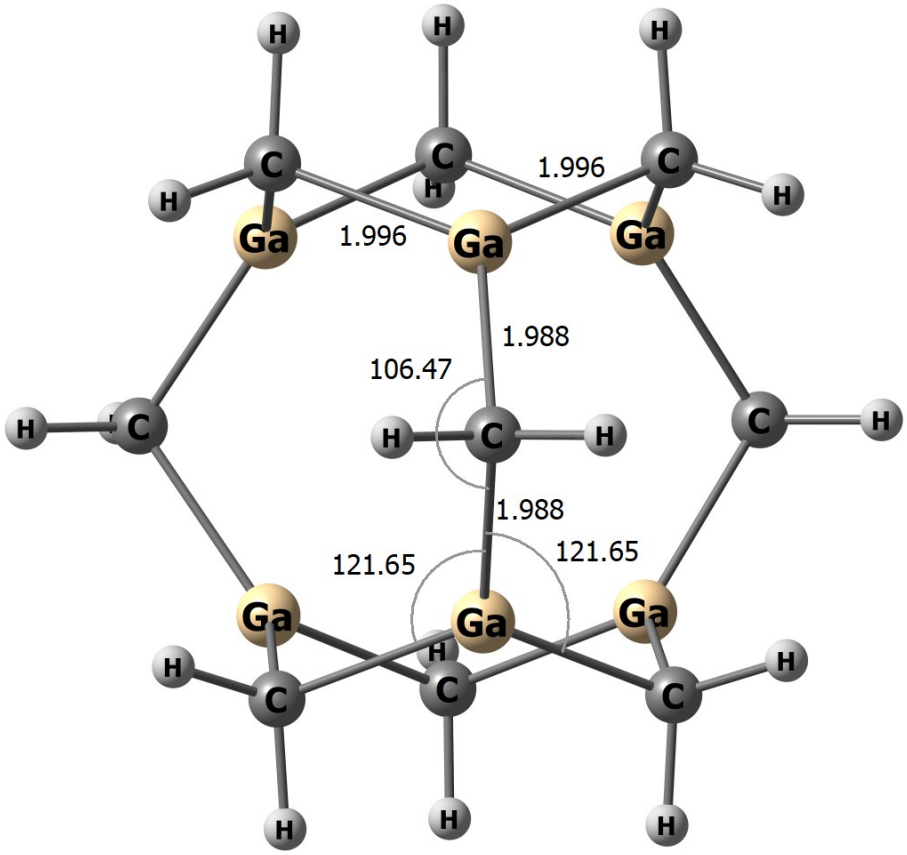

Fig. S44. Optimized geometry and selected geometrical parameters for the DFT-optimized model system $[Ga_6(\mu\text{-}CH_2)_9]$ in D_{3h} symmetry; distances in Å, angles in deg.

Cartesian Coordinates for $[Ga_6(\mu\text{-}CH_2)_9]$, D_{3h} symmetry:

6	1.671563000	0.965078000	2.248999000
6	0.000000000	3.026070000	0.000000000
6	-1.671563000	0.965078000	2.248999000
6	1.671563000	0.965078000	-2.248999000
6	0.000000000	-1.930155000	2.248999000
6	2.620653000	-1.513035000	0.000000000
6	-1.671563000	0.965078000	-2.248999000
6	-2.620653000	-1.513035000	0.000000000
6	0.000000000	-1.930155000	-2.248999000
1	1.608833000	0.928860000	3.343482000
1	0.895774000	3.651530000	0.000000000
1	2.581625000	1.490502000	1.956766000
1	-0.895774000	3.651530000	0.000000000
1	-1.608833000	0.928860000	3.343482000
1	-2.581625000	1.490502000	1.956766000
1	2.581625000	1.490502000	-1.956766000

1	0.000000000	-1.857721000	3.343482000
1	3.610205000	-1.050003000	0.000000000
1	1.608833000	0.928860000	-3.343482000
1	-2.581625000	1.490502000	-1.956766000
1	2.714431000	-2.601528000	0.000000000
1	0.000000000	-2.981004000	1.956766000
1	-1.608833000	0.928860000	-3.343482000
1	-3.610205000	-1.050003000	0.000000000
1	-2.714431000	-2.601528000	0.000000000
1	0.000000000	-1.857721000	-3.343482000
1	0.000000000	-2.981004000	-1.956766000
31	0.000000000	1.836338000	1.592357000
31	0.000000000	1.836338000	-1.592357000
31	1.590315000	-0.918169000	1.592357000
31	-1.590315000	-0.918169000	1.592357000
31	1.590315000	-0.918169000	-1.592357000
31	-1.590315000	-0.918169000	-1.592357000

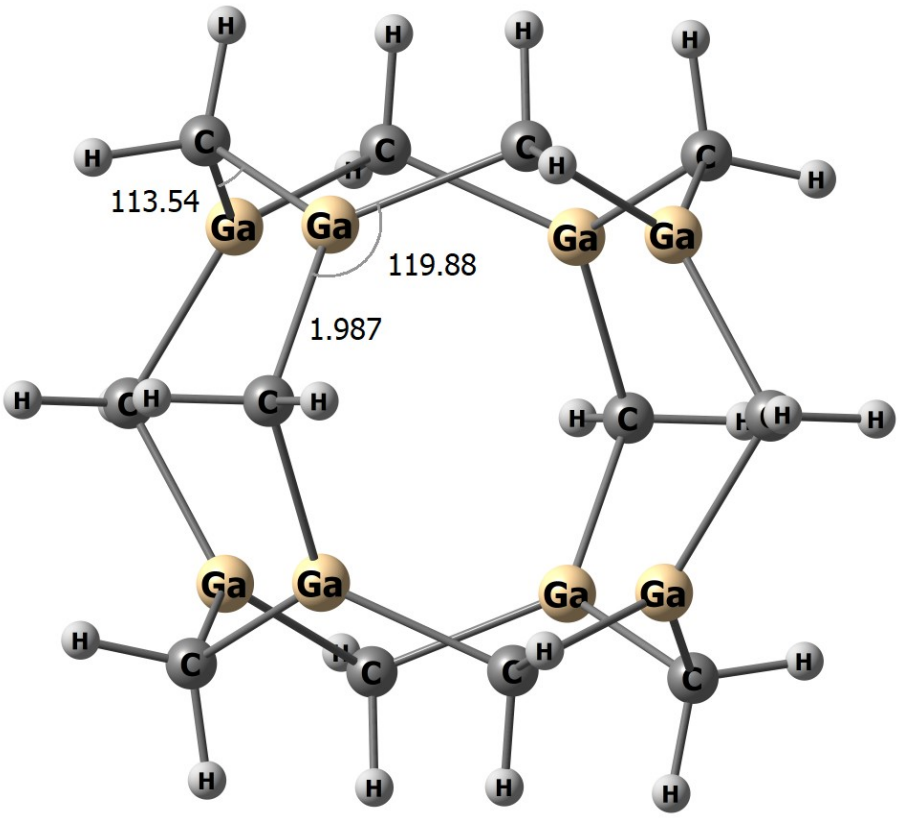

Fig. S45. Optimized geometry and selected geometrical parameters for the DFT-optimized model system [$Ga_8(\mu\text{-}CH_2)_{12}$] in *T* symmetry; distances in Å, angles in deg.

Cartesian Coordinates for [$Ga_8(\mu\text{-}CH_2)_{12}$], *T* symmetry:

6	0.000000000	2.429734000	2.433756000
1	0.000000000	2.242706000	3.511817000
1	0.000000000	3.508605000	2.251291000
6	2.433756000	0.000000000	2.429734000
1	2.251291000	0.000000000	3.508605000
1	3.511817000	0.000000000	2.242706000
6	2.429734000	2.433756000	0.000000000
1	2.242706000	3.511817000	0.000000000
1	3.508605000	2.251291000	0.000000000
6	-2.429734000	2.433756000	0.000000000
1	-3.508605000	2.251291000	0.000000000
1	-2.242706000	3.511817000	0.000000000
6	-2.433756000	0.000000000	2.429734000
1	-2.251291000	0.000000000	3.508605000
1	-3.511817000	0.000000000	2.242706000
6	0.000000000	2.429734000	-2.433756000
1	0.000000000	2.242706000	-3.511817000
1	0.000000000	3.508605000	-2.251291000
6	0.000000000	-2.429734000	2.433756000
1	0.000000000	-3.508605000	2.251291000
1	0.000000000	-2.242706000	3.511817000
6	-2.433756000	0.000000000	-2.429734000
1	-3.511817000	0.000000000	-2.242706000
1	-2.251291000	0.000000000	-3.508605000
6	-2.429734000	-2.433756000	0.000000000
1	-2.242706000	-3.511817000	0.000000000
1	-3.508605000	-2.251291000	0.000000000
6	2.429734000	-2.433756000	0.000000000
1	2.242706000	-3.511817000	0.000000000
1	3.508605000	-2.251291000	0.000000000
6	2.433756000	0.000000000	-2.429734000
1	3.511817000	0.000000000	-2.242706000
1	2.251291000	0.000000000	-3.508605000
6	0.000000000	-2.429734000	-2.433756000
1	0.000000000	-2.242706000	-3.511817000
1	0.000000000	-3.508605000	-2.251291000
31	1.661859000	1.661859000	1.661859000
31	-1.661859000	1.661859000	1.661859000
31	-1.661859000	1.661859000	-1.661859000
31	1.661859000	-1.661859000	1.661859000
31	1.661859000	1.661859000	-1.661859000
31	-1.661859000	-1.661859000	1.661859000
31	-1.661859000	-1.661859000	-1.661859000
31	1.661859000	-1.661859000	-1.661859000

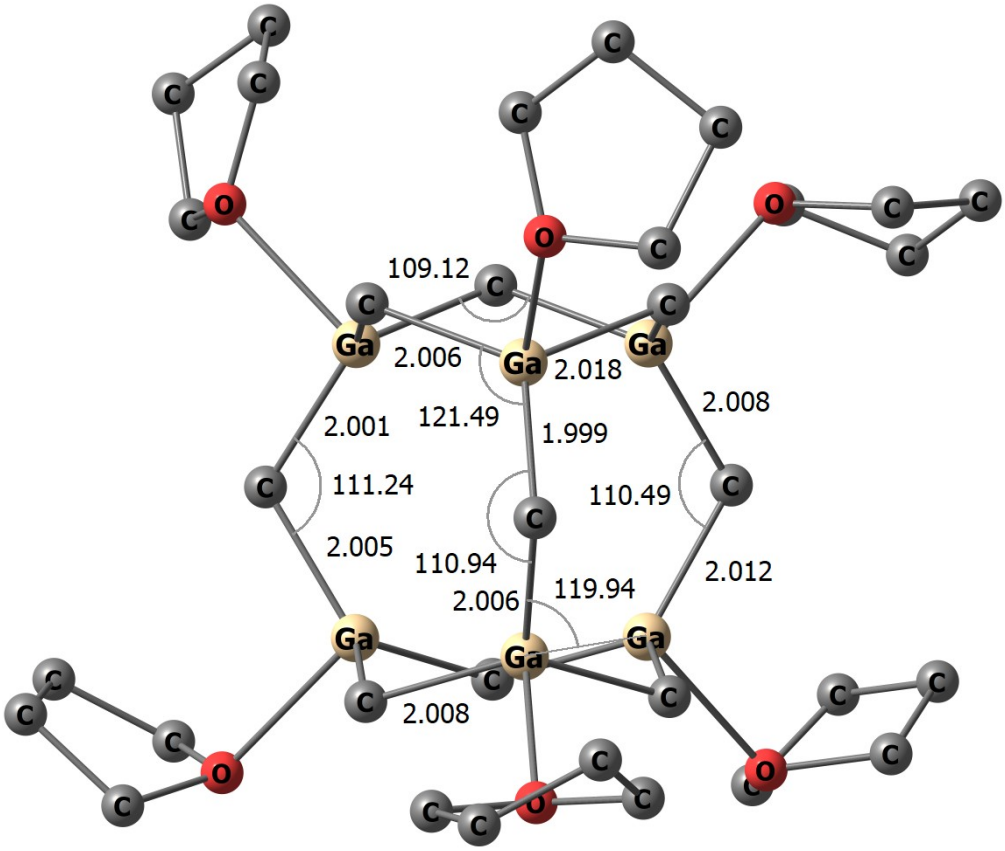

Fig. S46. Optimized geometry and selected geometrical parameters for the DFT-optimized model system $[Ga_6(\mu\text{-}CH_2)_9(thf)_6]$ in C_1 symmetry; distances in Å, angles in deg; all hydrogen atoms are omitted for clarity.

Cartesian Coordinates for $[Ga_6(\mu\text{-}CH_2)_9(thf)_6]$, C_1 symmetry:

6	4.141180000	-3.610261000	2.961585000
6	3.476807000	-4.749103000	2.151752000
6	4.780821000	-2.730779000	1.885242000
6	3.642265000	-4.309501000	0.685796000
6	3.033798000	0.169491000	1.006016000
6	4.352939000	3.352070000	1.500636000
6	0.862123000	-2.463926000	1.683537000
6	-3.180858000	-4.905896000	3.145163000
6	4.505243000	4.858910000	1.701292000
6	-1.852953000	-4.274266000	2.747298000
6	1.923822000	-1.816262000	-1.515070000
6	-4.145549000	-3.737774000	2.925583000
6	3.370676000	5.411447000	0.833477000
6	-3.324791000	-2.563523000	3.444852000
6	3.429022000	4.472390000	-0.362282000
6	1.858167000	-1.678057000	-5.024947000
6	-1.083301000	0.244064000	2.731707000
6	1.815923000	1.576299000	-1.845608000
6	0.761754000	2.786538000	1.202301000
6	0.507820000	-1.791832000	-5.737125000
6	-2.165785000	-1.704557000	0.197783000
6	1.236347000	0.498204000	-5.357136000
6	-0.944806000	-0.266420000	-2.702969000

6	0.144544000	-0.324006000	-6.065090000
6	-3.343419000	2.906958000	3.177606000
6	-2.230304000	1.667032000	-0.102162000
6	-2.315149000	4.565392000	1.845547000
6	-4.314509000	4.069820000	3.006201000
6	-4.272738000	-1.399780000	-2.756917000
6	-3.825560000	4.682943000	1.691378000
6	-4.247529000	-0.937144000	-4.206313000
6	-4.376148000	0.958305000	-2.773961000
6	-4.932449000	0.428225000	-4.095152000
31	2.162414000	-1.550168000	0.461525000
31	-0.885218000	-1.489664000	1.742342000
31	2.076666000	1.706600000	0.138940000
31	1.025333000	-0.207075000	-2.301137000
31	-0.949273000	1.783562000	1.453314000
31	-2.012345000	-0.109532000	-1.010099000
8	3.959636000	-2.916837000	0.731918000
8	3.765948000	3.189954000	0.193327000
8	-1.956138000	-2.894788000	3.148606000
8	1.837668000	-0.388923000	-4.412655000
8	-2.105511000	3.354325000	2.595925000
8	-4.062618000	-0.206330000	-1.984542000

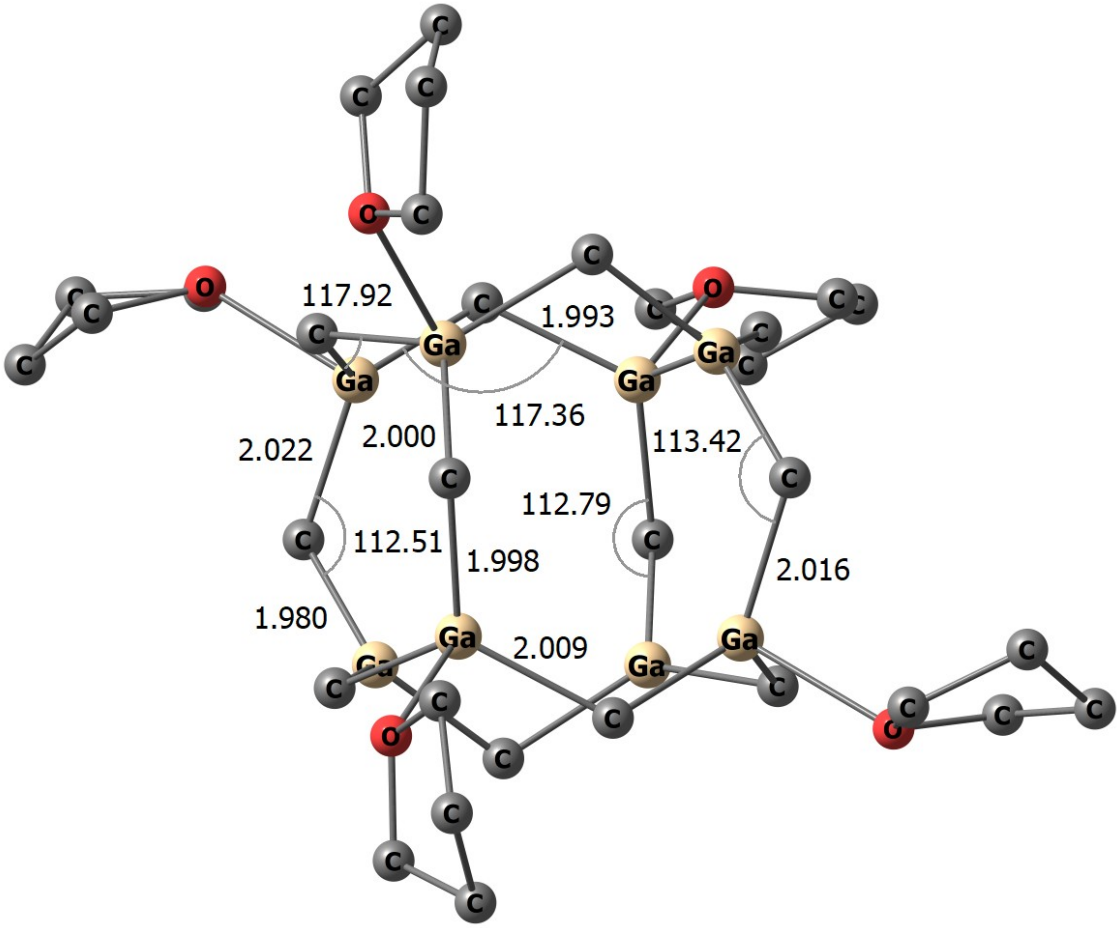

Fig. S47. Optimized geometry and selected geometrical parameters for the DFT-optimized model system $[Ga_8(\mu\text{-}CH_2)_{12}(thf)_5]$ in C_1 symmetry; distances in Å, angles in deg; all hydrogen atoms are omitted for clarity.

Cartesian Coordinates for $[Ga_8(\mu\text{-}CH_2)_{12}(thf)_5]$, C_1 symmetry:

8	-4.362057000	-2.801218000	-0.568422000
6	-4.155007000	-4.072383000	-1.213323000
6	-5.074069000	-4.057860000	-2.427736000
6	-6.255355000	-3.236460000	-1.905294000
6	-5.542157000	-2.162805000	-1.091222000
8	0.532544000	-3.939539000	2.801447000
6	-0.543568000	-4.152973000	3.733772000
6	0.083286000	-3.981221000	5.110445000
6	1.490660000	-4.535991000	4.874336000
6	1.801699000	-4.003479000	3.479463000
6	-1.351824000	-2.828752000	0.455680000
6	2.069773000	-2.264312000	0.569266000
6	0.031518000	-0.841122000	2.928054000
6	-3.400669000	0.001729000	0.616413000
6	-2.330463000	-1.247395000	-2.411241000
6	-1.234714000	2.256914000	2.129795000
6	1.059394000	-1.817563000	-2.722198000
6	-2.236579000	2.764325000	-1.108677000
6	-0.251589000	1.261088000	-3.462163000
6	3.185746000	0.450573000	-1.232749000
6	2.124983000	1.651170000	1.828095000

6	1.166905000	3.262769000	-1.057385000
6	-5.325261000	3.084585000	0.422186000
6	-5.460673000	4.552268000	0.040014000
6	-5.019529000	5.245161000	1.331865000
6	4.651463000	-2.035935000	-3.131691000
6	-3.862532000	4.357350000	1.776109000
6	6.064787000	-1.597152000	-2.773061000
6	6.418746000	-2.588862000	-1.661781000
6	5.099389000	-2.683477000	-0.902794000
6	5.248598000	2.706857000	0.768890000
6	3.861197000	4.598962000	0.476249000
31	0.264072000	-2.169788000	1.423638000
31	-2.537052000	-1.477179000	-0.413443000
31	-2.477723000	1.768210000	0.631153000
31	2.264672000	-1.334476000	-1.188242000
31	0.308988000	1.030938000	2.344777000
31	-0.516319000	-0.639898000	-2.920583000
31	-0.444719000	2.488308000	-1.909459000
31	2.348445000	1.908492000	-0.158483000
8	-4.204754000	3.031947000	1.324987000
8	4.073418000	-2.492532000	-1.894500000
8	4.143775000	3.258212000	0.029106000
6	5.441036000	3.641229000	1.956001000
6	5.048448000	4.990534000	1.348344000

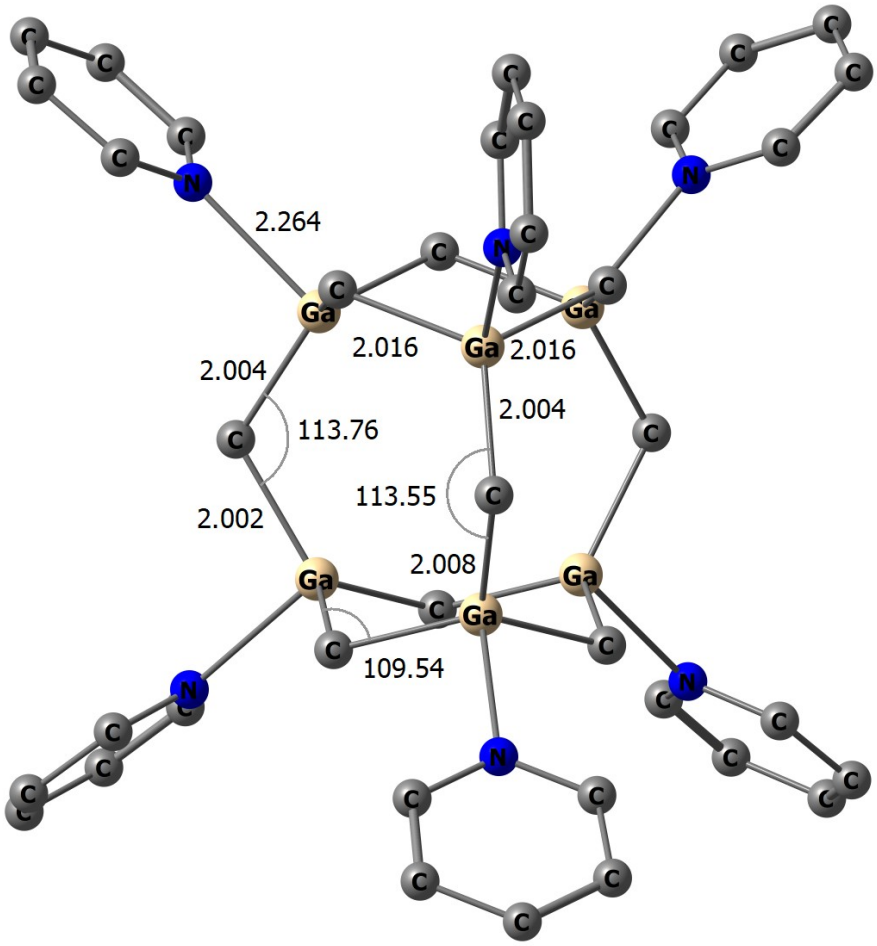

Fig. S48. Optimized geometry and selected geometrical parameters for the DFT-optimized model system $[Ga_6(\mu\text{-}CH_2)_9(pyr)_6]$ in C_s symmetry; distances in Å, angles in deg; all hydrogen atoms are omitted for clarity.

Cartesian Coordinates for $[Ga_6(\mu\text{-}CH_2)_9(pyr)_6]$, C_s symmetry:

6	-1.958022000	2.238143000	0.000000000
6	0.992407000	2.249266000	1.682232000
6	0.992407000	2.249266000	-1.682232000
6	-1.490705000	-0.001366000	2.596133000
6	3.012743000	-0.031083000	0.000000000
6	-1.490705000	-0.001366000	-2.596133000
6	0.975553000	-2.259726000	1.702907000
6	0.975553000	-2.259726000	-1.702907000
6	-1.969241000	-2.250026000	0.000000000
6	-1.027865000	3.624491000	-4.123326000
6	-1.532338000	4.473616000	-5.099535000
6	-2.860528000	4.871022000	-5.012460000
6	-3.634573000	4.407847000	-3.955681000
6	-3.047733000	3.561628000	-3.024536000
6	-3.047733000	3.561628000	3.024536000
6	-3.634573000	4.407847000	3.955681000
6	-3.067011000	-3.601168000	2.991586000
6	-3.662105000	-4.441874000	3.922735000
6	-2.913721000	-4.856070000	5.017296000
6	-1.601553000	-4.416881000	5.141251000
6	-1.087512000	-3.577216000	4.162307000
31	-0.936574000	1.672849000	-1.644790000
31	-0.936574000	1.672849000	1.644790000
31	1.932572000	1.656943000	0.000000000
31	-0.956329000	-1.682031000	-1.648401000
31	-0.956329000	-1.682031000	1.648401000
31	1.894599000	-1.699454000	0.000000000
7	-1.773414000	3.180483000	-3.111524000
7	-1.773414000	3.180483000	3.111524000
7	3.641357000	3.159919000	0.000000000
7	-1.808249000	-3.180330000	-3.113616000
7	-1.808249000	-3.180330000	3.113616000
7	3.580008000	-3.209292000	0.000000000
6	-2.860528000	4.871022000	5.012460000
6	-1.532338000	4.473616000	5.099535000
6	-1.027865000	3.624491000	4.123326000
6	3.349630000	4.461309000	0.000000000
6	4.328082000	5.444578000	0.000000000
6	5.661858000	5.053418000	0.000000000
6	5.964582000	3.698757000	0.000000000
6	4.919305000	2.782733000	0.000000000
6	-3.067011000	-3.601168000	-2.991586000
6	-3.662105000	-4.441874000	-3.922735000
6	-2.913721000	-4.856070000	-5.017296000
6	-1.601553000	-4.416881000	-5.141251000
6	-1.087512000	-3.577216000	-4.162307000
6	4.108518000	-3.627320000	1.150075000
6	5.198628000	-4.486051000	1.197070000
6	5.752506000	-4.922171000	0.000000000
6	5.198628000	-4.486051000	-1.197070000
6	4.108518000	-3.627320000	-1.150075000

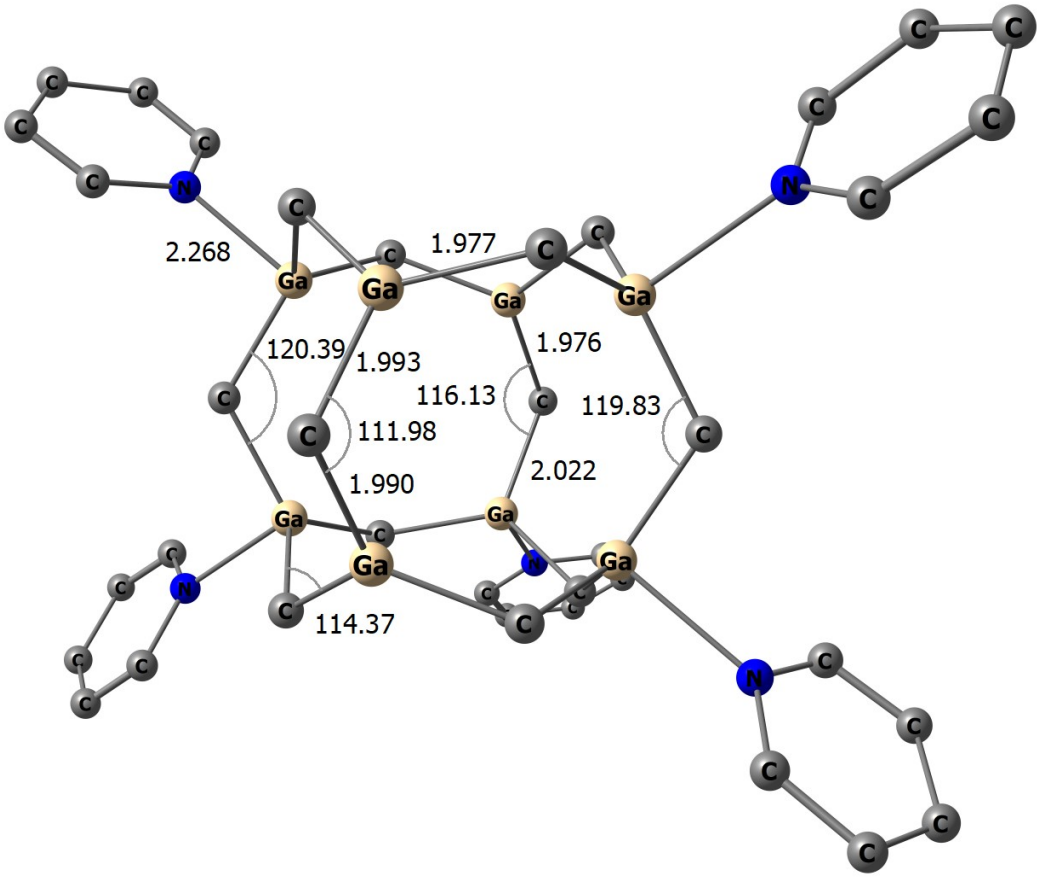

Fig. S49. Optimized geometry and selected geometrical parameters for the DFT-optimized model system $[Ga_8(\mu\text{-}CH_2)_{12}(pyr)_5]$ in C_1 symmetry; distances in Å, angles in deg; all hydrogen atoms are omitted for clarity.

Cartesian Coordinates for $[Ga_8(\mu\text{-}CH_2)_{12}(pyr)_5]$, C_1 symmetry:

6	-1.556115000	2.644874000	-0.215778000
6	1.898762000	2.319639000	-0.587571000
6	-0.281537000	0.833027000	-2.827877000
6	-3.445693000	-0.249799000	-0.019170000
6	-1.828198000	0.995749000	2.796887000
6	-1.568415000	-2.251826000	-2.116525000
6	1.591633000	1.409703000	2.725354000
6	-1.910597000	-3.100675000	1.211695000
6	0.269983000	-1.662355000	3.396012000
6	3.421620000	-0.586690000	0.597887000
6	1.832271000	-1.830523000	-2.237694000
6	1.513706000	-3.463176000	0.770283000
31	0.040710000	2.133009000	-1.313328000
31	-2.461713000	1.244251000	0.894289000
31	-2.518310000	-1.990220000	-0.361107000
31	2.493812000	1.158975000	0.937208000
31	0.004849000	-1.077075000	-2.410820000
31	-0.000467000	0.269355000	3.003219000
31	-0.044792000	-2.801172000	1.791091000
31	2.467091000	-2.075678000	-0.343529000
7	-4.346354000	-3.258677000	-0.804010000
6	-5.273369000	-3.368532000	0.149705000
6	-4.510251000	-3.927934000	-1.945122000
6	-6.408983000	-4.150186000	-0.001155000
6	-5.616623000	-4.734277000	-2.182149000

6	-6.582835000	-4.845692000	-1.191883000
7	-4.343967000	2.442814000	1.399220000
6	-4.701530000	2.776439000	2.638977000
6	-5.125367000	2.809139000	0.381595000
6	-5.857193000	3.498129000	2.912652000
6	-6.295785000	3.531416000	0.561137000
6	-6.667131000	3.883258000	1.853491000
7	0.068747000	3.976038000	-2.673504000
6	-0.989124000	4.184926000	-3.459160000
6	1.090137000	4.830290000	-2.727410000
6	-1.072440000	5.262242000	-4.329032000
6	1.093252000	5.936326000	-3.568729000
6	-0.009200000	6.155651000	-4.382894000
7	4.366371000	2.384311000	1.402482000
6	5.300555000	2.474766000	0.454012000
6	4.547271000	3.036936000	2.550401000
6	6.459582000	3.219302000	0.616162000
6	5.677256000	3.806603000	2.799563000
6	6.650554000	3.897613000	1.814298000
7	4.316090000	-3.311331000	-0.787118000
6	4.676925000	-3.674392000	-2.017932000
6	5.074885000	-3.682789000	0.246045000
6	5.814737000	-4.432019000	-2.266506000
6	6.226155000	-4.440348000	0.090699000
6	6.601439000	-4.822685000	-1.191743000

Cartesian Coordinates for thf, C_1 symmetry:

6	-1.158904000	-0.426668000	-0.137737000
1	-1.946038000	-0.822826000	0.506447000
1	-1.507328000	-0.463173000	-1.176812000
6	-0.726900000	0.989638000	0.238773000
1	-0.765703000	1.123671000	1.322883000
1	-1.341559000	1.758454000	-0.229484000
6	0.726974000	0.989554000	-0.238843000
1	1.341698000	1.758407000	0.229298000
1	0.765799000	1.123397000	-1.322960000
6	1.158853000	-0.426711000	0.137882000
1	1.946185000	-0.822961000	-0.505988000
1	1.506902000	-0.463115000	1.177072000
8	-0.000012000	-1.243342000	-0.000113000

Cartesian Coordinates for pyridine, C_{2v} symmetry:

6	0.000000000	1.136988000	0.719582000
1	0.000000000	2.051692000	1.304549000
6	0.000000000	1.193372000	-0.670307000
1	0.000000000	2.150236000	-1.176729000
7	0.000000000	0.000000000	1.414013000
6	0.000000000	0.000000000	-1.380200000
1	0.000000000	0.000000000	-2.463835000
6	0.000000000	-1.193372000	-0.670307000
1	0.000000000	-2.150236000	-1.176729000
6	0.000000000	-1.136988000	0.719582000
1	0.000000000	-2.051692000	1.304549000

Table S4. Energies of the optimized geometries [basis set 6-311G(2df,2p)], zero-point (ZP) and thermal corrections to the free enthalpy [basis set 6-311G(d,p), scale factor 0.970, 298 K] for all DFT model systems

System	*E* [a.u.]	ZP correction [a.u.]	Thermal correction (*G*) [a.u.]
$[Ga_6(\mu\text{-}CH_2)_9]$	−11902.7625152	0.227657	0.178013
$[Ga_8(\mu\text{-}CH_2)_{12}]$	−15870.3787709	0.303776	0.244082
$[Ga_6(\mu\text{-}CH_2)_9(thf)_6]$	−13297.4207755	0.922171	0.817684 (298 K) 0.866732 (200 K)
$[Ga_8(\mu\text{-}CH_2)_{12}(thf)_5]$	−17032.5883828	0.881752	0.775885 (298 K) 0.825870 (200 K)
$[Ga_6(\mu\text{-}CH_2)_9(pyr)_6]$	−13392.4348987	0.753695	0.646292
$[Ga_8(\mu\text{-}CH_2)_{12}(pyr)_5]$	−17111.7661770	0.742574	0.634900
$[Ga_8(\mu\text{-}CH_2)_{12}(thf)]$	−16102.8236898	0.419426	0.347842
$[Ga_8(\mu\text{-}CH_2)_{12}(thf)_2]$	−16335.2676523	0.535160	0.455260
$[Ga_8(\mu\text{-}CH_2)_{12}(thf)_3]$	−16567.7089215	0.650728	0.562290
$[Ga_8(\mu\text{-}CH_2)_{12}(thf)_4]$	−16800.1493647	0.766277	0.668707
$[Ga_8(\mu\text{-}CH_2)_{12}(thf)_6]$	−17265.0267979	0.997457	0.883005
$[Ga_8(\mu\text{-}CH_2)_{12}(thf)_7]$	−17497.4635619	1.112660	0.988846
$[Ga_8(\mu\text{-}CH_2)_{12}(thf)_8]$	−17729.8992584	1.228862	1.097967
thf	−232.416778994	0.114316	0.086081 (298 K) 0.096824 (200 K)
pyridine	−248.250920643	0.086758	0.059982

Table S5. Computed values for Δ*E* (zero-point corrected) and Δ*G*(298 K) for the reaction $[Ga_8(\mu\text{-}CH_2)_{12}(thf)_{n\text{-}1}] + thf \rightarrow [Ga_8(\mu\text{-}CH_2)_{12}(thf)_n]$ (*n* = 1-8)

n	Δ*E* [kJ/mol]	Δ*G* (298 K) [kJ/mol]
1	−70	−27
2	−68	−15
3	−61	−9.3
4	−59	−8.7
5	−55	−3.0
6	−53	−1.5
7	−50	−0.6
8	−45	+11

References

[1] H. M. Dietrich, K. W. Törnroos, E. Herdtweck, R. Anwander, *Organometallics* **2009**, *28*, 6739-6749.
[2] COSMO v. *1.61*, Bruker AXS Inc., Madison, WI **2012**.
[3] APEX2 v. *2012.10_0*, Bruker AXS Inc., Madison, WI **2012**.
[4] a) SAINT v. *8.34A*, Bruker AXS Inc., Madison, WI **2013**; b) SAINT v. *8.37A*, Bruker AXS Inc., Madison, WI **2015**.
[5] SADABS, L. Krause, R. Herbst-Irmer, G. M. Sheldrick, D. Stalke, *J. Appl. Cryst.* **2015**, *48*, 3-10.
[6] G. M. Sheldrick, TWINABS scaling for twinned crystals, version **2007/3**.
[7] G. Sheldrick, Shelx, *Acta Crystallogr.* **2008**, *Sect. A 64*, 112-122.
[8] a) SHELXTL, *Acta Crystallogr.* **2015**, *A71*, 3-8; b) Shelxl, *Acta Crystallogr.* **2015**, *C71*, 3-8.
[9] C. B. Hübschle, G. M. Sheldrick, B. Dittrich, SHELXLE, *J. Appl. Crystallogr.* **2011**, *44*, 1281-1284.
[10] D. Kratzert, J. J. Holstein, I. Krossing, *J. Appl. Crystallogr.* **2015**, *48*, 933-993.
[11] L. J. Farrugia, *J. Appl. Crystallogr.* **1999**, 32, 837-838.
[12] POV-Ray v. *3.6*, Persistence of Vision Pty. Ltd., Williamstown, Victoria, Australia, **2004** (http://www.povray.org/).
[13] M. J. Frisch, G. W. Trucks, H. B. Schlegel, G. E. Scuseria, M. A. Robb, J. R. Cheeseman, G. Scalmani, V. Barone, B. Mennucci, G. A. Petersson, H. Nakatsuji, M. Caricato, X. Li, H. P. Hratchian, A. F. Izmaylov, J. Bloino, G. Zheng, J. L. Sonnenberg, M. Hada, M. Ehara, K. Toyota, R. Fukuda, J. Hasegawa, M. Ishida, T. Nakajima, Y. Honda, O. Kitao, H. Nakai, T. Vreven, J. A. MontgomeryJr, J. E. Peralta, F. Ogliaro, M. Bearpark, J. J. Heyd, E. Brothers, K. N. Kudin, V. N. Staroverov, R. Kobayashi, J. Normand, K. Raghavachari, A. Rendell, J. C. Burant, S. S. Iyengar, J. Tomasi, M. Cossi, N. Rega, J. M. Millam, M. Klene, J. E. Knox, J. B. Cross, V. Bakken, C. Adamo, J. Jaramillo, R. Gomperts, R. E. Stratmann, O. Yazyev, A. J. Austin, R. Cammi, C. Pomelli, J. W. Ochterski, R. L. Martin, K. Morokuma, V. G. Zakrzewski, G. A. Voth, P. Salvador, J. J. Dannenberg, S. Dapprich, A. D. Daniels, Ö. Farkas, J. B. Foresman, J. V. Ortiz, J. Cioslowski and D. J. Fox, Gaussian 09, Revision D.01, Gaussian, Inc., Wallingford CT, **2013**.
[14] Y. Zhao, D. G. Truhlar, *Theo. Chem. Acc.* **2008**, *120*, 215-241.
[15] a) R. Krishnan, J. S. Binkley, R. Seeger, J. A. Pople, *J. Chem. Phys.* **1980**, *72*, 650-654; b) L. A. Curtiss, M. P. McGrath, J.-P. Blaudeau, N. E. Davis, R. C. Binning. Jr., L. Radom, *J. Chem. Phys.* **1995**, *103*, 6104-6113.
[16] a) I. M. Alecu, J. Zheng, Y. Zhao, D. G. Truhlar, *J. Chem. Theory Comput.* **2010**, *6*, 2872-2887; b) J. Zheng, D. G. Truhlar, unpublished, https://comp.chem.umn.edu/freqscale/version3b2.htm, **2014**.
[17] G. A. Zhurko, CHEMCRAFT, http://www.chemcraftprog.com.

Paper III

Rare-Earth-Metallocene Alkylaluminates Trigger Distinct Tetrahydrofuran Activation

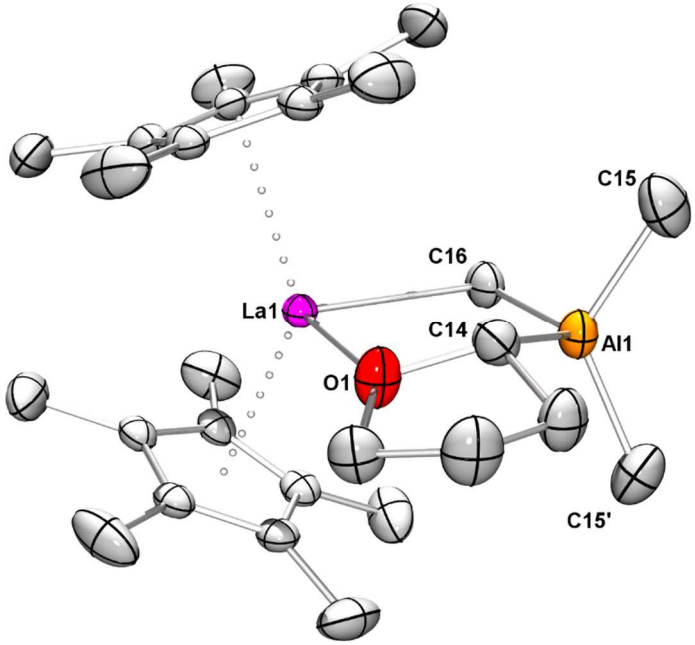

ChemComm

ROYAL SOCIETY OF CHEMISTRY

COMMUNICATION

Cite this: *Chem. Commun.*, 2021, **57**, 7918

Received 8th June 2021,
Accepted 7th July 2021

DOI: 10.1039/d1cc03024h

rsc.li/chemcomm

Rare-earth-metallocene alkylaluminates trigger distinct tetrahydrofuran activation†

Martin Bonath, Verena M. Birkelbach, Christoph Stuhl, Cäcilia Maichle-Mössmer and Reiner Anwander *

Thermal treatment of $Cp^*_2YMe(thf)$ ($Cp^* = C_5Me_5$), obtained from $Cp^*_2Y(AlMe_4)$ *via* donor-induced $AlMe_3$ cleavage, in THF resulted in the concomitant formation of vinyl oxide $Cp^*_2Y(OC_2H_3)(thf)$ and 2-ethylene-tetrahydrofuranyl complex $Cp^*_2Y(2\text{-}C_2H_4\text{-}OC_4H_7)$ *via* the release of methane. In stark contrast, dissolving $Cp^*_2La(AlMe_4)$ in THF/*n*-hexane led to the quantitative formation of $AlMe_3$-stabilized 2-tetrahydrofuranyl complex $Cp^*_2La(2\text{-}AlMe_3\text{-}OC_4H_7)$, with methane elimination.

(Half-)sandwich rare-earth-metal complexes are routinely used in catalytic polymerization[1] and heterofunctionalization/hydroelementation reactions,[2] involving hydrocarbyl or vinyl C–H-bond activation as pivotal mechanistic steps.[3,4] Moreover, the C–H-bond activation or *ortho*-metalation of heteroaromatics like pyridine or thiophene triggers a plethora of consecutive functionalization reactions[5] including olefin polymerization.[6] By contrast, the deprotonation/metalation of aliphatic cyclic ethers is far less effective and commonly results in either ring opening or intractable degradation reactions.[7,8] This can be ascribed to less Brønsted-acidic ring protons and the high negative charge at the oxygen atom causing severe destabilization of the ring system. Accordingly, it is quite challenging to master the delicate balance between the high basicity crucial for C–H-bond activation and stabilization of the emerging highly charged α-carbon atom. Hence, structurally characterized 2-tetrahydrofuranyl compounds are exceedingly rare and have not yet been described for the rare-earth metals (Fig. 1, **A**–**E**).[9–13] One approach to avoid ring-opening or cleavage reactions involves specific, heterobimetallic compounds like discrete (tmeda)Na(μ-tmp)(μ-CH_2SiMe_3)Zn(CH_2SiMe_3) (tmeda = *N*,*N*,*N*′,*N*′-tetramethylethylenediamine, tmp = 2,2,6,6-tetramethylpiperidido) as elegantly shown by Mulvey and co-workers in 2009 (Fig. 1, **D**).[12] While the organozinc moiety metalates THF, the adjacent alkali metal traps the highly reactive tetrahydrofuranyl anion *via* O-coordination (best yield of 53% after 2 weeks). Shortly after, the same group reported on a more efficient heterobimetallic system, when *in situ* formed [(thf)Li(tmp)(tmp)Al*i*Bu$_2$] (not isolable in pure form) afforded complex **E** (Fig. 1) in 35% yield overnight.[13]

Spurred on by the latter lithium-assisted metalation of THF by alkylaluminates, we wondered whether or not readily accessible heterobimetallic complexes $Cp^*_2Ln(AlMe_4)$ might display similar reactivity.

Yttrocene and lanthanocene tetramethylaluminates were chosen for their diamagnetic nature and any potential metal-size effect. It was clear that $Cp^*_2Y(AlMe_4)$ suffers $AlMe_3$ cleavage in THF to yield $Cp^*_2YMe(thf)$ (**1**).[14] Compound **1** was first synthesized by Teuben *et al.* applying a salt metathesis protocol [$Cp^*_2YCl(thf)$/MeLi/OEt_2/THF].[15] In contrast to solvent-free $[Cp^*_2YMe]_2$,[16] **1** does not activate hydrocarbons and aromatic solvents at ambient temperature and therefore proved to be a useful precursor in yttrocene chemistry. For example, **1** readily forms the tetramethylgallate $Cp^*_2Y(GaMe_4)$ upon addition of two equivalents of $GaMe_3$.[14] Furthermore, **1** metalates pyridine at the α position to afford the THF-stabilized yttrocene derivative

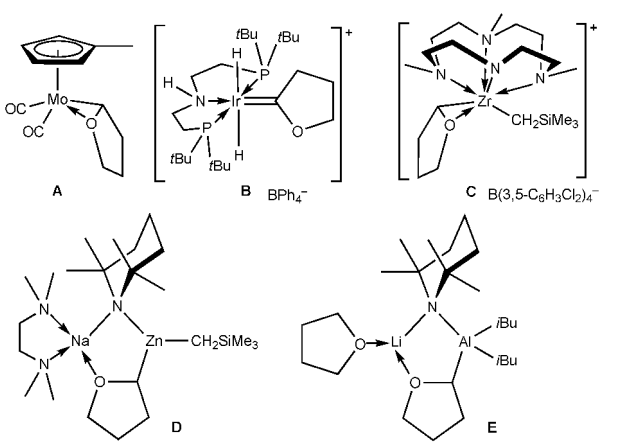

Fig. 1 Selected structurally authenticated 2-tetrahydrofuranyl complexes.

Institut für Anorganische Chemie, Eberhard Karls Universität Tübingen, Auf der Morgenstelle 18, Tübingen 72076, Germany.
E-mail: reiner.anwander@uni-tuebingen.de

† Electronic supplementary information (ESI) available. CCDC 2087233–2087236. For ESI and crystallographic data in CIF or other electronic format see DOI: 10.1039/d1cc03024h

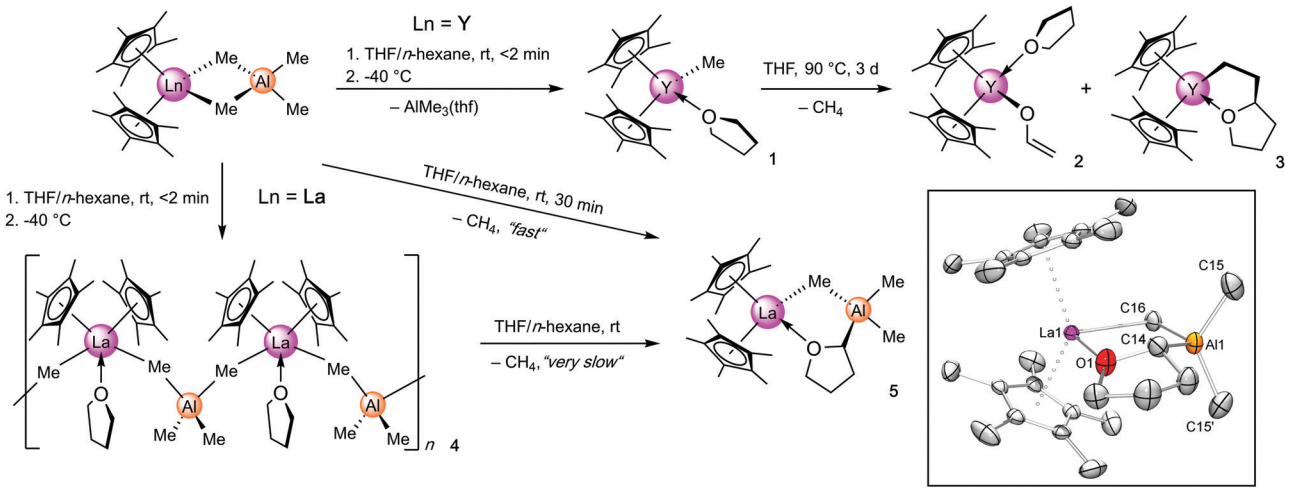

Scheme 1 Synthesis of THF-degradation/metalation products **2**, **3**, and **5** from $Cp^*_2Ln(AlMe_4)$ (Ln = Y and La). Crystal structure of $Cp^*_2La(2\text{-}AlMe_3\text{-}OC_4H_7)$ (**5**). All atoms are represented by atomic displacement ellipsoids set at 50% probability. Hydrogen atoms and disorder due to co-crystallized enantiomers are omitted for clarity. For detailed metrics, see ESI.†

$Cp^*_2Y(\eta^2\text{-}NC_5H_4)(thf)$.[17] Similarly, $[Cp^*_2LnMe]$ (Ln = Lu and Sc) form solvent-free $Cp^*_2Ln(\eta^2\text{-}NC_5H_4)$ upon addition of pyridine.[4b,18] Any activation/degradation of THF, however, was not observed in these reactions, although Bercaw *et al.* reported slow H/D exchange at the α position of THF in the scandium hydride complex $[Cp^*_2ScH(thf)]$ in THF-d_8 solutions.[4b] Since the reactivity of rare-earth-metallocene complexes tends to increase with increasing Ln(III) ionic radius, we were intrigued to find out whether **1** is prone to α activation of THF at elevated temperatures. Indeed, stirring **1** in THF solutions for three days at 90 °C consumed all the starting material. However, the ^{1}H NMR spectrum did not indicate the formation of a putative tetrahydrofuranyl compound such as $[Cp^*_2Y(\eta^2\text{-}OC_4H_7)(thf)]$. Instead, the ^{1}H NMR signal sets account for the presence of vinyloxide $Cp^*_2Y(OC_2H_3)(thf)$ (**2**) and the chiral ethylene-2-tetrahydrofuranyl compound $Cp^*_2Y(2\text{-}C_2H_4\text{-}OC_4H_7)$ (**3**) (Scheme 1) as the main products in an approximate ratio of 3 : 2. Fractional crystallization from *n*-pentane solutions allowed the separation of **2** and **3** and their isolation in high purity. The ^{1}H NMR spectrum of **2** in C_6D_6 shows three doublets of doublets at 7.25 (1H, $^3J(H,H)_{cis}$ = 5.5 Hz, $^3J(H,H)_{trans}$ = 13.7 Hz), 4.19 (1H, $^2J(H,H)_{geminal}$ = 0.6 Hz, $^3J(H,H)_{trans}$ = 13.7 Hz) and 4.03 ppm (1H, $^2J(H,H)_{geminal}$ = 0.5 Hz, $^3J(H,H)_{cis}$ = 5.7 Hz) for the OCH=CH_2 moiety and resonances at 2.01 ppm (30H) and 3.49/1.20 ppm for the Cp* ligands and coordinated THF, respectively.

The vinyloxy coordination in yttrocene **2** was unequivocally evidenced by X-ray diffraction (XRD) analysis, showing a C21–C22 distance of 1.33(1) Å (Fig. 2, left). The Y–O distances differ considerably in accordance with a neutral (Y1–$O1_{THF}$ = 2.384(2) Å) and anionic O-ligand (Y1–$O2_{alkoxy}$ = 2.08(2) Å), respectively. For comparison, similar Y–O_{THF} and Y–O_{alkoxy} distances were detected in $Cp^*_2YMe(thf)$[15] (2.379(8) Å) and $(Cp^*_2Y)_2(\mu\text{-}OC_2H_4O)(thf)_2$[19] (2.042(4) and 2.398(5) Å). The synthesis and utilization of **2** for the polymerization of acrylates was reported previously, but **2** was not fully characterized.[20] Furthermore, Evans found similar THF ring-opening reactions for $(C_5H_4R)_2Y(CH_2SiMe_3)(thf)$ (R = Me, and H) by thermolysis in toluene to afford solvent-free dimeric $[(C_5H_4R)_2Y(\mu\text{-}OC_2H_3)]_2$, featuring bridging vinyloxy moieties.[21] Other

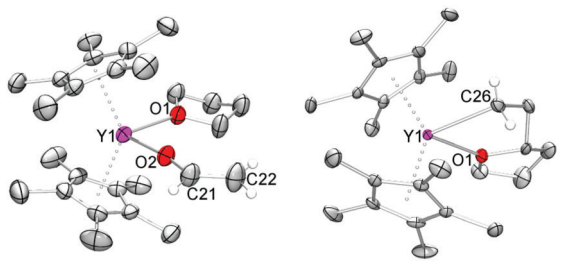

Fig. 2 Crystal structures of $Cp^*_2Y(OC_2H_3)(thf)$ (**2**, left) and $Cp^*_2Y(2\text{-}C_2H_4\text{-}OC_4H_7)$] (**3**, right). All atoms are represented by atomic displacement ellipsoids set at 50% probability. Hydrogen atoms, except at the vinyloxy ligand (**2**) and C26 (**3**), and disorder of the vinyloxy ligand and THF molecule (**2**) and the chiral ethylene-2-tetrahydrofuranyl ligand (**3**) are omitted for clarity. For detailed metrics, see ESI.†

ring-opening pathways include formation of the alkoxy derivative $Cp^*_2Ln[O(CH_2)_4C_5Me_5](thf)$ from the reaction of $LnCl_3$/3NaCp*/THF (Ln = La, Nd, Tm, Lu) and of the alkoxyalkyl decomposition product $[K(crypt)_2]_2[\{(C_5H_4Me)_3Ln\}_2\{\mu\text{-}O(CH_2)_3CH_2\}]$ *via* $(C_5H_4Me)_3Ln(thf)$/KC_8/2.2.2-cryptand/THF (Ln = La and Pr).[22,23]

The ^{1}H NMR spectrum of **3** in C_6D_6 revealed complicated signal splitting/coupling patterns of the asymmetrically substituted 2-ethylene-tetrahydrofuranyl ligand. ^{1}H,^{1}H COSY and ^{1}H,^{13}C HSQC NMR experiments allowed complete signal assignment (see ESI,† Fig. S9 and S10). XRD analysis of **3** revealed a monomeric complex, with the yttrocene entity additionally coordinated by the tetrahydrofuranyl oxygen atom and the terminal carbon atom of the fused ethylene moiety in a κ(C,O) mode (Fig. 2, right). Thus, the formed five-membered metallaheterocycle exhibits Y–C and Y–O distances of 2.439(2) and 2.349(1) Å, respectively. Similar Y–C distances were reported for **1** (2.44(2) Å)[15] and $[Cp^*_2YEt]$ (2.419(3) Å).[24]

A plausible mechanistic scenario for the formation of **2** and **3** involves THF degradation and ethylene insertion (Scheme 2). The reaction proceeds presumably *via* σ-bond metathesis at the

yttrium centre of **1** (step (i)) with the elimination of methane to form the transient tetrahydrofuranyl compound [Cp*$_2$Y(η^2-OC$_4$H$_7$)] (represented by the equilibrium between $\mathbf{I_1}$ and $\mathbf{I_2}$). Subsequent cleavage of THF with the release of ethylene[7] and coordination of a second THF molecule affords isolable complex **2** (step (ii)). Alternatively, the liberated ethylene (detectable by NMR spectroscopy, Fig. S12, ESI†) adds to $\mathbf{I_1}$ and inserts at the α position of the tetrahydrofuranyl moiety to produce compound **3** (step (iii)). Pathway (iii) features ethylene coordination and insertion as the elementary steps of α-olefin polymerization. It can be rationalized that step (iii) is much faster than (ii), because compounds **2** and **3** are formed in approximately equal quantities. Strikingly, Teuben *et al.* reported the similar insertion chemistry of the yttrocene pyridyl compound Cp*$_2$Y(η^2-NC$_5$H$_4$), which upon treatment with excess ethylene yielded [Cp*$_2$Y(2-C$_2$H$_4$-NC$_5$H$_4$)].[25] Moreover, the lanthanocene 2-thienyl complex [Cp*$_2$La(2-C$_4$H$_3$S)]$_2$ even gave access to thienyl-capped polyethylene (80 °C, ethylene pressure >7.5 bar), while the reaction with the yttrium congener was described as extremely sluggish.[6] It should be noted that thermal treatment of Cp*$_2$Y(AlMe$_4$) in THF generated complexes **2** and **3** as the main products as well. By contrast, heating of **1** in C$_6$D$_6$ to 90 °C (shortage of THF) did not produce **2** but a mixture of **3**, (Cp*$_2$Y)$_2$(μ-O) and Cp*$_2$Y(Ph-d_5)(thf) (Fig. S13 and S14, ESI†).[26]

In contrast to the yttrium reaction, the addition of THF to Cp*$_2$La(AlMe$_4$) (<2 min) and subsequent crystallization from THF/*n*-hexane mixtures at −40 °C did not result in tetramethylaluminato cleavage to form the elusive [Cp*$_2$LaMe(thf)] (Scheme 1). Instead, polymeric [Cp*$_2$La(μ-AlMe$_4$)(thf)]$_n$ (**4**) was obtained (XRD analysis) revealing a chain structure with the lanthanum centres bridged by almost linear La–C(Me)–Al linkages (165.4(1)°/166.1(1)°) (Fig. 3). The La–C distances of 2.910(3) and 2.917(3) Å are markedly elongated compared with those in [Cp*$_2$La(μ-AlMe$_4$)]$_2$ (2.849(2)/2.848(2) Å) and diamidopyridine-supported [*NNN*]La(AlMe$_4$)(thf) (2.825(7) Å),[27] bearing a terminal η^1-coordinated tetramethylaluminato ligand. A THF molecule saturates the coordination sphere of the lanthanum centre in **4**. Overall, the solid-state structure of **4** resembles that of divalent complex [Cp*Eu(μ-AlMe$_4$)(thf)$_3$]$_n$ with two additional thf donor molecules instead of a second Cp* ligand.[28]

Compound **4** readily dissolves in C$_6$D$_6$ and the ^{1}H NMR spectrum corroborates the disruption of the polymeric

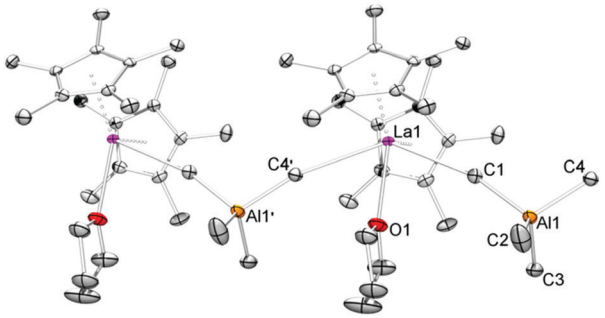

Fig. 3 Crystal structure of polymeric [Cp*$_2$La(AlMe$_4$)(thf)]$_n$ (**4**). All atoms are represented by atomic displacement ellipsoids set at 50% probability. Hydrogen atoms are omitted for clarity. For detailed metrics, see ESI.†

structure. The Cp* ligands resonate as a singlet at 1.89 ppm, while the broad singlet at −0.28 ppm is in accord with the [AlMe$_4$] moiety bearing highly fluxional methyl groups. Two multiplets at 3.48 and 1.31 ppm account for coordinated THF.

Even more surprisingly, stirring a solution of Cp*$_2$La(AlMe$_4$) in THF/*n*-hexane for 30 min at ambient temperature resulted in methane elimination and the quantitative formation of complex Cp*$_2$La(2-AlMe$_3$-OC$_4$H$_7$)] (**5**) (Scheme 1). In contrast to **3**, THF degradation and the formation of ethylene did not occur under these conditions. Presumably, the increased ionic character of the lanthanum compound hampers complete aluminate cleavage,[27] but rather leads to C–H-bond activation with the formation of the AlMe$_3$-stabilized tetrahydrofuranyl moiety. It is noteworthy that compound **4** is stable in C$_6$D$_6$ solution, but slowly converts into **5** upon addition of THF-d_8 (Scheme 1, and Fig. S21, ESI†). The ^{1}H NMR spectrum of **5** in C$_6$D$_6$ revealed rigid coordination of the tetrahydrofuranyl ligand: seven multiplets in accord with seven inequivalent protons. Hence, the resonance for the methine group at the α position appears as a doublet of doublets with coupling constants typical for vicinal coupling in the *gauche* (^3J(H,H) = 4.8 Hz) and *anti*-positions (^3J(H,H) = 13.6 Hz) according to the Karplus equation.[29] As such, **5** is formed as a racemic mixture. The bridging and terminal methyl groups at the aluminium centre resonate as very broad singlets at −0.08 ppm (3H) and −0.35 ppm (6H), indicative of fast exchange processes at ambient temperature. The two singlets at approximately 1.90 ppm account for the Cp* ligands in accord with the C_s symmetry of compound **5**.

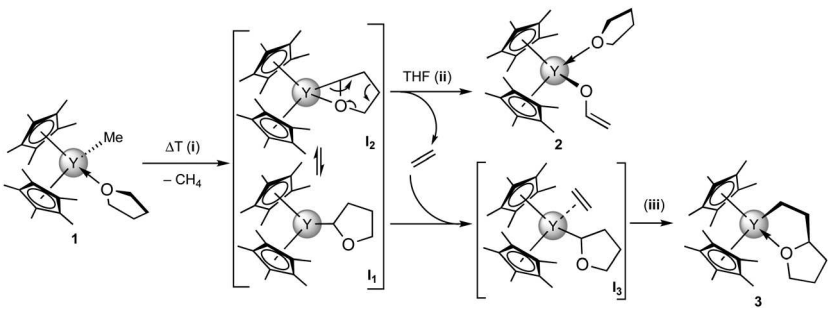

Scheme 2 Possible reaction sequence for the C–H-bond activation of THF and rearrangement reactions to afford **2** and **3**.

XRD analysis revealed a monomeric constitution of 8-coordinate **5** and unequivocally evidenced the formation of an $AlMe_3$-stabilized 2-tetrahydrofuranyl lanthanocene (Scheme 1). The aluminium atom binds at the α position of the tetrahydrofuranyl moiety, while the oxygen atom is attached to the lanthanum centre. One methyl group bridges between the aluminium and lanthanum atoms to form a five-membered bimetallic metallaheterocycle. The La–O distance of 2.425(2) Å is rather short compared with those observed for lanthanocenes **4** (2.657(2) Å), $[Cp^*_2La(1\text{-}C_3H_4\text{-}C_6H_5)(thf)]$[30] (2.634(2) Å), $[Cp^*_2La(HBEt_3)(thf)]$[31] (2.617(2) Å) or 5-coordinate [*NNN*]La($AlMe_4$)(thf) (2.538(4) Å).[27] The Al–C(Me) distances are within the expected range for terminal (1.97(1) Å) and bridging methyl groups (2.048(3) Å), while the Al–C14 distance of (2.080(4) Å) compares well to that found for Mulvey's structurally related $[(thf)Li(\mu\text{-}tmp)(\mu\text{-}SC_4H_7)Al(i\text{Bu})_2]$ (2.054(2) Å) (*cf.*, the sulphur analogue of **E**, Fig. 1).[13]

To conclude, metallocenes $Cp^*_2Ln(AlMe_4)$ (Ln = Y and La) display distinct reactivity towards THF that is dependent on the rare-earth-metal size. Yttrocene $Cp^*_2YMe(thf)$, obtainable *via* donor-induced cleavage of the [$AlMe_4$] moiety, is stable at ambient temperature; metalation of THF at the α position is prevalent only at elevated temperatures, leading to the vinyloxide $Cp^*_2Y(OC_2H_3)(thf)$ and the ethylene-inserted tetrahydrofuranyl complex $Cp^*_2Y(2\text{-}C_2H_4\text{-}OC_4H_7)$. By contrast, $AlMe_3$ displacement does not occur when $Cp^*_2La(AlMe_4)$ is dissolved in THF. The resulting bimetallic $[Cp^*_2La(AlMe_4)(thf)]$ is capable of selective THF metalation already at ambient temperature affording the $AlMe_3$-stabilized 2-tetrahydrofuranyl compound $Cp^*_2La(2\text{-}AlMe_3\text{-}OC_4H_7)$ quantitatively. Such unprecedented rare-earth-metal 2-tetrahydrofuranyl complexes point to heterobimetallic synergistic effects and might provide new opportunities for O-heterocycle functionalization and – in a broader sense – heterobimetallic cooperative catalysis.[32]

Conflicts of interest

There are no conflicts to declare.

Notes and references

1 (*a*) Z. Hou and Y. Wakatsuki, *Coord. Chem. Rev.*, 2002, **231**, 1–22; (*b*) J. Gromada, J.-F. Carpentier and A. Mortreux, *Coord. Chem. Rev.*, 2004, **248**, 397–410; (*c*) A. Fischbach and R. Anwander, *Adv. Polym. Sci.*, 2006, **204**, 155–281; (*d*) Z. Zhang, D. Cui, B. Wang, B. Liu and Y. Yang, in *Molecular Catalysis of Rare-Earth Elements*, ed. P. W. Roesky, Springer, Berlin Heidelberg, 2010, vol. 137, pp. 49–108; (*e*) M. Nishiura, F. Guo and Z. Hou, *Acc. Chem. Res.*, 2015, **48**, 2209–2220; (*f*) A. A. Trifonov and D. M. Lyubov, *Coord. Chem. Rev.*, 2017, **340**, 10–61.

2 C. J. Weiss and T. J. Marks, *Dalton Trans.*, 2010, **39**, 6576–6588.

3 R. Waterman, *Organometallics*, 2013, **32**, 7249–7263.

4 For early examples, see: (*a*) P. L. Watson, *J. Am. Chem. Soc.*, 1982, **104**, 337–339; (*b*) G. Jeske, H. Lauke, H. Mauermann, P. N. Swepston, H. Schumann and T. J. Marks, *J. Am. Chem. Soc.*, 1985, **107**, 8091–8103; (*c*) G. Jeske, L. E. Schock, P. N. Swepston, H. Schumann and T. J. Marks, *J. Am. Chem. Soc.*, 1985, **107**, 8103–8110; (*d*) M. E. Thompson, S. M. Baxter, A. R. Bulls, B. J. Burger, M. C. Nolan, B. D. Santarsiero, W. P. Schaefer and J. E. Bercaw, *J. Am. Chem. Soc.*, 1987, **109**, 203–219; (*e*) B. J. Burger, M. E. Thompson, W. D. Cotter and J. E. Bercaw, *J. Am. Chem. Soc.*, 1990, **112**, 1566–1577; (*f*) A. D. Sado and T. D. Tilley, *J. Am. Chem. Soc.*, 2003, **125**, 7971–7977.

5 H. Nagae, A. Kundu, M. Inoue, H. Tsurugi and K. Mashima, *Asian J. Org. Chem.*, 2018, **7**, 1256–1269.

6 S. N. Ringelberg, A. Meetsma, B. Hessen and J. H. Teuben, *J. Am. Chem. Soc.*, 1999, **121**, 6082–6083.

7 W. J. Evans, T. A. Ulibarri, L. R. Chamberlain, J. W. Ziller and D. Alvarez, *Organometallics*, 1990, **9**, 2124–2130.

8 R. Bates, L. Kroposki and D. Potter, *J. Org. Chem.*, 1972, **37**, 560–562.

9 H. Adams, N. A. Bailey, P. Cahill, D. Rogers and M. J. Winter, *J. Chem. Soc., Dalton Trans.*, 1986, **10**, 2119–2126.

10 J. Meiners, A. Friedrich, E. Herdtweck and S. Schneider, *Organometallics*, 2009, **28**, 6331–6338.

11 H. Kulinna, T. P. Spaniol, L. Maron and J. Okuda, *Chem. – Eur. J.*, 2013, **19**, 9468–9471.

12 (*a*) A. R. Kennedy, J. Klett, R. E. Mulvey and D. S. Wright, *Science*, 2009, **326**, 706–708; (*b*) R. E. Mulvey, V. L. Blair, W. Clegg, A. R. Kennedy, J. Klett and L. Russo, *Nat. Chem.*, 2010, **2**, 588–591.

13 E. Crosbie, P. García-Álvarez, A. R. Kennedy, J. Klett, R. E. Mulvey and S. D. Robertson, *Angew. Chem., Int. Ed.*, 2010, **49**, 9388–9391.

14 H. M. Dietrich, K. W. Törnroos, E. Herdtweck and R. Anwander, *Organometallics*, 2009, **28**, 6739–6749.

15 K. H. Den Haan, J. L. De Boer, J. H. Teuben, W. J. J. Smeets and A. L. Spek, *J. Organomet. Chem.*, 1987, **327**, 31–38.

16 P. L. Watson, *J. Am. Chem. Soc.*, 1983, **105**, 6491–6493.

17 K. H. Den Haan, Y. Wielstra and J. H. Teuben, *Organometallics*, 1987, **6**, 2053–2060.

18 P. L. Watson, *J. Chem. Soc., Chem. Commun.*, 1983, **6**, 276–277.

19 B.-J. Deelman, M. Booij, A. Meetsma, J. H. Teuben, H. Kooijman and A. L. Spek, *Organometallics*, 1995, **14**, 2306–2317.

20 E. Ihara, M. Morimoto and H. Yasuda, *Macromolecules*, 1995, **28**, 7886–7892.

21 W. J. Evans, R. Dominguez and T. P. Hanusa, *Organometallics*, 1986, **5**, 1291–1296.

22 H. Schumann, M. Glanz, H. Hemling and F. H. Gölitz, *J. Organomet. Chem.*, 1993, **462**, 155–161.

23 D. H. Woen, D. N. Huh, J. W. Ziller and W. J. Evans, *Organometallics*, 2018, **37**, 3055–3063.

24 M. R. MacDonald, R. R. Langeslay, J. W. Ziller and W. J. Evans, *J. Am. Chem. Soc.*, 2015, **137**, 14716–14725.

25 B.-J. Deelman, W. M. Stevels, J. H. Teuben, M. T. Lakin and A. L. Spek, *Organometallics*, 1994, **13**, 3881–3891.

26 (*a*) B.-J. Deelman, M. Booij, A. Meetsma, J. H. Teuben, H. Kooijman and A. L. Spek, *Organometallics*, 1995, **14**, 2306–2317; (*b*) S. N. Ringelberg, A. Meetsma, S. I. Troyanov, B. Hessen and J. H. Teuben, *Organometallics*, 2002, **21**, 1759–1765.

27 M. Zimmermann, K. W. Törnroos and R. Anwander, *Angew. Chem., Int. Ed.*, 2007, **46**, 3126–3130.

28 A. M. Bienfait, B. M. Wolf, K. W. Törnroos and R. Anwander, *Organometallics*, 2015, **34**, 5734–5744.

29 (*a*) M. Karplus, *J. Am. Chem. Soc.*, 1963, **85**, 2870–2871; (*b*) M. J. Minch, *Concepts Magn. Reson.*, 1994, **6**, 41–56.

30 W. P. Kretschmer, B. Ten Brummelhuis, A. Meetsma and J. H. Teuben, *Z. Anorg. Allg. Chem.*, 2006, **632**, 1933–1935.

31 W. J. Evans, J. M. Perotti and J. W. Ziller, *Inorg. Chem.*, 2005, **44**, 5820–5825.

32 For a recent perspective on main group bimetallic catalysis, see: J. M. Gil-Negrete and E. Hevia, *Chem. Sci.*, 2021, **12**, 1982–1992.

Electronic Supplementary Material (ESI) for ChemComm.

Supporting Information

Rare-earth-metallocene alkylaluminates trigger distinct tetrahydrofuran activation

Martin Bonath, Verena M. Birkelbach, Christoph Stuhl, Cäcilia Maichle-Mössmer, and Reiner Anwander*

Institut für Anorganische Chemie, Universität Tübingen, Auf der Morgenstelle 18, D-72076 Tübingen, (Germany)

* E-mail for R. A.: reiner.anwander@uni-tuebingen.de

Table of Contents

Experimental Section

General Consideration. Syntheses and manipulations of all organometallic compounds were carried out under dry argon by using standard *Schlenk*, high-vacuum, and glovebox techniques (MBraun MB 200B; <1 ppm O_2, <1 ppm H_20). *n*-Pentane, *n*-hexane, toluene and tetrahydrofurane (THF) were purified by using *Grubbs* columns (MBraun SPS-800, solvent purification system) and stored in a glovebox. C_6D_6 and THF-d_8 were obtained from Aldrich, dried over Na/K alloy for 24 h and distilled prior to use. $AlMe_3$ was purchased from Aldrich, Me_3SiI was purchased from abcr and used as received. Cp*$_2$Y($AlMe_4$) and Cp*$_2$La($AlMe_4$) were synthesized according to literature procedures.[1] NMR spectra of air and moisture sensitive compounds were recorded by using J. Young valve NMR tubes at 26 °C on a *Bruker* AVII+250 (^{1}H: 250.13 MHz; ^{13}C: 62.90 MHz), and on a *Bruker* AVII+400 (^{1}H: 400.13 MHz; ^{13}C: 100.61 MHz;). ^{1}H and ^{13}C NMR shifts are referenced to internal solvent resonances and reported in parts per million (ppm) relative to TMS. IR spectra were recorded on a NICOLET 6700 FTIR spectrometer using a DRIFT chamber with dry KBr/sample mixtures and KBr windows. For the latter the collected data were converted using the Kubelka-Munk refinement. Elemental analyses were performed on an *Elementar Vario MICRO cube*. Suitable crystals for X-ray structure analyses were selected in a glovebox and coated with Parabar 10312 (previously known as Paratone N, Hampton Research) and fixed on a nylon loop/glass fiber. X-ray data were collected on a Bruker APEX II DUO diffractometer by using QUAZAR optics and MoK_α radiation (λ = 0.71073 Å). The data collection strategy was determined using COSMO[2] employing ω-scans. Raw data were processed by using APEX[3] and SAINT[4] software; structure solution and final model refinement were performed by using SHELXL[5] and ShelXle.[6] Corrections for absorption effects were applied by using SADABS.[7] All nonhydrogen atoms were refined anisotropically. Disorder models were calculated using DSR,[8] a program for refining disordered structures in ShelXl. All plots were generated utilizing the programs ORTEP-3[9] and POV-Ray.[10] Further details of the refinement and crystallographic data are listed in Table S1, and in the CIF files. CCDC depositions 2087233-2087236 contain all the supplementary crystallographic data for this paper. These data can be obtained free of charge from The Cambridge Crystallographic Data Centre via www.ccdc.cam.ac.uk/structures/.

Cp*$_2$YMe(thf) (1). The synthesis of **1** was performed in a slightly modified procedure as described in the literature.[1] In a scintillation vial, Cp*$_2$Y($AlMe_4$) (159 mg, 0.36 mmol) was diluted in THF (0.8 mL). Then *n*-hexane (10 mL) was added, the reaction mixture filtered and the filtrate stored at –40 °C. After three days **1** crystallized as colorless crystals. To prevent partial back reaction the cold supernatant was removed, the solids washed with *n*-hexane and dried under reduced pressure to achieve pure **1** (124 mg, 78%). The ^{1}H NMR spectroscopic data are in accord with literature.[11]

Cp*$_2$YMe(OC$_2$H$_3$)(thf) (2). In a pressure tube, **1** (118 mg, 0.27 mmol) was dissolved in THF and stirred at 90 °C for three days. Then, all volatiles were removed under reduced pressure to obtain a pale yellow powder as the crude product. According to ^{1}H NMR spectral data the crude product contained **2** and **3** in an approximate ratio of 3:2. To obtain a pure sample of **2**, the crude product was subjected to fractional crystallization from *n*-pentane. Single crystals suitable for X-ray crystallography were grown from a saturated *n*-pentane solution at –40 °C (71 mg, 57%). ^{1}H NMR (C_6D_6, 400 MHz, 26 °C): δ = 7.25 (dd, 1 H, $^3J(H,H)_{cis}$ = 5.5 Hz, $^3J(H,H)_{trans}$ = 13.7 Hz, OC*H*=CH$_2$), 4.19 (dd, 1 H, $^2J(H,H)_{geminal}$ = 0.6 Hz, $^3J(H,H)_{trans}$ = 13.7 Hz , OCH=C*H*$_2$), 4.03 (dd, 1 H, $^2J(H,H)_{geminal}$ = 0.5 Hz, $^3J(H,H)_{cis}$ = 5.7 Hz, OCH=C*H*$_2$), 3.49 (m, 4 H, O(C*H*$_2$CH$_2$)$_2$), 2.01 (s, 30 H, C$_5$(C*H*$_3$)$_5$), 1.20 (m, 4 H, O(CH$_2$C*H*$_2$)$_2$) ppm. ^{13}C{^{1}H} NMR (C_6D_6, 101 MHz, 26 °C): δ = 156.0 (O*C*H=CH$_2$), 116.8 (d, ^1J(Y,C) = 1.4 Hz, *C*$_5$(CH$_3$)$_5$), 85.3 (OCH=*C*H$_2$), 71.7 (O(*C*H$_2$CH$_2$)$_2$), 25.4 (O(CH$_2$*C*H$_2$)$_2$), 11.3 (C$_5$(*C*H$_3$)$_5$) ppm. DRIFT (KBr): $\tilde{\nu}$ = 3096 (w), 2962 (m), 2901 (s), 2855 (m), 2722 (w), 1614 (vs), 1445 (m), 1486 (m), 1437 (m), 1391 (m), 1377 (m), 1317 (s), 1223 (vs), 1015 (m), 999 (s), 862 (m), 772 (w) cm^{-1}. Elemental analysis (%) calcd. for $C_{26}H_{41}O_2Y$ (474.52 g mol^{-1}): C 65.81, H 8.71. Found: C 66.00, H 8.72.

Cp*$_2$YMe(2-C$_2$H$_4$-OC$_4$H$_7$) (3). The residual supernatants from the crystallization of compound **2** were condensed, washed with toluene and recrystallized from *n*-pentane to afford pure samples of **3**. Single crystals suitable for X-ray crystallography were grown from a saturated *n*-pentane solution at –40 °C (44 mg, 36%). ^{1}H NMR (C_6D_6, 400 MHz, 26 °C): δ = 3.73 (m, 1 H, OC*H*(CH$_2$)$_2$), 3.15 (m, 1 H, OC*H*$_2$CH$_2$), 3.07 (m, 1 H, OC*H*$_2$CH$_2$), 2.50 (m, 1 H, YCH$_2$C*H*$_2$), 2.02 (s, 15 H, C$_5$(C*H*$_3$)$_5$), 2.00 (s, 15 H, C$_5$(C*H*$_3$)$_5$), 1.72 (m, 1 H, YCH$_2$C*H*$_2$), 1.41 (m, 1 H, OCH$_2$CH$_2$C*H*$_2$), 1.34 (m, 1 H, OCH$_2$C*H*$_2$CH$_2$), 1.24 (m, 1 H, OCH$_2$C*H*$_2$CH$_2$), 1.03 (m, 1 H, OCH$_2$CH$_2$C*H*$_2$), 0.45 (m, 1 H, YC*H*$_2$CH$_2$), –0.12 (m, 1 H, YC*H*$_2$CH$_2$) ppm. ^{13}C{^{1}H} NMR (C_6D_6, 101 MHz, 26 °C): δ = 115.9 (*C*$_5$(CH$_3$)$_5$), 90.6 (O*C*H(CH$_2$)$_2$), 67.8 (O*C*H$_2$CH$_2$), 36.3 (YCH$_2$*C*H$_2$), 31.2 (OCH$_2$CH$_2$*C*H$_2$), 29.7 (d, ^1J(Y,C) = 51.1 Hz, Y*C*H$_2$CH$_2$), 26.5 (OCH$_2$*C*H$_2$CH$_2$), 11.6 (C$_5$(*C*H$_3$)$_5$), 11.3 (C$_5$(*C*H$_3$)$_5$) ppm. DRIFT (KBr): $\tilde{\nu}$ = 2962 (s), 2906 (vs), 2860 (vs), 2791 (m), 2722 (w), 1614 (vs), 1454 (w), 1436 (m), 1377 (w), 1130 (w), 1020 (m), 988 (m), 947 (w), 913 (m), 845 (w), 780 (w), 519 (w) cm^{-1}. Elemental analysis (%) calcd. for $C_{26}H_{41}OY$ (458.52 g mol^{-1}): C 68.11, H 9.01. Found: C 67.28, H 8.90.

NMR-scale reaction of Cp*$_2$YMe(thf) (1) in C$_6$D$_6$. In a J.-Young-valve NMR tube, **1** (20 mg, 0.05 mmol) was dissolved in C_6D_6 (0.5 mL) and kept at 90 °C. After 11 h the colourless solution had turned to deep orange and all starting material had been consumed. Under these conditions formation of **2** was not observed. Hence, **3**, (Cp*$_2$Y)$_2$(μ-O)[12] and Cp*$_2$YPh-*d*$_5$(thf)/Cp*$_2$YPh(thf) were identified as the main products in an approximate ratio of 2:1:2. The oxy-bridged dimetallic complex is the least soluble and as such separable. Compounds Cp*$_2$YPh-*d*$_5$(thf)/Cp*$_2$YPh(thf) are likely formed via C–H-bond activation of C_6D_6/C_6H_6 by complex **3**. See, Figures S13 and S14.

[Cp*$_2$La{(μ-Me)$_2$AlMe$_2$)}(thf)]$_n$ (4). In a scintillation vial, Cp*$_2$La(AlMe$_4$) (309 mg, 0.62 mmol) was diluted quickly in THF (1.7 mL) at ambient temperature. Then *n*-hexane (10 mL) was added instantly, the mixture filtered and the filtrate stored at –40 °C immediately. After three days colourless crystals of **4** (302 mg, 86%) had grown, suitable for X-ray crystallography. ^{1}H NMR (C_6D_6, 400 MHz, 26 °C): δ = 4.48 (m, 4 H, O(C*H*$_2$CH$_2$)$_2$), 1.89 (s, 30 H, C$_5$(C*H*$_3$)$_5$), 1.31 (m, 4 H, O(CH$_2$C*H*$_2$)$_2$), –0.28(bs, 12 H, Al(C*H*$_3$)$_4$) ppm. ^{13}C{^{1}H} NMR (C_6D_6, 101 MHz, 26 °C): δ = 68.3 (THF, O*C*H$_2$CH$_2$), 25.6 (THF, OCH$_2$*C*H$_2$), 11.1 (C$_5$(*C*H$_3$)$_5$) ppm; signals for *C*$_5$(CH$_3$)$_5$ and Al(*C*H$_3$) moieties were not detected. DRIFT (KBr): $\tilde{\nu}$ = 2963 (m), 2903 (vs), 2869 (s), 2803 (w), 2728 (w), 1487 (w), 1436 (m), 1377 (w), 1172 (m), 1023 (s), 992 (s), 920 (w), 870 (w), 720 (s), 671 (w), 595 (w), 565 (w), 544 (m) cm^{-1}. Elemental analysis (%) calcd. for $C_{28}H_{50}AlLaO$ (568.59 g mol^{-1}): C 59.15, H 8.86. Found: C 58.87, H 8.46.

Cp*$_2$La(2-AlMe$_3$-OC$_4$H$_7$) (5). In a scintillation vial, Cp*$_2$La(AlMe$_4$) (117 mg, 0.23 mmol) was suspended in *n*-hexane (4 mL) and THF (1.5 mL). Within 30 minutes the suspension gradually dissolved to form a clear, colourless solution. Then, all volatiles were removed under reduced pressure and **5** (130 mg, 97%) was obtained analytically pure as white powder. Crystals of **5** suitable for X-ray crystallography were obtained from an *n*-hexane solution at –40 °C. ^{1}H NMR (C_6D_6, 400 MHz, 26 °C): δ = 3.43 (m, 1 H, OC*H*$_2$CH$_2$), 3.35 (m, 1 H, OC*H*$_2$CH$_2$), 2.82 (dd, ^3J(H,H)$_{gauche}$ = 4.8 Hz, ^3J(H,H)$_{anti}$ = 13.6 Hz, 1H, OC*H*(AlMe$_3$)CH$_2$), 2.15 (m, 1H, OCH(AlMe$_3$)C*H*$_2$), 1.90 (s, 15 H, C$_5$(C*H*$_3$)$_5$), 1.90 (s, 15 H, C$_5$(C*H*$_3$)$_5$), 1.79 (m, 1H, OCH(AlMe$_3$)C*H*$_2$), 1.63 (m, 1H, OCH$_2$C*H*$_2$), 1.43 (m, 1H, OCH$_2$C*H*$_2$), –0.06 (bs, 3 H, La(μ-C*H*$_3$)Al), –0.36 (bs, 6 H, Al(C*H*$_3$)$_2$) ppm. ^{13}C{^{1}H} NMR (C_6D_6, 101 MHz, 26 °C): δ = 121.1 (*C*$_5$(CH$_3$)$_5$), 120.9 (*C*$_5$(CH$_3$)$_5$), 78.3 (O*C*H(AlMe$_3$)CH$_2$), 69.2 (O*C*H$_2$CH$_2$), 30.7 (OCH(AlMe$_3$)*C*H$_2$), 29.6 (OCH$_2$*C*H$_2$), 11.1 (C$_5$(*C*H$_3$)$_5$), 11.1 (C$_5$(*C*H$_3$)$_5$) ppm; signals for Al(*C*H$_3$) moieties were not detected; probably due to fast exchange processes. DRIFT (KBr): $\tilde{\nu}$ = 2963 (m), 2906 (vs), 2857 (s), 2726 (w), 1436 (m), 1378 (w), 1180 (m), 1063 (w), 1022 (w), 990 (w), 971 (w), 889 (w), 798 (w), 716 (m), 684 (s), 601 (w), 567 (w), 544 (w) cm^{-1}. Elemental analysis (%) calcd. for $C_{27}H_{46}AlLaO$ (552.55 g mol^{-1}): C 58.69, H 8.39. Found: C 58.62, H 8.43.

Crystallographic Details

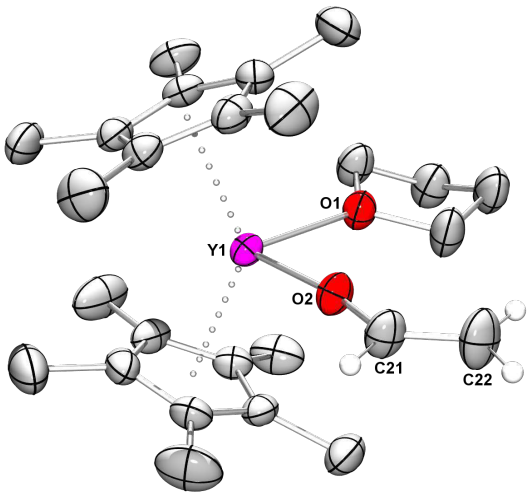

Figure S1. Crystal structure of $Cp^*_2Y(OC_2H_3)(thf)$ (**2**). All atoms are represented by atomic displacement ellipsoids set at 50% probability. Hydrogen atoms except at the vinyl alkoxide and disorders in the vinyl alkoxide and the THF molecule are omitted for clarity. Selected interatomic distances [Å] and angles [°]: Y1–O1 2.384(2), Y1–O2 2.08(2), C21–C22 1.33(1); O1–Y1–O2 92.4(4), Y1–O2–C21 171(1).

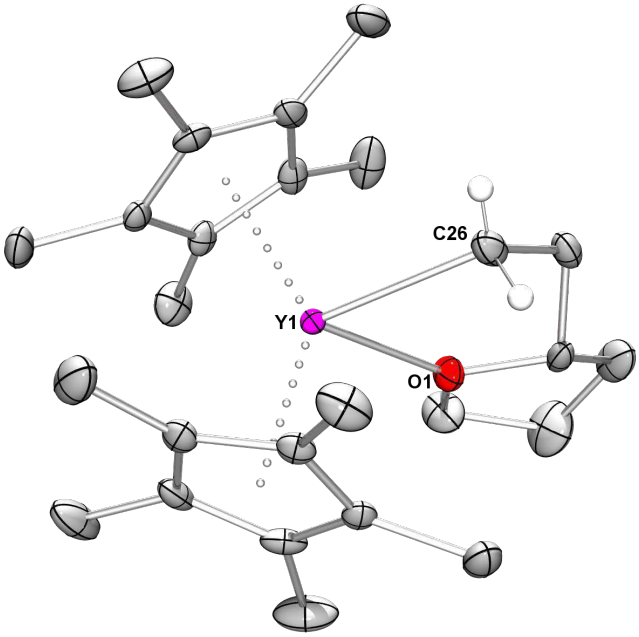

Figure S2. Crystal structure of $Cp^*_2Y(2\text{-}C_2H_4\text{-}OC_4H_7)$ (**3**). All atoms are represented by atomic displacement ellipsoids set at 50% probability. Hydrogen atoms except at C26 and the disorder in the chiral ethylene-2-tetrahydrofuranyl ligand are omitted for clarity. Selected interatomic distances [Å] and angles [°]: Y1–C26 2.439(2), Y1–O1 2.349(1); C26–Y1–O1 73.80(6).

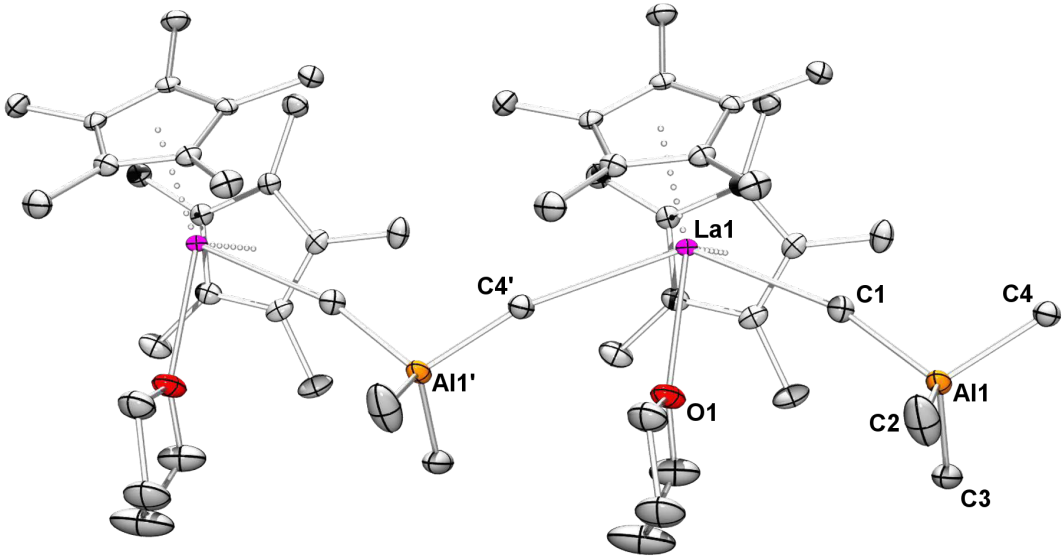

Figure S3. Crystal structure of $[Cp^*_2La(AlMe_4)(thf)]_n$ (**4**). All atoms are represented by atomic displacement ellipsoids set at 50% probability. Hydrogen atoms are omitted for clarity. Selected interatomic distances [Å] and angles [°]: La1–C1 2.910(3), La1–C4' 2.917(3), La1–O1 2.657(2), Al1–C1 2.025(3), Al1–C2 1.974(3), Al1–C3 1.983(3), Al1–C4 2.016(3); Al1–C1–La1 165.4(1), Al1–C4'–La1 166.1(1), C1–La1–C4' 135.64(4).

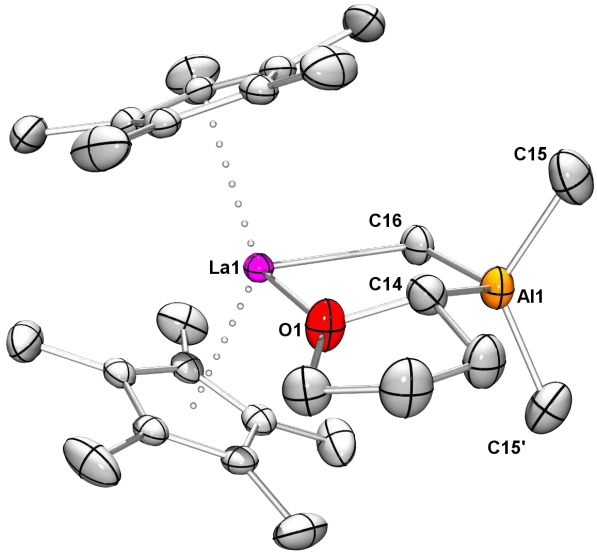

Figure S4. Crystal structure of $Cp^*_2La(2\text{-}AlMe_3\text{-}OC_4H_7)$ (**5**). All atoms are represented by atomic displacement ellipsoids set at 50% probability. Hydrogen atoms and disorder due to co-crystallized enantiomers are omitted for clarity. Selected interatomic distances [Å] and angles [°]: La1–C16 2.753(3), La1–O1 2.425(2), Al1–C14 2.080(4), Al1–C15 1.969(10), Al1–C16 2.048(3), C16–La1–O1 98.14(8), Al1–C16–La1 90.2(1), C14–Al1–C16 114.6(2).

Table S1. Crystallographic data of complexes **2**, **3**, **4** and **5**

	2	**3**	**4**	**5**
Formula	$C_{26}H_{41}O_2Y$	$C_{26}H_{41}OY$	$C_{28}H_{50}AlLaO$	$C_{27}H_{46}AlLaO$
CCDC	2087233	2087235	2087236	2087234
M_r [g mol^{-1}]	474.50	458.50	568.57	552.53
cryst syst	orthorhombic	monoclinic	monoclinic	orthorhombic
space group	*P*bca	$P2_1/n$	$P2_1/c$	*P*nma
a [Å]	14.0255(7)	10.5384(2)	18.808(16)	16.6514(15)
b [Å]	16.7687(9)	19.7009(4)	8.677(7)	15.0366(13)
c [Å]	21.8639(15)	11.5448(2)	19.029(16)	11.0355(10)
α [°]	90	90	90	90
β [°]	90	97.1483(10)	113.609(11)	90
γ [°]	90	90	90	90
V [Å^3]	5142.2(5)	2378.25(8)	2845(4)	2763.1(4)
Z	8	4	4	4
T [K]	180(2)	100(2)	100(2)	136(2)
ρ_{calcd} [g cm^{-3}]	1.226	1.281	1.327	1.328
μ [mm^{-1}]	2.285	2.465	1.548	1.593
F (000)	2016	976	1184	1144
R1/*w*R2 (I>2σ)[a]	0.0341/0.0714	0.0291/0.0651	0.0274/0.0521	0.0250/0.0576
R1/*w*R2 (all data)[a]	0.0627/0.0809	0.0330/0.0662	0.0420/0.0553	0.0289/0.0596
GOF[a]	1.006	1.123	0.935	1.055

[a] $R1 = \Sigma(||F_0|-|F_c||)/\Sigma|F_0|$, $F_0 > 4\sigma(F_0)$. $wR2 = \{\Sigma[w(F_0^2-F_c^2)^2/\Sigma[w(F_0^2)^2]\}^{1/2}$.

NMR Spectra

In general solvent peaks are marked with (°) or an asterisk (*).

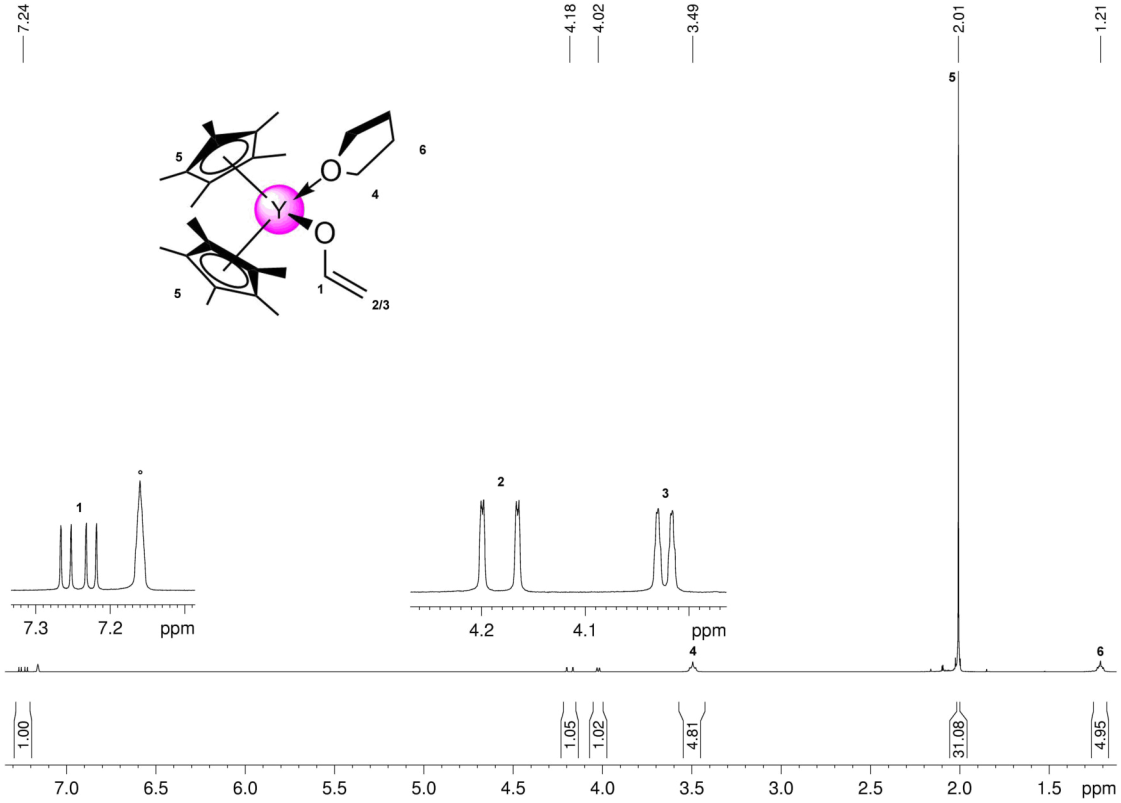

Figure S5. ^{1}H NMR spectrum (400 MHz) of **2** in C_6D_6 (°) at 26 °C.

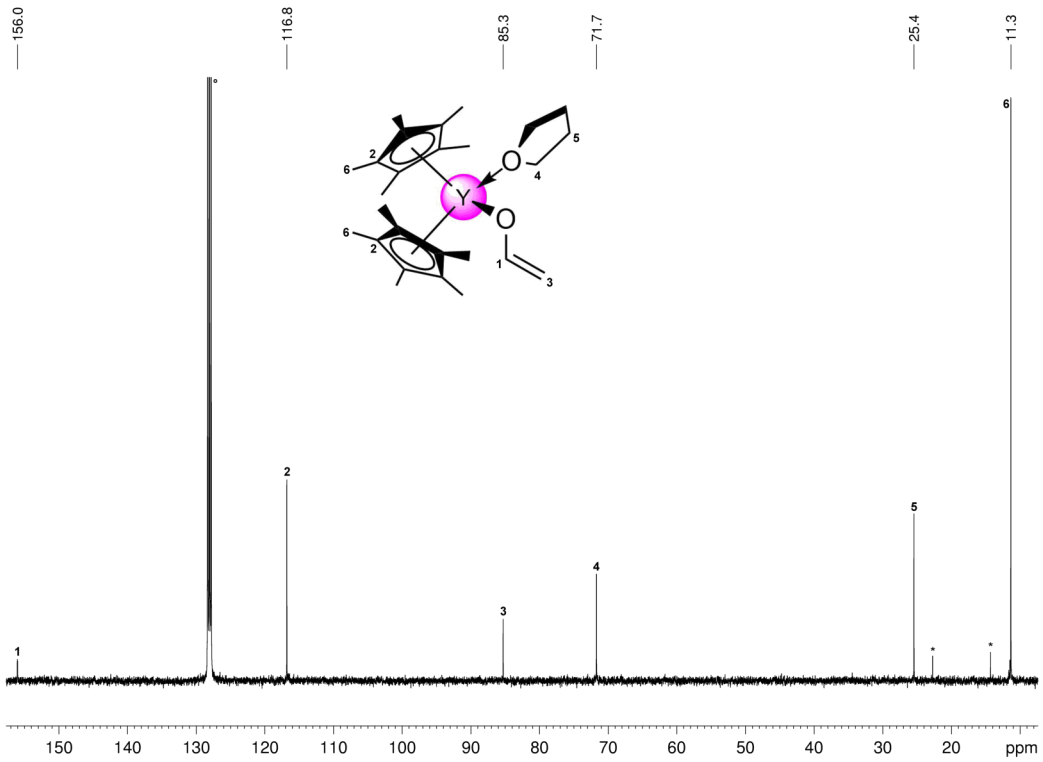

Figure S6. ^{13}C{^{1}H} NMR spectrum (101 MHz) of **2** in C_6D_6 (°) at 26 °C (* *n*-hexane).

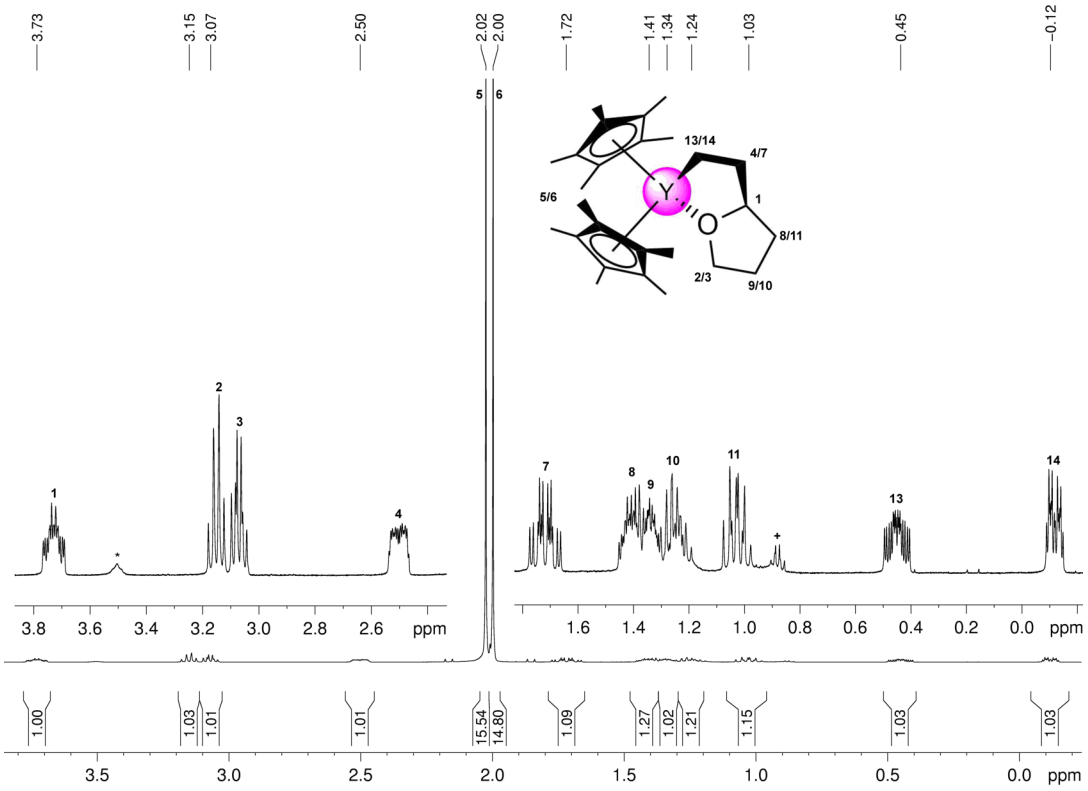

Figure S7. ^{1}H NMR spectrum (400 MHz) of **3** in C_6D_6 at 26 °C (* THF, + *n*-hexane).

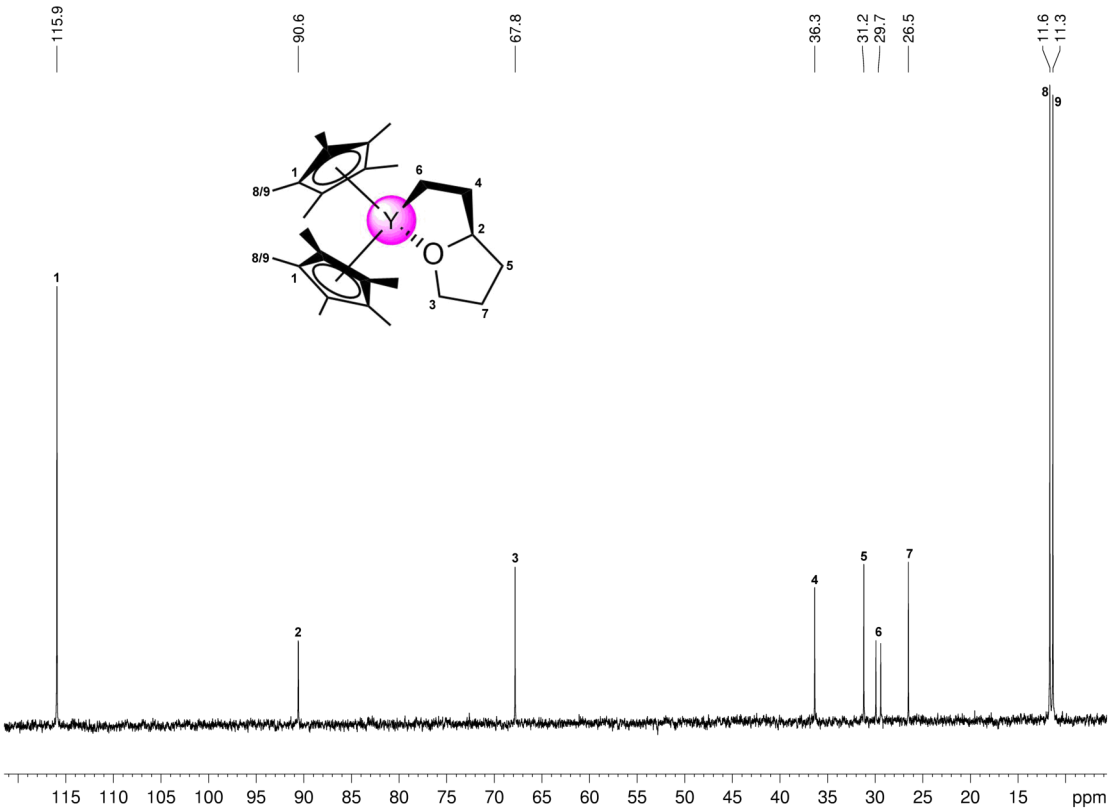

Figure S8. ^{13}C{^{1}H} NMR spectrum (101 MHz) of **3** in C_6D_6 at 26 °C.

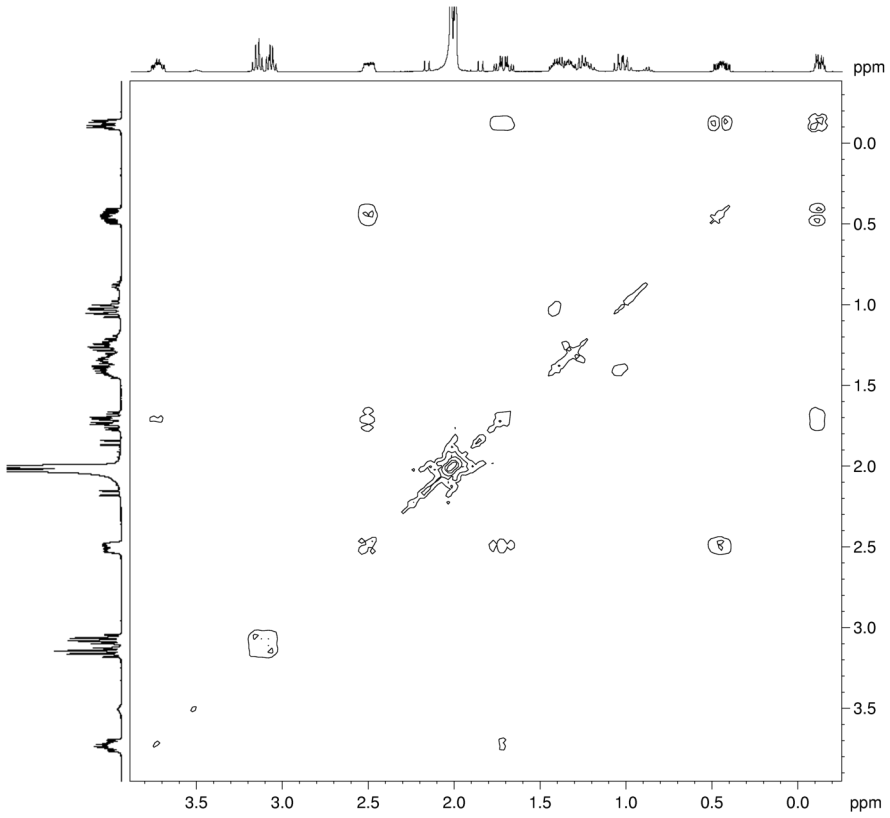

Figure S9. ^{1}H-^{1}H COSY NMR spectrum (400 MHz) of **3** in C_6D_6 at 26 °C.

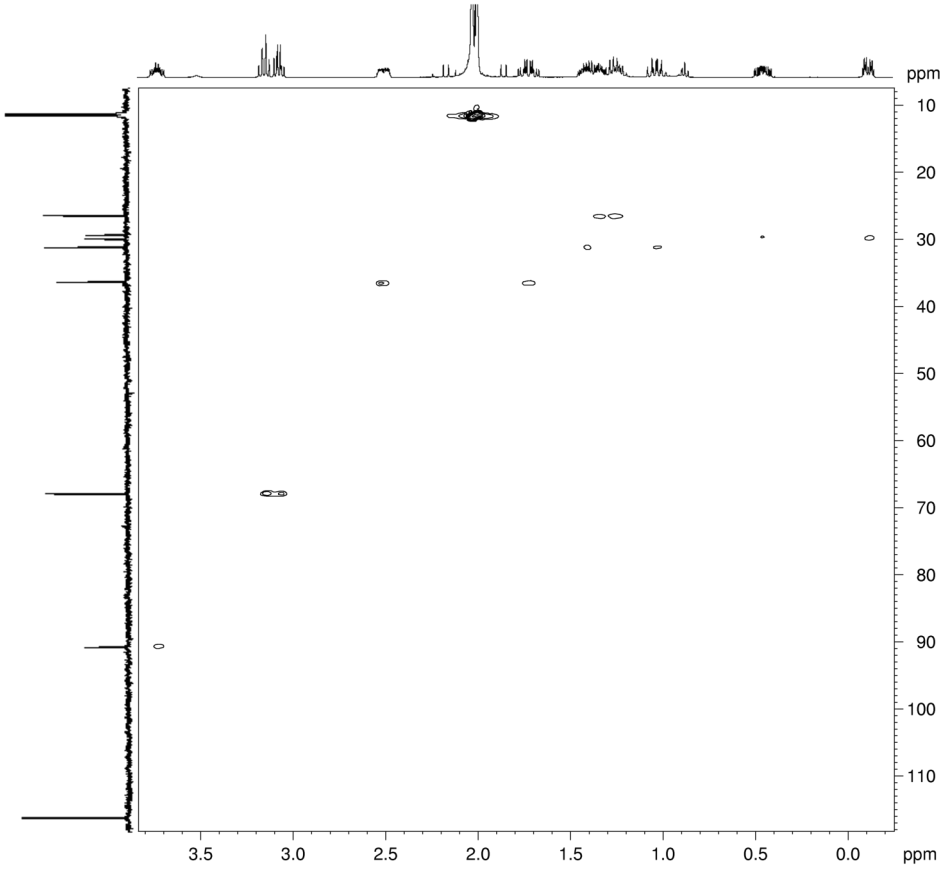

Figure S10. ^{1}H-^{13}C HSQC NMR spectrum (400 MHz, 101 MHz) of **3** in C_6D_6 at 26 °C.

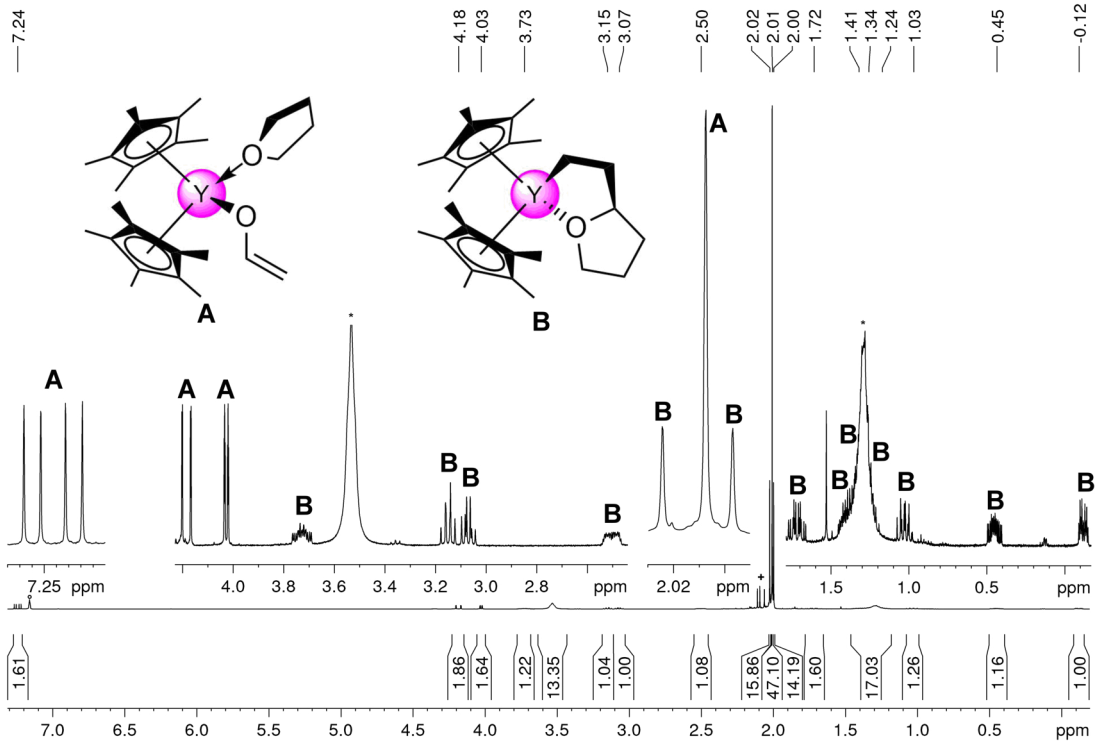

Figure S11. ^{1}H NMR spectrum (400 MHz) of crude product mixture of **2** and **3** in C_6D_6 at 26 °C (* THF, + minor side products).

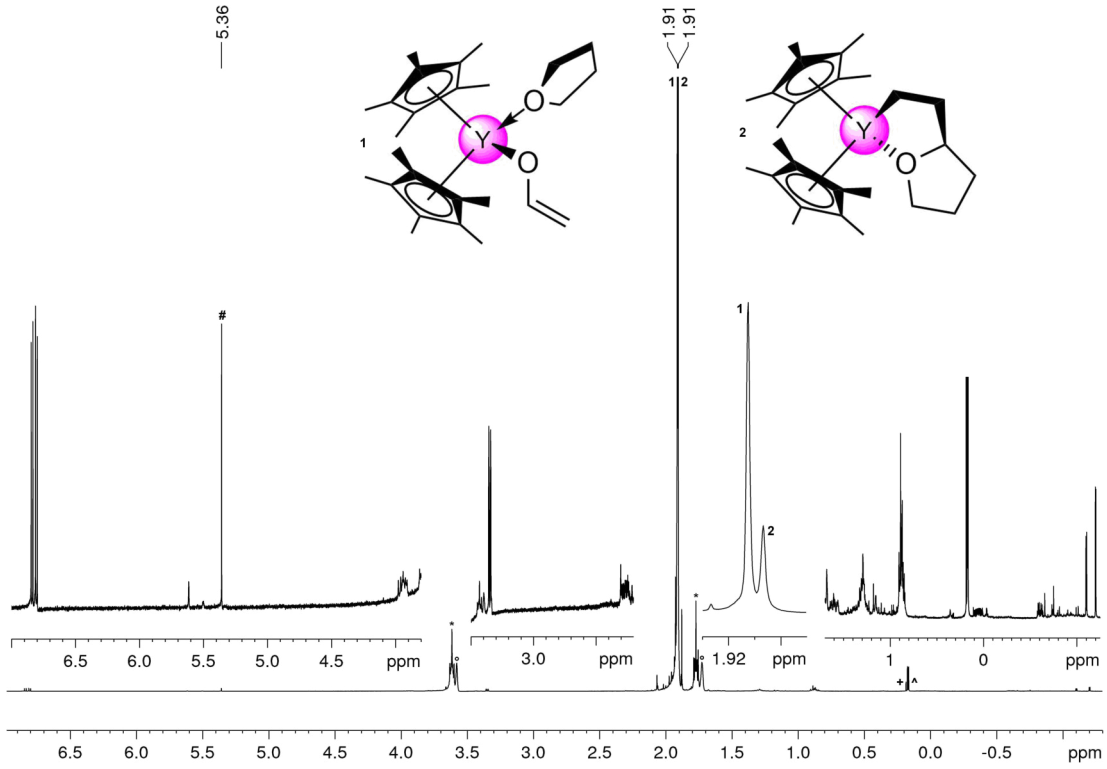

Figure S12. ^{1}H NMR spectrum (400 MHz) of crude product mixture of **2** and **3** in THF-d_8 at 26 °C (* THF, # ethylene, + CH_4, ^ CDH_3).

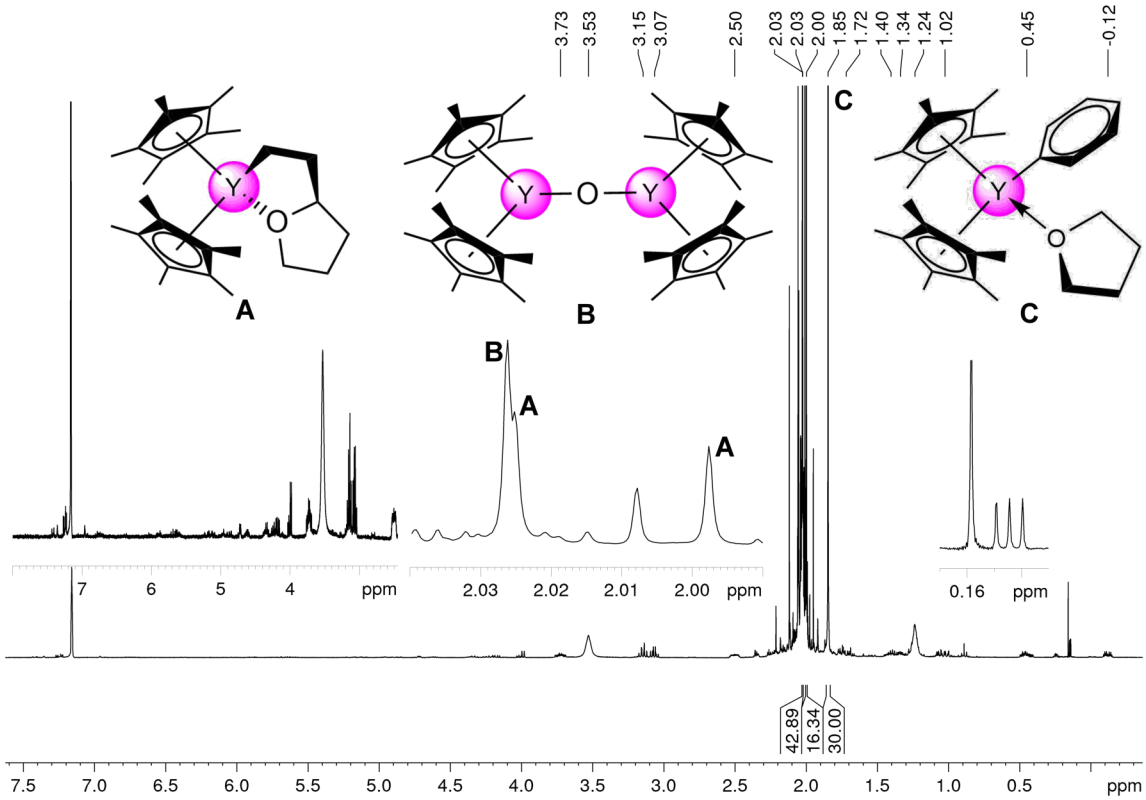

Figure S13. ^{1}H NMR spectrum (400 MHz) of **1** in C_6D_6 (°) after heating to 90 °C for 11 h. CH_4 und CDH_3 are formed in an approximate ratio of 1:1. Complex **2** is not detected

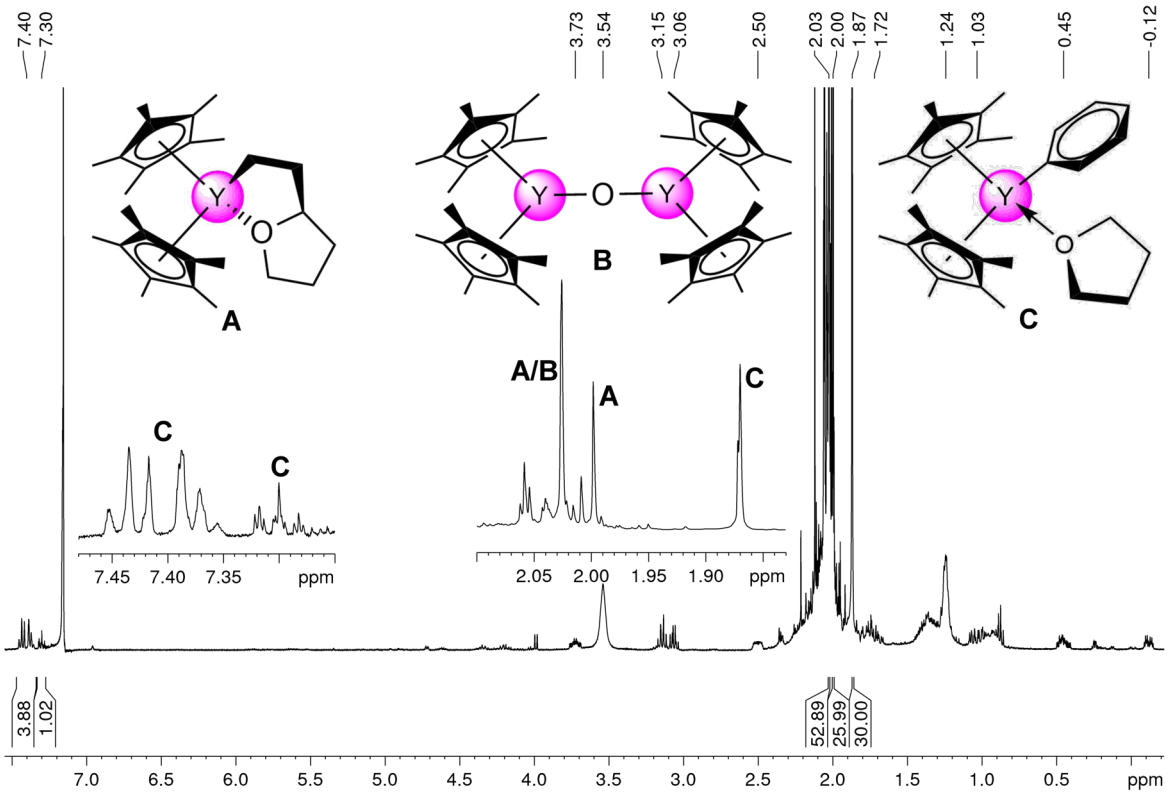

Figure S14. ^{1}H NMR spectrum (400 MHz) of **1** in C_6D_6 after heating to 90 °C for 11 h, evaporation to dryness, extracting with C_6H_6, evaporation to dryness and re-dissolving in C_6D_6. Complex **2** is not detected.

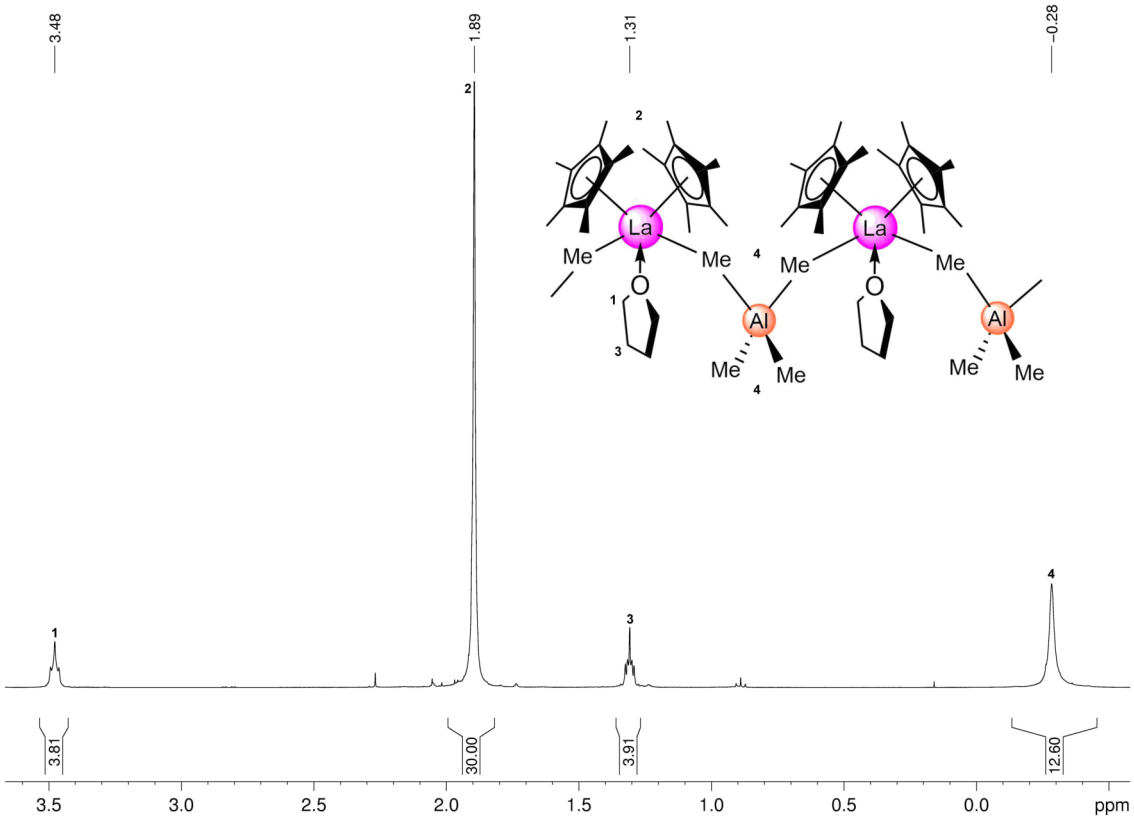

Figure S15. ^{1}H NMR spectrum (400 MHz) of **4** in C_6D_6 at 26 °C.

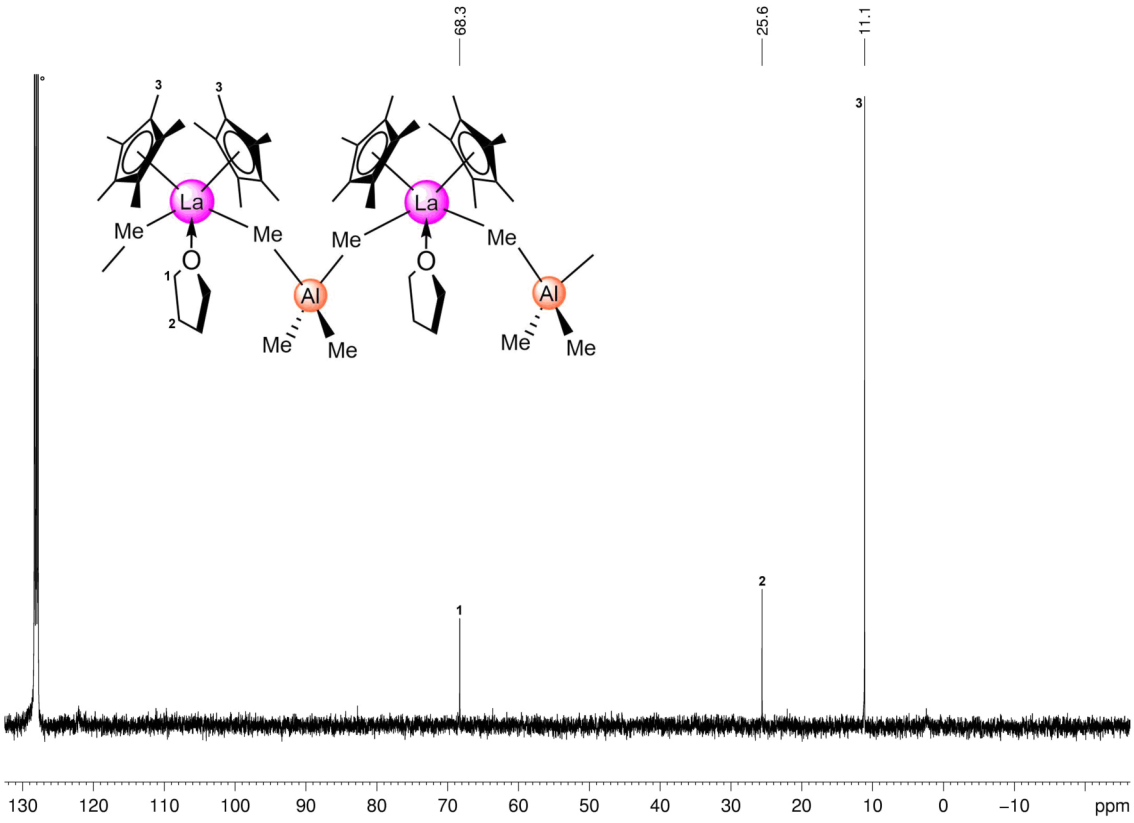

Figure S16. ^{13}C{^{1}H} NMR spectrum (101 MHz) of **4** in C_6D_6 at 26 °C.

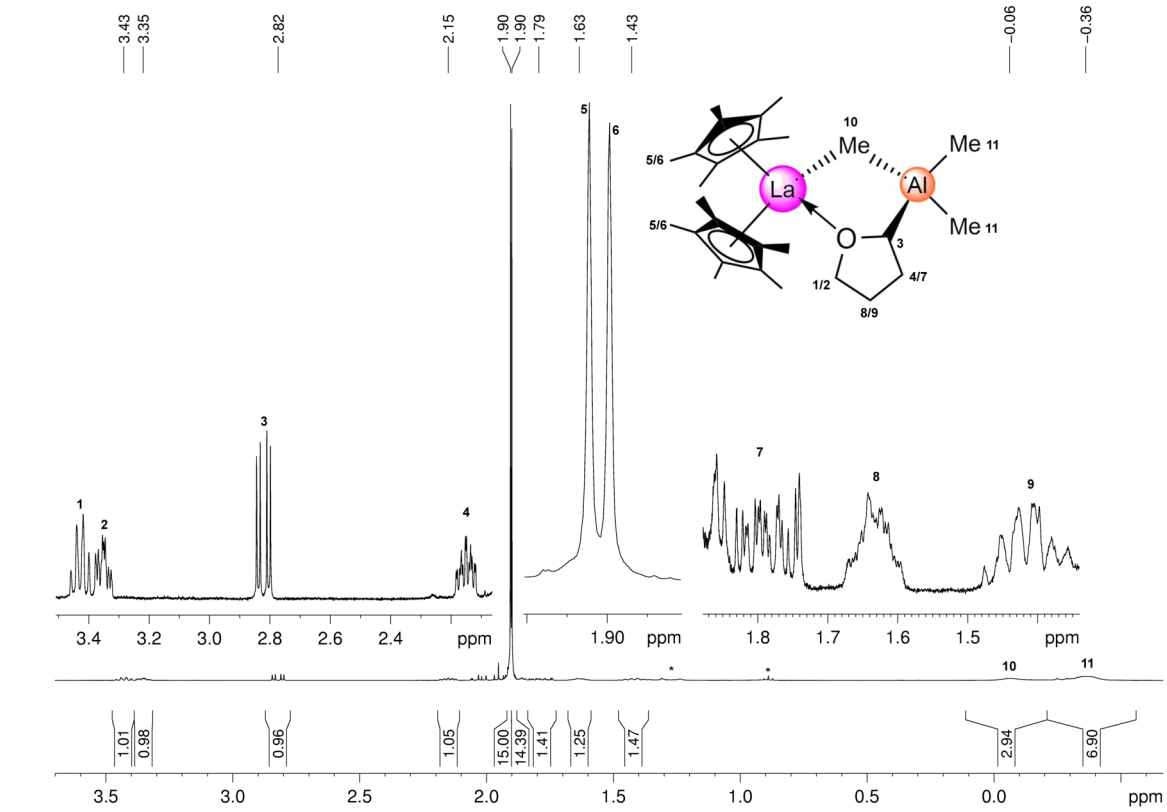

Figure S17. ^{1}H NMR spectrum (400 MHz) of **5** in C_6D_6 at 26 °C.

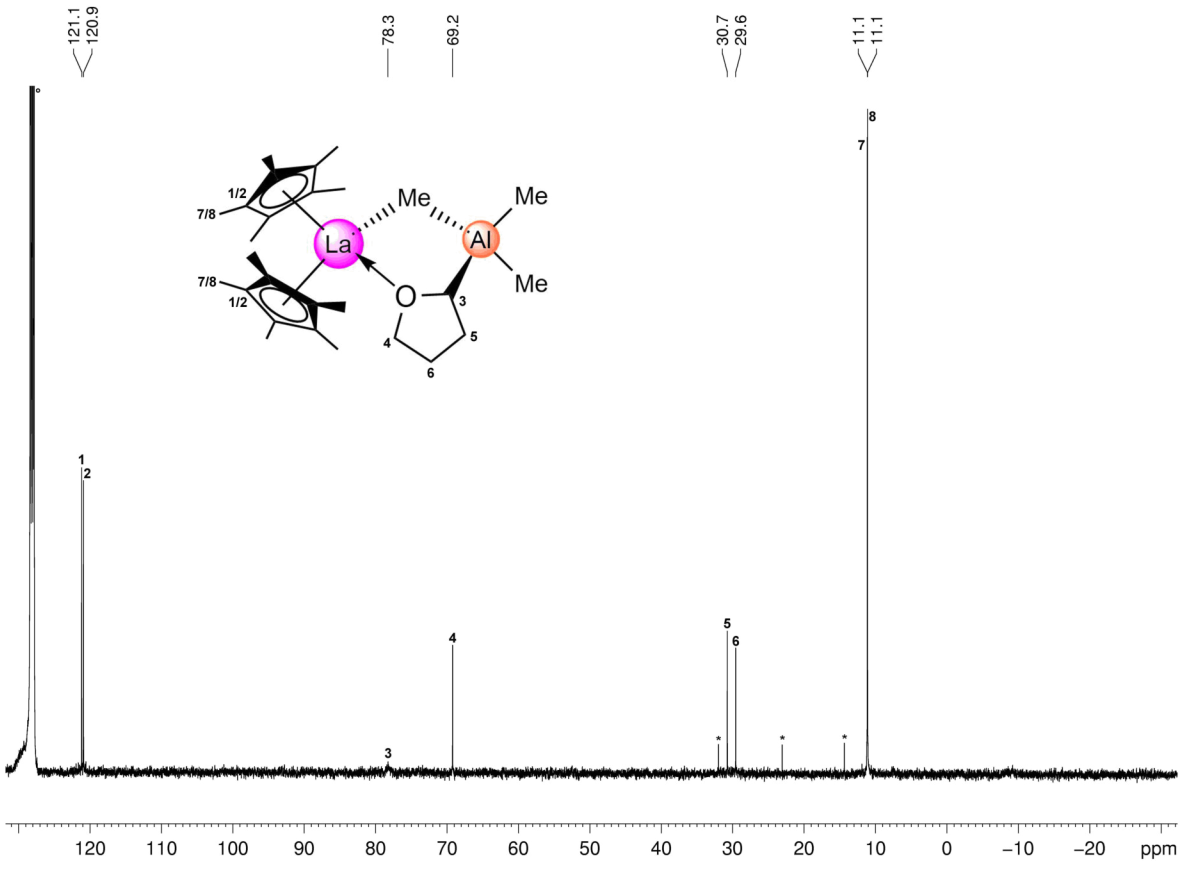

Figure S18. ^{13}C{^{1}H} NMR spectrum (101 MHz) of **5** in C_6D_6 (°) at 26 °C (* *n*-hexane).

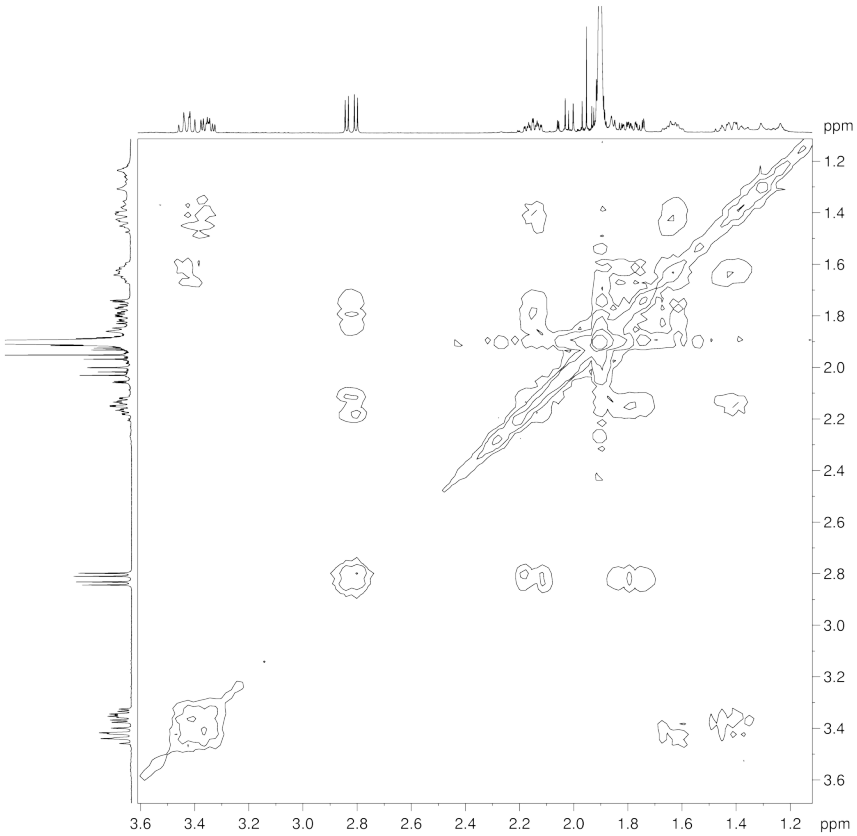

Figure S19. ^{1}H-^{1}H COSY NMR spectrum (400 MHz) of **5** in C_6D_6 at 26 °C.

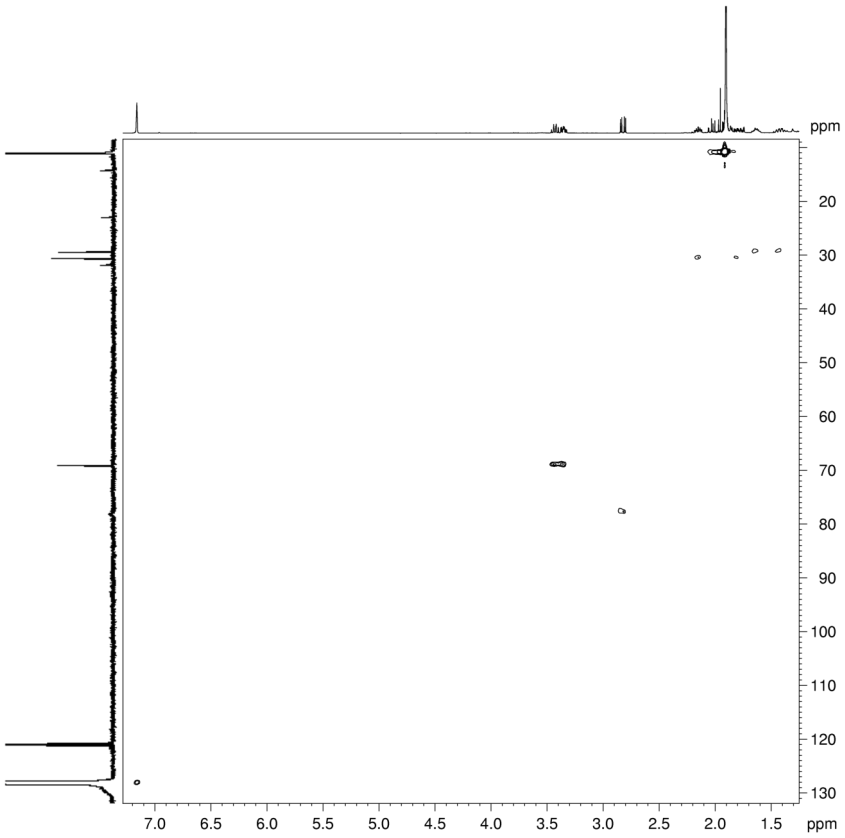

Figure S20. ^{1}H-^{13}C HSQC NMR spectrum (400 MHz, 101 MHz) of **5** in C_6D_6 at 26 °C.

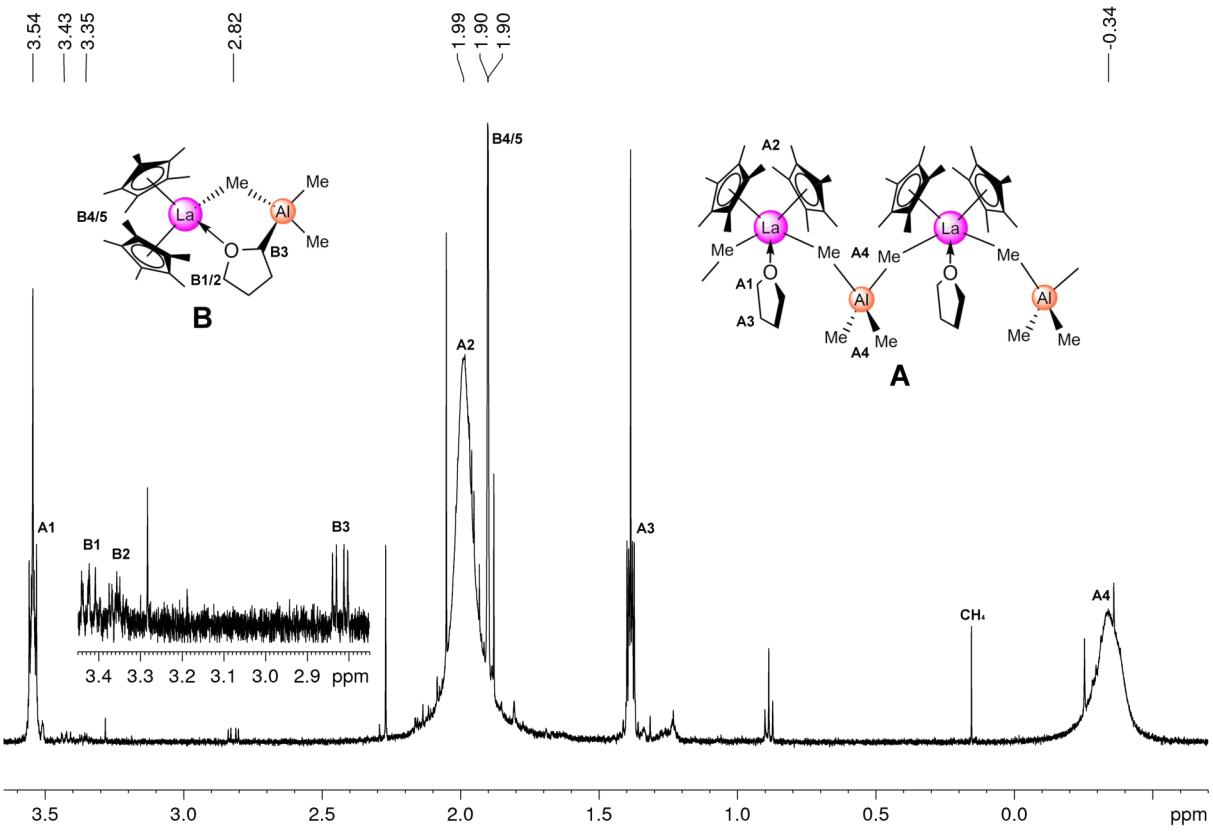

Figure S21. ^{1}H NMR spectrum (400 MHz) of **4** (**A**) in C_6D_6 at 26 °C, recorded after 1 h upon addition of some drops of THF-d_8, revealing the formation of methane and compound **5** (**B**).

References

1. H. M. Dietrich, K. W. Törnroos, E. Herdtweck and R. Anwander, *Organometallics*, 2009, **28**, 6739-6749.
2. COSMO, v. 1.61; Bruker AXS Inc.: Madison, WI, 2012.
3. APEX 3, v. 2017.3-0; Bruker AXS Inc., Madison, WI, 2017; APEX 2, v. 2012.10-0; Bruker AXS Inc., Madison, WI, 2012.
4. SAINT, v. 8.34A; Bruker AXS Inc., Madison, WI, 2013.
5. SHELXTL: G. M. Sheldrick, *Acta Crystallogr.*, 2015, **A71**, 3–8.
6. SHELXLE: C. B. Hübschle, G. M. Sheldrick and B. Dittrich, *J. Appl. Crystallogr.*, 2011, **44**, 1281-1284.
7. SADABS: L. Krause, R. Herbst-Irmer, G. M. Sheldrick and D. Stalke, *J. Appl. Crystallogr.* 2015, **48**, 3.
8. DSR: enhanced modelling and refinement of disordered structures with SHELXL: D. Kratzert, J. J. Holstein and I. Krossing, *J. Appl. Cryst.*, 2015, **48**, 933-938.
9. L. J. Farrugia, *J. Appl. Crystallogr.,* 1997, **30**, 565-566.
10. POV-Ray v. 3.6; Persistence of Vision Pty. Ltd.: Williamstown, Victoria, Australia, 2004. http://www.povray.org/.
11. K. H. Den Haan, J. L. De Boer, J. H. Teuben, W. J. J. Smeets and A. L. Spek, *J. Organomet. Chem.*, 1987, **327**, 31-38.
12. a) B.-J. Deelman, M. Booij, A. Meetsma, J. H. Teuben, H. Kooijman and A. L. Spek, *Organometallics*, 1995, **14**, 2306-2317; b) S. N. Ringelberg, A.Meetsma, S. I. Troyanov, B. Hessen and J. H. Teuben, *Organometallics*, 2002, **21**, 21759-1765.

Paper IV

The Alkylaluminate/gallate Trap: Metalation of Benzene by Heterobimetallic Yttrocene Complexes [Cp*$_2$Y(MMe$_3$R)] (M = Al, Ga)

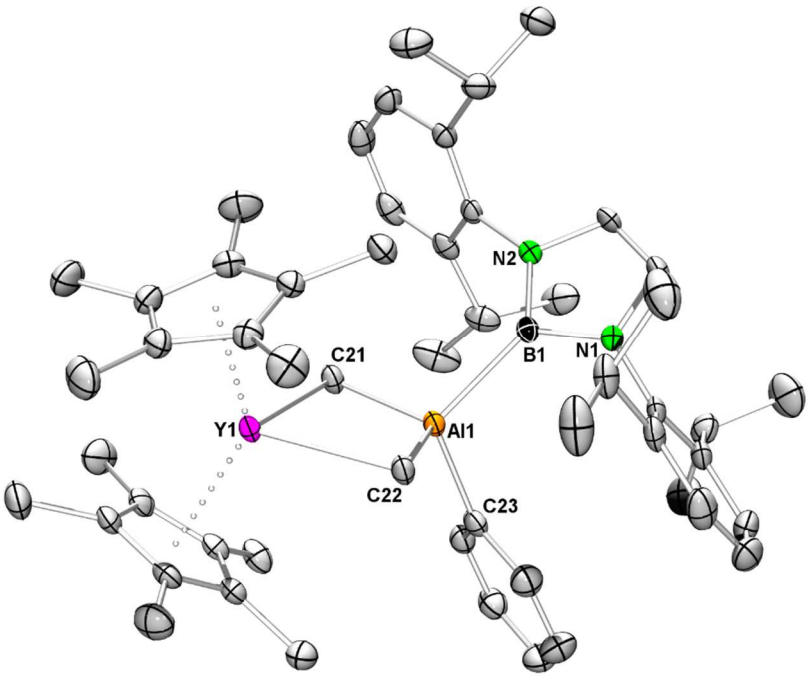

Inorganic Chemistry

pubs.acs.org/IC

Article

The Alkylaluminate/Gallate Trap: Metalation of Benzene by Heterobimetallic Yttrocene Complexes [Cp*$_2$Y(MMe$_3$R)] (M = Al, Ga)

Martin Bonath, Dorothea Schädle, Cäcilia Maichle-Mössmer, and Reiner Anwander*

Cite This: *Inorg. Chem.* 2021, 60, 14952−14968

Read Online

ACCESS | Metrics & More | Article Recommendations | Supporting Information

ABSTRACT: Yttrocene derivatives [Cp*$_2$Y(MMe$_4$)] (Cp* = C$_5$Me$_5$; M = Al, Ga) and Cp*$_2$Y[Me$_3$Al{B(NDippCH)$_2$}] (Dipp = C$_6$H$_3$*i*Pr$_2$-2,6) deprotonate benzene at elevated temperatures via the release of methane. The formation of [Cp*$_2$Y(Me$_2$MPh$_2$)] (M = Al, Ga), Cp*$_2$Y(MPh$_4$) (M = Al, Ga), Cp*$_2$Y[Me$_2$AlPh{B(NDippCH)$_2$}], and Cp*$_2$Y[AlPh$_3${B(NDippCH)$_2$}] can be controlled via the temperature applied. The activation temperature and formation of the coordinatively unsaturated "reactive" [Cp*$_2$YMe] strongly depend on the coordination strength of the displaceable Lewis acids [AlMe$_3$]$_2$, GaMe$_3$, and [Me$_2$Al{B(NDippCH)$_2$}]$_2$. Hence, [Cp*$_2$Y(AlMe$_4$)] requires temperatures above 100 °C to metalate benzene, while Cp*$_2$Y[AlMe$_3${B(NDippCH)$_2$}] undergoes C−H-bond activation even at ambient temperatures. A kinetic deuterium isotope effect was observed for the reactions in C$_6$D$_6$ solutions. Distinct differences in the stabilities of the bulky Group 13 anions ([Me$_2$MPh$_2$]$^-$, [MPh$_4$]$^-$, [Me$_3$Al{B(NDippCH)$_2$}]$^-$, [Me$_2$AlPh{B(NDippCH)$_2$}]$^-$, and [AlPh$_3${B(NDippCH)$_2$}]$^-$) are assessed by detailed studies of the coordination chemistry with tetrahydrofuran (THF) and by variable-temperature ^{1}H NMR spectroscopy. Thus, increased steric bulk or a reduced Lewis acidity of the Group 13 metal center promote temperature-sensitive dissociation of trivalent Group 13 alkyl entities. Consequently, compound Cp*$_2$Y[AlPh$_3${B(NDippCH)$_2$}] was found to engage in a dissociation equilibrium with [Cp*$_2$YPh] and AlPh$_2${B(NDippCH)$_2$} in a C$_6$D$_6$ solution at ambient temperature. The reaction of Cp*$_2$Y[AlPh$_3${B(NDippCH)$_2$}] with THF results in the concomitant formation of monometallic Cp*$_2$YPh(THF) and the solvent-separated ion pair [Cp*$_2$Y(THF)$_2$][AlPh$_3${B(NDippCH)$_2$}].

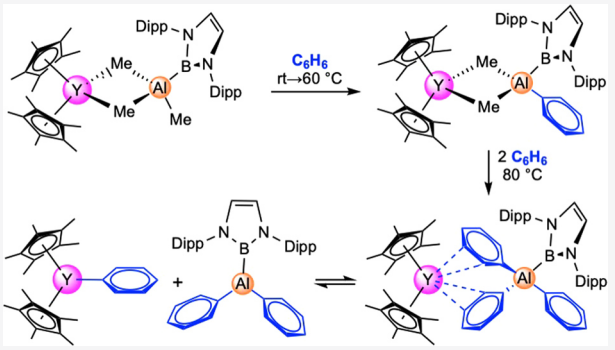

INTRODUCTION

In 1983, Watson marked a milestone in organolanthanide-promoted C−H-bond-activation chemistry by discovering reversible methane-exchange reactions of donor-solvent-free rare-earth-metallocene compounds [Cp*$_2$LnMe]$_2$ (Ln = Y, Lu; Cp* = C$_5$Me$_5$).[1−3] Detailed kinetic studies revealed that the monomer [Cp*$_2$LnMe] is the active species to engage with methane in a four-centered transition state (Scheme 1). Watson also pointed out that intramolecular C−H-bond activation and the formation of a tuck-in complex are competing with the bimolecular process. Shortly after, Bercaw and co-workers reported on a very similar reactivity for [Cp*$_2$ScMe], coining the term "σ-bond metathesis".[4,5]

Scheme 1. Methane Activation by Unsolvated Rare-Earth Metallocenes [Cp*$_2$LnMe]$_x$ (*x* = 1, Ln = Sc; *x* = 2, Ln = Y, Lu) via the Formation of "Tuck-in" Complexes (Left) and Four-Centered Transition States (Right)[1−5]

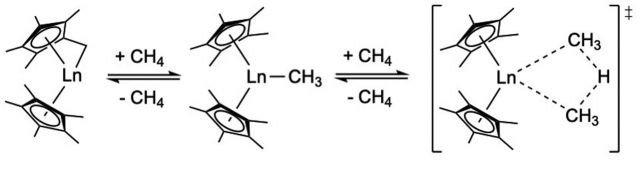

The synthesis of other coordinatively unsaturated metallocenes [Cp*$_2$LnMe]$_x$ has remained challenging because the reactivity was shown to increase with increasing size of the ionic radii of the rare-earth-metal center, tantamount to enhanced steric unsaturation.[2] It was not until 2005 that Evans et al. reported on the congener of the larger-sized samarium(III), revealing the asymmetric trimer [Cp*$_2$SmMe]$_3$ instead of an asymmetric dimer (Ln = Y, Lu) in the solid state.[6] Not surprisingly, the samarium derivative performs in a multitude of C−H-bond-activation reactions, and its comparatively higher reactivity was ascribed to the formation of doubly metalated Cp* ligands. Only recently did Walter et al. successfully prepare the ytterbium derivative [Cp*$_2$YbMe]$_2$

Received: August 3, 2021
Published: September 11, 2021

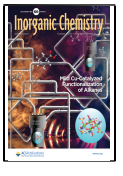

https://doi.org/10.1021/acs.inorgchem.1c02349
Inorg. Chem. 2021, 60, 14952−14968

via oxidative methylation.[7] Unexpectedly and "mysteriously", the redox-active $[Cp^*_2YbMe]_2$ (open-shell, f^{13} isomorphous with the lutetium analogue) does not engage in the C−H-bond-activation chemistry typically observed for the closed-shell congeners scandium and yttrium, as well as for samarium.

Extensive research works on rare-earth-metallocene methyl complexes revealed a rich chemistry and an outstanding performance in the hydrogenolysis and C−H-bond activation of numerous substrates including benzene, toluene, pyridine, and tetramethylsilane (Scheme 2).[1−5,8−11] As such, σ-bond

Scheme 2. Reactivity of $[Cp^*_2LnMe]_x$ (x = 1, Ln = Sc; x = 2, Ln = Y, Lu; x = 3, Ln = Sm) and Reaction Products Characterized by Single-Crystal XRD or NMR Spectroscopy Only

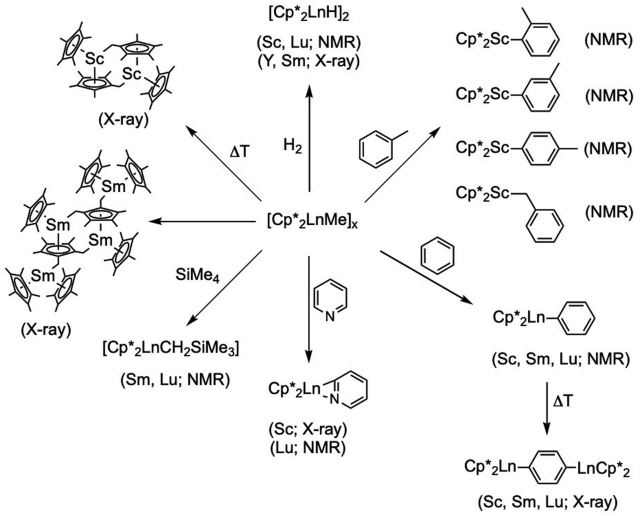

metathesis is considered to be the crucial mechanistic pathway for Ln(III)-promoted C−H-bond activation, and therefore $[Cp^*_2LnMe]_x$ are regarded as archetypical compounds of extraordinary reactivity.[12] While most of the reaction products were isolable and characterized by X-ray diffraction (XRD), the isolation of $[Cp^*_2LnPh]$ from benzene solutions proved to be delicate. Instead, the p-phenylene-bridged $Cp^*_2Ln(\mu\text{-}1,4\text{-}C_6H_4)LnCp^*_2$ (Ln = Sc, Sm, Lu) could be obtained (Scheme 2).[6,8,13,14]

The associated rare-earth-metallocene tetramethylaluminates $[Cp^*_2Ln(AlMe_4)]$ can be accessed via (a) the addition of $AlMe_3$ to $[Cp^*_2LnMe]$,[15,16] (b) $LiAlMe_4$ salt extrusion from $Cp^*_2LnMe_2Li/AlMe_3$,[17] (c) protonolysis of $Ln(AlMe_4)_3$ with Cp*H,[16] (d) redox methylation of $Cp^*_2Sm(THF)_2$ (THF = tetrahydrofuran) with $AlMe_3$,[15] or (e) allyl displacement in $[C_5Me_4(SiMe_2CH_2CH{=}CH_2)]_2Y(C_3H_5)$ with $AlMe_3$.[18] While such heterobimetallics are available for the entire Ln(III) size range, the coordination sphere of the rare-earth-metal center is now "saturated" by an additional methyl group. In addition to the relatively high thermal robustness and reasonable solubility in aromatic solvents, $[Cp^*_2Ln(AlMe_4)]$ ["methyls in disguise": $Cp^*_2LnMe(AlMe_3)$] exhibit reactivities comparable to those of $[Cp^*_2LnMe]_x$, e.g., as precatalysts in ethylene polymerization.[17,19]

Considering the concept of reversible donor-induced tetramethylaluminate cleavage reactions,[20] we were intrigued by the idea of further tracing analogies in the chemistry of $[Cp^*_2LnMe]_x$ and $[Cp^*_2Ln(AlMe_4)]$. The potential metalation of benzene was selected as an exemplary reaction for C−H-bond activation, and the impact of Group 13 methyls was probed by a comparative study of the yttrocene complexes $[Cp^*_2Y(AlMe_4)]$, $[Cp^*_2Y(GaMe_4)]$, and $Cp^*_2Y[Me_3Al\{B(NDippCH)_2\}]$ (Dipp = $C_6H_3iPr_2$-2,6).

RESULTS AND DISCUSSION

Metalation of Benzene by $[Cp^*_2Y(AlMe_4)]$ (1^{Al}). Already the initial papers on rare-earth-metallocene tetramethylaluminate complexes pointed to their remarkable thermal stability. For example, the parent $(C_5H_5)_2(LnAlMe_4)$ compounds were described as sublimable without decomposition (Ln = Sc, 100 °C/0.1 mmHg; Y, 120 °C/0.05 mmHg).[20,21] A similar sublimation behavior was reported for homoleptic $Y(AlMe_4)_3$ (80 °C/10^{-3} mbar).[22] Further important properties of this compound class were described by Watson.[23] Accordingly, $[Cp^*_2Lu(AlMe_4)]$ was found to engage in a monomer−dimer equilibrium (vide infra; a very slow process on the NMR time scale, as evidenced by sharp signals) but undergoes rapid exchange reactions with $Al(CD_3)_3$, while $AlMe_3$ binds much more strongly to $[Cp^*_2LuMe]$ than ethereal molecules.[24]

Not unexpectedly, our benchmark compound $[Cp^*_2Y(AlMe_4)]$ ($\mathbf{1}^{Al}$) was found to be chemically inert to aliphatic and aromatic solvents at temperatures ≤90 °C.[25] However, heating benzene solutions of $\mathbf{1}^{Al}$ at a slightly increased temperature of 100 °C for 42 h resulted in the selective formation of heteroaluminate $[Cp^*_2Y(Me_2AlPh_2)]$ ($\mathbf{3}^{Al}$) in almost quantitative yield under the release of methane (Scheme 3). In accordance with $\mathbf{1}^{Al}$,[23,26] the ^1H NMR

Scheme 3. Multiple Methyl/Phenyl Exchange in $[Cp^*_2Y(MMe_4)]$ [M = Al ($\mathbf{1}^{Al}$), Ga ($\mathbf{1}^{Ga}$] at Elevated Temperatures in Benzene

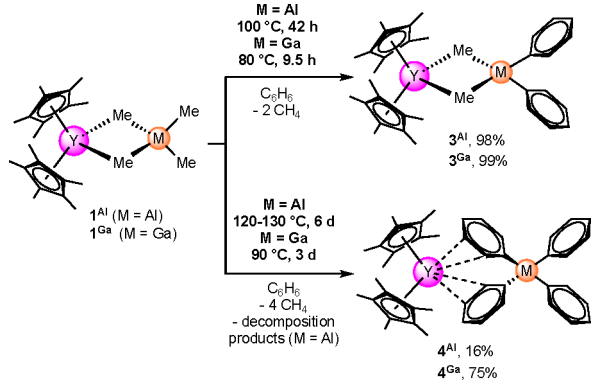

spectrum of $\mathbf{3}^{Al}$ in C_6D_6 shows two sets of signals accounting for monomeric $Cp^*_2Y(Me_2AlPh_2)$ ($\mathbf{3}^{Al}_M$) and dimeric $Cp^*_2Y\{(\mu\text{-Me})AlPh_2(\mu\text{-Me})\}_2YCp^*_2$ ($\mathbf{3}^{Al}_D$). In contrast to the sterically less encumbered $\mathbf{1}^{Al}$, which was reported to form the entropically favored monomer as the dominant species at 20 °C (a ratio of approximately 4:1; cf. Table 1), complex $\mathbf{3}^{Al}$ displays an almost equal distribution of monomer and dimer at ambient temperature. This indicates that the enthalpy term in the linear binding situation[27,28] of the bridging methyl groups increases markedly because of methyl/phenyl exchange. The lower basicity of Ph^- [pK_a(benzene) = 43] compared to that of Me^- [pK_a(methane) = 48] possibly increases the Lewis acidity at the aluminum center and therefore strengthens already existing Al−C bonds.[29]

https://doi.org/10.1021/acs.inorgchem.1c02349
Inorg. Chem. 2021, 60, 14952−14968

Table 1. Relative Distribution of Monomer versus Dimer of Compounds 1^{Al}, 3^{Al}, 1^{Ga}, 3^{Ga}, and 6 at 26 °C in C_6D_6 Solutions, Derived from the Methyl Group Integral Ratio of the ^1H NMR Spectra (cf. the Supporting Information)

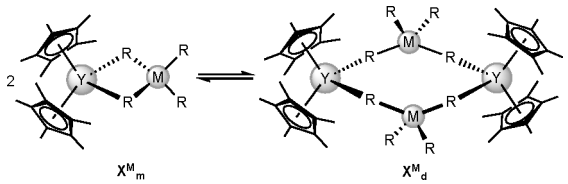

	monomer (rel %)	dimer (rel %)
1^{Al}	84	16
3^{Al}	54	46
1^{Ga}	98	2
3^{Ga}	77	23
6	100	0

The methyl groups resonate as sharp doublets at −0.11 ppm ($3^{Al}{}_M$) and −0.53 ppm ($3^{Al}{}_D$) because of a scalar ^2J(Y,H) yttrium−hydrogen coupling of 5.0 and 3.0 Hz, respectively. Accordingly, the methyl groups are exclusively in the bridging positions. The variable-temperature (VT) ^1H NMR experiment of 3^{Al} indicated that dimeric $3^{Al}{}_D$ is favored at lower temperatures, while monomeric $3^{Al}{}_M$ dominates at T > 30 °C, similar to 1^{Al}.[23,26] At 100 °C, $3^{Al}{}_M$ is present exclusively. However, the molecular structure in the solid state is exclusively represented by the dimer $3^{Al}{}_D$ (Figure 1), even

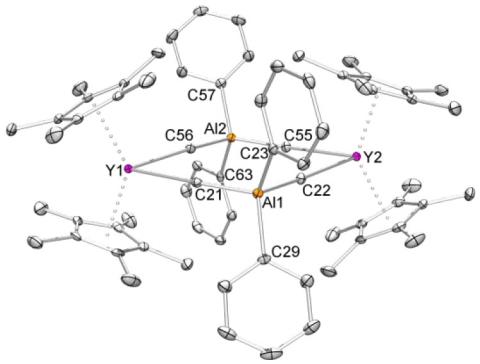

Figure 1. Crystal structure of $3^{Al}{}_D$. For the structural analogue $3^{Ga}{}_D$, compare Figure S6. All atoms are represented by atomic displacement ellipsoids set at 50% probability. Hydrogen atoms are omitted for clarity.

when crystallized at ambient temperature. Compound $3^{Al}{}_D$ features the same structural motif as $1^{Al}{}_D$, with a virtually planar eight-membered heterobimetallic ring.[23] The Al−C distances in $3^{Al}{}_D$ (av 2.012 Å) match those in $1^{Al}{}_D$ (av 2.010 Å; because of the low-quality XRD data published in the original work, the crystal structure of $1^{Al}{}_D$ was reexamined; cf. Figure S1 and Table S1).[23] The Y−C(Cp*) distances in $3^{Al}{}_D$ (av 2.750 Å) appear significantly elongated compared to those in $1^{Al}{}_D$ (av 2.678 Å) most likely because of increased steric repulsion between the terminal phenyl moieties and Cp* ligands.

In contrast to the well-established homoalkylaluminate (AlR_4^-) complexes, heteroalkylaluminates ($AlR_xR'_y^-$) are rare[30] for the rare-earth elements and have been structurally authenticated for, e.g., $(C_5Me_5)_2Sm[(\mu\text{-}Me)_2Al(C_5Me_5)\text{-}Me]_2Sm(C_5Me_5)_2$[31] and *rac*-$[Me_2Si(2\text{-}Me\text{-}C_9H_5)_2]Y(\mu\text{-}Me)(\mu\text{-}Et)AlEt_2$.[32] Mixed alkyl/phenyl aluminates were predominantly obtained as adducts of $Al(C_6F_5)_3$ and d-block metal alkyl compounds.[33−37] Moreover, Krieck et al. prepared a series of solvent-separated calcium bis(aluminate) complexes $[Ca(THF)_6][(Me_{4-n}AlPh_n)]_2$ (n = 0−4),[38] whereas lanthanum compounds $[Cp^*La(Me_3Al\{C_6F_5\})(Me_2Al\{C_6F_5\}_2)]_2$[39] and $[(2,4\text{-dtbp})La(Me_3Al\{C_6F_5\})(Me_2Al\{C_6F_5\}_2)]_2$ (2,4-dtbp = 2,4-di-*tert*-butylpentadienyl)[40] feature the characteristic eight-membered heterobimetallic ring with two terminal aryl moieties at the aluminum center.[24]

Prolonged thermal treatment of 1^{Al} (or 3^{Al}) in benzene solutions at $T \geq 120$ °C led to continuous methane extrusion and a color change of the colorless solution to bright yellow after 6 days. The ^1H NMR spectrum of the crude product revealed the absence of Al−Me groups and resonances in the Cp* and aromatic region accounting for decomposition reactions under these conditions. However, after workup, an off-white powder of pure $Cp^*{}_2Y(AlPh_4)$ (4^{Al}) could be isolated in low yield. Attempts to optimize the yield of 4^{Al} failed because product formation proceeds very slowly at T < 120 °C (and stops at T < 100 °C), while decomposition reactions seem to be far less temperature-dependent in the range between 100 and 130 °C. At 26 °C, the ^1H NMR spectrum in C_6D_6 of compound 4^{Al} shows one broad singlet at 1.52 ppm for the Cp* ligands and one set of signals in the range of 7.17−8.07 ppm for the phenyl groups, with the latter showing strong dynamic broadening. It is noteworthy that the $^{13}C\{^1H\}$ NMR spectrum at ambient temperature shows one very broad signal for the Al−C(*ipso*-Ph) moieties shifted considerably to low field at 162.6 ppm. For deeper insights into the dynamic behavior of 4^{Al}, VT ^1H NMR studies in toluene-d_8 were performed. Thus, at temperatures below 0 °C, the Cp* ligands and the signal of the *o*-phenyl protons shifted to lower fields and resonated as sharp signals. Upon cooling to −40 °C, aside the dominant sharp singlet resonance at 1.52 ppm ascribed to 4^{Al}, another weak Cp* signal at 1.78 ppm (approximately 1:15) indicated the presence of traces of $[Cp^*{}_2YPh]$ via $AlPh_3$ dissociation (vide infra). Heating the sample to 80 °C resulted in a line sharpening of the Cp* resonance at 1.52 ppm, as well, while the signal of the *o*-phenyl protons merged to a broad singlet under these conditions. The *m*-phenyl and *p*-phenyl proton resonances show no significant temperature sensitivity. This might be due to the conversion of 4^{Al} from a weakly coordinated contact ion pair at low temperature, and hence decreased dynamic processes, to dissociated ions at elevated temperature and therefore undistorted $[Cp^*{}_2Y]^+$ cations and solvent-separated $[AlPh_4]^-$ anions. Rotation of the phenyl moieties mainly influence the *o*-phenyl proton resonance, resulting in effective line broadening at T > 60 °C.

The solid-state structure of 4^{Al} (Figure 2) is reminiscent of the tetraphenylborate complex $Cp^*{}_2Y(BPh_4)$ (4^B).[41] For comparison, the Al−C bond distances of av 2.007 Å match those found in alkaline-earth-metal complexes coordinated by $[AlPh_4]^-$[38,42−44] but are longer than the B−C bond distances of av 1.638 Å in 4^B with respect to the differences of the ionic radii (Al^{3+}, 53 pm; B^{3+}, 25 pm).[45] As a consequence, the $[AlPh_4]^-$ anion is sterically more demanding than $[BPh_4]^-$ and the closest interatomic distances between the yttrium center and *o*-carbon atoms are 2.887(1) and 2.872(1) Å, respectively, which are somewhat longer than those in 4^B [2.819(3) and 2.813(3) Å], in accordance with the elongated Y···M distance (4.786 Å, M = Al; 4.442 Å, M = B). The distances between Y^{3+} and the *m*-carbon atoms C23 and C29 [3.155(2) and 3.154(2)

https://doi.org/10.1021/acs.inorgchem.1c02349
Inorg. Chem. 2021, 60, 14952−14968

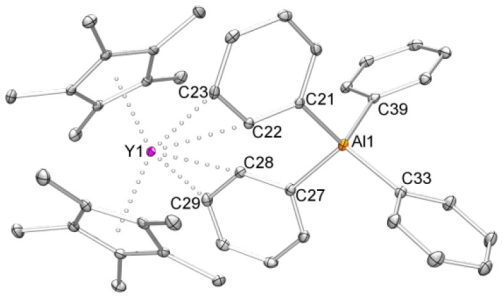

Figure 2. Crystal structure of tetraphenylaluminate $\mathbf{4}^{Al}$. For the structural analogue $\mathbf{4}^{Ga}$, compare Figure S7. All atoms are represented by atomic displacement ellipsoids set at 50% probability. Hydrogen atoms and cocrystallized benzene are omitted for clarity.

Å], however, are comparable to those in $\mathbf{4}^{B}$ [3.152(3) and 3.118(3) Å].

Considering [$AlMe_4$] moieties as "alkyls in disguise" dissociation of $AlMe_3$ from $\mathbf{1}^{Al}$ and liberation of [Cp^*_2YMe] under forcing thermal conditions would be a plausible scenario (Scheme 4). Note that a loss of $AlMe_3$ is presumed to be the main decomposition pathway of $Sc(AlMe_4)_3$.[46,47] Accordingly, the sterically demanding Cp* ligands in [$Cp^*_2Y(AlMe_4)$] might impart sufficient steric destabilization of the [$AlMe_4$] moiety. [Cp^*_2YMe] is well-known for its outstanding performance in various C−H-bond-activation reactions; e.g., [Cp^*_2YMe] activates benzene under the evolution of methane and the formation of [Cp^*_2YPh].[1] Hence, compound $\mathbf{4}^{Al}$ can be considered to be a Lewis acid−base adduct of [Cp^*_2YPh] stabilized by $AlPh_3$ and therefore represents the first structurally characterized derivative of donor-solvent-free metallocenes [Cp^*_2LnPh].

Metalation of Benzene by [$Cp^*_2Y(GaMe_4)$] ($\mathbf{1}^{Ga}$). Considering a dissociation scenario and the in situ formation of highly reactive [Cp^*_2YMe], a more labile yttrocene derivative, compared to $\mathbf{1}^{Al}$, should activate benzene at even lower temperature. We and others have demonstrated previously that alkylgallate/aluminate derivatives (Ga^{3+} vs Al^{3+}) feature similar structural motifs[16,48−53] but differ markedly in terms of thermal robustness and dissociation of $GaMe_3$/$AlMe_3$ because $GaMe_3$ is a considerably weaker Lewis acid.[14,35] For example, while $Y(AlMe_4)_3$ is sublimable,[22] $Y(GaMe_4)_3$ separates $GaMe_3$ under vacuum, affording pure [YMe_3]$_n$.[50] Thus, it was reasonable to probe whether the corresponding gallate compound $\mathbf{1}^{Ga}$ exhibits enhanced reactivity in benzene metalation.

Indeed, $\mathbf{1}^{Ga}$ metalates benzene already at $T \geq 80$ °C (Scheme 3) in an identical fashion to afford the gallate analogues [$Cp^*_2Y(Me_2GaPh_2)$] ($\mathbf{3}^{Ga}$) and $Cp^*_2Y(GaPh_4)$ ($\mathbf{4}^{Ga}$) in high yields. Compounds $\mathbf{3}^{Ga}$ and $\mathbf{4}^{Ga}$ represent structural analogues of the aluminum congeners with almost identical structural parameters (cf. Figures S6 and S7). For comparison, the chemistry of bulky gallate anions seems limited to [$Li\{Cp^*_3Ti_3O_3(CH)\}_2$][$PhLi(GaPh_3\{C_6H_4Me-4\})$],[54] [$Ga(CH_2SiMe_3)_3CH_{5-m}F_m$][$Li(PMDETA)$] ($m$ = 1−3; PMDETA = *N*,*N*,*N*′,*N*″,*N*″-pentamethyldiethylenetriamine)[55] and complexes with the weakly coordinating anion $[Ga(C_6F_5)_4]^-$.[56−62]

The ^{1}H NMR spectrum of $\mathbf{3}^{Ga}$ in C_6D_6 revealed a similar monomer−dimer equilibrium, as observed for related compounds $\mathbf{1}^{Ga}$ and $\mathbf{3}^{Al}$, with the monomer being the dominant species at ambient temperature (cf. Table 1). According to a VT ^{1}H NMR experiment of $\mathbf{3}^{Ga}$, the equilibrium is shifted completely to the monomeric species already at 80 °C. Moreover, the finding for $\mathbf{3}^{Al}$, that exchange of terminal methyl groups by phenyl groups stabilizes the dimer, also applies for $\mathbf{3}^{Ga}$. Finally, a higher monomer content in solution at ambient temperature correlates with a higher reactivity toward benzene activation.

The VT ^{1}H NMR experiment of $\mathbf{4}^{Ga}$ is indicative of a pronounced equilibrium involving [Cp^*_2YPh] and $GaPh_3$. At temperatures above 40 °C, a singlet resonance is present at 1.78 ppm, which may be attributed to [Cp^*_2YPh] (vide infra) because this resonance merges to a broad signal (1.67 ppm) at 10 °C. Further cooling provokes splitting to a minor signal at 1.78 ppm and a dominant singlet at 1.48 ppm, attributed to $\mathbf{4}^{Ga}$. Apparently, $\mathbf{4}^{Ga}$ is labile in solution and dissociates to [Cp^*_2YPh] and $GaPh_3$. This parallels the dynamic behavior observed for $\mathbf{4}^{Al}$ at low temperatures. However, for $\mathbf{4}^{Al}$, no further dissociation was observed at temperatures up to 80 °C. Probably, temperatures higher than 80 °C are necessary to dissociate the [$AlPh_4$]$^-$ anion. The different dissociation behavior of the anions [$GaPh_4$]$^-$ and [$AlPh_4$]$^-$, respectively, seems plausible considering that $AlPh_3$ forms dimers in the solid state, while $GaPh_3$ prefers a monomeric trigonal coordination mode.[63]

Scheme 4. Possible Scenario for Benzene Activation by $\mathbf{1}^{Al}$ and $\mathbf{1}^{Ga}$

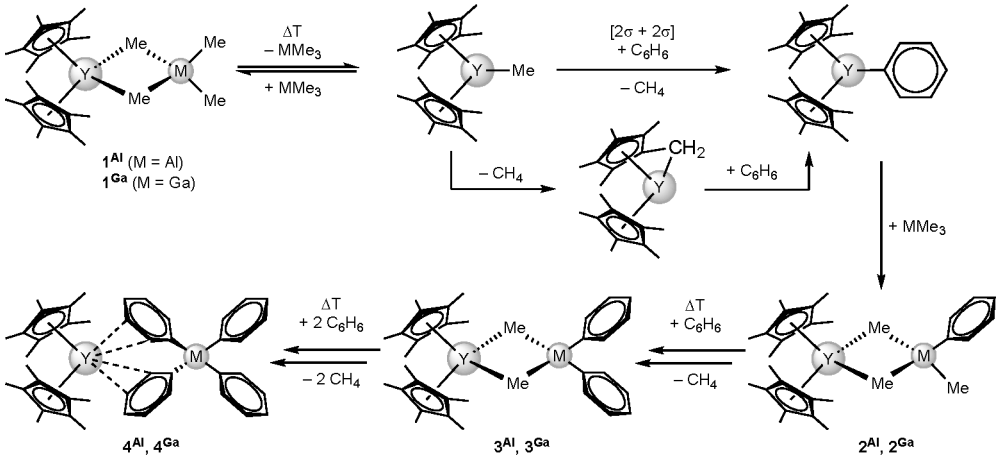

https://doi.org/10.1021/acs.inorgchem.1c02349
Inorg. Chem. 2021, 60, 14952−14968

Mechanistic Considerations. A rational reaction sequence is illustrated in Scheme 4. Starting from monomeric $\mathbf{1}^{Al}_{M}$ and $\mathbf{1}^{Ga}_{M}$, respectively, an initial dissociation of the Lewis acid MMe_3 would release highly reactive [Cp*$_2$YMe]. This is a plausible scenario because $\mathbf{1}^{Al}_{M}$ and $\mathbf{1}^{Ga}_{M}$ significantly differ in activation temperature, as is expected because of the markedly different Lewis acid strength of the corresponding Group 13 metal alkyl MMe_3. Alternatively, Teuben et al. suggested the formation of ions, $[Cp^*_2Y]^+$ and $[AlMe_4]^-$, at temperatures above 70 °C because the resonances of the methyl protons in the ^{1}H NMR spectrum merge into one broad singlet and hence do not account for yttrium−hydrogen coupling.[26] Line broadening and loss of fine resolution is, however, indicative of the rapid exchange of bridging and terminal positions. Furthermore, an ion-pair formation scenario would not explain the different activation temperatures of $\mathbf{1}^{Al}$ compared to $\mathbf{1}^{Ga}$ because ion separation would not be favored by the tetramethylgallate $\mathbf{1}^{Ga}$. The $AlMe_3$-dissociation pathway is also supported by early catalytic investigations of complex $(C_5H_4SiMe_3)_2Y(AlMe_4)$, which feature a threshold effect in ethylene polymerization. While this complex is not active at 70 °C/5 bar C_2H_4 like $[(C_5H_4SiMe_3)_2YMe]_x$ is, it promotes polymerization at >95 °C/33 bar C_2H_4.[19] Moreover, a low excess of $AlMe_3$ was reported to completely stop ethylene polymerization by [Cp*$_2$LuMe] via alkylaluminate formation.[24]

Once liberated, [Cp*$_2$YMe] is capable of activating benzene either in a bimolecular process via a four-centered transition state or according to an intramolecular C−H-bond-activation reaction to form the transient "tuck-in" complex [Cp*Y-$(CH_2C_5Me_4)$], which engages in benzene activation. Both pathways ultimately yield [Cp*$_2$YPh]. Monitoring this process for $\mathbf{1}^{Al}$ and $\mathbf{1}^{Ga}$ by ^{1}H NMR spectroscopy in C_6D_6 indicated a competitive scenario because extrusion of CDH_3 and CH_4 was observed in a relative ratio of approximately 13:1 for both proposed reactions. This is in line with the findings of Thompson et al. when treating [Cp*$_2$ScMe] with C_6D_6.[4] At 80 °C in neat benzene solutions, [Cp*$_2$ScMe] generated methane to form [Cp*$_2$ScPh] cleanly, while in C_6D_6 solutions, a mixture of CDH_3 and CH_4 was observed. Because the "tuck-in" complex [Cp*Sc$(CH_2C_5Me_4)$] was isolable, Thompson et al. could verify that its reaction with C_6D_6 cleanly afforded CDH_3 and [Cp*(Cp*-d_1)ScC_6D_5], corroborating a competing reaction scenario. Following this idea, [Cp*$_2$Y(Me$_2$Al{Ph-d_5}$_2$)] was generated from $\mathbf{1}^{Al}$ in C_6D_6 solutions. Subsequent ^{2}H NMR measurements, however, were not indicative of the presence of a Cp*-d_1 moiety, and only the Ph-d_5 groups were detected, which is in stark contrast to the intermediate "tuck-in" scenario. On the other hand, on the basis of the CDH_3/CH_4 ratio of 13:1, only 7% of [Cp*(Cp*-d_1)Y(Me$_2$Al{Ph-d_5}$_2$)] is estimated to be present, and hence the integrals accounting for Cp*-d_1 would be of very low intensity.

However, monitoring the reaction of $\mathbf{1}^{M}$ in C_6D_6 revealed a strong kinetic deuterium isotope effect, typical for reactions mediated by σ-bond metathesis.[4] This behavior was examined for $\mathbf{1}^{Ga}$ in more detail. Thus, activation of benzene by $\mathbf{1}^{Ga}$ follows first-order kinetics until about 80% conversion into $\mathbf{3}^{Ga}$. As pointed out before, methyl/phenyl exchange seems to stabilize the unreactive dimer. Therefore, the proceeding methyl/phenyl exchange would result in reduced reactivity regarding benzene activation. The activation of C_6D_6 proceeded approximately 4 times slower, corresponding to a kinetic isotope effect of approximately k_H/k_D = 3.8, as determined by a comparison of the relative integral ratios in the ^{1}H NMR spectra. This value compares well to kinetic isotope data found in the literature for σ-bond metathesis of C−H bonds.[1,4,12,64]

Upon formation of [Cp*$_2$YPh], the addition of the previously dissociated Lewis acid MMe_3 and immediate methyl/phenyl exchange at the bridging position would afford compounds [Cp*$_2$Y(Me$_3$MPh)] ($\mathbf{2}^{M}$). Naturally, the sterically more demanding phenyl groups would be accommodated in the ligand periphery.[29,32] Finally, repeating this reaction sequence would lead to complete methyl/phenyl exchange along with decelerated conversion rates. Accordingly, the formation of $\mathbf{3}^{Ga}$ is accomplished within 10 h, while complete methyl/phenyl exchange to afford $\mathbf{4}^{Ga}$ requires 3 days at even higher temperatures.

Ligand-Exchange Experiments. The rapid exchange of bridging and terminal alkyl groups is routinely observed within $[MR_4]$ moieties (M = Al, Ga) and selectively afforded complexes $\mathbf{3}^{Al}$ and $\mathbf{3}^{Ga}$ in high purity. Thus, the oddly substituted aluminates and gallates $\mathbf{2}^{M}$ and [Cp*$_2$Y(MeMPh$_3$)] should be formed prior to compounds $\mathbf{3}^{M}$ and $\mathbf{4}^{M}$, respectively. Indeed, additional signal sets accounting for the presence of mixed aluminates/gallates are indicated by ^{1}H NMR spectroscopy when monitoring the complete exchange process. Most unfortunately, attempts to crystallize any of those intermediates from the crude product mixture failed, and only crystals of $\mathbf{3}^{M}$ and $\mathbf{4}^{M}$ were obtained. Hence, $\mathbf{1}^{M}$ and $\mathbf{3}^{M}$ were mixed in a 1:1 ratio to afford putative compounds $\mathbf{2}^{M}$ in a rational approach. However, the ^{1}H NMR spectra indicated that compounds $\mathbf{2}^{M}$ are in equilibrium with $\mathbf{1}^{M}$, $\mathbf{3}^{M}$, and $[(Cp^*_2Y)_2(M_2Me_{8-n}Ph_n)]$ (n = 1−3). Consequently, crystals of $\mathbf{2}^{M}$ contain approximately 25−50% of cocrystallized $\mathbf{1}^{M}$ (cf. Figures S2 and S3). In a similar vein, $\mathbf{3}^{M}$ and $\mathbf{4}^{M}$ were mixed to afford compounds [Cp*$_2$Y(MeMPh$_3$)]. This triphenylmethylaluminate, however, seems to be disfavored, and crystallization led to disproportionation and the exclusive formation of $\mathbf{3}^{M}$ and $\mathbf{4}^{M}$. This observation is in line with VT ^{1}H NMR spectral data of a 1:1 mixture of $\mathbf{3}^{Ga}$ and $\mathbf{4}^{Ga}$ in C_6D_6. At temperatures above 60 °C, two broad singlets at 1.74 ppm (Cp*) and −0.04 ppm (Me) with an integral ratio of approximately 30:3 account for the presence of [Cp*$_2$Y(MeGaPh$_3$)], while upon cooling to 0 °C, these resonances decreased and signals appeared clearly assignable to $\mathbf{3}^{Ga}$ and $\mathbf{4}^{Ga}$ (cf. Figure S43).

Metalation of Benzene by Cp*$_2$Y[Me$_3$Al{B(NDippCH)$_2$}] (6). The aluminum/gallium exchange ($\mathbf{1}^{Al}$ vs $\mathbf{1}^{Ga}$) proved to be a viable strategy for lending support to the dissociation mechanism depicted in Scheme 4. Alternatively, we envisaged the use of a sterically demanding aluminate functionality as another approach to promoting dissociative aluminate cleavage. Previously, our group introduced organoaluminum boryl compound [Me$_2$Al{B(NDippCH)$_2$}]$_2$ (Dipp = $C_6H_3iPr_2$-2,6) as a bulky Lewis acid, deaggregating polymeric $[YMe_3]_n$ and trimeric $[Cp^*YMe_2]_3$ into the monomeric heteroaluminate complexes Y(Me$_3$Al[B(NDippCH)$_2$])$_3$ and Cp*Y(Me$_3$Al[B(NDippCH)$_2$])$_2$ (**5**), respectively.[65,66] In both the homoleptic and half-sandwich complexes, the bulky boryl ligand adopts a terminal position at the aluminum center. Accordingly, we were intrigued to access the respective metallocene complex **6** for comparative studies in benzene activation.

The salt-metathesis reaction of **5** and KCp* afforded Cp*$_2$Y[Me$_3$Al{B(NDippCH)$_2$}] (**6**) in almost quantitative yields along with the polymeric coproduct [K(Me$_3$Al{B-

https://doi.org/10.1021/acs.inorgchem.1c02349
Inorg. Chem. 2021, 60, 14952−14968

$(NDippCH)_2\})]_n$ (**7**; Scheme 5). Compound **7** is insoluble in aliphatic solvents but dissolves in benzene to a low extent. The

Scheme 5. Synthesis of 6 via the Salt-Metathesis Reaction of the Half-Sandwich Compound 5 and KCp*

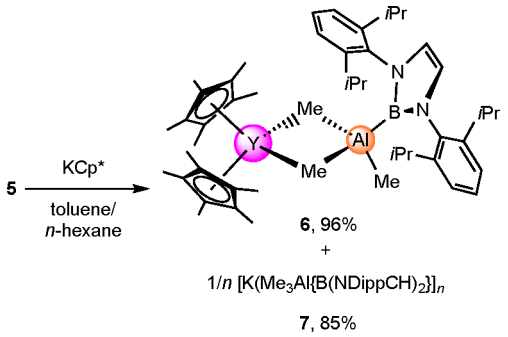

^{1}H NMR spectrum of **7** confirms the typical set of signals accounting for the boryl moiety accompanied by the singlet at −1.25 ppm assignable to the organoaluminum moiety (9H, $AlMe_3$). The methyl groups are highly fluxional in solution, similar to that observed for $Ln(Me_3Al[B(NDippCH)_2])_3$[65] and $Cp^*Ln(Me_3Al[B(NDippCH)_2])_2$ (Ln = Lu, Y).[66]

Single crystals of **7** were obtained from refluxing benzene solutions as very thin needles. The poor quality of the XRD data allowed for only depiction of the connectivity of **7** (Figure 3), but ruling out any detailed discussion of metrical parameters. Notwithstanding, compound **7** adopts a paired polymeric chain arrangement in the solid state comprising alternating 8- and 12-memberd rings with two distinct potassium environments (Figure S9). The peripheral potassium atoms coordinate to four methyl groups and feature weak interactions with the π systems of two aryl rings, which are aligned almost orthogonally. The central potassium atoms interconnect the two molecular branches and bind to three methyl groups with additional interactions to two aryl rings in an almost linear alignment. For comparison, structurally characterized solvent-free potassium tetraorganoaluminates, $[K(Me_3AlCN)]_n$[67] and $[K(AlEt_4)]_n$,[68] respectively, form three-dimensional networks, while tetraorganoaluminates of the lighter alkaline metals $[AM(AlR_4)]_n$ (R = Me, Et, *n*-Pr) exhibit linear chain structures (AM = Li)[63] or three-dimensional networks (AM = Na).[69,70] Moreover, our group reported previously on the synthesis of tetrameric $[Li(Me_3Ga\{B(NDippCH)_2\})]_4$[71] featuring a 16-membered ring, with the lithium atoms in a coordination mode similar to that described for the central potassium atoms in **7**. However, the smaller lithium allows only for one π−arene interaction, as a consequence of the difference in the ionic radii of lithium (73 pm) and potassium (151 ppm).[45]

In contrast to the low solubility in aromatic solvents, **7** dissolves readily upon the addition of THF to a benzene suspension. The single-crystal structure determination of the THF adduct $[(THF)_2K(Me_3Al\{B(NDippCH)_2\})]_n$ (**8**) revealed a zigzag chain structure (Figure 4), with μ_2-η^2:η^1 $[Me_3Al\{B(NDippCH)_2\}]$ moieties interconnecting the potassium centers. Each potassium atom is coordinated by three methyl carbon atoms and two THF oxygen atoms. While the Al−C distances are all within the expected range of av 2.024 Å, the K−C distances differ considerably because of the different binding modes of the methyl groups. Accordingly, two relatively short K−C distances of 3.093(5) and 3.072(5) Å

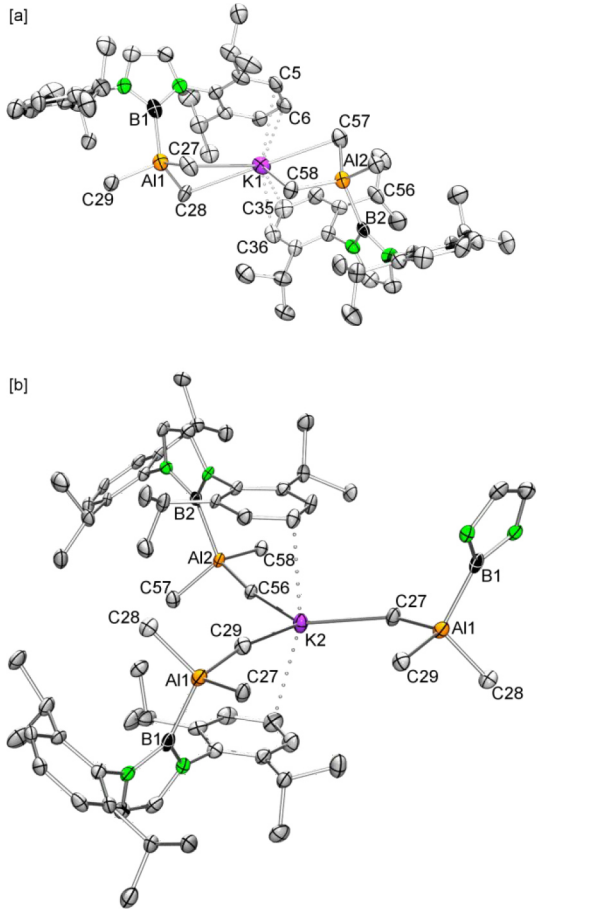

Figure 3. Molecular connectivity of polymeric **7** comprising two distinct binding situations for potassium with coordination numbers of (a) 6 and (b) 5. All atoms are represented by atomic displacement ellipsoids set at 50% probability. Hydrogen atoms and the disorder in one Dipp moiety are omitted for clarity; in part b, two Dipp moieties are omitted.

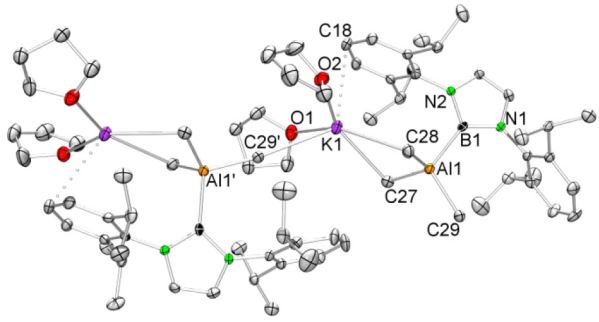

Figure 4. Section of the polymeric network in the solid-state structure of the THF adduct **8**. All atoms are represented by atomic displacement ellipsoids set at 50% probability. Hydrogen atoms and the disorder in one THF molecule are omitted for clarity.

are found in the bent unit [K−C(CH$_3$)−Al], along with one elongated K−C distance of 3.215(3) Å in the almost linear K1−C29′−Al1′ linkage (171.6°), with an additional close contact of the potassium center to the *p*-carbon atom [3.324(4) Å] of one aryl ring of the boryl unit.

The ^{1}H NMR spectrum of the yttrocene complex **6** in C_6D_6 shows a set of signals attributable to the boryl moiety. The reduced symmetry is indicated by two singlets at 1.69 ppm

https://doi.org/10.1021/acs.inorgchem.1c02349
Inorg. Chem. 2021, 60, 14952−14968

(15H) and 1.83 ppm (15H), which can be assigned to the Cp* ligands. The singlet at −0.49 ppm (3H) and the doublet at −0.89 ppm [6H, ^2J(Y,H) = 5.3 Hz] in the high-field region are attributed to the terminal and bridging methyl groups, respectively. However, the ^{1}H NMR spectrum gave no indication of the existence of a monomer−dimer equilibrium (not even upon cooling to −80 °C), diagnostic for related compounds $\mathbf{1}^{Al}$ and $\mathbf{3}^{Al}$ (vide supra). These findings clearly evidence the reduced mobility of the methyl groups compared to the starting material **5**, with highly fluxional methyl groups, which resonate as a single doublet in the ^{1}H NMR spectrum at ambient temperature. At elevated temperatures, compound **6** displayed coalescence of the Cp* signals ($T \geq 60$ °C) and methyl group resonances ($T \geq 80$ °C). Obviously, the steric demand of the terminal boryl moiety in close proximity to the Cp* ligands effectively prevents aggregation to dimers. The presence of a three-coordinate boron center in complex **6** is evidenced by the ^{11}B{^{1}H} NMR resonance at δ = 32.9 ppm, comparable to those detected for Lu(Me$_3$Al[B(NDippCH)$_2$])$_3$ (28.6 ppm), Cp*Ln(Me$_3$Al[B(NDippCH)$_2$])$_2$ (Ln = Y, 31.4 ppm; Ln = Lu, 31.0 ppm), and [Me$_2$Al{B(NDippCH)$_2$}]$_2$ (27.9 ppm).[65,66]

The XRD analysis of **6** revealed a monomeric complex in accordance with NMR spectroscopy (Figure 5). The

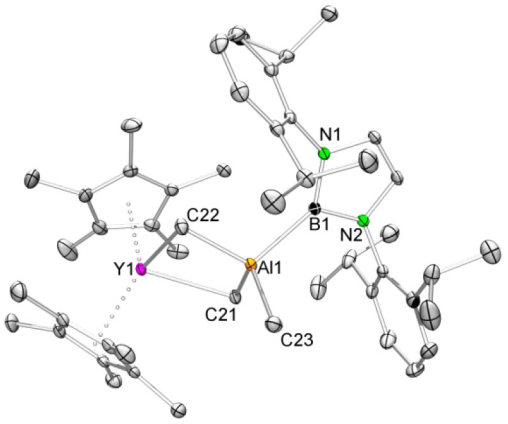

Figure 5. Crystal structure of **6**. All atoms are represented by atomic displacement ellipsoids set at 50% probability. Hydrogen atoms are omitted for clarity.

heteroaluminate moiety coordinates in a η^2 fashion, forming a planar [Y(μ-CH$_3$)$_2$Al] metallacycle, as was observed for the yttrium tetramethylaluminates Y(AlMe$_4$)$_3$[72] and Cp*Y(AlMe$_4$)$_2$.[16] However, the [AlMe$_4$] unit of the corresponding rare-earth-metallocene alkylaluminates [Cp*$_2$Ln(AlMe$_4$)] coordinates in a classical μ_2-η^1:η^1 fashion. For comparison, monomeric metallocene alkylaluminates were reported for less encumbered rare-earth-metal centers in (C$_5$H$_5$)$_2$Ln(AlMe$_4$) (Ln = Y,[73] Yb[21]), (C$_5$H$_4$SiMe$_3$)$_2$Ce(AlMe$_4$),[74] (C$_{13}$H$_9$)$_2$Lu(AlMe$_4$)[75] and Cp*$_2$Ln(AlEt$_4$) (Ln = Sm,[76] Yb[77]). A very similar structural motif has been found for the monomeric tetramethylgallate compound Cp*$_2$La(GaMe$_4$).[16] The B−Al distance of 2.161(2) Å in compound **6** is in the same range as that in complex Lu(Me$_3$Al[B(NDippCH)$_2$])$_3$ (av 2.153 Å)[65] and somewhat longer than those in complexes Cp*Lu(Me$_3$Al[B(NDippCH)$_2$])$_2$ (av 2.136 Å)[66] and [Me$_2$Al{B(NDippCH)$_2$}]$_2$ [2.119(3) Å].[65]

In agreement with prior considerations, the monomeric molecular structure of **6** is associated with enhanced reactivity of the [Y−C(CH$_3$)−Al] moiety in C−H-bond-activation reactions. In fact, compound **6** activates C$_6$D$_6$ slowly at ambient temperature, as evidenced by the characteristic resonance of CDH$_3$ in the ^{1}H NMR spectrum after 24 h at ambient temperature. At 60 °C, metalation of benzene proceeds comparatively fast and **6** converts into Cp*$_2$Y(Me$_2$AlPh[B(NDippCH)$_2$]) (**9**) almost quantitatively within 36 h (Scheme 6). A kinetic isotope effect of k_H/k_D = 3.0 was determined from the ^{1}H NMR data and is in line with the value calculated for benzene activation by $\mathbf{1}^{Ga}$ (k_H/k_D = 3.8).

Scheme 6. Reactivity of the Heteroaluminate Yttrocene Compound 6 toward Benzene

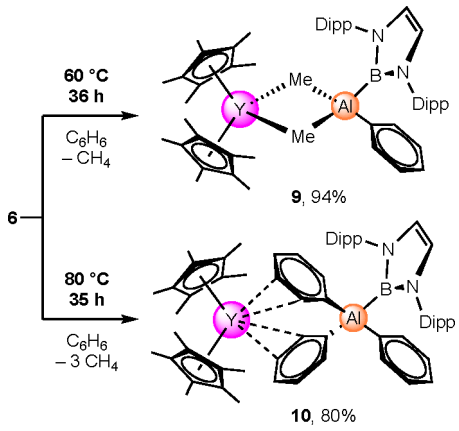

Unsurprisingly, compound **9** is monomeric in the solid state (Figure 6) with structural parameters almost identical with

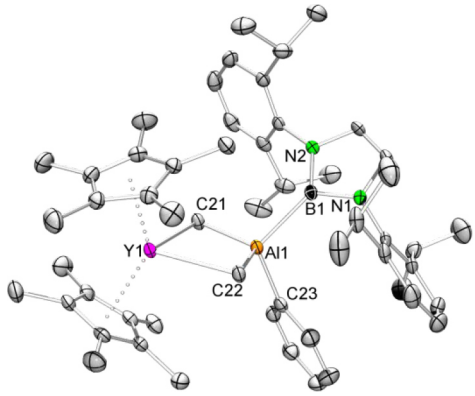

Figure 6. Crystal structure of **9**. All atoms are represented by atomic displacement ellipsoids set at 50% probability. Hydrogen atoms are omitted for clarity.

those of **6**. The aluminum-bonded terminal phenyl group is in proximity to the boryl moiety, which displays a slightly elongated Al−B distance of 2.171(2) Å. The phenyl group in **9** is also clearly detectable in the ^{1}H NMR spectrum in C$_6$D$_6$. Moreover, in the high-field region, only one doublet appeared at δ = −0.53 ppm [6H, ^2J(Y,H)], accounting for the methyl groups in the bridging positions. Broad singlets at 1.51 and 1.81 ppm are assigned to the Cp* ligands. This indicates increased mobility at ambient temperature and hence a more labile aluminato moiety attached to the metallocene fragment (compared to **6**). Accordingly, VT ^{1}H NMR measurements revealed coalescence of the Cp* resonances already at 40 °C (Figure S58). At low temperatures, the doublets at 1.20 ppm

https://doi.org/10.1021/acs.inorgchem.1c02349
Inorg. Chem. 2021, 60, 14952−14968

(12H, 6.7 Hz) and 1.25 ppm (12H, 6.6 Hz), which are attributed to the isopropyl groups, merged into a broad resonance at −20 °C and split into four doublets upon further cooling, in accordance with four independent isopropyl moieties. Simultaneously, the methine septet split into two separate signals. This finding clearly indicates a sterically encumbered aluminum center with an increased rotational barrier around the Al−B and N−C(Dipp) axes. The $^{11}B\{^1H\}$ NMR spectrum shows a signal at 31.2 ppm, accounting for the expected three-coordinate boron nuclei.

Finally, prolonged thermal treatment of **6** in benzene at 80 °C resulted in complete methyl/phenyl exchange within 35 h to afford $Cp^*_2Y[Ph_3Al\{B(NDippCH)_2\}]$ (**10**) in high yields. The solid-state structure of **10** (Figure 7) contains two

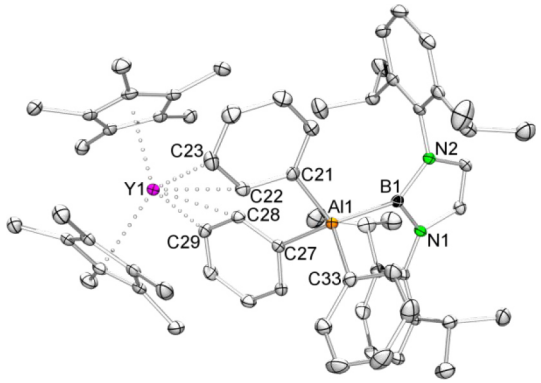

Figure 7. Crystal structure of **10**. All atoms are represented by atomic displacement ellipsoids set at 50% probability. Hydrogen atoms, cocrystallized benzene, and a second independent molecule in the unit cell are omitted for clarity (cf. the Supporting Information).

independent molecules in the asymmetric unit with metrical parameters similar to those of $\mathbf{4}^{Al}$. The yttrocene fragment is coordinated by two phenyl groups through interaction with the *o*- and *m*-carbon atoms (av $Y-C_{ortho}$ = 2.888 Å; av $Y-C_{meta}$ = 3.047 Å). Because of steric constraints, the boryl moiety is in the terminal position and the aluminum-bonded phenyls are slightly directed toward the $[Cp^*_2Y]^+$ entity, and hence the average Y···Al distance of 4.885 Å is elongated compared to that of $\mathbf{4}^{Al}$ (4.786 Å).

Interestingly, at ambient temperature, the ^1H NMR spectrum of compound **10** in C_6D_6 revealed the presence of two different species, as indicated by the signal sets for two independent boryl moieties and two resonances at 1.47 and 1.78 ppm for the Cp* ligands in a ratio of approximately 3:1. The resonances in the aromatic region overlap, hampering a complete signal assignment. However, at 3 °C a set of signals in good agreement with the structure of **10** is clearly dominant. Upon heating, the second species gets more and more pronounced, being present exclusively at 80 °C (Figure 8). Repeated cooling to ambient temperature gave the original ^1H NMR spectrum. Apparently, complex **10** is in equilibrium with $[Cp^*_2YPh]$ and $[Ph_2Al\{B(NDippCH)_2\}]$, hence exhibiting a dissociation behavior similar to that of compounds $\mathbf{4}^{Al}$ and $\mathbf{4}^{Ga}$ at variable temperatures. The $^{11}B\{^1H\}$ NMR spectrum revealed the presence of a three-coordinate boron center, while the strong asymmetric singlet at 28.6 ppm possibly reflects overlap with a second resonance.

To probe the particular importance of the $[Cp^*_2Y]$ fragment for C−H-bond activation by yttrocene heteroaluminate

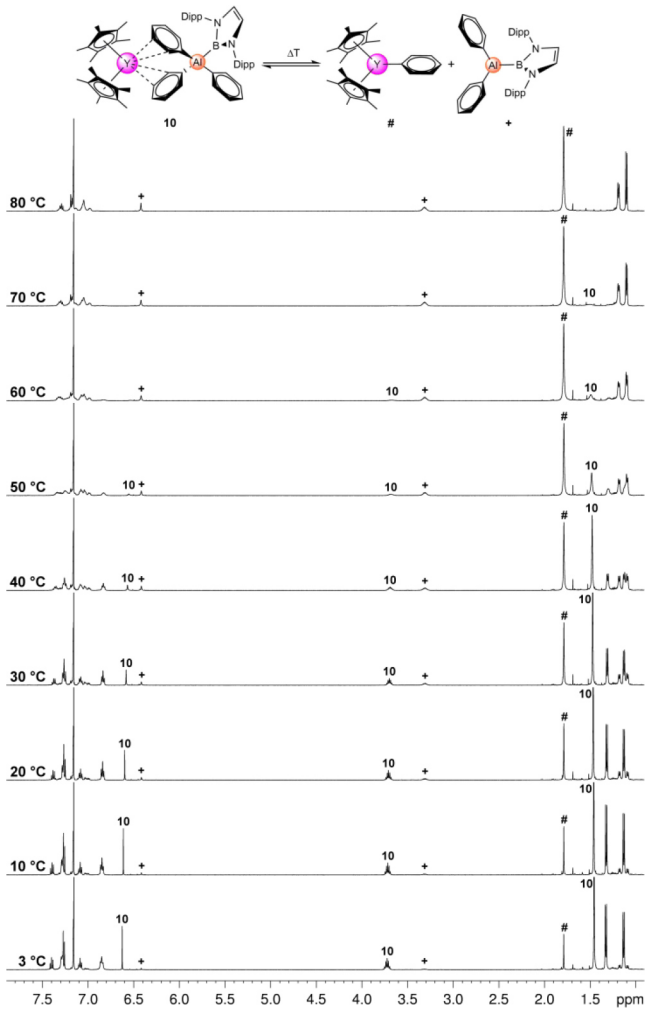

Figure 8. VT ^1H NMR spectra (500 MHz) of **10**, $[Cp^*_2YPh]$ (#), and $[Ph_2Al\{B(NDippCH)_2\}]$ (+) in C_6D_6.

compounds, the sterically less encumbered complex $Cp_2Y[Me_3Al\{B(NDippCH)_2\}]$ (**11**; Cp = C_5H_5) was synthesized by the addition of 1 equiv of $[Me_2Al\{B(NDippCH)_2\}]_2$ to $[Cp_2Y(\mu\text{-Me})]_2$ in hydrocarbon solutions (Scheme 7). In contrast to $[Cp^*_2YMe]_2$, $[Cp_2Y(\mu\text{-Me})]_2$ features two bridging methyl groups in the solid state and is stable in hydrocarbon solutions.[78]

The ^1H NMR spectrum of **11** in C_6D_6 shows the characteristic signals of the boryl moiety aside broad singlets attributed to the Cp ligands at 5.79 ppm (5H) and 5.74 ppm (5H). Broad resonances at −0.67 ppm (3H) and −0.73 ppm (6H) are in accordance with a terminal and two bridging methyl groups and their fluxional behavior at ambient

Scheme 7. Synthesis of 11 via Addition of the Organoaluminum Boryl Compound $[Me_2Al\{B(NDippCH)_2\}]_2$ to $[Cp_2YMe]_2$

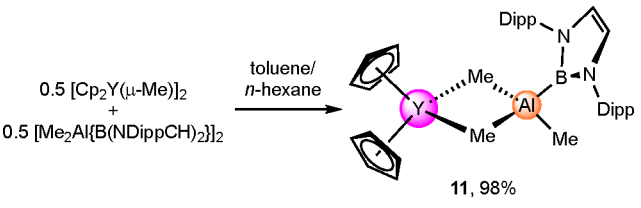

https://doi.org/10.1021/acs.inorgchem.1c02349
Inorg. Chem. 2021, 60, 14952−14968

temperatures. Dynamic processes were studied in more detail by VT ^{1}H NMR measurements in toluene-d_8. Accordingly, the Cp resonances coalesce at temperatures above 40 °C and split into two sharp singlets upon cooling to 0 °C. The resonances attributed to the methyl groups overlap as two broad singlets around −0.75 ppm at temperatures above 30 °C. However, coalescence did not occur even at 80 °C. At temperatures below 10 °C, these resonances separated into a singlet and a doublet [^2J(Y,H) = 5.3 Hz].

The solid-state structure of **11** displays a structural analogue to that of **6** (Figure 9). In good agreement with $(C_5H_5)_2$Y-

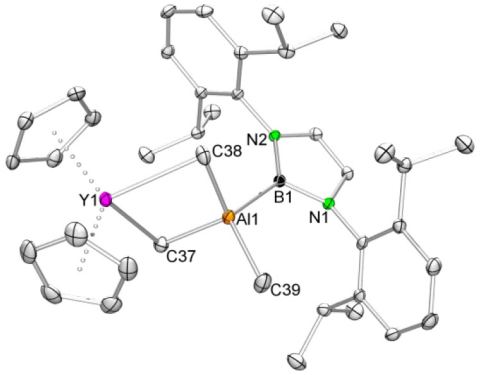

Figure 9. Crystal structure of **11**. All atoms are represented by atomic displacement ellipsoids set at 50% probability. Hydrogen atoms and cocrystallized toluene are omitted for clarity.

$(AlMe_4)$,[73] the terminal methyl group is slightly bent toward the yttrium center, and, hence, the Y···Al distance (3.068 Å) is somewhat shorter than that found in **6** (3.127 Å).

Heating a sample of **11** in a J. Young-valved NMR tube in C_6D_6 up to 130 °C for 2 days did not result in any detectable benzene activation (the absence of CDH_3). Only traces of CH_4 accounted for minor decomposition (cf. Figure S69). Furthermore, $AlMe_3$, $GaMe_3$, and $[Me_2Al\{B(NDippCH)_2\}]_2$ display inert behavior in C_6D_6 solutions at 110 °C. As such, these findings are in line with a dissociative scenario to liberate $[Cp^*_2YMe]_2$ in situ as the reactive intermediate.

Reactivity of Heterometallates 3^{Al}, 3^{Ga}, 6, and 9 toward THF. We assumed that methyl-bridged heteroaluminates 3^{Al}, **6**, and **9** and heterogallate 3^{Ga} would undergo donor-induced cleavage to form $Cp^*_2YMe(THF)$ and the corresponding THF-coordinated Group 13 trialkyl compounds, in accordance with the parent complexes 1^{Al} and 1^{Ga}.[16] For compounds 3^{Al}, **6**, and **9**, clean cleavage reactions of the heteroaluminate functionality were observed after THF was added to a C_6D_6 solution (Scheme 8a,c,d), as indicated by a sharp singlet at 1.98 ppm (30H) and doublets between −0.71 and −0.67 ppm (3H) assigned to $Cp^*_2YMe(THF)$ (the resonances differ slightly due to varying THF contents).[23,26]

Compound 3^{Ga} revealed a reaction behavior toward THF in a benzene solution markedly distinct from that of the heteroaluminate derivatives. The cleavage of the heterogallate moiety is clearly indicated by broad singlets at 1.82 ppm (30H, Cp*) and −0.48 ppm (3H, Me) in the ^{1}H NMR spectrum. However, additional signals appeared in the organogallium region as two sharp singlets at −0.05 and +0.11 ppm, as well as a broad singlet resonance at 0.35 ppm. Hence, the latter seems to represent a gallium alkyl species in fast exchange with the yttrocene unit. In the aromatic region, several multiplets revealed the presence of permuted gallium alkyl compounds.

Scheme 8. Reactivity of Yttrocene Compounds 3^{Al} (a), 3^{Ga} (b), 6 (c), and 9 (d) toward THF in C_6D_6 Solutions

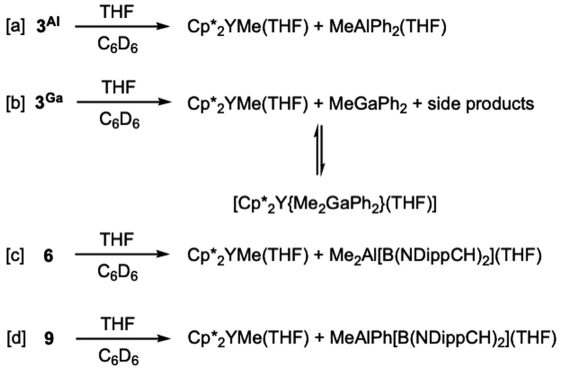

Presumably, this behavior results from the relatively low Lewis acidity of the gallium center. In line with these findings, donor adducts of $GaPh_3$ are not described in the literature. Hence, the transient cleavage product $MeGaPh_2$ engages in weak interactions with $Cp^*_2YMe(THF)$ rather than with THF (Scheme 8b). Additionally, redistribution reactions could lead to the formation of $GaPh_3$, Me_2GaPh, and $GaMe_3$, as previously reported for Me_2GaPh.[79] The latter two compounds are more prone to donor adduct formation, which could be a possible stimulus for ligand rearrangement reactions. The ^{1}H NMR spectrum of 3^{Ga} in THF-d_8 is consistent with this assumption because similar spectral data are obtained but the relative intensities are shifted toward the resonances presumed to correlate to $GaMe_3(THF)$ and $Me_2GaPh(THF)$. However, unequivocal peak assignment is hampered by multiple signal interferences.

Reactivity of Fully Me/Ph-Exchanged 4^{Al}, 4^{Ga}, and 10 toward THF. The coordination chemistry of 4^B toward donor molecules was extensively investigated by MacDonald et al., usually resulting in the separated ion pairs $[Cp^*_2Y(Do)_2][BPh_4]$ (Do = THF, $OCMe_2$, $OCPh_2$, pyridine, phenanthroline).[80] Similarly, the formation of donor adducts was anticipated for the treatment of compounds 4^M with THF. However, boryl-functionalized compound **10** dissociates in solution to form monometallic $[Cp^*_2YPh]$, as indicated by the Cp* resonance at 1.78 ppm in the ^{1}H NMR spectrum (Figure 8). Strikingly, the VT ^{1}H NMR spectra of compounds 4^{Al} and 4^{Ga} show singlet resonances at the same chemical shift. Hence, donor addition might also lead to $[MPh_4]$ cleavage to produce $Cp^*_2YPh(THF)$ (**13**) accompanied by $AlPh_3(THF)$ or $GaPh_3$, respectively.

In fact, according to the ^{1}H NMR spectrum, a THF-d_8 solution of 4^{Al} indicated quantitative formation of the solvent-separated ion pair $[Cp^*_2Y(THF)_2][AlPh_4]$ (**12**). The phenyl groups of **12** resonate as a broad doublet at 7.70 ppm (8H, *o*-C_6H_5), a triplet at 6.99 ppm (8H, *m*-C_6H_5), and a triplet of triplets at 6.92 ppm (4H, *p*-C_6H_5). The sharp singlet at 1.90 ppm (30H) can be assigned to the Cp* ligands. However, upon treatment of a C_6D_6 solution of 4^{Al} with THF, the presence of **12** is indicated only as a minor coproduct by resonances at 1.50 ppm (30H, 2 Cp*) and 8.35 ppm (8H, *o*-C_6H_5) (signals assigned to *m*- and *p*-C_6H_5 protons are interfered with by other resonances). The dominant signals at 1.88 ppm (Cp*) and 7.95 ppm (*o*-C_6H_5; *m*-C_6H_5 and *p*-C_6H_5 are interfered with) with relative intensities of 30 and 6, respectively, indicate cleavage of the $[AlPh_4]$ functionality to form **13** and $AlPh_3(THF)$ (Scheme 9a). Furthermore, at 70

https://doi.org/10.1021/acs.inorgchem.1c02349
Inorg. Chem. 2021, 60, 14952−14968

°C, **12** is completely converted to **13** and $AlPh_3(THF)$ (Figure 10).

Scheme 9. Reactivity of Yttrocene Compounds 4^{Al} (a), 4^{Ga} (b), and 10 (c) toward THF in C_6D_6 Solutions

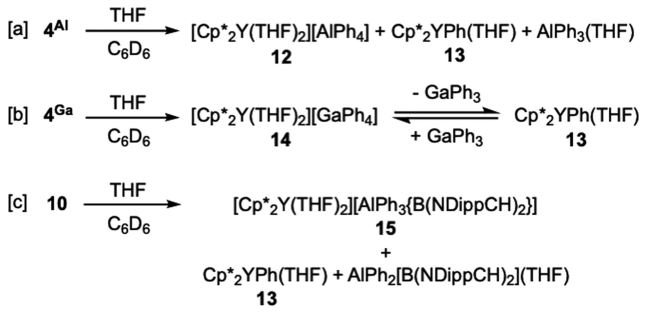

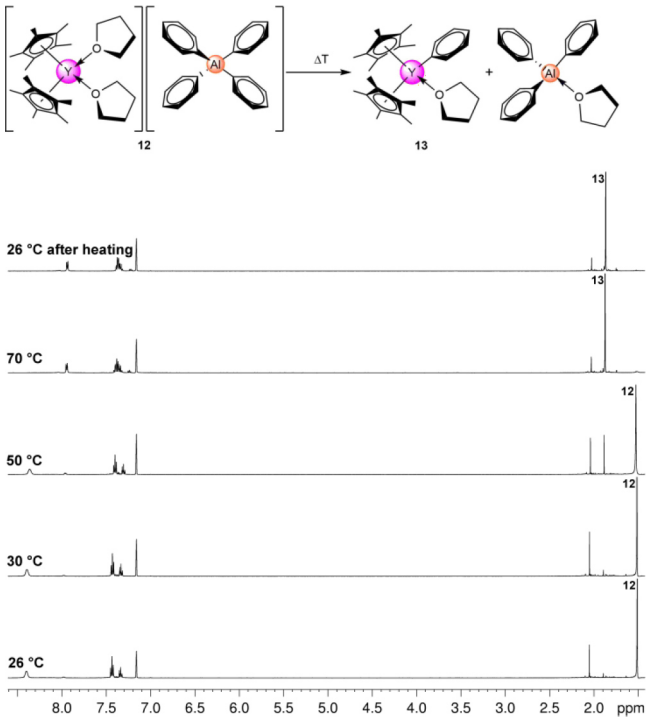

Figure 10. VT ^1H NMR spectra (500 MHz) monitoring the thermal transformation of **12** into **13** and $AlPh_3(THF)$ in C_6D_6.

Compound **13** could not be isolated from the reaction mixtures because $AlPh_3(THF)$ cannot be separated by extraction with benzene or fractional crystallization. Moreover, treating the crude product with THF resulted in the back-formation of **12**. Apparently, in noncoordinating solvents, the $[Cp^*_2Y(THF)_2]^+$ cation is prone to phenyl abstraction and, hence, triggers phenyl transfer from the $[AlPh_4]^-$ anion to form neutral $AlPh_3(THF)$ and **13**. On the other hand, donor solvents stabilize the $[Cp^*_2Y(THF)_2]^+$ cation. The THF adduct **12** precipitates from benzene/THF solutions at ambient temperature with an induction time of several minutes after the initial THF addition and crystallizes at −40 °C from saturated THF solutions as very thin needles or platelets. Most unfortunately, several attempts to determine the solid-state structure of **12** failed.[81]

A THF-d_8 solution of 4^{Ga} also revealed formation of the respective solvent-separated ion pair $[Cp^*_2Y(THF)_2][GaPh_4]$ (**14**). The ^1H NMR resonances of **14** were detected at 7.63, 6.99, and 6.90 ppm for the phenyl groups and at 1.89 ppm for the Cp* ancillary ligand. Moreover, two products were observed when THF was added to a C_6D_6 solution of 4^{Ga} in approximately a 1:1 ratio, at ambient temperature (Scheme 9b). The ^1H NMR data in C_6D_6 are consistent with the formation of **14**, as indicated by the Cp* resonance at 1.52 ppm and an aryl resonance at 8.27 ppm (Ph). In addition, a second set of signals at 1.87 ppm (Cp*) and 7.90 ppm can be assigned to **13** and $GaPh_3$. Further aromatic resonances appeared between 7.24 and 7.48 ppm; however, a conclusive peak assignment was ruled out because of massive signal overlap. Compound **14** was investigated in more detail by VT ^1H NMR spectroscopy in C_6D_6 to reveal that **14** and **13** are in fast equilibrium (Figure 11). Accordingly, increasing the

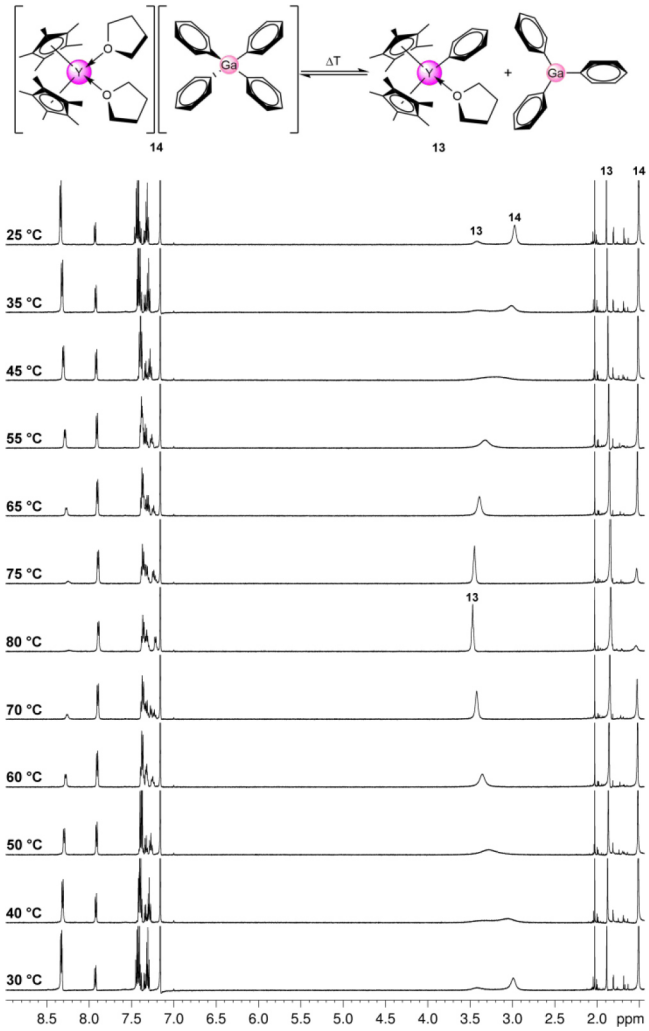

Figure 11. VT ^1H NMR spectra (500 MHz) monitoring the temperature-dependent equilibrium between **13**, $GaPh_3$, and **14** and in C_6D_6.

temperature to 80 °C resulted in almost complete conversion of **14** to **13** and $GaPh_3$, while cooling to ambient temperature led to a gradual back-conversion to **14**. At ambient temperature, **14** is the dominant species and precipitates instantaneously at even lower temperatures. This might be a consequence of the low affinity of $GaPh_3$ to THF, favoring abstraction of the yttrium-bonded phenyl group to form **14**. In

https://doi.org/10.1021/acs.inorgchem.1c02349
Inorg. Chem. 2021, 60, 14952−14968

contrast, strong THF adduct formation of $AlPh_3$ seems to impede back-conversion to **12**.

Because compound **10** is in equilibrium with $[Cp^*_2YPh]$ and $Ph_2Al[B(NDippCH)_2]$ in C_6D_6 solutions, as depicted in Figure 8 (top), we anticipated that the addition of THF would result in the formation of putative THF adducts **13** and $Ph_2Al[B(NDippCH)_2](THF)$. Indeed, the ^1H NMR spectrum shows signal sets in accordance with two boryl entities. However, only the singlet at 1.88 ppm accounting for the Cp* moieties indicated the formation of **13**. A second singlet is most likely interfered with by the THF resonances. To obtain deeper insight into the dynamic processes, compound **10** was synthesized in C_6D_6 and treated with THF-d_8. The ^1H NMR spectroscopic analysis confirmed a second yttrocene species resonating at 1.42 ppm, consistent with formation of the solvent-separated ion pair $[Cp^*_2Y(THF)_2][AlPh_3\{B(NDippCH)_2\}]$ (**15**; Scheme 9c). A reversible dissociation of sterically encumbered Group 13 tetraalkyl anions $[M(CH_2SiMe_3)_4]^-$ (M = Al, Ga, In) was reported previously by Kramer et al. for the solvent-separated ion pair $[Y(CH_2SiMe_3)_2(THF)_4][M(CH_2SiMe_3)_4]$ in aromatic solvents to form neutral $Y(CH_2SiMe_3)_3(THF)_2$ and $M(CH_2SiMe_3)_3(THF)$.[82]

The crude reaction mixture of **10** in C_6D_6 and THF led to concomitant crystallization of compounds **13** and **15** as colorless and pale-yellow crystals, respectively. The XRD analysis of compound **13** revealed that the metal center of the yttrocene entity is coordinated by a phenyl ring and a THF donor molecule (Figure 12), being isostructural to $Cp^*_2SmPh(THF)$.[83] The metrical parameters of **13** [Y−C(alkyl), 2.464(2) Å; Y−O, 2.391(1) Å] compare well with those of yttrocene derivatives $Cp^*_2YMe(THF)$ [2.44(2) and 2.379(8) Å],[84] $Cp^*_2Y(CH_2Ph)(THF)$ [2.484(6) and 2.398(4) Å],[85] $Cp^*_2Y(C{\equiv}CPh)(THF)$ [2.407(2) and 2.399(1) Å],[86] and $Cp^*_2Y(C_4H_3O)(THF)$ [2.436(9) and 2.373(7) Å].[87] Accordingly, the ^1H NMR spectrum of the crystalline compound **13** in C_6D_6 shows signals at 7.44 and 7.31 ppm for the phenyl ligand and at 3.53 and 1.24 ppm for coordinating THF. The resonance at 1.88 ppm can be assigned to the Cp* methyl groups. This finding unambiguously evidences cleavage of the $[AlPh_3\{B(NDippCH)_2\}]$ unit and suggests similar behavior for $\mathbf{4^{Al}}$ and $\mathbf{4^{Ga}}$ under these conditions because the corresponding ^1H NMR spectra exhibit a diagnostic singlet at 1.88 ppm for the yttrocene fragment.

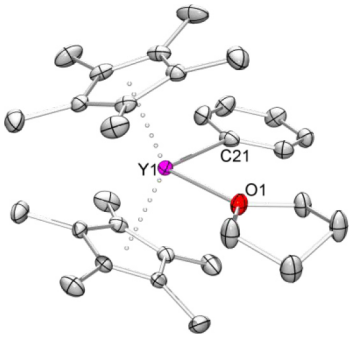

Figure 12. Crystal structure of the THF adduct **13**. All atoms are represented by atomic displacement ellipsoids set at 50% probability. Hydrogen atoms are omitted for clarity.

The XRD analysis of the solvent-separated ion pair **15** revealed that the yttrocenium cation $[Cp^*_2Y]^+$ is coordinated by two THF molecules with Y−O distances in the expected range [Y−O1, 2.388(3) Å; Y−O2, 2.359(3) Å; Figure 13].

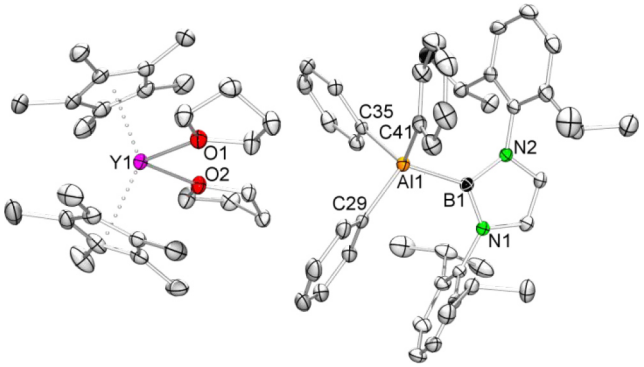

Figure 13. Crystal structure of **15**. All atoms are represented by atomic displacement ellipsoids set at 50% probability. Hydrogen atoms and cocrystallized *n*-pentane are omitted for clarity.

This structural motif has been previously reported for tetraphenylborate complexes $[Cp^*_2Ln(THF)_2][BPh_4]$ (Ln = Sc,[88] Sm,[89] Yb[90]). The separated $[AlPh_3\{B(NDippCH)_2\}]^-$ counteranion (Y···Al = 7.436 Å) features an aluminum center adopting a tetrahedral geometry that is less distorted [angles ranging from 104.3(1) to 113.3(1)°; av 109.4°] than that in compound **10** [from 100.5(1) to 121.6(1)°; av 109.3°].

These final findings nicely document the decreased stability of $[MPh_4]^-$ anions (M = Al, Ga) compared to that of the corresponding borate $[BPh_4]^-$ and therefore increased ability for phenyl transfer.

CONCLUSIONS

Yttrocene derivatives $[Cp^*_2Y(MMe_4)]$ (M = Al, Ga) metalate benzene at elevated temperatures under the release of methane. The associated methyl/phenyl exchange can be effectively trapped via heteroaluminate/gallate formation. Depending on the temperature and reaction time, complete or partial methyl/phenyl exchange can be achieved to form $[Cp^*_2Y(Me_2MPh_2)]$ and $Cp^*_2Y(MPh_4)$. A possible reaction sequence involves the dissociation of MMe_3 to liberate $[Cp^*_2YMe]$, which is highly reactive, easily undergoing C−H-bond activation via σ-bond metathesis. This scenario is supported by an enhanced reactivity of the tetramethylgallate compound $[Cp^*_2Y(GaMe_4)]$ due to a more facile displacement of the associated Lewis acid $GaMe_3$. A substantial H/D kinetic isotope effect is diagnostic for a σ-bond metathesis pathway. The concomitant extrusion of CDH_3 and CH_4 upon activation of C_6D_6 accounts for two competing reaction pathways, namely, a four-center transposition involving $[Cp^*_2YMe]$ and C_6D_6 versus a "tuck-in" complex, resembling benzene activation by $[Cp^*_2LnMe]$ (Ln = Sc, Y, Lu). The occurrence of a dissociative process is further corroborated by use of the kinetically labile yttrocene derivative $Cp^*_2Y[Me_3Al\{B(NDippCH)_2\}]$ bearing a sterically demanding peripheral boryl moiety instead of a methyl group. As anticipated, this highly congested yttrium complex shows enhanced reactivity in benzene activation and readily forms the corresponding complexes $Cp^*_2Y[Me_2AlPh\{B(NDippCH)_2\}]$ and $Cp^*_2Y[Ph_3Al\{B(NDippCH)_2\}]$ under mild conditions. VT ^1H NMR investigations on the yttrocene complexes $Cp^*_2Y(MPh_4)$ and $Cp^*_2Y[Ph_3Al\{B(NDippCH)_2\}]$ featuring "weakly coordinating" anions revealed a high propensity for phenyl

https://doi.org/10.1021/acs.inorgchem.1c02349
Inorg. Chem. 2021, 60, 14952−14968

group transfer to form [Cp*$_2$YPh]. Accordingly, donor addition results in the temperature-dependent formation of solvent-separated ion pairs [Cp*$_2$Y(THF)$_2$][MPh$_3$R] (M = Al, R = Ph, {B(NDippCH)$_2$}; M = Ga, R = Ph) and monometallic Cp*$_2$YPh(THF), respectively. This is in stark contrast to the reaction behavior of the borate congener Cp*$_2$Y(BPh$_4$).[80]

To conclude, the thermal treatment of readily accessible yttrocene derivatives [Cp*$_2$Y(MMe$_4$)] (M = Al, Ga) led to a powerful deprotonating agent, as emphasized by benzene metalation.[91] The reactivity shows striking parallels to that of rare-earth-metallocene methyl compounds [Cp*$_2$LnMe]$_x$. Given the easy access to rare-earth-metal compounds [Cp*$_2$Ln(MMe$_4$)], further investigations focus on extending this concept to the lanthanide series and the activation of chemically inert substrates.

EXPERIMENTAL SECTION

General Consideration. *Caution! The group 13 and yttrium methyl derivatives are highly pyrophoric and react violently when exposed to air and/or moisture.* Therefore, the syntheses and manipulations of all organometallic compounds were carried out under dry argon by using standard Schlenk, high-vacuum, and glovebox techniques (MBraun MB 200B; <1 ppm of O_2 and <1 ppm of H_2O). *n*-Pentane, *n*-hexane, toluene, and tetrahydrofuran (THF) were purified by using Grubbs-type columns (MBraun SPS-800, solvent purification system) and stored in a glovebox. Benzene, C_6D_6, toluene-d_8, and THF-d_8 were obtained from Aldrich, dried over Na/K alloy for 24 h, and distilled prior to use. AlMe$_3$ was purchased from Aldrich, GaMe$_3$ was purchased from Dockweiler Chemicals (optoelectronic grade), and both were used as received. KCp*, [Cp$_2$Y(μ-Me)]$_2$,[92] [Cp*$_2$Y(AlMe$_4$)] (**1^{Al}**),[23,26] [Cp*$_2$Y(GaMe$_4$)] (**1^{Ga}**),[16,23] and Cp*Y[Me$_3$Al{B(NDippCH)$_2$}]$_2$ (**5**;[66] Dipp = C$_6$H$_3$*i*Pr$_2$-2,6) were synthesized according to literature procedures. NMR spectra of air- and moisture-sensitive compounds were recorded by using J. Young-valved NMR tubes at 26 °C on Bruker AVII+250 (^{1}H, 250.13 MHz; ^{13}C, 62.90 MHz; ^{11}B, 80.25 MHz), Bruker AVII+400 (^{1}H, 400.13 MHz; ^{13}C, 100.61 MHz), and Bruker AVII+500 (^{1}H, 500.13 Hz; ^{13}C, 125.76 MHz; ^{89}Y, 24.51 MHz) spectrometers. ^{1}H and ^{13}C shifts are referenced to internal solvent resonances and reported in parts per million relative to tetramethylsilane. IR spectra were recorded on a Nicolet 6700 FTIR spectrometer using a DRIFT chamber with dry KBr/sample mixtures and KBr windows. For the latter, the collected data were converted using Kubelka–Munk refinement. Elemental analyses were performed on an Elementar Vario MICRO cube. Single crystals suitable for X-ray structure analyses were selected in a glovebox and coated with Paratone-N (Hampton Research). X-ray data were collected on a Bruker APEX III DUO diffractometer by using QUAZAR optics and Mo K_α radiation (λ = 0.71073 Å). The data collection strategy was determined using *COSMO*[93,94] employing ω scans. Raw data were processed by using *APEX*[95] and *SAINT*[96] software; structure solution and final model refinement were performed by using *SHELXTL* and *SHELXLE*.[97,98] Corrections for absorption effects were applied by using *SADABS*,[99] whereas in the case of complexes **1** and **8**, *TWINABS* was applied.[100] All plots were generated utilizing the programs *ORTEP-3*[101] and *POV-Ray*.[102]

[Cp*$_2$Y(Me$_2$AlPh$_2$)] (3^{Al}). In a pressure tube, **1^{Al}** (93 mg, 0.21 mmol) was suspended in benzene (4 mL) and stirred at 100 °C for 42 h. Subsequent ^{1}H NMR spectroscopic analysis revealed a mixture of products representing **3^{Al}** and [Cp*$_2$Y(MeAlPh$_3$)] (72% vs 28%). Hence, an appropriate amount of **1^{Al}** (13 mg, 0.03 mmol) was added to the reaction mixture. After stirring at ambient temperature for 30 min, all volatiles were removed, and the white residue was washed with *n*-hexane (2 mL) and dried under reduced pressure to yield **3^{Al}** as a white powder (132 mg, 98%). Single crystals suitable for XRD analysis were grown at ambient temperature by condensing *n*-pentane onto a saturated benzene solution. ^{1}H NMR (C_6D_6, 500 MHz, 26 °C): dimer, δ 8.18 (m, 4H, *o*-C$_6H_5$), 7.52 (m, 4H, *m*-C$_6H_5$), 7.39 (m, 2H, *p*-C$_6H_5$), 1.81 (s, 30H, C$_5$(CH_3)$_5$), −0.53 (d, 6H, ^2J(Y,H) = 3.0 Hz, Y(μ-CH_3)$_2$); monomer, δ 7.85 (m, 4H, *o*-C$_6H_5$), 7.37 (m, 4H, *m*-C$_6H_5$), 7.27 (m, 2H, *p*-C$_6H_5$), 1.71 (s, 30H, C$_5$(CH_3)$_5$), −0.11 (d, 6H, ^2J(Y,H) = 5.0 Hz, Y(μ-CH_3)$_2$). ^{13}C{^{1}H} NMR (C_6D_6, 126 MHz, 26 °C): dimer, δ 138.5 (*o*-C$_6H_5$), 127.3 (*m*-C$_6H_5$), 127.1 (*p*-C$_6H_5$), 121.0 (d, ^1J(Y,C) = 1.3 Hz, C$_5$(CH$_3$)$_5$), 11.8 (C$_5$(CH$_3$)$_5$), 1.5 (Y(μ-CH$_3$)$_2$); monomer, δ 137.5 (*o*-C$_6H_5$), 127.5 (*m*-C$_6H_5$), 127.3 (*p*-C$_6H_5$), 120.0 (d, ^1J(Y,C) = 1.4 Hz, C$_5$(CH$_3$)$_5$), 11.6 (C$_5$(CH$_3$)$_5$), 2.5 (Y(μ-CH$_3$)$_2$). ^{89}Y−^{1}H HSQC (C_6D_6, 25 MHz, 26 °C): dimer, δ 14.3 (^{89}Y); monomer, δ −45.8 (^{89}Y). DRIFT (KBr): $\tilde{\nu}$ 3117 (w), 3052 (m), 2987 (s), 2905 (vs), 2859 (s), 2728 (w), 1951 (w), 1876 (w), 1822 (w), 1435 (s), 1418 (s), 1245 (m), 1082 (vs), 950 (s), 929 (s), 786 (m), 706 (vs), 551 (s) cm^{-1}. Elem anal. Calcd for C$_{34}$H$_{46}$AlY (570.63 g mol^{-1}): C, 71.57; H, 8.13. Found: C, 71.85; H, 8.13.

Cp*$_2$Y(AlPh$_4$) (4^{Al}). In a pressure tube, **1^{Al}** (586 mg, 1.31 mmol) was suspended in benzene (8 mL) and stirred first at 120 °C for 43 h and then at 130 °C for a further 112 h. The colorless solution turned bright yellow. All volatiles were removed under reduced pressure to obtain a sticky yellow residue. The residue was washed with *n*-hexane (4 × 3 mL) and toluene (3 × 1 mL) and dried in vacuo to afford an off-white powder (146 mg, 16%). Single crystals suitable for XRD analysis were grown at ambient temperature by condensing *n*-pentane onto a saturated benzene solution. ^{1}H NMR (C_6D_6, 500 MHz, 26 °C): δ 8.07 (d br, 4.0 Hz, 8H, *o*-C$_6H_5$), 7.24 (m, 4H, *p*-C$_6H_5$), 7.17 (t, 7.0 Hz, 8H, *m*-C$_6H_5$), 1.52 (bs, 30H, C$_5$(CH_3)$_5$). ^{13}C{^{1}H} NMR (C_6D_6, 126 MHz, 26 °C): δ 162.6 (*i*-C$_6H_5$), 137.8 (*o*-C$_6H_5$), 128.4 (*p*-C$_6H_5$), 127.4 (*m*-C$_6H_5$), 123.3 (C$_5$(CH$_3$)$_5$), 11.6 (C$_5$(CH$_3$)$_5$). DRIFT (KBr): $\tilde{\nu}$ 3115 (w), 3042 (vs), 2986 (s), 2944 (s), 2900 (vs), 2861 (s), 2733 (w), 1948 (w), 1876 (w), 1819 (w), 1492 (m), 1448 (m), 1418 (vs), 1383 (m), 1251 (m), 1078 (vs), 1022 (m), 735 (vs), 704 (vs), 668 (m), 478 (vs), 470 (vs) cm^{-1}. Elem anal. Calcd for C$_{44}$H$_{50}$AlY (694.77 g mol^{-1}): C, 76.07; H, 7.25. Found: C, 75.71; H, 7.22.

[Cp*$_2$Y(Me$_2$GaPh$_2$)] (3^{Ga}). In a J. Young-valved NMR tube, equipped with a sealed C_6D_6 glass capillary to allow in situ ^{1}H NMR measurements, **1^{Ga}** (33 mg, 0.07 mmol) was suspended in benzene (0.7 mL) and heated at 80 °C for 9.5 h, and then all volatiles were removed under reduced pressure to yield 41 mg (99%) of **3^{Ga}** as a white powder. Single crystals suitable for XRD analysis were grown at ambient temperature by condensing *n*-pentane onto a saturated benzene solution. ^{1}H NMR (C_6D_6, 500 MHz, 26 °C): dimer, δ 8.11 (m, 4H, *o*-C$_6H_5$), 7.51 (m, 4H, *m*-C$_6H_5$), 7.36 (m, 2H, *p*-C$_6H_5$; interfered with by the multiplet at 7.35 ppm), 1.82 (s, 30H, C$_5$(CH_3)$_5$), −0.39 (d, 6H, ^2J(Y,H) = 3.0 Hz, Y(μ-CH_3)$_2$); monomer, δ 7.77 (m, 4H, *o*-C$_6H_5$), 7.35 (m, 4H, *m*-C$_6H_5$), 7.23 (m, 2H, *p*-C$_6H_5$), 1.71 (s, 30H, C$_5$(CH_3)$_5$), −0.06 (d, 6H, ^2J(Y,H) = 4.9 Hz, Y(μ-CH_3)$_2$). ^{13}C{^{1}H} NMR (C_6D_6, 126 MHz, 26 °C): dimer, δ 154.5 (*i*-C$_6H_5$), 137.6 (*o*-C$_6H_5$), 127.5 (*m*-C$_6H_5$), 126.9 (*p*- C$_6H_5$), 121.0 (d, ^1J(Y,C) = 1.4 Hz, C$_5$(CH$_3$)$_5$), 11.8 (C$_5$(CH$_3$)$_5$), 1.8 (Y(μ-CH$_3$)$_2$); monomer, δ 152.9 (*i*-C$_6H_5$), 136.3 (*o*-C$_6H_5$), 127.7 (*m*-C$_6H_5$), 126.6 (*p*- C$_6H_5$), 120.0 (d, ^1J(Y,C) = 1.5 Hz, C$_5$(CH$_3$)$_5$), 11.6 (C$_5$(CH$_3$)$_5$), 3.3 (Y(μ-CH$_3$)$_2$). ^{89}Y−^{1}H HSQC (C_6D_6, 25 MHz, 26 °C): dimer, δ 21.6 (^{89}Y); monomer, δ −50.0 (^{89}Y). DRIFT (KBr): $\tilde{\nu}$ 3125 (w), 3054 (m), 3037 (m), 2979 (m), 2906 (s), 2862 (s), 2729 (w), 1948 (w), 1872 (w), 1818 (w), 1479 (m), 1435 (m), 1422 (s), 1386 (m), 1251 (m), 1077 (s), 1022 (m), 937 (s), 811 (m), 725 (s), 705 (vs), 492 (s), 458 (s) cm^{-1}. Elem anal. Calcd for C$_{34}$H$_{46}$GaY (613.37 g mol^{-1}): C, 66.56; H, 7.56. Found: C, 66.18; H, 7.45.

Cp*$_2$Y(GaPh$_4$) (4^{Ga}). In a pressure tube, **1^{Ga}** (315 mg, 0.64 mmol) was suspended in benzene (5 mL) and stirred at 90 °C for 72 h. Then all volatiles were removed, and the yellow residue was washed with five portions of 3 mL of *n*-hexane and dried under reduced pressure to yield an off-white powder of **4^{Ga}** (359 mg, 75%). Single crystals suitable for XRD analysis were grown at ambient temperature by condensing *n*-pentane onto a saturated benzene solution. ^{1}H NMR (C_6D_6, 400 MHz, 26 °C): δ 7.86 (bs, 8H, *o*-C$_6H_5$), 7.25 (bs, 12H, *m*-C$_6H_5$ and *p*-C$_6H_5$), 1.63 (bs, 30H, C$_5$(CH_3)$_5$). ^{13}C{^{1}H} NMR (C_6D_6, 101 MHz, 26 °C): δ 137.3 (*o*-C$_6H_5$), 131.5 (*m*-C$_6H_5$ or *p*-C$_6H_5$), 127.7 (*m*-C$_6H_5$ or *p*-C$_6H_5$, interfered with by C_6D_6 resonance), 121.7 (C$_5$(CH$_3$)$_5$), 11.3 (C$_5$(CH$_3$)$_5$). A *i*-C$_6H_5$ resonance was not detected; apart of the signal at 11.3 ppm, all signals are very broad because of

https://doi.org/10.1021/acs.inorgchem.1c02349
Inorg. Chem. 2021, 60, 14952−14968

the highly dynamic behavior in solution. ^{1}H NMR (toluene-d_8, 400 MHz, 26 °C): δ 7.77 (bs, 8H, *o*-C_6H_5), 7.22 (bs, 12H, *m*-C_6H_5 and *p*-C_6H_5), 1.66 (bs, 30H, $C_5(CH_3)_5$). ^{13}C{^{1}H} NMR (toluene-d_8, 101 MHz, 26 °C): δ 129.0 (*m*-C_6H_5 or *p*-C_6H_5, according to ^{1}H−^{13}C HSQC NMR, interfered with by toluene-d_8 resonance), 127.7 (*m*-C_6H_5 or *p*-C_6H_5, according to ^{1}H−^{13}C HSQC NMR, interfered with by toluene-d_8 resonance), 120.6 ($C_5(CH_3)_5$), 11.1 ($C_5(CH_3)_5$). *i*-C_6H_5 and *p*-C_6H_5 resonances were not detected, and *p*-C_6H_5 was probably interfered with by the toluene-d_8 signal at 137.5 ppm; apart of the signal at 11.3 ppm, all signals are very broad because of to high dynamic behavior in solution. DRIFT (KBr): $\tilde{\nu}$ 3044 (vs), 2983 (s), 2975 (s), 2941 (s), 2899 (vs), 2859 (s), 1958 (w), 1873 (w), 1819 (w), 1475 (s), 1449 (s), 1420 (s), 1383 (m), 1257 (m), 1075 (vs), 1022 (m), 737 (vs), 725 (m), 703 (vs), 682 (s), 468 (s), 456 (s) cm^{-1}. Elem anal. Calcd for $C_{44}H_{50}GaY$ (737.51 g mol^{-1}): C, 71.66; H, 6.83. Found: C, 71.95; H, 6.68.

Cp*$_2$Y[Me$_3$Al{B(NDippCH)$_2$}] (6) and [K(Me$_3$Al{B(NDippCH)$_2$})]$_n$ (7). In a glovebox, to a suspension of KCp* (59 mg, 0.34 mmol) in toluene (2 mL) precooled to −40 °C was added dropwise under vigorous stirring a solution of **5** (386 mg, 0.34 mmol) in *n*-hexane (6 mL). The suspension was allowed to warm to ambient temperature with stirring for 16 h. Then the solid was separated by centrifugation, and the white precipitate was washed with three portions of *n*-hexane (3 mL) and dried under vacuum to yield 163 mg (85%) of **7** as a white powder. The combined extracts were filtered and dried in vacuo to obtain a colorless powder. Fractional crystallization at ambient temperature from saturated *n*-pentane solutions afforded 265 mg (96%) of pure product **6** as colorless crystals.

6. ^{1}H NMR (C_6D_6, 400 MHz, 26 °C): δ 7.29 (s, 6H, H_{Dipp}), 6.53 (s, 2H, NC*H*), 3.68 (sept, 4H, ^3J(H,H) = 6.8 Hz, C*H*(CH$_3$)$_2$), 1.83 (s, 15H, $C_5(CH_3)_5$), 1.69 (s, 15H, $C_5(CH_3)_5$), 1.55 (d, 12H, ^3J(H,H) = 6.8 Hz, CH(C*H*$_3$)$_2$), 1.28 (d, 12H, ^3J(H,H) = 6.7 Hz, CH(C*H*$_3$)$_2$), −0.49 (s, 3H, AlC*H*$_3$), −0.88 (d, 6H, ^2J(Y,H) = 5.3 Hz, Y(μ-C*H*$_3$)$_2$). ^{13}C{^{1}H} NMR (C_6D_6, 101 MHz, 26 °C): δ 146.5 (*o*-C_{Dipp}), 143.2 (*i*-C_{Dipp}), 127.1 (*p*-C_{Dipp}), 123.4 (*m*-C_{Dipp}), 121.6 (NCH), 119.2 ($C_5(CH_3)_5$), 118.9 ($C_5(CH_3)_5$), 28.9 (CH(CH$_3$)$_2$), 27.3 (CH(CH$_3$)$_2$), 23.2 (CH(C*H*$_3$)$_2$), 12.2 ($C_5(CH_3)_5$), 11.4 ($C_5(CH_3)_5$), 7.9 (Y(μ-C*H*$_3$)), 7.7 (Y(μ-C*H*$_3$)), −3.5 (AlC*H*$_3$). ^{11}B{^{1}H} NMR (C_6D_6, 80 MHz, 26 °C): δ 32.9 (*B*Al). ^{89}Y−^{1}H HSQC (C_6D_6, 25 MHz, 26 °C): δ −52.0 (^{89}Y). DRIFT (KBr): $\tilde{\nu}$ 3063 (w), 2959 (vs), 2927 (vs), 2865 (vs), 2726 (w), 1925 (w), 1852 (w), 1782 (w), 1461 (vs), 1439 (vs), 1381 (s), 1367 (vs), 1256 (s), 757 (s), 696 (s) cm^{-1}. Elem anal. Calcd for $C_{49}H_{75}AlBN_2Y$ (818.85 g mol^{-1}): C, 71.87; H, 9.23; N, 3.42. Found: C, 71.76; H, 9.33; N, 3.40.

7. ^{1}H NMR (C_6D_6, 500 MHz, 26 °C): δ 7.20 (m, 6H, H_{Dipp}), 6.46 (s, 2H, NC*H*), 3.66 (sept, 4H, ^3J(H,H) = 6.9 Hz, C*H*(CH$_3$)$_2$), 1.47 (d, 12H, ^3J(H,H) = 6.9 Hz, CH(C*H*$_3$)$_2$), 1.31 (d, 12H, ^3J(H,H) = 6.9 Hz, CH(C*H*$_3$)$_2$), −1.25 (s, 9H, Al(C*H*$_3$)$_3$). ^{13}C{^{1}H} NMR (C_6D_6, 125 MHz, 26 °C): δ 147.6 (*o*-C_{Dipp}), 144.9 (*i*-C_{Dipp}), 126.3 (*p*-C_{Dipp}), 123.0 (*m*-C_{Dipp}), 120.5 (NCH), 28.7 (CH(CH$_3$)$_2$), 25.8 (CH(CH$_3$)$_2$), 23.7 (CH(C*H*$_3$)$_2$). Al(C*H*$_3$)$_3$ resonances were not detected. DRIFT (KBr): $\tilde{\nu}$ 3063 (w), 2959 (vs), 2905 (s), 2868 (s), 2801 (m), 2719 (w), 1927 (w), 1862 (w), 1796 (w), 1580 (w), 1461 (vs), 1442 (s), 1381 (m), 1367 (vs), 1327 (m), 1268 (m), 1235 (m), 1129 (m), 805 (m), 764 (s), 695 (m), 554 (m) cm^{-1}. Elem anal. Calcd for $C_{29}H_{45}AlBKN_2$ (498.58 g mol^{-1}): C, 69.86; H, 9.10; N, 5.62. Found: C, 69.62; H, 8.98; N, 5.59.

Cp*$_2$Y[Me$_2$AlPh{B(NDippCH)$_2$}] (9). In a J. Young-valved NMR tube, equipped with a sealed C_6D_6 glass capillary to allow in situ ^{1}H NMR measurements, **6** (49 mg, 0.06 mmol) was dissolved in benzene (0.6 mL) and heated to 60 °C for 36.5 h. The crude product was dried under reduced pressure and washed with *n*-pentane (0.5 mL) to yield a white crystalline solid (30 mg). Additional colorless crystals of **9** (19 mg) were obtained from the *n*-pentane solution at −40 °C to give an overall yield of 94%. ^{1}H NMR (C_6D_6, 500 MHz, 26 °C): δ 7.34 (m, 2H, *p*-H_{Dipp}), 7.28 (m, 4H, *m*-H_{Dipp}), 7.21 (m, 3H, *m*-C_6H_5 and *p*-C_6H_5), 7.13 (m, 2H, *o*-C_6H_5), 6.55 (s, 2H, NC*H*), 3.58 (sept, 4H, ^3J(H,H) = 6.7 Hz, C*H*(CH$_3$)$_2$), 1.82 (bs, 15H, $C_5(CH_3)_5$), 1.51 (bs, 15H, $C_5(CH_3)_5$), 1.25 (d, 12H, ^3J(H,H) = 6.6 Hz, CH(C*H*$_3$)$_2$), 1.20 (d, 12H, ^3J(H,H) = 6.7 Hz, CH(C*H*$_3$)$_2$), −0.54 (d, 6H, ^2J(Y,H) = 5.4 Hz, Y(μ-C*H*$_3$)$_2$). ^{13}C{^{1}H} NMR (C_6D_6, 126 MHz, 26 °C): δ 153.6 (*i*-C_6H_5), 146.2 (*o*-C_{Dipp}), 143.2 (*i*-C_{Dipp}), 138.4 (*o*-C_6H_5), 126.9 (*p*-C_{Dipp}), 126.9 (*m*-C_6H_5), 126.6 (*p*-C_6H_5), 123.8 (*m*-C_{Dipp}), 121.7 (NCH), 119.5 ($C_5(CH_3)_5$), 29.1 (CH(CH$_3$)$_2$), 27.2 (CH(CH$_3$)$_2$), 22.4 (CH(C*H*$_3$)$_2$), 11.7 ($C_5(CH_3)_5$), 3.5 (Y(μ-C*H*$_3$)), 3.6 (Y(μ-C*H*$_3$)). ^{11}B{^{1}H} NMR (toluene-d_8, 80 MHz, 26 °C): δ 31.2 (*B*Al). ^{89}Y−^{1}H HSQC (C_6D_6, 25 MHz, 26 °C): δ −55.7 (^{89}Y). DRIFT (KBr): $\tilde{\nu}$ 3051 (w), 3028 (w), 2959 (vs), 2923 (s), 2864 (s), 2726 (w), 1925 (w), 1862 (w), 1815 (w), 1459 (vs), 1440 (vs), 1382 (s), 1367 (vs), 1322 (m), 1267 (m), 802 (w), 759 (s), 704 (s) cm^{-1}. Elem anal. Calcd for $C_{54}H_{77}AlBN_2Y$ (880.92 g mol^{-1}): C, 73.63; H, 8.81; N, 3.18. Found: C, 73.27; H, 8.84; N, 3.21.

Cp*$_2$Y[AlPh$_3${B(NDippCH)$_2$}] (10). In a J. Young-valved NMR tube, equipped with a sealed C_6D_6 glass capillary to allow in situ ^{1}H NMR measurements, **6** (56 mg, 0.07 mmol) was dissolved in benzene (0.6 mL) and heated to 80 °C for 35 h. All volatiles were removed under reduced pressure, and the solid residue was washed with *n*-pentane (0.5 mL). After drying in vacuo, 33 mg of a white powder was obtained. Additional product crystallized from the *n*-pentane solution at −40 °C (22 mg) to obtain a total yield of 80%. Single crystals suitable for XRD analysis were grown from a saturated *n*-pentane solution at −40 °C. ^{1}H NMR (C_6D_6, 400 MHz, 26 °C): **10**, δ 7.38 (t, 2H, ^3J(H,H) = 7.7 Hz, *p*-H_{Dipp}), 7.27 (d, 6H, ^3J(H,H) = 6.5 Hz, *o*-C_6H_5), 7.25 (d, 4H, ^3J(H,H) = 7.8 Hz, *m*-H_{Dipp}), 7.08 (tt, 3H, ^3J(H,H) = 7.3 Hz, ^4J(H,H) = 1.4 Hz, *p*-C_6H_5), 6.84 (t, 6H, ^3J(H,H) = 7.1 Hz, *m*-C_6H_5), 6.59 (s, 2H, NC*H*), 3.70 (sept, 4H, ^3J(H,H) = 6.8 Hz, C*H*(CH$_3$)$_2$), 1.47 (s, 30H, $C_5(CH_3)_5$), 1.32 (d, 12H, ^3J(H,H) = 6.8 Hz, CH(C*H*$_3$)$_2$), 1.13 (d, 12H, ^3J(H,H) = 6.8 Hz, CH(C*H*$_3$)$_2$); [Cp*$_2$YPh], δ 1.78 (s, 30H, $C_5(CH_3)_5$); [AlPh$_2${B(NDippCH)$_2$}], δ 7.31 (t, 2H, ^3J(H,H) = 7.7 Hz, *p*-H_{Dipp}), 7.18 (d, 4H, ^3J(H,H) = 7.7 Hz, *m*-H_{Dipp}), 6.42 (s, 2H, NC*H*), 3.31 (sept, 4H, ^3J(H,H) = 6.8 Hz, C*H*(CH$_3$)$_2$), 1.18 (d, 12H, ^3J(H,H) = 6.8 Hz, CH(C*H*$_3$)$_2$), 1.09 (d, 12H, ^3J(H,H) = 7.0 Hz, CH(C*H*$_3$)$_2$). Because of major interference by the dominant resonances of **10**, further aromatic resonances of the phenyl moieties could not be assigned to [Cp*$_2$YPh] or [AlPh$_2${B(NDippCH)$_2$}], respectively. ^{13}C{^{1}H} NMR (C_6D_6, 101 MHz, 26 °C): **10**, δ 168.0 (*i*-C_6H_5), 147.2 (*o*-C_{Dipp}), 144.4 (*i*-C_{Dipp}), 137.7 (*o*-C_6H_5), 127.7 (*p*-C_6H_5), 126.8 (*p*-C_{Dipp}), 125.9 (*m*-C_6H_5), 123.5 (*m*-C_{Dipp}), 122.8 (d, ^1J(Y,C) = 1.2 Hz, $C_5(CH_3)_5$), 121.7 (NCH), 28.7 (CH(CH$_3$)$_2$), 26.1 (CH(CH$_3$)$_2$), 23.8 (CH(CH$_3$)$_2$), 11.6 ($C_5(CH_3)_5$); [Cp*$_2$YPh], δ 118.8 ($C_5(CH_3)_5$), 10.8 ($C_5(CH_3)_5$)); [AlPh$_2${B(NDippCH)$_2$}], δ 122.0 (NCH), 25.0 (CH(CH$_3$)$_2$), 24.9 (CH(CH$_3$)$_2$). Further resonances at δ 146.2, 141.3, 138.4, 134.3, 129.3, 127.5, 127.2 125.7 and 124.2 could not be assigned unambiguously. ^{1}H NMR (C_6D_6, 400 MHz, 3 °C): **10**, δ 7.40 (t, 2H, ^3J(H,H) = 7.7 Hz, *p*-H_{Dipp}), 7.29 (d, 6H, ^3J(H,H) = 6.5 Hz, *o*-C_6H_5), 7.26 (d, 4H, ^3J(H,H) = 7.7 Hz, *m*-H_{Dipp}), 7.09 (tt, 3H, ^3J(H,H) = 7.3 Hz, ^4J(H,H) = 1.4 Hz, *p*-C_6H_5), 6.85 (t, 6H, ^3J(H,H) = 6.6 Hz, *m*-C_6H_5), 6.62 (s, 2H, NC*H*), 3.72 (sept, 4H, ^3J(H,H) = 6.9 Hz, C*H*(CH$_3$)$_2$), 1.46 (s, 30H, $C_5(CH_3)_5$), 1.33 (d, 12H, ^3J(H,H) = 6.9 Hz, CH(C*H*$_3$)$_2$), 1.13 (d, 12H, ^3J(H,H) = 6.9 Hz, CH(C*H*$_3$)$_2$). ^{13}C{^{1}H} NMR (C_6D_6, 101 MHz, 3 °C): **10**, δ 168.0 (*i*-C_6H_5), 147.1 (*o*-C_{Dipp}), 144.3 (*i*-C_{Dipp}), 137.6 (*o*-C_6H_5), 127.7 (*p*-C_6H_5), 126.8 (*p*-C_{Dipp}), 125.8 (*m*-C_6H_5), 123.5 (*m*-C_{Dipp}), 122.7 (d, ^1J(Y,C) = 1.3 Hz, $C_5(CH_3)_5$), 121.6 (NCH), 28.7 (CH(CH$_3$)$_2$), 26.1 (CH(CH$_3$)$_2$), 23.8 (CH(CH$_3$)$_2$), 11.6 ($C_5(CH_3)_5$). ^{11}B{^{1}H} NMR (C_6D_6, 80 MHz, 26 °C): δ 28.6 (*B*Al). DRIFT (KBr): $\tilde{\nu}$ 3101 (w), 3042 (m) 2957 (vs), 2922 (s), 2863 (s), 2801 (w), 1974 (w), 1932 (w), 1866 (w), 1583 (w), 1461 (s), 1415 (m), 1381 (m), 1367 (vs), 1326 (m), 1267 (m), 1070 (m), 761 (m), 735 (m), 699 (m), 478 (s) cm^{-1}. Elem anal. Calcd for $C_{64}H_{81}AlBN_2Y$ (1005.06 g mol^{-1}): C, 76.48; H, 8.12; N, 2.79. Found: C, 77.11; H, 7.95; N, 2.64.

Cp$_2$Y[Me$_3$Al{B(NDippCH)$_2$}] (11). A solution of [Me$_2$Al{B(NDippCH)$_2$}]$_2$ (133 mg, 0.30 mmol) in *n*-hexane (6 mL) was added dropwise to a stirred solution of [Cp$_2$Y(μ-Me)]$_2$ (70 mg, 0.30 mmol) in toluene (4 mL). After 16 h, all volatiles were removed in vacuo. The resulting sticky solid was washed with *n*-pentane (2 mL) and dried under reduced pressure to obtain **11** as a white powder (199 mg, 98%). Single crystals suitable for XRD analysis were grown

https://doi.org/10.1021/acs.inorgchem.1c02349
Inorg. Chem. 2021, 60, 14952−14968

from a saturated *n*-pentane/toluene (1:1) solution at −40 °C. ^{1}H NMR (C_6D_6, 400 MHz, 26 °C): δ 7.31 (m, 2H, *p*-H_{Dipp}), 7.26 (m, 4H, *m*-H_{Dipp}), 6.41 (s, 2H, NC*H*), 5.79 (bs, 5H, C_5H_5), 5.74 (bs, 5H, C_5H_5), 3.52 (sept, 4H, ^{3}J(H,H) = 6.9 Hz, $CH(CH_3)_2$), 1.45 (d, 12H, ^{3}J(H,H) = 6.9 Hz, $CH(CH_3)_2$), 1.27 (d, 12H, ^{3}J(H,H) = 6.9 Hz, $CH(CH_3)_2$), −0.67 (bs, 3H, $AlCH_3$), −0.73 (bs, 6H, $Y(\mu\text{-}CH_3)_2$). $^{13}C\{^{1}H\}$ NMR (C_6D_6, 101 MHz, 26 °C): δ 146.5 (*o*-C_{Dipp}), 142.9 (*i*-C_{Dipp}), 127.3 (*p*-C_{Dipp}), 123.4 (*m*-C_{Dipp}), 121.5 (NCH), 112.5 (C_5H_5), 28.7 ($CH(CH_3)_2$), 26.1 ($CH(CH_3)_2$), 23.6 ($CH(CH_3)_2$), 6.8 ($Y(\mu\text{-}CH_3)$), 6.7 ($Y(\mu\text{-}CH_3)$), −5.4 ($AlCH_3$). $^{11}B\{^{1}H\}$ NMR (C_6D_6, 80 MHz, 26 °C): δ 32.7 (BAl). DRIFT (KBr): $\tilde{\nu}$ 3066 (w), 3030 (w), 2959 (vs), 2926 (m), 2890 (m), 2866 (m), 2769 (w), 2707 (w), 1668 (w), 1558 (w), 1497 (w), 1457 (s), 1443 (m), 1370 (s), 1326 (m), 1267 (m), 1241 (m), 1223 (w), 1185(w), 1151 (w), 1113 (w), 1057 (w), 1013 (s), 936 (w), 896 (w), 799 (s), 783 (vs), 762 (s), 697 (m), 616 (m) cm^{-1}. Elem anal. Calcd for $C_{39}H_{55}AlBN_2Y$ (678.58 g mol^{-1}): C, 69.03; H, 8.17; N, 4.13. Found: C, 68.66; H, 8.20; N, 4.11.

[Cp*$_2$Y(THF)$_2$][AlPh$_4$] (12). In a pressure tube, **4^{Al}** (94 mg, 0.14 mmol) was suspended in benzene (3 mL) and stirred while THF (1 mL) was added dropwise. The suspension turned clear immediately. The solution was stirred at 80 °C for 30 min, and then all volatiles were removed under vacuum. The resulting sticky residue was suspended with *n*-pentane (2 mL), dried in vacuo, and washed with benzene (3 × 1 mL) to obtain **12** as a white powder (67 mg, 59%). ^{1}H NMR (THF-d_8, 500 MHz, 26 °C): δ 7.70 (d br, J = 5.1 Hz, 8H, *o*-C_6H_5), 6.99 (t, J = 7.2 Hz, 8H, *m*-C_6H_5), 6.92 (tt, ^{3}J(H,H) = 7.2 Hz, ^{4}J(H,H) = 2.5 Hz, 4H, *p*-C_6H_5), 1.90 (s, 30H, $C_5(CH_3)_5$). Because of exchange with THF-d_8, free THF was found (approximately 2 equiv). $^{13}C\{^{1}H\}$ NMR (THF-d_8, 126 MHz, 26 °C): δ 139.8 (*o*-C_6H_5), 126.0 (*m*-C_6H_5), 124.6 (*p*-C_6H_5), 121.5 (d, ^{1}J(Y,C) = 1.7 Hz, $C_5(CH_3)_5$), 68.0 (free THF), 67.7 (OCH_2, THF), 26.2 (free THF), 25.6 (CH_2, THF), 11.5 ($C_5(CH_3)_5$). Resonances for *i*-C_6H_5 were not detected. DRIFT (KBr): $\tilde{\nu}$ 3112 (w), 3043 (vs), 2984 (vs), 2964 (s), 2903 (s), 2861 (s), 2723 (w), 1943 (w), 1868 (w), 1818 (w), 1474 (m), 1454 (m), 1416 (s), 1380 (m), 1244 (m), 1074 (vs), 1002 (s), 858 (m), 832 (m), 731 (s), 705 (vs), 664 (s), 480 (vs), 463 (m) cm^{-1}. Elem anal. Calcd for $C_{52}H_{66}O_2AlY$ (838.99 g mol^{-1}): C, 74.44; H, 7.93. Found: C, 74.12; H, 7.69.

[Cp*$_2$Y(THF)$_2$][GaPh$_4$] (14). Dissolving **4^{Ga}** in THF-d_8 led to complete conversion to **14**. ^{1}H NMR (THF-d_8, 400 MHz, 26 °C): δ 7.63 (d br, J = 6.5 Hz, 8H, *o*-C_6H_5), 6.99 (t, J = 7.1 Hz, 8H, *m*-C_6H_5), 6.90 (tt, ^{3}J(H,H) = 7.2 Hz, ^{4}J(H,H) = 1.6 Hz, 4H, *p*-C_6H_5), 1.89 (s, 30H, $C_5(CH_3)_5$).

Cp*$_2$YPh(THF) (13) and [Cp*$_2$Y(THF)$_2$][Ph$_3$Al{B(NDippCH)$_2$}] (15). In a glovebox, a sample of **10** (12 mg, 0.01 mmol) was dissolved in benzene (0.4 mL) and THF (0.1 mL) was added after 30 min. The colorless solution was frozen at −40 °C and dried cold under vacuum to obtain a voluminous colorless powder. The powder was dissolved in *n*-pentane (0.3 mL), filtered, and stored at −40 °C. After 3 days, single crystals suitable for XRD analysis of **15** (pale yellow) and **13** (colorless) were obtained.

■ ASSOCIATED CONTENT

Supporting Information

The Supporting Information is available free of charge at https://pubs.acs.org/doi/10.1021/acs.inorgchem.1c02349.

Supporting figures, detailed crystallographic data, spectroscopic data (NMR), and analytical details (PDF)

Accession Codes

CCDC 2093598−2093611 contain the supplementary crystallographic data for this paper. These data can be obtained free of charge via www.ccdc.cam.ac.uk/data_request/cif, or by emailing data_request@ccdc.cam.ac.uk, or by contacting The Cambridge Crystallographic Data Centre, 12 Union Road, Cambridge CB2 1EZ, UK; fax: +44 1223 336033.

■ AUTHOR INFORMATION

Corresponding Author

Reiner Anwander − *Institut für Anorganische Chemie, Eberhard Karls Universität Tübingen, Tübingen 72076, Germany;* orcid.org/0000-0002-1543-3787; Email: reiner.anwander@uni-tuebingen.de

Authors

Martin Bonath − *Institut für Anorganische Chemie, Eberhard Karls Universität Tübingen, Tübingen 72076, Germany*

Dorothea Schädle − *Institut für Anorganische Chemie, Eberhard Karls Universität Tübingen, Tübingen 72076, Germany*

Cäcilia Maichle-Mössmer − *Institut für Anorganische Chemie, Eberhard Karls Universität Tübingen, Tübingen 72076, Germany;* orcid.org/0000-0001-7638-1610

Complete contact information is available at: https://pubs.acs.org/10.1021/acs.inorgchem.1c02349

Notes

The authors declare no competing financial interest.

■ ACKNOWLEDGMENTS

We thank the German Science Foundation (Grant AN238/15-2) for support.

■ REFERENCES

(1) Watson, P. L. Methane Exchange Reactions of Lanthanide and Early-Transition-Metal Methyl Complexes. *J. Am. Chem. Soc.* **1983**, *105*, 6491−6493.

(2) Watson, P. L.; Parshall, G. W. Organolanthanides in Catalysis. *Acc. Chem. Res.* **1985**, *18*, 51−56.

(3) Mindiola, D. J. Pioneers and Influencers in Organoemtallic Chemistry: Dr. Patricia Watson and the Molecualr Dance of M−C and C−H Bonds. *Organometallics* **2020**, *39*, 1135−1138.

(4) Thompson, M. E.; Bercaw, J. E. Some Aspects of the Chemistry of Alkyl and Hydride Derivatives of Permethylscandocene. *Pure Appl. Chem.* **1984**, *56*, 1−11.

(5) Thompson, M. E.; Baxter, S. M.; Bulls, A. R.; Burger, B. J.; Nolan, M. C.; Santarsiero, B. D.; Schaefer, W. P.; Bercaw, J. E. σ-Bond Metathesis for Carbon-Hydrogen Bonds of Hydrocarbons and Sc-R (R = H, Alkyl, Aryl) Bonds of Permethylscandocene Derivatives. Evidence for Noninvolvement of the π System in Electrophilic Activation of Aromatic and Vinylic C-H Bonds. *J. Am. Chem. Soc.* **1987**, *109*, 203−219.

(6) Evans, W. J.; Perotti, J. M.; Ziller, J. W. Synthetic Utility of $[(C_5Me_5)_2Ln][(\mu\text{-}Ph)_2BPh_2]$ in Accessing $[(C_5Me_5)_2LnR]_x$ Unsolvated Alkyl Lanthanide Metallocenes, Complexes with High C−H Activation Reactivity. *J. Am. Chem. Soc.* **2005**, *127*, 3894−3909.

(7) Walter, M. D.; Matsunaga, P. T.; Burns, C. J.; Maron, L.; Andersen, R. A. Synthesis and Reactions of $[Cp^*_2Yb]_2(\mu\text{-Me})$ and $[Cp^*_2Yb]_2(\mu\text{-Me})(Me)$ and Related Yb_2(II, III) and Yb_2(III, III) Compounds. *Organometallics* **2017**, *36* (23), 4564−4578.

(8) Watson, P. L. Facile C-H Activation by Lutetium-Methyl and Lutetium-Hydride Complexes. *J. Chem. Soc., Chem. Commun.* **1983**, 276−277.

(9) Hajela, S.; Schaefer, W. P.; Bercaw, J. E. Structure of a Permethylcyclopentadienyl-μ-tetramethylcyclopentadienylmethylene Scandium Dimer. *Acta Crystallogr., Sect. C: Cryst. Struct. Commun.* **1992**, *C48*, 1771−1773.

(10) Webster, C. L.; Ziller, J. W.; Evans, W. J. Solvent-Free Organometallic Reactivity: Synthesis of Hydride and Carboxylate Complexes of Uranium and Yttrium from Gas/Solid Reactions. *Organometallics* **2014**, *33*, 433−436.

(11) Evans, W. J.; Bloom, I.; Hunter, W. E.; Atwood, J. L. Reactivity of Low-Valent Samarium with Unsaturated Hydrocarbons Leading to

a Structurally Characterized Samarium Hydride Complex. *J. Am. Chem. Soc.* **1983**, *105*, 1401−1403.
(12) Waterman, R. σ-Bond Metathesis: A 30-Year Retrospective. *Organometallics* **2013**, *32*, 7249−7263.
(13) Jahns, V.; Köstlmeier, S.; Kotzian, M.; Röusch, N.; Watson, P. L. On the Agostic Interaction in Lanthanide Phenylene Complexes: An INDO Study of $[(CpM)_2C_6H_4]$ (M = Sc, Lu) Employing an Energy-Partitioning Analysis. *Int. J. Quantum Chem.* **1992**, *44*, 853−867.
(14) Castillo, I.; Tilley, T. D. Mechanistic Aspects of Samarium-Mediated σ-Bond Activations of Arene C−H and Arylsilane Si−C Bonds. *J. Am. Chem. Soc.* **2001**, *123*, 10526−10534.
(15) Evans, W. J.; Chamberlain, L. R.; Ulibarri, T. A.; Ziller, J. W. Reactivity of Trimethylaluminum with $(C_5Me_5)_2Sm(THF)_2$: Synthesis, Structure, and Reactivity of the Samarium Methyl Complexes $(C_5Me_5)_2Sm[(\mu\text{-}Me)AlMe_2(\mu\text{-}Me)]_2Sm(C_5Me_5)_2$ and $(C_5Me_5)_2SmMe(THF)$. *J. Am. Chem. Soc.* **1988**, *110*, 6423−6432.
(16) Dietrich, H. M.; Törnroos, K. W.; Herdtweck, E.; Anwander, R. Tetramethylaluminate and Tetramethylgallate Coordination in Rare-Earth Metal Half-Sandwich and Metallocene Complexes. *Organometallics* **2009**, *28*, 6739−6749.
(17) Watson, P. L. Ziegler−Natta Polymerization: The Lanthanide Model. *J. Am. Chem. Soc.* **1982**, *104*, 337−339.
(18) Evans, W. J.; Kozimor, S. A.; Brady, J. C.; Davis, B. L.; Nyce, G. W.; Seibel, C. A.; Ziller, J. W.; Doedens, R. J. Metallocene Allyl Reactivity ind the Presence of Alkenes Tethered to Cyclopentadienyl Ligands. *Organometallics* **2005**, *24*, 2269−2278.
(19) Ballard, D. G. H.; Courtis, A.; Holton, J.; McMeeking, J.; Pearce, R. Alkyl Bridged Complexes of the Group 3A and Lanthanoid Metals as Homogeneous Ethylene Polymerisation Catalysts. *J. Chem. Soc., Chem. Commun.* **1978**, 994−995.
(20) Holton, J.; Lappert, M. F.; Scollary, G. R.; Ballard, D. G. H.; Pearce, R.; Atwood, J. L.; Hunter, W. E. μ-Dialkyl Inner Transition Metal(III) Tetra-alkylaluminates; the Crystal and Molecular Structure of Di-μ-methyl-(dimethylaluminium)biscyclopentadienyl-yttrium and -ytterbium. *J. Chem. Soc., Chem. Commun.* **1976**, 425−426.
(21) Holton, J.; Lappert, M. F.; Ballard, D. G. H.; Pearce, R.; Atwood, J. L.; Hunter, W. E. Alkyl-Bridged Complexes of the d- and f-Block Elements. Part 1. Di-μ-alkyl-bis(η-cyclopentadienyl)metal(III)-dialkylaluminium(III) Complexes and the Crystal and Molecular Structure of the Ytterbium Methyl Species. *J. Chem. Soc., Dalton Trans.* **1979**, 45−53.
(22) Dietrich, H. M.; Raudaschl-Sieber, G.; Anwander, R. Trimethylyttrium and Trimethyllutetium. *Angew. Chem., Int. Ed.* **2005**, *44*, 5303−5306.
(23) Busch, M. A.; Harlow, R.; Watson, P. L. Unusual Eight-Membered Rings with Linear Symmetric Methyl Groups from Yttrium and Lutetium Methyl Complexes. *Inorg. Chim. Acta* **1987**, *140*, 15−20.
(24) Watson, P. L.; Herskovitz, T. Homogeneous Lanthanide Complexes as Polymerization and Oligomerization Catalysts: Mechanistic Studies. *ACS Symp. Ser.* **1983**, *212*, 459−479.
(25) Heating a sample of **1** at 90 °C in a J. Young-valved NMR tube in C_6D_6 for 7 days did not result in any detectable decomposition.
(26) Den Haan, K. H.; Wielstra, Y.; Eshuis, J. J. W.; Teuben, J. H. Synthesis of Permethylyttrocene Alkyl Complexes. *J. Organomet. Chem.* **1987**, *323*, 181−192.
(27) Jemmis, E. D.; Chandrasekhar, J.; Schleyer, P. v. R. Stabilization of D_{3h} Pentacoordinate Carbonium Ions. Linear Three-Center-Two-Electron Bonds. Implications for Aliphatic Electrophilic Substitution Reactions. *J. Am. Chem. Soc.* **1979**, *101*, 527−533.
(28) Schleyer, P. v. R.; Tidor, B.; Jemmis, E. D.; Chandrasekhar, J.; Würthwein, E. U.; Kos, A. J.; Luke, B. T.; Pople, J. A. Lithium-Stabilized Methanonium Ions, $CLi_{5-n}H_n^+$. A Theoretical Study. *J. Am. Chem. Soc.* **1983**, *105*, 484−488.
(29) Zimmermann, M.; Anwander, R. Homoleptic Rare-Earth Metal Complexes Containing Ln−C σ-Bonds. *Chem. Rev.* **2010**, *110*, 6194−6259.
(30) Fischbach, A.; Anwander, R. Rare-Earth Metals and Aluminium Getting Close in Ziegler-type Organometallics. *Adv. Polym. Sci.* **2006**, *204*, 155−281.
(31) Evans, W. J.; Forrestal, K. J.; Ansari, M. A.; Ziller, J. W. Reactions of Olefin Polymerization Activators with Complexed Pentamethylcyclopentadienyl Ligands: Abstraction of Tetramethyl-fulvalene. *J. Am. Chem. Soc.* **1998**, *120*, 2180−2181.
(32) Klimpel, M. G.; Eppinger, J.; Sirsch, P.; Scherer, W.; Anwander, R. The Lanthanide Ziegler−Natta Model: Aluminum-Mediated Chain Transfer. *Organometallics* **2002**, *21*, 4021−4023.
(33) Chen, E. Y. X.; Kruper, W. J.; Roof, G.; Wilson, D. R. Double Activation" of Constrained Geometry and *ansa*-Metallocene Group 4 Metal Dialkyls: Synthesis, Structure, and Olefin Polymerization Study of Mono- and Dicationic Aluminate Complexes. *J. Am. Chem. Soc.* **2001**, *123*, 745−746.
(34) Liu, Z.; Somsook, E.; Landis, C. R. A ^{2}H-Labeling Scheme for Active-Site Counts in Metallocene-Catalyzed Alkene Polymerization. *J. Am. Chem. Soc.* **2001**, *123*, 2915−2916.
(35) Stahl, N. G.; Salata, M. R.; Marks, T. J. $B(C_6F_5)_3$- vs $Al(C_6F_5)_3$-Derived Metallocenium Ion Pairs. Structural, Thermochemical, and Structural Dynamic Divergences. *J. Am. Chem. Soc.* **2005**, *127*, 10898−10909.
(36) Mathis, D.; Couzijn, E. P. A.; Chen, P. Structure, Dynamics, and Polymerization Activity of Zirconocenium Ion Pairs Generated with Boron-C_6F_5 Compounds and Al_2R_6. *Organometallics* **2011**, *30*, 3834−3843.
(37) Theurkauff, G.; Bader, M.; Marquet, N.; Bondon, A.; Roisnel, T.; Guegan, J.-P.; Amar, A.; Boucekkine, A.; Carpentier, J.-F.; Kirillov, E. Discrete Ionic Complexes of Highly Isoselective Zirconocenes. Solution Dynamics, Trimethylaluminum Adducts, and Implications in Propylene Polymerization. *Organometallics* **2016**, *35*, 258−276.
(38) Krieck, S.; Görls, H.; Westerhausen, M. Synthesis and Properties of Calcium Tetraorganylalanates with $[Me_{4-n}AlPh_n]^-$ Anions. *Organometallics* **2008**, *27*, 5052−5057.
(39) Zimmermann, M.; Törnroos, K. W.; Anwander, R. Cationic Rare-Earth-Metal Half-Sandwich Complexes for the Living *trans*-1,4-Isoprene Polymerization. *Angew. Chem., Int. Ed.* **2008**, *47*, 775−778.
(40) Barisic, D.; Buschmann, D. A.; Schneider, D.; Maichle-Mössmer, C.; Anwander, R. Rare-Earth Metal Pentadienyl Half-Sandwich and Sandwich Tetramethylaluminates − Synthesis, Structure, Reactivity, and Performance in Isoprene Polymerization. *Chem. - Eur. J.* **2019**, *25*, 4821−4832.
(41) Evans, W. J.; Davis, B. L.; Champagne, T. M.; Ziller, J. W. C−H Bond Activation Through Steric Crowding of Normally Inert Ligands in the Sterically Crowded Gadolinium and Yttrium $(C_5Me_5)_3M$ Complexes. *Proc. Natl. Acad. Sci. U. S. A.* **2006**, *103*, 12678−12683.
(42) Langer, J.; Krieck, S.; Gorls, H.; Kreisel, G.; Seidel, W.; Westerhausen, M. Organic Heterobimetallic Complexes of the Alkaline Earth Metals (Ae = Ca, Sr, Ba) with Tetrahedral Metallate Anions of Three-Valent Metals (M = B, Al, Ga, and V). *New J. Chem.* **2010**, *34*, 1667−1677.
(43) Pour, N.; Gofer, Y.; Major, D. T.; Aurbach, D. Structural Analysis of Electrolyte Solutions for Rechargeable Mg Batteries by Stereoscopic Means and DFT Calculations. *J. Am. Chem. Soc.* **2011**, *133*, 6270−6278.
(44) Koch, A.; Krieck, S.; Görls, H.; Westerhausen, M. Alkaline Earth Metal-Carbene Complexes with the Versatile Tridentate 2,6-Bis(3-mesitylimidazol-2-ylidene)pyridine Ligand. *Organometallics* **2017**, *36*, 994−1000.
(45) Shannon, R. Revised Effective Ionic Radii and Systematic Studies of Interatomic Distances in Halides and Chalcogenides. *Acta Crystallogr., Sect. A: Cryst. Phys., Diffr., Theor. Gen. Crystallogr.* **1976**, *A32*, 751−767.
(46) Occhipinti, G.; Meermann, C.; Dietrich, H. M.; Litlabø, R.; Auras, F.; Törnroos, K. W.; Maichle-Mössmer, C.; Jensen, V. R.; Anwander, R. Synthesis and Stability of Homoleptic Metal(III) Tetramethylaluminates. *J. Am. Chem. Soc.* **2011**, *133*, 6323−6337.
(47) Barisic, D.; Diether, D.; Maichle-Mössmer, C.; Anwander, R. Trimethylscandium. *J. Am. Chem. Soc.* **2019**, *141*, 13931−13940.

https://doi.org/10.1021/acs.inorgchem.1c02349
Inorg. Chem. 2021, 60, 14952−14968

(48) Evans, W. J.; Anwander, R.; Doedens, R. J.; Ziller, J. W. The Use of Heterometallic Bridging Moieties To Generate Tractable Lanthanide Complexes of Small Ligands. *Angew. Chem., Int. Ed. Engl.* **1994**, *33*, 1641−1644.
(49) Dietrich, H. M.; Meermann, C.; Törnroos, K. W.; Anwander, R. Sounding out the Reactivity of Trimethylyttrium. *Organometallics* **2006**, *25*, 4316−4321.
(50) Zimmermann, M.; Litlabø, R.; Törnroos, K. W.; Anwander, R. "Metastable" $Lu(GaMe_4)_3$ Reacts Like Masked $[LuMe_3]$: Synthesis of an Unsolvated Lanthanide Dimethyl Complex. *Organometallics* **2009**, *28*, 6646−6649.
(51) Dietrich, H. M.; Maichle-Mössmer, C.; Anwander, R. Donor-Assisted Tetramethylaluminate/Gallate Exchange in Organolanthanide Complexes: Pushing the Limits of Pearson's HSAB Concept. *Dalton Trans.* **2010**, *39*, 5783−5785.
(52) Schädle, D.; Meermann-Zimmermann, M.; Schädle, C.; Maichle-Mössmer, C.; Anwander, R. Rare-Earth Metal Complexes with Terminal Imido Ligands. *Eur. J. Inorg. Chem.* **2015**, *2015*, 1334−1339.
(53) Schädle, D.; Meermann-Zimmermann, M.; Maichle-Mössmer, C.; Schädle, C.; Törnroos, K. W.; Anwander, R. Rare-Earth Metal Methylidene Complexes with $Ln_3(\mu_3\text{-}CH_2)(\mu_3\text{-}Me)(\mu_2\text{-}Me)_3$ Core Structure. *Dalton Trans.* **2015**, *44*, 18101−18110.
(54) Gómez-Pantoja, M.; Gómez-Sal, P.; Hernán-Gómez, A.; Martín, A.; Mena, M.; Santamaría, C. Co-Complexation of Lithium Gallates on the Titanium Molecular Oxide $\{[Ti(\eta^5\text{-}C_5Me_5)(\mu\text{-}O)\}_3(\mu_3\text{-}CH)]$. *Inorg. Chem.* **2012**, *51*, 8964−8972.
(55) McLellan, R.; Uzelac, M.; Kennedy, A. R.; Hevia, E.; Mulvey, R. E. LiTMP Trans-Metal-Trapping of Fluorinated Aromatic Molecules: A Comparative Study of Aluminum and Gallium Carbanion Traps. *Angew. Chem., Int. Ed.* **2017**, *56*, 9566−9570.
(56) Tebbe, K.-F.; Gilles, T.; Conrad, F.; Tyrra, W. Bis-(triphenylphosphin)iminium-Tetrakis(pentafluorphenyl)gallat. *Acta Crystallogr., Sect. C: Cryst. Struct. Commun.* **1996**, *C52*, 1663−1666.
(57) King, W. A.; Scott, B. L.; Eckert, J.; Kubas, G. J. Reversible Displacement of Polyagostic Interactions in 16e $[Mn(CO)(R_2PC_2H_4PR_2)_2]^+$ by H_2, N_2, and SO_2. Binding and Activation of η^2-H_2 *trans* to CO Is Nearly Invariant to Changes in Charge and *cis* Ligands. *Inorg. Chem.* **1999**, *38*, 1069−1084.
(58) Guzei, I. A.; Dagorne, S.; Jordan, R. F. Bis(isopropylamino)-methylcarbenium Tetrakis(pentafluorophenyl)gallate. *Acta Crystallogr., Sect. C: Cryst. Struct. Commun.* **2000**, *C56*, e134−e135.
(59) Ren, K.; Mejiritski, A.; Malpert, J. H.; Grinevich, O.; Gu, H.; Neckers, D. C. Tetrakis(pentafluorophenyl)gallates (I). *Tetrahedron Lett.* **2000**, *41*, 8669−8672.
(60) Cowley, A. H.; Macdonald, C. L. B.; Silverman, J. S.; Gorden, J. D.; Voigt, A. Triple-Decker Main Group Cations. *Chem. Commun.* **2001**, 175−176.
(61) Kaafarani, B. R.; Gu, H.; Alan Pinkerton, A.; Neckers, D. C. The Crystal and Molecular Structures of 1-Naphthylphenyliodonium tetrafluoroborate and 1-Naphthylphenyliodonium Tetrakis-(pentafluorophenyl)gallate. *J. Chem. Soc., Dalton Trans.* **2002**, 2318−2321.
(62) Ren, K.; Malpert, J. H.; Gu, H.; Li, H.; Neckers, D. C. Synthesis, Properties and Photolysis of New Iodonium Tetrakis-(pentafluorophenyl)gallate Photoinitiators and Comparison with Their Indate and Aluminate Analogs. *Tetrahedron* **2002**, *58*, 5267−5273.
(63) Malone, J. F.; McDonald, W. S. Crystal Structures of Triphenylgallium and Triphenylindium. *J. Chem. Soc. A* **1970**, 3362−3367.
(64) Sadow, A. D.; Tilley, T. D. Homogeneous Catalysis with Methane. A Strategy for the Hydromethylation of Olefins Based on the Nondegenerate Exchange of Alkyl Groups and σ-Bond Metathesis at Scandium. *J. Am. Chem. Soc.* **2003**, *125*, 7971−7977.
(65) Dettenrieder, N.; Dietrich, H. M.; Schädle, C.; Maichle-Mössmer, C.; Törnroos, K. W.; Anwander, R. Organoaluminum Boryl Complexes. *Angew. Chem., Int. Ed.* **2012**, *51*, 4461−4465.
(66) Dettenrieder, N.; Hollfelder, C. O.; Jende, L. N.; Maichle-Mössmer, C.; Anwander, R. Half-Sandwich Rare-Earth-Metal Alkylaluminate Complexes Bearing Peripheral Boryl Ligands. *Organometallics* **2014**, *33*, 1528−1531.
(67) Atwood, J. L.; Cannon, R. E. The Synthesis and Structure of Potassium Cyanotrimethylaluminate. *J. Organomet. Chem.* **1973**, *47*, 321−329.
(68) Michel, O.; Dietrich, H. M.; Litlabø, R.; Törnroos, K. W.; Maichle-Mössmer, C.; Anwander, R. Tris(pyrazolyl)borate Complexes of the Alkaline-Earth Metals: Alkylaluminate Precursors and Schlenk-Type Rearrangements. *Organometallics* **2012**, *31*, 3119−3127.
(69) Gerteis, R. L.; Dickerson, R. E.; Brown, T. L. The Crystal Structure of Lithium Aluminum Tetraethyl. *Inorg. Chem.* **1964**, *3*, 872−875.
(70) Medley, J. H.; Fronczek, F. R.; Ahmad, N.; Day, M. C.; Rogers, R. D.; Kerr, C. R.; Atwood, J. L. The Crystal Structures of $NaAlR_4$, R = Methyl, Ethyl, and *n*-Propyl. *J. Crystallogr. Spectrosc. Res.* **1985**, *15*, 99−107.
(71) Dettenrieder, N.; Schädle, C.; Maichle-Mössmer, C.; Sirsch, P.; Anwander, R. A Dimethylgallium Boryl Complex and Its Methyllithium Addition Compound. *J. Am. Chem. Soc.* **2014**, *136*, 886−889.
(72) Evans, W. J.; Anwander, R.; Ziller, J. W. Inclusion of Al_2Me_6 in the Crystalline Lattice of the Organometallic Complexes $LnAl_3Me_{12}$. *Organometallics* **1995**, *14*, 1107−1109.
(73) Scollary, G. The Crystal Structure of the Methyl-Bridged Yttrium-Aluminium Complex, $[(\mu\text{-}C_5H_5)_2YMe_2AlMe_2]$. *Aust. J. Chem.* **1978**, *31*, 411−414.
(74) Schneider, D.; Harmgarth, N.; Edelmann, F. T.; Anwander, R. Ceric Cyclopentadienides Bearing Alkoxy, Aryloxy, Chlorido, or Iodido Co-Ligands. *Chem. - Eur. J.* **2017**, *23*, 12243−12252.
(75) Diether, D.; Tyulyunov, K.; Maichle-Mössmer, C.; Anwander, R. Fluorenyl Half-Sandwich Bis(tetramethylaluminate) Complexes of the Rare-Earth Metals: Synthesis, Structure, and Isoprene Polymerization. *Organometallics* **2017**, *36*, 4649−4659.
(76) Evans, W. J.; Chamberlain, L. R.; Ziller, J. W. Synthesis and X-ray Crystal Structure of a Heterobimetallic Ethyl-Bridged Organoaluminum Complex: $(C_5Me_5)_2Sm(\mu\text{-}C_2H_5)_2Al(C_2H_5)_2$. *J. Am. Chem. Soc.* **1987**, *109*, 7209−7211.
(77) Bienfait, A. M.; Wolf, B. M.; Törnroos, K. W.; Anwander, R. Ln(II)/Pb(II)−Ln(III)/Pb(0) Redox Approach toward Rare-Earth-Metal Half-Sandwich Complexes. *Organometallics* **2015**, *34*, 5734−5744.
(78) Holton, J.; Lappert, M. F.; Ballard, D. G. H.; Pearce, R.; Atwood, J. L.; Hunter, W. E. Alkyl-Bridged Complexes of the d- and f-Block Elements. Part 2. Bis[bis(μ-cyclopentadienyl)methylmetal(III)] Complexes, and the Crystal and Molecular Structure of the Yttrium and Ytterbium Species. *J. Chem. Soc., Dalton Trans.* **1979**, 54−61.
(79) Jutzi, P.; Izundu, J.; Neumann, B.; Mix, A.; Stammler, H.-G. Aryl(dimethyl)gallium Compounds and Methyl(diphenyl)gallium: Synthesis, Structure, and Redistribution Reactions. *Organometallics* **2008**, *27*, 4565−4571.
(80) MacDonald, M. R.; Ziller, J. W.; Evans, W. J. Coordination and Reductive Chemistry of Tetraphenylborate Complexes of Trivalent Rare Earth Metallocene Cations, $[(C_5Me_5)_2Ln][(\mu\text{-}Ph)_2BPh_2]$. *Inorg. Chem.* **2011**, *50*, 4092−4106.
(81) Compounds **12** and **14** eluded to XRD analyses, and only cell parameters could be determined. **12**: monoclinic angle β = 91.8°; a = 15.52 Å, b = 11.67 Å, and c = 26.55 Å. **14**: monoclinic angle β = 112.9°; a = 15.33 Å, b = 35.65 Å, and c = 19.56 Å.
(82) Kramer, M. U.; Robert, D.; Nakajima, Y.; Englert, U.; Spaniol, T. P.; Okuda, J. Alkyl Abstraction from a Trialkylyttrium Complex $[YR_3(thf)_2]$ (R = CH_2SiMe_3) Using a Group-13 Element Lewis Acid ER_3 (E = B, Al, Ga, In) − Structural Characterisation of the Ion Pair $[YR_2(thf)_4]^+[GaR_4]^-$ and of ER_3 (E = B, Al, Ga). *Eur. J. Inorg. Chem.* **2007**, *2007*, 665−674.
(83) Evans, W. J.; Bloom, I.; Hunter, W. E.; Atwood, J. L. Metal Vapor Synthesis of $(C_5Me_5)_2Sm(THF)_2$ and $(C_5Me_4Et)_2Sm(THF)_2$ and Their Reactivity with Organomercurial Reagents. Synthesis and

https://doi.org/10.1021/acs.inorgchem.1c02349
Inorg. Chem. 2021, 60, 14952−14968

X-ray Structural Analysis of $(C_5Me_5)_2Sm(C_6H_5)(THF)$. *Organometallics* **1985**, *4*, 112−119.
(84) Den Haan, K. H.; De Boer, J. L.; Teuben, J. H.; Smeets, W. J. J.; Spek, A. L. Formation and Molecular Structure of Permethylyttrocene Methyl Tetrahydrofuranate. *J. Organomet. Chem.* **1987**, *327*, 31−38.
(85) Mandel, A.; Magull, J. Neue Benzylkomplexe der Lanthanoiden. Darstellung und Kristallstrukturen von $[(C_5Me_5)_2Y(CH_2C_6H_5)(thf)]$, $[(C_5Me_5)_2Sm(CH_2C_6H_5)_2K(thf)_2]_\infty$ und $[(C_5Me_5)Gd(CH_2C_6H_5)_2(thf)]$. *Z. Anorg. Allg. Chem.* **1996**, *622*, 1913−1919.
(86) Casely, I. J.; Ziller, J. W.; Evans, W. J. C−H Activation via Carbodiimide Insertion into Yttrium−Carbon Alkynide Bonds: An Organometallic Alder-ene Reaction. *Organometallics* **2011**, *30*, 4873−4881.
(87) Ringelberg, S. N.; Meetsma, A.; Troyanov, S. I.; Hessen, B.; Teuben, J. H. Permethyl Yttrocene 2-Furyl Complexes: Synthesis and Ring-Opening Reactions of the Furyl Moiety. *Organometallics* **2002**, *21*, 1759−1765.
(88) Bouwkamp, M. W.; Budzelaar, P. H. M.; Gercama, J.; Del Hierro Morales, I.; de Wolf, J.; Meetsma, A.; Troyanov, S. I.; Teuben, J. H.; Hessen, B. Naked $(C_5Me_5)_2M$ Cations (M = Sc, Ti, and V) and Their Fluoroarene Complexes. *J. Am. Chem. Soc.* **2005**, *127*, 14310−14319.
(89) Evans, W. J.; Ulibarri, T. A.; Chamberlain, L. R.; Ziller, J. W.; Alvarez, D. Synthesis and Reactivity of the Cationic Organosamarium(III) Complex $[(C_5Me_5)_2Sm(THF)_2][BPh_4]$, Including the Synthesis and Structure of a Metallocene with an Alkoxy-tethered C_5Me_5 Ring, $(C_5Me_5)_2Sm[O(CH_2)_4C_5Me_5](THF)$. *Organometallics* **1990**, *9*, 2124−2130.
(90) Schumann, H.; Winterfeld, J.; Keitsch, M. R.; Herrmann, K.; Demtschuk, J. Metallorganische Verbindungen der Lanthanoide. 111. Synthese und Charakterisierung kationischer Metallocen-Komplexe der Lanthanoide. Röntgenstrukturanalyse von $[CpYb(THF)_2][BPh_4]$. *Z. Anorg. Allg. Chem.* **1996**, *622*, 1457−1461.
(91) For review artcles, see: (a) Mulvey, R. E. Modern Ate Chemistry: Applications of Synergic Mixed Alkali-Metal−Magnesium or − Zinc Reagents in Synthesis and Structure Building. *Organometallics* **2006**, *25*, 1060−1075. (b) Mulvey, R. E.; Mongin, F.; Uchiyama, M.; Kondo, Y. Deprotonative Metalation Using Ate Compounds: Synergy, Synthesis, and Structure Building. *Angew. Chem., Int. Ed.* **2007**, *46*, 3802−3824. (c) Mulvey, R. E. Avant-Garde Metalating Agents: Structural Basis of Alkali-Metal-Mediated Metalation. *Acc. Chem. Res.* **2009**, *42*, 743−755.
(92) For representative examples, see: (a) Armstrong, D. R.; Clegg, W.; Dale, S. H.; Graham, D. V.; Hevia, E.; Hogg, L. M.; Honeyman, G. W.; Kennedy, A. R.; Mulvey, R. E. Dizincation and dimagnesation of benzene unsing alkali-mediated metallation. *Chem. Commun.* **2007**, 598−600. (b) Ohsato, T.; Okuno, Y.; Ishida, S.; Iwamoto, T.; Lee, K.-H.; Lin, Z.; Yamashita, M.; Nozaki, K. A Potassium Diboryllithate: Synthesis, Bonding Properties, and the Deprotonation of Benzene. *Angew. Chem., Int. Ed.* **2016**, *55*, 11426−11430.
(93) Evans, W. J.; Meadows, J. H.; Hunter, W. E.; Atwood, J. L. Organolanthanide and Organoyttrium Hydride Chemistry. 5. Improved Synthesis of $[(C_5H_4R)_2YH(THF)]_2$ Complexes and Their Reactivity with Alkenes, Alkynes, 1,2-Propadiene, Nitriles, and Pyridine, Including Structural Characterization of an Alkylideneamido Product. *J. Am. Chem. Soc.* **1984**, *106*, 1291−1300.
(94) *COSMO*, version 1.61; Bruker AXS Inc.: Madison, WI, 2012.
(95) *APEX 3*, version 2016.5-0; Bruker AXS Inc.: Madison, WI, 2012.
(96) *SAINT*, version 8.34A; Bruker AXS Inc.: Madison, WI, 2010.
(97) Sheldrick, G. M. SHELXTL − Integrated space-group and crystal-structure determination. *Acta Crystallogr., Sect. A: Found. Adv.* **2015**, *71*, 3−8.
(98) Hübschle, C. B.; Sheldrick, G. M.; Dittrich, B. ShelXle: a Qt graphical user interface for SHELXL. *J. Appl. Crystallogr.* **2011**, *44*, 1281−1284.
(99) Krause, L.; Herbst-Irmer, R.; Sheldrick, G. M.; Stalke, D. Comparison of silver and molybdenum microfocus X-ray sources for single-crystal structure determination. *J. Appl. Crystallogr.* **2015**, *48*, 3−10.
(100) Sheldrick, G. M. *TWINABS*; University of Göttingen: Göttingen, Germany, 2002.
(101) Farrugia, L. J. ORTEP-3 for Windows − a version of ORTEP-III with a Graphical User Interface (GUI). *J. Appl. Crystallogr.* **1997**, *30*, 565−566.
(102) *POV-Ray*, version 3.6; Persistence of Vision Pty. Ltd.: Williamstown, Victoria, Australia, 2004; http://www.povray.org/.

https://doi.org/10.1021/acs.inorgchem.1c02349
Inorg. Chem. 2021, 60, 14952−14968

Supporting Information

The Alkylaluminate/gallate Trap: Metalation of Benzene by Heterobimetallic Yttrocene Complexes [Cp*$_2$Y(MMe$_3$R)] (M = Al, Ga)

Martin Bonath, Dorothea Schädle, Cäcilia Maichle-Mössmer, and Reiner Anwander*

Institut für Anorganische Chemie, Universität Tübingen, Auf der Morgenstelle 18, D-72076 Tübingen, (Germany)

* E-mail for R. A.: reiner.anwander@uni-tuebingen.de

Table of Contents

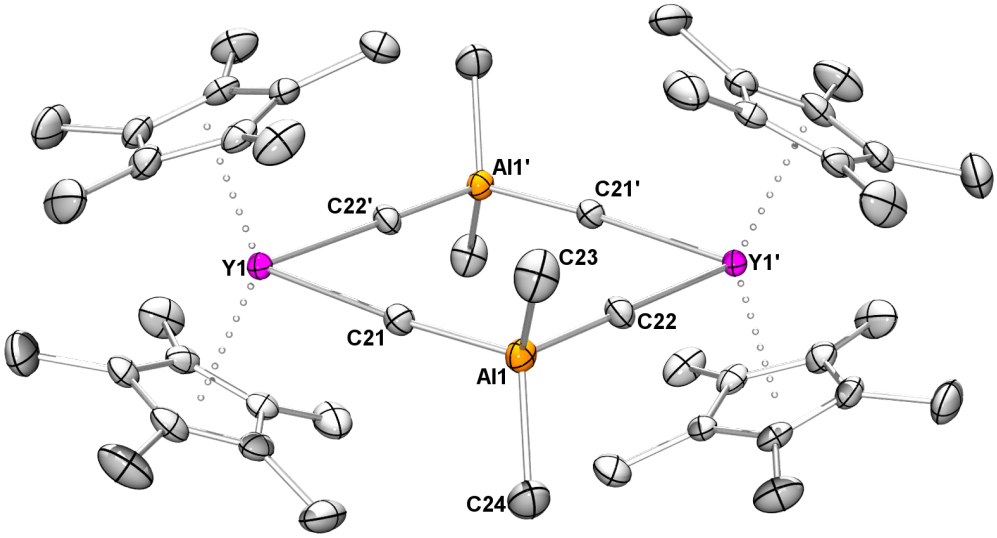

Figure S1. Crystal structure of $[Cp^*_2Y(AlMe_4)]_2$ ($\mathbf{1^{Al}_D}$). Single crystals for X-ray diffraction were grown at ambient temperature by condensing *n*-pentane to a concentrated benzene solution. All atoms are represented by atomic displacement ellipsoids set at 50% probability. Hydrogen atoms and a second independent molecule in the unit cell are omitted for clarity.

Table S1. Selected interatomic distances [Å] and angles [°] for $\mathbf{1^{Al}_D}$

molecule 1 (depicted)		molecule 2 (omitted)	
Y1–C21	2.675(3)	Y2–C45	2.655(4)
Y1'–C22	2.680(3)	Y2'–C47	2.684(3)
Al1–C21	2.041(4)	Al2–C45	2.048(4)
Al1–C22	2.046(4)	Al2–C47	2.039(3)
Al1–C23	1.971(4)	Al2–C46	1.985(4)
Al1–C24	1.980(4)	Al2–C48	1.969(5)
C21–Y1–C22'	86.8(1)	C45–Y2–C47'	84.9(1)
Y1–C21–Al1	174.6(2)	Y2–C45–Al2	177.0(2)
Y1–C22'–Al1'	177.6(2)	Y2–C47'–Al2'	174.5(2)
C21–Al1–C22	100.4(2)	C45–Al2–C47	102.1(2)
C23–Al1–C24	115.2(2)	C46–Al2–C48	116.7(2)

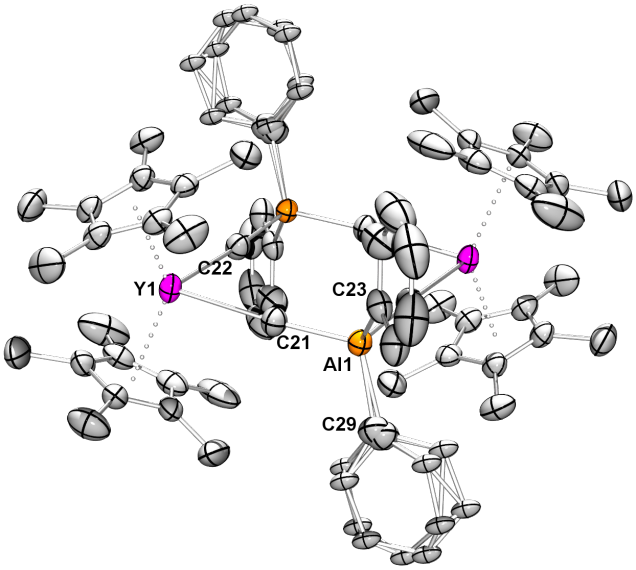

Figure S2. Crystal structure of $[Cp^*_2Y(Me_3AlPh)]_2$ ($\mathbf{2^{Al}_D}$), including disordered phenyl moieties at C29 due to concomitantly crystallized $\mathbf{3^{Al}_D}$ in about 25%. All atoms are represented by atomic displacement ellipsoids set at 50% probability. Disorder in the Cp* moieties, hydrogen atoms and co-crystallized benzene are omitted for clarity. Selected interatomic distances [Å] and angles [°]: Y1–C21 2.717(3), Y1–C22' 2.717(3), Al1–C21 2.042(3), Al1–C22 2.043(3), Al1–C23 1.991(3), Al1–C29 1.954(4); Y1–C21–Al1 173.1(2), Y1'–C22–Al1' 174.6(2), C21–Al1–C22 101.0(1), C23–Al1–C29 111.1(2), C21–Al1–C29 112.0(2).

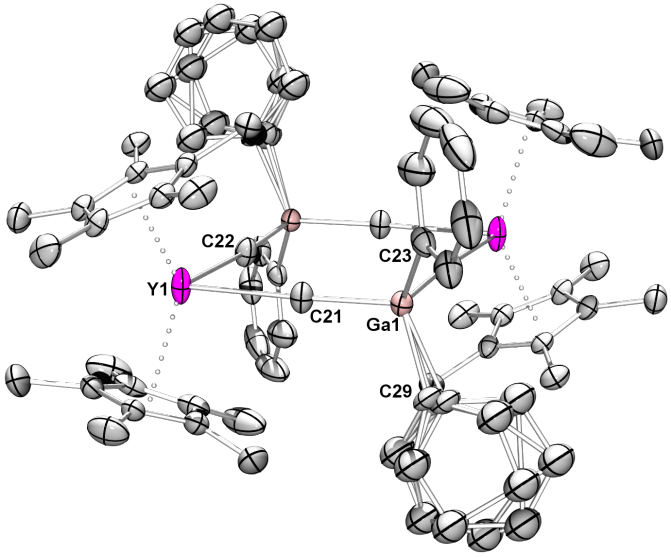

Figure S3. Crystal structure of $[Cp^*_2Y(Me_3GaPh)]_2$ ($\mathbf{2^{Ga}_D}$), including disordered phenyl moieties at C29 due to concomitantly crystallized $\mathbf{3^{Ga}_D}$ in about 50%. All atoms are represented by atomic displacement ellipsoids set at 50% probability. Disorder in the Cp* moieties, hydrogen atoms and co-crystallized benzene are omitted for clarity. Selected interatomic distances [Å] and angles [°]: Y1–C21 2.701(3), Y1–C22' 2.709(3), Ga1–C21 2.059(3), Ga1–C22 2.062(3), Ga1–C23 1.992(3), Ga1–C29 1.944(7); Y1–C21–Ga1 173.3(2), Y1'–C22–Ga1 174.5(2), C21–Ga1–C22 100.0(1), C23–Ga1–C29 112.1(2), C22–Ga1–C29 111.9(3).

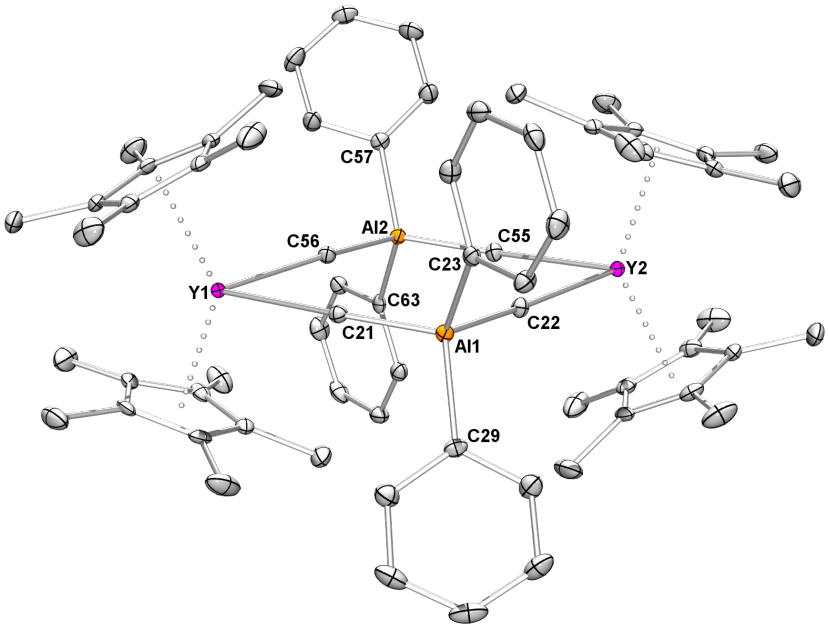

Figure S4. Crystal structure of $[Cp^*_2Y(Me_2AlPh_2)]_2$ ($\mathbf{3^{Al}_D}$). All atoms are represented by atomic displacement ellipsoids set at 50% probability. Hydrogen atoms are omitted for clarity. Selected interatomic distances [Å] and angles [°]: Y1–C21 2.779(3), Y1–C56 2.717(3), Y2–C22 2.720(3), Y2–C55 2.782(3), Al1–C21 2.040(3), Al1–C22 2.045(3), Al1–C23 1.994(3), Al1–C29 2.001(3), Al2–C55 2.036(3), Al2–C56 2.043(3), Al2–C57 1.999(3), Al2–C63 1.999(3); Y1–C21–Al1 169.1(2), Y1–C56–Al2 174.8(2), Y2–C22–Al1 176.0(2), Y2–C55–Al2 167.6(2), C21–Al1–C22 102.4(1), C23–Al1–C29 108.4(1), C21–Al1–C23 114.7(1), C55–Al2–C56 102.5(1), C57–Al2–C63 109.4(1), C55–Al2–C57 116.4(1).

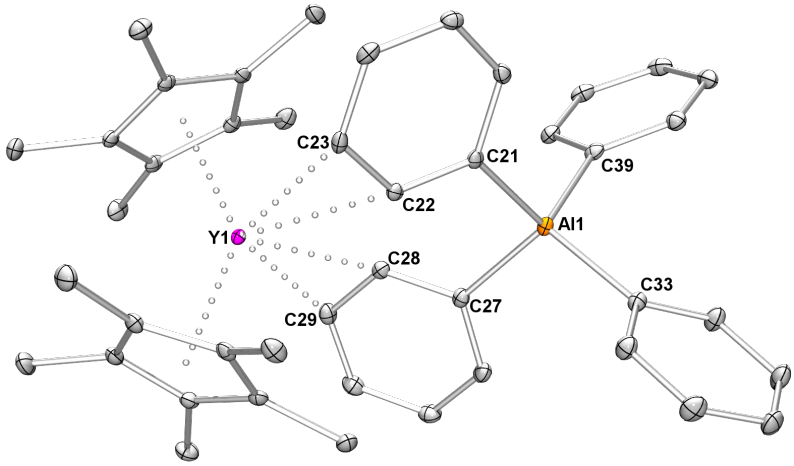

Figure S5. Crystal structure of $Cp^*_2Y(AlPh_4)$ ($\mathbf{4^{Al}}$). All atoms are represented by atomic displacement ellipsoids set at 50% probability. Hydrogen atoms and co-crystallized benzene are omitted for clarity. Selected interatomic distances [Å] and angles [°]: Y1–C22 2.887(1), Y1–C23 3.155(2), Y1–C28 2.872(1), Y1–C29 3.154(2), Al1–C21 2.015(1), Al1–C27 2.011(2), Al1–C33 1.996(2), Al1–C39 2.004(2); C21–Al1–C27 105.15(6), C33–Al1–C39 111.15(6), C21–Al1–C39 112.12(6).

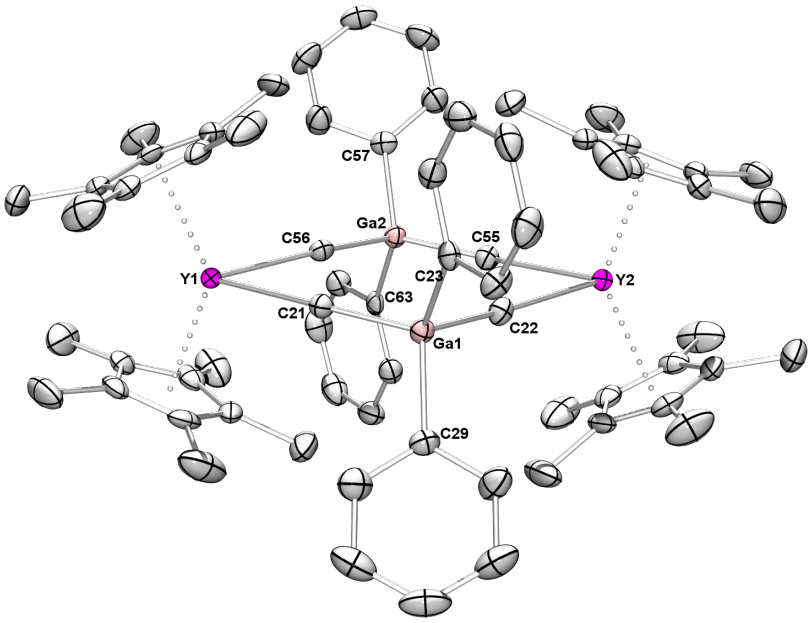

Figure S6. Crystal structure of $[Cp^*_2Y(Me_2GaPh_2)]_2$ ($\mathbf{3^{Ga}_D}$). All atoms are represented by atomic displacement ellipsoids set at 50% probability. Hydrogen atoms are omitted for clarity. Selected interatomic distances [Å] and angles [°]: Y1–C21 2.768(3), Y1–C56 2.706(3), Y2–C22 2.715(3), Y2–C55 2.770(3), Ga1–C21 2.060(3), Ga1–C22 2.061(3), Ga1–C23 1.999(3), Ga1–C29 1.999(3), Ga2–C55 2.060(3), Ga2–C56 2.066(3), Ga2–C57 1.996(3), Ga2–C63 2.001(3); Y1–C21–Ga1 169.2(2), Y1–C56–Ga2 174.5(2), Y2–C22–Ga1 175.5(2), Y2–C55–Ga2 167.6(2), C21–Ga1–C22 101.8(1), C23–Ga1–C29 109.0(1), C21–Ga1–C23 114.4(1), C55–Ga2–C56 101.9(1), C57–Ga2–C63 109.9(1), C55–Ga2–C57 116.6(1).

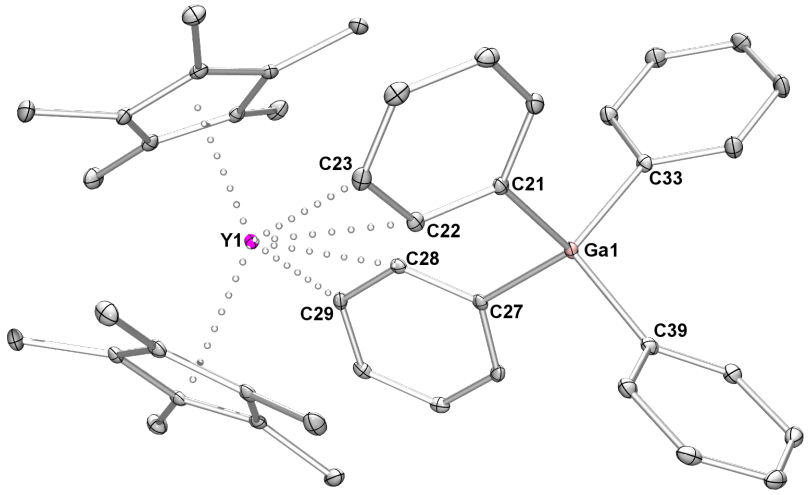

Figure S7. Crystal structure of $Cp^*_2Y(GaPh_4)$ ($\mathbf{4^{Ga}}$). All atoms are represented by atomic displacement ellipsoids set at 50% probability. Hydrogen atoms and co-crystallized benzene are omitted for clarity. Selected interatomic distances [Å] and angles [°]: Y1–C22 2.858(2), Y1–C23 3.144(2), Y1–C28 2.890(2), Y1–C29 3.165(2), Ga1–C21 2.015(2), Ga1–C27 2.017(2), Ga1–C33 1.998(2), Ga1–C39 2.005(2); C21–Ga1–C27 105.53(7), C33–Ga1–C39 111.11(7), C27–Ga1–C39 112.25(7).

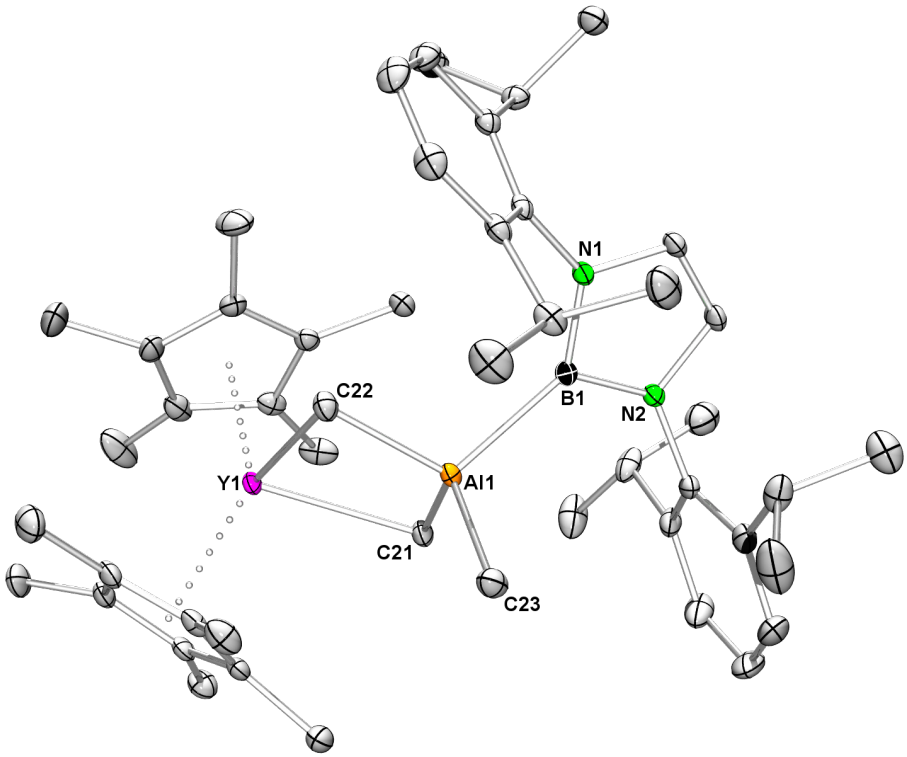

Figure S8. Crystal structure of $Cp^*_2Y[Me_3Al\{B(NDippCH)_2\}]$ (**6**). All atoms are represented by atomic displacement ellipsoids set at 50% probability. Hydrogen atoms are omitted for clarity. Selected interatomic distances [Å] and angles [°]: Y1–C21 2.591(1), Y1–C22 2.605(1), Al1–C21 2.078(1), Al1–C22 2.087(1), Al1–C23 1.988(1), Al1–B1 2.161(2); Y1–C21–Al1 83.32(5), Y1–C22–Al1 82.82(5), C21–Al1–C22 110.84(6), B1–Al1–C21 107.63(6), B1–Al1–C22 111.00(6), B1–Al1–C23 110.50(6).

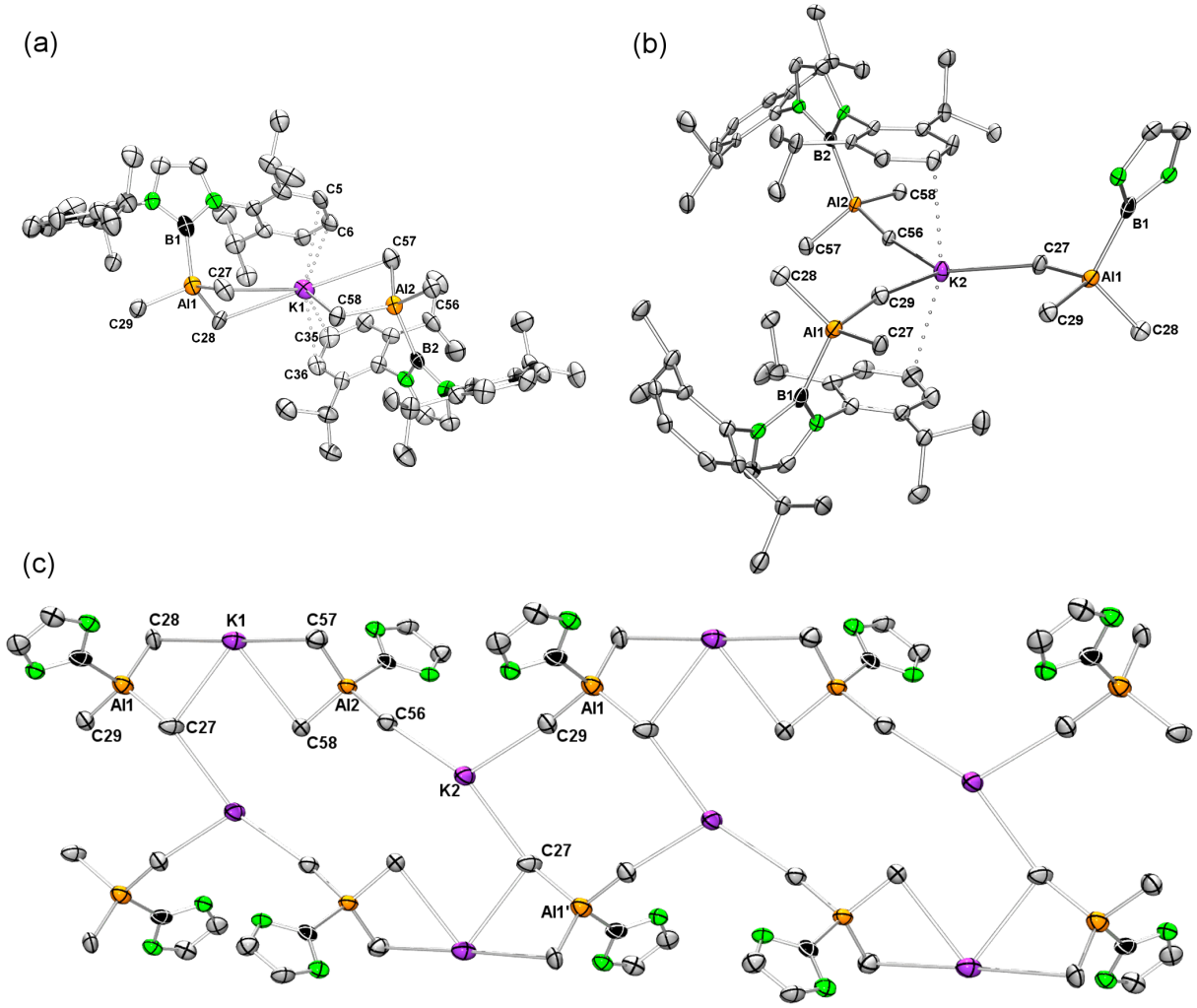

Figure S9. Molecular connectivity of $[K(Me_3Al\{B(NDippCH)_2\})]_n$ (**7**) in the solid state, comprising two different binding situations for potassium; (a) coordination number (CN) = 6, (b) CN = 5, (c) section of the polymeric chain arrangement. All atoms are represented by atomic displacement ellipsoids set at 50% probability. Hydrogen atoms and the disorder in one Dipp moiety are omitted for clarity; in (c) all Dipp moieties are omitted.

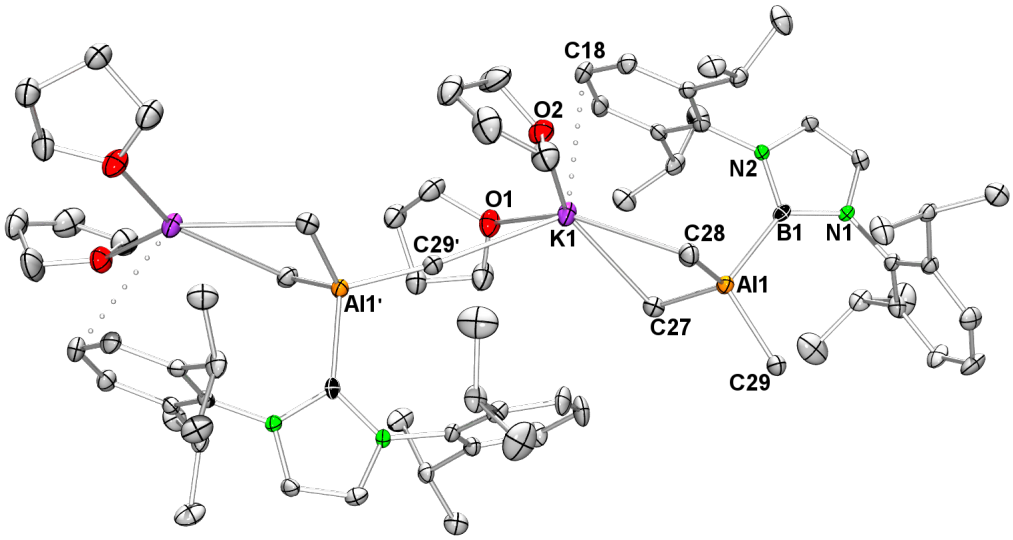

Figure S10. Section of the polymeric chain arrangement of THF adduct $[(THF)_2K(Me_3Al\{B(NDippCH)_2\})]_n$ (**8**) in the solid state. All atoms are represented by atomic displacement ellipsoids set at 50% probability. Hydrogen atoms and the disorder in one THF molecule are omitted for clarity. Selected interatomic distances [Å] and angles [°]: K1···C18 3.324(4), K1–C27 3.093(5), K1–C28 3.072(5), K1–C29' 3.215(3), K1–O1 2.715(3), K1–O2 2.713(4), Al1–C27 2.023(5), Al1–C28 2.028(5), Al1–C29 2.021(3), Al1–B1 2.164(4); K1–C27–Al1 88.5(2), K1–C28–Al1 89.0(2), K1'–C29–Al1 171.6(2), C27–Al1–C28 109.4(2), B1–Al1–C29 111.5(1).

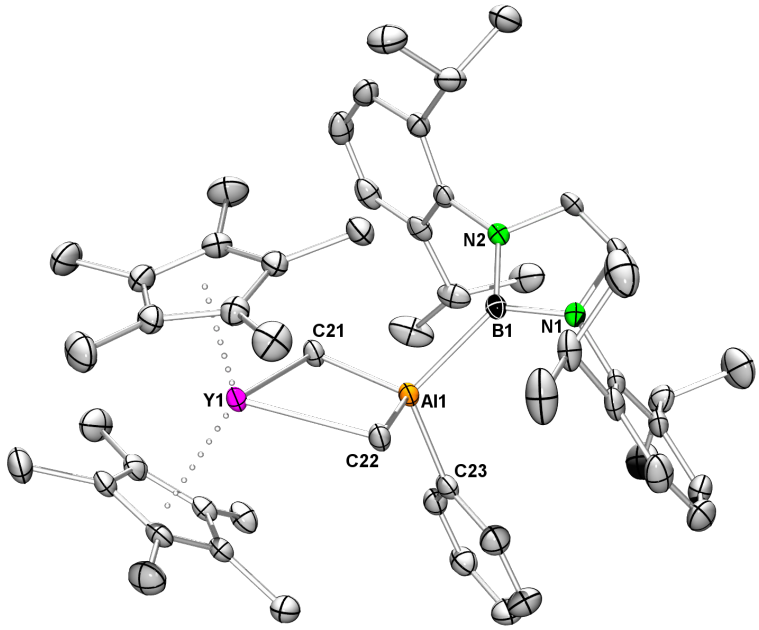

Figure S11. Crystal structure of $Cp^*_2Y[Me_2AlPh\{B(NDippCH)_2\}]$ (**9**). All atoms are represented by atomic displacement ellipsoids set at 50% probability. Hydrogen atoms are omitted for clarity. Selected interatomic distances [Å] and angles [°]: Y1–C21 2.636(2), Y1–C22 2.592(2), Al1–C21 2.072(2), Al1–C22 2.072(2), Al1–C23 2.008(2), Al1–B1 2.171(2); Y1–C21–Al1 83.82(7), Y1–C22–Al1 84.97(7), C21–Al1–C22 110.10(8), B1–Al1–C21 108.14(8), B1–Al1–C22 115.48(8), B1–Al1–C23 109.56(7).

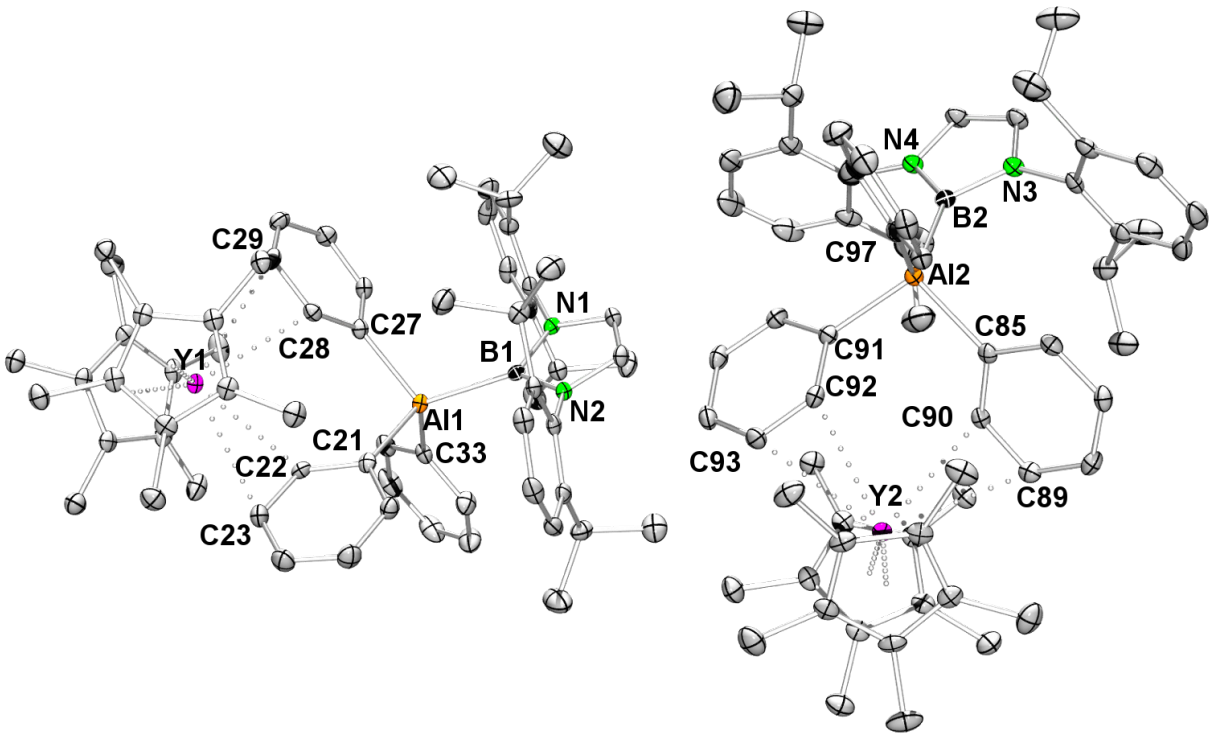

Figure S12. Crystal structure of $Cp^*_2Y[AlPh_3\{B(NDippCH)_2\}]$ (**10**). All atoms are represented by atomic displacement ellipsoids set at 50% probability. Hydrogen atoms and co-crystallized benzene are omitted for clarity.

Table S2. Selected interatomic distances [Å] and angles [°] for **10**

molecule 1 (left)		molecule 2 (right)	
Y1–C22	2.857(2)	Y2–C90	2.899(2)
Y1–C23	3.025(2)	Y2–C89	3.043(2)
Y1–C28	2.893(2)	Y2–C92	2.903(2)
Y1–C29	3.124(2)	Y2–C93	2.996(2)
Al1–C21	2.030(2)	Al2–C85	2.033(2)
Al1–C27	2.032(2)	Al2–C91	2.029(2)
Al1–C33	2.014(2)	Al2–C97	2.024(2)
Al1–B1	2.179(2)	Al2–B2	2.179(2)
C21–Al1–C27	101.51(8)	C85–Al2–C91	100.49(8)
B1–Al1–C21	121.56(8)	B2–Al2–C85	112.61(8)
B1–Al1–C27	111.90(9)	B2–Al2–C91	118.56(8)
B1–Al1–C33	109.61(8)	B2–Al2–C97	110.97(9)

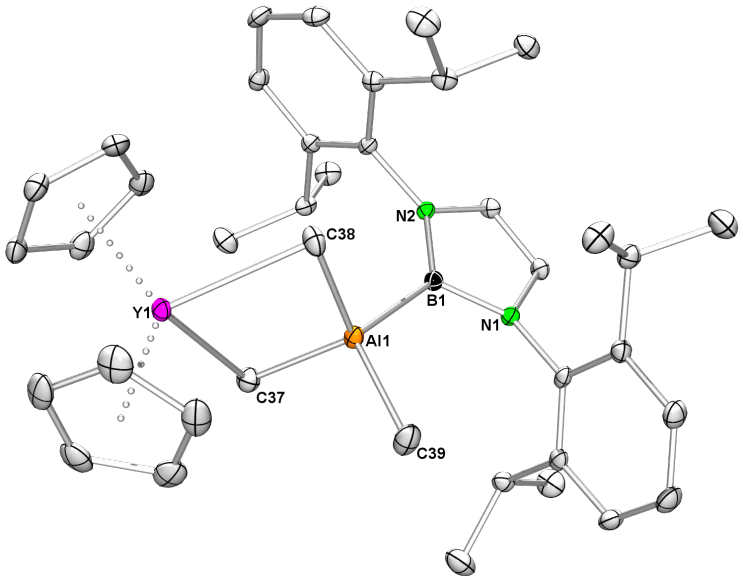

Figure S13. Crystal structure of $Cp_2Y[Me_3Al\{B(NDippCH)_2\}]$ (**11**). All atoms are represented by atomic displacement ellipsoids set at 50% probability. Hydrogen atoms and co-crystallized toluene are omitted for clarity. Selected interatomic distances [Å] and angles [°]: Y1–C37 2.584(1), Y1–C38 2.554(1), Al1–C37 2.095(1), Al1–C38 2.092(2), Al1–C39 1.981(1), Al1–B1 2.147(1); Y1–C37–Al1 81.21(5), Y1–C38–Al1 82.98(5), C37–Al1–C38 109.60(6), B1–Al1–C37 106.14(5), B1–Al1–C38 109.50(6), B1–Al1–C39 114.36(6).

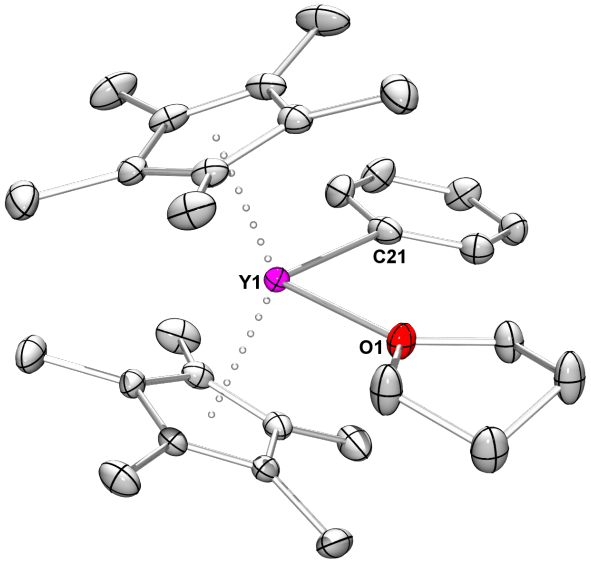

Figure S14. Crystal structure of $Cp^*_2YPh(THF)$ (**13**). All atoms are represented by atomic displacement ellipsoids set at 50% probability. Hydrogen atoms are omitted for clarity. Selected interatomic distances [Å] and angles [°]: Y1–O1 2.391(1), Y1–C21 2.464(2); C21–Y1–O1 96.72(5).

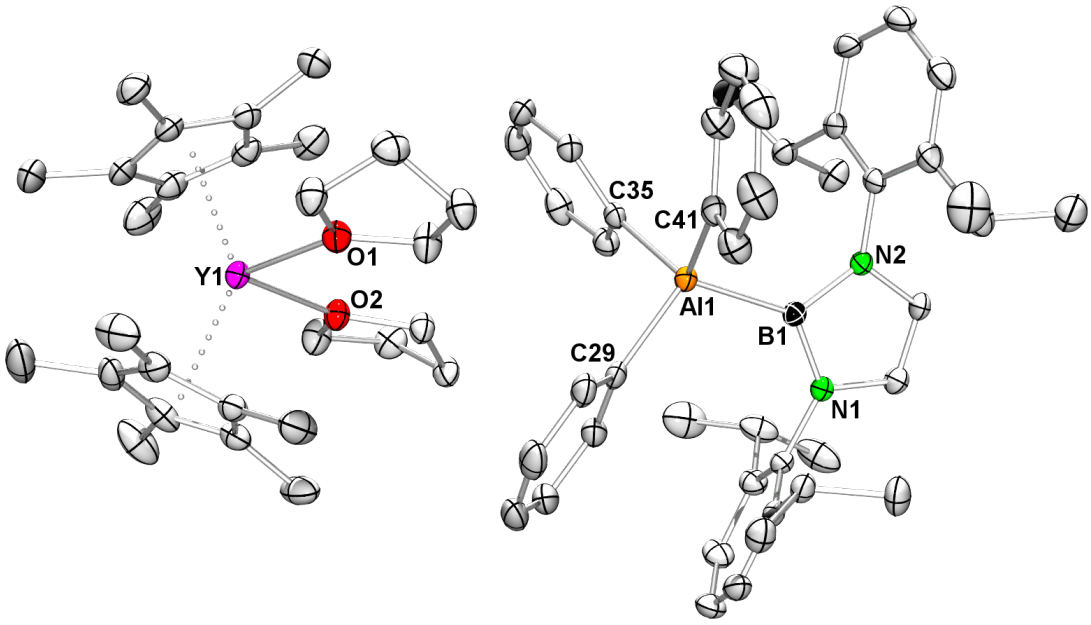

Figure S15. Crystal structure of $[Cp^*_2Y(THF)_2][AlPh_3\{B(NDippCH)_2\}]$ (**15**). All atoms are represented by atomic displacement ellipsoids set at 50% probability. Hydrogen atoms and co-crystallized *n*-pentane are omitted for clarity. Selected interatomic distances [Å] and angles [°]: Y1–O1 2.388(3), Y1–O2 2.359(3), Al1–C29 2.036(2), Al1–C35 2.039(3), Al1–C41 2.027(3), Al1–B1 2.181(3); C29–Al1–C35 104.3(1), B1–Al1–C29 113.3(1), B1–Al1–C35 110.8(1), B1–Al1–C41 110.0(1).

Crystallographic Data

Table S3. Crystallographic data of complexes $\mathbf{1^{Al}_D}$, $\mathbf{2^{Al}_D}$, $\mathbf{3^{Al}_D}$, and $\mathbf{4^{Al}}$

	$\mathbf{1^{Al}_D}$	$\mathbf{2^{Al}_D}$	$\mathbf{3^{Al}_D}$	$\mathbf{4^{Al}}$
CCDC	2093598	2093601	2093600	2093607
Formula	$C_{48}H_{84}Al_2Y_2$	$C_{58}H_{88}Al_2Y_2 \cdot C_6H_6$	$C_{68}H_{72}D_{20}Al_2Y_2$	$C_{44}H_{50}AlY \cdot (C_6H_6)_{0.5}$
M_r [g mol^{-1}]	892.93	1126.20	1161.31	733.78
cryst syst	triclinic	triclinic	monoclinic	monoclinic
space group	$P\bar{1}$	$P\bar{1}$	$P2_1/c$	$P2_1/n$
a [Å]	12.1291(8)	11.8055(5)	12.340(6)	14.0698(3)
b [Å]	12.2983(9)	12.6143(5)	26.476(13)	15.4604(3)
c [Å]	17.2484(12)	12.8998(5)	18.992(9)	18.2533(4)
α [°]	102.908(2)	67.7380(10)	90	90
β [°]	98.081(2)	63.8330(10)	98.973(7)	101.3120(10)
γ [°]	90.174(2)	81.227(2)	90	90
V [Å^3]	2481.4(3)	1595.38(11)	6129(5)	3893.41(14)
Z	2	1	4	4
T [K]	180(2)	180(2)	150(2)	100(2)
ρ_{calcd} [g cm^{-3}]	1.195	1.172	1.259	1.252
μ [mm^{-1}]	2.391	1.873	1.951	1.552
F (000)	952	598	2416	1548
Data/param/rest	11980/519/0	7094/559/2247	13364/717/0	9268/452/0
R1/*w*R2 (I>2σ)[a]	0.0466/0.0879	0.0426/0.1008	0.0440/0.0835	0.0260/0.0607
R1/*w*R2 (all data)[a]	0.0678/0.0938	0.0642/0.1091	0.0832/0.0955	0.0345/0.0639
GOF[a]	1.046	1.101	1.018	1.032

[a] $R1 = \Sigma(||F_0|-|F_c||)/\Sigma|F_0|$, $F_0 > 4\sigma(F_0)$. $wR2 = \{\Sigma[w(F_0^2-F_c^2)^2/\Sigma[w(F_0^2)^2]\}^{1/2}$.

Table S4. Crystallographic data of complexes $\mathbf{2^{Ga}_D}$, $\mathbf{3^{Ga}_D}$, and $\mathbf{4^{Ga}}$

	$\mathbf{2^{Ga}_D}$	$\mathbf{3^{Ga}_D}$	$\mathbf{4^{Ga}}$
CCDC	2093603	2093605	2093604
Formula	$C_{63}H_{90}Ga_2Y_2 \cdot C_6H_6$	$C_{68}H_{72}D_{20}Ga_2Y_2$	$C_{44}H_{30}D_{20}GaY \cdot (C_6D_6)_{0.5}$
M_r [g mol^{-1}]	1242.71	1246.79	799.66
cryst syst	triclinic	monoclinic	monoclinic
space group	$P\bar{1}$	$P2_1/c$	$P2_1/n$
a [Å]	11.7229(5)	12.3220(11)	14.1131(9)
b [Å]	12.5458(5)	26.467(2)	15.4344(10)
c [Å]	12.8342(5)	18.9958(17)	18.2425(12)
α [°]	67.9410(10)	90	90
β [°]	64.0690(10)	99.064(2)	101.5890(10)
γ [°]	81.5240(10)	90	90
V [Å^3]	1572.95(11)	6117.6(9)	3892.7(4)
Z	1	4	4
T [K]	173(2)	150(2)	100(2)
ρ_{calcd} [g cm^{-3}]	1.312	1.354	1.364
μ [mm^{-1}]	2.712	2.788	2.207
F (000)	650	2560	1620
Data/param/rest	6940/559/2249	12507/733/3	9659/480/106
R1/wR2 (I>2σ)[a]	0.0395/0.0937	0.0366/0.0690	0.0279/0.0600
R1/wR2 (all data)[a]	0.0470/0.0970	0.0721/0.0803	0.0396/0.0639
GOF[a]	1.138	1.033	1.022

[a] $R1 = \Sigma(||F_0|-|F_c||)/\Sigma|F_0|$, $F_0 > 4\sigma(F_0)$. $wR2 = \{\Sigma[w(F_0^2-F_c^2)^2/\Sigma[w(F_0^2)^2]\}^{1/2}$.

Table S5. Crystallographic data of complexes **6**, **7**, **8**, and **9**

	6	**7**	**8**	**9**
CCDC	2093599		2093602	2093611
Formula	$C_{49}H_{75}N_2BAlY$	$C_{29}H_{45}N_2BAlK$	$C_{37}H_{61}O_2N_2BAlK$	$C_{54}H_{77}N_2BAlY$
M_r [g mol^{-1}]	818.81	498.58	642.76	880.87
cryst syst	triclinic	triclinic	monoclinic	monoclinic
space group	$P\bar{1}$	$P\bar{1}$	$P2_1/c$	$P2_1/n$
a [Å]	10.7284(3)	12.5115(37)	13.2538(6)	11.0256(4)
b [Å]	13.8937(3)	15.5048(43)	14.9214(7)	23.4038(9)
c [Å]	16.1669(4)	18.5960(57)	20.5957(10)	21.3880(9)
α [°]	80.5380(10)	104.658(7)	90	90
β [°]	86.4220(10)	106.136(7)	106.667(3)	95.386(2)
γ [°]	76.8690(10)	106.023(6)	90	90
V [Å^3]	2314.07(10)		3902.0(3)	5494.6(4)
Z	2		4	4
T [K]	173(2)		173(2)	130(2)
ρ_{calcd} [g cm^{-3}]	1.175		1.094	1.065
μ [mm^{-1}]	1.312		0.190	1.110
F (000)	880		1400	1888
Data/param/rest	10582/530/0		8010/425/0	12108/575/0
R1/*w*R2 (I>2σ)[a]	0.0265/0.0641		0.0674/0.1355	0.0354/0.0818
R1/*w*R2 (all data)[a]	0.0314/0.0661		0.1158/0.1588	0.0548/0.0882
GOF[a]	1.032		1.018	1.028

[a] $R1 = \Sigma(||F_0|-|F_c||)/\Sigma|F_0|$, $F_0 > 4\sigma(F_0)$. $wR2 = \{\Sigma[w(F_0^2-F_c^2)^2/\Sigma[w(F_0^2)^2]\}^{1/2}$.

Table S6. Crystallographic data of complexes **10**, **11**, **13**, and **15**

	10	**11**	**13**	**15**
CCDC	2093608	2093606	2093610	2093609
Formula	$C_{64}H_{66}D_{15}N_2BAlY\cdot(C_6D_6)_{0.5}$	$C_{39}H_{55}AlBN_2Y\cdot C_7H_8$	$C_{30}H_{43}OY$	$C_{72}H_{97}O_2N_2BAlY\cdot(C_5H_{12})_2$
M_r [g mol^{-1}]	1062.17	770.68	508.55	1293.50
cryst syst	monoclinic	triclinic	monoclinic	triclinic
space group	$P2_1/c$	$P\bar{1}$	$P2_1/c$	$P\bar{1}$
a [Å]	14.6405(3)	10.2691(2)	9.4293(4)	15.981(15)
b [Å]	37.6604(8)	11.6747(3)	17.1736(8)	16.363(17)
c [Å]	21.2051(5)	19.3277(4)	16.8407(8)	17.003(15)
α [°]	90	74.8594(10)	90	86.73(4)
β [°]	95.8740(10)	85.4672(11)	102.8110(10)	62.36(2)
γ [°]	90	69.6399(11)	90	74.19(3)
V [Å^3]	11630.4(4)	2096.82(8)	2659.2(2)	3777(6)
Z	8	2	4	2
T [K]	100(2)	100(2)	100(2)	100(2)
ρ_{calcd} [g cm^{-3}]	1.213	1.221	1.270	1.137
μ [mm^{-1}]	1.059	1.444	2.212	0.829
F (000)	4456	820	1080	1400
Data/param/rest	28864/1333/0	10411/494/0	7155/299/0	18013/824/21
R1/*w*R2 (I>2σ)[a]	0.0428/0.0851	0.0266/0.0637	0.0289/0.0659	0.0440/0.1088
R1/*w*R2 (all data)[a]	0.0788/0.0955	0.0311/0.0653	0.0407/0.0697	0.0613/0.1181
GOF[a]	1.016	1.032	1.048	1.025

[a] $R1 = \Sigma(||F_0|-|F_c||)/\Sigma|F_0|$, $F_0 > 4\sigma(F_0)$. $wR2 = \{\Sigma[w(F_0^2-F_c^2)^2/\Sigma[w(F_0^2)^2]\}^{1/2}$.

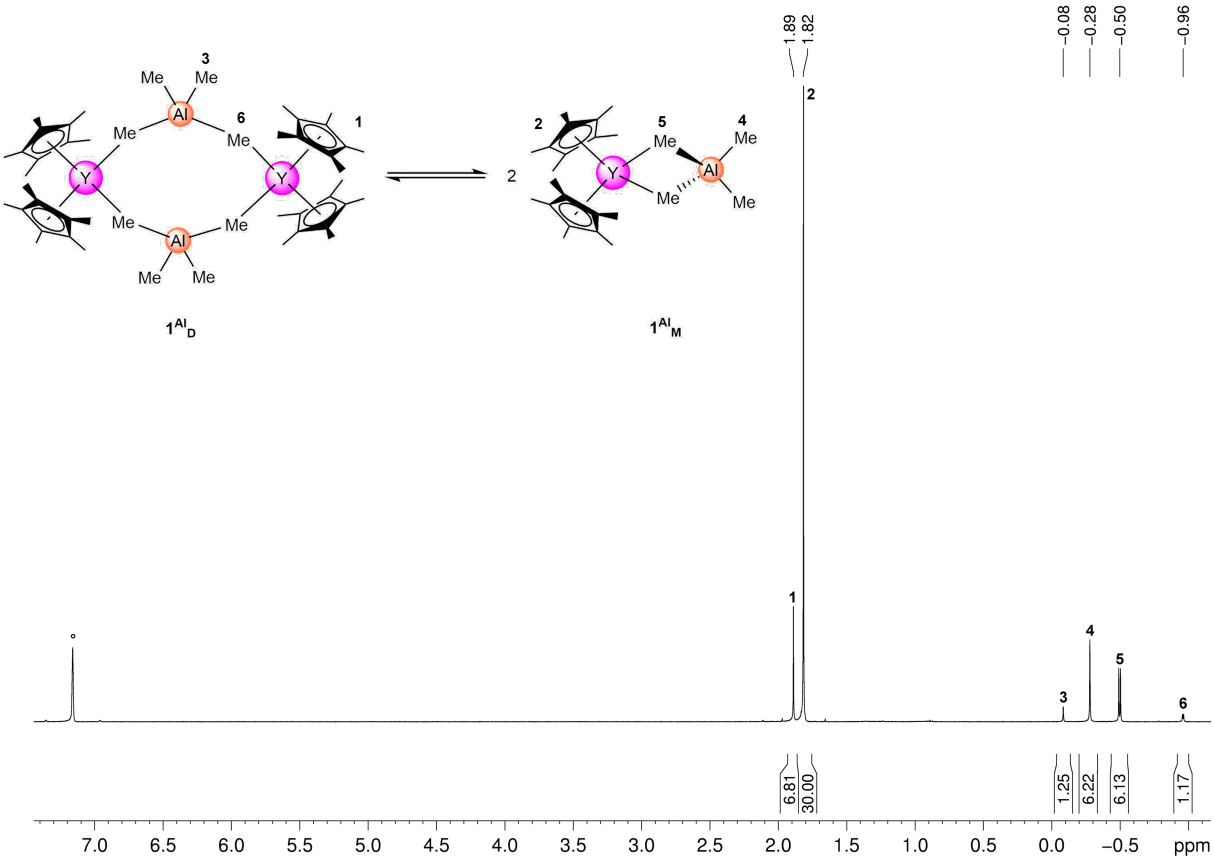

Figure S16. ^{1}H NMR spectrum (400 MHz) of $\mathbf{1^{Al}}$ in C_6D_6 (°) at 26 °C.

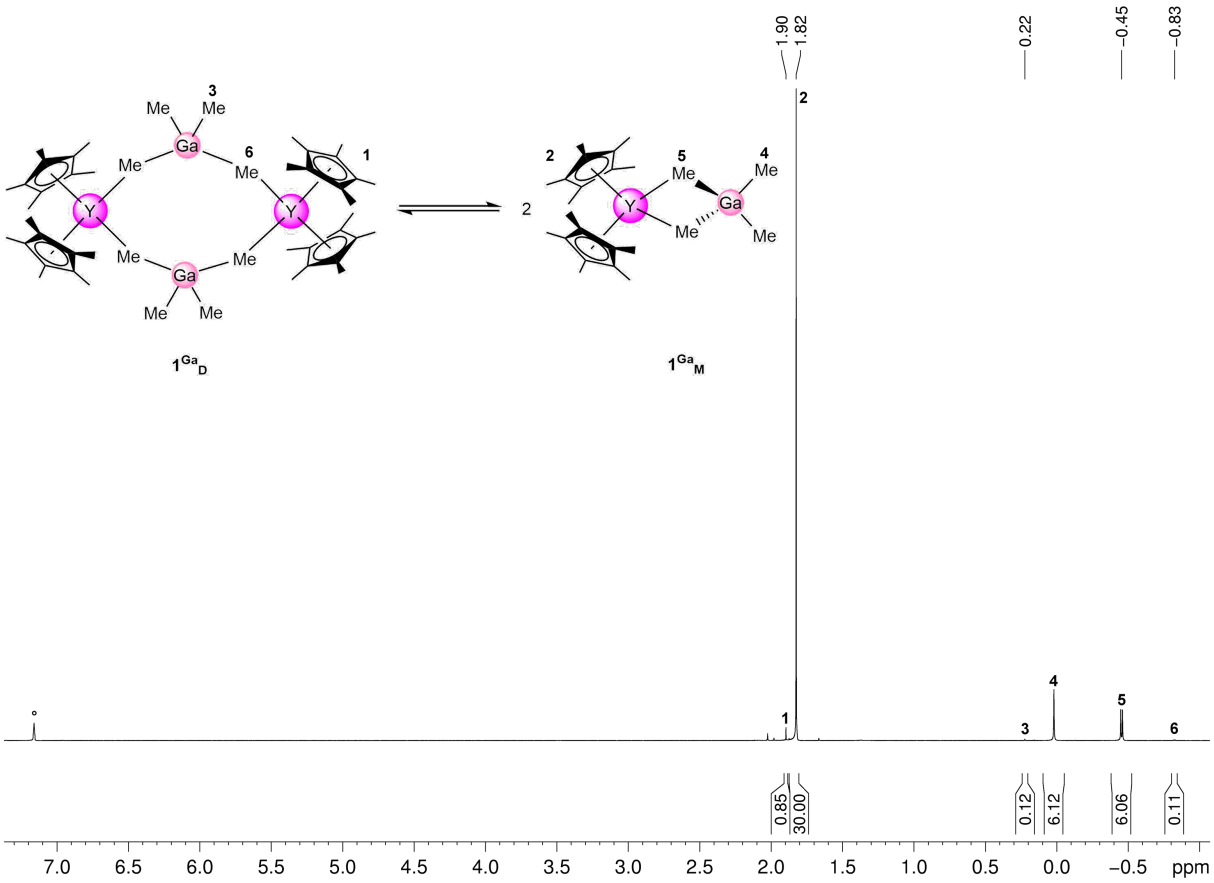

Figure S17. ^{1}H NMR spectrum (400 MHz) of $\mathbf{1^{Ga}}$ in C_6D_6 (°) at 26 °C.

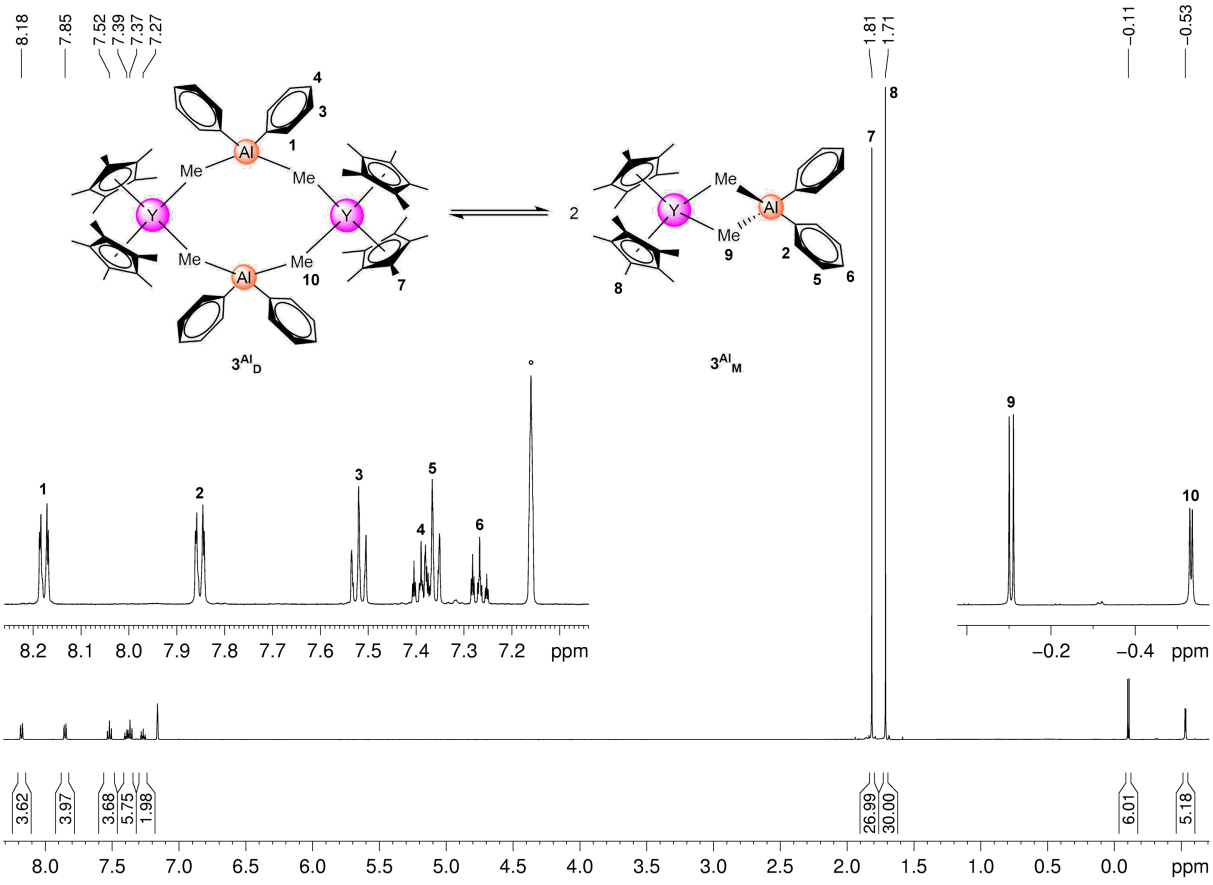

Figure S18. ^{1}H NMR spectrum (500 MHz) of $\mathbf{3^{Al}}$ in C_6D_6 (°) at 26 °C.

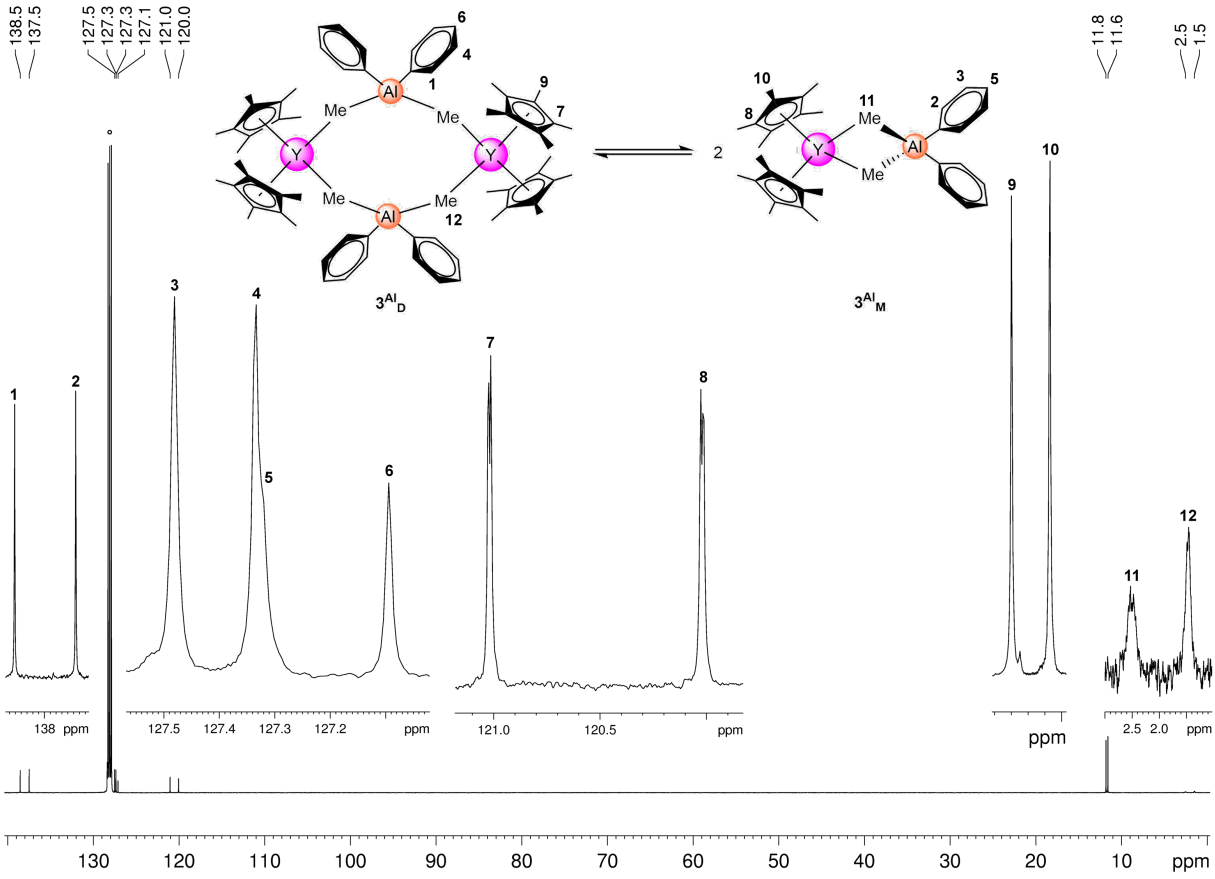

Figure S19. $^{13}C\{^{1}H\}$ NMR spectrum (126 MHz) of $\mathbf{3^{Al}}$ in C_6D_6 (°) at 26 °C.

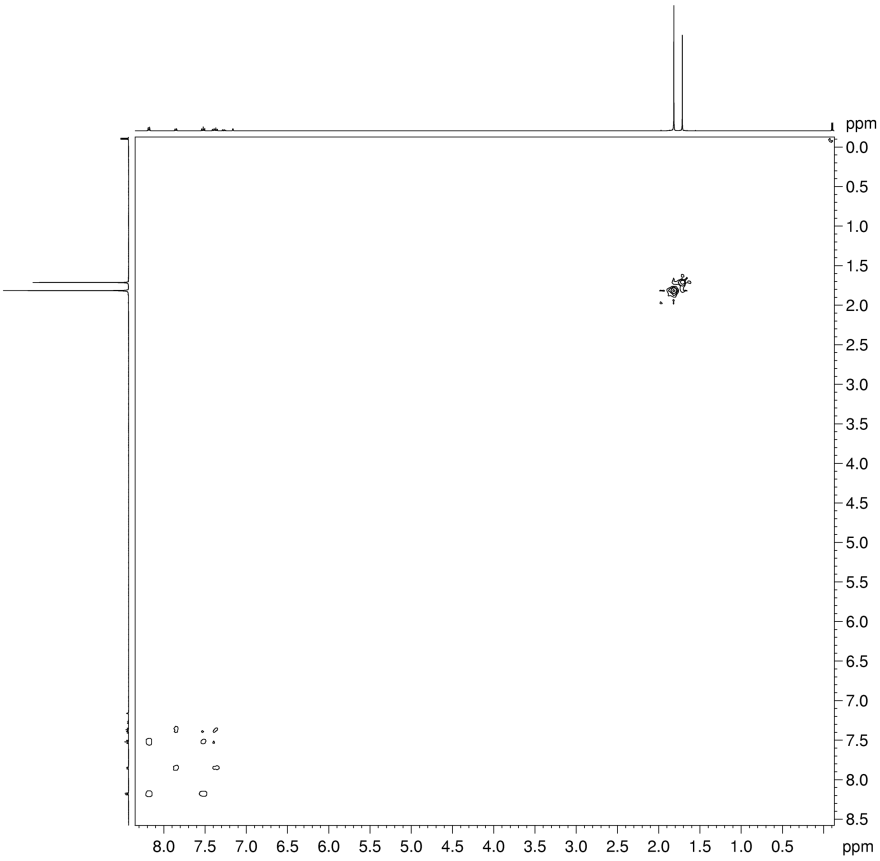

Figure S20. ^{1}H-^{1}H COSY NMR spectrum (400 MHz) of **3^{Al}** in C_6D_6 at 26 °C.

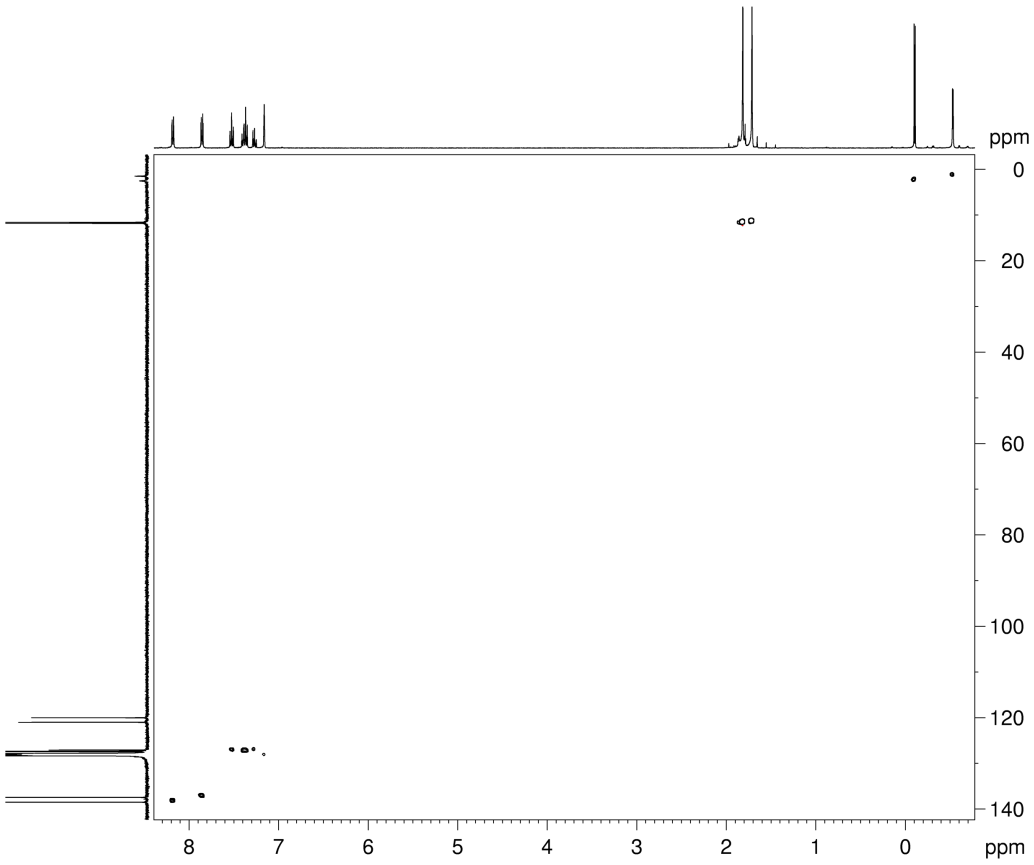

Figure S21. ^{1}H-^{13}C HSQC NMR spectrum (400 MHz, 101 MHz) of **3^{Al}** in C_6D_6 at 26 °C.

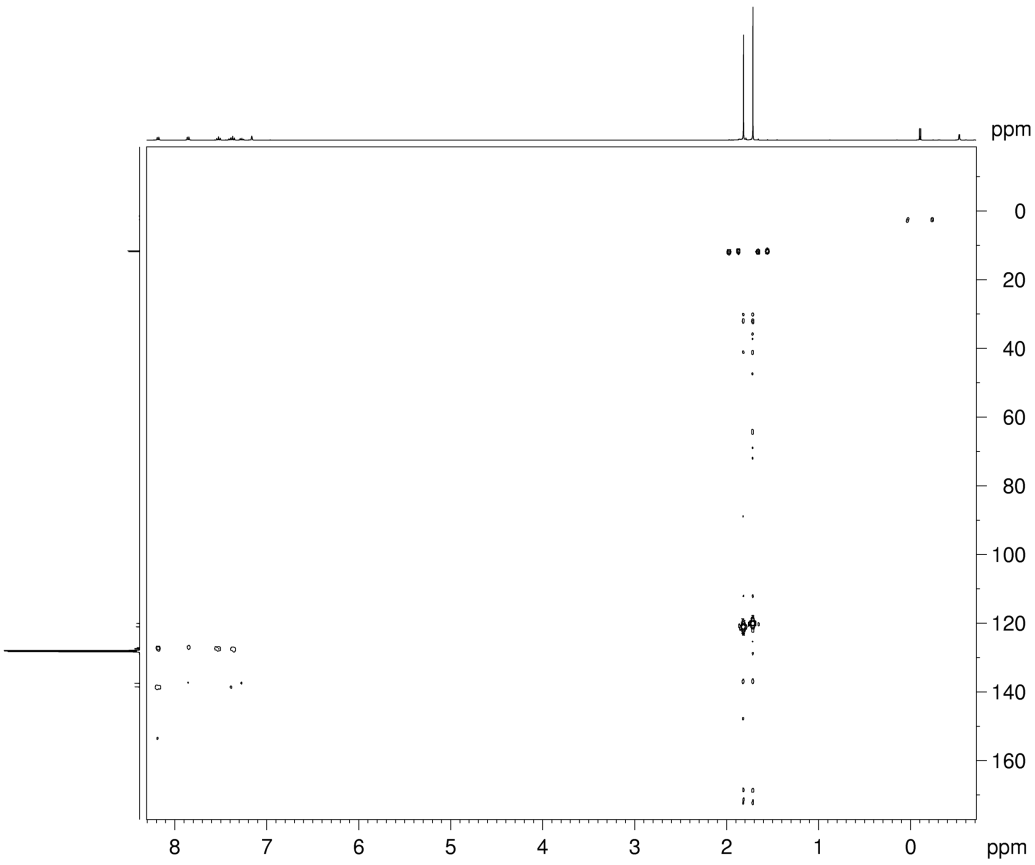

Figure S22. ^{1}H-^{13}C HMBC NMR spectrum (400 MHz, 101 MHz) of **3^{Al}** in C_6D_6 at 26 °C.

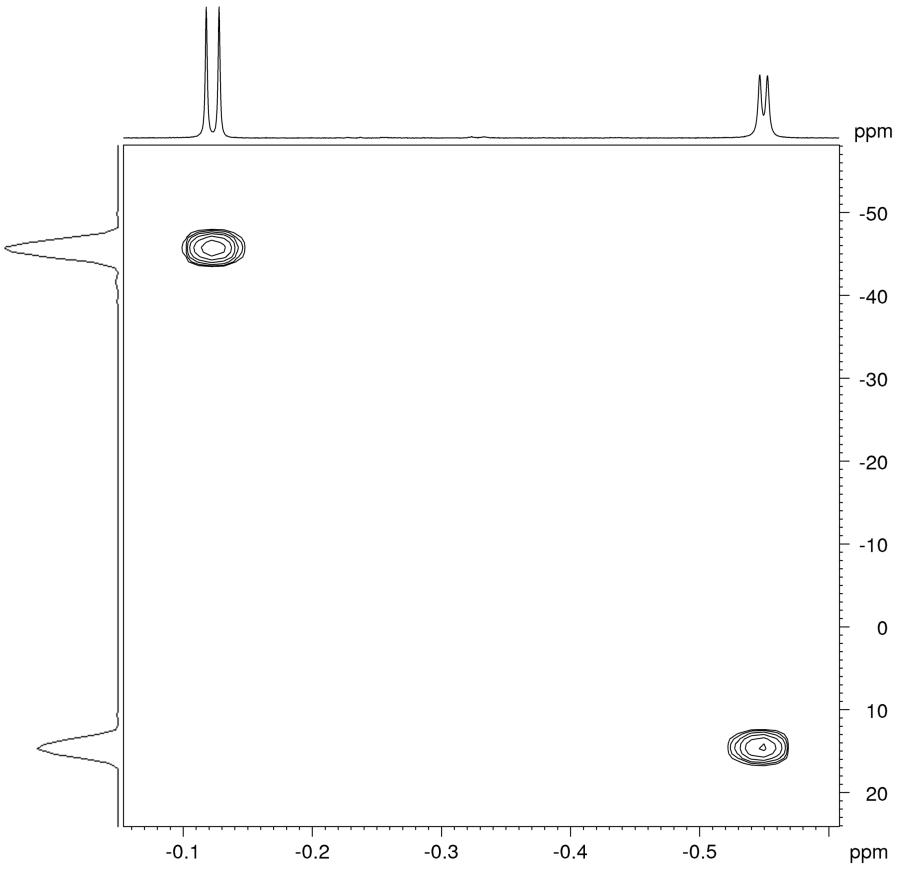

Figure S23. ^{1}H-^{89}Y HSQC NMR spectrum (500 MHz, 25 MHz) of **3^{Al}** in C_6D_6 at 26 °C.

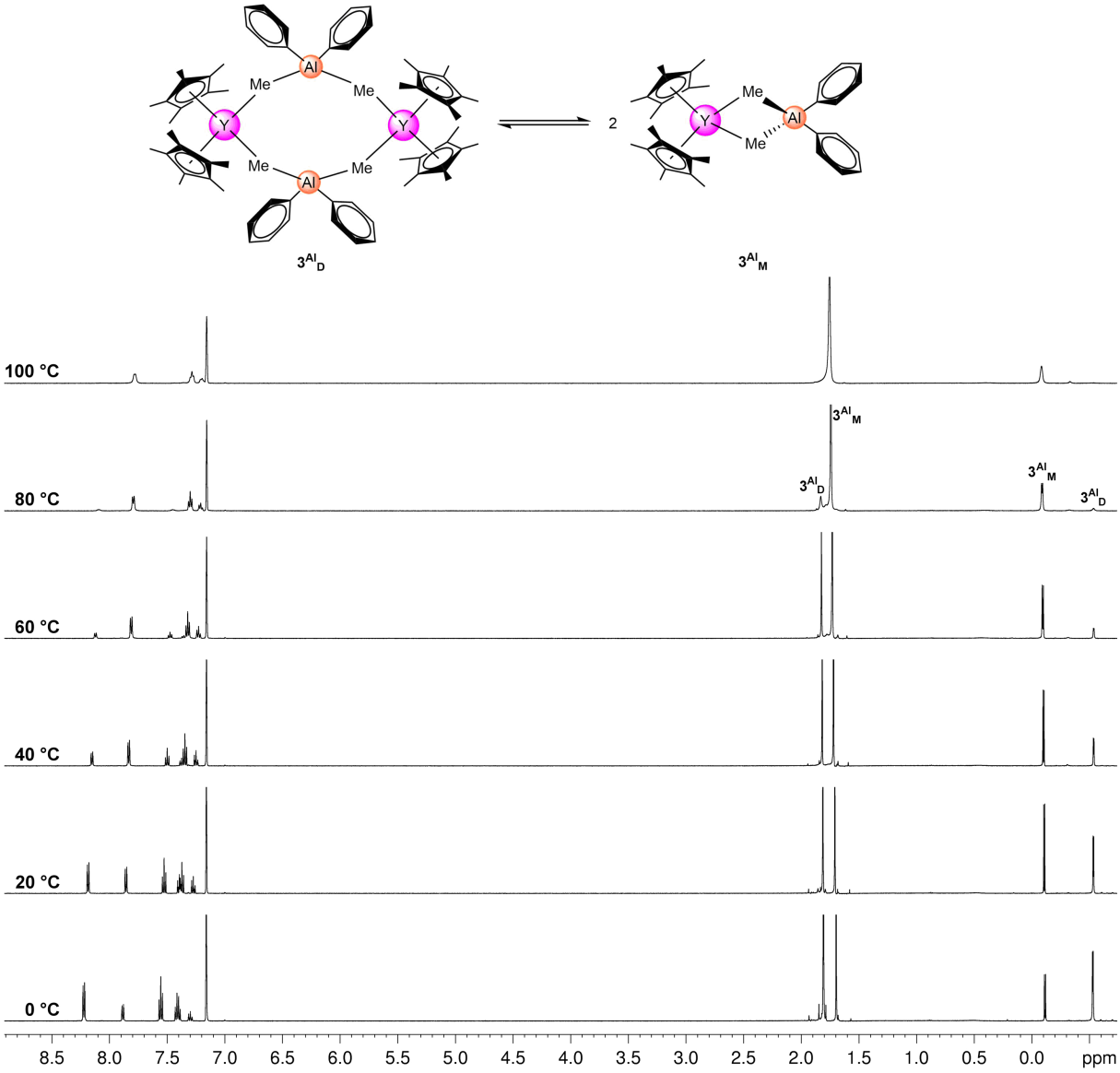

Figure S24. Variable-temperature ^{1}H NMR spectra (500 MHz) of $\mathbf{3^{Al}}$ in C_6D_6.

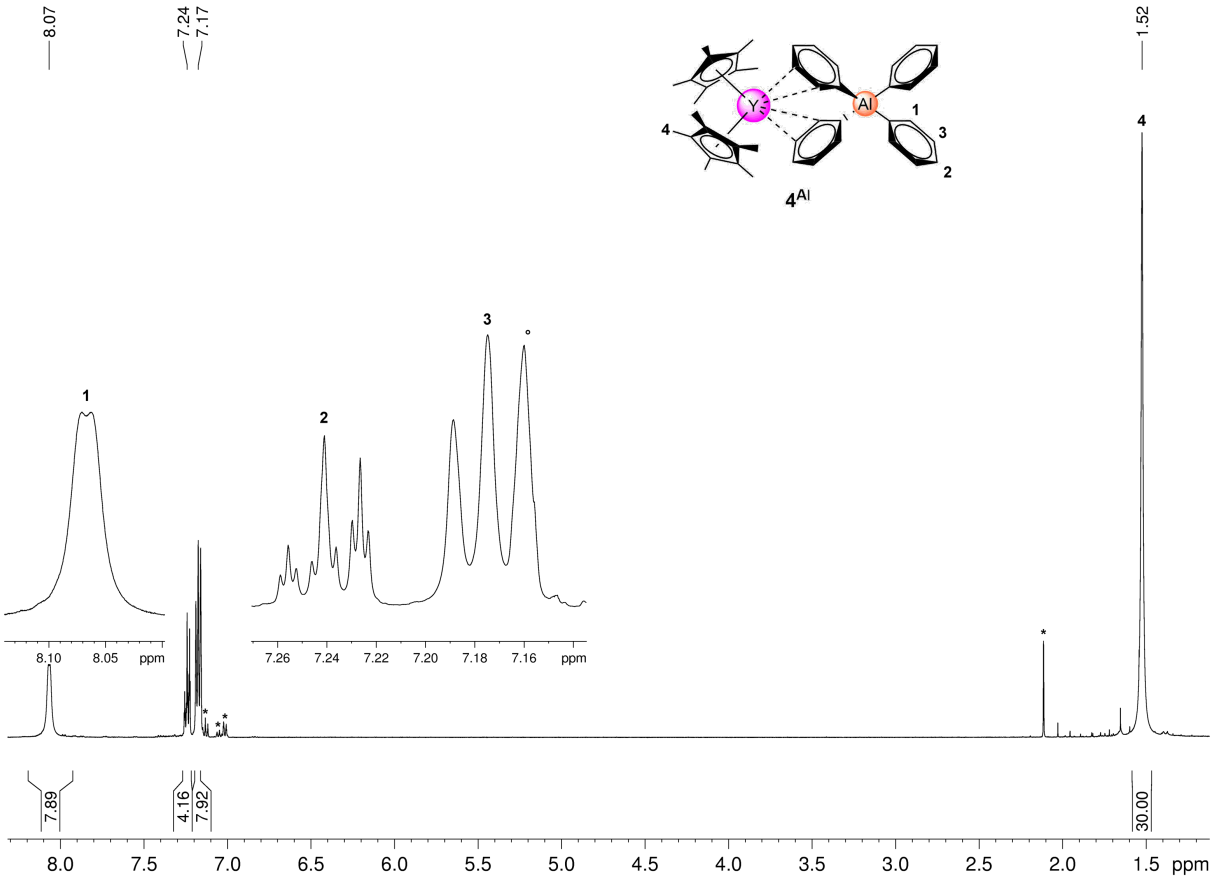

Figure S25. ^{1}H NMR spectrum (500 MHz) of **4^{Al}** in C_6D_6 (°) at 26 °C (* toluene).

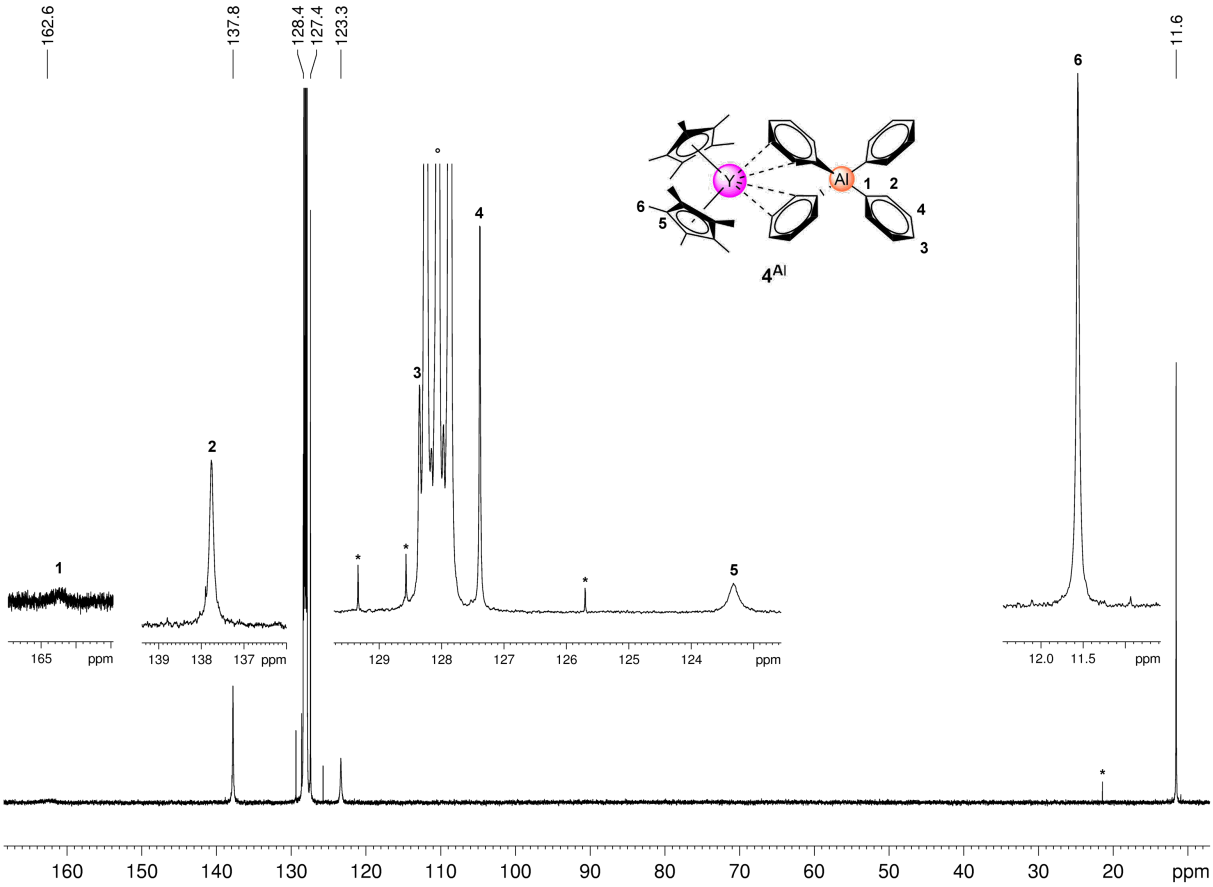

Figure S26. ^{13}C{^{1}H} NMR spectrum (126 MHz) of **4^{Al}** in C_6D_6 (°) at 26 °C (* toluene).

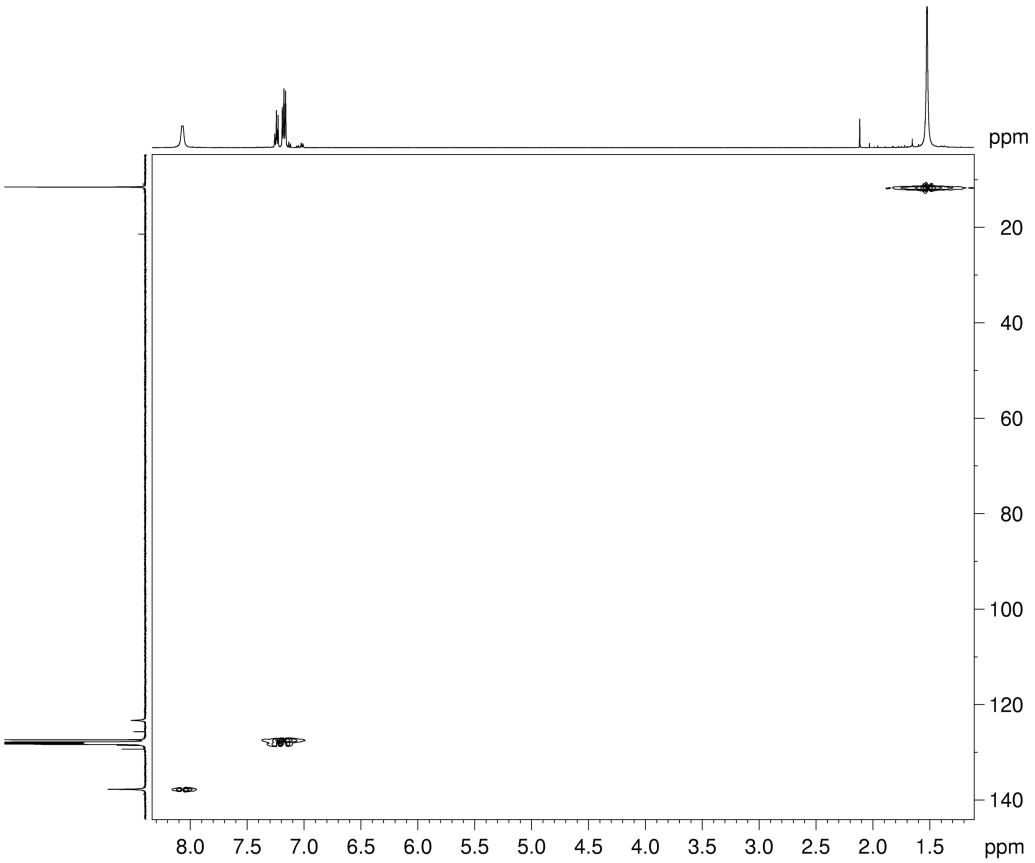

Figure S27. ^{1}H-^{13}C HSQC NMR spectrum (500 MHz, 126 MHz) of **4^{Al}** in C_6D_6 at 26 °C.

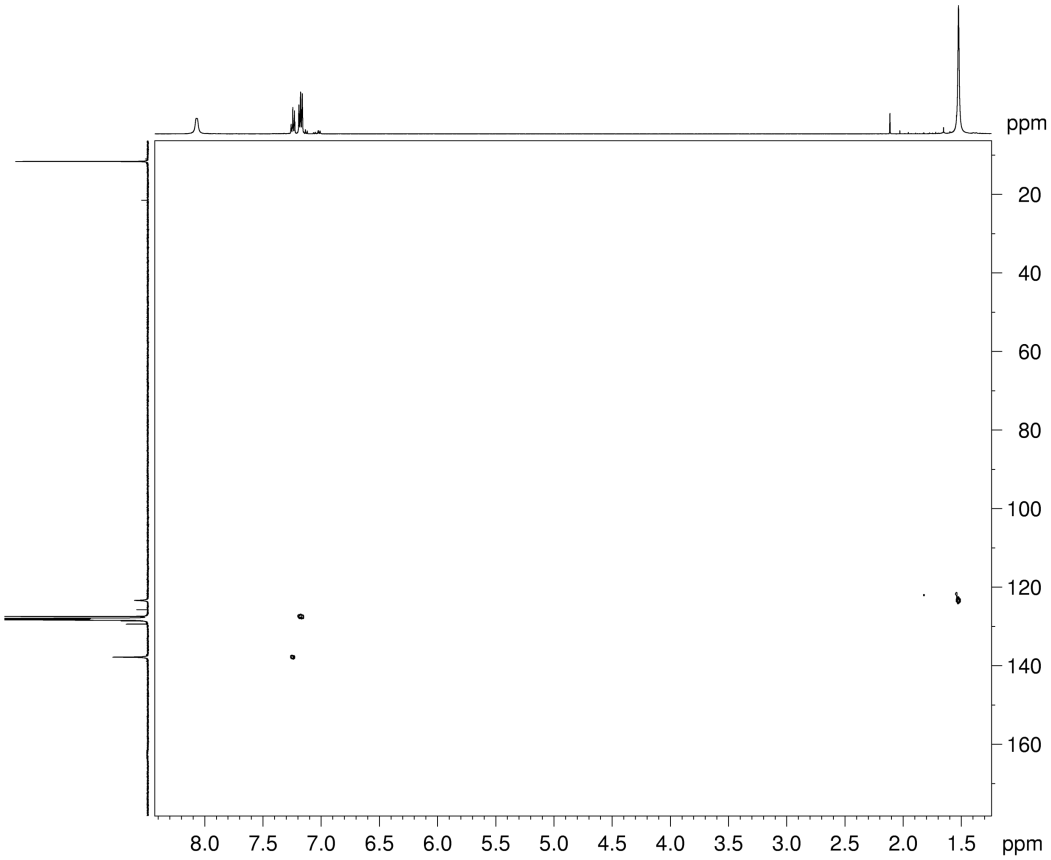

Figure S28. ^{1}H-^{13}C HMBC NMR spectrum (500 MHz, 126 MHz) of **4^{Al}** in C_6D_6 at 26 °C.

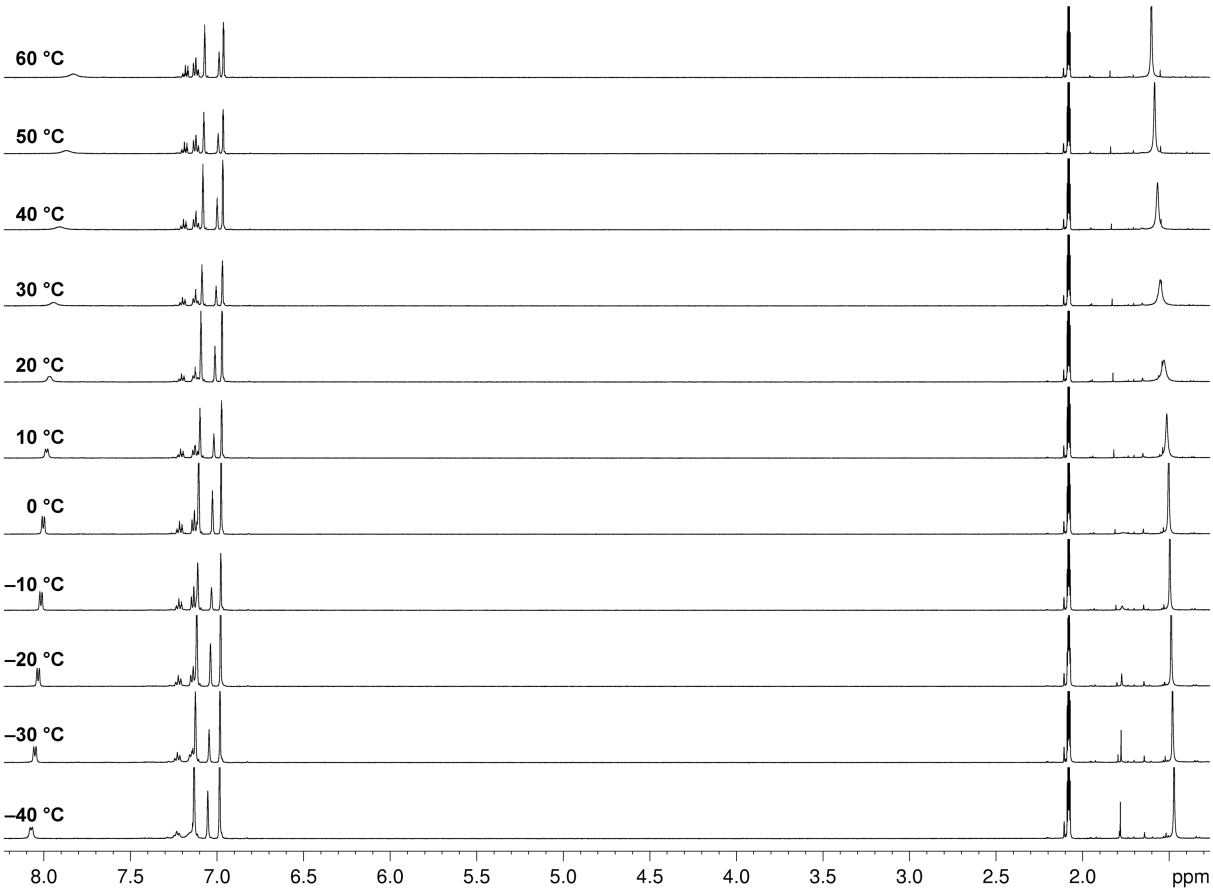

Figure S29. Variable-temperature ^{1}H NMR spectra (500 MHz) of $\mathbf{4^{Al}}$ in toluene-d_8.

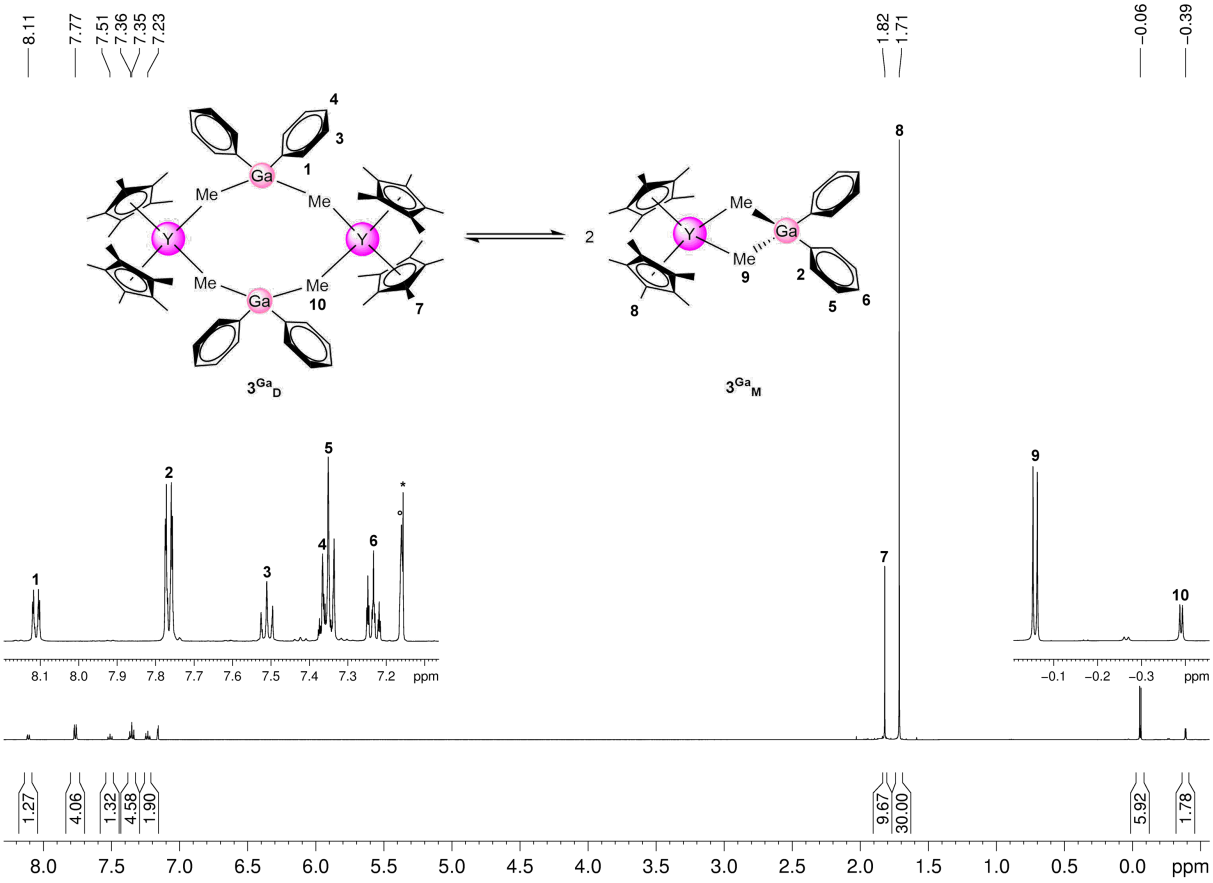

Figure S30. ^{1}H NMR spectrum (500 MHz) of $\mathbf{3^{Ga}}$ in C_6D_6 (°) at 26 °C (* benzene).

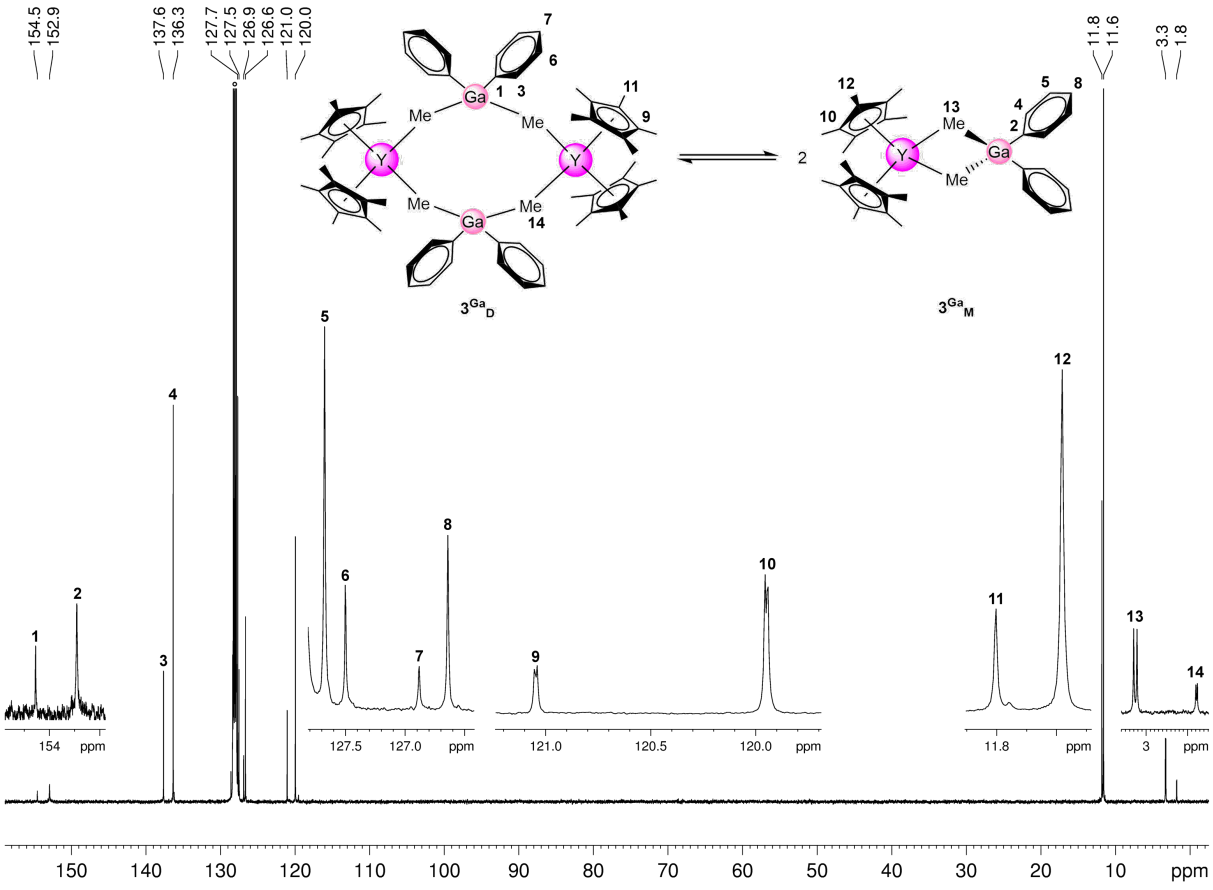

Figure S31. $^{13}C\{^{1}H\}$ NMR spectrum (126 MHz) of $\mathbf{3^{Ga}}$ in C_6D_6 (°) at 26 °C.

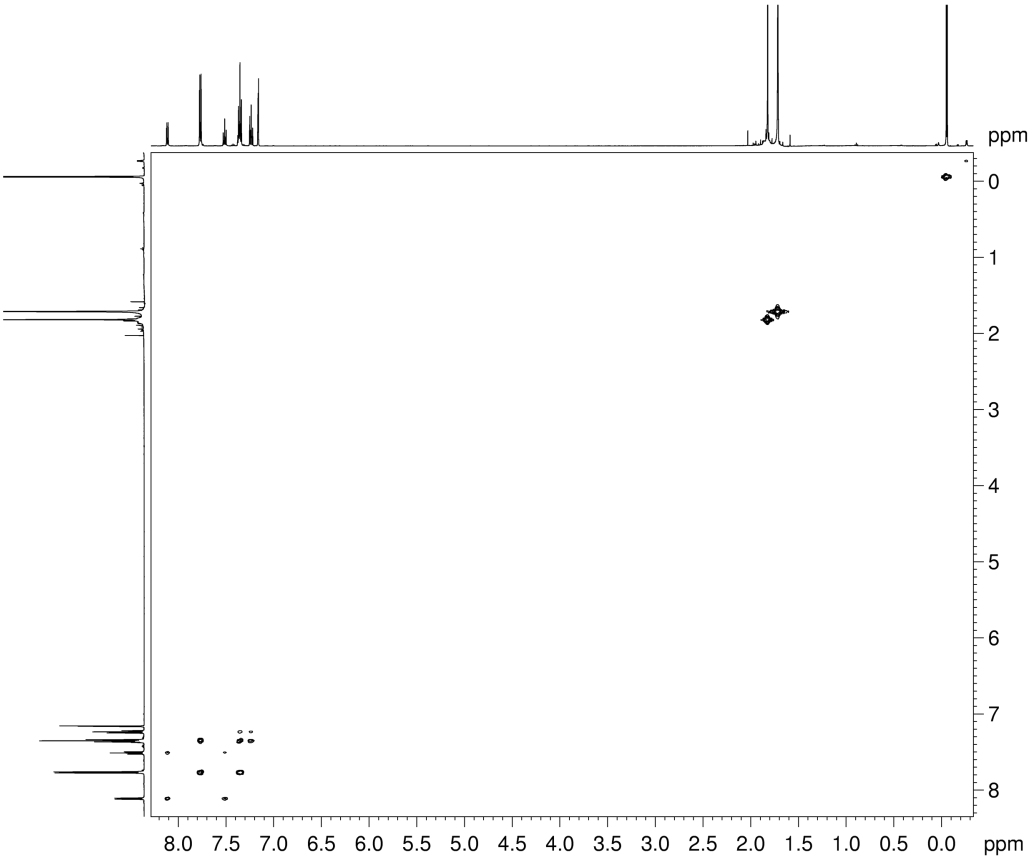

Figure S32. ^{1}H-^{1}H COSY NMR spectrum (500 MHz) of $\mathbf{3^{Ga}}$ in C_6D_6 at 26 °C.

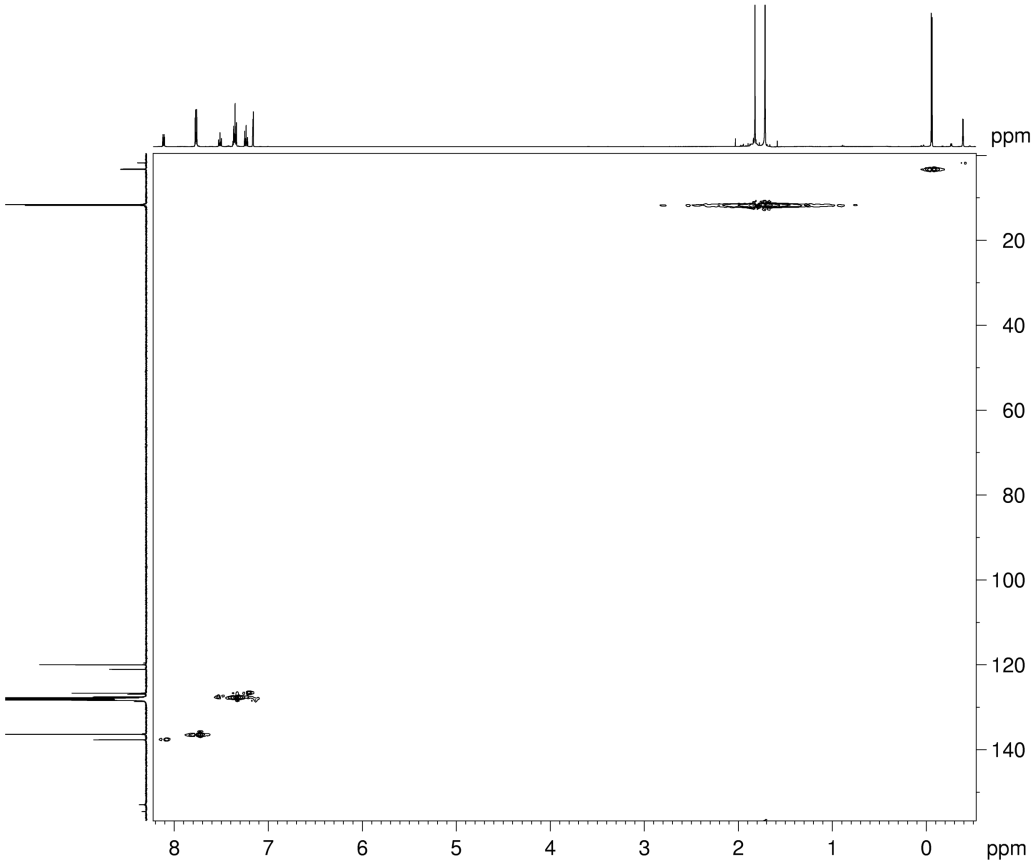

Figure S33. ^{1}H-^{13}C HSQC NMR spectrum (500 MHz, 126 MHz) of **3^{Ga}** in C_6D_6 at 26 °C.

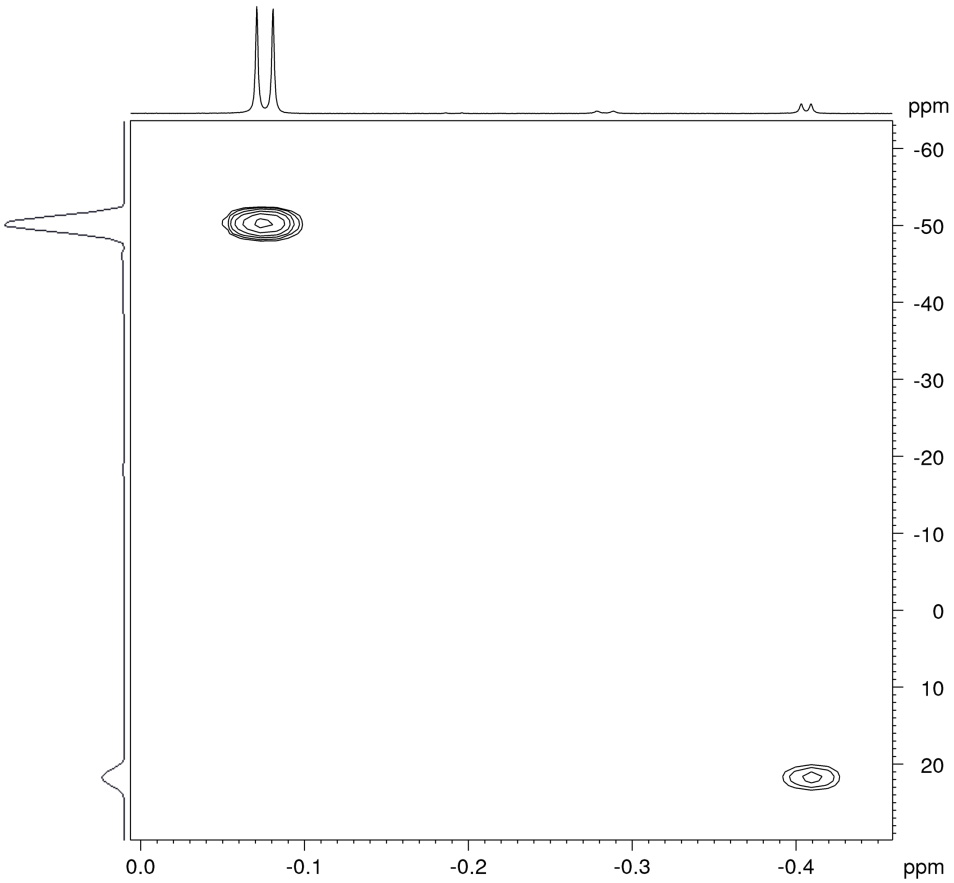

Figure S34. ^{1}H-^{89}Y HSQC NMR spectrum (500 MHz, 25 MHz) of **3^{Ga}** in C_6D_6 at 26 °C.

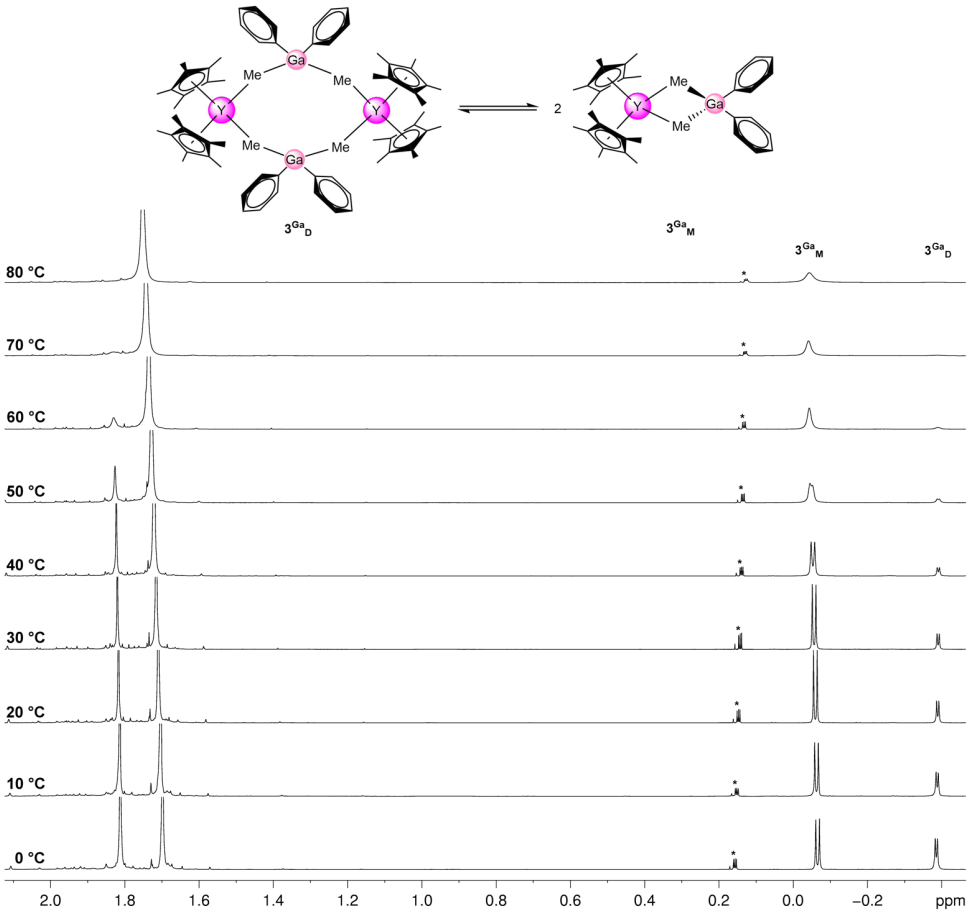

Figure S35. Variable-temperature ^{1}H NMR spectra (500 MHz) of $\mathbf{3^{Ga}}$ in C_6D_6 (* CH_4/CDH_3).

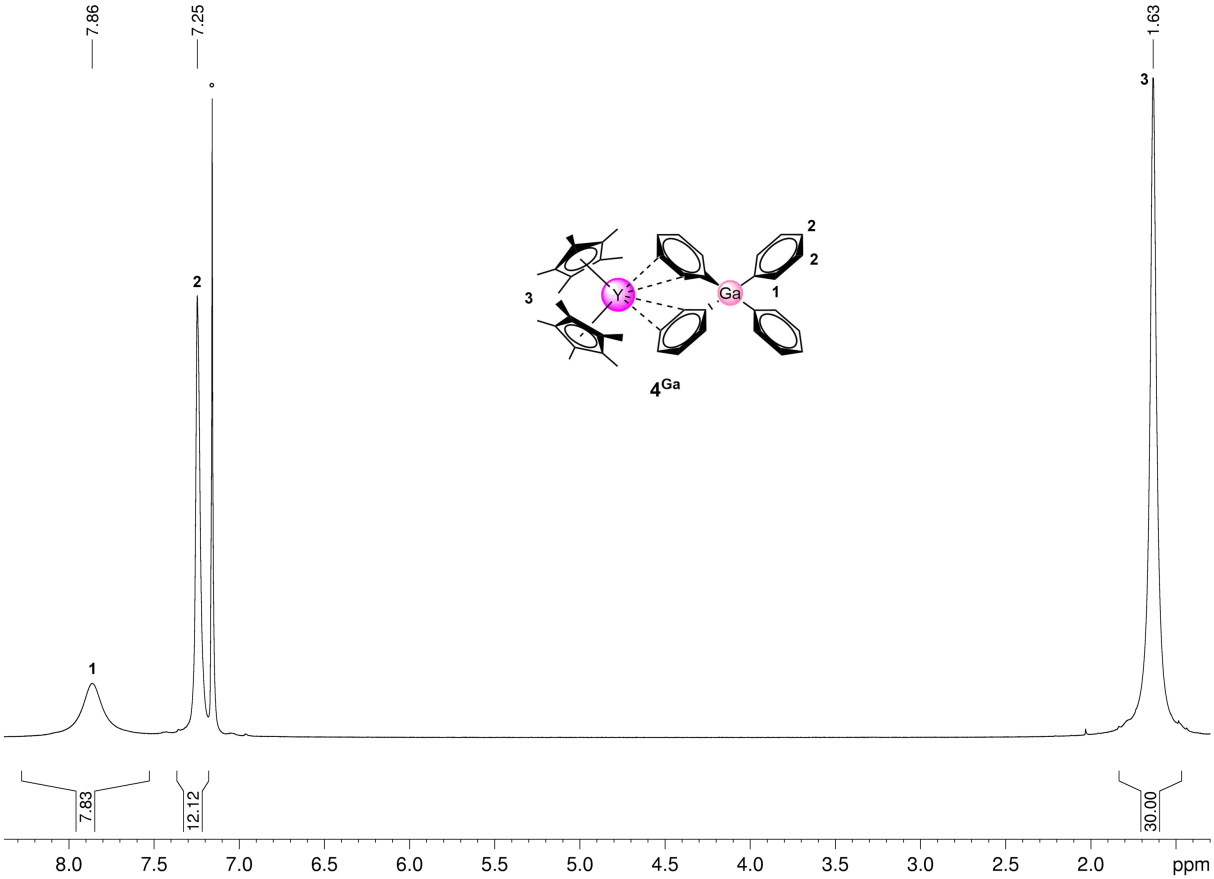

Figure S36. ^{1}H NMR spectrum (400 MHz) of $\mathbf{4^{Ga}}$ in C_6D_6 (°) at 26 °C.

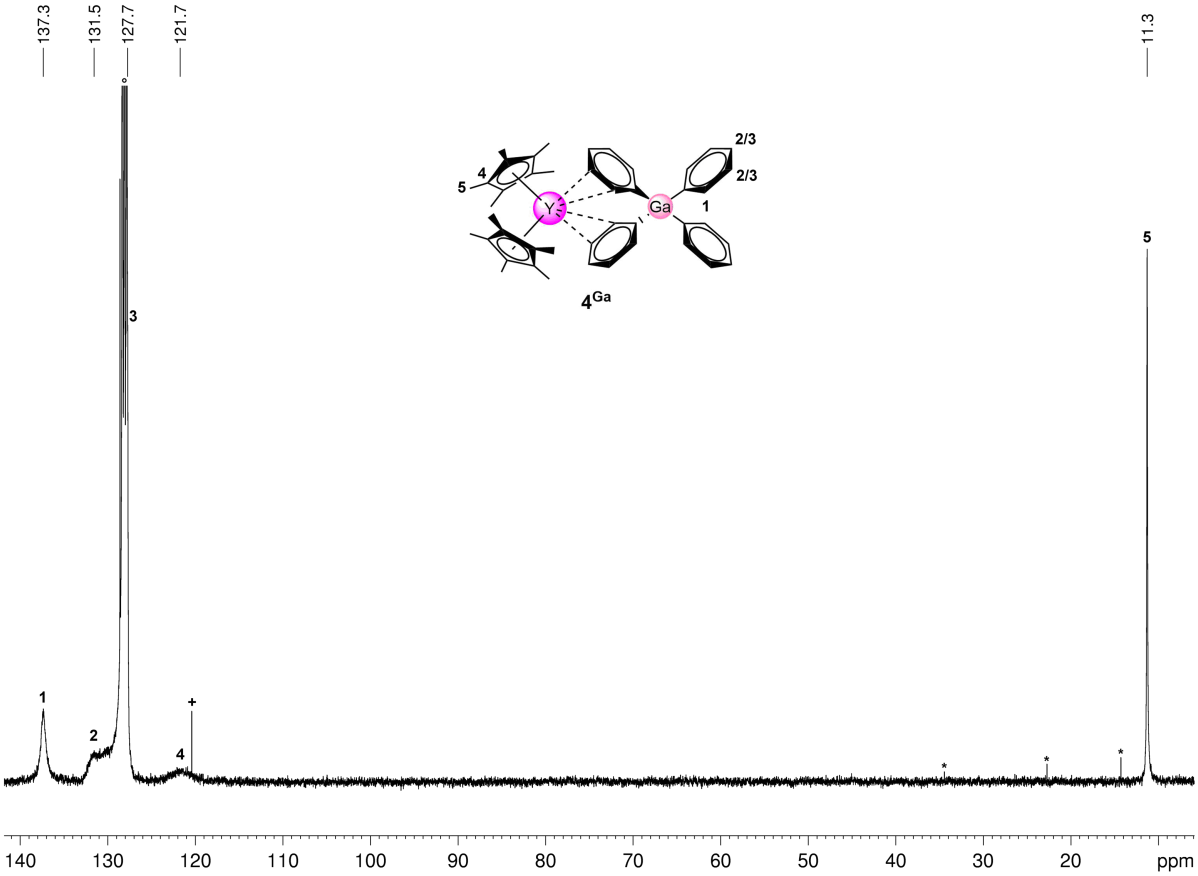

Figure S37. $^{13}C\{^{1}H\}$ NMR spectrum (400 MHz) of $\mathbf{4^{Ga}}$ in toluene-d_8 (°) at 26 °C (* *n*-pentane; + minor side product).

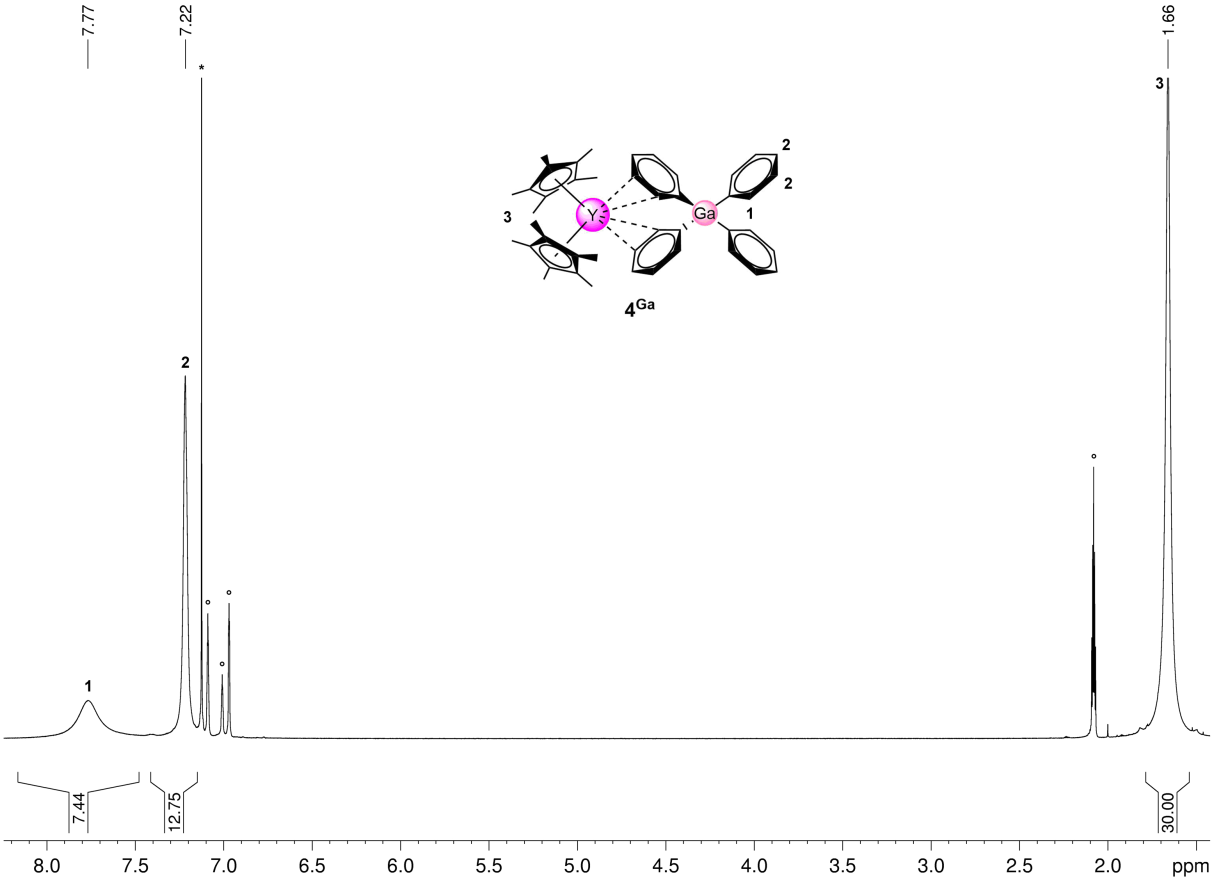

Figure S38. ^{1}H NMR spectrum (400 MHz) of $\mathbf{4^{Ga}}$ in toluene-d_8 (°) at 26 °C (* benzene).

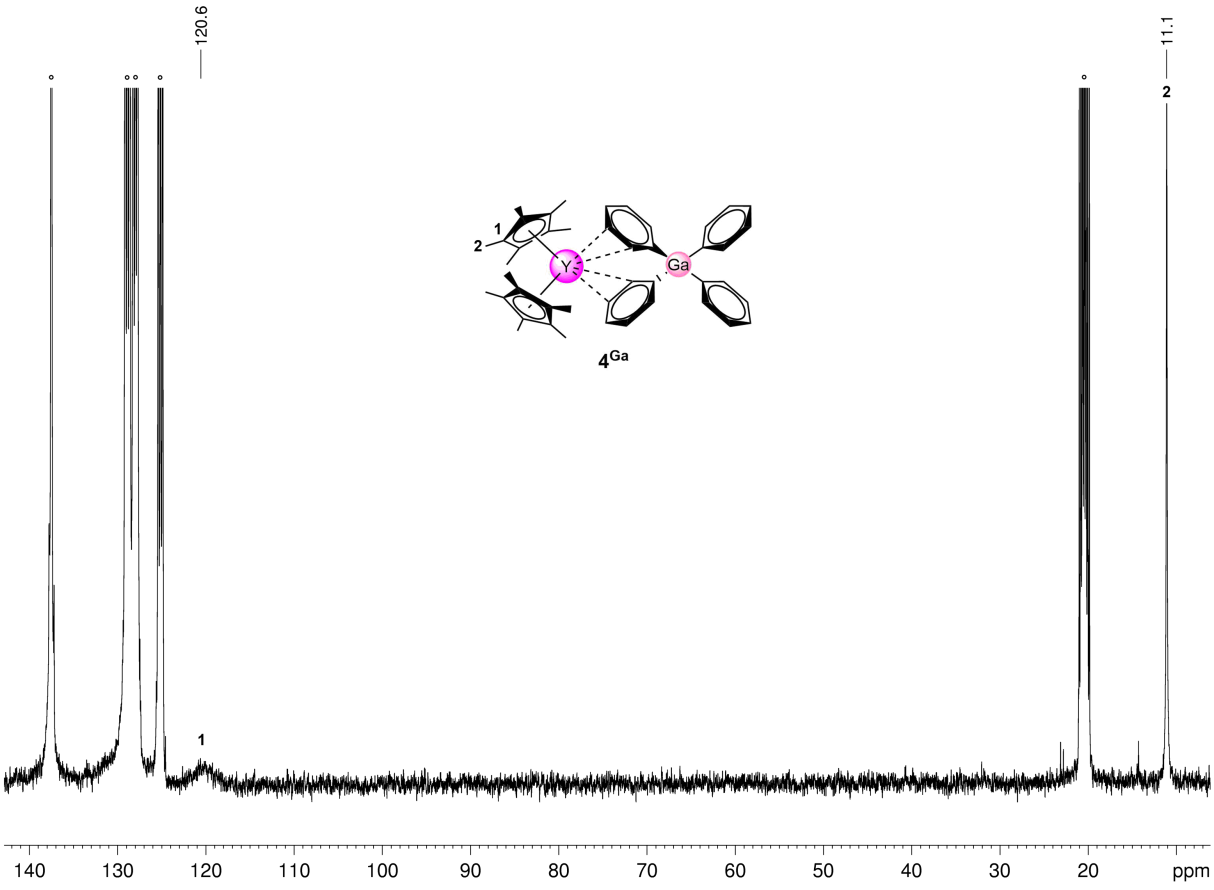

Figure S39. $^{13}C\{^{1}H\}$ NMR spectrum (101 MHz) of $\mathbf{4^{Ga}}$ in toluene-d_8 (°) at 26 °C.

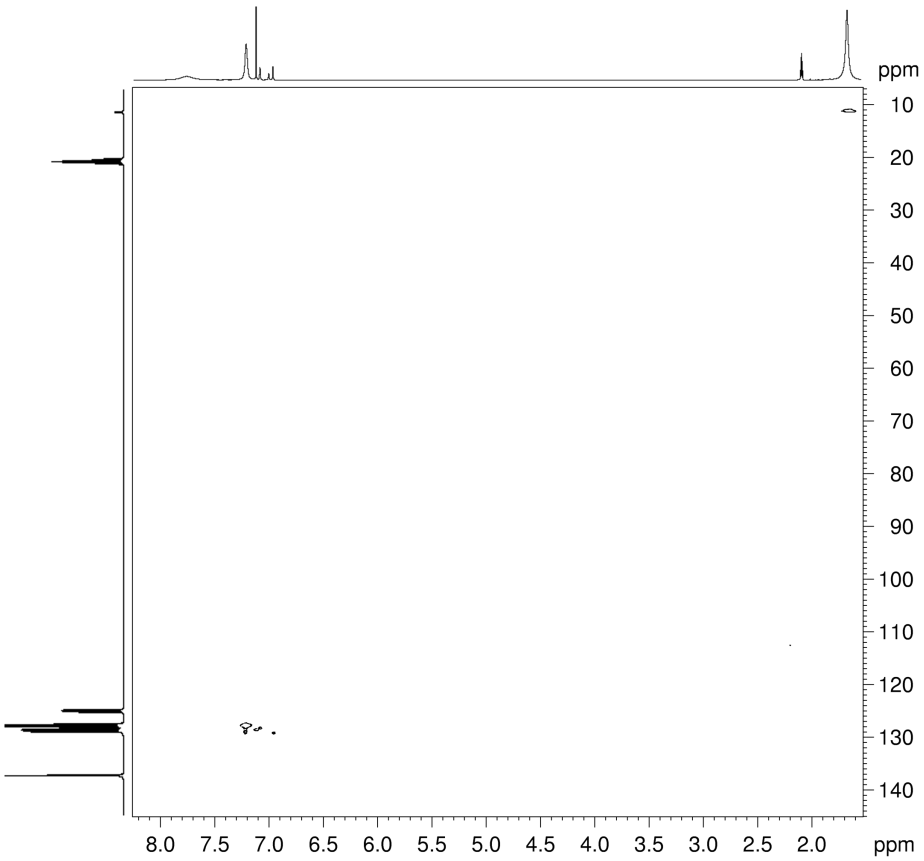

Figure S40. ^{1}H-^{13}C HSQC NMR spectrum (400 MHz, 101 MHz) of $\mathbf{4^{Ga}}$ in toluene-d_8 at 26 °C.

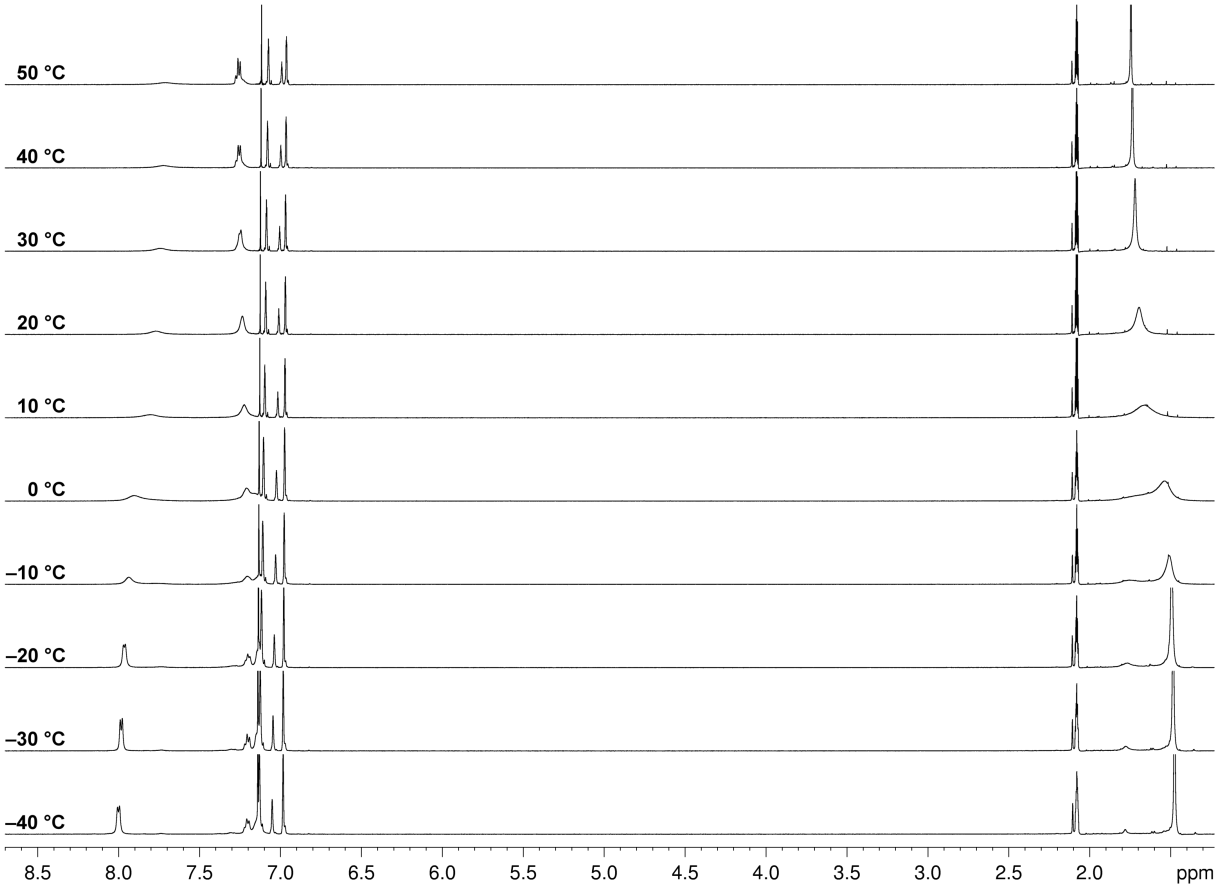

Figure S41. Variable-temperature ^{1}H NMR spectra (500 MHz) of **4^{Ga}** in toluene-d_8.

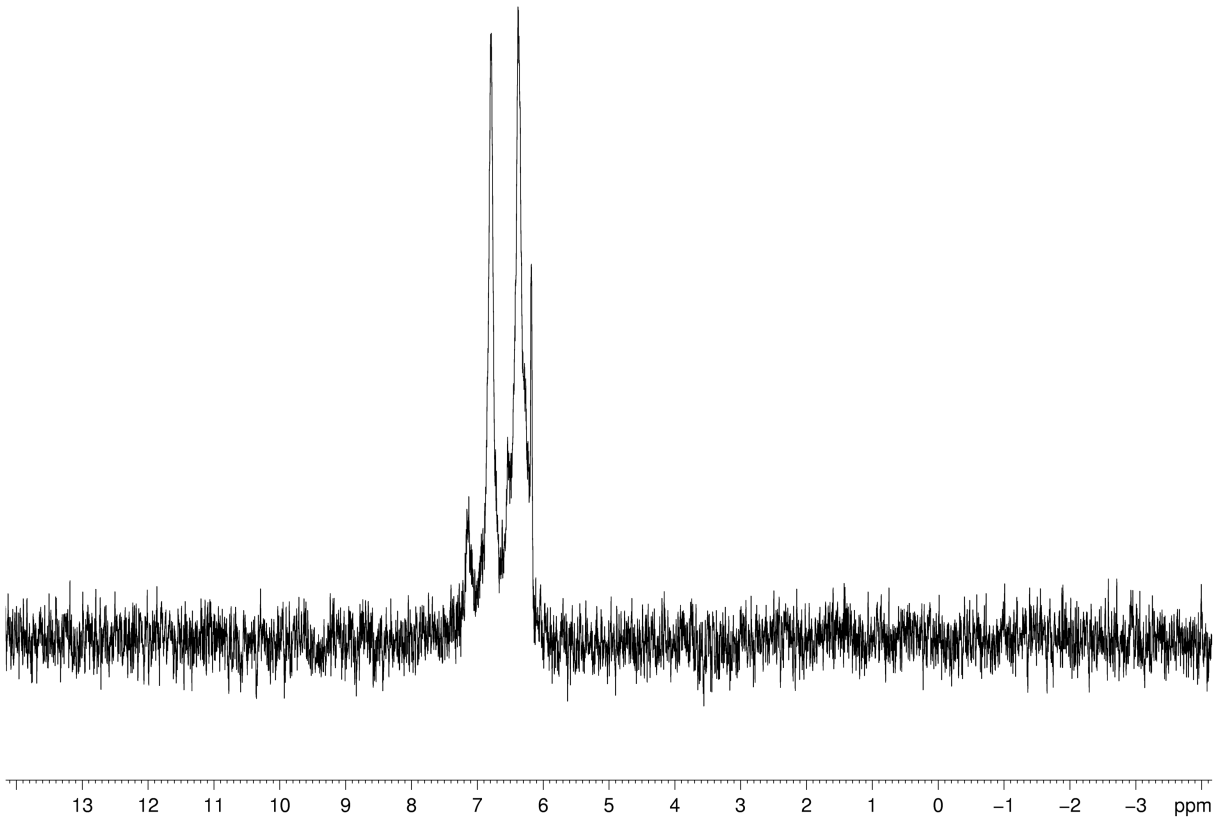

Figure S42. ^{2}H NMR spectrum (500 MHz) of [Cp*$_2$Y(Me$_2$Ga{Ph-*d5*}$_2$)] in benzene.

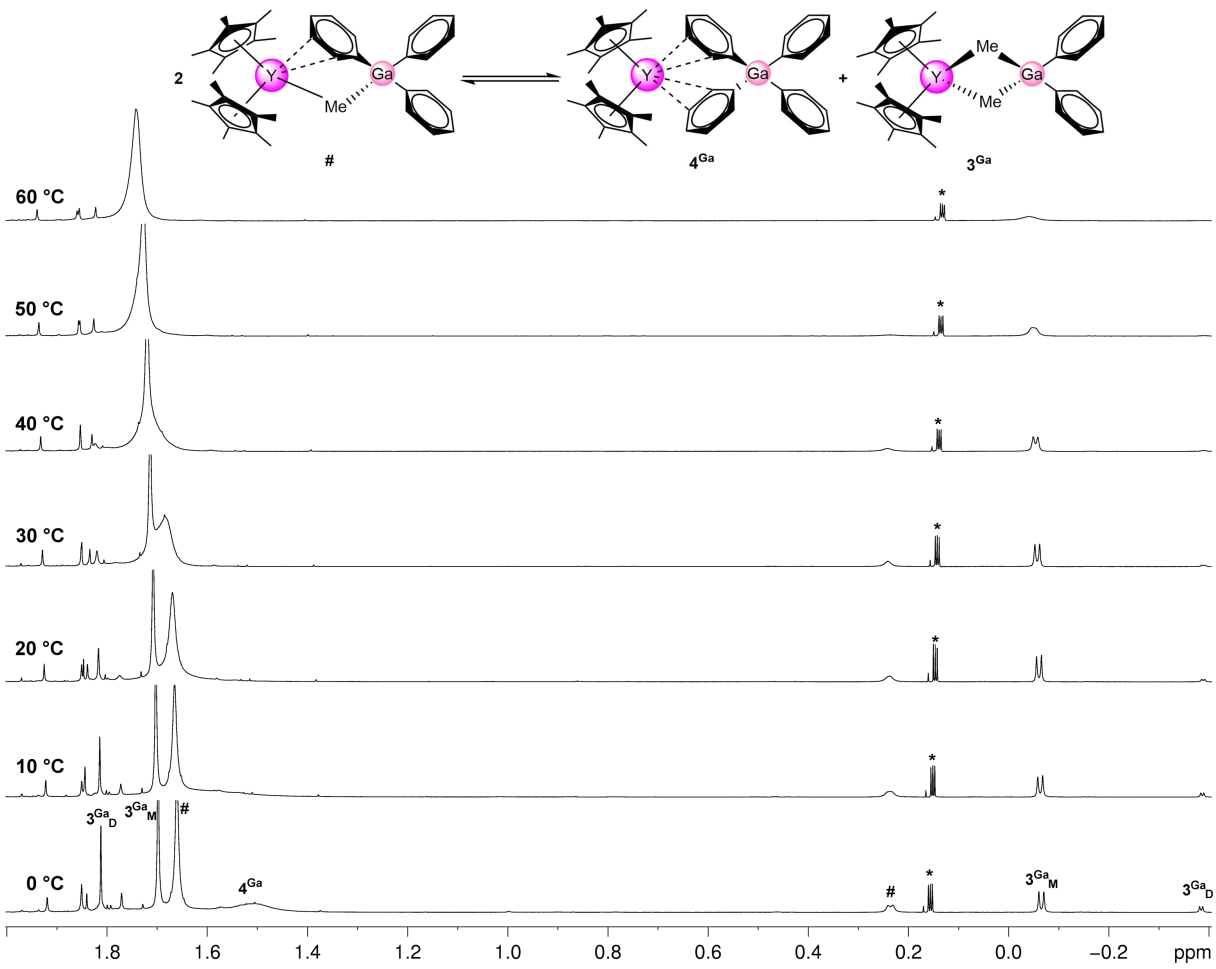

Figure S43. Variable-temperature ^{1}H NMR spectra (500 MHz) of $\mathbf{3^{Ga}}$ + $\mathbf{4^{Ga}}$ in C_6D_6 (* CH_4/CDH_3).

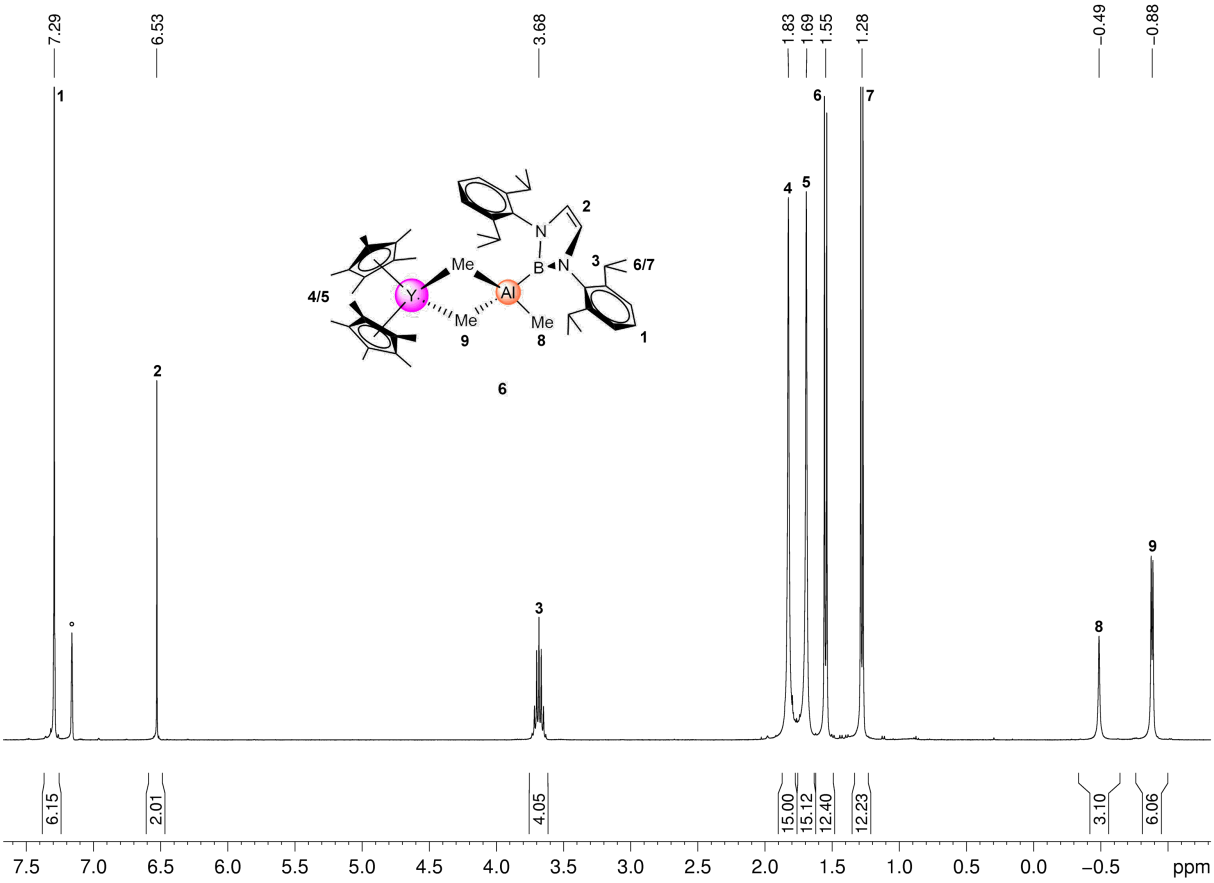

Figure S44. ^{1}H NMR spectrum (400 MHz) of **6** in C_6D_6 (°) at 26 °C.

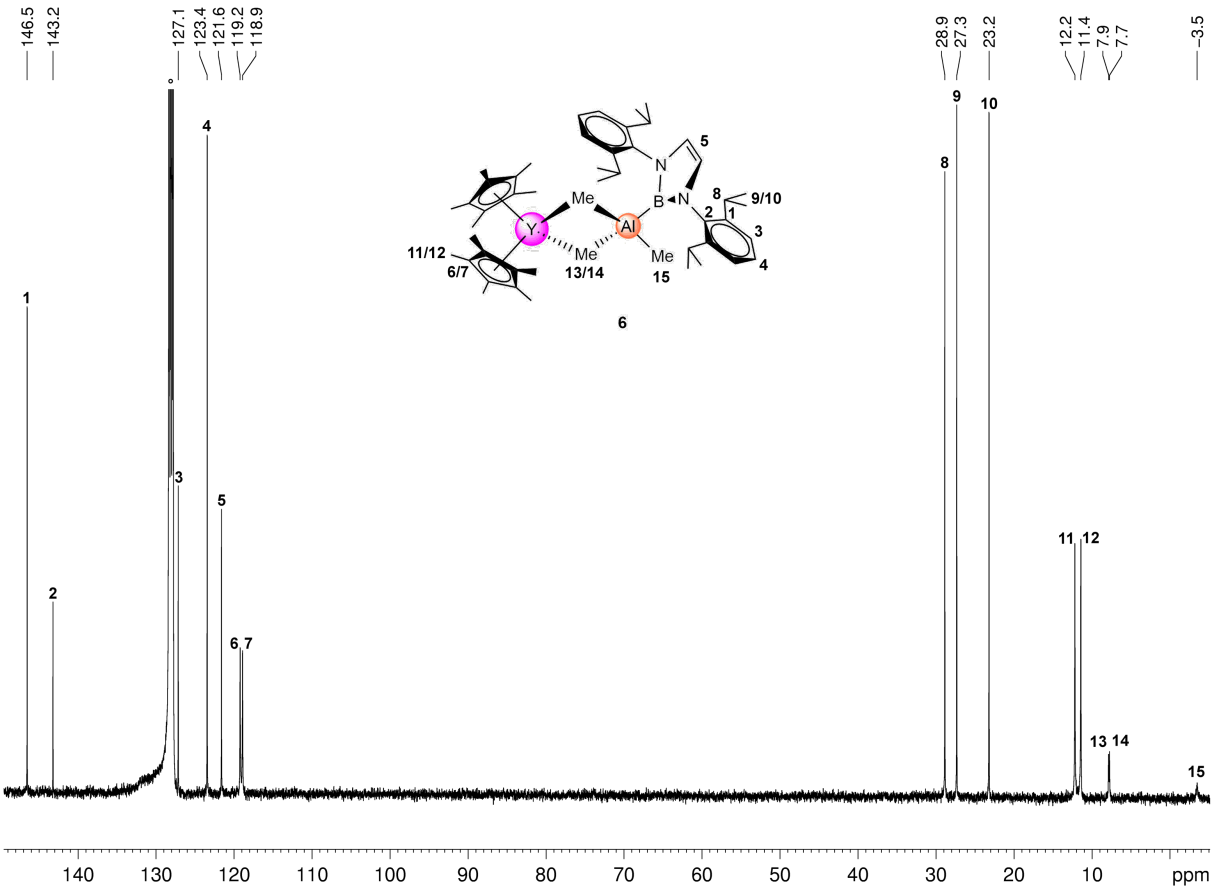

Figure S45. ^{13}C{^{1}H} NMR spectrum (101 MHz) of **6** in C_6D_6 (°) at 26 °C.

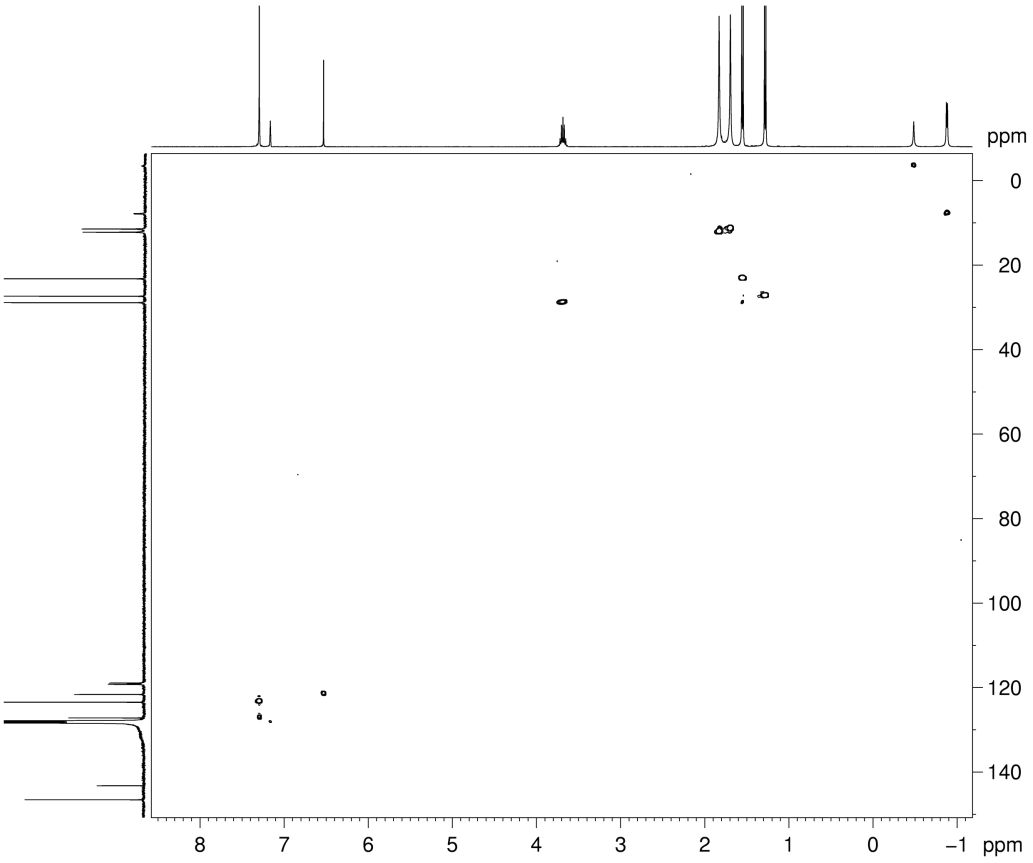

Figure S46. ^{1}H-^{13}C HSQC NMR spectrum (400 MHz, 101 MHz) of **6** in C_6D_6 at 26 °C.

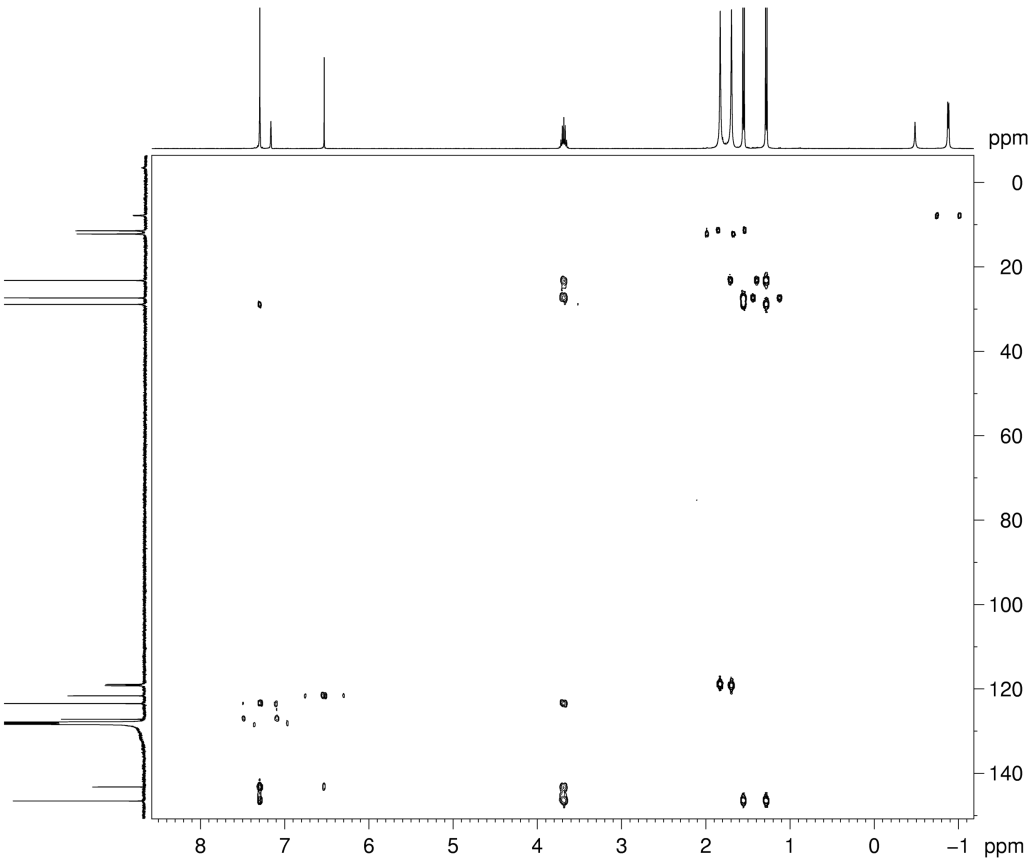

Figure S47. ^{1}H-^{13}C HMBC NMR spectrum (400 MHz, 101 MHz) of **6** in C_6D_6 at 26 °C.

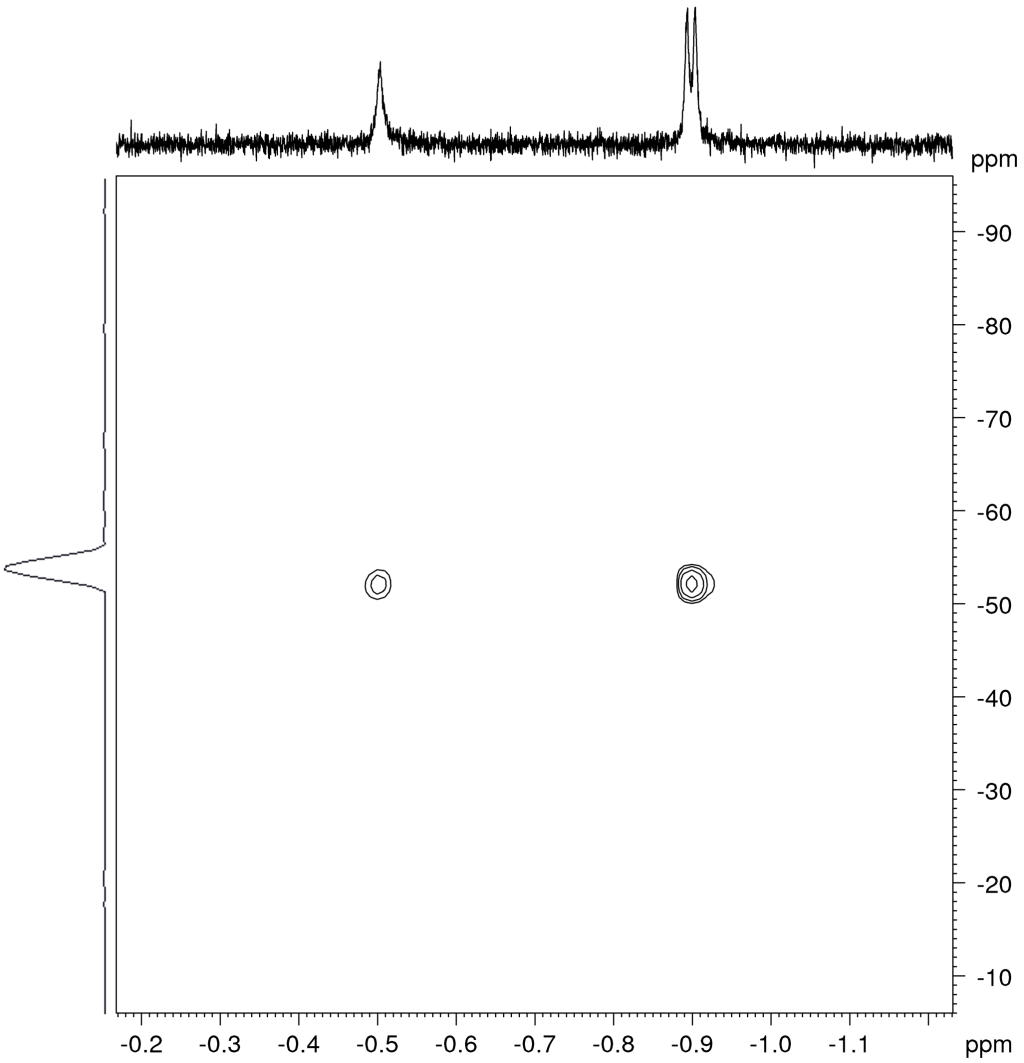

Figure S48. ^{1}H-^{89}Y HSQC NMR spectrum (500 MHz, 25 MHz) of **6** in C_6D_6 at 26 °C.

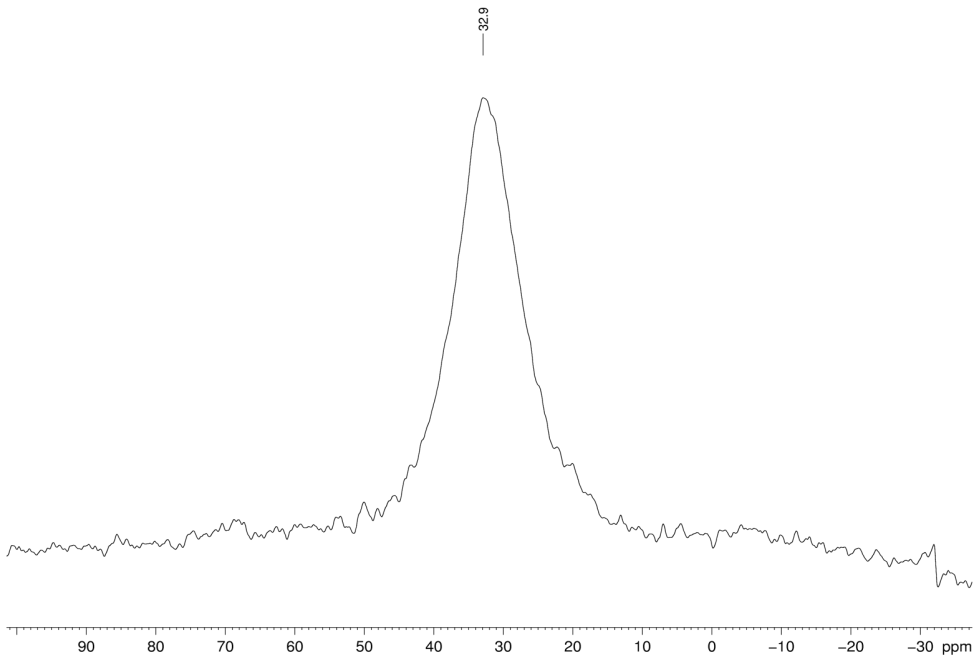

Figure S49. $^{11}B\{^{1}H\}$ NMR spectrum (80 MHz) of **6** in C_6D_6 at 26 °C.

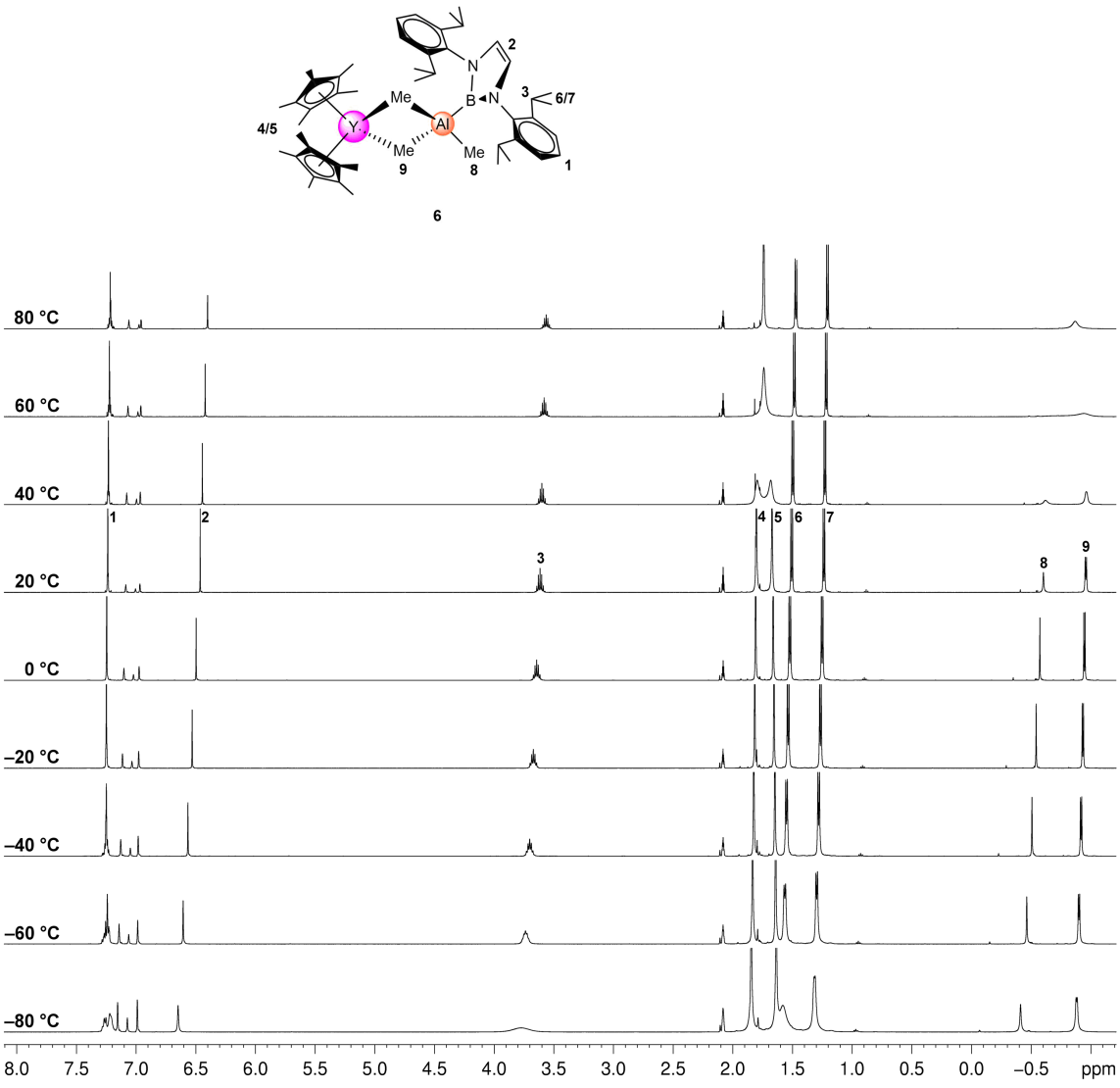

Figure S50. Variable-temperature ^{1}H NMR spectra (500 MHz) of **6** in toluene-d_8.

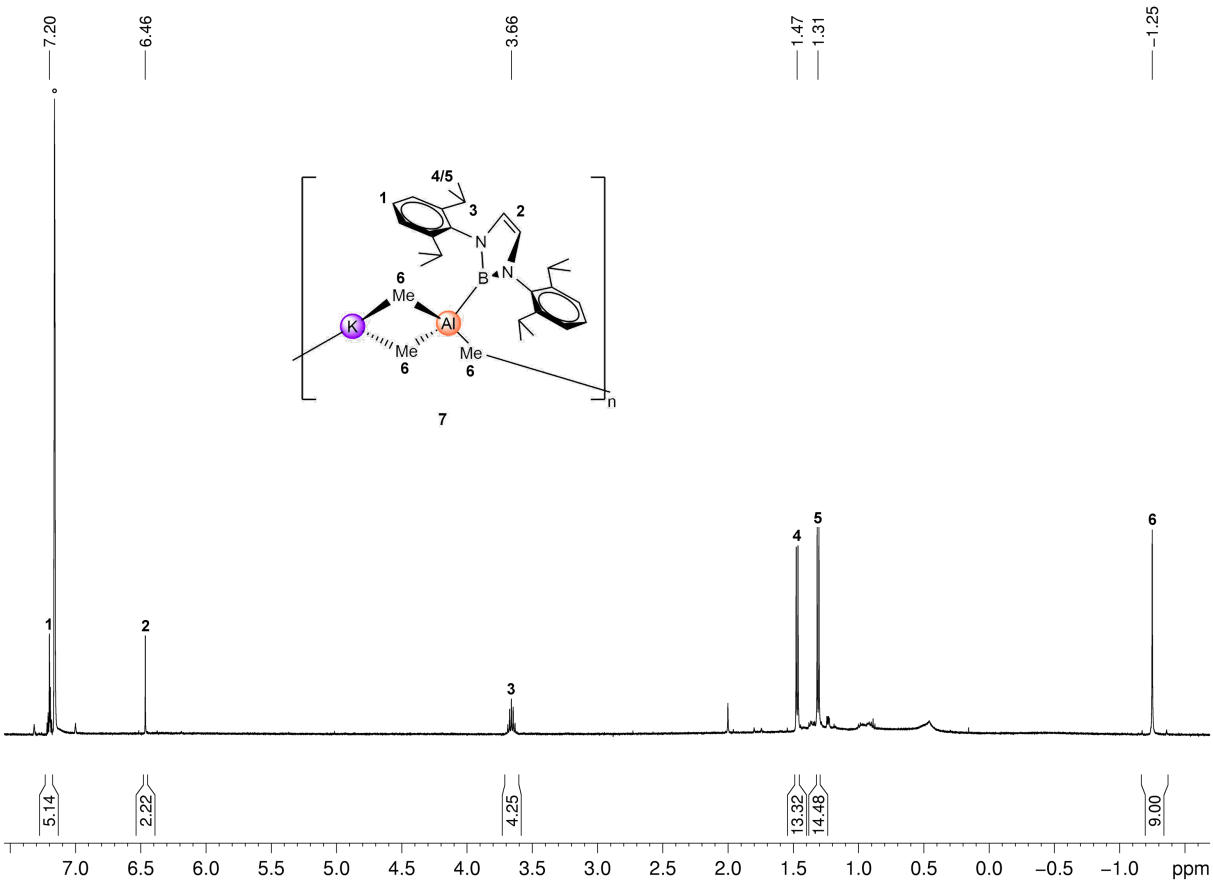

Figure S51. ^{1}H NMR spectrum (500 MHz) of **7** in C_6D_6 (°) at 26 °C.

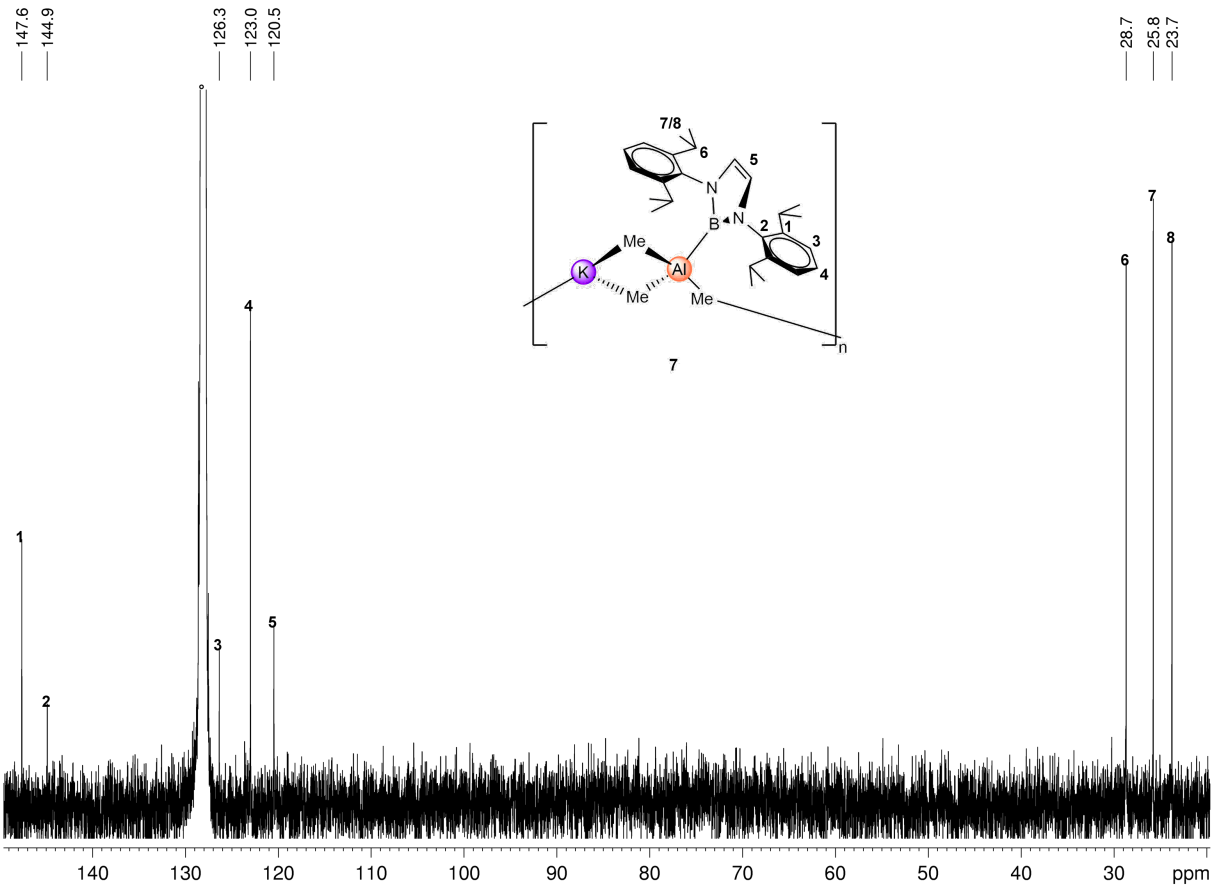

Figure S52. ^{13}C{^{1}H} NMR spectrum (126 MHz) of **7** in C_6D_6 (°) at 26 °C.

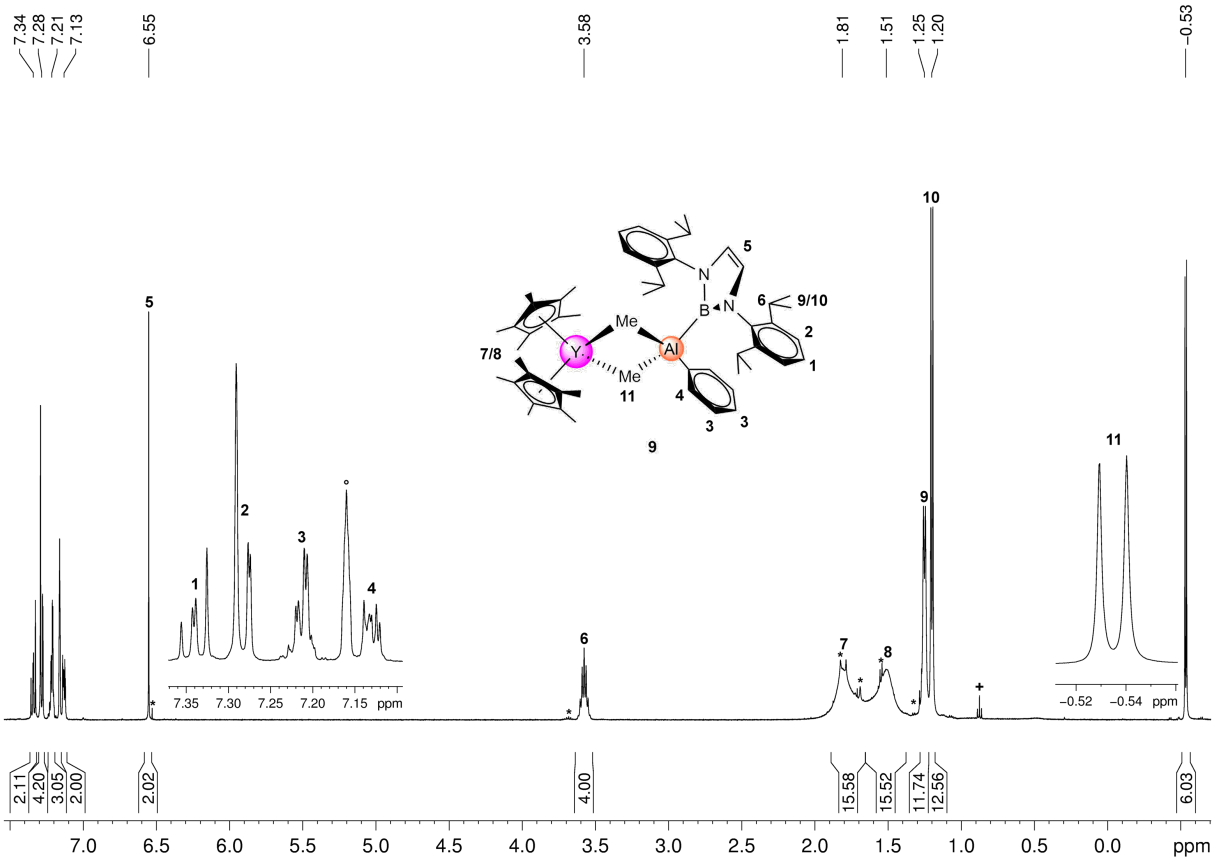

Figure S53. ^{1}H NMR spectrum (500 MHz) of **9** in C_6D_6 (°) at 26 °C (+ *n*-pentane; * traces of starting material).

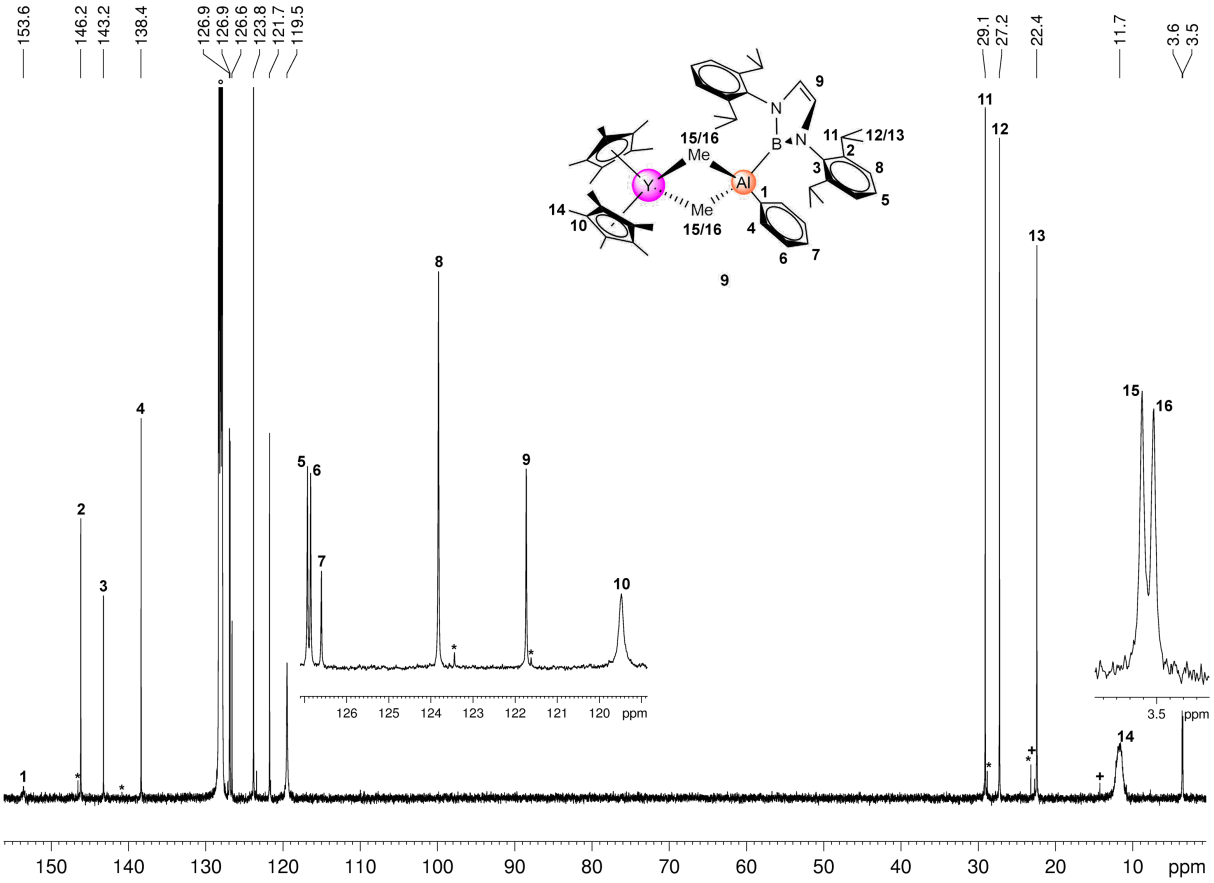

Figure S54. $^{13}C\{^{1}H\}$ NMR spectrum (126 MHz) of **9** in C_6D_6 (°) at 26 °C (+ *n*-pentane; * traces of starting material).

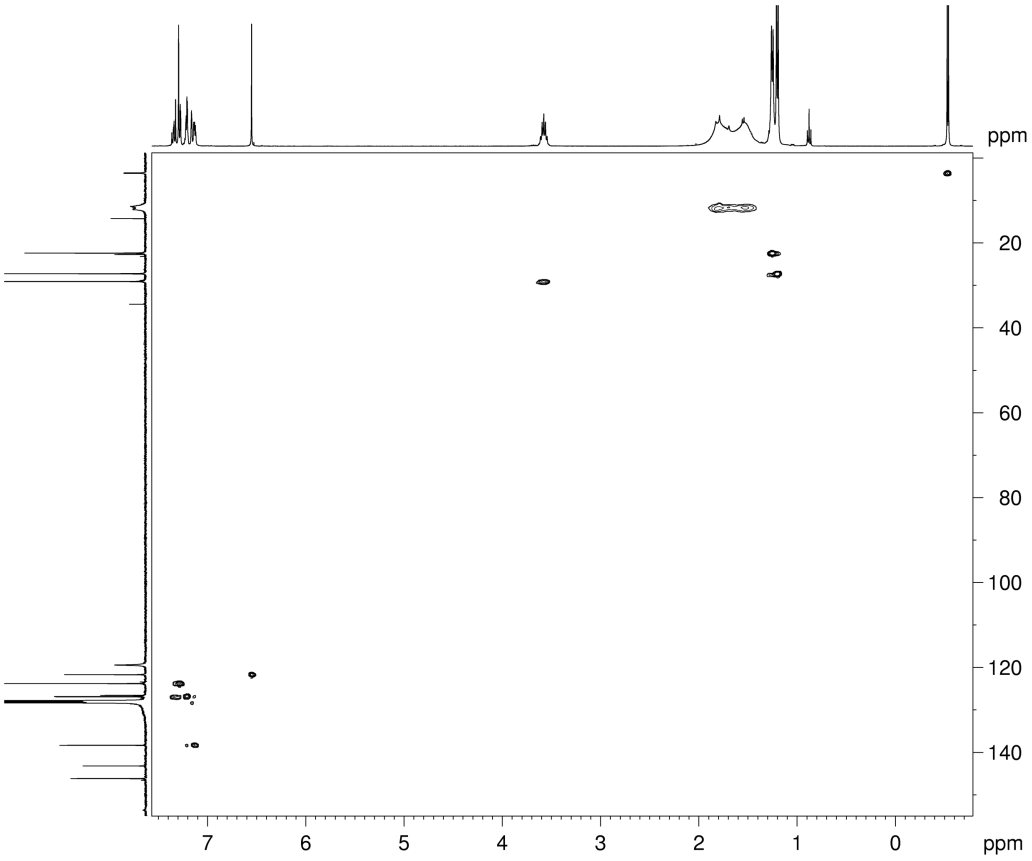

Figure S55. ^{1}H-^{13}C HSQC NMR spectrum (400 MHz, 101 MHz) of **9** in C_6D_6 at 26 °C.

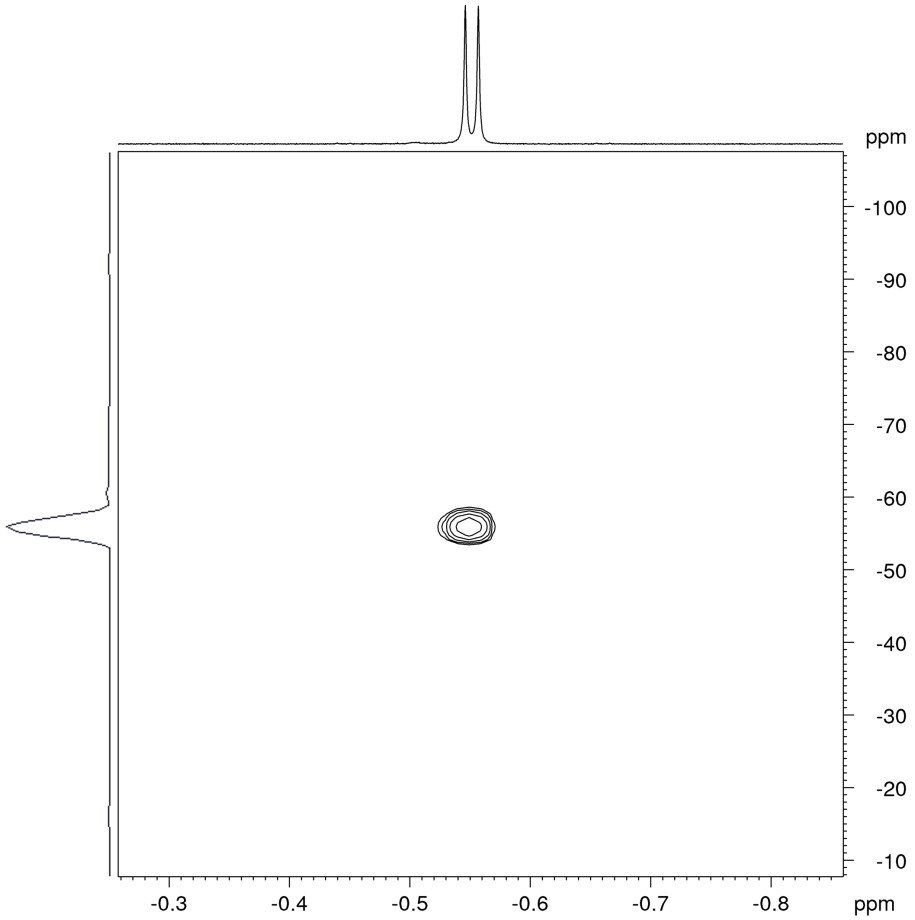

Figure S56. ^{1}H-^{89}Y HSQC NMR spectrum (500 MHz, 25 MHz) of **9** in C_6D_6 at 26 °C.

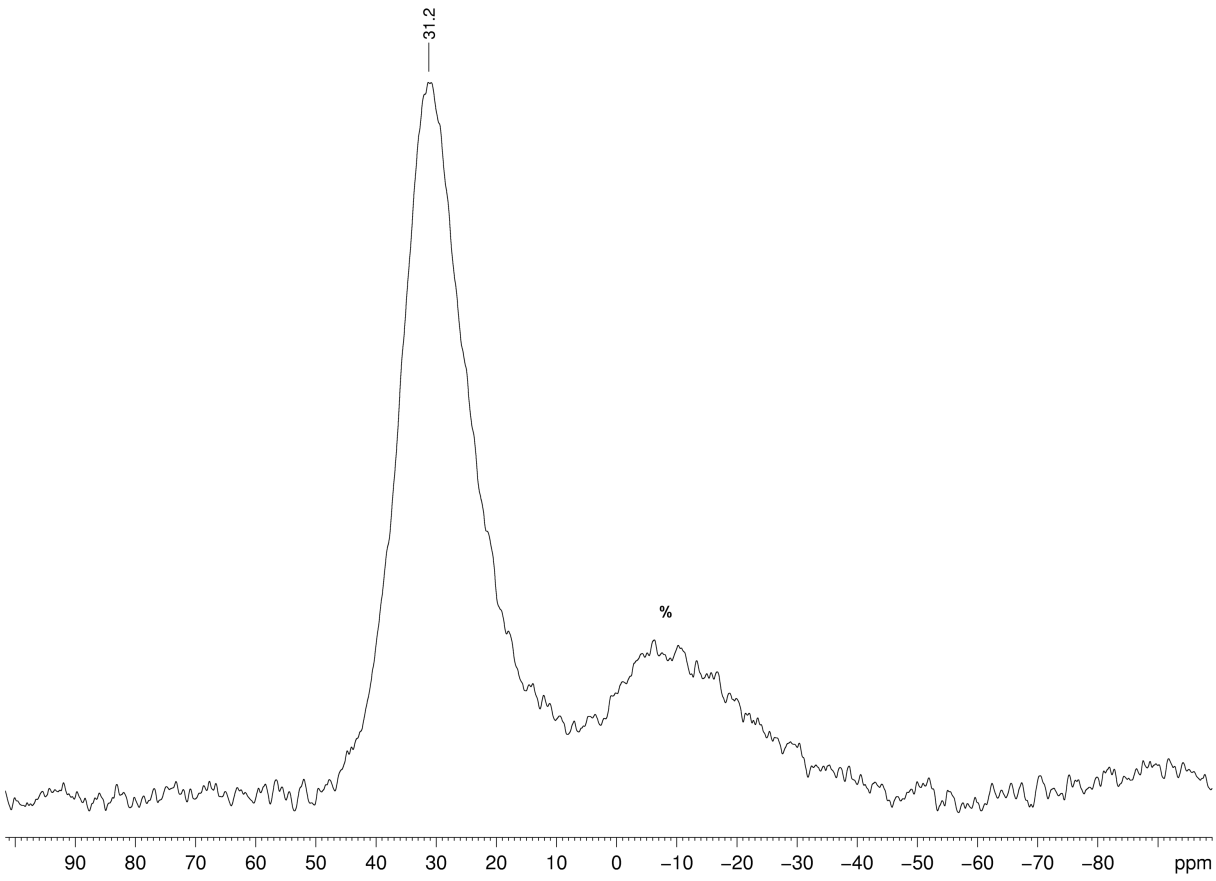

Figure S57. $^{11}B\{^{1}H\}$ NMR spectrum (80 MHz) of **9** in C_6D_6 at 26 °C (% borosilicate glass background).

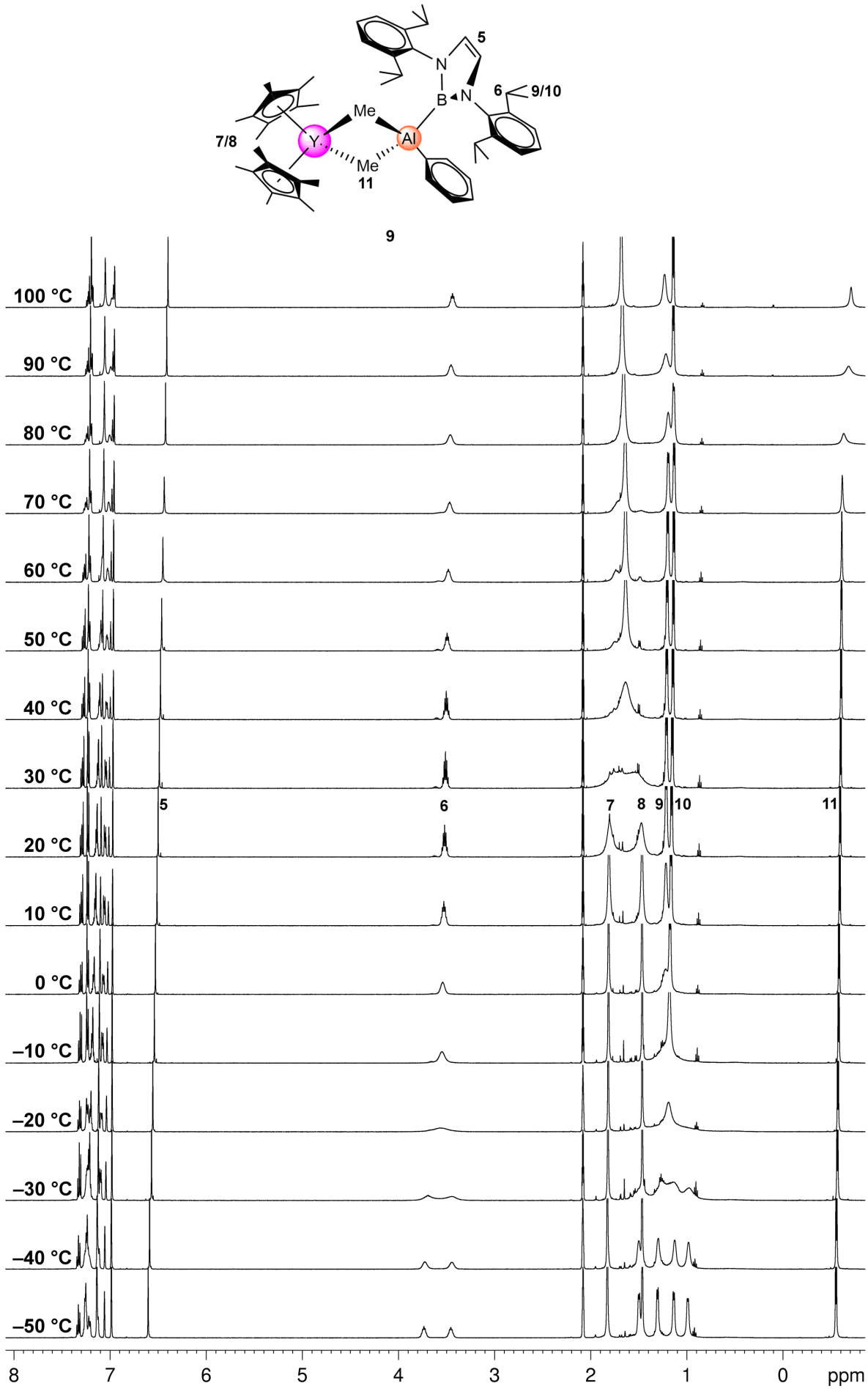

Figure S58. Variable-temperature ^{1}H NMR spectra (500 MHz) of **9** in toluene-d_8.

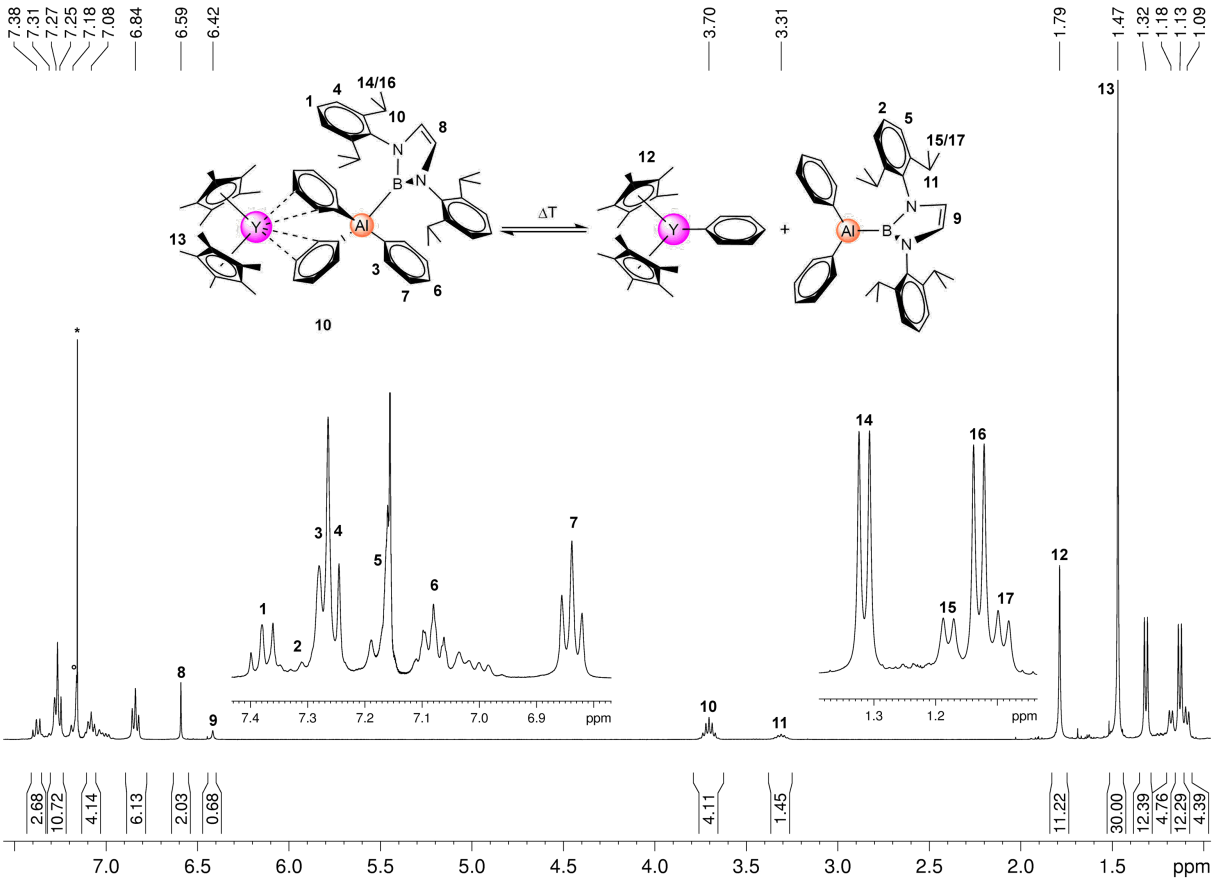

Figure S59. ^{1}H NMR spectrum (400 MHz) of **10** in C_6D_6 (°) at 26 °C (* benzene).

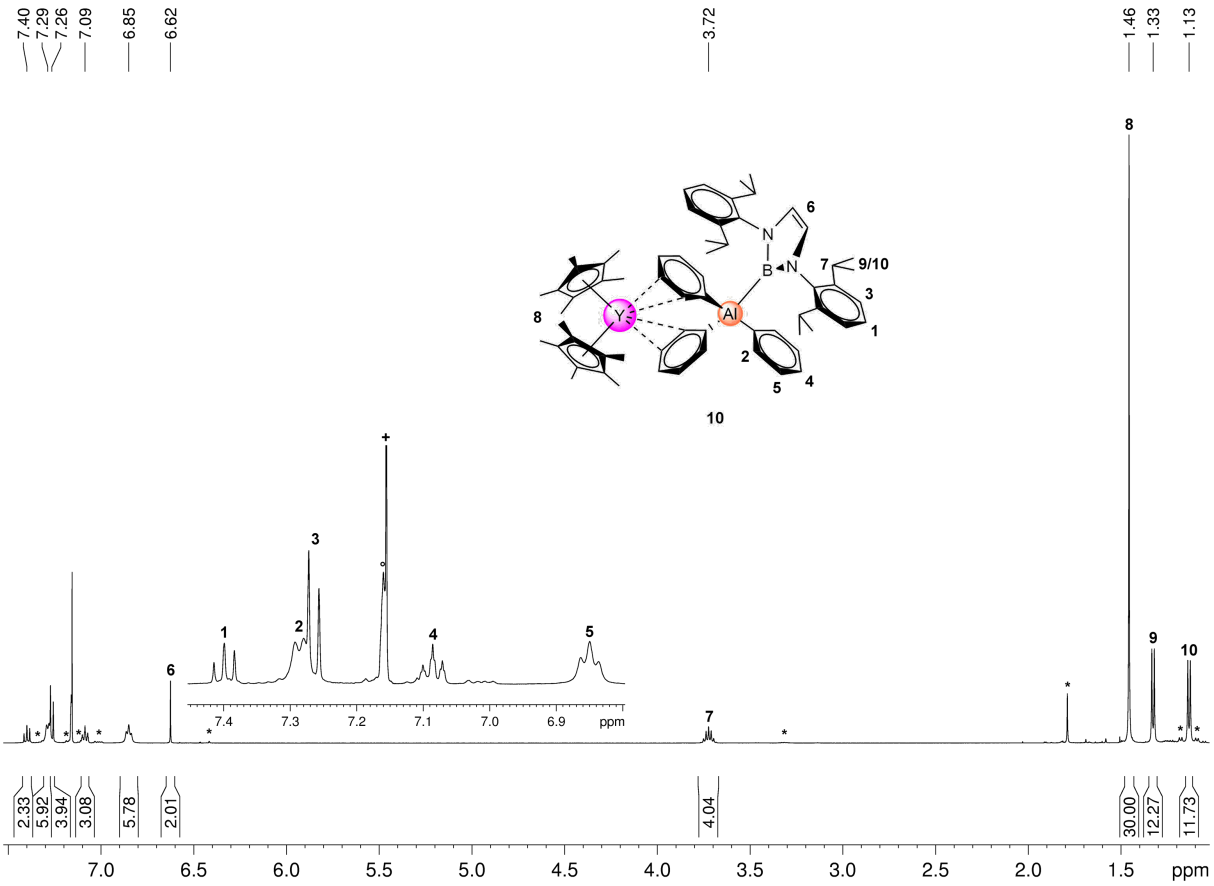

Figure S60. ^{1}H NMR spectrum (400 MHz) of **10** in C_6D_6 (°) at 3 °C (+ benzene; * traces of $[Cp^*_2YPh]$ + $[Ph_2Al\{B(NDippCH)_2\}]$).

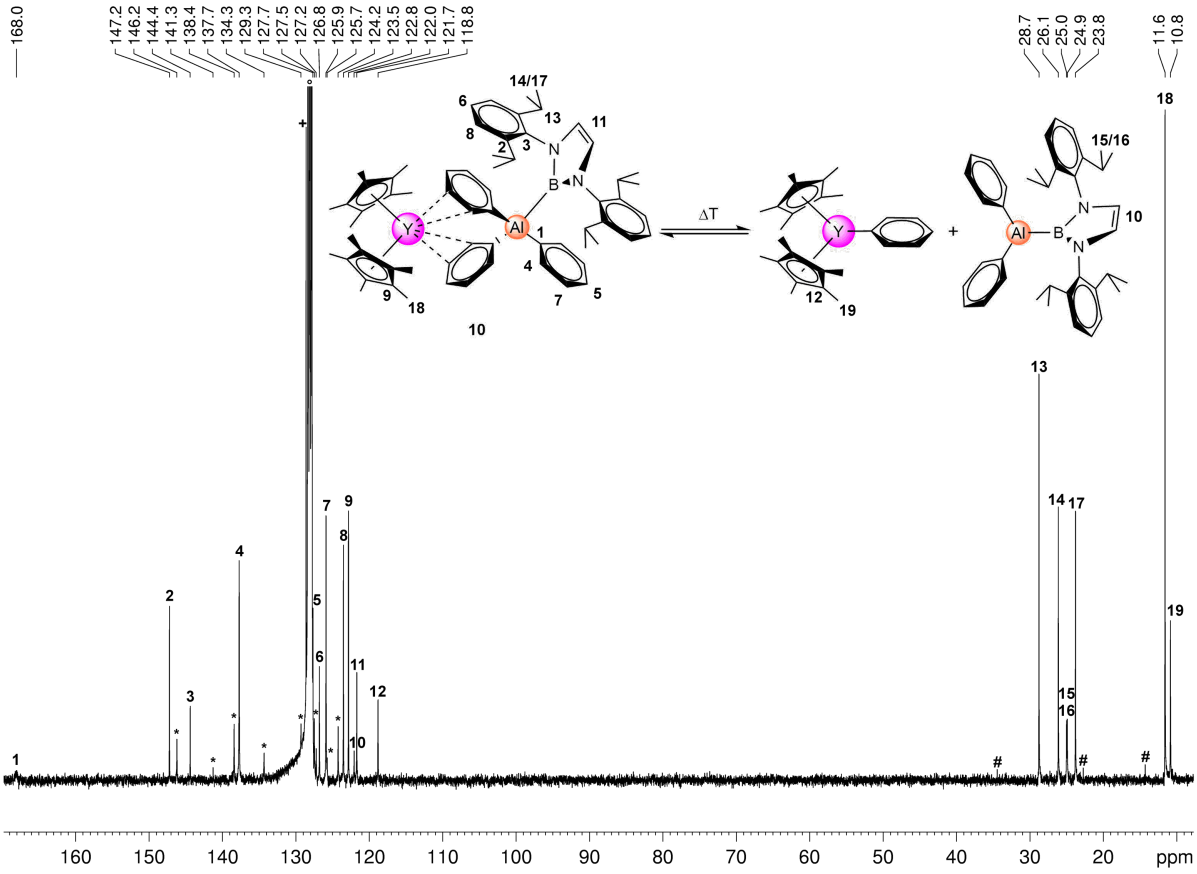

Figure S61. $^{13}C\{^{1}H\}$ NMR spectrum (101 MHz) of **10** in C_6D_6 (°) at 26 °C (# *n*-pentane; + C_6H_6; * aromatic resonances of [Cp*$_2$YPh] + [Ph$_2$Al{B(NDippCH)$_2$}]).

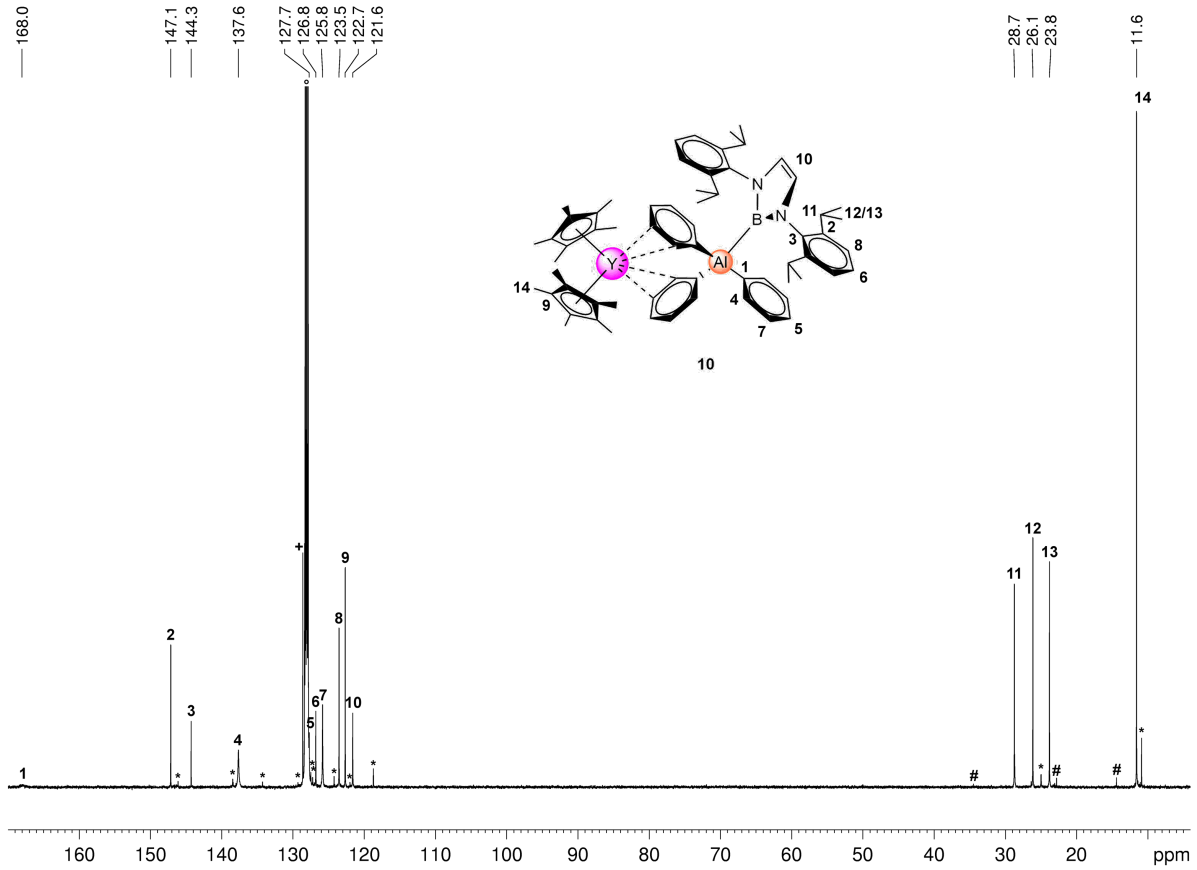

Figure S62. $^{13}C\{^{1}H\}$ NMR spectrum (101 MHz) of **10** in C_6D_6 (°) at 3 °C (# *n*-pentane; + C_6H_6; * traces of [Cp*$_2$YPh] + [Ph$_2$Al{B(NDippCH)$_2$}]).

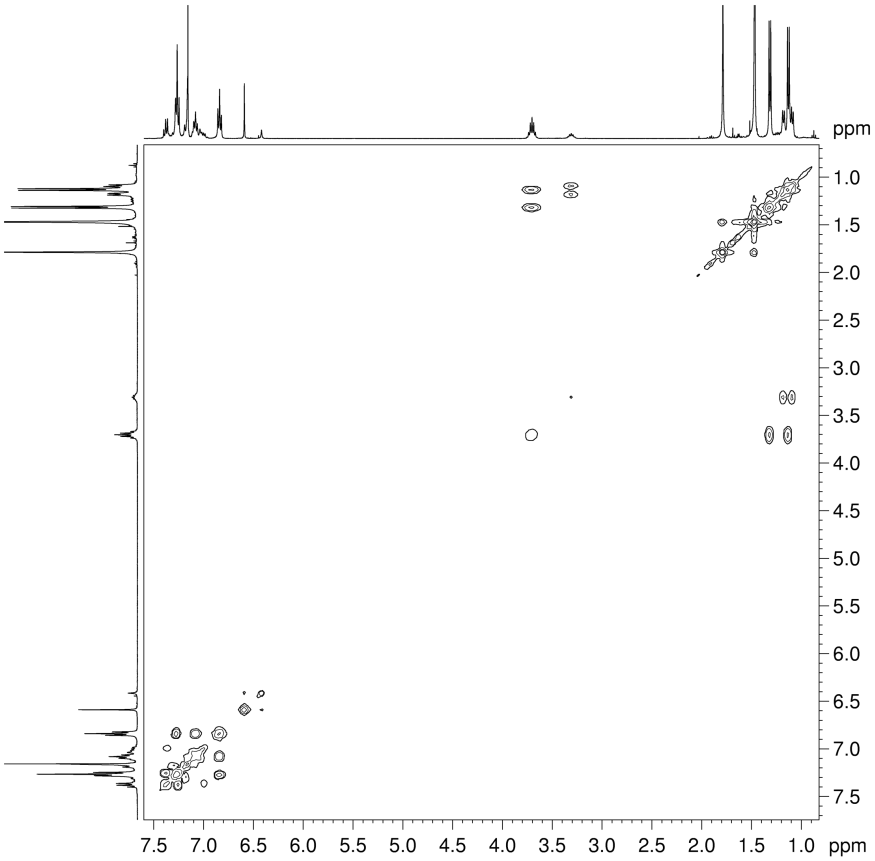

Figure S63. ^{1}H-^{1}H COSY NMR spectrum (400 MHz) of **10** in C_6D_6 at 26 °C.

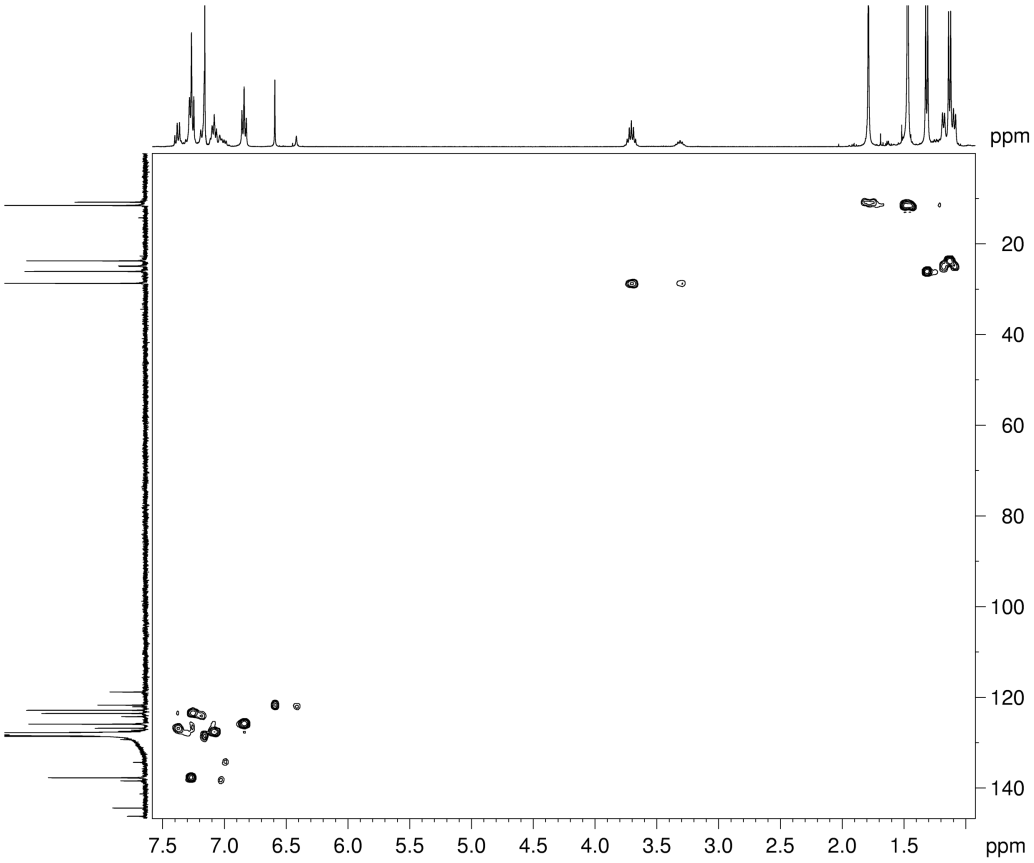

Figure S64. ^{1}H-^{13}C HSQC NMR spectrum (400 MHz, 101 MHz) of **10** in C_6D_6 at 26 °C.

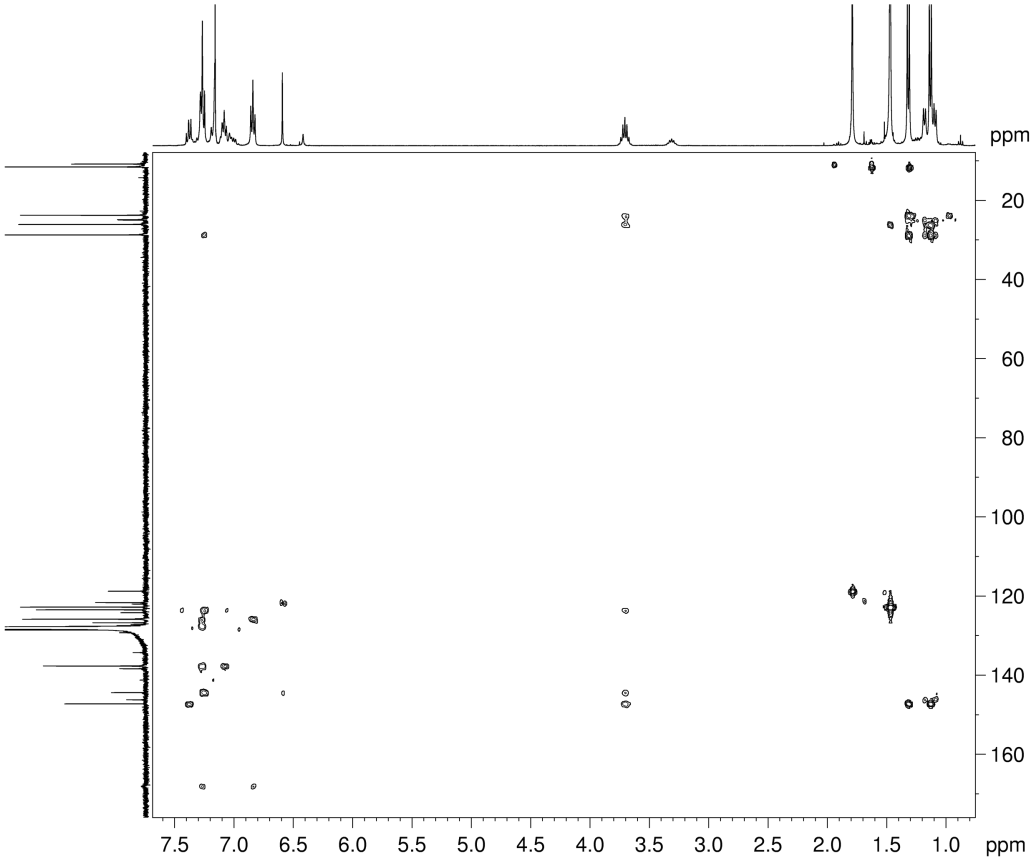

Figure S65. ^{1}H-^{13}C HMBC NMR spectrum (400 MHz, 101 MHz) of **10** in C_6D_6 at 26 °C.

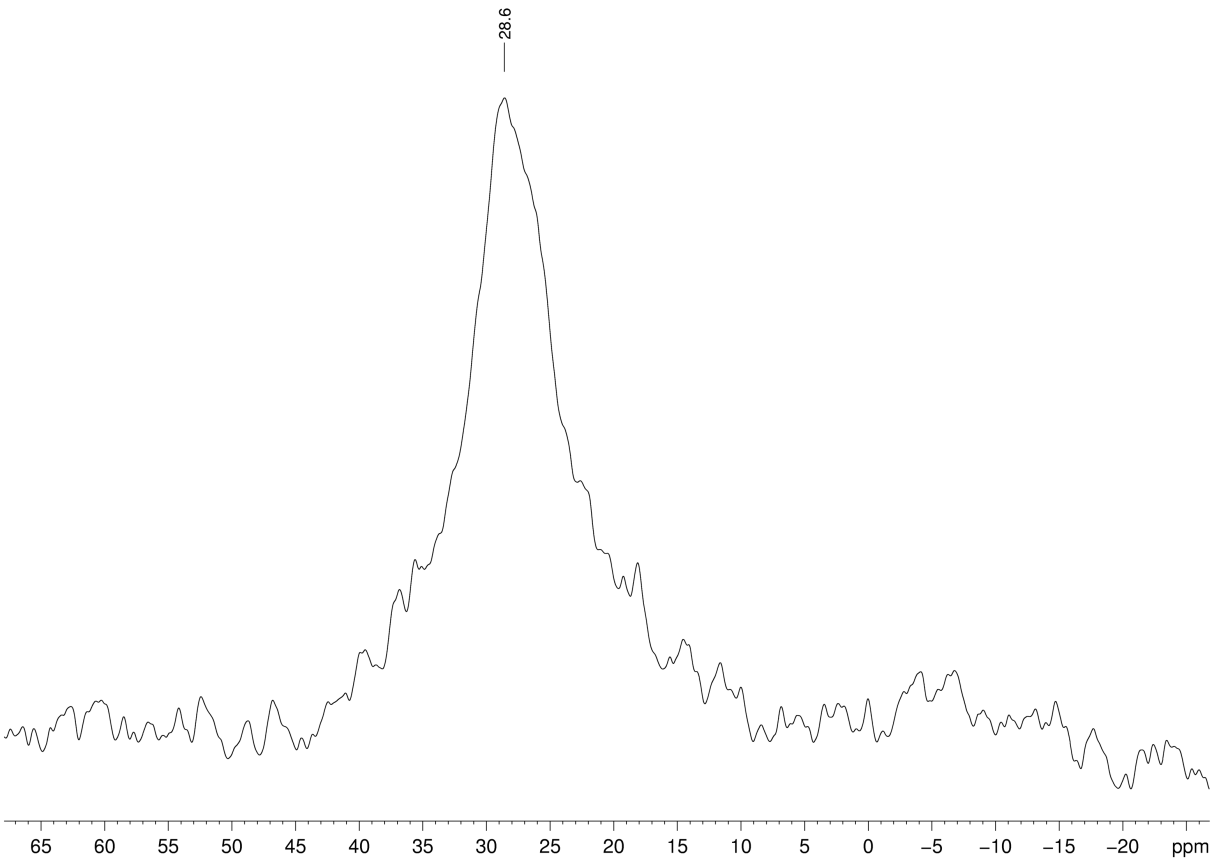

Figure S66. $^{11}B\{^{1}H\}$ NMR spectrum (80 MHz) of **10** in C_6D_6 at 26 °C.

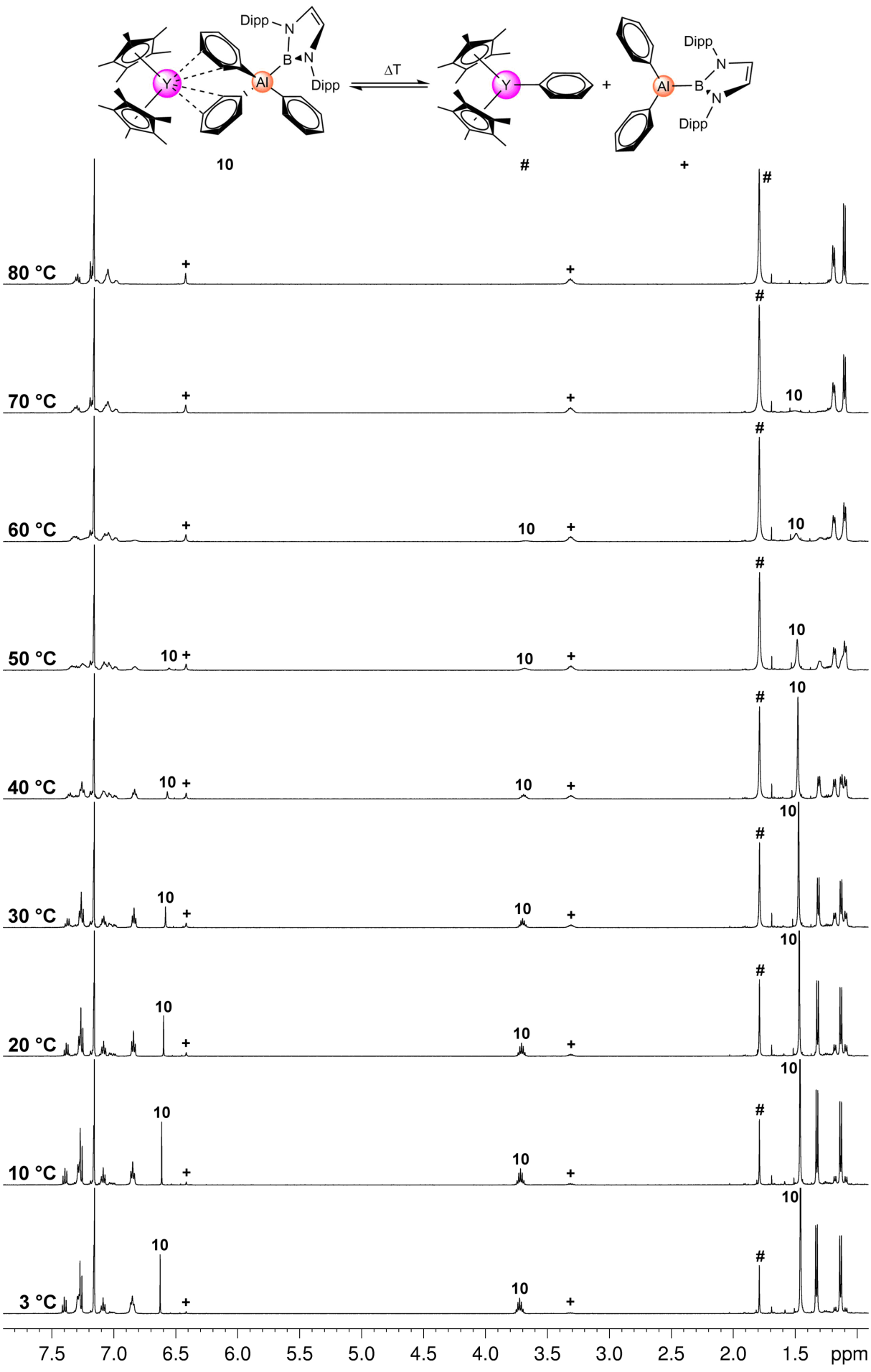

Figure S67. Variable-temperature ^{1}H NMR spectra (500 MHz) of **10** in C_6D_6.

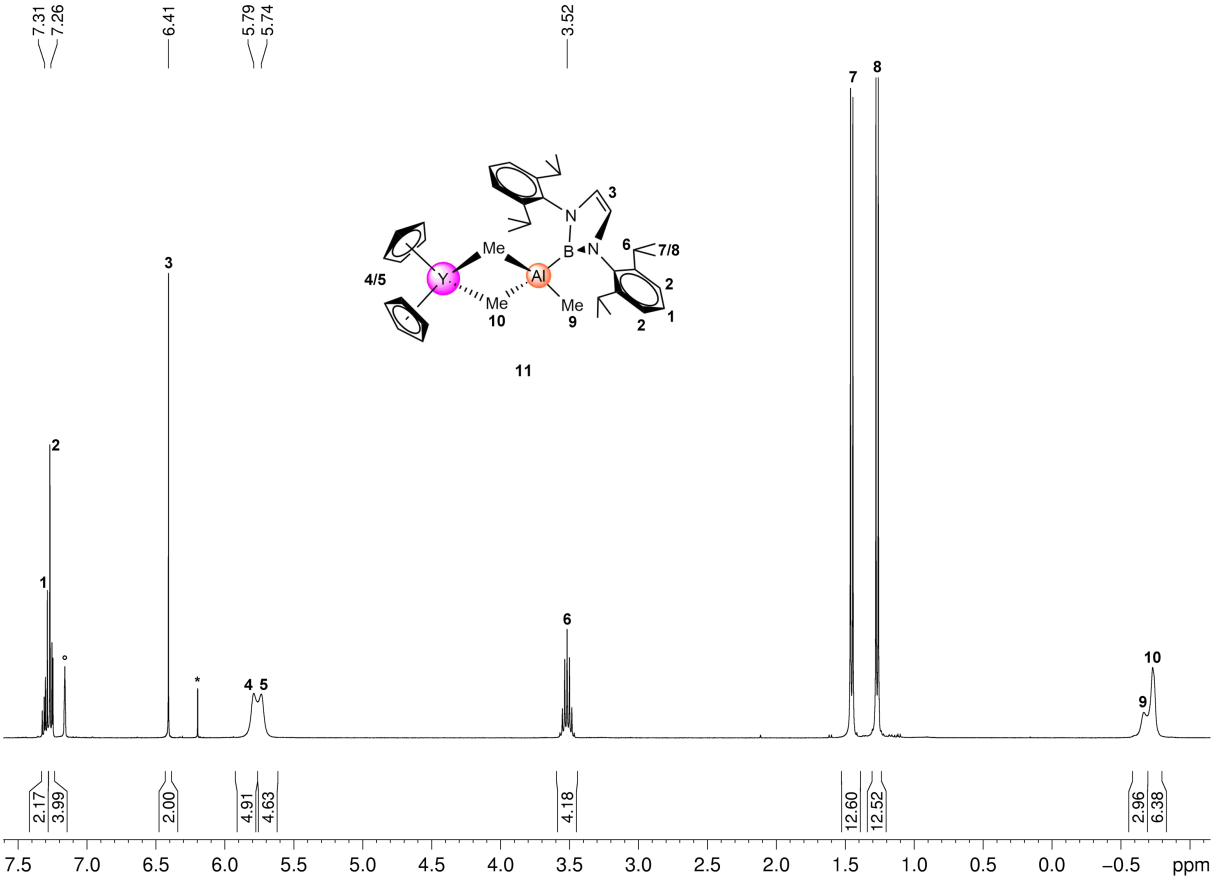

Figure S68. ^{1}H NMR spectrum (400 MHz) of **11** in C_6D_6 (°) at 26 °C (* residual $[Cp_2YCl]_2$).

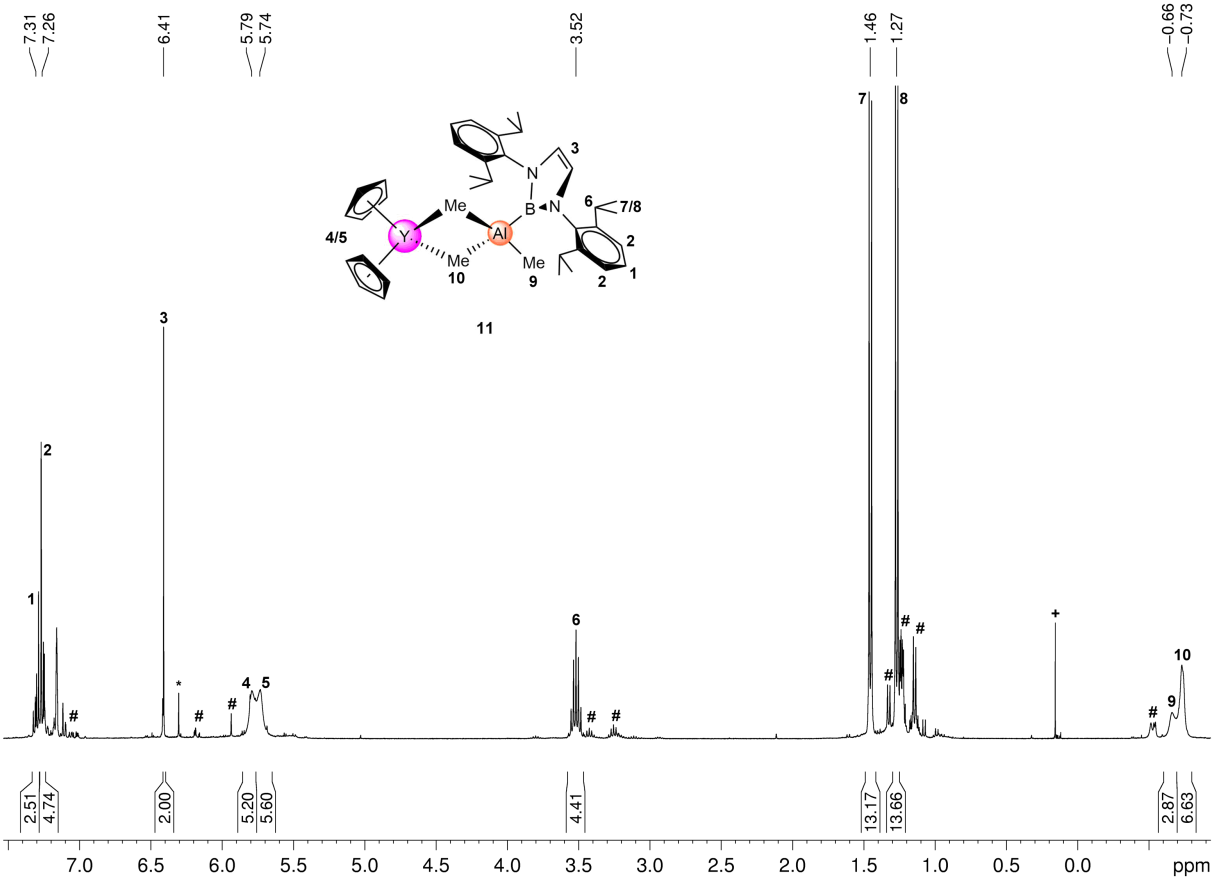

Figure S69. ^{1}H NMR spectrum (400 MHz) of **11** in C_6D_6 (°) after thermal treatment at 130 °C for 50 h. (* residual $[Cp_2YCl]_2$; + methane; # decomposition products).

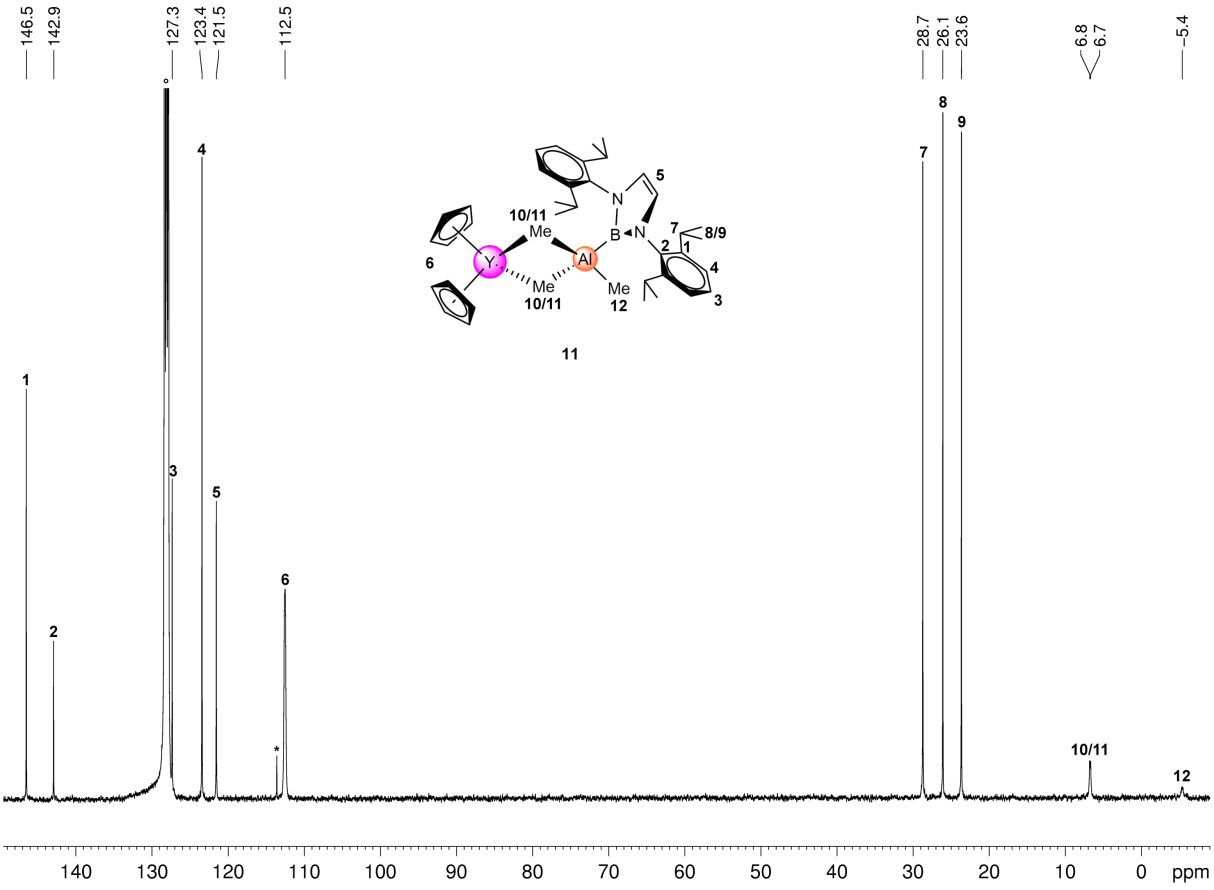

Figure S70. $^{13}C\{^{1}H\}$ NMR spectrum (101 MHz) of **11** in C_6D_6 (°) at 26 °C (* residual $[Cp_2YCl]_2$).

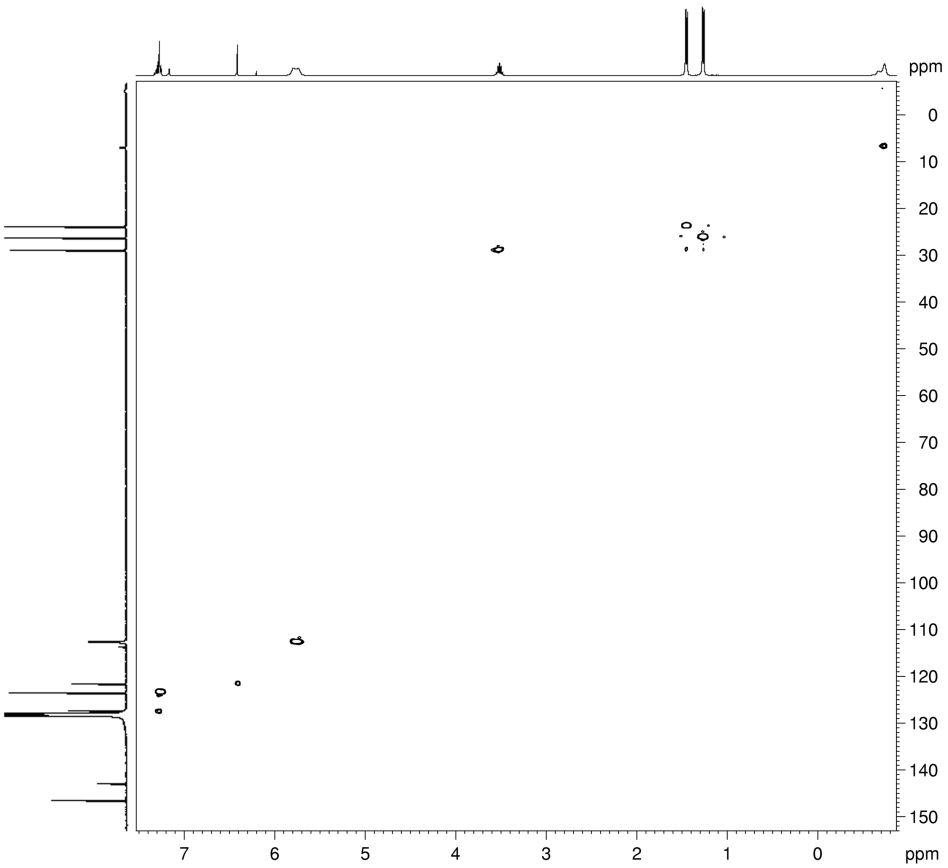

Figure S71. ^{1}H-^{13}C HSQC NMR spectrum (400 MHz, 101 MHz) of **11** in C_6D_6 at 26 °C.

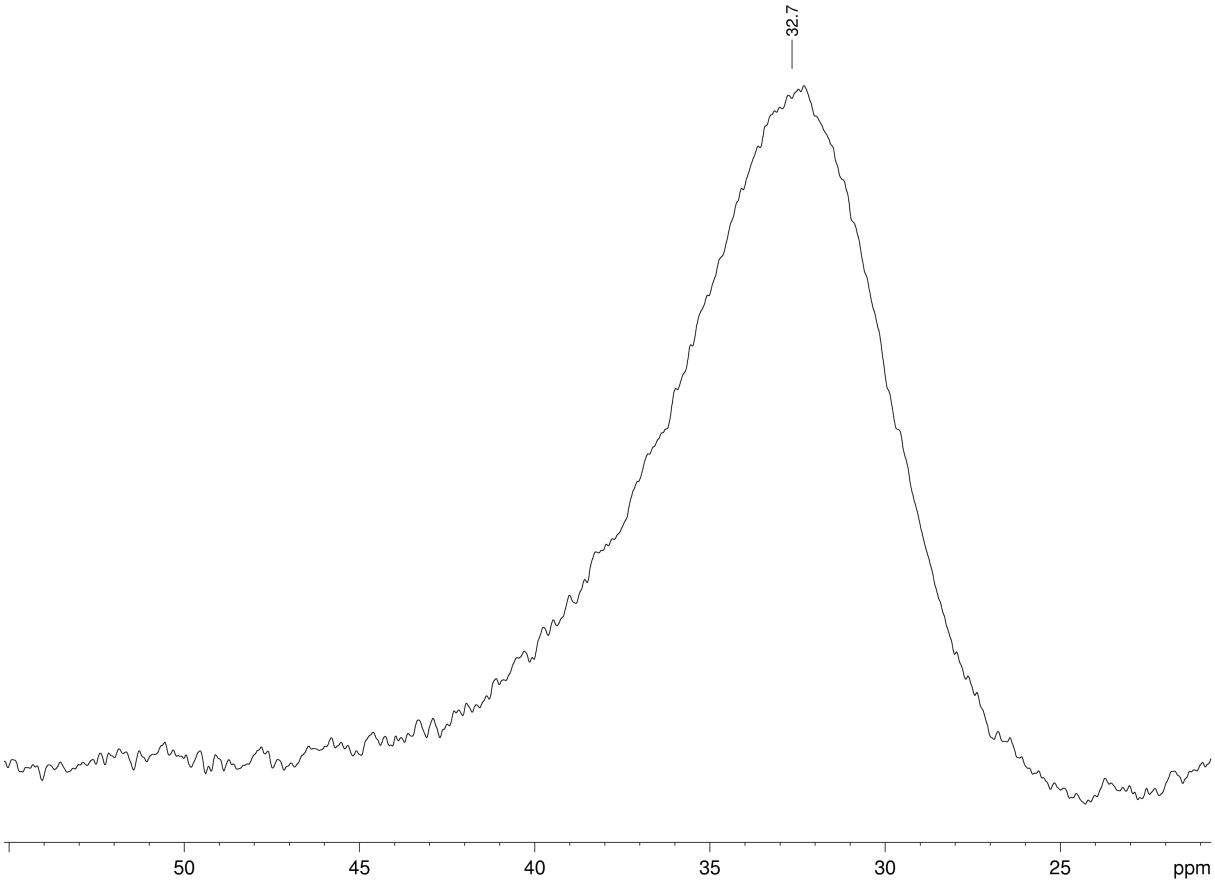

Figure S72. $^{11}B\{^{1}H\}$ NMR spectrum (80 MHz) of **11** in C_6D_6 at 26 °C.

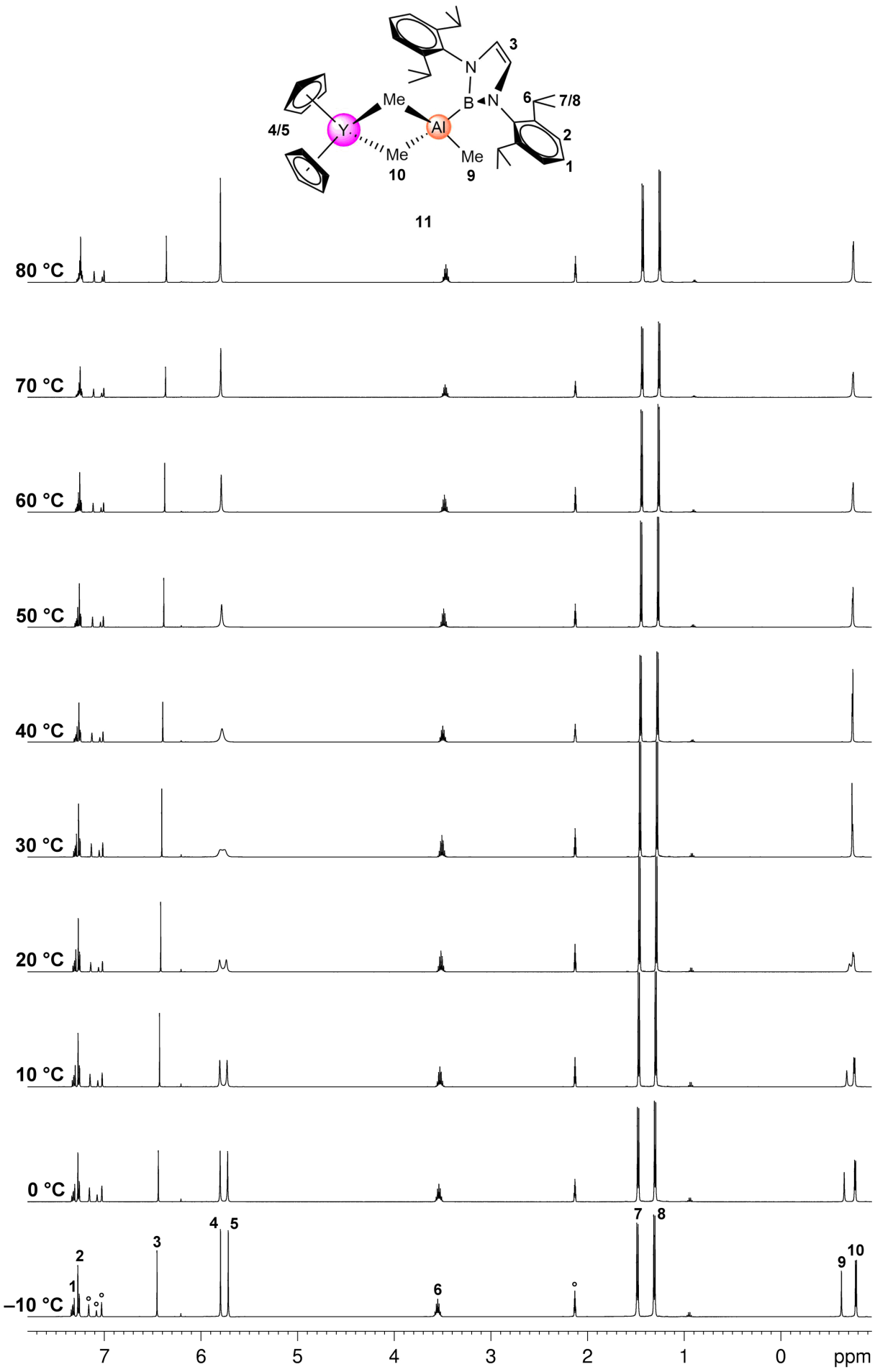

Figure S73. Variable-temperature ^{1}H NMR spectra (500 MHz) of **11** in toluene-d_8.

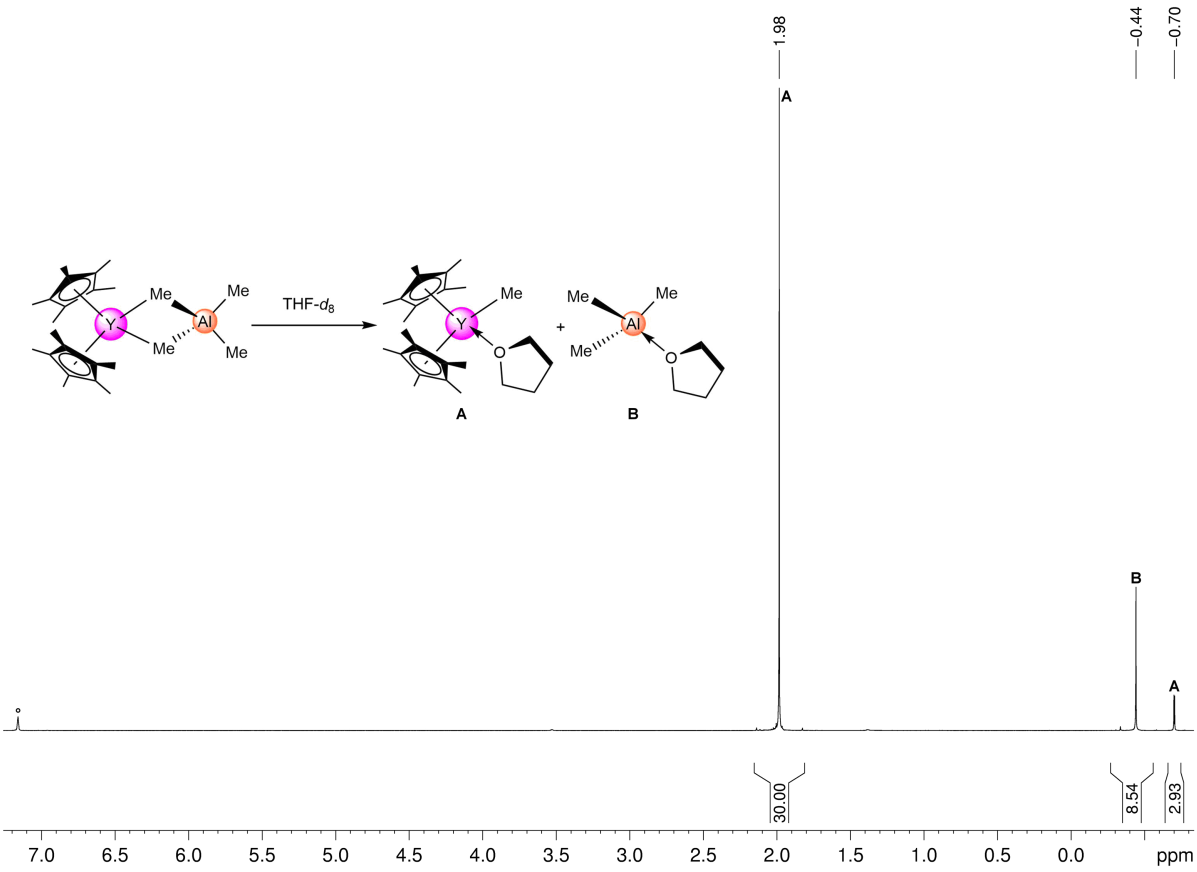

Figure S74. ^{1}H NMR spectrum (400 MHz) of [Cp*$_2$Y(AlMe$_4$)] (**1^{Al}**) and one equiv. THF-d_8 in C_6D_6 (°) to form[Cp*$_2$YMe(THF) and AlMe$_3$(THF) via [AlMe$_4$] cleavage.

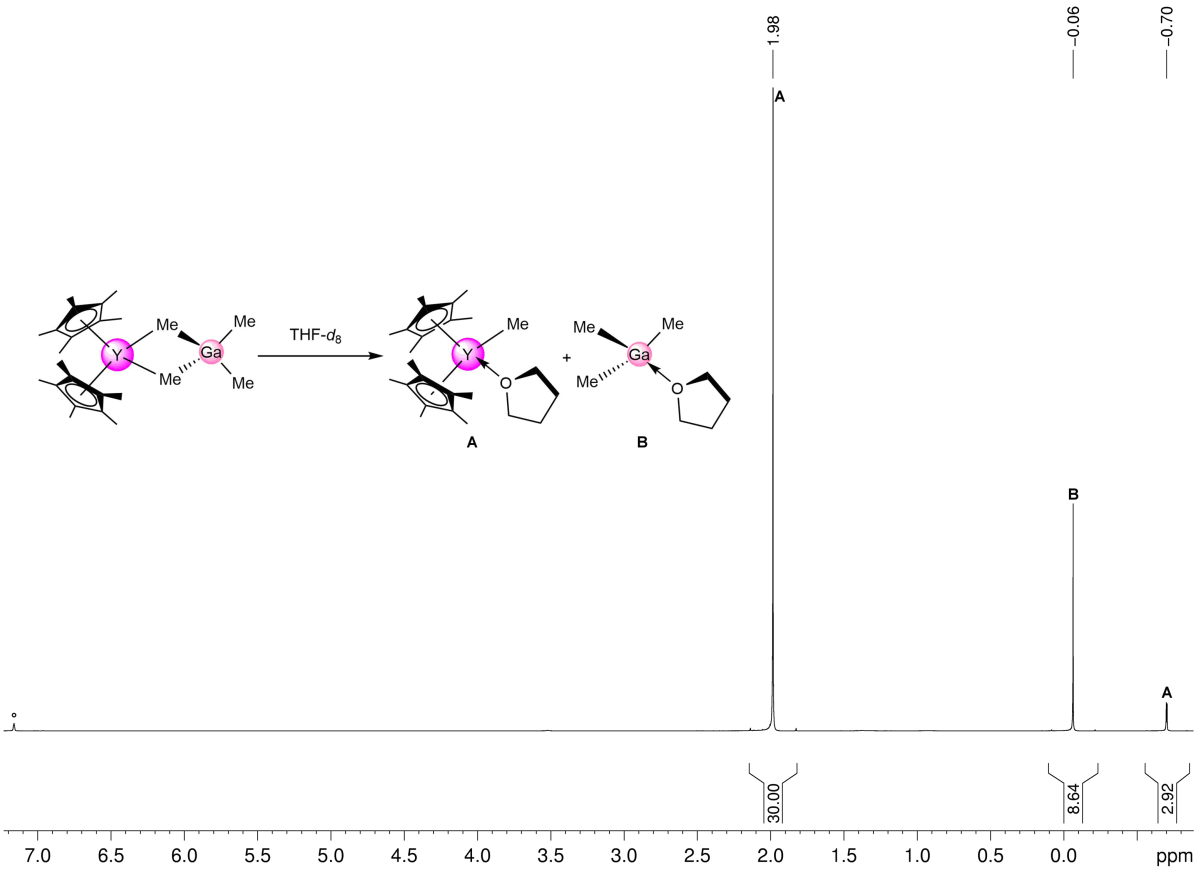

Figure S75. ^{1}H NMR spectrum (400 MHz) of [Cp*$_2$Y(GaMe$_4$)] (**1^{Ga}**) and one equiv. THF-d_8 in C_6D_6 (°) to form Cp*$_2$YMe(THF) and GaMe$_3$(THF) via [GaMe$_4$] cleavage.

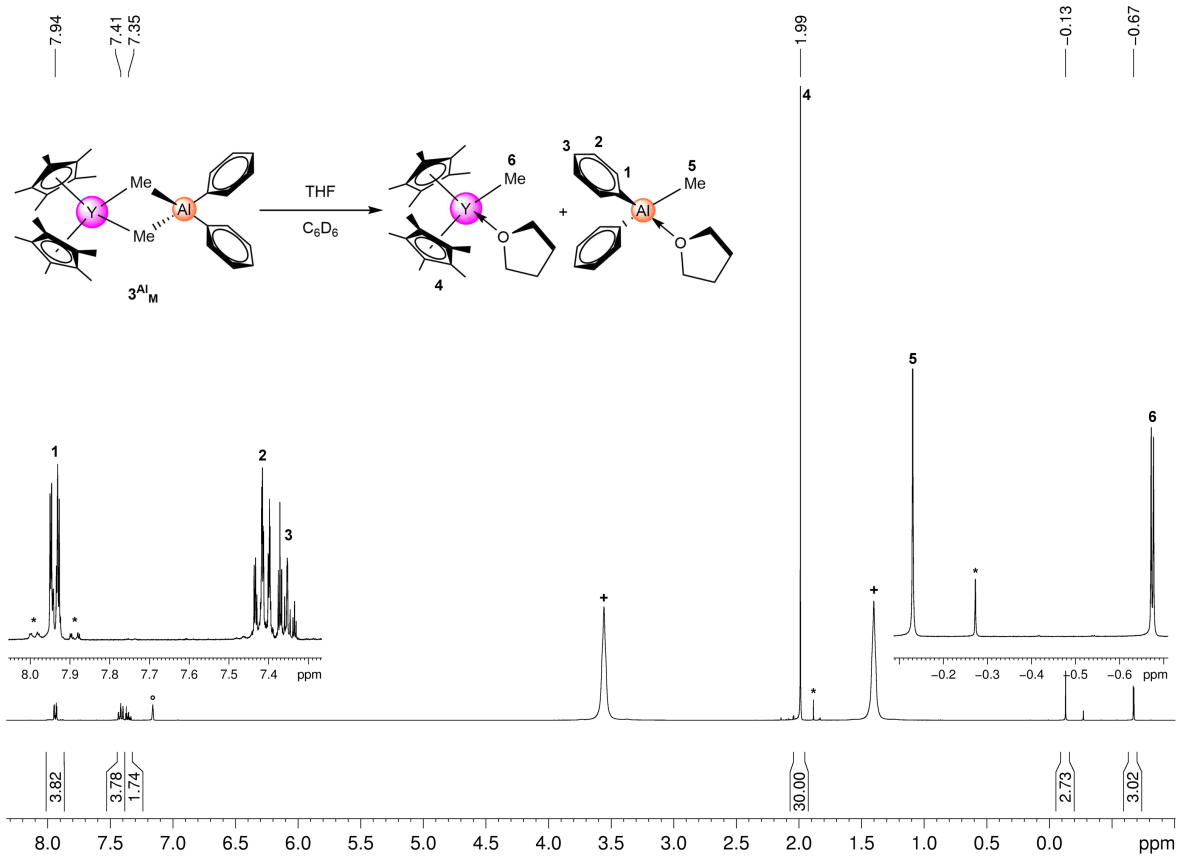

Figure S76. ^{1}H NMR spectrum (400 MHz) of $\mathbf{3^{Al}_{M}}$ and THF (+) in C_6D_6 (°) to form Cp*$_2$YMe(THF) and $Me_2AlPh(THF)$ via [Me_2AlPh_2] cleavage (* minor side products).

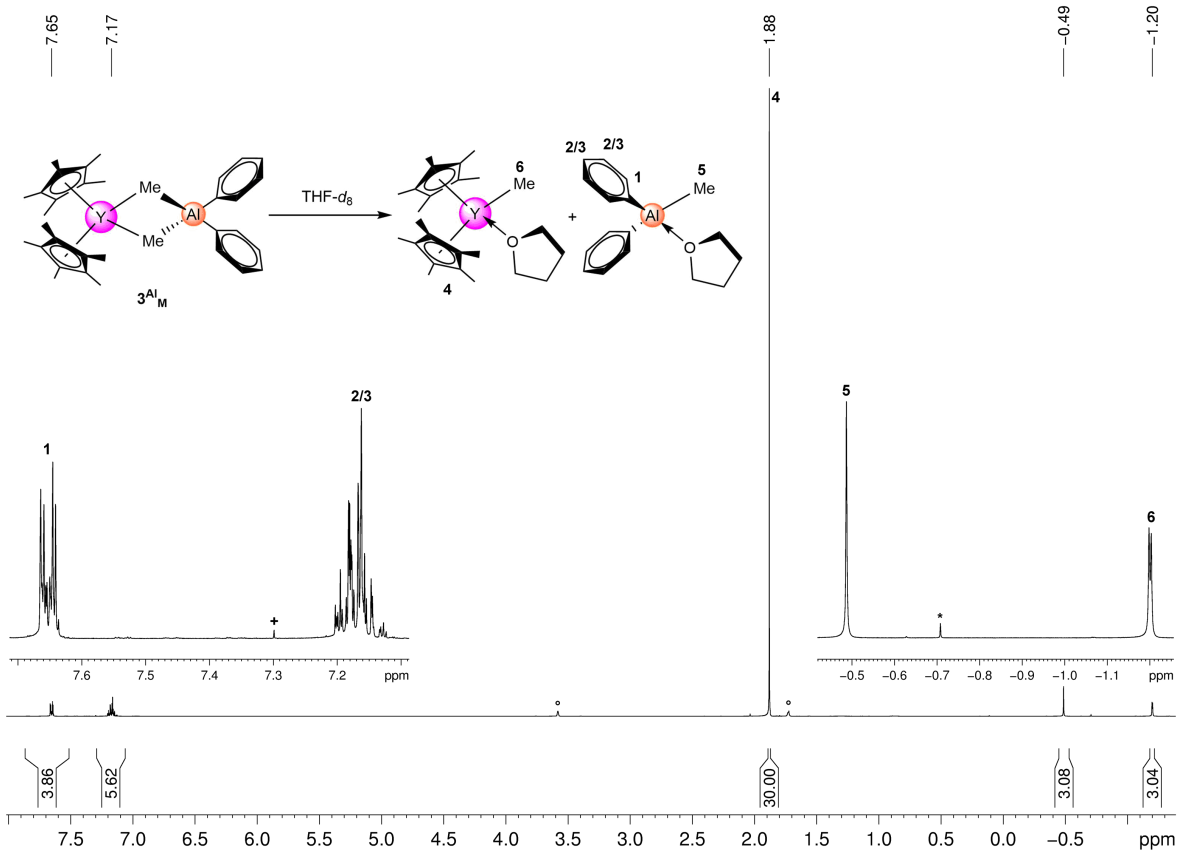

Figure S77. ^{1}H NMR spectrum (400 MHz) of $\mathbf{3^{Al}_{M}}$ in THF-d_8 (°) to form [Cp*$_2$YMe(THF) and $Me_2AlPh(THF)$ via [Me_2AlPh_2] cleavage (+ benzene; * minor side products).

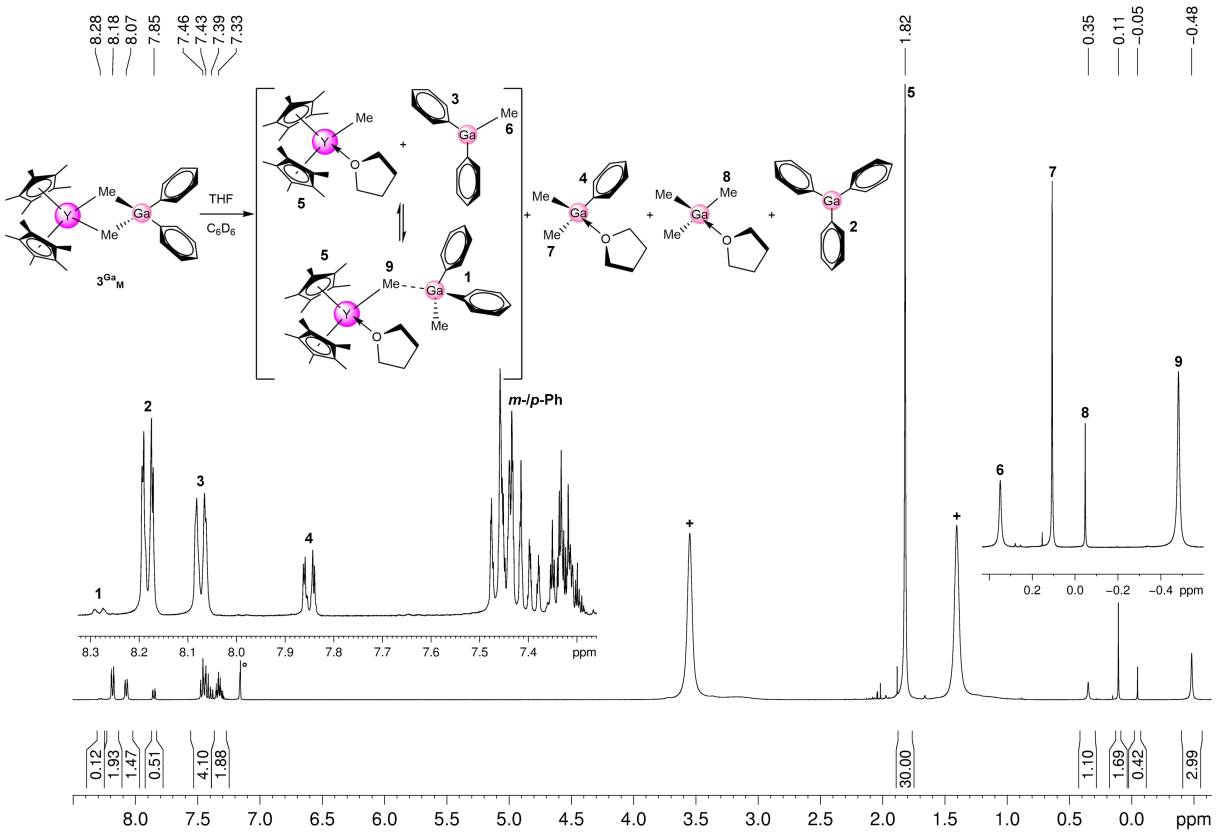

Figure S78. ^{1}H NMR spectrum (400 MHz) of $\mathbf{3^{Ga}_{M}}$ and THF (+) in C_6D_6 (°) to form $Cp^*_2YMe(THF)$ and organogallium compounds via $[Me_2GaPh_2]$ cleavage.

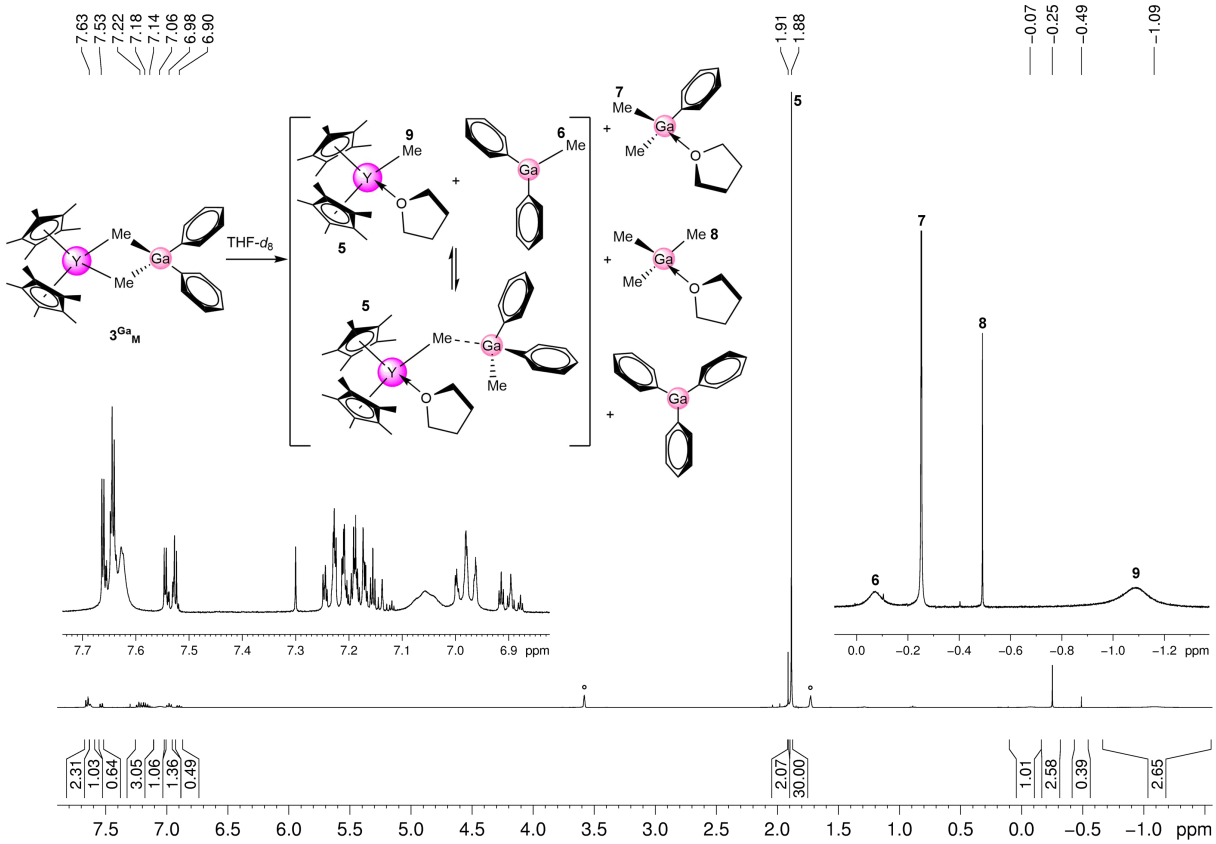

Figure S79. ^{1}H NMR spectrum (400 MHz) of $\mathbf{3^{Ga}_{M}}$ in THF-d_8 (°) to form $Cp^*_2YMe(THF)$ and organogallium compounds via $[Me_2GaPh_2]$ cleavage.

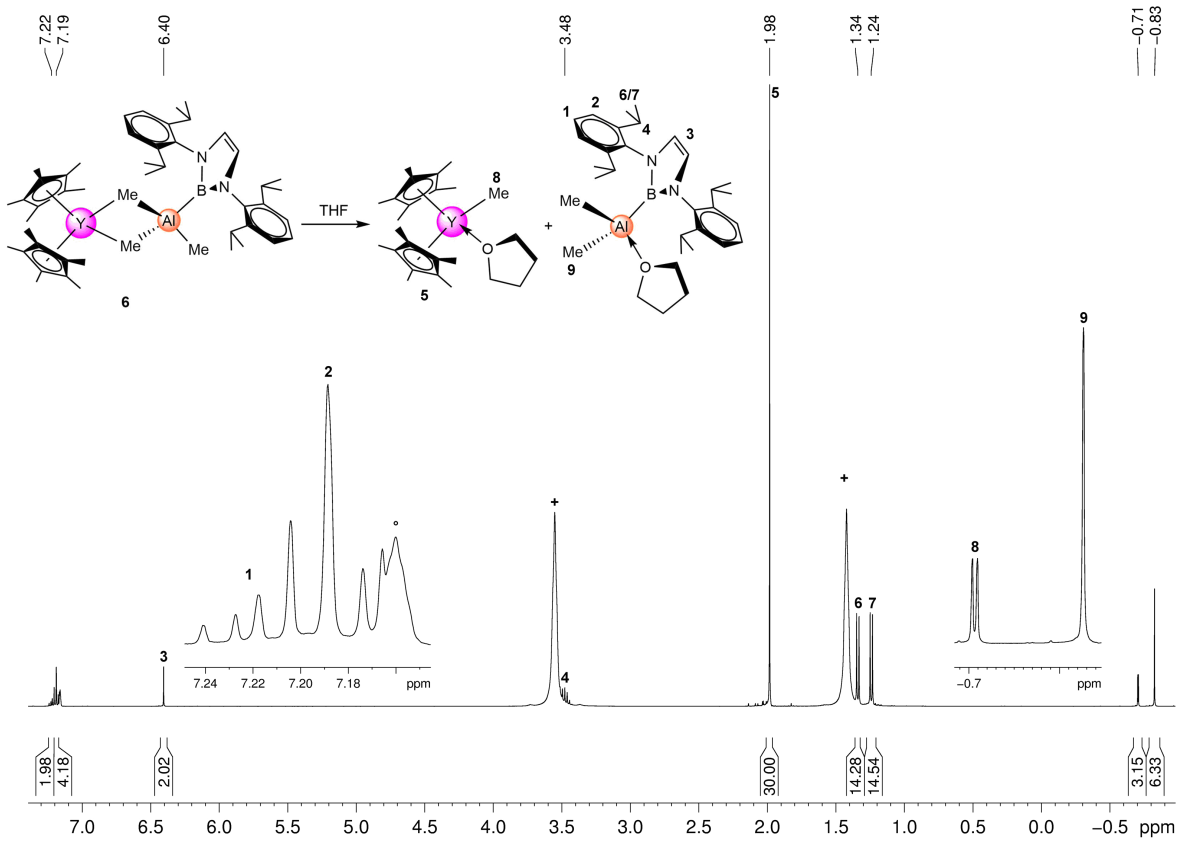

Figure S80. ^{1}H NMR spectrum (400 MHz) of **6** and THF (+) in C_6D_6 (°) to afford Cp*$_2$YMe(THF) and [Me$_2$Al{B(NDippCH)$_2$}(THF)] via [Me$_3$Al{B(NDippCH)$_2$}] cleavage.

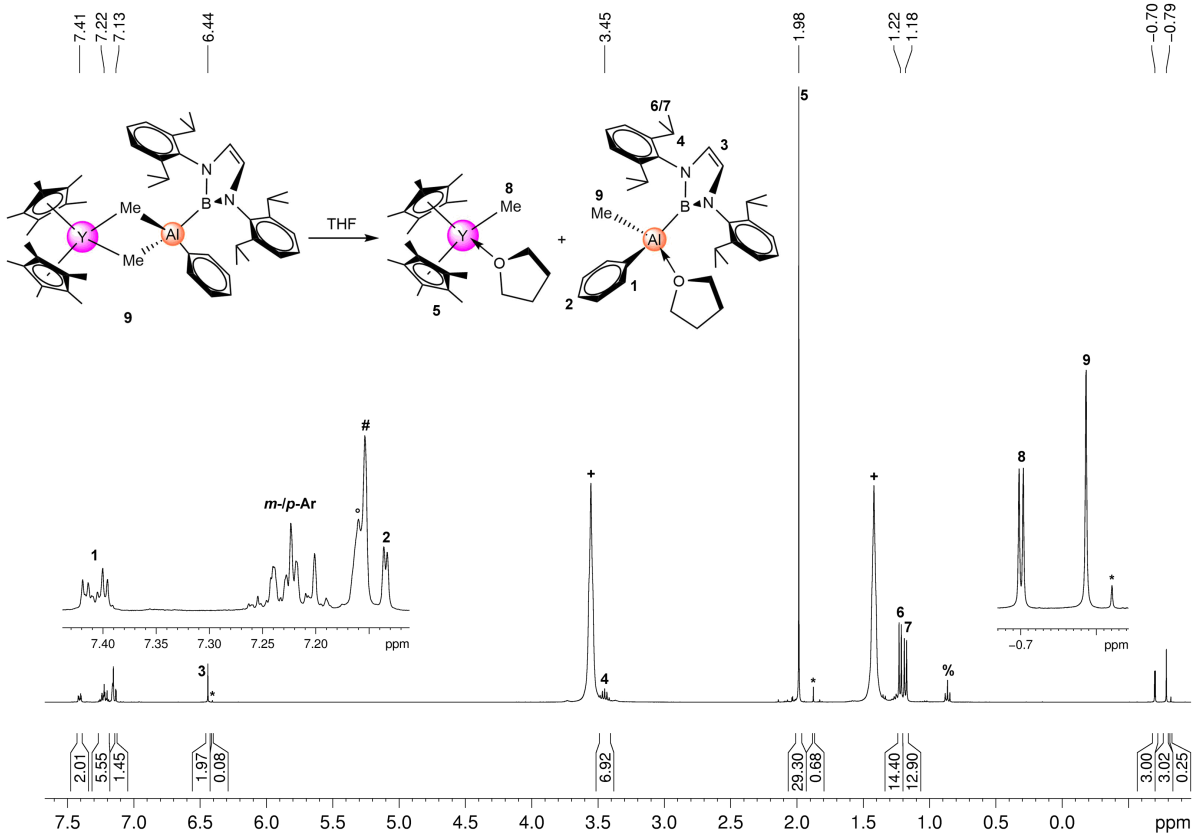

Figure S81. ^{1}H NMR spectrum (400 MHz) of **9** and THF (+) in C_6D_6 (°) to afford Cp*$_2$YMe(THF) and [MeAlPh{B(NDippCH)$_2$}(THF)] via [Me$_2$AlPh{B(NDippCH)$_2$}] cleavage (* minor side products; # benzene; % *n*-pentane).

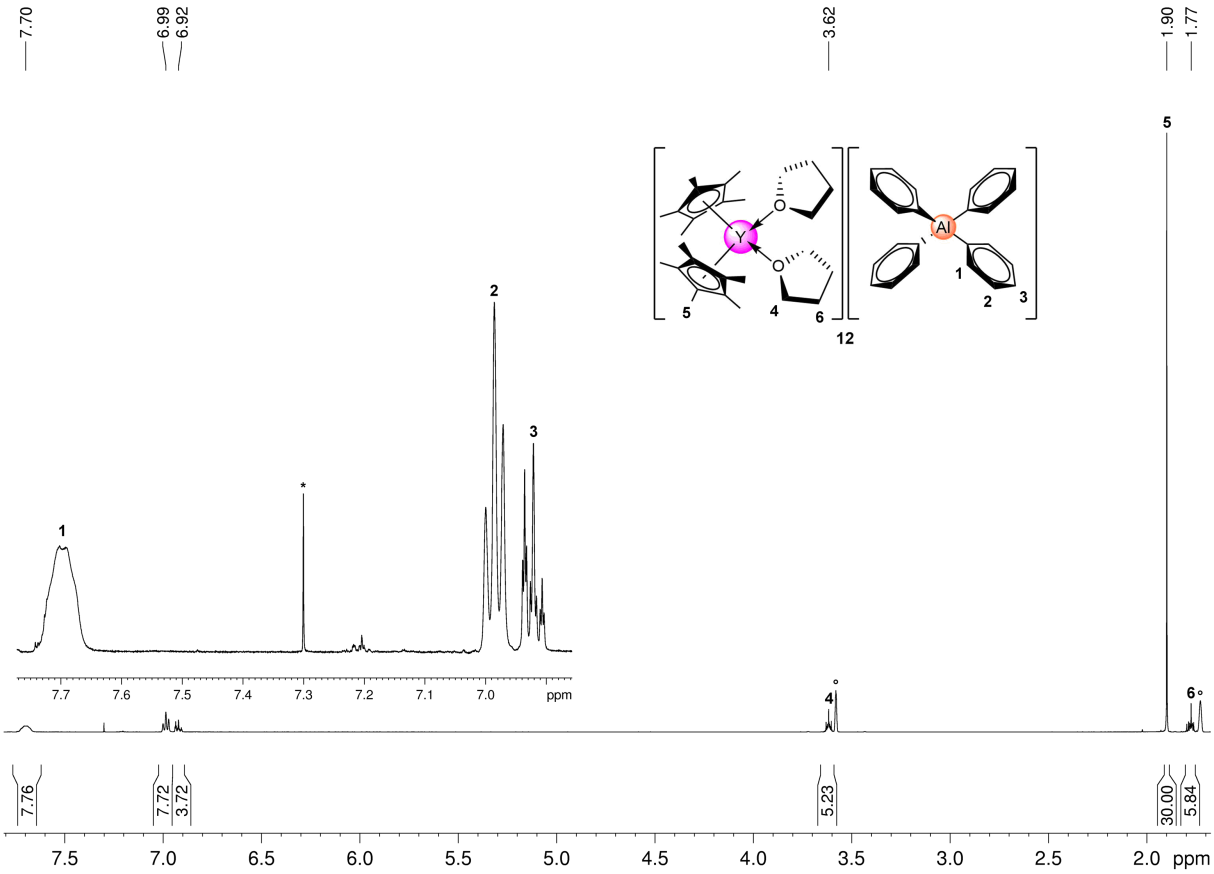

Figure S82. ^{1}H NMR spectrum (500 MHz) of **12** in THF-d_8 (°) at 26 °C (* benzene).

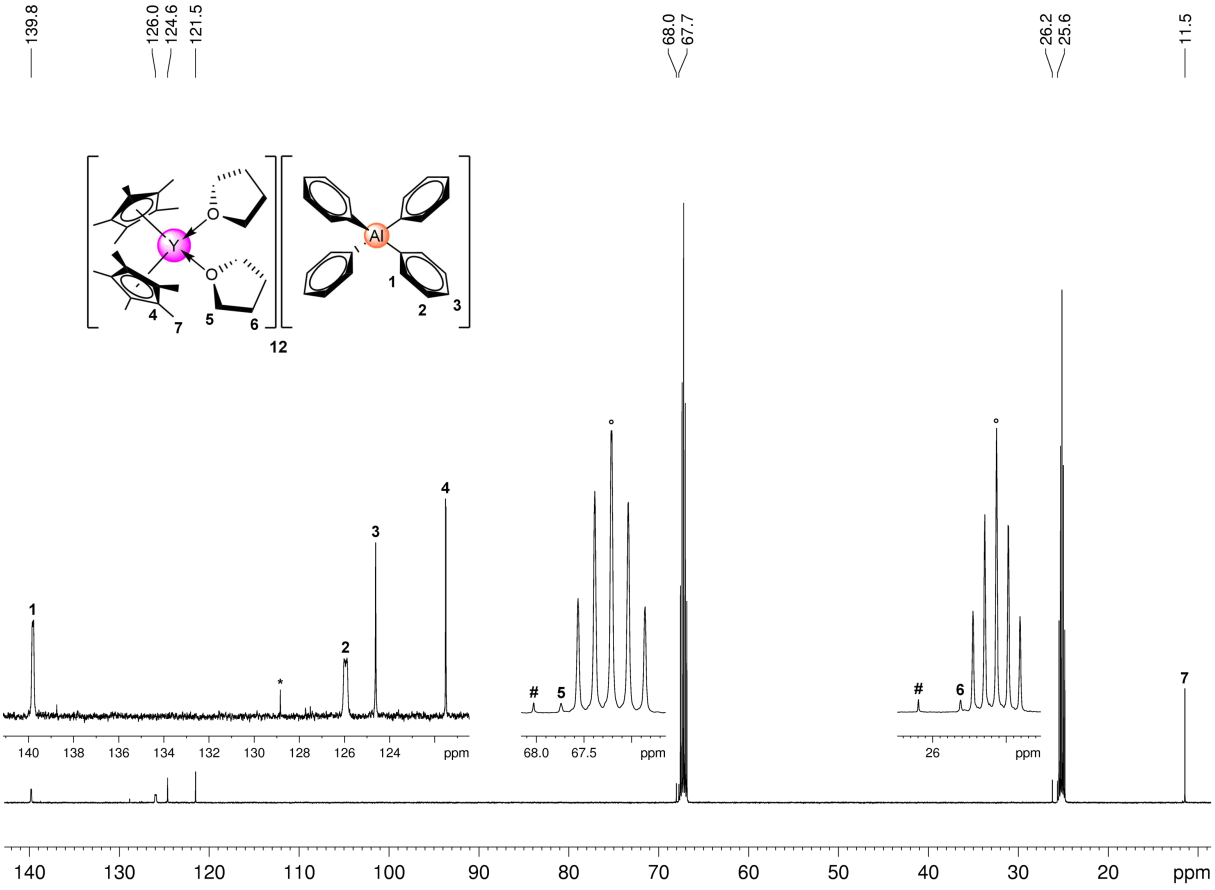

Figure S83. ^{13}C{^{1}H} NMR spectrum (126 MHz) of **12** in THF-d_8 (°) at 26 °C (* benzene; # THF).

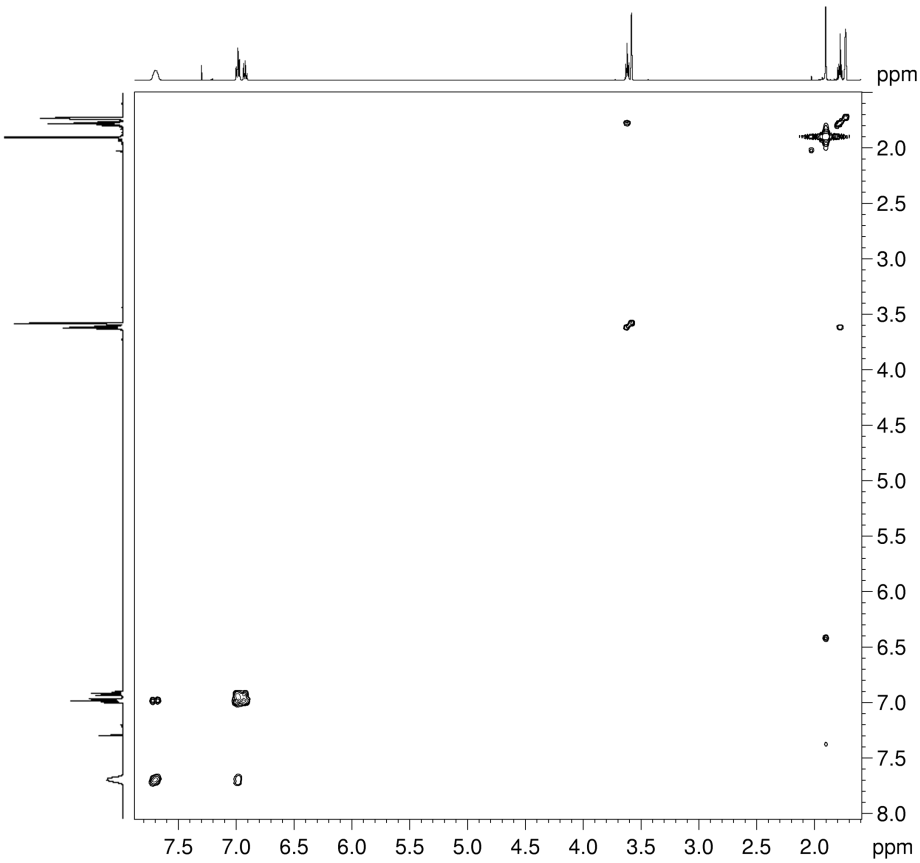

Figure S84. ^{1}H-^{1}H COSY NMR spectrum (500 MHz) of **12** in THF-d_8 at 26 °C.

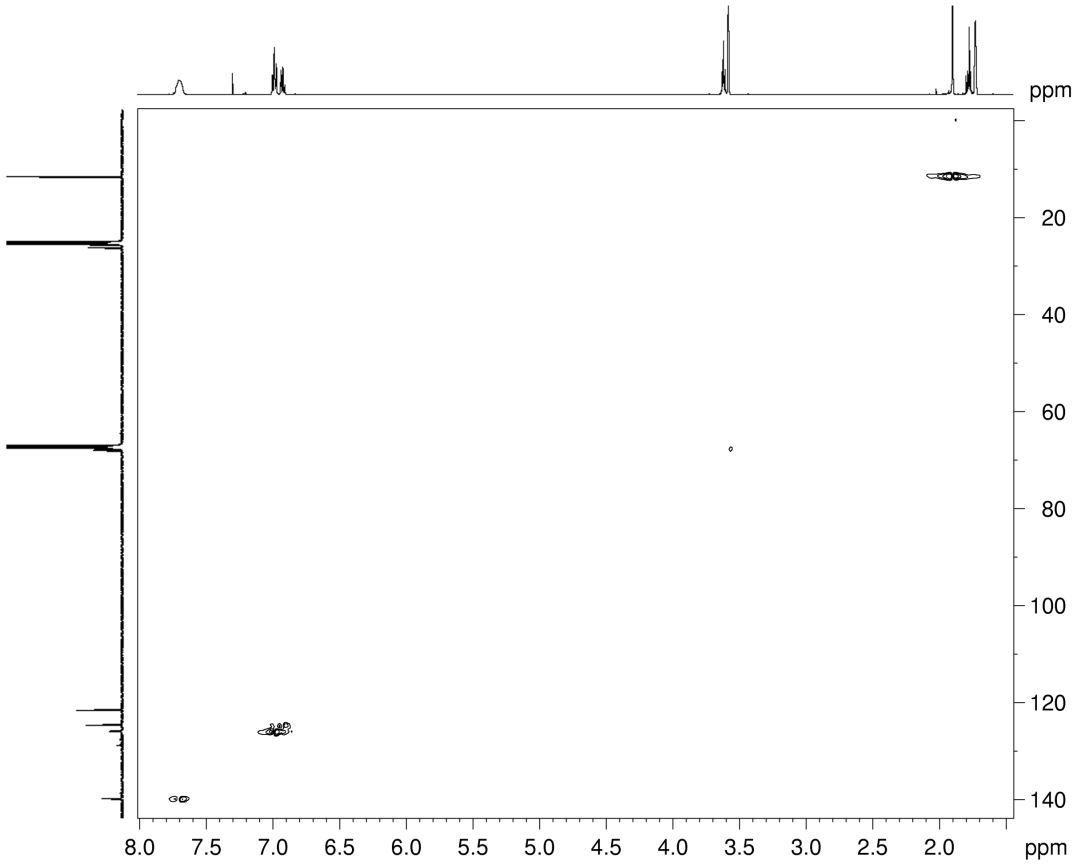

Figure S85. ^{1}H-^{13}C HSQC NMR spectrum (500 MHz, 126 MHz) of **12** in THF-d_8 at 26 °C.

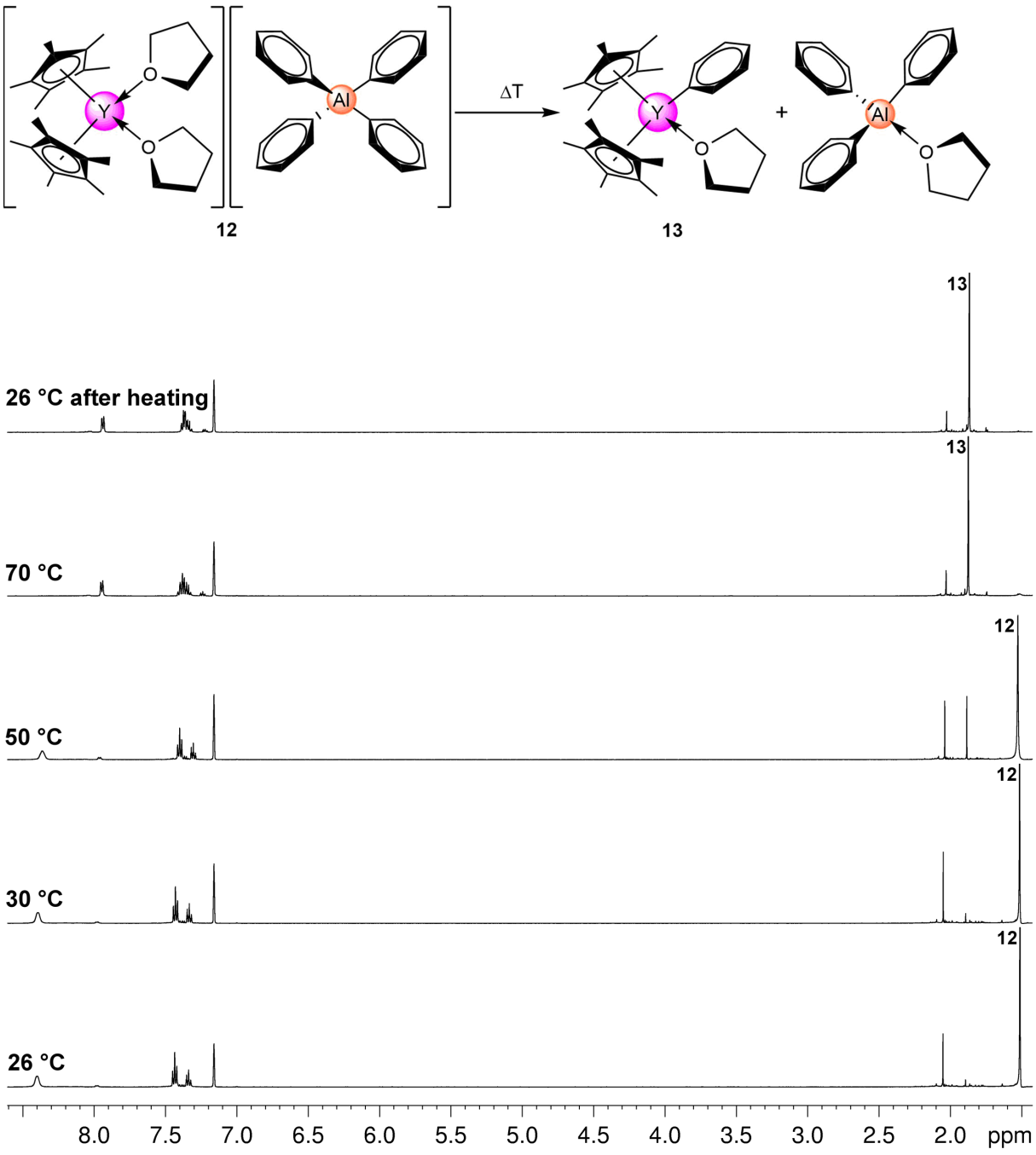

Figure S86. Variable-temperature ^{1}H NMR spectra (500 MHz) monitoring the transformation of **12** to **13** in C_6D_6.

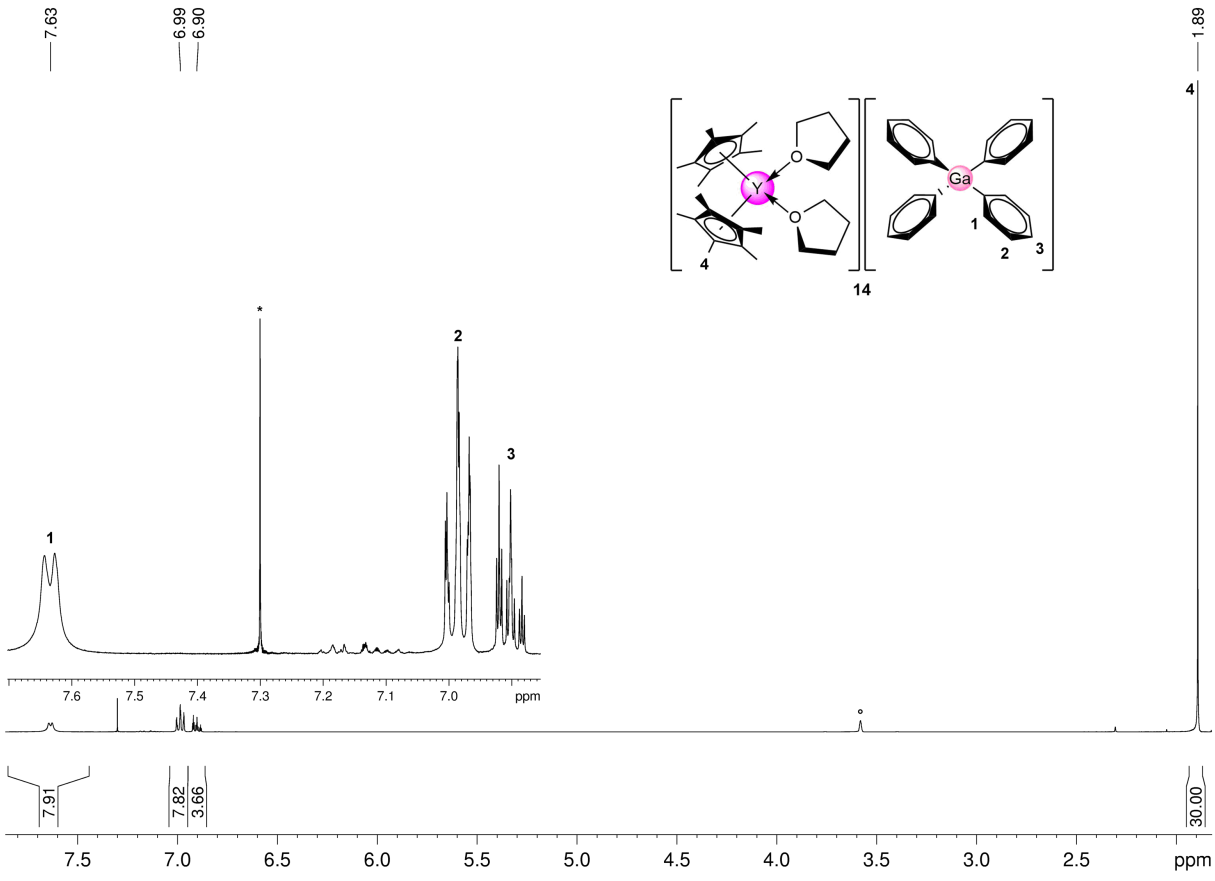

Figure S87. ^{1}H NMR spectrum (400 MHz) of **14** in THF-d_8 (°) at 26 °C (* benzene).

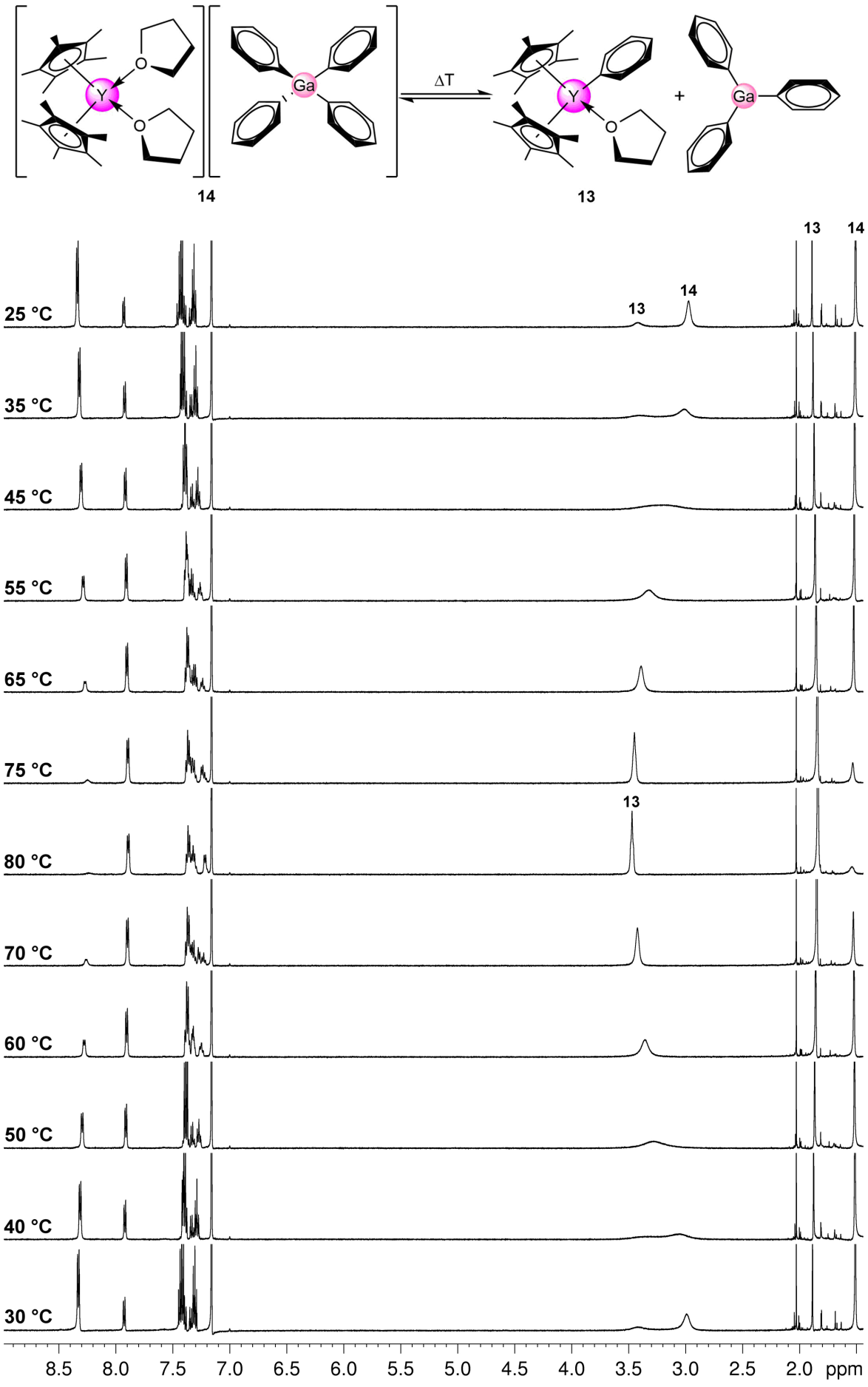

Figure S88. Variable-temperature ^{1}H NMR spectra (500 MHz) of temperature dependent equilibrium between **14** and **13** in C_6D_6.

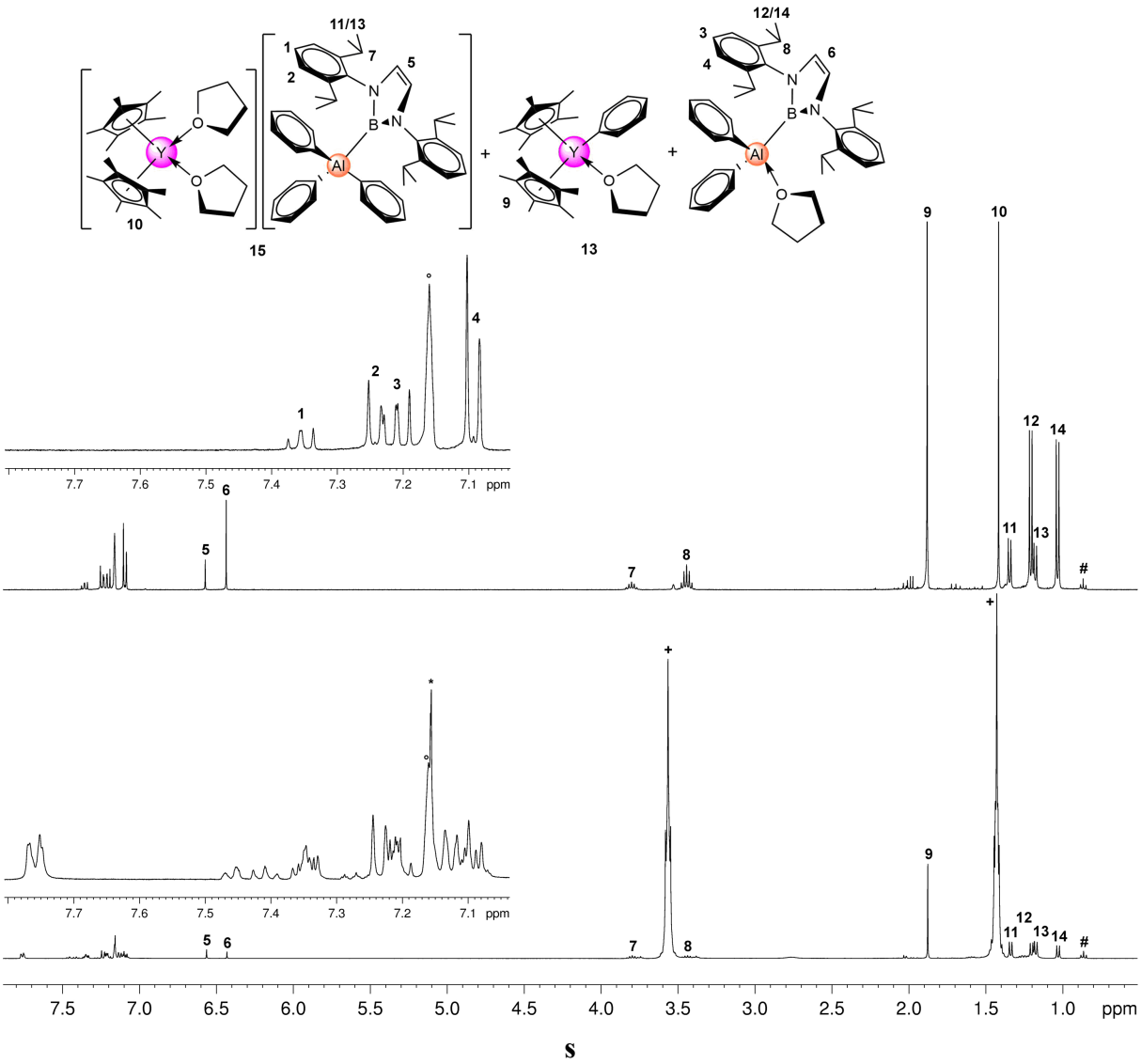

S

Figure S89. ^{1}H NMR spectra (400 MHz) of **15** + **13** + [(THF)AlPh$_2${B(NDippCH)$_2$}] (bottom) and **15-*d*$_{15}$** + **13-*d*$_5$** + [(THF)Al{Ph-*d*$_5$}$_2${B(NDippCH)$_2$}] (top) in C_6D_6 (°) at 26 °C (* benzene; + THF; # *n*-pentane).

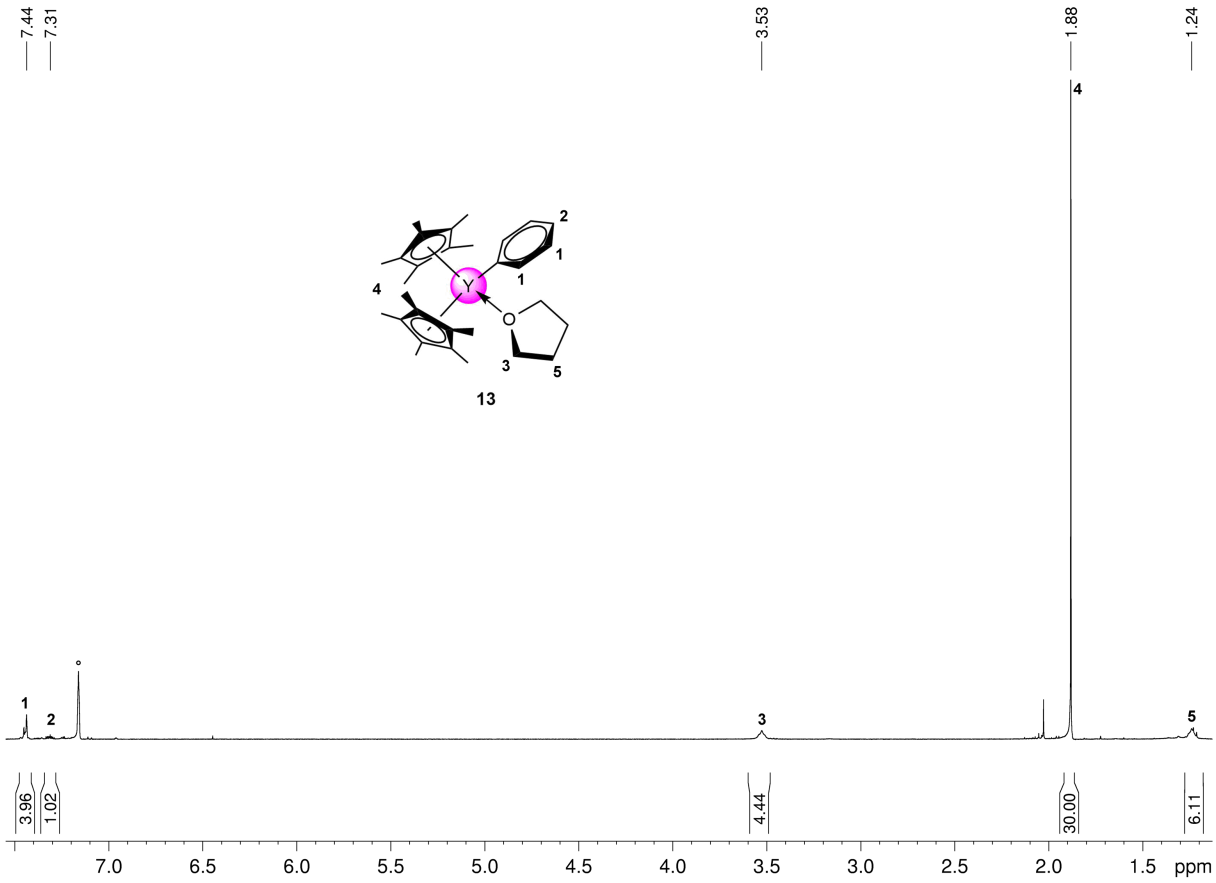

Figure S90. ^{1}H NMR spectrum (400 MHz) of **13** in C_6D_6 (°) at 26 °C.

Determination of the Kinetic Isotope Effect

The kinetic isotope effect for the benzene/benzene-d_6 C–H/C–D activation by [Cp*$_2$Y(GaMe$_4$)] (**1^{Ga}**) to form [Cp*$_2$Y(Me$_2$GaPh$_2$)] (**3^{Ga}**) was determined by monitoring NMR-scale experiments of 14 mg samples in 0.4 mL C_6H_6 or C_6D_6, respectively, at 80 °C. To allow *in situ* ^{1}H NMR measurements of the C_6H_6 activation the J-Young-valved NMR tube was equipped with a sealed C_6D_6 glass capillary. Activation of benzene was monitored every 20 minutes, while activation of C_6D_6 was evaluated every 60 minutes by ^{1}H NMR spectroscopy at ambient temperature. Since the reaction stops immediately at temperatures below 70 °C no significant error is expected by that routine. The conversion rates were determined by the relative ratio of the overall Cp* resonance signals (≙ [Cp*]) versus the overall Me resonance signals (≙ [Me]). Thus, the relative concentration [A] can be estimated from the [Me]/[Cp*] ratio. Accordingly, the reaction coefficients (k_H and k_D) can be calculated from the gradient (m_H and m_D) of the linear fit of the ln([A]/[A]$_0$) vs. time plot.

$k_H = -m_H = 0.002215$ $\quad$ $k_D = -m_D = 0.000584$ $\quad$ $k_H/k_D = 3.8$

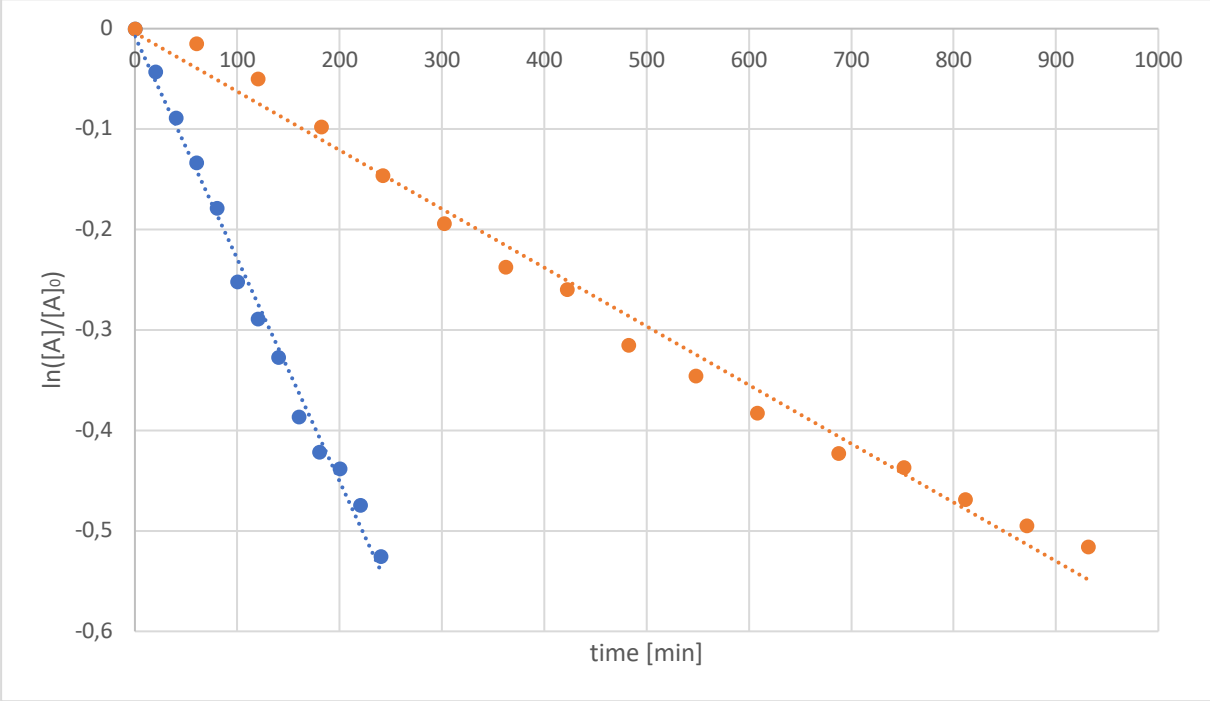

Figure S91. Plot of ln([A]/[A]$_0$) vs. time (min) for the reactions of **1^{Ga}** in C_6H_6 (blue) and C_6D_6 (orange) at 80 °C to form **3^{Ga}** and **3^{Ga}-*d*$_{10}$**, respectively, up to approximately 80% conversion.

The formation of Cp*$_2$Y[Me$_2$AlPh{B(NDippCH)$_2$}] (**9**) from Cp*$_2$Y[Me$_3$Al{B(NDippCH)$_2$}] (**6**) was monitored following the aforementioned procedure to determine the kinetic isotope effect of this reaction.

$k_H = -m_H = 0.001332$ $k_D = -m_D = 0.000445$ $k_H/k_D = 3.0$

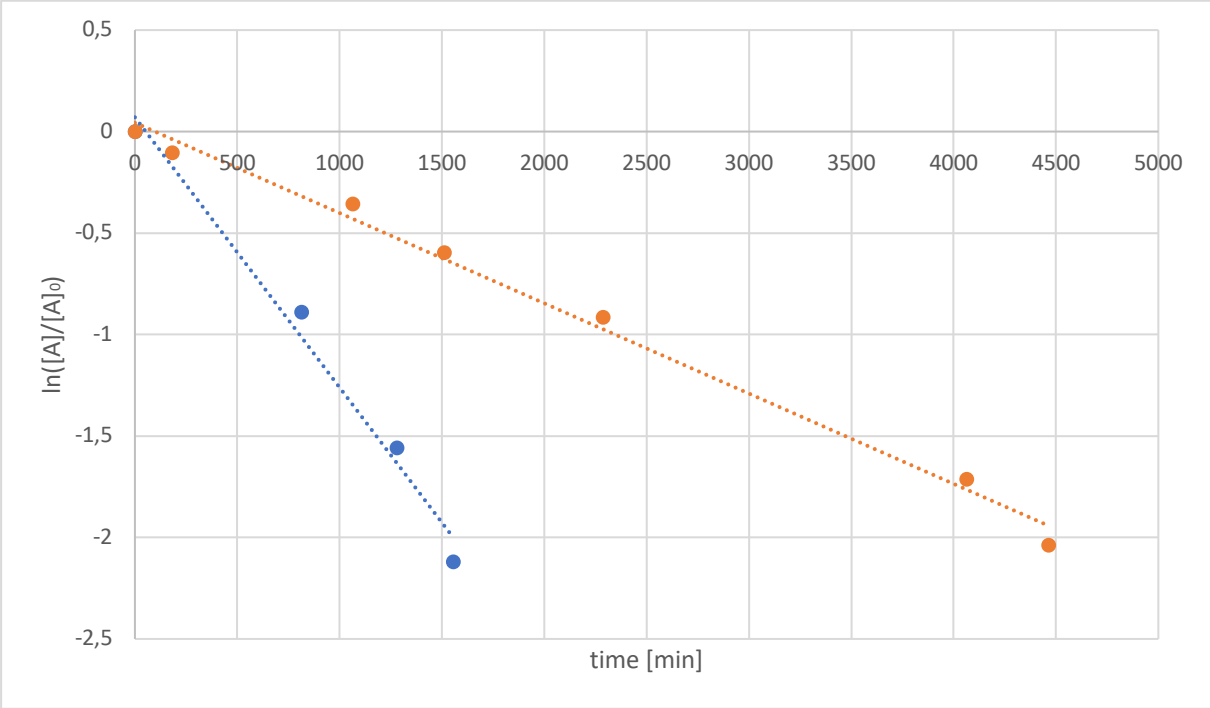

Figure S92. Plot of ln([A]/[A]$_0$) vs. time (min) for the reactions of **6** in C_6H_6 (blue) and C_6D_6 (orange) at 60 °C to form **9** and **9-*d*$_5$**, respectively, up to approximately 90% conversion.

Paper V

[Cp*Y{C_5Me_4(μ-CH_2)MPh_3}] (M = Al, Ga): Group 13-Assisted Metalation of Permethylyttrocene

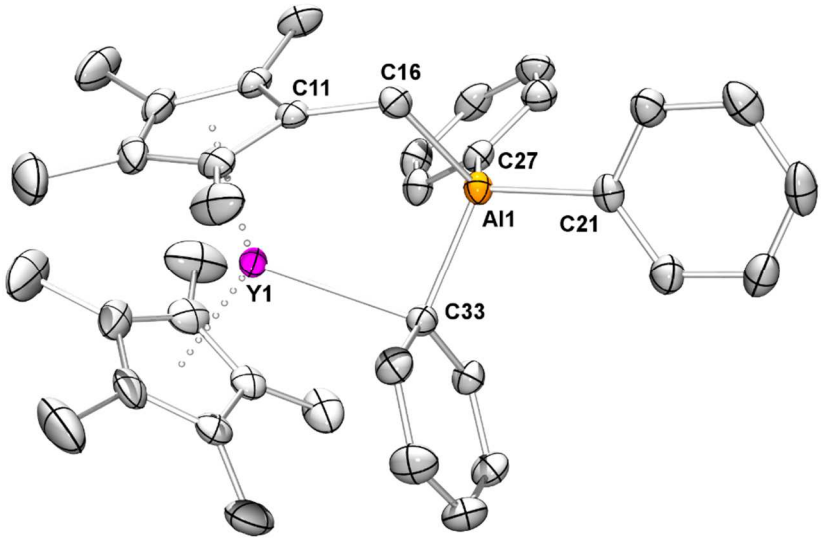

Cp*Y[C_5Me_4(μ-CH_2)MPh_3] (M = Al, Ga): Group 13-Assisted Metalation of Permethylyttrocene

Martin Bonath, Cäcilia Maichle-Mössmer, and Reiner Anwander*

Institut für Anorganische Chemie, Eberhard Karls Universität Tübingen, Auf der Morgenstelle 18, 72076 Tübingen, Germany

Supporting Information Placeholder

ABSTRACT: In a recent study we demonstrated that thermal treatment of complexes [Cp*$_2$Y(MMe_4)] (M = Al, Ga; Cp* = C_5Me_5) in benzene solutions leads to partial or complete methyl/phenyl exchange via σ-bond metathesis to form [Cp*$_2$Y(Me_2MPh_2)] and Cp*$_2$Y(MPh_4), respectively. Here we report that prolonged thermal treatment of Cp*$_2$Y(MPh_4) results in metalation of the ancillary ligand and concomitant elimination of methane to obtain the zwitterionic complexes Cp*Y[C_5Me_4(μ-CH_2)MPh_3] (M = Al, Ga).

INTRODUCTION

Metalation of the pentamethylcyclopentadienyl (Cp*) ligand is a recurrent phenomenon in rare-earth-metallocene chemistry. So-called "tuck-in" species have been already established for the first isolated donor solvent free rare-earth-metallocene methyl compounds [Cp*$_2$LnMe]$_x$ (x = 1, Ln = Sc; x = 2, Ln = Y, Lu) by Watson and Bercaw in the 1980's as a competing process to methane activation.[1] However, monomeric rare-earth-metal "tuck-in" complexes [Cp*Ln{η^5,μ-η^1-$C_5Me_4(CH_2)$}] are not isolable since they readily activate saturated and aromatic hydrocarbons or form oligomeric "tuck-over" complexes in order to stabilize the coordinatively unsaturated rare-earth-metal center (Chart 1, **A**-**B**).[2] Similarly, Teuben found Cp* metalation in yttrocene hydride compound [Cp*$_2$YH]$_2$ to form mixed hydride "tuck-over" complex **C**.[3]

In contrast, "tuck-in" complexes can be isolated for group 4 metallocenes. As such, the "tuck-in" structural motif has been authenticated for group 4 metal compounds **D**-**F** (Chart 1).[4] The accessibility of Zr(IV) "tuck-in" complexes allowed for the synthesis of zwitterionic Lewis acid adducts by addition of the perfluorinated phenyl borane $HB(C_6F_5)_2$ to Cp*($C_5Me_4CH_2$)ZrR (R = Cl, Ph) (Chart 1, **G**).[5] Piers et al. isolated a series of such zwitterionic Zr(IV) complexes of relevance for olefin polymerization catalysis. The Ti(III) variant **H** was found by Rosenthal from the reaction of the Ti(III) metallocene alkyne compound Cp*$_2$Ti(η^2-PhC_2SiMe_3) with borane $B(C_6F_5)_3$ under elimination of the alkyne and H_2.[6] Only recently, Arnold and co-workers observed C–H-bond activation of the Cp* ligand in the reaction of [Cp*$_2$TiCl] with $(THF)_2LiH_3AlC(SiMe_3)_3$ at 25 °C to form the zwitterionic complex **I**.[7]

Chart 1. Structurally Authenticated "Tuck-over", "Tuck-in", and Zwitterionic Complexes Derived from Metallocene Metalation.

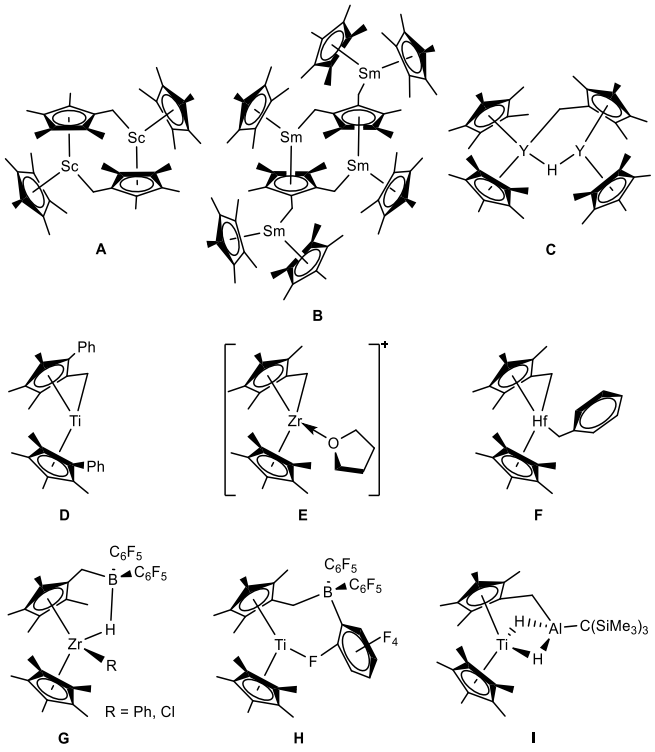

Despite the comprehensive studies on zwitterionic group 4 metallocene complexes, somewhat surprisingly, rare-earth-metal congeners have not been reported so far.

RESULTS AND DISSCUSION

In a recent study we showed that [Cp*$_2$Y(MMe_4)] is a remarkable deprotonating agent at elevated temperatures in benzene solutions. Depending on the temperature applied, partial or complete methyl/phenyl exchange was observed, affording compounds [Cp*$_2$Y(Me_2MPh_2)] and Cp*$_2$Y(MPh_4),

respectively, under methane elimination [8] Prolonged thermal treatment of $Cp^*_2Y(MPh_4)$, however, led to further C–H-bond activation involving the Cp* ligand via benzene elimination, generating the zwitterionic complexes $Cp^*Y[C_5Me_4(\mu\text{-}CH_2)MPh_3]$ (M = Al, **1**; Ga, **2**; Scheme 2).

The ^1H NMR spectroscopic data of **1** in C_6D_6 were indicative of derivatization of one Cp* ligand. Accordingly, three singlets with a relative integral ratio of 2:6:6 appeared at 2.19 (2H), 1.95 (6H) and 1.60 ppm (6H) for the cyclometalated $C_5Me_4CH_2Al$ moiety and one singlet at 1.54 ppm (15H) for the "innocent" C_5Me_5 ligand. Noteworthy, at ambient temperature the diastereotopic methylene protons of the metalated Cp* ligand appear as a single resonance. In the aromatic region three multiplets at 7.73 (*o*-Ph, 6H), 7.26 (*m*-Ph, 6H) and 7.20 ppm (*p*-Ph, 3 H) account for the presence of three equivalent phenyl groups in solution at ambient temperature, indicating a highly fluxional $AlPh_3$ moiety involving unrestricted rotations about both the Al–C_{ipso} and Al–CH_2 bonds, and consequently weak interactions between the phenylaluminate counterion and the yttrium center. While compound **1** is very stable in C_6D_6 solutions and Ph/Ph-d_5 exchange or decomposition cannot be observed after 5 weeks at ambient temperature, NMR spectroscopic experiments on the gallate compound **2** are indicative for a Ph/Ph-d_5 exchange at elevated temperatures in C_6D_6 solutions.

Scheme 2. Metalation of the Cp* Ancillary Ligand in $Cp^*_2Y(MPh_4)$ to Form the Zwitterionic Compounds $Cp^*Y[C_5Me_4(\mu\text{-}CH_2)MPh_3]$ (M = Al, Ga).

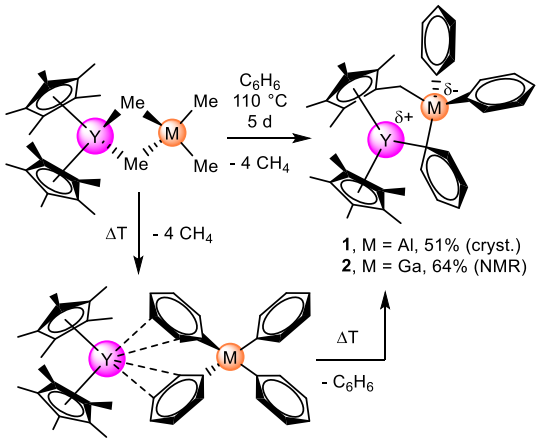

Since $[Cp^*_2Y(MPh_4)]$ (M = Al, Ga) are labile in solution,[8] a rational reaction sequence to form compounds **1** and **2**, respectively, involves dissociation of $[Cp^*_2Y(MPh_4)]$ to form $[Cp^*_2YPh]$ and MPh_3 (Scheme 3). $[Cp^*_2YPh]$ possibly engages in an intramolecular σ-bond metathesis reaction to eliminate benzene and formation of the highly reactive "tuck in" complex $[Cp^*Y\{C_5Me_4(\mu\text{-}CH_2)\}]$ followed by MPh_3-promoted CH_2 abstraction to generate **1** and **2**, respectively.

Scheme 3. Possible Scenario for the Activation of the Ancillary Ligand Cp* by $[Cp^*_2Y(MPh_4)]$ (M = Al, Ga).

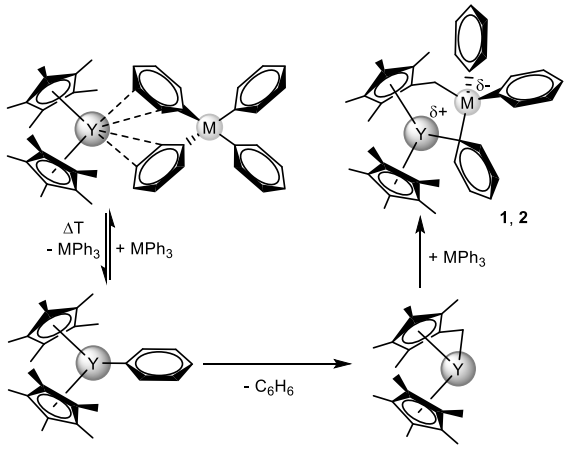

Single crystal X-ray diffraction analysiss unequivocally evidenced C-H-bond activation of one Cp* methyl by the $AlPh_4$ moiety. Metalation of the Cp* ligand, however, does not result in considerable distortion compared to the unsubstituted Cp* ligand. Hence, typical metrical values for the ytrocene scaffold of **1** are found (Y1–Ct1 = 2.333, Y1–Ct2 = 2.341 Å; Ct1–Y–Ct2 = 135.8 °), similar to $Cp^*_2Y(MPh_4)$[8] (av. Y–Ct = 2.355 Å; Ct–Y–Ct = 137.6 °). In the solid state, **1** features different binding modes of the phenyl groups (Figure 1), which is in stark contrast to the dynamic processes in solution. While one phenyl group is in the bridging position between the yttrium and aluminum center with an almost perpendicular Y1-C_{ipso}-Al1 bond angle of 94.1(6) °, the two terminal phenyl groups at the aluminum atom face the ytrocene scaffold almost orthogonally. Accordingly, any σ- or π-bonding between the terminal phenyl groups and the rare-earth metal center is not implicated. The Al–C distances are within the expected range. As such, the Al–C distance of the bridging phenyl group (2.064(2) Å) is slightly elongated compared to the terminal phenyl groups (1.991(2) / 2.000(2)Å). For comparison, similar metrical parameters were found in $[Me_2AlPh]_2$[9] (av. Al–C(μ-Ph) = 2.144 Å), $[AlPh_3]_2$[10] (Al–C(μ-Ph) = 2.184(5); Al–C(Ph) = 1.960(4) Å) and $Cp^*_2Y(AlPh_4)$ (av. Al–C(Ph) = 2.007 Å).

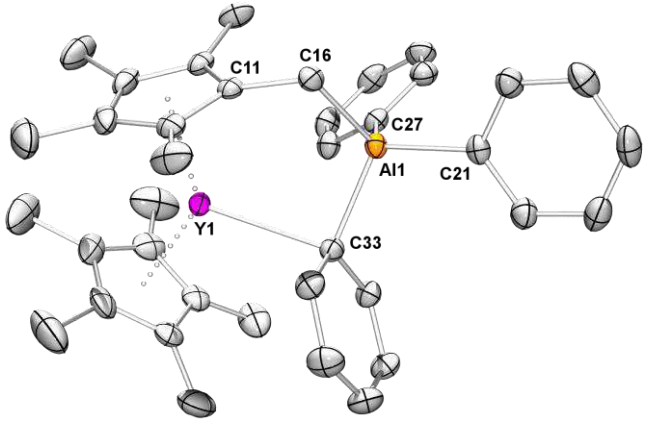

Figure 1. Crystal structure of zwitterionic compound Cp*Y[C_5Me_4(μ-CH_2)$AlPh_3$] (**1**). All atoms are represented by atomic displacement ellipsoids set at 50% probability. Hydrogen atoms are omitted for clarity. Selected interatomic distances (Å) and angles (°): Y1···Al1 3.501(1), Y1–C33 2.685(2), Al1–C16 2.003(2), Al1–C21 1.991(2), Al1–C27 2.000(2), Al1–C33 2.064(2), Y1–C33–Al1 94.1(6).

*+

In analogy to **1**, the gallate variant Cp*Y[C_5Me_4(μ-CH_2)$GaPh_3$] (**2**) shows singlet resonances in the ^{1}H NMR spectrum at 2.42 (2H), 1.96 (6H), 1.71 (6H) and 1.52 (15H), characteristic for the metalated and unsubstituted Cp* ligands, respectively. Unsurprisingly, **2** features almost identical metrical parameters in the solid state as found for **1** (Figure 2). Consequently, one phenyl group is in the bridging position (Y–C_{ipso}–Ga = 94.2(1)°) with the phenyl plane orthogonal to the Y···Ga axis and two phenyl groups of the heterogallate moiety bind terminally to the gallium center.

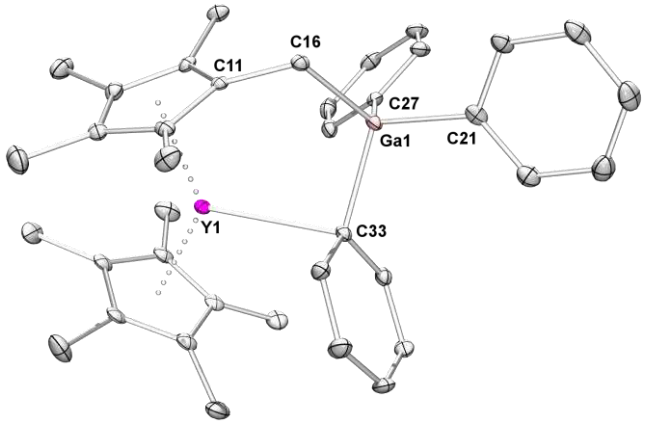

Figure 2. Crystal structure of zwitterionic compound Cp*Y[C_5Me_4(μ-CH_2)$GaPh_3$] (**2**). All atoms are represented by atomic displacement ellipsoids set at 50% probability. Hydrogen atoms and disorder of the Cp* ligands are omitted for clarity. Selected interatomic distances (Å) and angles (°): Y1···Ga1 3.513, Y1–C33 2.686(4), Ga1–C16 2.020(5), Ga1–C21 1.986(4), Ga1–C27 1.996(4), Ga1–C33 2.075(3), Y1–C33–Ga1 94.2(1).

CONCLUSION

Zwitterionic rare-earth metallocene complexes Cp*Y[C_5Me_4(μ-CH_2)MPh_3] (M = Al, Ga) are accessible by prolonged thermal treatment of [Cp*$_2$Y(MMe_4)] or Cp*$_2$Y(MPh_4), respectively. The structural motif is reminiscent of "tuck-in" complexes that have not yet been isolated for rare-earth metallocenes, though, have been authenticated for group 4 metallocene compounds. Accordingly, Cp*Y[C_5Me_4(μ-CH_2)MPh_3] can be considered as Lewis acid stabilized "tuck-in" compounds of [Cp*Y{C_5Me_4(μ-CH_2)}]. In solution the phenyl groups undergo fast rotation around the (μ-CH_2)–M axis. In the solid state one phenyl group is in the bridging position between the yttrium center and the group 13 metal center while two phenyl groups are terminally arranged without additional arene interactions to the rare-earth metal center. At ambient temperature Cp*Y[C_5Me_4(μ-CH_2)$AlPh_3$] is stable in C_6D_6 solutions and activation of benzene C–D bonds is not observed.

The investigation of the corresponding lanthanum and lutetium compounds [Cp*Ln(C_5Me_4{μ-CH_2)MPh_3}] for comparative studies is in progress.

EXPERIMENTAL SECTION

General Consideration. Syntheses and manipulations of all organometallic compounds were carried out under dry argon by using standard *Schlenk*, high-vacuum, and glovebox techniques (MBraun MB 200B; <1 ppm O_2, <1 ppm H_2O). *n*-Pentane was purified by using *Grubbs* columns (MBraun SPS-800, solvent purification system) and stored in a glovebox. C_6D_6 and C_6H_6 were obtained from Aldrich, dried over Na/K alloy for 24 h and distilled prior to use. $AlMe_3$ was purchased from Aldrich, $GaMe_3$ was purchased from Dockweiler Chemicals (optoelectronic grade) and used as received. [Cp*$_2$Y($AlMe_4$)] and [Cp*$_2$Y($GaMe_4$)] were synthesized according to literature procedures.[11] NMR spectra of air and moisture sensitive compounds were recorded by using J. Young valve NMR tubes at 26 °C on a *Bruker* AVII+250 (^{1}H: 250.13 MHz; ^{13}C: 62.90 MHz) and a *Bruker* AVII+400 (^{1}H: 400.13 MHz; ^{13}C: 100.61 MHz;). ^{1}H and ^{13}C NMR shifts are referenced to internal solvent resonances and reported in parts per million (ppm) relative to TMS. IR spectra were recorded on a NICOLET 6700 FTIR spectrometer using a DRIFT chamber with dry KBr/sample mixtures and KBr windows. For the latter the collected data were converted using the Kubelka-Munk refinement. Elemental analyses were performed on an *Elementar Vario MICRO cube*. Single crystals suitable for X-ray structure analyses were selected in a glovebox, coated with Paratone-N (Hampton Research). X-ray data were collected on a Bruker APEX III DUO diffractometer by using QUAZAR optics and MoK_α radiation (λ = 0.71073 Å). The data collection strategy was determined using COSMO[12] employing ω-scans. Raw data were processed by using APEX[13] and SAINT[14] software; structure solution and final model refinement were performed by using SHELXL[15] and ShelXle.[16] Corrections for absorption effects were applied by using SADABS.[17] All plots were generated utilizing the programs ORTEP-3[18] and POV-Ray.[19]

[Cp*Y{C_5Me_4(μ-CH_2)$AlPh_3$}] (1). In a pressure tube, [Cp*$_2$Y($AlMe_4$)] (95 mg, 0.21 mmol) was stirred in benzene (4 mL) at 110 °C for five days. The colorless solutions turned into bright yellow. Then, all volatiles were removed under reduced pressure and the yellow residue washed with *n*-pentane (2 mL) to obtain a yellow powder of **1** (67 mg, 51%). Bright yellow single crystals suitable for X-ray crystallography were grown by condensing *n*-pentane onto a saturated benzene solution at ambient temperature. ^{1}H NMR (C_6D_6, 400 MHz, 26 °C): δ = 7.73 (m, 6 H, *o*-C_6H_5), 7.26 (m, 6 H, *m*-C_6H_5), 7.20 (m, 3 H, *p*-C_6H_5), 2.19 (s, 2 H, $C_5(CH_3)_4$(μ-CH_2)), 1.95 (s, 6 H, C(CH_3)C(CH_3)C(μ-CH_2)), 1.60 (s, 6 H, C(CH_3)C(CH_3)C(μ-CH_2)), 1.54 (s, 15 H, $C_5(CH_3)_5$) ppm. ^{13}C{^{1}H} NMR (C_6D_6, 101 MHz, 26 °C): δ = 153.6 (*i*-C_6H_5), 139.2 (*o*-C_6H_5), 129.9 (*p*-C_6H_5), 129.5 (*m*-C_6H_5), 121.5 (d, ^2J(Y,C) = 1.3 Hz, $C_5(CH_3)_5$), 120.8 (d, ^2J(Y,C) = 1.5 Hz,

$C(CH_3)C(CH_3)C(\mu\text{-}CH_2)$), 119.6 (d, ^2J(Y,C) = 2.1 Hz, $C(CH_3)C(CH_3)C(\mu\text{-}CH_2)$ and $C(CH_3)C(CH_3)C(\mu\text{-}CH_2)$), 12.7 ($C(CH_3)C(CH_3)C(\mu\text{-}CH_2)$), 11.8 ($C(CH_3)C(CH_3)C(\mu\text{-}CH_2)$) 10.9 ($C_5(CH_3)_5$), 10.3 ($C(CH_3)C(CH_3)C(\mu\text{-}CH_2)$) ppm. DRIFT (KBr): $\tilde{\nu}$ = 3115 (w), 3049 (m), 2989 (m), 2907 (s), 2723 (w), 1417 (m), 1379 (w), 1245 (w), 1081 (m), 1048 (m), 854 (w), 726 (m), 717 (s), 704 (vs), 675 (s), 640 (m), 533 (m), 466 (s), 452 (s) cm^{-1}. Elemental analysis (%) calcd. for $C_{38}H_{44}AlY$ (616.66 g mol^{-1}): C 74.01, H 7.19. Found: C 73.51, H 7.09.

[Cp*Y{C_5Me_4(μ-CH_2)Ga(Ph-d_5)$_3$}] (2). In a J.-Young-valved NMR tube, [Cp*$_2$Y($GaMe_4$)] (17 mg, 0.03 mmol) in C_6D_6 (0.4 mL) was treated at 110 °C for four days. The colorless solutions turned into bright orange. Condensing *n*-pentane onto the concentrated solution at ambient temperature afforded bright orange single crystals suitable for X-ray crystallography. ^{1}H NMR (C_6D_6, 400 MHz, 26 °C): δ = 2.42 (s, 2 H, $C_5(CH_3)_4(\mu\text{-}CH_2)$), 1.96 (s, 6 H, $C(CH_3)C(CH_3)C(\mu\text{-}CH_2)$), 1.71 (s, 6 H, $C(CH_3)C(CH_3)C(\mu\text{-}CH_2)$), 1.52 (s, 15 H, $C_5(CH_3)_5$) ppm.

ASSOCIATED CONTENT

Supporting Information

The Supporting Information is available free of charge on the ACS Publications website.

AUTHOR INFORMATION

Corresponding Author

*reiner.anwander@uni-tuebingen.de

Orchid

Reiner Anwander: 0000-0002-1543-3787

Notes

The authors declare no competing financial interest.

ACKNOWLEDGMENT

We thank the German Science Foundation (Grant: ???) for support.

REFERENCES

1. (a) Watson, P. L., *J. Am. Chem. Soc.* **1983,** *105*, 6491-6493; (b) Thompson, M. E.; Baxter, S. M.; Bulls, A. R.; Burger, B. J.; Nolan, M. C.; Santarsiero, B. D.; Schaefer, W. P.; Bercaw, J. E., *J. Am. Chem. Soc.* **1987,** *109*, 203-219.
2. (a) Hajela, S.; Schaefer, W. P.; Bercaw, J. E., *Acta Crystallogr.* **1992,** *C48*, 1771-1773; (b) Evans, W. J.; Perotti, J. M.; Ziller, J. W., *J. Am. Chem. Soc.* **2005,** *127*, 3894-3909.
3. Booij, M.; Deelman, B. J.; Duchateau, R.; Postma, D. S.; Meetsma, A.; Teuben, J. H., *Organometallics* **1993,** *12*, 3531-3540.
4. (a) Pinkas, J.; Císařová, I.; Conde, A.; Fandos, R.; Horáček, M.; Kubišta, J.; Mach, K., *Inorg. Chem. Commun.* **2009,** *12*, 11-14; (b) Novarino, E.; Guerrero Rios, I.; van der Veer, S.; Meetsma, A.; Hessen, B.; Bouwkamp, M. W., *Organometallics* **2011,** *30*, 92-99; (c) Bulls, A. R.; Schaefer, W. P.; Serfas, M.; Bercaw, J. E., *Organometallics* **1987,** *6*, 1219-1226.
5. Sun, Y.; Spence, R. E. v. H.; Piers, W. E.; Parvez, M.; Yap, G. P. A., *J. Am. Chem. Soc.* **1997,** *119*, 5132-5143.
6. Burlakov, V. V.; Pellny, P.-M.; Arndt, P.; Baumann, W.; Spannenberg, A.; Shur, V. B.; Rosenthal, U., *Chem. Commun.* **2000,** *3*, 241-242.
7. Brown, A. C.; Altman, A. B.; Lohrey, T. D.; Hohloch, S.; Arnold, J., *Chem. Sci.* **2017,** *8*, 5153-5160.
8. Bonath, M.; Schädle, C.; Maichle-Mössmer, C.; Anwander, R., *Inorg. Chem.* **2021**, *XX*, XXX.
9. Malone, J. F.; McDonald, W. S., *J. Chem. Soc., Dalton Trans.* **1972,** *23*, 2649-2652.
10. Malone, J. F.; McDonald, W. S., *J. Chem. Soc., Dalton Trans.* **1972,** *23*, 2646-2648.
11. Dietrich, H. M.; Törnroos, K. W.; Herdtweck, E.; Anwander, R., *Organometallics* **2009,** *28*, 6739-6749.
12. COSMO, v. 1.61; Bruker AXS Inc.: Madison, WI, **2012**.
13. APEX 3, v. 2016.5-0; Bruker AXS Inc., Madison, WI, **2012**.
14. SAINT, v. 8.34A; Bruker AXS Inc., Madison, WI, **2010**.
15. SHELXTL: Sheldrick, G. M. *Acta Crystallogr.* **2015**, *A71*, 3–8.
16. SHELXLE: Hübschle, C. B.; Sheldrick, G. M.; Dittrich, B. *J. Appl. Crystallogr.* **2011**, *44*, 1281-1284.
17. SADABS: Krause, L.; Herbst-Irmer, R.; Sheldrick, G. M.; Stalke, D. *J. Appl. Crystallogr.* **2015**, *48*, 3.
18. Farrugia, L. J. *J. Appl. Crystallogr.* **1997**, *30*, 565-566.
19. POV-Ray v. 3.6; Persistence of Vision Pty. Ltd.: Williamstown, Victoria, Australia, **2004**. http://www.povray.org/.

Supporting Information

[Cp*Y{C_5M_4(μ-CH_2)MPh_3}] (M = Al, Ga): Group 13-Assisted Metalation of Permethylyttrocene

Martin Bonath, Cäcilia Maichle-Mössmer, and Reiner Anwander*

Institut für Anorganische Chemie, Universität Tübingen, Auf der Morgenstelle 18, D-72076 Tübingen, (Germany)

* E-mail for R. A.: reiner.anwander@uni-tuebingen.de

Table of Contents

Crystallographic Data

Table S1. Crystallographic data of complexes **1** and **2**

	1	**2**
Formula	$C_{38}H_{44}AlY$	$C_{38}H_{29}D_{15}GaY$
M_r [g mol^{-1}]	616.62	674.45
cryst syst	monoclinic	monoclinic
space group	$P2_1/n$	$P2_1/n$
a [Å]	10.3106(11)	10.3616(8)
b [Å]	27.596(3)	27.206(2)
c [Å]	11.2165(12)	11.2071(9)
α [°]	90	90
β [°]	90.686(2	91.310(2)
γ [°]	90	90
V [Å^3]	3191.3(6)	3158.4(4)
Z	4	4
T [K]	150(2)	100(2)
ρ_{calcd} [g cm^{-3}]	1.283	1.418
μ [mm^{-1}]	1.879	2.706
F (000)	1296	1368
R1/wR2 (I>2σ)[a]	0.0307/0.0708	0.0541/0.1036
R1/wR2 (all data)[a]	0.0442/0.0758	0.0725/0.1083
GOF[a]	1.031	1.172

[a] $R1 = \Sigma(||F_0|-|F_c||)/\Sigma|F_0|$, $F_0 > 4\sigma(F_0)$. $wR2 = \{\Sigma[w(F_0^2-F_c^2)^2/\Sigma[w(F_0^2)^2]\}^{1/2}$.

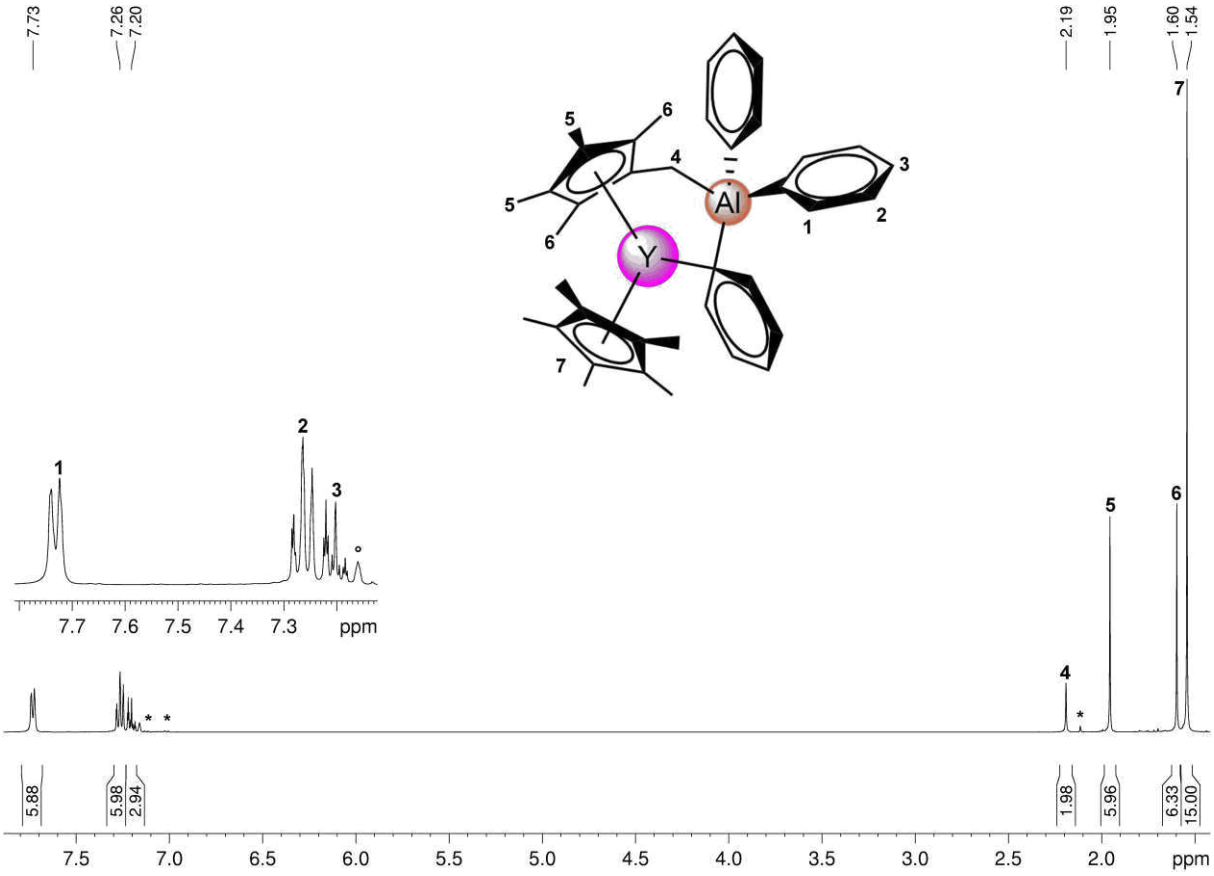

Figure S1. ^{1}H NMR spectrum (400 MHz) of **1** in C_6D_6 (°) at 26 °C (* toluene).

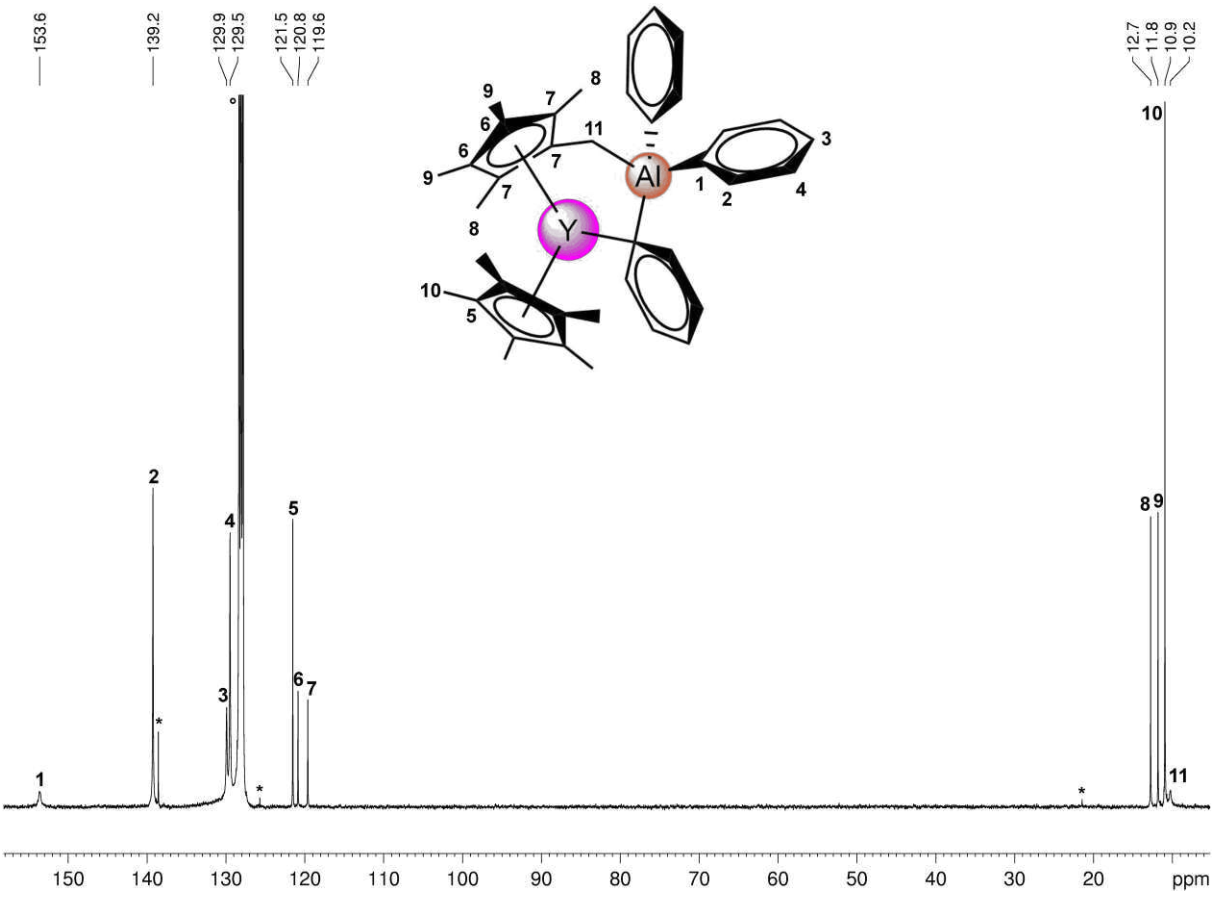

Figure S2. ^{13}C{^{1}H} NMR spectrum (101 MHz) of **1** in C_6D_6 (°) at 26 °C (* toluene).

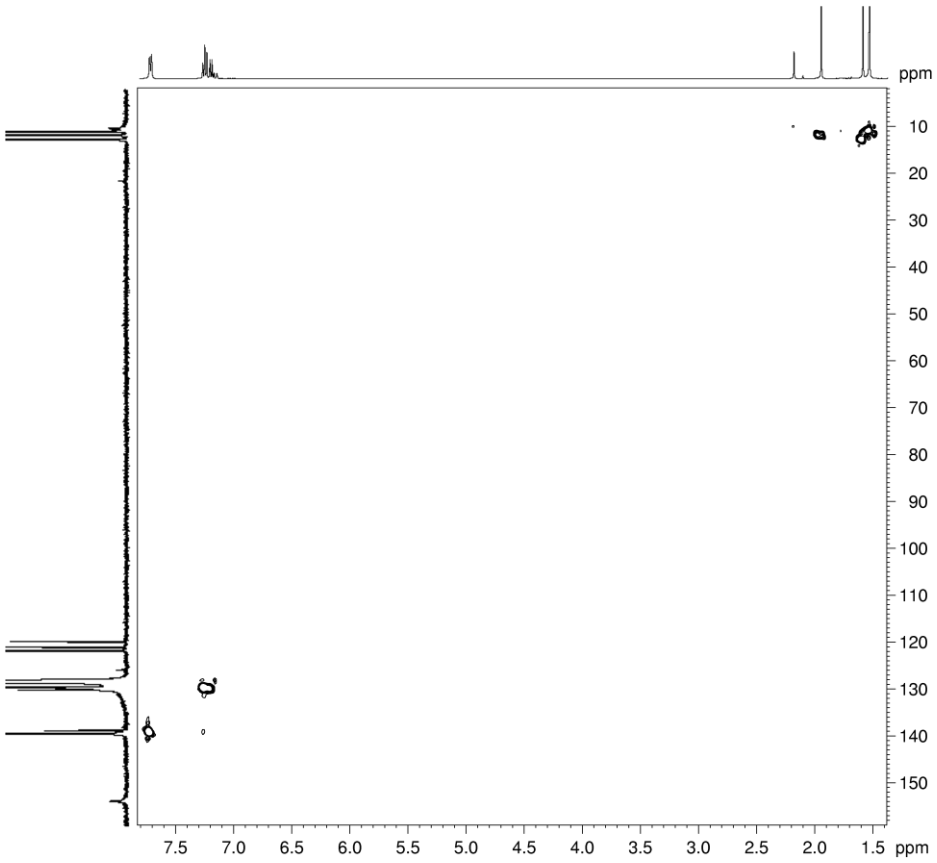

Figure S3. ^{1}H-^{13}C HSQC NMR spectrum (400 MHz, 101 MHz) of **1** in C_6D_6 at 26 °C.

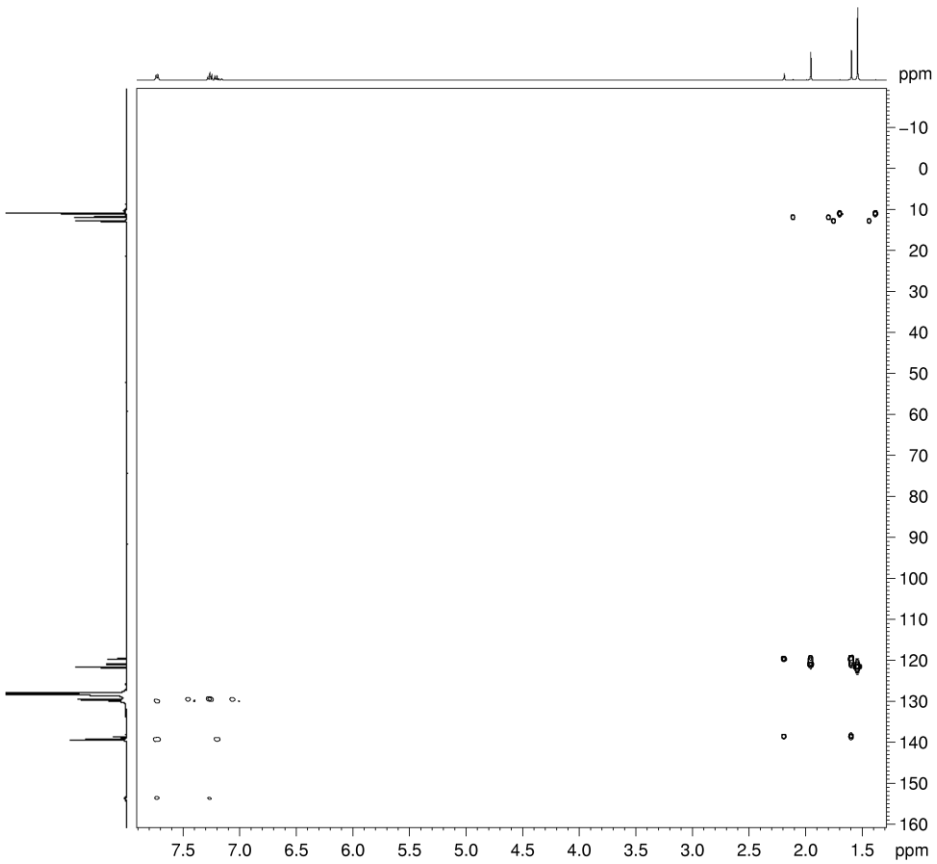

Figure S4. ^{1}H-^{13}C HMBC NMR spectrum (400 MHz, 101 MHz) of **1** in C_6D_6 at 26 °C.

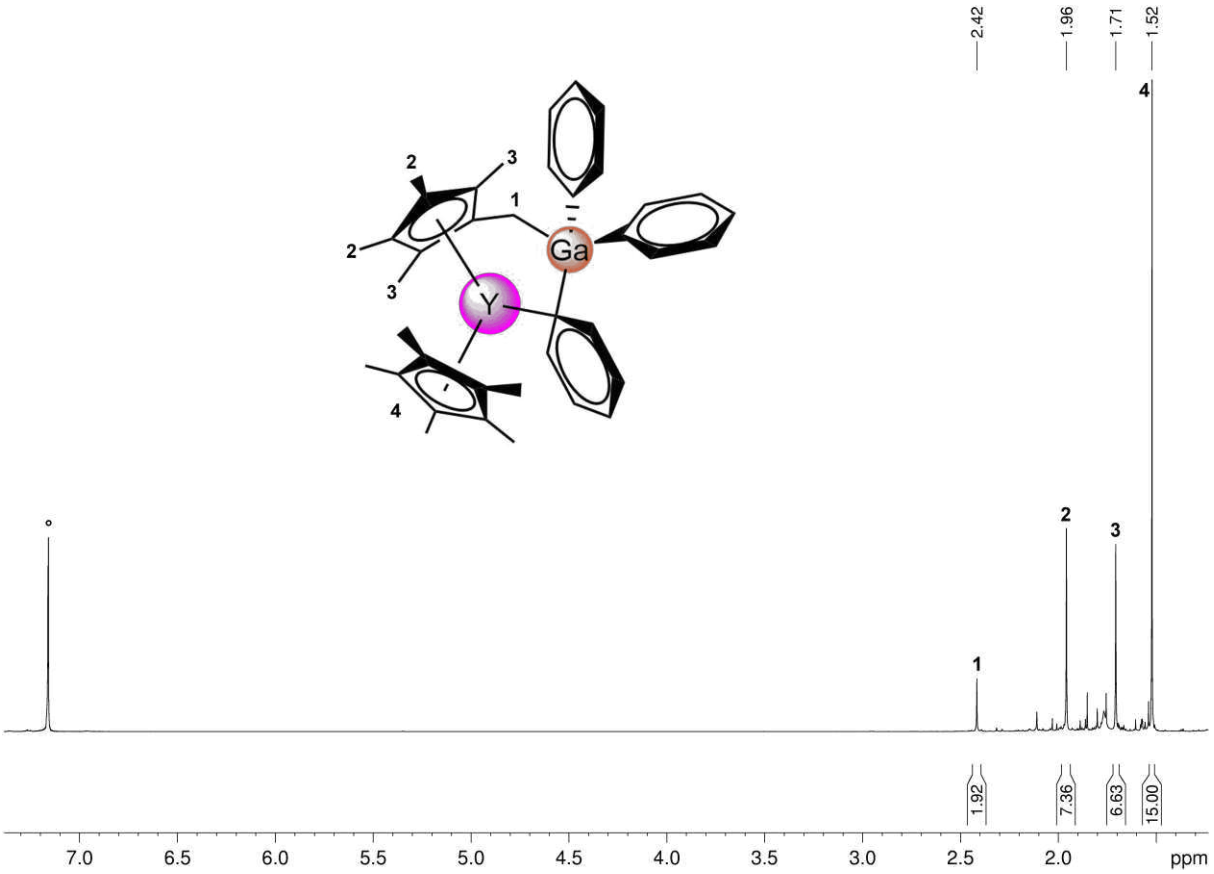

Figure S5. ^{1}H NMR spectrum (400 MHz) of crude **2-*d*$_{15}$** in C_6D_6 (°) at 26 °C.